WOODHEAD PUBLISHING SERIES IN ELECTRONIC AND OPTICAL MATERIALS

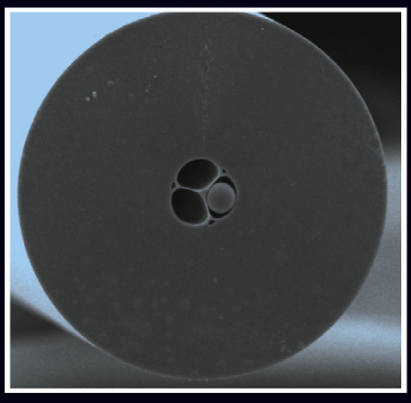

# Optofluidics, Sensors and Actuators in Microstructured Optical Fibers

Edited by Stavros Pissadakis and Stefano Selleri

WP
WOODHEAD PUBLISHING

# Optofluidics, Sensors and Actuators in Microstructured Optical Fibers

## Related titles

*Fundamentals of femtosecond optics*
(ISBN 978-1-78242-128-3)

*Modeling, characterization and production of nanomaterials: Electronics, photonics and energy applications*
(ISBN 978-1-78242-228-0)

*Optical biomimetics: Materials and applications*
(ISBN 978-1-84569-802-7)

Woodhead Publishing Series in Electronic and Optical Materials: Number 79

# Optofluidics, Sensors and Actuators in Microstructured Optical Fibers

*Edited by*

*Stavros Pissadakis and Stefano Selleri*

AMSTERDAM • BOSTON • CAMBRIDGE • HEIDELBERG
LONDON • NEW YORK • OXFORD • PARIS • SAN DIEGO
SAN FRANCISCO • SINGAPORE • SYDNEY • TOKYO
Woodhead Publishing is an imprint of Elsevier

Woodhead Publishing is an imprint of Elsevier
80 High Street, Sawston, Cambridge, CB22 3HJ, UK
225 Wyman Street, Waltham, MA 02451, USA
Langford Lane, Kidlington, OX5 1GB, UK



**Notice**
No responsibility is assumed by the publisher for any injury and/or damage to persons or property as a matter of products liability, negligence or otherwise, or from any use or operation of any methods, products, instructions or ideas contained in the material herein. Because of rapid advances in the medical sciences, in particular, independent verification of diagnoses and drug dosages should be made.

**British Library Cataloguing-in-Publication Data**
A catalogue record for this book is available from the British Library

**Library of Congress Control Number:** 2015931794

ISBN 978-1-78242-329-4 (print)
ISBN 978-1-78242-347-8 (online)

# Contents

This page intentionally left blank

# List of contributors

**A. Argyros** Institute of Photonics and Optical Science (IPOS), The University of Sydney, NSW, Australia

**F. Berghmans** Vrije Universiteit Brussel (VUB), Brussels, Belgium

**A. Candiani** University of Parma, Parma, Italy

**P. Christodoulides** Cyprus University of Technology, Limassol, Cyprus

**M. Consales** University of Sannio, Benevento, Italy

**A. Cucinotta** University of Parma, Parma, Italy

**A. Cusano** University of Sannio, Benevento, Italy

**A. Cutolo** University of Sannio, Benevento, Italy

**E. Davies** Cyprus University of Technology, Limassol, Cyprus

**F. Dias** University College Dublin, Dublin, Ireland; Centre de Mathématiques et de Leurs Applications, Ecole Normale Supérieure de Cachan, Cachan, France

**S. Ertman** Warsaw University of Technology, Warsaw, Poland

**S.C. Fleming** Institute of Photonics and Optical Science (IPOS), The University of Sydney, NSW, Australia

**G.A. Florides** Cyprus University of Technology, Limassol, Cyprus

**T. Geernaert** Vrije Universiteit Brussel (VUB), Brussels, Belgium

**K. Kalli** Cyprus University of Technology, Limassol, Cyprus

**I. Konidakis** Foundation for Research and Technology – Hellas (FORTH), Institute of Electronic Structure and Laser (IESL), Heraklion, Greece

**E.E. Kriezis** Department of Electrical and Computer Engineering, Aristotle University of Thessaloniki, Thessaloniki, Greece

**B.T. Kuhlmey** Institute of Photonics and Optical Science (IPOS), The University of Sydney, NSW, Australia

**J. Li** Genie Physique, Ecole Polytechnique de Montreal, Montreal, QC, Canada

**G.D. Peng** School of Electrical Engineering and Telecommunications, UNSW Australia, Sydney, NSW, Australia

**M. Pisco** University of Sannio, Benevento, Italy

**A. Pitilakis** Department of Electrical and Computer Engineering, Aristotle University of Thessaloniki, Thessaloniki, Greece

**H. Qu** Genie Physique, Ecole Polytechnique de Montreal, Montreal, QC, Canada

**G. Rajan** School of Electrical Engineering and Telecommunications, UNSW Australia, Sydney, NSW, Australia

**K.A. Rutkowska** Warsaw University of Technology, Warsaw, Poland

**M. Skorobogatiy** Genie Physique, Ecole Polytechnique de Montreal, Montreal, QC, Canada

**C. Sonnenfeld** Vrije Universiteit Brussel (VUB), Brussels, Belgium

**S. Sulejmani** Vrije Universiteit Brussel (VUB), Brussels, Belgium

**H. Thienpont** Vrije Universiteit Brussel (VUB), Brussels, Belgium

**A. Tuniz** Institute of Photonics and Optical Science (IPOS), The University of Sydney, NSW, Australia

**T.R. Woliński** Warsaw University of Technology, Warsaw, Poland

**D.C. Zografopoulos** Istituto per la Microelettronica e Microsistemi (IMM), Consiglio Nazionale delle Ricerche (CNR), Roma, Italy

# Woodhead Publishing Series in Electronic and Optical Materials

1 **Circuit analysis**
*J. E. Whitehouse*
2 **Signal processing in electronic communications: For engineers and mathematicians**
*M. J. Chapman, D. P. Goodall and N. C. Steele*
3 **Pattern recognition and image processing**
*D. Luo*
4 **Digital filters and signal processing in electronic engineering: Theory, applications, architecture, code**
*S. M. Bozic and R. J. Chance*
5 **Cable engineering for local area networks**
*B. J. Elliott*
6 **Designing a structured cabling system to ISO 11801: Cross-referenced to European CENELEC and American Standards**
**Second edition**
*B. J. Elliott*
7 **Microscopy techniques for materials science**
*A. Clarke and C. Eberhardt*
8 **Materials for energy conversion devices**
*Edited by C. C. Sorrell, J. Nowotny and S. Sugihara*
9 **Digital image processing: Mathematical and computational methods**
**Second edition**
*J. M. Blackledge*
10 **Nanolithography and patterning techniques in microelectronics**
*Edited by D. Bucknall*
11 **Digital signal processing: Mathematical and computational methods, software development and applications**
**Second edition**
*J. M. Blackledge*
12 **Handbook of advanced dielectric, piezoelectric and ferroelectric materials: Synthesis, properties and applications**
*Edited by Z.-G. Ye*
13 **Materials for fuel cells**
*Edited by M. Gasik*
14 **Solid-state hydrogen storage: Materials and chemistry**
*Edited by G. Walker*
15 **Laser cooling of solids**
*S. V. Petrushkin and V. V. Samartsev*

16 **Polymer electrolytes: Fundamentals and applications**
*Edited by C. A. C. Sequeira and D. A. F. Santos*
17 **Advanced piezoelectric materials: Science and technology**
*Edited by K. Uchino*
18 **Optical switches: Materials and design**
*Edited by S. J. Chua and B. Li*
19 **Advanced adhesives in electronics: Materials, properties and applications**
*Edited by M. O. Alam and C. Bailey*
20 **Thin film growth: Physics, materials science and applications**
*Edited by Z. Cao*
21 **Electromigration in thin films and electronic devices: Materials and reliability**
*Edited by C.-U. Kim*
22 ***In situ* characterization of thin film growth**
*Edited by G. Koster and G. Rijnders*
23 **Silicon-germanium (SiGe) nanostructures: Production, properties and applications in electronics**
*Edited by Y. Shiraki and N. Usami*
24 **High-temperature superconductors**
*Edited by X. G. Qiu*
25 **Introduction to the physics of nanoelectronics**
*S. G. Tan and M. B. A. Jalil*
26 **Printed films: Materials science and applications in sensors, electronics and photonics**
*Edited by M. Prudenziati and J. Hormadaly*
27 **Laser growth and processing of photonic devices**
*Edited by N. A. Vainos*
28 **Quantum optics with semiconductor nanostructures**
*Edited by F. Jahnke*
29 **Ultrasonic transducers: Materials and design for sensors, actuators and medical applications**
*Edited by K. Nakamura*
30 **Waste electrical and electronic equipment (WEEE) handbook**
*Edited by V. Goodship and A. Stevels*
31 **Applications of ATILA FEM software to smart materials: Case studies in designing devices**
*Edited by K. Uchino and J.-C. Debus*
32 **MEMS for automotive and aerospace applications**
*Edited by M. Kraft and N. M. White*
33 **Semiconductor lasers: Fundamentals and applications**
*Edited by A. Baranov and E. Tournie*
34 **Handbook of terahertz technology for imaging, sensing and communications**
*Edited by D. Saeedkia*
35 **Handbook of solid-state lasers: Materials, systems and applications**
*Edited by B. Denker and E. Shklovsky*
36 **Organic light-emitting diodes (OLEDs): Materials, devices and applications**
*Edited by A. Buckley*
37 **Lasers for medical applications: Diagnostics, therapy and surgery**
*Edited by H. Jelínková*
38 **Semiconductor gas sensors**
*Edited by R. Jaaniso and O. K. Tan*

39 **Handbook of organic materials for optical and (opto)electronic devices: Properties and applications**
*Edited by O. Ostroverkhova*
40 **Metallic films for electronic, optical and magnetic applications: Structure, processing and properties**
*Edited by K. Barmak and K. Coffey*
41 **Handbook of laser welding technologies**
*Edited by S. Katayama*
42 **Nanolithography: The art of fabricating nanoelectronic and nanophotonic devices and systems**
*Edited by M. Feldman*
43 **Laser spectroscopy for sensing: Fundamentals, techniques and applications**
*Edited by M. Baudelet*
44 **Chalcogenide glasses: Preparation, properties and applications**
*Edited by J.-L. Adam and X. Zhang*
45 **Handbook of MEMS for wireless and mobile applications**
*Edited by D. Uttamchandani*
46 **Subsea optics and imaging**
*Edited by J. Watson and O. Zielinski*
47 **Carbon nanotubes and graphene for photonic applications**
*Edited by S. Yamashita, Y. Saito and J. H. Choi*
48 **Optical biomimetics: Materials and applications**
*Edited by M. Large*
49 **Optical thin films and coatings**
*Edited by A. Piegari and F. Flory*
50 **Computer design of diffractive optics**
*Edited by V. A. Soifer*
51 **Smart sensors and MEMS: Intelligent devices and microsystems for industrial applications**
*Edited by S. Nihtianov and A. Luque*
52 **Fundamentals of femtosecond optics**
*S. A. Kozlov and V. V. Samartsev*
53 **Nanostructured semiconductor oxides for the next generation of electronics and functional devices: Properties and applications**
*S. Zhuiykov*
54 **Nitride semiconductor light-emitting diodes (LEDs): Materials, technologies and applications**
*Edited by J. J. Huang, H. C. Kuo and S. C. Shen*
55 **Sensor technologies for civil infrastructures**
**Volume 1: Sensing hardware and data collection methods for performance assessment**
*Edited by M. Wang, J. Lynch and H. Sohn*
56 **Sensor technologies for civil infrastructures**
**Volume 2: Applications in structural health monitoring**
*Edited by M. Wang, J. Lynch and H. Sohn*
57 **Graphene: Properties, preparation, characterisation and devices**
*Edited by V. Skákalová and A. B. Kaiser*
58 **Silicon-on-insulator (SOI) technology**
*Edited by O. Kononchuk and B.-Y. Nguyen*

59 **Biological identification: DNA amplification and sequencing, optical sensing, lab-on-chip and portable systems**
*Edited by R. P. Schaudies*
60 **High performance silicon imaging: Fundamentals and applications of CMOS and CCD sensors**
*Edited by D. Durini*
61 **Nanosensors for chemical and biological applications: Sensing with nanotubes, nanowires and nanoparticles**
*Edited by K. C. Honeychurch*
62 **Composite magnetoelectrics: Materials, structures, and applications**
*G. Srinivasan, S. Priya and N. Sun*
63 **Quantum information processing with diamond: Principles and applications**
*Edited by S. Prawer and I. Aharonovich*
64 **Advances in non-volatile memory and storage technology**
*Edited by Y. Nishi*
65 **Laser surface engineering: Processes and applications**
*Edited by J. Lawrence, C. Dowding, D. Waugh and J. Griffiths*
66 **Power ultrasonics: Applications of high-intensity ultrasound**
*Edited by J. A. Gallego-Juárez and K. F. Graff*
67 **Advances in delay-tolerant networks (DTNs): Architectures, routing and challenges**
*Edited by J. J. P. C. Rodrigues*
68 **Handbook of flexible organic electronics: Materials, manufacturing and applications**
*Edited by S. Logothetidis*
69 **Machine-to-machine (M2M) communications: Architecture, performance and applications**
*Edited by C. Anton-Haro and M. Dohler*
70 **Ecological design of smart home networks: Technologies, social impact and sustainability**
*Edited by N. Saito and D. Menga*
71 **Industrial tomography: Systems and applications**
*Edited by M. Wang*
72 **Vehicular communications and networks: Architectures, protocols, operation and deployment**
*Edited by W. Chen*
73 **Modeling, characterization and production of nanomaterials: Electronics, photonics and energy applications**
*Edited by V. Tewary and Y. Zhang*
74 **Reliability characterisation of electrical and electronic systems**
*Edited by J. Swingler*
75 **Handbook of industrial wireless sensor networks: Monitoring, control and automation**
*Edited by R. Budampati S. Kolavennu*
76 **Epitaxial growth of complex metal oxides**
*Edited by G. Koster, M. Huijben and G. Rijnders*
77 **Semiconductor nanowires: Materials, synthesis, characterization and applications**
*Edited by J. Arbiol and Q. Xiong*

78 **Superconductors in the power grid**
*Edited by C. Rey*
79 **Optofluidics, sensors and actuators in microstructured optical fibers**
*Edited by S. Pissadakis and S. Selleri*
80 **Magnetic nano- and microwires: design, synthesis, properties and applications**
*Edited by M. Vázquez*
81 **Robust design of microelectronic assemblies against mechanical shock, temperature and moisture**
*E-H. Wong and Y-W. Mai*
82 **Biomimetic technologies: Principles and applications**
*Edited by T. D. Ngo*
83 **Directed self-assembly of block co-polymers for nano-manufacturing**
*Edited by Gronheid and P. Nealey*

This page intentionally left blank

# Preface

The invention of the Photonic Crystal Fiber (PCF) was a cornerstone demonstration, inaugurating the field of Microstructured Optical Fibers (MOFs), where light confinement into the fiber core was departed from the traditional total internal reflection mechanism. The guiding mode confinement within a microstructured optical fiber core by employing mechanisms such as the modified total internal reflection, the antiresonant guidance, or the photonic band gap localization imparted new optical characteristics to those new fibers not being available before. Since then, several research groups spanning all over the world have directed their experimental and theoretical efforts into this rapidly growing field, illustrating new light confinement and propagation effects and exotic device designs. In addition, the hollow structure of MOFs naturally pushed the integration of fluidic functionalities into the fiber itself. Thus, numerous scientific and technical challenges have emerged since the early days of the establishment of the microstructured optical fibers field, indicatively related to the tailoring of the optical mode guiding characteristics, to the implementation of standard processing procedures (tapering, splicing, grating recording, etc.) into the MOF fashion, and to the investigation and potential exploitation of fluidic actuation into the MOFs/PCFs capillaries. During the last twenty years the field of PCFs and MOFs has been massively grown, new fiber types have been presented, and disruptive photonic devices have been demonstrated, while the new insights into the field are constantly augmented. Moreover, the technology of PCFs and MOFs has been commercialized through the deployment of broadband super-continuum sources and the development of high efficient and power fiber lasers. In parallel, the research carried out within the field of PCFs and MOFs has been largely interconnected with other photonic fields, such as those of Optofluidics, Imaging, Metrology, and Optical Sensing as well as with other nonphotonic fields such as those of Biology, Nanomaterials, and Chemistry, leading to the development of device designs with novel functionalities and/or improved performance. The last statement that there are constantly new advancements into the field of MOFs/PCFs, while attracting significant attention from both the academic and industrial photonic communities.

The book *Optofluidics, Sensors and Actuators in Microstructured Optical Fibres* reviews and updates recent advances in the vibrant field of PCF and MOF devices, focusing on fabrication methods and materials as well as related applications. The progress undergone within the field during the last few years spans beyond the pure photonic aspect, wherein new materials and processing/infiltration methods prompt the implementation of the "Lab-in-a-Fiber" protocol, where the guiding modes localized

with PCFs and MOFs are used for probing (or even inducing/catalyzing) biological, chemical, or physical actuations occurring within the MOFs/PCFs capillaries, opening new horizons for them into high socioeconomical impact application fields. In this volume there are 10 chapters authored by high caliber research groups working in the field of PCFs and MOFs photonic devices, covering the thematic aspects discussed above, while being analyzed as follows.

In Chapter 1 K. Kalli and coauthors present a mathematical model for the flow along a microchannel also accounting for heat transfer and provide numerical results for given flow and heat configurations along single or multiple microchannel fibers.

In Chapter 2 A. Argyros and coauthors explore fabrication approaches and fiber drawing methods as potential techniques for metamaterial fabrication. Specific types of drawn metamaterial with designed electric and magnetic responses are discussed in more detail with a further emphasis on hyperlenses that beat the diffraction limit.

In Chapter 3 E. Kriezis and coauthors investigate the natural possibility for infiltrating fiber capillaries with fluid materials, like liquid crystals, in order to introduce a means for dynamic control by electro-optical addressing, in the context of switching applications. In particular they present design and performance of three switching elements, namely a single-polarization switch, a complete polarization controller, and a dual-core polarization splitter.

In Chapter 4 M. Pisco and coauthors present interesting results on the layering of carbon nanotubes into the capillaries of MOFs, their corresponding waveguiding behavior, and finally their chemosensing response to organic substances and solvents.

In Chapter 5 I. Konidakis reviews recent investigations on the infiltration of silica glass PCFs with high refractive index soft glasses for developing photonic band gap guidance fibers and studying light propagation, plasmonic absorption, and glass transition effects in those.

In Chapter 6 H. Thienpont and coauthors deal with optical fiber sensors based on fiber Bragg gratings that have evolved into one of the most mature fiber sensor technologies, combining all the advantages of optical fiber sensors with excellent resistance to fatigue at high loads, thus being the most successful approach for structural health monitoring applications.

In Chapter 7 T. Wolinski and coauthors demonstrate features of photonic liquid crystal fibers used for dynamically controlled and tunable electromagnetic field sensors. Considering the fiber as a matrix of parallel waveguide channels, when optical nonlinearity is taken into account, spatial light localization and delocalization can be obtained, paving the way not only for all-optical sensing but also for switching.

In Chapter 8 G. Rajan and G.D. Peng present an overview of the recent progress in the development of polymer optical fiber Bragg grating sensors, including polymer microstructured FBGs, polymer microfiber Bragg gratings, and grating arrays. They discuss some of the recent developments in this area, such as accelerometers, fast-response humidity sensors, force, and pressure measurements.

In Chapter 9 A. Cucinotta and A. Candiani explore a novel DNA photonic-sensing approach based on peptide nucleic acids functionalized microstructured fibers. By employing Bragg gratings, the signal is monitored in reflection mode, allowing the

use of the fiber itself as a probe. The detection of DNA chains of great relevance for the medical and food industries is reported.

In Chapter 10 Hang Qu and coauthors demonstrate new designs for photonic band gap and Bragg fibers for liquid refractometry, analyze the protocols of detection, and utilize those specialty fibers for analytes sensing.

From the above presentation of the content of the chapters the academic audience of this volume can be easily drawn. This audience is thematically diverse, covering scientists from optics and photonics, optical fiber sensors, materials science, biosensing, and instrumentation; also, scientists from the industrial sector (mainly the optical fiber sensor sector) may find hybrid PCF and MOF components and fabrication methods presented herein useful for their devices under development. In addition, this book can be equally valuable for young postdoctoral researchers and doctorate and Msc students for obtaining a niche update on related technologies developed in PCFs and MOFs and being familiarized with infiltration techniques and sensing protocols.

Both editors would like to acknowledge Elsevier Publishing services for their help in organizing and editing this book, and especially Laura Pugh, Anneka Hess, Josh Bennett, Adam Hooper, and Poulouse Joseph for their continuous help. Also, a warm acknowledgment is directed to our scientific colleagues who work immensely hard at producing the high quality scientific results as presented in this book. Finally, Stavros and Stefano would like to deeply thank all of the authors who contributed their high impact scientific work into this new volume, rendering a final result of the highest quality possible.

Stavros Pissadakis and Stefano Selleri

This page intentionally left blank

# Part One

# Materials and fabrication of microstructured optical fibres

This page intentionally left blank

# Microfluidics flow and heat transfer in microstructured fibers of circular and elliptical geometry

1

*P. Christodoulides*[1], *G.A. Florides*[1], *E. Davies*[1], *K. Kalli*[1], *F. Dias*[2,3]
[1]Cyprus University of Technology, Limassol, Cyprus; [2]University College Dublin, Dublin, Ireland; [3]Centre de Mathématiques et de Leurs Applications, Ecole Normale Supérieure de Cachan, Cachan, France

## 1.1 Introduction

The field of microfluidics utilizes micron-scale devices to control the flow of fluids. The principal application is the manipulation of very small volumes of fluids on the order of nanoliters to femtoliters that are typically seeded with nanoparticles. Hence the control and sorting of nanoparticles is a primary goal using this technology. With this in mind the analysis of DNA in the fluid streams has proven to be of great interest for the high throughput of chemical and biological analysis. There is particular interest in the use of microstructured optical fibers, whereby the guided light in the "core" region can interact with a fluid residing in the region of the air-hole structure, for many applications that are principally related to optical sensing and new forms of optical spectroscopy (Fan & White, 2011; Hassani & Skorobogatiy, 2006; Kerbage & Eggleton, 2004; Monat, Domachuk, & Eggleton, 2007; Russell, 2003). Recently there has been a move toward microfluidic fiber microreactors (as flow-through systems) (Sazio, Amezcua-Correa, Finlayson, Hayes, et al., 2006; Unterkofler et al., 2012). Microstructured fibers are considered to be strong candidates for their use as microfluidic devices (as optical fiber or more precisely as optofluidic sensors with applications in chemical and biological sensing), given the minute sample volumes that are required. Figure 1.1(a) shows such a system that has great potential as a novel integrated method for the online analysis of photochemical reactions. A hollow-core photonic crystal fiber is used as an optofluidic channel (Figure 1.1(b)), which provides a low loss method of guiding light in a liquid medium. There is an overlap between the light field in the micron-size core and the dissolved specimen that proves to be greatly enhanced compared to traditional bioanalytical methods, and this offers a highly efficient photoactivation process. Moreover, if a continuous flow is applied through the fiber, then photochemical reaction products can be applied to a mass spectrometer in a rapid, online manner, which is highly advantageous over conventional cuvette-based approaches (Figure 1.1(c) and (d)). Other advantages include the ability to detect

**Optofluidics, Sensors and Actuators in Microstructured Optical Fibers.** http://dx.doi.org/10.1016/B978-1-78242-329-4.00001-1

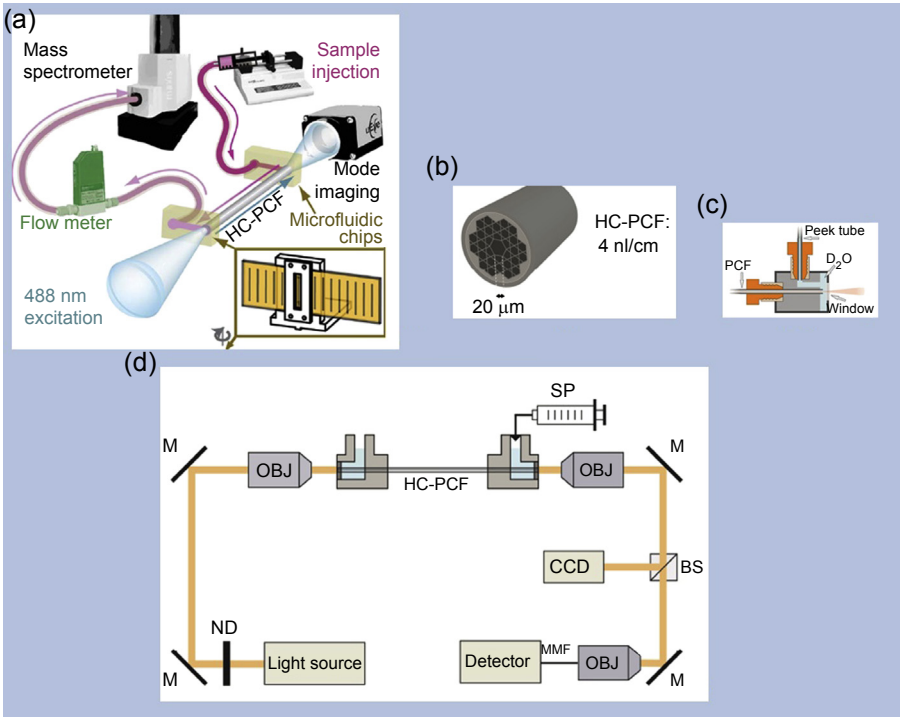


**Figure 1.1** Microreactor system using flow-through photonic crystal fiber.
(a) Overview of microreactor system concept, (b) cross-section of photonic crystal fiber, (c) combining flow-through and optical information, (d) schematic of key components. After: Unterkofler et al. (2012).

short-lived reaction species, improved handling of low fluid volumes, the analysis of new types of photoactivated metal-based anticancer prodrugs (Farrer, Salassa, & Sadler, 2009), and the potential for integration with other lab-on-a-chip devices (Brivio et al., 2002; Oleschuk & Harrison, 2000) for sample preparation, separation, and (multimodal) analysis in a straightforward fashion.

Given the development of new types of microstructured fibers with cross-sections containing circular or elliptical holes, or more complex cross-sectional geometries, it is important to be able to model the fluid transport capabilities of these fiber types. Furthermore, complex cross-sectional geometries can affect the transfer of heat into the fiber, creating local changes in the behavior of the fluid system. Hence in this work we study the fluid transport capabilities of microstructured fibers with cross-sections containing circular or elliptical holes, while considering the effects of flow rates, fluid viscosity, and the channel shape. The role of heat flux is considered in relation to the fluid characteristics. These effects are studied using a numerical application of a system of partial differential equations consisting of the time-dependent Navier–Stokes equations and the convection–diffusion

equation. We examine the effects of flow rates, fluid viscosity, compressibility, and the channel diameter. The role of heat flux is considered in relation to the fluid characteristics, but also with regard to the material properties of the microstructured fiber. This work is of importance as one cannot assume that the flow dynamics in microstructured fibers will be the same as conventional microfluidic channels. Through the study of the heat transfer, for pressure-driven and other flows and for low Reynolds numbers, we confirm the anticipated behavior of the fluids in the microchannel structure.

We note that it is necessary to undertake a study of how microstructured fibers behave as microfluidic channels, as their dimensions are typically on the same scale as transitional microchannels. One cannot assume that the flow dynamics in microstructured fibers will be the same as conventional microfluidic channels, where the length scales are a factor of 10, or more, greater. The features of a flow and any potential heat transfer are governed by the length scales and material properties, which in turn are governed by the Reynolds number and the convection heat transfer coefficient. Of course one should also consider the effect of external heating, as this will prove important for dynamic microfluidic devices.

From numerous studies on microfluidic flows, one can mention as cases motivating the work presented in this chapter, but with particular consideration for microfluidic microreactors the work of Sazio et al. (2006) and Unterkofler et al. (2012). Yahng and collaborators fabricated microfluidic devices with multiple channels having trapezoidal and triangular cross-sections and investigated the fluid dynamics of the devices as a function of the flow rate, the channel depth, and the channel's geometry (Yahng et al., 2005). Moreover, Colin and Tancogne studied the stability of jets in microchannels and computed the length on which a jet is stable for a given configuration with respect to the flow rates, viscosities, diameter of the channel, and surface tension (Colin & Tancogne, 2011), whereas Sahu and collaborators studied the stability of a co-flow composed of Newtonian and non-Newtonian fluid (Sahu, Valluri, Splet, & Matar, 2007). Lien and Vollmer detected minimum flow rates based on integrated optical fiber cantilevers (Lien & Vollmer, 2007). Regarding heat transfer related to microfluidics, the literature includes the work of Beskok and Karniadakis, who performed simulations of heat and momentum transfer in microgeometries (Beskok & Karniadakis, 1994), Chen and Wu's study of the thermal properties of a microchannel flow in miniature thermal conductivity detectors (Chen & Wu, 2000), and Damean and collaborators' study of the fluid and flow characteristics through a one-dimensional model for the heat transfer in a micro electromechanical system for microfluidics (Damean, Regtien, & Elwenspock, 2003), as well as Christodoulides and collaborators (Christodoulides, Florides, Kalli, & Komodromos, 2012; Christodoulides et al., 2014), in addition to other more complex microfluidic design methods (Plouffe, Lewis, & Murthy, 2011).

This chapter is organized as follows. In Section 1.2 the mathematical model for the flow along a microchannel is formulated in conjunction with heat transfer. Numerical results for certain flow and heat configurations based on the finite element method (FEM) are presented in Section 1.3. Finally, Section 1.4 is devoted to a discussion for further numerical and experimental applications.

## 1.2 Governing equations of flows along a microchannel

We begin by considering the general form of the momentum equation (Navier–Stokes equations) governing a three-dimensional motion of an incompressible fluid given, in summation convention notation, by

$$\rho \frac{\partial u_i}{\partial t} + \rho u_j \frac{\partial u_i}{\partial x_j} = f_i, \tag{1.1}$$

where $\rho$ is the density of the fluid (in kg/m$^3$), $u_i$ is the velocity component of the fluid in the $i$-direction (in m/s), and $f_i$ is the total force per volume (in kg/m$^2$ s) acting on the fluid consisting of pressure gradient, friction forces, and body forces. In its turn the continuity equation is given by

$$\frac{\partial u_i}{\partial x_i} = 0. \tag{1.2}$$

For small Knudsen numbers and in the absence of body forces, following the microfluidics simplifications (according to which gravity may be neglected and as the influence of convection is small, there is no convecting momentum transport) the governing equations reduce to

$$\rho \frac{\partial u_i}{\partial t} = -\frac{\partial p}{\partial x_i} + \mu \frac{\partial^2 u_i}{\partial x_i^2}, \tag{1.3}$$

with an extra equation for $p$, the fluid pressure (in Pa), arising by simply applying the divergence operator to the Navier–Stokes equation, and where $\mu$ is the dynamic viscosity of the fluid (in kg/m s).

It is commonplace to express the system of equations above in dimensionless form. In such cases the resulting dimensionless Reynolds number is given by

$$\mathrm{Re} = \frac{\rho u_0 L}{\mu}. \tag{1.4}$$

This number describes the balance between inertial forces and viscosity, where $u_0$ is a fixed mean velocity relative to the fluid and $L$ is some fixed characteristic linear dimension. In general, microfluidic flows can be classified, according to their Reynolds number, as (1) creeping/Stokes (laminar) flows with no lateral convection ($\mathrm{Re} < 1$), (2) "intermediate" (still laminar) flows with lateral convection becoming increasingly important ($1 < \mathrm{Re} < 2300$) (where time dependence becomes more important), or (3) turbulent flows, where there is a curling of field lines, perturbations are amplified, and the development of field of velocity vectors over time is unpredictable ($\mathrm{Re} > 2300$). Note that it is typical that for flows in microchannels, viscous forces, corresponding to low Reynolds numbers, are dominant.

Figure 1.2 shows a typical parabolic flow profile for an incompressible fluid, where the residence time near walls is high, meaning a low velocity. As we move to the middle of the channel the velocity peaks and the residence time is minimized. We note that any liquid plug can be rapidly diluted, and this is particularly important for the injection of biochemical samples.

When interested in the energy transport into the material region, the energy equation is given by the convection−diffusion equation

$$\rho c_p \frac{\partial T}{\partial t} + \rho u_3 \frac{\partial T}{\partial x_3} + \frac{\partial}{\partial x_i}\left(-\lambda \frac{\partial T}{\partial x_i}\right) + h(T_{\text{fluid}} - T_{\text{int}}) = 0. \tag{1.5}$$

Here $h$ is the convection heat transfer coefficient (in W/m$^2$ K), $\lambda$ is the thermal fluid conductivity (in W/m K), $c_p$ is the fluid specific heat capacity (in J/kg K), and $T_{\text{fluid}}$ and $T_{\text{int}}$ are respectively the temperature of the fluid and the temperature at the wall of the channel. Coupling Eqn (1.5) to set of Eqn (1.3) will yield the full system describing the heat transfer in a flow domain.

We also need to consider the change of the heat transfer coefficient $h$ and its relationship to pressure (Kandlikar et al., 2006). The effect of hydraulic diameter on heat transfer and pressure drop is shown in Figure 1.3(a) and (b), respectively, for water and air flowing in a square channel under constant heat flux and laminar flow conditions. We first note that $h$ is independent of the Reynolds number, and is given by

$$h = N_{\text{u}} \frac{\lambda}{D_{\text{h}}}, \tag{1.6}$$

where $D_{\text{h}}$ is the channel's hydraulic diameter and $N_{\text{u}}$ is the Nusselt number. $N_{\text{u}} = 3.61$ in the case of a fully developed laminar flow in a square channel under constant heat flux conditions. In Figure 1.3(a) we observe the variation of $h$ for flow of water and air with channel hydraulic diameter under these conditions for which $h$ greatly increases as the channel size is reduced. Figure 1.3(b) shows the variation for the pressure gradient with the channel size for a square channel with a mass flux of 200 kg/m$^2$ s, for air and water under incompressible flow conditions. The pressure gradient decreases dramatically as the channel diameter increases. We note that these plots are only a

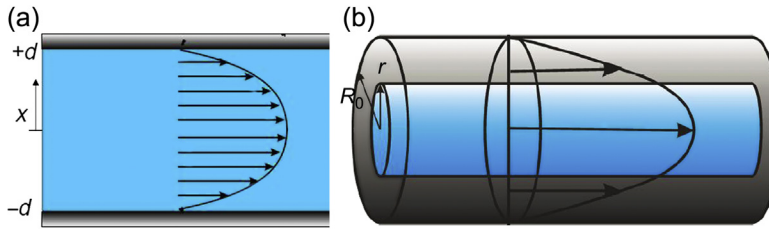


**Figure 1.2** (a) The typical parabolic flow profile of an incompressible fluid in a channel and (b) the fiber cross-section.

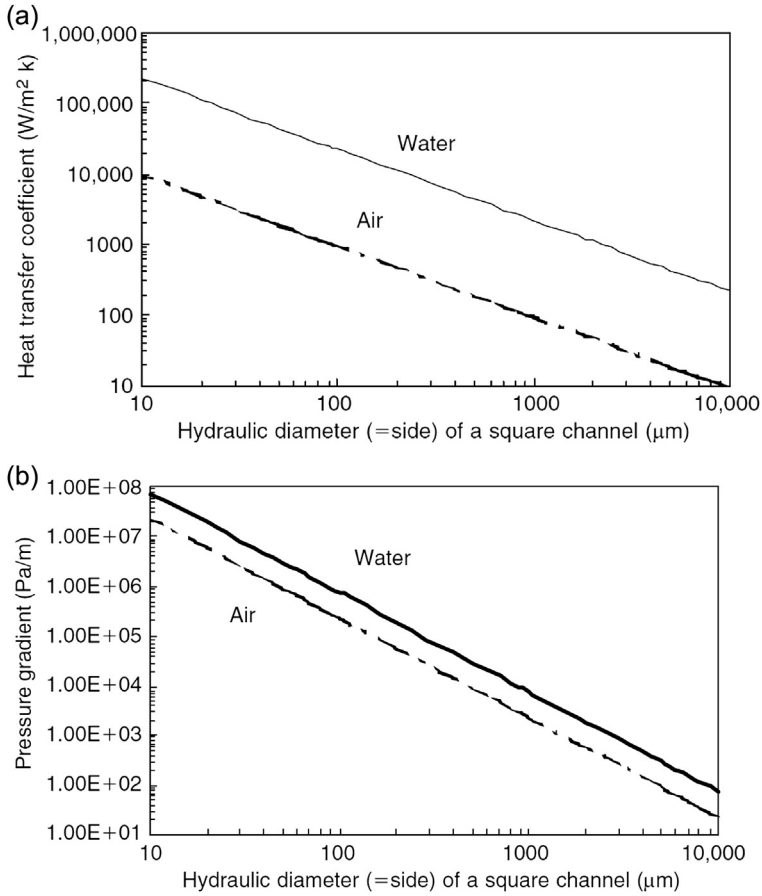


**Figure 1.3** Variation of (a) the heat transfer coefficient $h$ and (b) the pressure with channel size for fully developed laminar flow for air and water.
After: Kandlikar et al. (2006).

guide and deviations can occur, particularly for gases flowing through smaller diameter channels.

This information acquires a new relevance as microchannels become ever more important for microfluidics and in particular for the biosensing community. Microchannels are found in many biological systems; the lungs and kidneys are capable of extremely efficient heat and mass transfer processes. The key issue is one of system stability, as the movement and control of biological macromolecules places critical demands on sample conditions. If we consider human cells then the ideal environment requires a temperature of 37 °C and a pH of 7.4; any deviation exceeding 10% will result in cell necrosis. High temperatures and unsuitable pH conditions can adversely affect protein molecules, leading to denaturation and loss of biological activity due to unfolding. Conversely, in a polymerase chain reaction, rapid temperature cycling (∼1 min/cycle for approximately 40 cycles, from 94 to 54 °C) induces repeated

**Table 1.1 Channel classification**

| Category | $D$: smallest channel dimension |
|---|---|
| Conventional | $D > 3$ mm |
| Minichannel | 200 μm $< D \leq 3$ mm |
| Microchannel | 10 μm $< D \leq 200$ μm |
| Transitional microchannel | 1 μm $< D \leq 10$ μm |
| Transitional nanochannel | 0.1 μm $< D \leq 1$ μm |
| Nanochannel | $D \leq 0.1$ μm |

denaturation and annealing of DNA chains. Hence the microchannel geometry can be utilized to rapidly change the temperature of small liquid volumes and control reactions in microchannel bioreactors.

It should be noted that fibers can be classified as channels according to their cross-sectional diameter. Table 1.1 shows the conventional descriptions, where $D$ is the channel diameter. In the case of noncircular channels, the short side of a rectangular cross-section should be used in place of the diameter $D$. We will use this classification scheme for defining minichannels and microchannels. The definitions in Table 1.1 are principally for ease in use and are based on the so-called "hydraulic diameter"; they are intended to offer a simple means for assigning a range of dimensions that are under consideration. The applicability of continuum theory or slip flow conditions for any gas flow needs to be considered for any channel.

With each channel size reduction we observe different effects on different processes; however, the number of processes and parameters that govern transitions from regular to microscale phenomena are many and varied, hence a simple dimensional classification is generally adopted and preferred. For example, in biological systems, the flow in capillaries occurs at very low Reynolds numbers and a modified modeling approach is needed. In this chapter we concentrate on microchannels.

## 1.3 Numerical results

Following the formulation of Section 1.2, we concentrate on pressure-driven flows along single or multiple microchannels, where circular or elliptical microcapillaries running along the length of the fiber axis may be surrounded by a ring filled with gas. These types of fiber configurations can be seen as nothing other than "approximations" (with regard to their thermal properties) of existing structures, as shown in Figure 1.4 (van Eijkelenborg et al., 2001; Yu et al., 2006). Based on these configurations and choosing appropriate boundary conditions, the coupled differential Eqns (1.3) and (1.5) are solved numerically, by application of the FEM. The FEM mesh is shown in Figure 1.5 for an indicative case with a single circular capillary. Unless

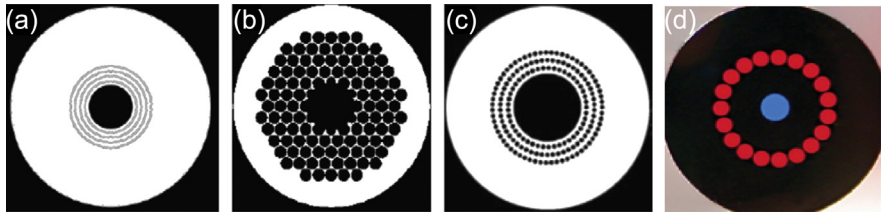


**Figure 1.4** A typical set of fiber cross-sectional configurations, such as (a) Bragg fiber, (b) photonic bandgap fiber, and (c) and (d) ring-structured fibers.
After: Yu et al. (2006).

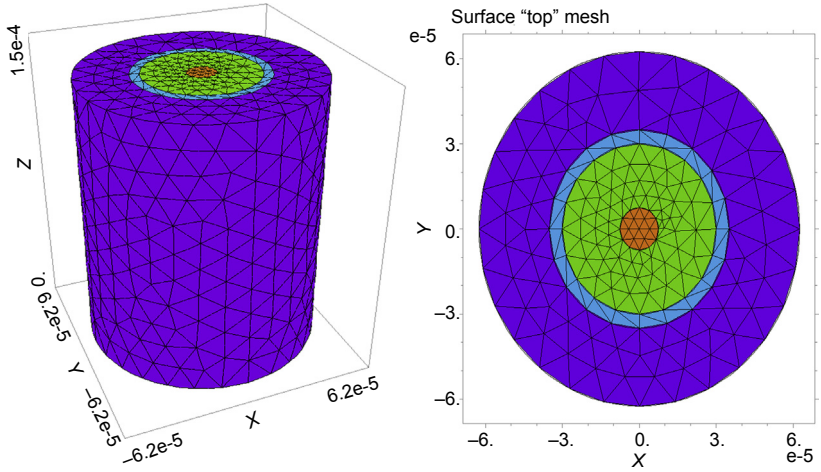


**Figure 1.5** FEM mesh for a microstructured fiber with a single circular capillary running along the length of the fiber axis and surrounded by a gas ring.

otherwise specified, for all cases presented in the following sections the fiber length is taken to be of an infinite extent (practically a 3 cm length in the mesh is sufficient) with a diameter of $D = 125$ μm, while the ring has an internal radius of 30 μm and an external one of 35 μm and the single circular channel is of radius $r = 7.5$ μm. Moreover, the fiber material is silica ($SiO_2$), the gas in the ring is air, the fluid is water (refer to Table 1.2 for thermal properties), the fluid temperature is 20 °C, and the fixed external temperature is 90 °C. Considering the laminar character of the flow, we present here flows of constant velocity (unless otherwise stated, the fluid velocity is 0.001 m/s). This velocity is chosen as being realistic for experimental systems.

The case of a single circular microchannel within a gas ring is presented in Figure 1.6 for the flow regime described above. In Figure 1.6(a) the axial temperature distribution along the fiber is shown for a time of $t = 10$ s. One can observe steady-state temperatures between 20 and 90 °C within the channel. The fluid flow seems to have a cooling effect for a microchannel of length of just over 0.8 mm, where the temperature is about 90 °C. Figure 1.6(b)−(d) shows three cross-sectional temperature distributions (inlet, middle, and outlet, respectively).

**Table 1.2 Physical properties of fluids and glass fiber materials**

| Fluid or glass fiber | $\rho$ (kg/m$^3$) | $\mu$ (kg/m s) | $\lambda$ (W/m K) | $c_p$ (J/kg K) |
|---|---|---|---|---|
| Water | 1000 | 0.001 | 0.609 | 4185 |
| Oil[a] | 916 | 0.084 | 0.170 | 1970 |
| Glycerin | 1260 | 1.490 | 0.290 | 2430 |
| Air | 0.93 | – | 0.032 | 1010 |
| $SiO_2$ | 2250 | – | 1.400 | 700 |
| PMMA | 1170 | – | 0.150 | 1380 |

[a]An indicative case of oil (here olive oil).

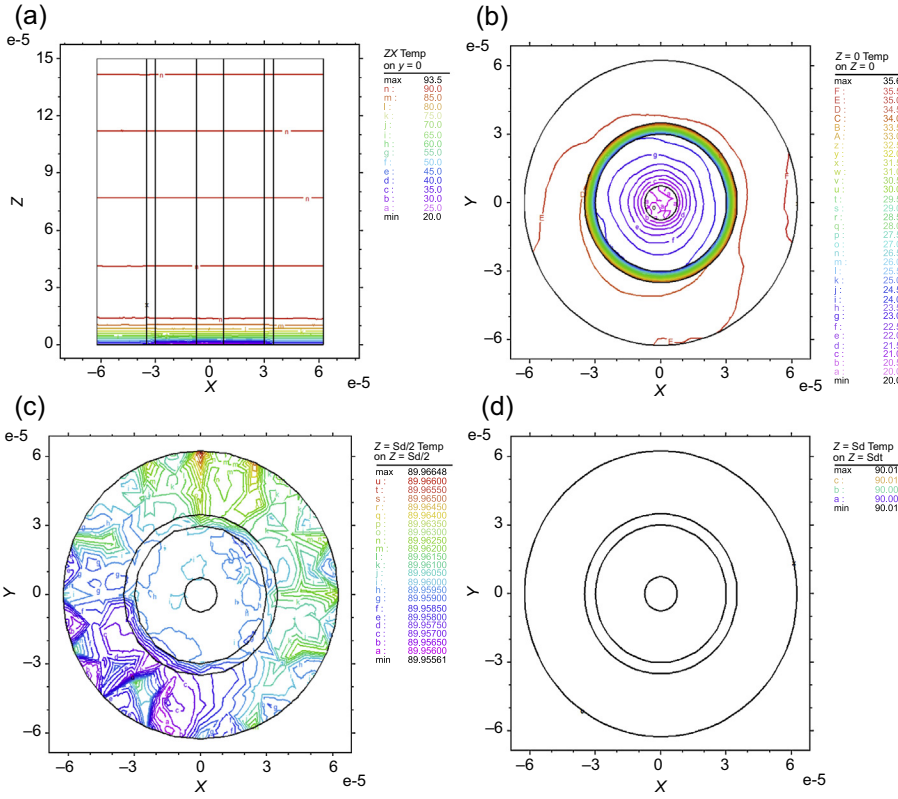


**Figure 1.6** (a) Axial temperature distribution of the fiber with the circular microchannel within a gas ring for a flow of water with velocity of 0.001 m/s and temperature of 20 °C and an external temperature of 90 °C ($z$ is scaled for computational purposes), (b) inlet, (c) middle, (d) outlet cross-sectional temperature distribution.

It must also be mentioned that the heat transfer coefficient of the air surrounding the fiber, $h_{air}$, relies heavily on the type and the strength of the heat source. For the case of Figure 1.6 and the sequel (unless otherwise stated) $h_{air}$ is of order $O(10^4)$ W/m$^2$ K. The effect of $h_{air}$ on the cooling of the circular microchannel as well as on the time to reach steady state is shown in Figure 1.7. On the other hand it turns out that the corresponding heat transfer coefficients for the fluid in the microchannel as well as the air in the ring have a negligible effect on the time to reach steady state.

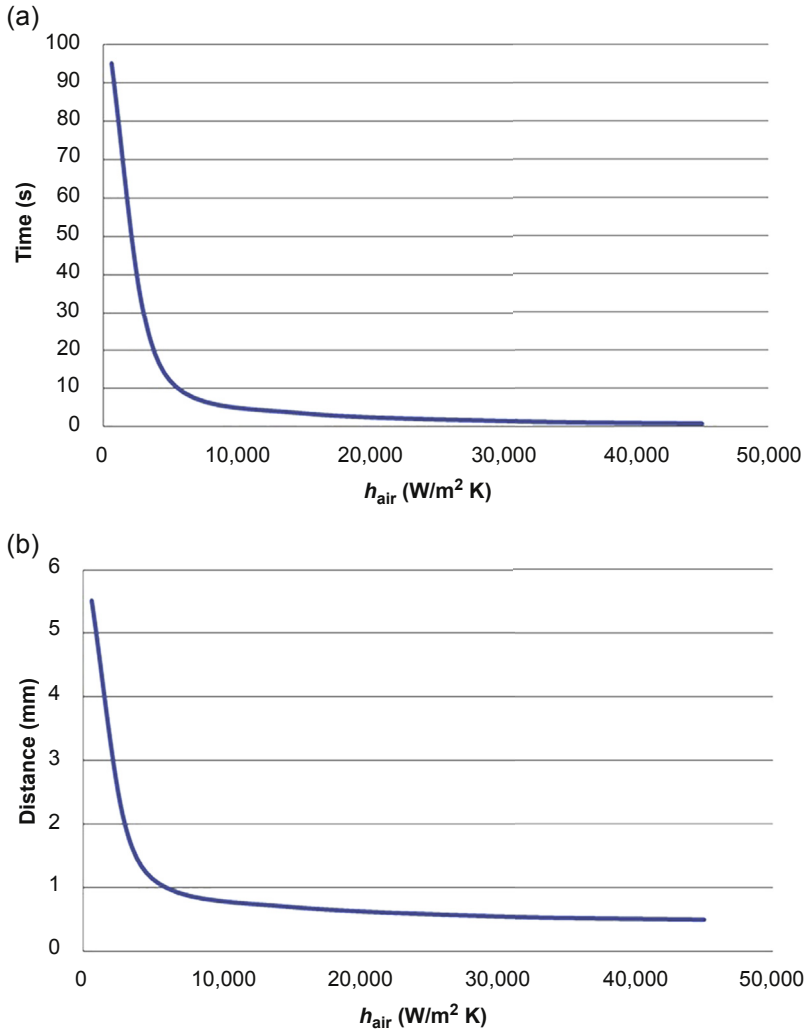


**Figure 1.7** (a) Time for the heat flow to reach steady state and (b) distance within the microchannel where the cooling is present as a function of the heat transfer coefficient of the surrounding air for a fiber with the circular microchannel within a gas ring for a flow of water with velocity of 0.001 m/s and temperature of 20 °C and an external temperature of 90 °C.

We then move to the case of an elliptical microchannel of semiaxes 7.5 and 5 μm. A flow with the same characteristics as the one presented in Figure 1.6 is shown in Figure 1.8. In Figure 1.8(a) the axial temperature distribution along the fiber is shown for a time of $t = 10$ s. One can observe steady-state temperatures between 20 and 90 °C within the channel. The fluid flow appears to have a cooling effect for a microchannel of length of just below 1.1 mm, where the temperature is about 90 °C. Figure 1.8(b)−(d) show three cross-sectional temperature distributions (inlet, middle, and outlet, respectively).

Finally we consider the case of three circular microchannels of equal *total* area ($\approx 177$ μm$^2$) to the circular microchannel studied above. The radius of each circle is 4.33 μm with all circles' centers being equidistant at 12 μm from the center of the fiber cross-section. A flow with the same characteristics as the one presented in Figures 1.6 and 1.8 is presented in Figure 1.9. In Figure 1.9(a) the axial temperature distribution along the fiber is shown for a time of $t = 10$ s. One can observe steady-state temperatures between 20 and 90 °C within the channel. Similarly to

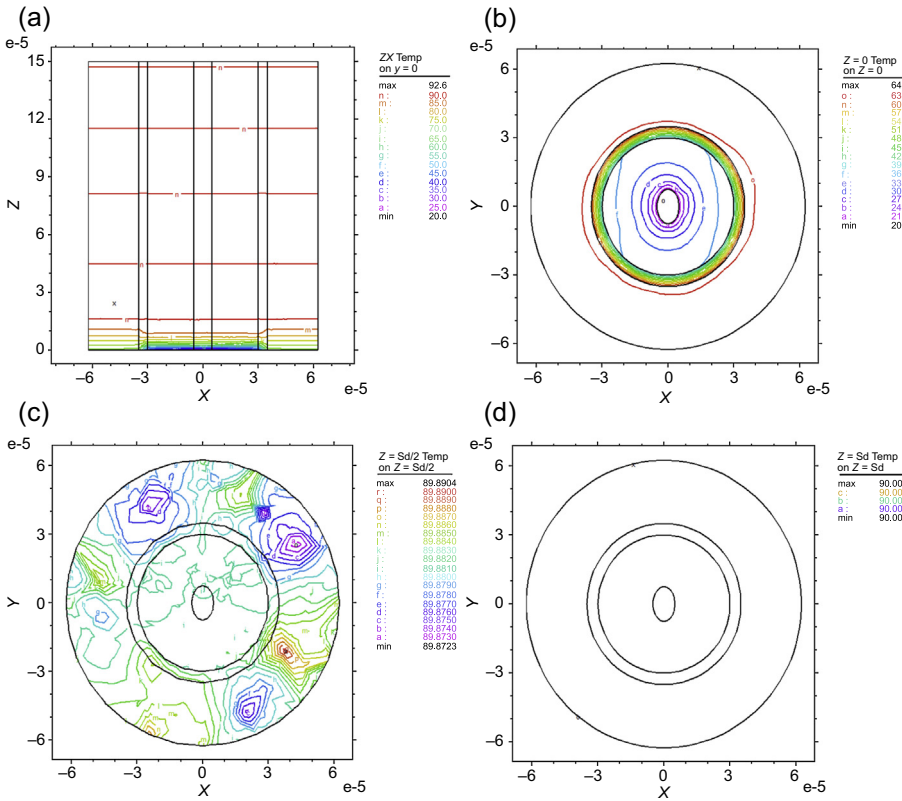


**Figure 1.8** (a−d) An elliptical microchannel, under the same conditions and perspectives as shown in Figure 1.6.

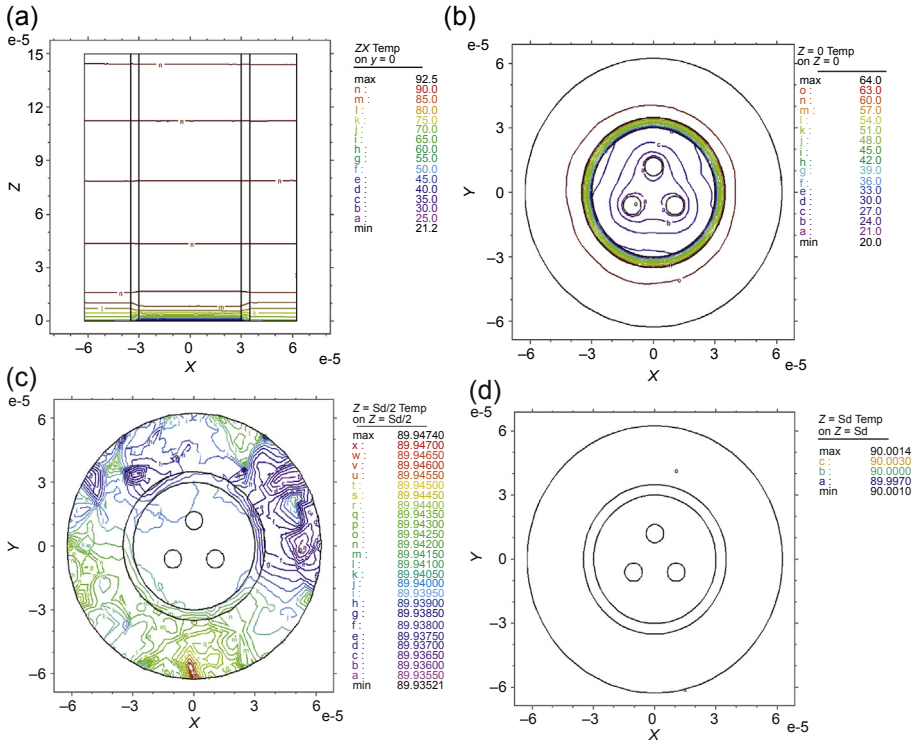


**Figure 1.9** (a–d) A triple-circular microchannel under the flow and temperature conditions and perspectives shown in Figures 1.6 and 1.7.

the cases considered above, the fluid flow has a cooling effect for a microchannel of length of just over 1.1 mm, where the temperature is 90 °C. Figure 1.9(b)–(d) show three cross-sectional temperature distributions (inlet, middle, and outlet, respectively).

For the three cases considered above, the mid-channel temperature with respect to time is plotted in Figure 1.10. As is observed in Figure 1.10(a), for the single circular microchannel the steady-state temperature is attained in about 0.8 s as opposed to 0.5 s for the elliptical microchannel (Figure 1.10(b)) and 0.4 s for the triple-circular configuration (Figure 1.10(c)). It must be stressed that the decisive factor is not the shape of the channel but rather the length of the circumference ($15\pi$, $12.7\pi$, and $8.66\pi$, for each circle, respectively) as well as the position of the microchannel with respect to the gas ring. In other words, microchannels of the same circumference (and position) behave in an identical manner with regard to their thermal properties. On the other hand, considering the cooling effect with regard to distance within the fiber, it would seem that the fluid velocity, rather than the shape and circumference of the microchannels, is the significant factor (with reference to Figures 1.6(a), 1.8(a), and 1.9(a), and later in Section 1.3.2).

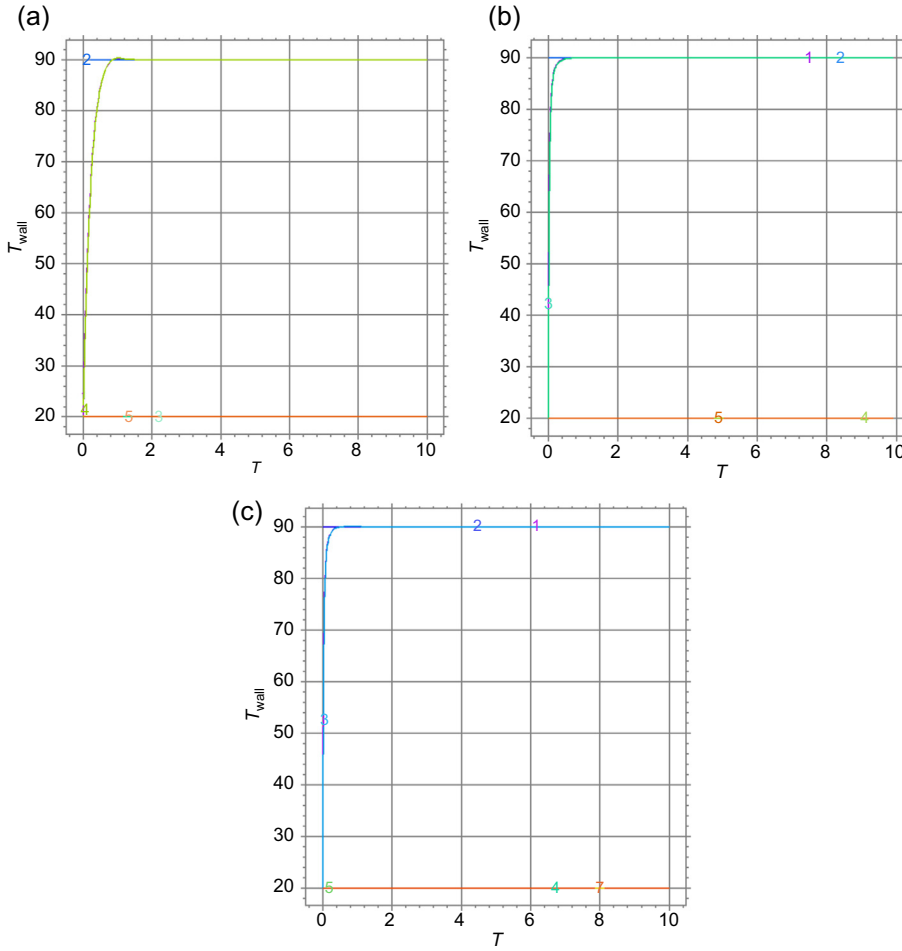


**Figure 1.10** Temperature with respect to time for water flow with velocity of 0.001 m/s and initial temperature of 20 °C for an external temperature of 90 °C. (a) Circular, (b) elliptical, (c) triple-circular microchannels within a gas ring.

### 1.3.1 Effect of gas ring

When the gas ring is not present, the same procedure for the three configurations and surrounding conditions as above is repeated. We discern that the cooling effect is a little slower, as is actually anticipated.

In Figure 1.11, for a flow of water with temperature of 20 °C, external temperature of 90 °C, and fluid velocity of 0.001 m/s, the inlet cross-sectional temperature distribution of the fiber is shown at a time of $t = 10$ s for each of the three configurations. One can observe that the steady-state temperatures are lower than the corresponding ones for the gas-ring example (with reference to Figures 1.6(b), 1.8(b), 1.9(b)), owing to the higher homogeneity of the total fiber area.

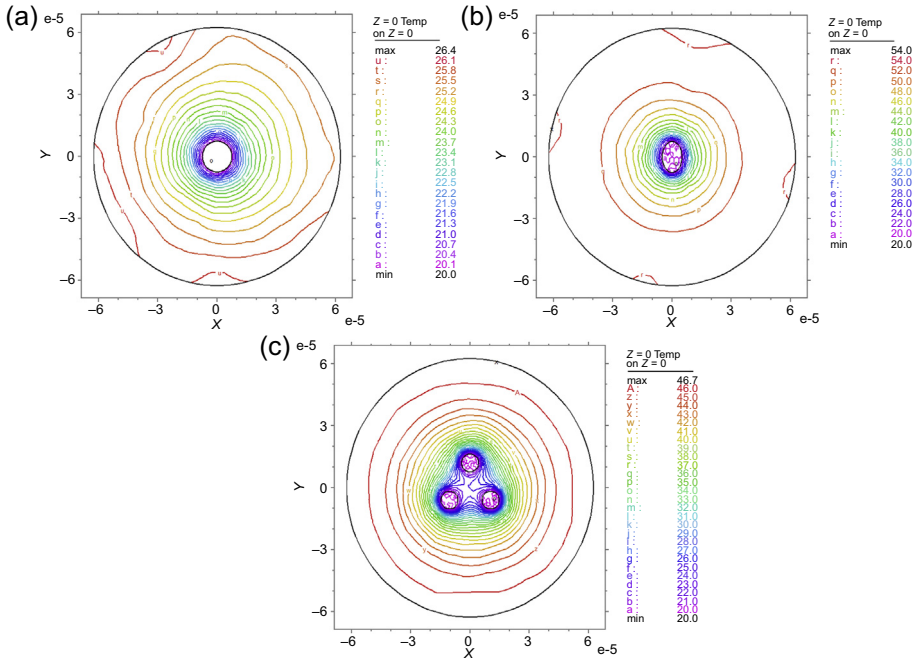


**Figure 1.11** Inlet cross-sectional temperature distribution of the fiber with no gas ring at $t = 10$ s for a flow of water with temperature of 20 °C, an external temperature of 90 °C and fluid velocity of 0.001 m/s. (a) Circular, (b) elliptical, (c) triple-circular microchannels.

On the other hand, in Figure 1.12, where the mid-channel temperature with respect to time is plotted, one observes that the steady-state temperature is attained at slightly longer times than is the corresponding case for the gas-ring example (with reference to Figure 1.10).

We now consider the effect of the width of the gas ring relative to the size of the inner microchannel. In Figure 1.13(a) the axial temperature distribution along the fiber is shown for a time of $t = 10$ s when the gas ring is still 5 μm wide and the circular microchannel is of a radius of 20 μm (as opposed to the 7.5 μm radius of the case studied previously). One observes steady-state temperatures between 20 and 90 °C within the channel. The fluid flow appears to display a cooling effect for a microchannel of length close to 1 mm (slightly longer than the earlier case of Figure 1.6), where the temperature is about 90 °C. In Figure 1.13(b) the axial temperature distribution along the fiber is shown for a time of $t = 10$ s when the gas ring is now 10 μm wide and the circular microchannel is (as before) of a radius of 7.5 μm. One observes steady-state temperatures between 20 and 90 °C within the channel. The fluid flow seems to have a cooling effect for a microchannel of length of about 0.8 mm (same as for the case of Figure 1.6), where the temperature is about 90 °C.

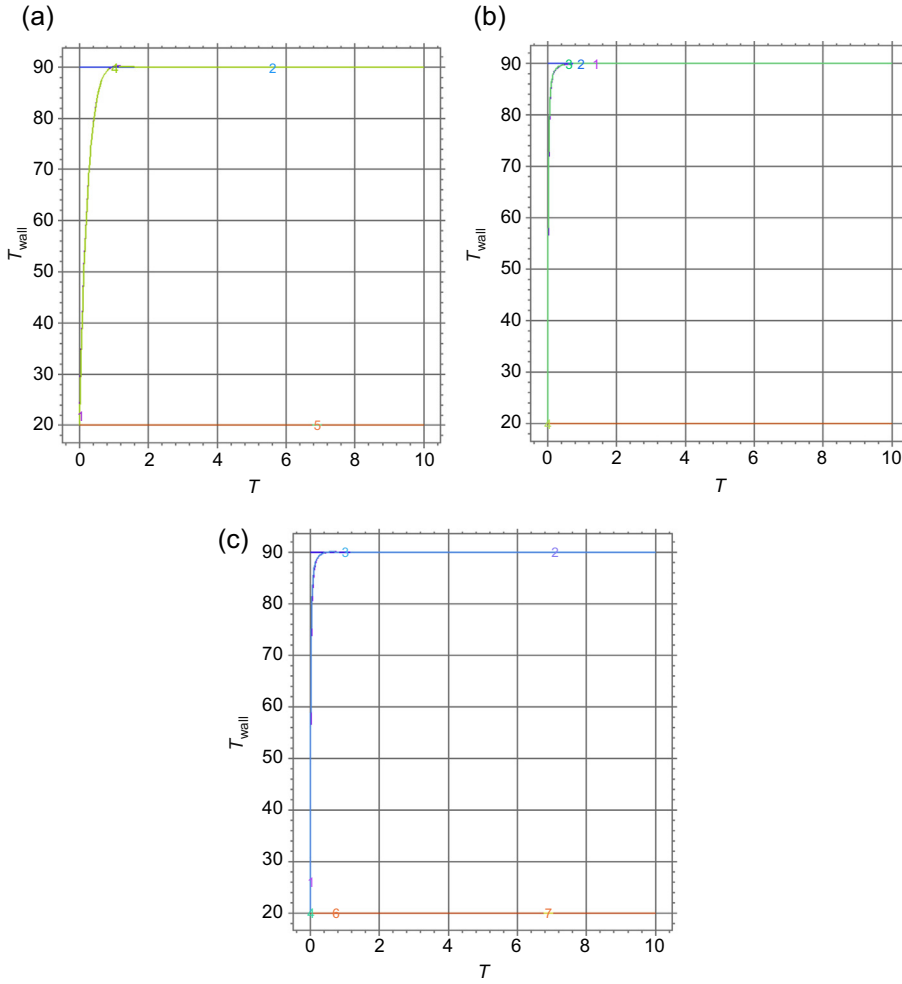


**Figure 1.12** Temperature with respect to time for water flow with velocity of 0.001 m/s and initial temperature of 20 °C for an external temperature of 90 °C. (a) Circular, (b) elliptical, (c) triple-circular microchannels (no gas ring present).

Finally in Figure 1.14, where the mid-channel temperature with respect to time is plotted, one observes that the steady-state temperature is attained in slightly larger (for case (a)) and roughly the same (case (b)) times as for the case of Figure 1.6, showing no significantly different behavior.

Combining the results discussed above, one can conclude that, at least for "realistically small to medium size" gas (*air*)-ring widths, the latter is not a significant factor with regard to the fiber thermal properties.

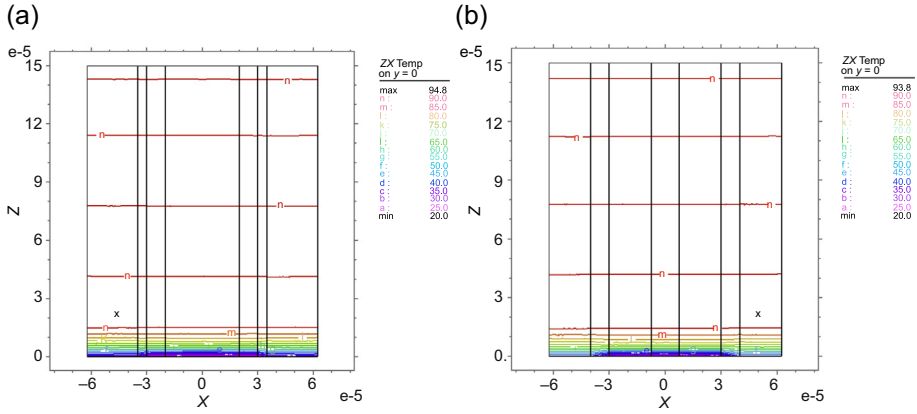


**Figure 1.13** Axial temperature distribution of the fiber with the circular microchannel within a gas ring for a flow of water with velocity of 0.001 m/s and temperature of 20 °C and an external temperature of 90 °C ($z$ is scaled). (a) Gas-ring width = 5 μm, microchannel radius = 20 μm, (b) gas-ring width = 10 μm, microchannel radius = 7.5 μm.

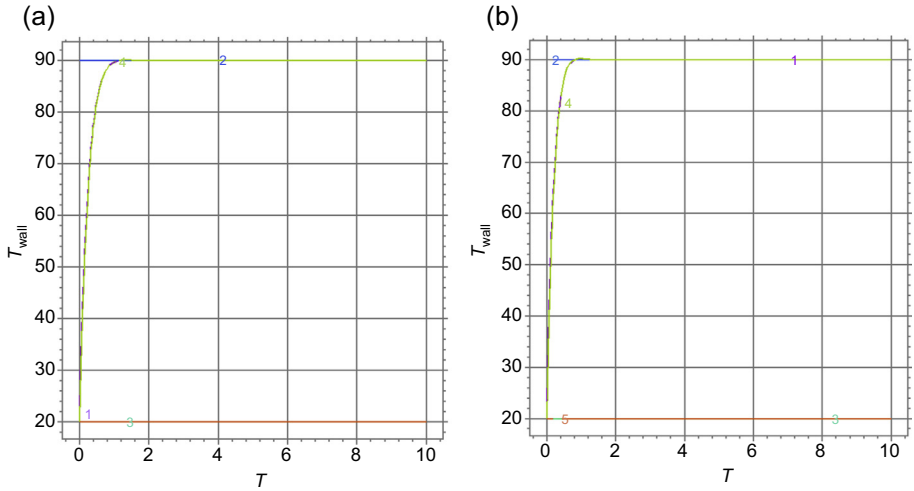


**Figure 1.14** (a, b) Temperature with respect to time under the details and the conditions shown in Figure 1.13.

### 1.3.2 Effect of fluid velocity

Following the thermal behavior of fibers studied thus far—all in cases for a fluid velocity of 0.001 m/s—the next step is to let the fluid velocity vary within "reasonable" values for microfluidics. We may consider that given that steady state was reached (for all cases studied) after a short distance of about 1 mm from the inlet, we now consider the "inlet" maximum steady-state temperature of the fiber attained for different velocities. Figure 1.15 shows that for water, flowing through a circular

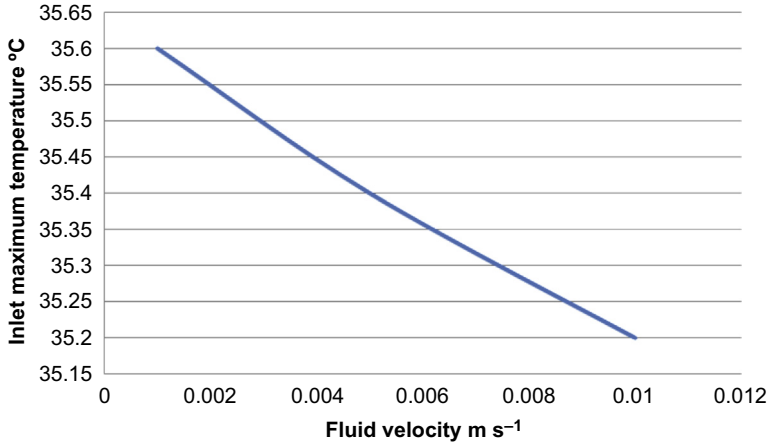


**Figure 1.15** The steady-state inlet maximum temperature of the fiber with the circular microchannel within a gas ring for a flow of water with temperature of 20 °C and an external temperature of 90 °C as a function of velocity for Reynolds number values of Re << 1.

microchannel and the regime of Figure 1.6, the greater the velocity the lower the temperature, as anticipated. Such flows can be considered as creeping laminar, as the Reynolds numbers corresponding to these velocities are all low (Re << 1). Note that the change in maximum temperature is almost insignificant, owing to the large $h_{air}$. For relatively low values of $h_{air}$ (e.g., order $O(10^2)$, not shown here) the effect is much more significant (Christodoulides et al., 2014).

Moreover, two more indicative cases of a fiber with a circular microchannel (the regime of Figure 1.6) with respective fluid velocities of 0.005 and 0.01 m/s this

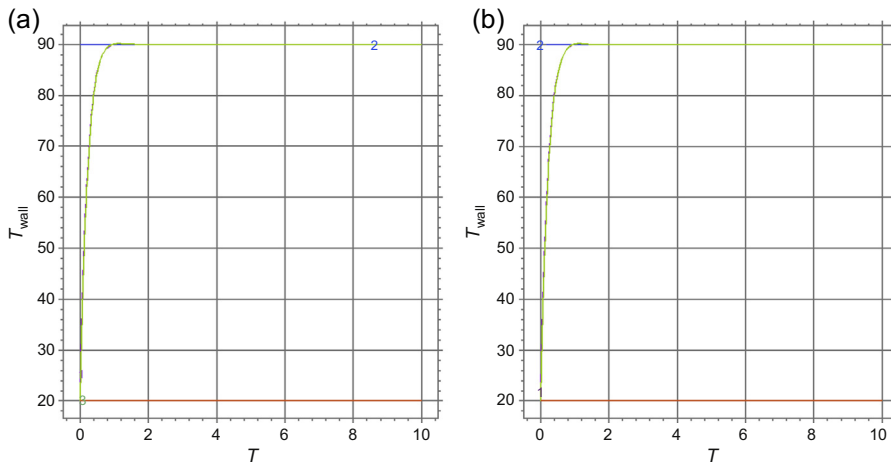


**Figure 1.16** Temperature with respect to time for water flow (in the circular microchannel) with initial temperature of 20 °C, an external temperature of 90 °C and velocity of (a) 0.005 m/s and (b) 0.01 m/s.

time, are shown in Figure 1.16. It is clear that the fluid velocity has very little effect on steady-state times. Again (not shown here) for relatively low values of $h_{air}$ the steady-state times are significantly lower for large velocities (Christodoulides et al., 2014).

Finally, in order to assess the capillary action for different fluid velocities at the inlet of the microchannel, we consider the steady-state temperature at $t = 10$ s for an initial temperature of 20 °C and a fixed external temperatures of 90 °C for the circular microchannel. The effect of velocity change is shown to be negligible as one can observe maximum temperatures of 35.6 (Figure 1.6(b)), 35.4 (Figure 1.17(a)), and 35.2 (Figure 1.17(b)) for velocities of 0.001, 0.005, and 0.01 m/s respectively. Note again that (not shown here) the effect is much more significant for relatively low values of $h_{air}$.

### 1.3.3 Effect of fluid type

In order to study the effect of the fluid chosen (with reference to Table 1.2 for relevant fluid thermal properties) on the steady-state mid-channel temperature, we chose the circular microchannel configuration studied in Figure 1.6, for a fixed fluid velocity of 0.001 m/s. The results are shown in Figures 1.10(a) and 1.18, where one can observe that water has the best cooling effect along the microchannel, followed by glycerin and then oil (with references to the steady-state times of 0.8, 1.0, and 1.2 s, respectively, for each liquid), as actually one would expect given the respective values of $\lambda$ (thermal fluid conductivity) and $c_p$ (fluid specific heat capacity). Again this kind of effect can be best demonstrated for relatively low values of $h_{air}$ (Christodoulides et al., 2014).

The behavior of each fluid with respect to velocity is also examined by recording the steady-state inlet maximum temperature of the fiber with the circular microchannel within a gas ring for a flow with temperature of 20 °C and an external temperature of 90 °C. Figure 1.19 shows that for each fluid the behavior is nearly identical

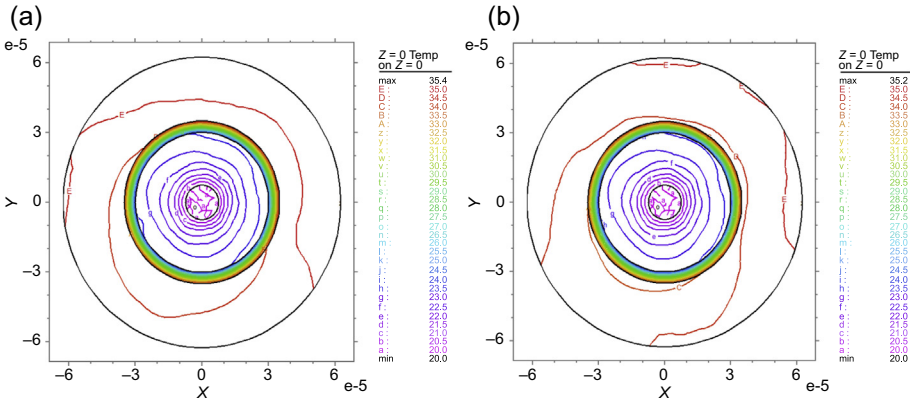


**Figure 1.17** Inlet cross-sectional temperature distribution of the fiber with the circular microchannel within a gas ring at $t = 10$ s for a flow of water with temperature of 20 °C, an external temperature of 90 °C and fluid velocity of (a) 0.005 m/s and (b) 0.01 m/s.

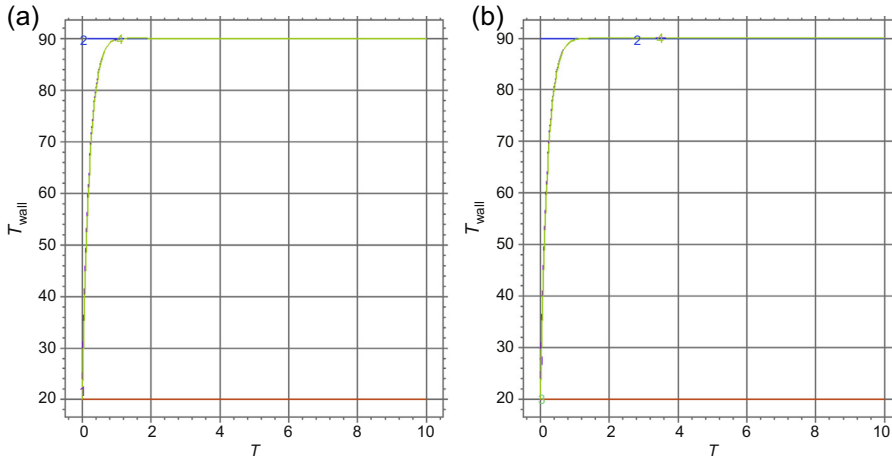


**Figure 1.18** Temperature with respect to time for a flow (in the circular microchannel) with initial temperature of 20 °C, an external temperature of 90 °C and velocity of 0.001 m/s when the fluid is (a) glycerin and (b) oil.

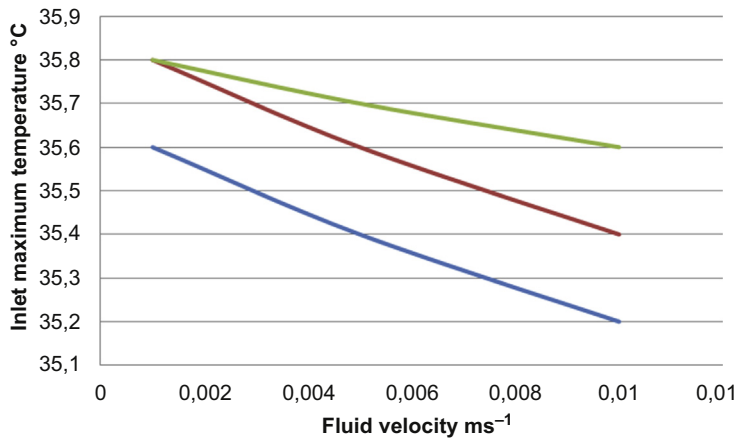


**Figure 1.19** The steady-state inlet maximum temperature of the fiber with the circular microchannel within a gas ring for a flow with temperature of 20 °C and an external temperature of 90 °C as a function of velocity for water (blue line), glycerin (red line), oil (green line).

(as expected), and that for laminar (low Re << 1) flows the greater the velocity the lower the maximum temperature, re-confirming the results of Section 1.3.2.

### *1.3.4 Effect of fiber material*

Thus far we have focused on $SiO_2$-based microstructured fibers, with cross-sections containing circular or elliptical holes, or more complex cross-sectional

geometries, for use as microfluidic devices. However, there is a fundamental limitation with glass fibers as they are essentially two-dimensional photonic crystal structures having infinite length. To gain the advantage offered by a third dimension, one has to move to other materials. Polymers are a desirable choice as they can be cast into any shape prior to fiber drawing. We have chosen polymethyl methacrylate (PMMA) as a host material, as it practically offers far more flexibility in the fiber design than could be achieved with silica-based fibers (Argyros, van Eijkelenborg, Large, & Bassett, 2005; van Eijkelenborg et al., 2003); moreover, microfluidic devices are often PMMA based. However, the use of a polymer such as PMMA has some limitations as a waveguide as significant optical losses arise due to the intrinsic absorption loss of carbon−hydrogen stretching vibration. This can be somewhat circumvented by adopting a hollow-core fiber geometry with suitable fine mesh cladding structure. PMMA can be used to create a fiber having relatively low transmission loss, moderate bandwidth, and large core. Moreover it is possible to transmit light over a very broad wavelength range, from the visible to the near infrared.

We can compare PMMA and $SiO_2$ solid structures in the case of heat transfer. We observe from Figure 1.20 that $SiO_2$ is a better thermal conductor than PMMA, offering more uniform heating. For a uniform 3-cm-length fiber of diameter of $D = 125$ μm and a medium-size $h_{air}$ of order $O(10^3)$, in the case of $SiO_2$, we observe after 2 s a temperature of 64.8 °C, whereas for PMMA there is almost uniform heating, and after 2 s, the temperature has reached 64.2 °C, a very small difference. In both cases the external temperature is 90 °C, which can be reached throughout the microchannel in about 10 s for both materials.

For the case of a fiber with a circular microchannel within a gas ring for a flow of water with temperature of 20 °C and an external temperature of 50 °C and velocity of 0.001 m/s, one can observe in Figure 1.21 that at a time of 10 s the water flow seems to

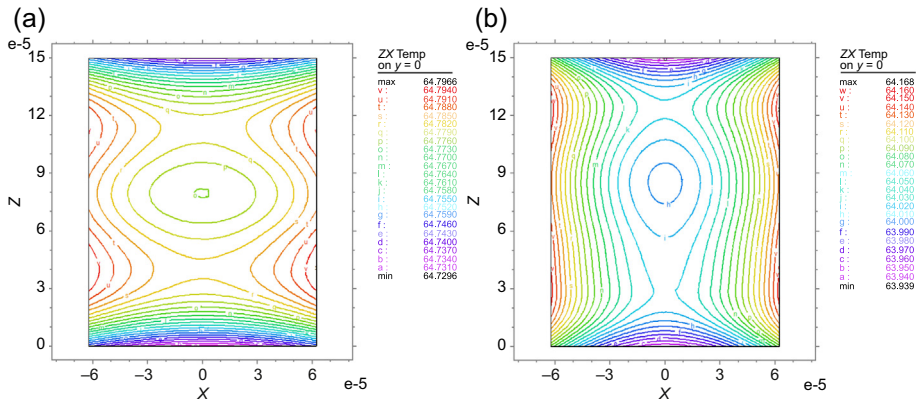


**Figure 1.20** Axial temperature distribution of the fiber (no microchannel) ($z$ is scaled) for an external temperature of 50 °C when the fiber material is (a) $SiO_2$, (b) PMMA.

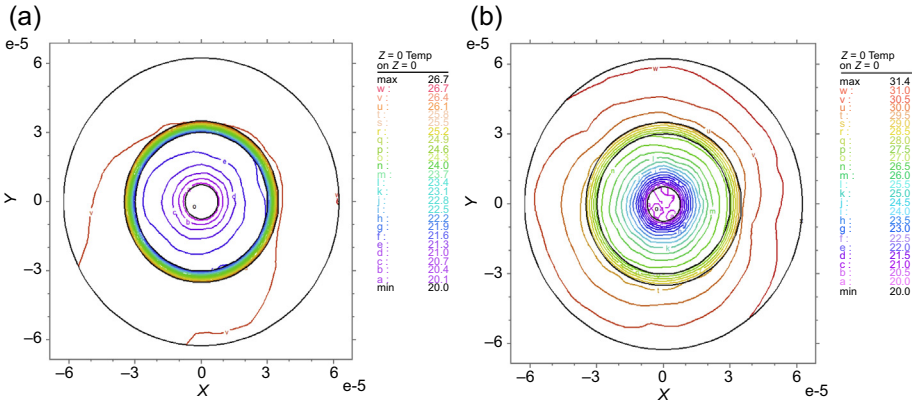


**Figure 1.21** Inlet cross-sectional of the fiber with the circular microchannel within a gas ring at $t = 10$ s for a flow of water with temperature of 20 °C and an external temperature of 50 °C and velocity of 0.001 m/s, when the fiber material is (a) $SiO_2$ and (b) PMMA.

have a cooling effect at the inlet of the microchannel where one can observe maximum temperatures of 26.7 for $SiO_2$ (Figure 1.21(a)), as opposed to 31.4 for PMMA (Figure 1.21(b)). This shows that PMMA is not as good a conductor as $SiO_2$. For the two cases considered above, the mid-channel temperature with respect to time is plotted in Figure 1.22, exhibiting no difference in behavior (the steady state can be reached in about 0.8 s for both materials). Analogous results are obtained for an external temperature of 90 °C for (see Figures 1.6(b), 1.10(a), and 1.23).

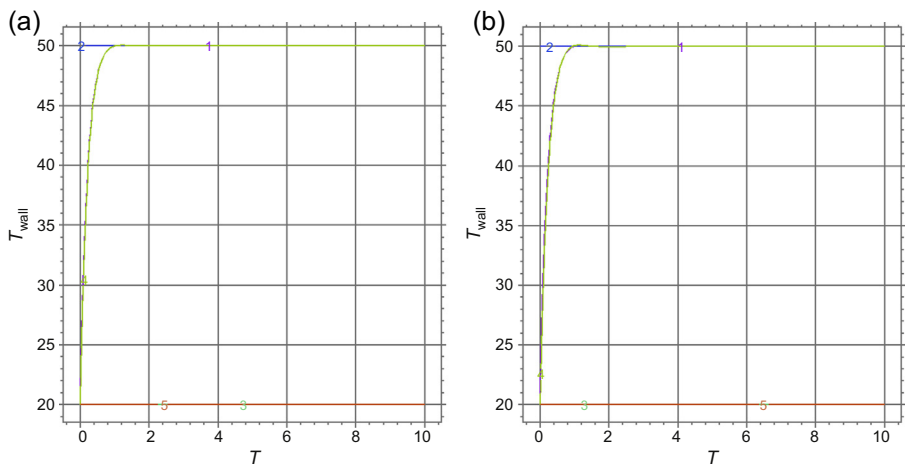


**Figure 1.22** Temperature with respect to time for water flow (in the circular microchannel) with velocity of 0.001 m/s and initial temperature of 20 °C, for an external temperature of 50 °C when the fiber material is (a) $SiO_2$, (b) PMMA.

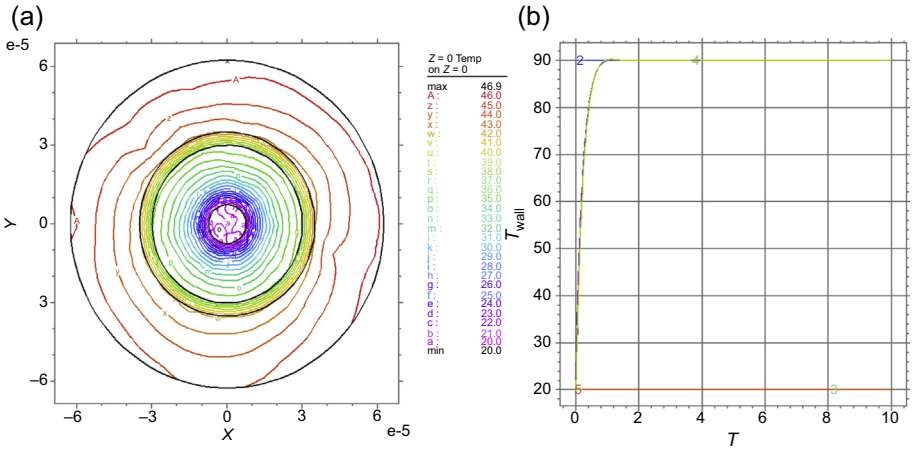


**Figure 1.23** (a) Inlet cross-sectional of the fiber with the circular microchannel within a gas ring at $t = 10$ s and (b) temperature with respect to time for water flow with velocity of 0.001 m/s, initial temperature of 20 °C and an external temperature of 90 °C, when the fiber material is PMMA.

Finally, going back to reconfirm the effect of the fluid type on the thermal behavior of the fiber (see Section 1.3.3), we consider the capillary action in PMMA for three different liquids. For a fixed flow of 0.001 m/s with temperature of 20 °C and an external temperature of 90 °C the results are shown in Figures 1.23(b) and 1.24. One can observe that water (Figure 1.23(b)) has the best cooling effect along the microchannel, followed

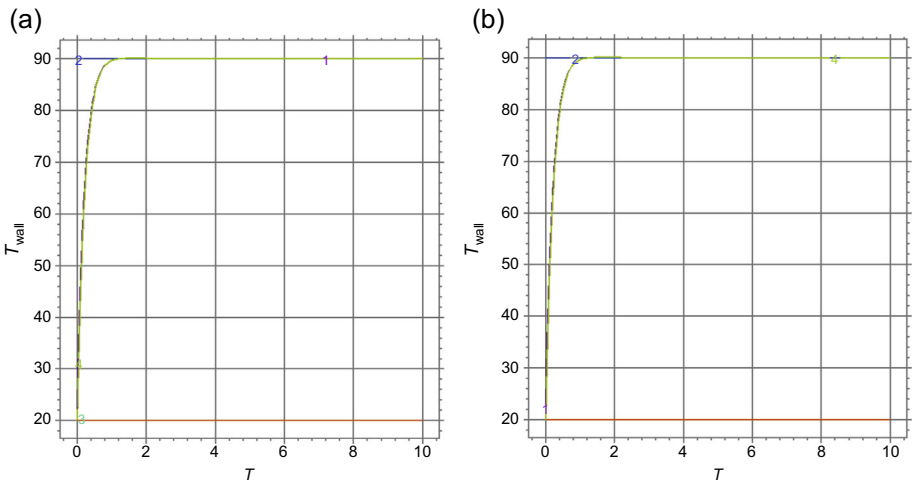


**Figure 1.24** Temperature with respect to time for a flow in the circular microchannel within a gas ring (fiber material is PMMA), with initial temperature of 20 °C, an external temperature of 90 °C and velocity of 0.001 m/s, when the fluid is (a) glycerin and (b) oil.

by glycerin (Figure 1.24(a)) and then oil (Figure 1.24(b)) with references to the steady-state times of 0.8, 1.0, and 1.2 s respectively for each liquid.

## 1.4 Conclusions

The presented results are relevant to the development of microstructured fibers with cross-sections containing circular or elliptical holes, or more complex cross-sectional geometries, with consideration given to silica and polymer materials. These can be applied for the use of microstructured fibers as microfluidic devices. The rationale behind this work is to couple the fluid transport to the transfer of heat into the fiber, creating local changes in the behavior of the fluid system. An implemented numerical solution of the time-dependent Navier−Stokes equations and the convection−diffusion equation examined the effects of flow rates and the role of heat flux in relation to the fluid characteristics. This work is of importance as one cannot assume that the flow dynamics in microstructured fibers will be the same as conventional microfluidic channels. Through the study of the heat transfer, for low Reynolds numbers, we have confirmed anticipated behavior of the fluids in the microchannel structure.

The case of the single circular microchannel surrounded by a ring of air can be seen as nothing other than an approximation of an air guiding photonic crystal fiber with a typical fine mesh lattice that forms the band gap structure. The elliptical structures are variations based on the so-called "grapefruit" fiber designs. Based on the possibility of flexible fiber designs, the rationale behind this work is to couple the fluid transport to the transfer of heat into the fiber, creating local changes in the behavior of the fluid system. Therefore, the time-dependent Navier–Stokes equations can be numerically analyzed along with the convection–diffusion equation, in order to ascertain the effects of flow rates, fluid viscosity and the channel diameter. The role of heat flux has been considered in relation to the fluid characteristics. This work is of importance as one cannot assume that the flow dynamics in microstructure fibers will be the same as conventional microfluidics channels. Through the study of the heat transfer, for low Reynolds numbers, we have confirmed anticipated behavior of the fluids in the micro-channel structure. Our approach proves to be versatile for all cases examined. The model can easily be extended for other configurations, such as multiple circular or elliptical microchannels, surrounded (or not) by a ring of gas (not necessarily air), or instead by a ring consisting of small circles or complex ellipses.

## Acknowledgments

The authors acknowledge the co-financing by the Cyprus Research Promotion Foundation and the European Fund of Regional Growth of the EU under the project ΑΝΑΒΑΘΜΙΣΗ/ΠΑΓΙΟ/308/27. P. Christodoulides, G.A. Florides, E. Davies, and K. Kalli acknowledge support by the People Program (Marie Curie Actions) of the European Union's 7th Framework Program FP7/2007-2013 under REA Grant Agreement number 608382.

## References


Argyros, A., van Eijkelenborg, M. A., Large, M. C. J., & Bassett, I. M. (2005). Hollow-core microstructured polymer optical fibre. In *The 14th international conference on polymer optical fiber*. Hong Kong: China.

Beskok, A., & Karniadakis, G. E. (1994). Simulation of heat and momentum transfer in complex microgeometries. *Journal of Thermophysics and Heat Transfer, 8*, 647−655.

Brivio, M., Fokkens, R. H., Verboom, W., Reinhoudt, D. N., Tas, N. R., Goedbloed, M., et al. (2002). Integrated microfluidic system enabling (bio)chemical reactions with on-line MALDI-TOF mass spectrometry. *Analytical Chemistry, 74*, 3972−3976.

Chen, K., & Wu, T.-E. (2000). Thermal analysis and simulation of a microchannel flow in miniature thermal conductivity detectors. *Sensors and Actuators A, 79*, 211−218.

Christodoulides, P., Florides, G., Kalli, K., & Komodromos, M. Z. (2012). *Modeling microfluidic flow and heat transfer in circular and elliptical channels in microstructure fibers*. Brussels, Belgium: SPIE Photonics Europe.

Christodoulides, P., Florides, G., Kalli, K., Koutsides, C., Lazari, L., Komodromos, M., et al. (2014). Microfluidics in microstructure optical fibers: heat flux and pressure-driven and other flows. *Procedia IUTAM, 11*, 23−33. IUTAM symposium on nonlinear interfacial wave phenomena from the micro- to the macro-scale 2013, Limassol, Cyprus.

Colin, T., & Tancogne, S. (2011). Stability of bifluid jets in microchannels. *European Journal of Mechanics B/Fluids, 30*, 409−420.

Damean, N., Regtien, P. P. L., & Elwenspock, M. (2003). Heat transfer in a MEMS for microfluidics. *Sensors and Actuators A, 105*, 137−149.

van Eijkelenborg, M., Large, M., Argyros, A., Zagari, J., Manos, S., Issa, N., et al. (2001). Microstructured polymer optical fibre. *Optics Express, 9*, 319−327.

van Eijkelenborg, M. A., Argyros, A., Barton, G., Bassett, I. M., Fellew, M., Henry, G., et al. (2003). Recent progress in microstructured polymer optical fibre fabrication and characterisation. *Optical Fiber Technology, 9*(4), 199−209.

Fan, X., & White, I. M. (2011). Optofluidic microsystems for chemical and biological analysis. *Nature Photonics, 5*, 591−597.

Farrer, N. J., Salassa, L., & Sadler, P. J. (2009). Photoactivated chemotherapy (PACT): the potential of excited-state d-block metals in medicine. *Dalton Transactions, 48*, 10690−10701.

Hassani, A., & Skorobogatiy, M. (2006). Design of the microstructured optical fiber-based surface plasmon resonance sensors with enhanced microfluidics. *Optics Express, 14*, 11616−11621.

Kandlikar, S. G., et al. (2006). *Heat transfer and fluid flow in minichannels and microchannels*. Elsevier.

Kerbage, C., & Eggleton, B. J. (2004). Manipulating light by microfluidic motion in microstructured optical fibers. *Optical Fiber Technology, 10*, 133−149.

Lien, V., & Vollmer, F. (2007). Microfluidic flow rate detection based on integrated optical fibre cantilever. *Lab Chip, 7*, 1352−1356.

Monat, C., Domachuk, P., & Eggleton, B. J. (2007). Integrated optofluidics: a new river of light. *Nature Photonics, 1*, 106−114.

Oleschuk, R. D., & Harrison, D. J. (2000). Analytical microdevices for mass spectrometry. *Trends in Analytical Chemistry, 19*, 379−388.

Plouffe, B. D., Lewis, L. H., & Murthy, S. K. (2011). Computational design optimization for microfluidic magnetophoresis. *Biomicrofluidics, 5*, 013413.

Russell, P. St J. (2003). Photonic crystal fibers. *Science, 299*, 358−362.

Sahu, K. C., Valluri, P., Splet, P. D. M., & Matar, O. K. (2007). Linear instability of pressure-driven channel flow of a Newtonian and a Herschel-Bulkley fluis. *Physics of Fluids, 19*, 122101.

Sazio, P. J. A., Amezcua-Correa, A., Finlayson, C. E., Hayes, J. R., et al. (2006). Microstructured optical fibers as high-pressure microfluidic reactors. *Science, 311*(5767), 1583−1586.

Unterkofler, S., McQuitty, R. J., Euser, T. G., Farrer, N. J., Sadler, P. J., & Russell, P. St J. (2012). Microfluidic integration of photonic crystal fibers for online photochemical reaction analysis. *Optics Letters, 37*, 1952−1954.

Yahng, J. S., Jeoung, S. C., Choi, D. S., Cho, D., Kim, J. H., Choi, H. M., et al. (2005). Fabrication of microfluidic devices by using a femtosecond laser micromachining technique and μ-PIV studies on its fluid dynamics. *Journal of the Korean Physical Society, 47*(6), 977−981.

Yu, R.-J., Zhang, B., Chen, M.-Y., Huo, L., Tiam, Z.-G., & Bai, X.-Z. (2006). A new solution of reducing polymer optical fiber losses. *Optics Communications, 266*, 536−540.

This page intentionally left blank

# Drawn metamaterials

2

*A. Argyros, A. Tuniz, S.C. Fleming, B.T. Kuhlmey*
Institute of Photonics and Optical Science (IPOS), The University of Sydney, NSW, Australia

## 2.1 Introduction

Metamaterials are composite materials typically composed of arrays of small metallic resonators structured on the microscale or nanoscale (McPhedran, Shadrivov, Kuhlmey, & Kivshar, 2011; Walser, 2003). For electromagnetic waves with wavelengths larger than the scale of the resonators and their periodicity, each resonator acts as an artificial atom, providing electromagnetic properties that can be engineered and go beyond anything available in natural materials. This versatility in design, and therefore achievable electromagnetic properties, has made metamaterials a very exciting and promising research area in recent years, yielding many interesting and unique phenomena such as negative refraction and left-handed materials (Smith & Kroll, 2000; Veselago, 1968), effective magnetic responses at high frequency and from non-magnetic materials and negative permeability (Smith, Padilla, Vier, Nemat-Nasser, & Schultz, 2000), invisibility cloaking (Leonhardt, 2006; Pendry, Schurig, & Smith, 2006; Schurig et al., 2006), invisible materials (Tuniz, Kuhlmey, Chen, & Fleming, 2010), a variety of lens designs that beat the diffraction limit (Belov et al., 2010; Lemoult, Fink, & Lerosey, 2011; Pendry, 2000) and extremely subwavelength cavities (Lemoult, Kaina, Fink, & Lerosey, 2013).

This active interest in metamaterials has seen a rapid development in their design and fabrication. Given the requirement of subwavelength structure, much work has taken place at radio and microwave frequencies, where the wavelength is large and subwavelength structures are easier to fabricate (e.g. Belov et al., 2010; Lemoult et al., 2013; Smith & Kroll, 2000). Subsequently, smaller scales were achieved through various microfabrication and nanofabrication techniques to demonstrate metamaterials operating all the way through to the optical and UV (Xu, Agrawal, Abashin, Chau, & Lezec, 2013; Yao et al., 2008). The corresponding decrease in feature size creates considerable fabrication challenges, particularly with regard to the geometry of metamaterials that can be made and the volumes of metamaterial that can be produced.

The topic of this chapter is the use of fibre drawing as a technique for metamaterial fabrication. As such, this chapter does not aim to give a comprehensive overview of the vast field of metamaterials in its entirety. Instead, it will begin by considering two of the earliest proposed designs — a wire array metamaterial which has a designed electric permittivity and split-ring resonators which have designed magnetic permeability — which have now become canonical examples that illustrate important concepts. Following that discussion, fabrication approaches will be explored in order to place

**Optofluidics, Sensors and Actuators in Microstructured Optical Fibers.** http://dx.doi.org/10.1016/B978-1-78242-329-4.00002-3

the topic of this chapter in context, before describing the fibre drawing methods in Section 2.2. In Sections 2.3 and 2.4 specific types of drawn metamaterial with designed electric and magnetic response will be discussed in more detail, before describing one of the most promising applications of drawn metamaterial in Section 2.5 – hyperlenses that beat the diffraction limit. Finally, the limitations of the drawing method and future directions of this field will be discussed in Sections 2.6 and 2.7.

### 2.1.1 Wire arrays – electric metamaterials

The first canonical example of metamaterials is a wire array (Figure 2.1), which allows control over the electric response. While such arrays had already been studied in the 1950s and 1960s in the context of antennas and radio and microwave manipulation (Barlow & Cullen, 1953; Rotman, 1962), their potential in conjunction with magnetic resonators as metamaterials was made clear by Pendry, Holden, Stewart, and Youngs, (1996). The array is periodic with period $a$, containing wires of diameter $d$, embedded in a dielectric background of index $n_d$. Its properties are considered at a frequency such that the free-space wavelength $\lambda \gg a$. This structure is clearly anisotropic, as the wires are conducting along their length but not conducting across the array.

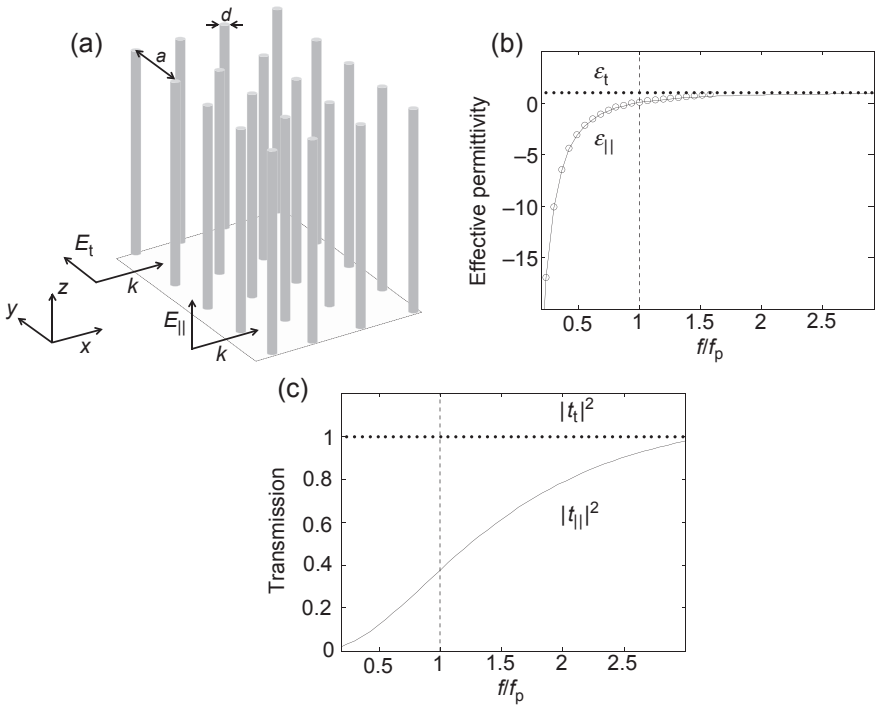


**Figure 2.1** (a) Structure of wire array metamaterial. (b) Resulting permittivity and (c) typical transmission of a thin slab of wire medium for polarisations in the transverse plane and parallel to the wires.

As such, for radiation polarised transversely (in the plane of the array), the structure will behave as a dielectric with a permittivity close to $\varepsilon_d = n_d^2$. However, electric fields polarised parallel to the wires can cause currents to flow along the wires, and the structure will exhibit metallic behaviour, allowing its permittivity $\varepsilon_{zz}$ to be described by a Drude model (Simovski, Belov, Atrashchenko, & Kivshar, 2012). The currents will create magnetic fields around each wire, which will result in additional forces on the electrons through induction, changing their net acceleration. This can be considered as a change in the electrons' effective mass, with the consequence that the plasmonic response will not be the same as for the bulk metal (Pendry et al., 1996). It can be shown that the electromagnetic response of wire arrays is well described by a geometry-dependent Drude-like axial permittivity (Belov et al., 2003)

$$\frac{\varepsilon_{zz}(k)}{\varepsilon_d} = 1 - \frac{k_p^2}{k^2 - i\gamma k - k_z^2}, \tag{2.1}$$

where $k$ is the wavenumber in the dielectric, $k_p$ is a geometry-dependent plasma wavenumber and $\gamma$ is a damping factor. In particular, this response is dependent on the component of the wavevector parallel to the wires $k_z$ – a manifestation of nonlocality (Belov et al., 2003). Expressing this in terms of frequency $f = kc/n_d 2\pi$ at normal incidence ($k_z = 0$) one obtains

$$\frac{\varepsilon_{zz}(f)}{\varepsilon_d} = 1 - \frac{f_p^2}{f^2 - i\xi f}, \tag{2.2}$$

where $\xi$ is a damping factor, and $f_p$ is a lowered, geometry-dependent, effective plasma frequency, which can be approximated by (Maslovski & Silveirinha, 2009)

$$f_p^2 = \frac{(c/n_d)^2}{2\pi A_{cell} \ln\left[a^2/d(2a-d)\right]}, \tag{2.3}$$

for $A_{cell}$ the average area per wire of the metamaterial. Overall, below the effective plasma frequency the wire array can be described as an *indefinite* medium (Smith & Schurig, 2003) with permittivity tensor

$$\underline{\varepsilon} = \begin{pmatrix} \varepsilon_t & 0 & 0 \\ 0 & \varepsilon_t & 0 \\ 0 & 0 & \varepsilon_{zz} \end{pmatrix}, \tag{2.4}$$

where $\varepsilon_t \approx \varepsilon_d > 0$ and $\mathrm{Re}(\varepsilon_{zz}) < 0$, reflecting the metallic behaviour for one polarisation, as shown in Figure 2.1(b).

Since the effective plasma frequency depends on the size and spacing of the wires, the internal structure of the metamaterial determines its bulk properties. In this case a desired permittivity is achieved through the tailored effective plasma frequency.

Periodicity and uniformity of the array are assumed for these bulk descriptions to be valid, otherwise the values of $a$ and $d$ are not uniquely defined and the strength of the induction between neighbouring wires would vary. In addition, if the period is not small compared to the wavelength, propagation of waves can no longer be described by a single permittivity tensor. In particular when the period approaches $\lambda/2n_d$ Bragg scattering modifies the propagation of light, and multiple bands and bandgaps can emerge.

The indefinite permittivity tensor results in unusual effects in such metamaterials. Waves propagating across the array, as in Figure 2.1(a), experience either a dielectric material if polarised in the transverse plane or a Drude metal if polarised parallel to the wires. The wire medium is thus transparent for one polarisation and a high-pass filter in the other, as in Figure 2.1(c). Waves at oblique propagation angles compared with the array as in Figure 2.2 also have very different properties depending on their polarisation. Transverse Electric (TE) waves only experience the positive transverse permittivity and propagate as ordinary waves in a dielectric. Transverse Magnetic (TM) waves, however, have electric field components along the wires as well as across the wires and are thus affected simultaneously by both the positive transverse and negative longitudinal permittivity components, fully experiencing the dual metal-dielectric nature of the wire array. As outlined in detail in Section 2.5, such waves have hyperbolic, unbounded isofrequency curves, which allow propagation of arbitrarily large wavevectors, and thus are not subject to the diffraction limit, meaning propagation without diffraction can be achieved. Hence, such wire arrays can be used as a diffraction limit-beating *hyperlens* (Belov et al., 2010; Casse et al., 2010), in which otherwise evanescent waves propagate, enabling subdiffraction limited imaging.

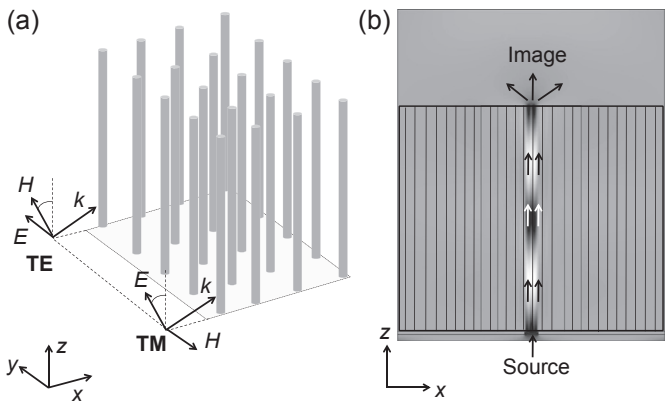


**Figure 2.2** Geometry of wire array metamaterial showing the case of (a) transverse electric (TE) (ordinary) and transverse magnetic (TM) (extraordinary) waves. (b) The TM waves, having an electric field component parallel to the wires, can propagate along the wire array without diffracting.

### 2.1.2 Split-ring resonators – magnetic metamaterials

The second canonical example of metamaterials, also introduced by Pendry, Holden, Robbins, and Stewart (1999), is an array of split-ring resonators (SRR) which allow control of the magnetic response (Figure 2.3). Each resonator consists of an open loop of wire, which can be described by an LC circuit. Current flowing around the loop can be induced by an oscillating magnetic field perpendicular to the plane of the loop. This produces a magnetic dipole moment perpendicular to the plane of the loop, which results in the self-inductance $L$, and a potential difference across the gap of the loop, described by the capacitance $C$. The shape and size of the resonator determine $L$ and $C$ and thus the resonance frequency. If the resonance frequency corresponds to wavelengths much larger than the period of the array, the medium's response can be described in terms of the averaged induced magnetic dipole moment, which is particularly strong around the resonance frequency, yielding a nonzero magnetic susceptibility and thus an engineered magnetic permeability. For appropriately sized resonators, the LC resonance can yield an artificial magnetic response at any frequency from otherwise non-magnetic materials. The permeability is only resonant in the direction of the magnetic field that can excite the current in the loop – so that the component of the relative permittivity tensor perpendicular to the plane of the loop takes the form (Pendry et al., 1999)

$$\mu_{zz}(f) = 1 - \frac{F}{(1 - f_0^2/f^2) + i\zeta/f}, \tag{2.5}$$

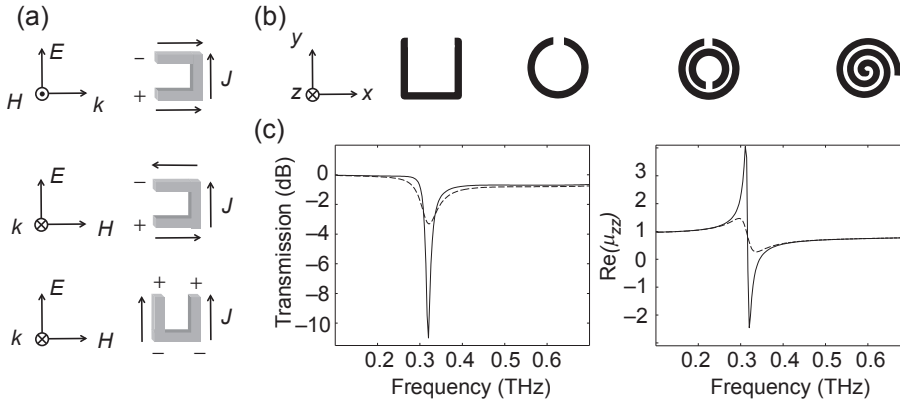


**Figure 2.3** (a) Split-ring resonator structure showing possibilities for exciting the magnetic resonance through a magnetic field perpendicular to the plane of the resonator (upper panel) or an electric field parallel to the capacitive gap (middle panel). The arrangement in the lower panel does not excite the resonance. (b) Variations of the resonator structure. (c) Manifestation of a magnetic resonance in the transmission spectrum, giving rise to a reduced transmission, and the resulting real part of the permeability, for a weaker (dashed line) and stronger (solid line) resonance. Note that the permeability can be negative for a sufficiently strong resonance.

where $F$ is a volumetric filling factor, $f_0$ is the resonance frequency and $\zeta$ is a damping factor. If the resonance is sufficiently strong and the resonators sufficiently densely packed, the permeability can even become negative – in which case magnetic reflection can be observed (Figure 2.3(c)).

Magnetic fields in the plane of the loop do not result in an induced current around the loop and thus cannot excite the magnetic resonance so that the relative permeability tensor components in that plane remain unchanged. However, an electric field parallel to the gap of the loops can also excite the resonance, leading to an electric dipole moment and a resonant permittivity. As the magnetic and electric resonances are two manifestations of the same resonance of currents, the material is in fact bi-anisotropic: an electric field excitation also generates a magnetic response, and a magnetic field excitation generates an electric response. Electric fields orthogonal to the resonator gap cannot excite the fundamental resonance (Pendry et al., 1999).

At frequencies below the resonance the magnetic dipole and currents are weak and in phase quadrature with the exciting field (in phase with the time derivative of the flux). At resonance, the amplitude of the dipoles is much enhanced and goes through a $\pi$ phase shift; currents are maximum and thus so are ohmic losses. At frequencies much above the resonance, the currents and induced magnetic dipole are again weaker. The resonant permeability is thus accompanied by strong losses at resonance. A more complete treatment needs to incorporate strong coupling through the mutual inductance of resonators in the array and other resonances than the fundamental resonance. This leads to a complex frequency-dependent set of permittivity, permeability and magnetoelectric coupling.

Variants in shape and complexity of magnetic resonators have been reported, for example double resonators, as shown in Figure 2.3(b). These operate also as LC resonators, following the same principles as the single split-ring – however, the currents of their fundamental magnetic resonance lead to induced dipoles of opposite signs in the two gaps, which compensate each other – this means that the fundamental magnetic resonance is not dipolar but quadrupolar to lowest order and cannot be excited by electric fields. Double split-ring resonators (DSRR) can thus provide a pure magnetic response without associated resonant dielectric response and without magnetoelectric coupling and bi-anisotropy. Furthermore, because with the same outer dimensions DSRR have higher capacitance and inductance, their fundamental resonance frequency corresponds to longer wavelengths. The principle of a loop of current resulting in a magnetic field remains the fundamental mechanism behind all metal-based artificial magnetic responses. More complex electromagnetic behaviour can arise through combinations of the basic electric and magnetic responses described here. For example, the appropriate combination of negative permittivity and permeability will give rise to negative refractive index (Veselago, 1968).

### 2.1.3 Fabrication of metamaterials

Apart from the wire arrays and resonators described above, other metamaterial designs have been proposed and demonstrated, based on phased-array antennas, fishnet designs, metal–dielectric multilayer stacks and many others. As for the basic examples

of the previous sections, their properties arise from the subwavelength structure, and their description in terms of bulk parameters is appropriate. The subwavelength requirement, however, can pose a challenge in the fabrication.

Metamaterials for (low) frequencies of order 1−10 GHz ($\lambda = 3-30$ cm) can be assembled easily by hand from wire, or by utilising PCB writing techniques, as features on the sub-mm-to-cm scale are sufficient. This provided a useful experimental tool for the demonstration of, for example, the first invisibility cloak (Schurig et al., 2006) (at 10 GHz using PCB techniques) and wire array-based hyperlens with a resolution beyond the diffraction limit (Belov et al., 2010) (at 1 GHz by manual assembly).

Moving to higher frequencies, from 100's of GHz to the UV, requires correspondingly smaller structures, and techniques such as lithography, nanoimprinting, self-assembly and electrochemical techniques have been employed. Whilst capable of producing the required structures, these techniques can suffer from two drawbacks: (1) they produce planar structures, with limited reach along a third axis, and (2) they can be expensive, time-consuming and low-yield, meaning that they would not be commercially viable. Whilst a large range of metamaterials has been demonstrated using these methods, they do limit the geometries and arrangements that have been experimentally investigated. For example, a hyperlens is intrinsically a three-dimensional object, being a two-dimensional array of wires in one plane that extends along a third axis, that would be difficult to fabricate using planar techniques. This chapter will focus on using fibre drawing techniques to produce metamaterials and address these two drawbacks.

## 2.2 Fibre-based metamaterials

Fibre drawing is an established industrial technique, and in the context of microstructured optical fibres (MOF) − the topic of this book − is used to produce large volumes (kms) of fibre which contain structure on the micron scale in the form of the microscopic holes along the fibre's length (Russell, 2006). Hence, it was recognised as an efficient and cost-effective way to produce large volumes of material structures on the micron scale, as required for metamaterials, and furthermore produce 3D metamaterials not being restricted to planar geometries. The aim of developing such a method was to address the fabrication challenges mentioned above − both in the efficiency of fabrication and the range of metamaterials that can be fabricated.

It is clear that filling the longitudinal holes of an MOF with metal will produce a wire array metamaterial. Wire arrays are inherently longitudinally invariant and thus compatible with such a process. Drawing multiple metallic wires in glass represents an extension of the Taylor wire process, which has been used to produce thin (single) wires encased in a dielectric since the 1920s (Taylor, 1924). Other structures, such as resonators, will also operate using the same principles if they extend longitudinally, for example, to form a slotted cylinder. Continuing to work with the dimensions of MOF − with micron-sized features in the structure − means that these drawn structures will be metamaterials at correspondingly larger wavelengths, of 10s of microns, up to

several mm. Hence, this work has been focused on the mid-IR to the THz frequency range to which those wavelengths correspond.

The specific fabrication technique employed (Tuniz, Lwin, Argyros, Fleming, & Kuhlmey, 2012) is an extension of the methods developed for MOF (Knight, Birks, Russell, & Atkin, 1996) and in particular, microstructured polymer optical fibres (mPOF) (Argyros, 2009, 2013). A large cm-scale preform with the correct structure is assembled from polymer and metal and drawn to fibre using an optical fibre draw tower. In principle, the structure is scaled down unperturbed to the correct dimensions, whilst long lengths (large volumes) of metamaterial fibre containing the micron-scaled metallic inclusions are produced. The technique relies on using a compatible metal-polymer combination, such that the metal's melting point is below the drawing temperature of the polymer. Thus, the metal is liquid during the fibre draw and in principle no different to having any other fluid in the holes (such as air in MOF fabrication); however, as discussed in Section 2.6, differences do arise from the properties of the fluid. The technique also relies on the ability to assemble a preform of the correct structure, which can be achieved through variation of stacking methods and other techniques already developed for MOF fabrication. A schematic of the fabrication method is shown in Figure 2.4, whilst details of the fabrication of specific structures are given in Sections 2.3–2.6.

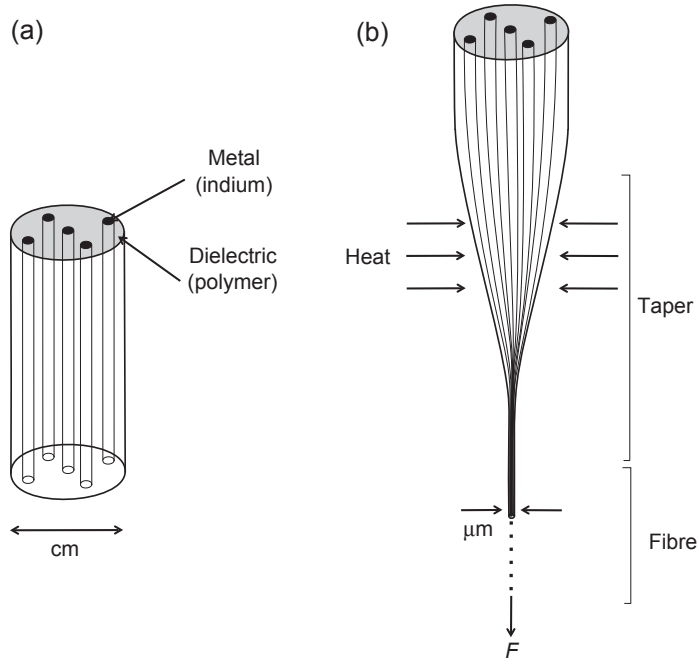


**Figure 2.4** Schematic of the drawn metamaterial fabrication method in which (a) a cm-scale preform containing the desired metal–dielectric structure is (b) drawn to fibre with micron-scale dimensions.

Metamaterials have been fabricated using this drawing method and polymethylmethacrylate (PMMA), polycarbonate (PC) and the cyclo olefin polymer Zeonex®, which had already been used in mPOF fabrication. Their glass transition temperatures ($T_g$) range from 115 to 150 °C, and fibre drawing is done at higher temperatures in the range 160−220 °C (Argyros, 2013). The compatible metal used was indium, which has a melting point of 157 °C and is thus liquid during fibre drawing. There are specific advantages to this material system − the metal and polymers are readily available and inexpensive, they require low processing temperatures and the polymers are easily machined − which allowed the work to progress quickly. For work at THz frequencies, polymers such as Zeonex also offer higher transparency (Anthony, Leonhardt, Argyros, & Large, 2011).

Apart from addressing the scalability of fabrication and extending the metamaterial geometries that can be made, the drawing method is itself limited to producing (1) the longitudinally invariant fibre and (2) the tapered neck-down region (Figure 2.4(b)), thus it is limited to producing metamaterials that are either invariant along one direction or consist of a tapered geometry. As noted, wire arrays and resonators are compatible with this, as are wire array hyperlenses. One additional consideration is nonlocal effects. As the structures are electrically conducting along one axis, fields in one position may result in currents and fields in a different position along that axis. This is also referred to as spatial dispersion, which describes the dependence of the properties of the metamaterial on the wavevector (Belov et al., 2003), in addition to frequency (see for example Eqn (2.1)); this is discussed further in Section 2.4.

## 2.3 Drawn wire array metamaterials

A schematic of the fabrication method for wire array metamaterials is shown in Figure 2.5 and begins with the making of single wires, using the Taylor wire process. A polymer tube made of PMMA or Zeonex with approximately 1-mm inner diameter and 5 mm outer diameter is prepared, and molten indium is introduced into the hole using a vacuum. This single-wire preform is drawn to a fibre of 300−500 μm diameter, and many such fibres are stacked inside a larger consolidating tube to form the wire array preform as in Figure 2.5(c). Depending on the desired final dimensions, the wire array preform is drawn directly to fibre, or stretched to an intermediate size, placed in further consolidating jackets and drawn further. These additional consolidating jackets may be removed post-drawing by controlled etching, or by using different polymers for the wire array and the jacket, such that the jacket can be dissolved without affecting the remaining structure. Both PMMA and Zeonex were used for such structures, although Zeonex is preferred for work at THz frequencies due to its higher transparency (Anthony et al., 2011).

This basic method allowed the first drawn metamaterials to be fabricated − a wire array metamaterial with 8 μm diameter wires at 100 μm spacing (Tuniz et al., 2010), shown in Figure 2.6(b). Individual fibres were manually consolidated into an array one fibre thick and several cm in size, as in Figure 2.6(a). Such arrays were characterised as

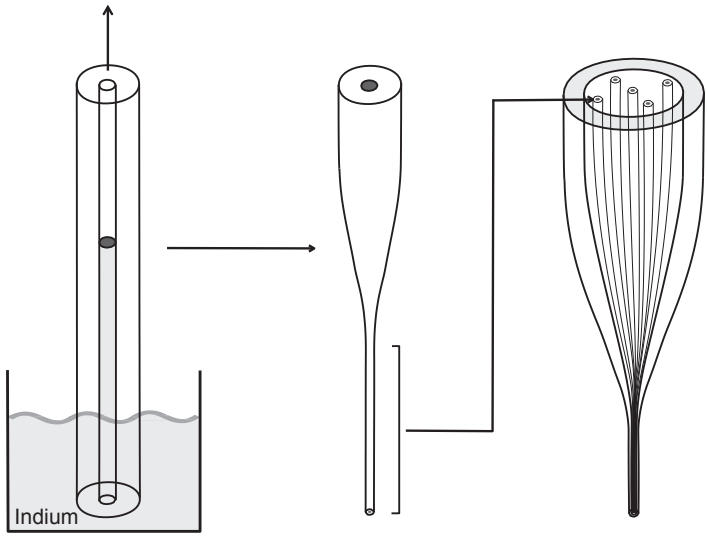


**Figure 2.5** Schematic of fabrication method for wire array metamaterials.

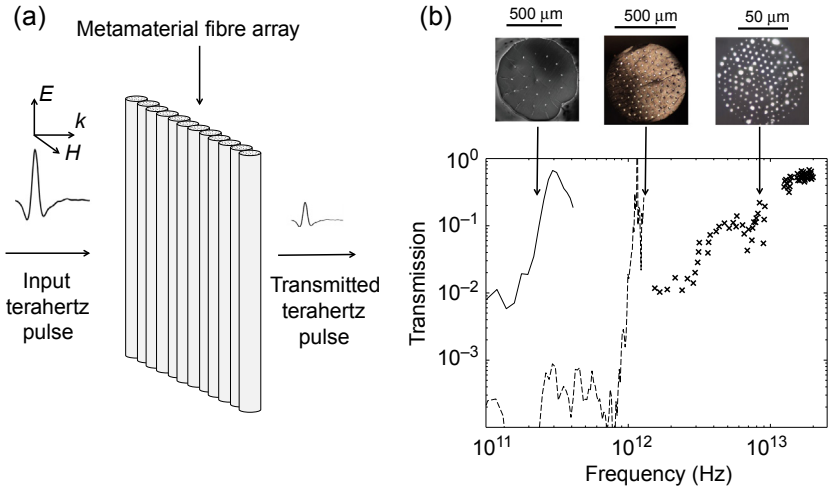


**Figure 2.6** (a) Metamaterial wire array fibres are assembled into an array one fibre thick and their transmission spectra are measured. (b) The results for three examples are shown, with the expected high-pass filtering behaviour clearly observed. Microscope images of the arrays are also shown in each case.
Adapted from Tuniz et al. (2010) and Naman et al. (2013).

a Drude metal in the THz frequency range using THz time domain spectroscopy (TDS). The expected high-pass filtering behaviour was observed, and the effective plasma frequency was shown to be approximately 100 GHz. Further drawing of

similar structures to smaller dimensions (Naman et al., 2013) shifts the plasma frequency higher, for example to 1 THz with 12 μm wires at 56 μm spacing and to approximately 15 THz with 2 μm wires at 6 μm spacing (Figure 2.6(b)). These structures were characterised using THz TDS and FTIR spectroscopy, respectively. This fabrication technique can thus produce large volumes of wire array materials with an effective plasma frequency that can be tuned over two orders of magnitude, up to the edge of the mid-IR. The observed plasma frequencies were in agreement with Eqn (2.2). While Eqn (2.2) is derived for perfect metal wires much thinner than the wire spacing, the agreement indicates that the cases considered here sufficiently satisfy this approximation.

## 2.4 Drawn magnetic metamaterials

Drawn magnetic metamaterials based on single and double split-ring resonators (SRR/DSRR) have also been produced, using the method shown in Figure 2.7 (Singh et al., 2012; Tuniz et al., 2011). A sheet of indium is rolled into a cylinder around a polymer tube such that a gap remains along its length, which forms the capacitive gap in the resonator. The gap is kept open by a polymer rod, and the entire structure is inserted into a consolidating tube. In the case of the SRR, this forms the final preform. In the case of the DSRR, this forms the inner ring, and a second sheet of indium is wrapped around this in a similar manner, followed by a further consolidating tube. The preform is then drawn to fibre through one or multiple steps, depending on the required dimensions. The result is perhaps more appropriately described as a slotted *cylinder* resonator.

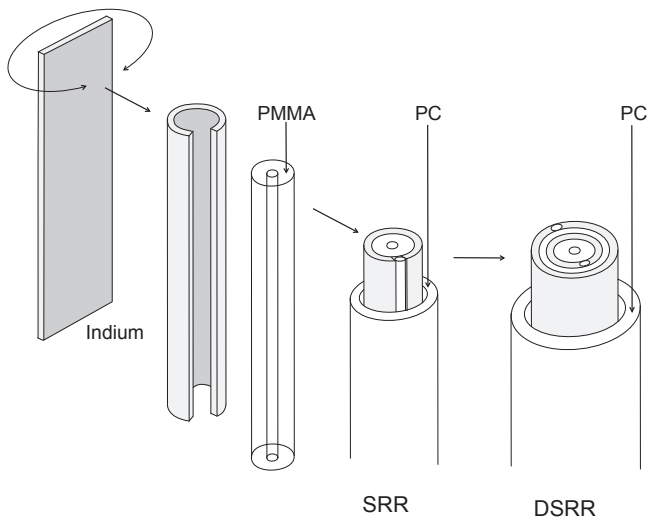


**Figure 2.7** Schematic of fabrication method for drawn single and double split-ring resonators (slotted cylinder resonators).

The larger amount of metal and the geometry of the structure caused complications in the fabrication. The furnace used to heat the preforms is a radiative furnace; thus, encasing the preform in layers of metal serves to insulate the inner parts, resulting in an undesirable temperature gradient, which translates to a viscosity gradient. This creates a problem as the inner region of the preform remains cold and too viscous to be drawn. This was solved by using a hollow tube made of PMMA on the inner part ($T_g = 115\ ^\circ C$) and a PC tube on the outer part ($T_g = 150\ ^\circ C$) of the preform. The lesser quantity of material in the centre and the lower $T_g$ meant that whilst the temperature gradient could not be avoided, the viscosity gradient was sufficiently reduced to allow successful drawing (Tuniz et al., 2011).

Examples of the resonators produced are shown in Figure 2.8(b). Again, these resonator fibres were manually assembled into arrays one fibre thick and several cm in size and characterised using THz-TDS, as in Figure 2.8(a). A transmission dip corresponding to excitation of the magnetic resonance was observed in the 100−500 GHz frequency range, depending on the size and structure of the resonators (Singh et al., 2012; Tuniz et al., 2010).

These resonators can be used to illustrate the onset of spatial dispersion arising from their longitudinal invariance (Tuniz et al., 2012). Figure 2.8(a) and (c) show that changing the incidence angle of the radiation such that the wavevector has a component along the fibres results in a shift of the resonance to higher frequency. This is understood by considering the excitation of the resonance as the coupling between the incoming plane wave and the resonant mode of the longitudinally invariant resonator. Such a mode (treated as a waveguide mode) will correspond to a particular longitudinal wavenumber $k_z$ and will be excited when phase matched to the plane wave in the longitudinal direction

$$k_z = \frac{n\omega}{c}\sin\theta, \tag{2.6}$$

for $\omega$ the angular frequency of the wave and $n$ a uniform index in which the resonator is assumed to be embedded. The resonant mode will also satisfy the Helmholtz equation

$$\left(\nabla_t^2 + \frac{n^2\omega^2}{c^2} - k_z^2\right)\mathbf{E} = 0. \tag{2.7}$$

Taking the metal to be a perfect conductor, the resonant modes satisfy $\mathbf{E} = 0$ at the metal boundary in addition to Eqn (2.7). This occurs independently of $\omega$ and $k_z$, so combinations of these that produce a constant $n^2\omega^2/c^2 - k_z^2$ term in Eqn (2.7) will correspond to the resonant mode. Taking the resonance frequency to be $\omega_0$ at normal incidence ($k_z = 0$) and considering Eqn (2.6) allow the resonance frequency as a function of incident angle to be determined as

$$\omega(\theta) = \frac{\omega_0}{\sqrt{1 - \sin^2\theta}}. \tag{2.8}$$

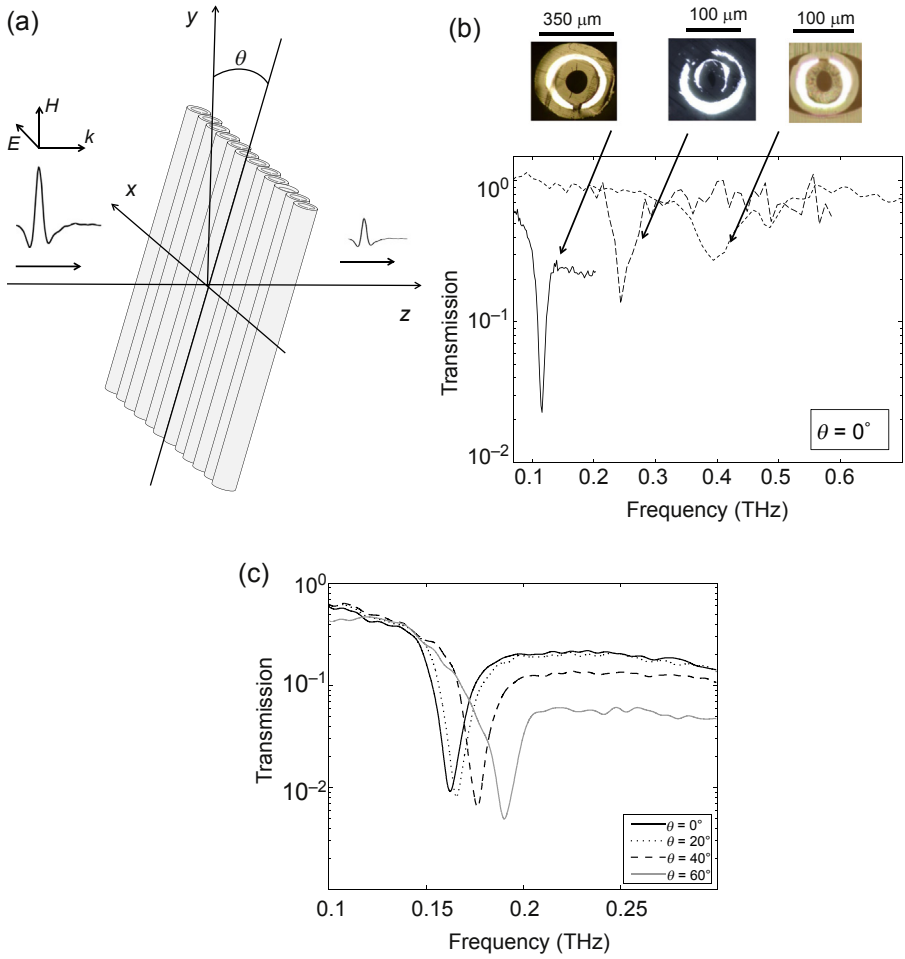


**Figure 2.8** (a) Resonator fibres are assembled into an array one fibre thick and their transmission spectra are measured. Spatial dispersion becomes evident when the wavevector has a component along the fibres, for $\theta > 0$. (b) The results for three examples at normal incidence are shown, with the magnetic resonance corresponding to the dip in transmission. (c) The spatial dispersion causes the resonance to shift to higher frequencies for larger incidence angles. Adapted from Tuniz et al. (2011) and Singh et al. (2012).

The resonators fabricated here, however, are not embedded in a uniform medium – they are embedded in polymer whilst the radiation is incident from air. To account for this, the index in Eqn (2.6) is set to 1 for air, defining $k_z$ in air, whilst the index in Eqn (2.7) is set to the polymer index $\tilde{n}$. This modifies the resonance frequency to

$$\omega(\theta) = \frac{\omega_0}{\sqrt{1 - \sin^2 \theta/\tilde{n}^2}}. \tag{2.9}$$

The observed spatial dispersion of the resonators, such as in Figure 2.8(c), shows excellent agreement with Eqn (2.9), taking $\tilde{n} = 1.65$, which is the average refractive index of the polymers used, in which the field is mostly concentrated.

## 2.5 Applications

The transverse transmission properties of metamaterial fibres discussed above can straightforwardly be used for simple applications. Wire arrays can behave as polarisers or high-pass filters and magnetic resonators as a notch filter (e.g. Figure 2.1(c) and 2.3(c)). Whilst this in itself is interesting and important, particularly at THz frequencies where options for optical components are limited, it does not exploit the behaviour that is unique to metamaterials.

More interesting applications can be obtained by exploiting one of the unique features of metamaterials. The relevant example here is of wire array fibres and their indefinite permeability tensor. These fibres' behaviour as a metal along the fibre but as a dielectric across the fibre can be used to build a hyperlens for THz frequencies. Two such hyperlenses were demonstrated: straight hyperlenses from drawing a wire array preform and a tapered hyperlens from the neck-down region of the preform. These have the unique property of transmitting subwavelength information from the near field of an object over long distances and are perfectly matched to the drawing method. The tapered neck-down region can also focus light to subdiffraction-limited spot sizes or conversely magnify subwavelength details from the near field to sizes where they can be seen in the far field.

To describe the operation of the hyperlenses, the wire array metamaterial described in Section 2.1.1 and Figures 2.1 and 2.2 is considered in more detail. Its permittivity tensor is given in Eqn (2.4), with $\varepsilon_t > 0$ in the transverse plane ($xy$ plane), and with $\varepsilon_{zz} < 0$ along $z$ to which the wires are directed. Spatial features in $x$ form an image, which will be transmitted along the hyperlens in the $z$ direction, such that the electric field is given by

$$E = E_0 \exp[i(k_x x + k_z z - \omega t)]. \tag{2.10}$$

As for any uniaxial material, the wire medium supports ordinary and extraordinary waves (e.g. the TE and TM waves, respectively, in Figure 2.2(a)). The extraordinary waves, having a nonzero electric field component along $z$, satisfy the dispersion relation

$$\frac{k_x^2}{\varepsilon_{zz}} + \frac{k_z^2}{\varepsilon_t} = k_0^2. \tag{2.11}$$

As the wire medium is indefinite below its plasma frequency, that is the diagonal components differ in sign, the $\mathbf{k}$ vector components for a given frequency all lie on a hyperbola (see Figure 2.9). Since the hyperbola extends to infinity, there are propagating solutions to the wave equation for $\mathbf{k}$ vectors with arbitrarily large values of $k_x$, meaning

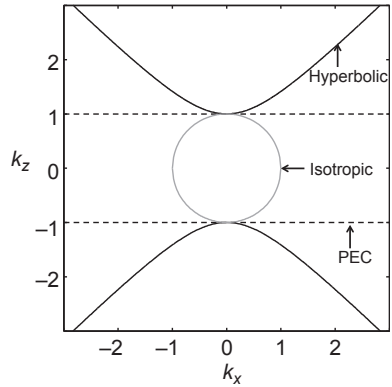


**Figure 2.9** Schematic of the spatial isofrequency contours for isotropic media ($\varepsilon_{zz} = \varepsilon_t$, here taken to be unity), hyperbolic media ($\varepsilon_t > 0$, $\varepsilon_{zz} < 0$) and wire media composed of perfect electric conductors (PEC) ($\varepsilon_t > 0$, $|\varepsilon_{zz}| \to \infty$).

that all spatial frequencies along $x$ can propagate. As a result, small features along $x$ which correspond to high spatial frequency components (large $k_x$) can propagate along the fibre, overcoming the classical diffraction limit. For comparison, in isotropic media Eqn (2.11) describes a circle, which has a finite range in $k_x$. Larger $k_x$ containing information about small features in an image correspond to evanescent modes which exist only in the near field and decay exponentially. The evanescent decay of these high spatial frequencies (higher than $\varepsilon^{1/2}k_0$) is what gives rise to the diffraction limit — however, as these do not decay in the example here, the diffraction limit does not apply. A resolution limit is, however, imposed by the spacing between the wires.

If the wires in the medium are good conductors then $|\varepsilon_{zz}| \gg \varepsilon_t$ and Eqn (2.11) can be simplified to

$$k_z(k_x) \sim n_d \omega / c. \tag{2.12}$$

This means that $k_z$ is constant for all values of $k_x$, and therefore all spatial frequencies propagate with the same phase velocity and with the energy flowing along the wires. The wire medium then constitutes a highly directive, diffractionless imaging device, and the electromagnetic waves are said to be 'canalized' (Belov, Simovski, & Ikonen, 2005). This canalisation regime (illustrated in Figure 2.2(b)) requires that the wavelength be much larger than the spacing between wires, which in turn must be larger than the skin depth of the metal (Silveirinha, Belov, & Simovski, 2008). (At terahertz frequencies, the skin depth is of the order of a few hundred nanometres.)

Wire media thereby allow the transport of subdiffraction spatial field distributions, without loss in resolution. This can occur over propagation distances of several wavelengths and with relatively low losses, since the field does not penetrate far into the metallic wires. Additionally, the imaging process is not particularly sensitive to the dielectric losses or to small surface irregularities on the wires (a decay in intensity does not result in substantial image corruption), to fluctuations in wire location or to

variation in wire thickness or cross-sectional shape (Capolino, 2009), thereby making it very tolerant of fabrication inaccuracies.

It should be noted that in general, the transmission properties of a wire medium depend on both spatial and temporal frequencies. It is well known that for a wire medium slab (with endfaces perpendicular to the wires), imaging performance is in fact optimal near the Fabry−Perot (FP) resonances of the slab, where the transmission amplitude and phase are independent of the spatial frequency, resulting in perfect imaging (Belov & Silveirinha, 2006). Away from the FP resonance, slab modes lead to the amplification of selected high spatial frequencies, resulting in artefacts in the images formed (see for example Figure 2.12). It was recently shown that this type of behaviour applies to the wider class of uniaxial media with large negative or positive axial permittivity (Tuniz et al., 2014).

An alternative viewpoint is to consider that the modes of the wire medium are a superposition of individual wire modes, so that the metamaterial acts as a subwavelength endoscope. If the wire array tapers along the length of the device, 'pixels' of the endoscope become more separated, and images can be magnified or focussed by a factor corresponding to the ratio between wire spacing at both ends of the taper.

Until recently, difficulties in fabricating high aspect ratio metallic wire arrays (and in particular tapered arrays) have prevented their demonstration at frequencies above microwaves. Most metals behave as good conductors up to frequencies of several terahertz; the fabrication method presented in Figure 2.4 and Section 2.3 is thus ideally suited to produce tapered and untapered wire medium hyperlenses at terahertz frequencies. Both straight and tapered hyperlenses for the THz have been fabricated using the drawing method.

The fabrication of the wire array hyperlenses followed the method given in Figure 2.5, with Zeonex used in the wire array for its transparency to THz and PMMA for the consolidating jacket. Figure 2.10(a) and (b) show a photograph and X-ray computer tomography scan of the taper, respectively. The taper and fibre contain 453 hexagonally arranged indium wires of nominally 10 μm diameter and 50 μm pitch at the fibre end, as shown in the cross-sectional microscope image of Figure 2.10(c). The diameter of the region containing the wire medium varies between 8 mm on the larger end of the taper and 1 mm on the smaller end of the taper and fibre.

The subwavelength imaging properties of the wire medium fibre and taper were characterised using a near-field scanning terahertz TDS system (Bitzer, Ortner, & Walther, 2010). To highlight the resolution potential, a range of subwavelength apertures in contact with the hyperlens, illuminated by focused THz pulses, were imaged. The TDS antenna detecting transverse field components was placed in close proximity to the output of the aperture, fibre or taper, and raster scanned along the $x$ and $y$ coordinates, recording the full time-dependent amplitude and phase of the $x$ component of the electric field. Spectrally resolved images were then obtained from the Fourier transform of the time-dependent THz signals.

Figure 2.11 shows (1) the direct near-field image of a double aperture at 0.1 THz, and (2) after a 3.4 mm straight section of wire array hyperlens at 0.11 THz ($\lambda = 2.7$ mm in vacuum, $\lambda = 1.7$ mm in Zeonex, corresponding to the lowest resolved FP resonance of the fibre). The 100 μm gap in the $x$ direction between the two 200 μm

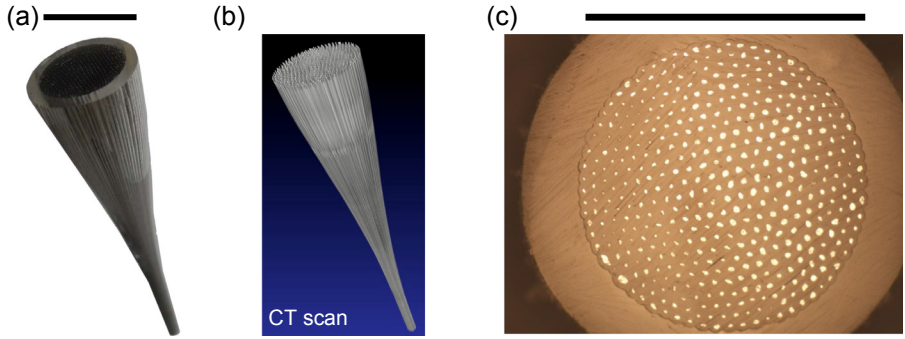


**Figure 2.10** (a) Photograph and (b) X-ray tomography scan of a tapered wire array hyperlens for the THz. (c) Optical microscope image of the cross section of the fibre (and fibre end of the tapered hyperlens). The scale bar is 8 mm in (a) and 1 mm in (c).
Adapted from Tuniz et al. (2013).

apertures is clearly imaged through the fibre, indicating a resolution better than $\lambda/27$, significantly away from the object such that the near-field information would have ordinarily decayed. For comparison, Figure 2.11(c) shows the image of a single 200 μm aperture. Figure 2.11(d)−(f) show the intensity along $x$ for all three cases, averaged around the centre of the image ($y = 0$).

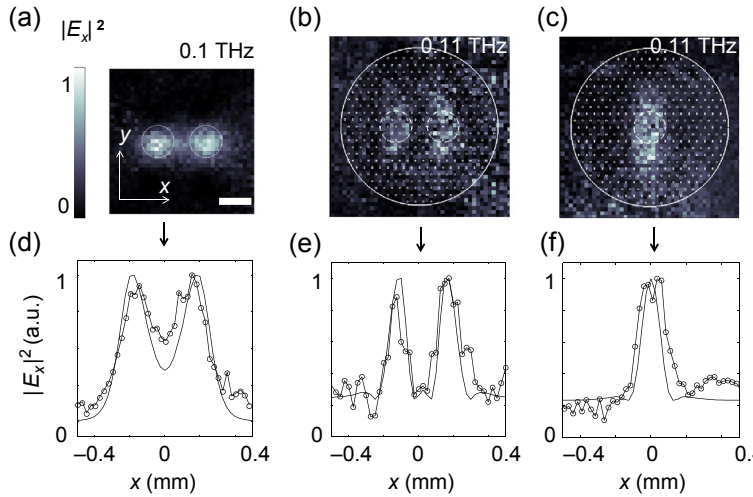


**Figure 2.11** Images at the frequencies indicated of (a) two 200 μm apertures separated by 100 μm, (b) the same apertures through the straight wire array hyperlens and (c) a single 200 μm aperture through the straight wire array hyperlens. Scale bar: 0.2 mm. The intensity through the centre of the image ($y = 0$) is shown in (d)−(f), with the experimental measurements (line with data points) compared to simulation results (solid line with no data points). The hyperlens used was 3.4 mm long.
Adapted from Tuniz et al. (2013).

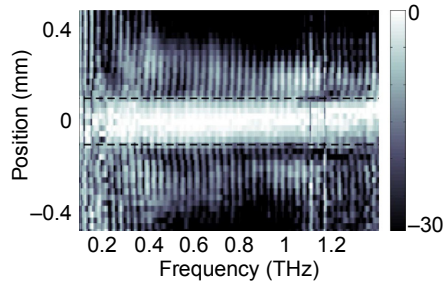


**Figure 2.12** Intensity of an image of a 200 μm aperture as a function of frequency and $x$-coordinate, with the intensity averaged at the centre of the image ($y = 0$) (see Figure 2.11(c) and (f)).
Adapted from Tuniz et al. (2013).

To further illustrate the imaging characteristics of this hyperlens, Figure 2.12 shows the output intensity of the 200 μm aperture imaged by the fibre, as a function of frequency and $x$ coordinate, averaged around the centre of the image ($y = 0$). The intensity at each frequency is normalised to the maximum in $x$ and plotted using a logarithmic colour scale, showing the important field characteristics. Note the periodic appearance of side lobes at FP antiresonances, at which imaging is suboptimal; the frequency spacing between these side lobes is 29 GHz − corresponding to the free spectral range of the 3.4-mm Zeonex FP slab.

In addition to the straight hyperlens, the tapered hyperlens was also characterised in a similar manner. Figure 2.13 demonstrates its focussing properties, whereby an $x$-polarised THz beam, without an aperture, was focussed on the large side of the taper. The frequency-dependent beam profile along $x$ at $y = 0$, as shown in Figure 2.13(a). Subsequently, the near field at the narrow end of the taper (Figure 2.13(c)) was measured, showing a compression along $x$. Figure 2.13(b) and (d) show the complete intensity images before and after the taper at 50 GHz, where the near field at the output of the fibre has a full-width at half-maximum (FWHM) of $\lambda/9$. Remarkably, transmission losses at the low frequencies (<0.1 THz) are negligible, and an actual increase in power density due to focussing was observed. However, at high frequencies, losses become larger both because of the increase in material losses and because the wire array at the large end of the taper is no longer subwavelength and thus does not behave as an indefinite metamaterial.

Figure 2.13(e)−(h) illustrate the focussing of an image of a 1 mm aperture with the tapered hyperlens. Figure 2.13(e) and (f) show the near field directly at the aperture without the tapered hyperlens for comparison. Figure 2.13(h) shows that the field at the small end of the taper is strongly focussed in the $x$ direction, down to a FWHM of $\lambda/28$. (Subsequent, yet unpublished, work extended this to $\lambda/50$.) The spread in the $y$ direction is due to contributions from ordinary waves of the indefinite medium, which diffract but are confined by the lateral boundaries of the fibre. Figure 2.13(g) shows the frequency-dependent intensity distribution along $x$ (for $y = 0$) at the output of the taper, showing effective and consistent focussing-down

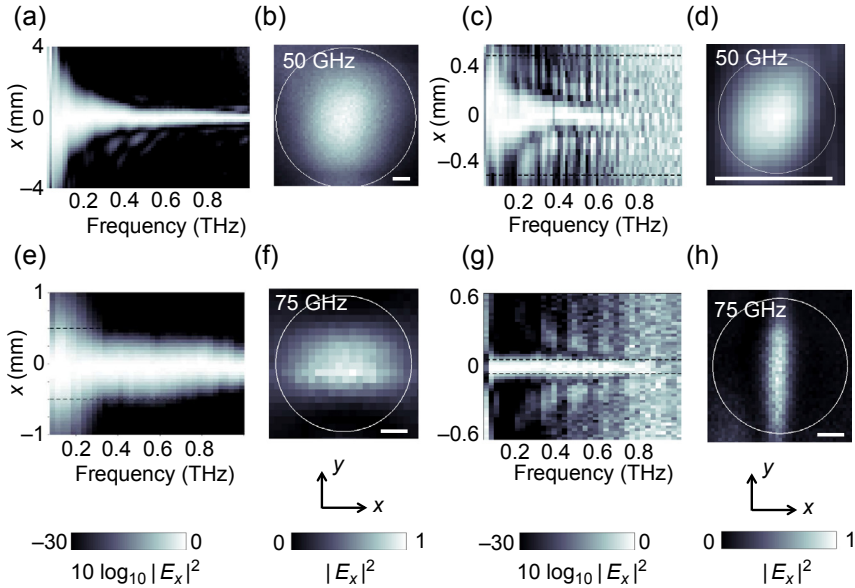


**Figure 2.13** Characterisation of the tapered hyperlens. (a) Width of a focused beam and (b) cross section of the beam at the frequency shown. This beam was directed on to the large end of the taper, and the output at the fibre end is shown in (c) and (d), with a reduction in size equal to the ratio of the taper. The field of a 1 mm aperture (e), (f) before the taper and (g), (h) after the taper, again showing focussing. Scale bars in (b), (d): 1 mm. Scale bars in (f), (h): 0.2 mm. Adapted from Tuniz et al. (2013).

of the aperture across frequencies from 50 GHz to 0.9 THz, with some artefacts appearing at some frequencies above 0.3 THz. The length of the taper corresponds to 182 wavelengths in Zeonex at 0.9 THz and 10 wavelengths at 0.05 THz.

This work on hyperlenses clearly demonstrates the application of metamaterial wire array fibres to the transmission of subwavelength images over optically long distances. In particular, the same tapered wire array lens could in principle be used for magnification if the experiments described above in Figure 2.13 had the light incident on the narrow end of the taper instead. Such wire array tapers with long propagation lengths used in reflection could be used as subdiffraction-limited THz endoscopes and with higher density of wires could even image with high resolution down to single cells within living tissue. THz imaging by conventional means within tissues is typically impossible because of the high absorption of water at these frequencies and the severe restrictions imposed by the diffraction limit. The metamaterial fibres could also enable increased THz power extraction (Jacob et al., 2010) through a higher density of states and even be used for spectral measurement-based far-field subwavelength-resolved imaging (Lemoult et al., 2011). The fabrication method lends itself to mass production, and hyperlenses thus have a realistic prospect of finding widespread use in THz imaging technology.

## 2.6 Future directions—challenges and opportunities

The current level of development of this technology is very exciting, in that a novel and practical technique has been demonstrated for fabricating metamaterials, and the realisation of devices such as the hyperlens demonstrates new and important functionality. This can be taken as a starting point as there are several directions to explore to substantially extend this capability, provided some challenges can be overcome.

The combination of polymers (PMMA and Zeonex) with indium has proven excellent for demonstrating the possibilities of applying microstructured fibre drawing to metamaterial fabrication. Furthermore, this platform is a very good combination for the THz wavelength range, both in terms of the dimensions on the microscale of structures that are readily drawn and the high transparency of Zeonex, being one of the most transparent solids known in that wavelength range. While the THz spectrum is of rapidly growing technological importance, the application of this fabrication method to metamaterials for a wide frequency range is one obvious extension of the work.

Operation over a wide spectral range was explored in the context of wire arrays, and whilst operation at wavelengths as short as 20 μm was demonstrated, for example Figure 2.6(b) (Naman et al., 2013), for shorter wavelengths this combination of materials presents severe limitations arising from three different aspects. Firstly, the polymer becomes highly absorbing into the mid- and near-IR, making the dielectric used here undesirable. Secondly, for shorter wavelengths the assumption that indium is a perfect metal becomes increasingly less applicable and the metallic losses increase. Finally, the shorter wavelengths require smaller structure, that is, thinner wires more closely spaced. The limitation in making smaller structure arises from the Rayleigh−Plateau instability (Tomotika, 1935, 1936), which describes the tendency of a column of liquid (the liquid metal during drawing) to break up and form droplets due to the effect of surface tension.

A relatively small number of metals have complex permittivities suitable for metamaterials at near-IR or visible wavelengths, with the most promising candidates being silver, gold, copper and aluminium. These have melting temperatures above 650 °C and mostly above 900 °C. These higher melting temperatures are clearly incompatible with polymers, and hence glasses will be required. There is a very large range of glasses, and their softening (drawing) temperatures extend from 100 °C to 1700 °C. This expanded choice of dielectric materials also provides a wider range in terms of other important properties such as strength and transparency in the mid- and near-IR. For example, combinations of aluminium and soda lime, or silver and boro-alumino-silicate, should be co-drawable based on melting and softening temperatures and are comprised of materials with good optical properties at shorter wavelengths right into the visible spectrum. As an example, in another context copper wires have been drawn within silica fibres (Hou et al., 2008). Thus the first two constraints of the metal's and dielectric's optical properties could in principle be solved through a different choice of materials.

The remaining challenge is to what scale the materials of choice may be drawn in view of the Rayleigh−Plateau instability. In the modified form of fibre drawing employed here, one fluid (liquid metal) is drawn inside another (viscous polymer or

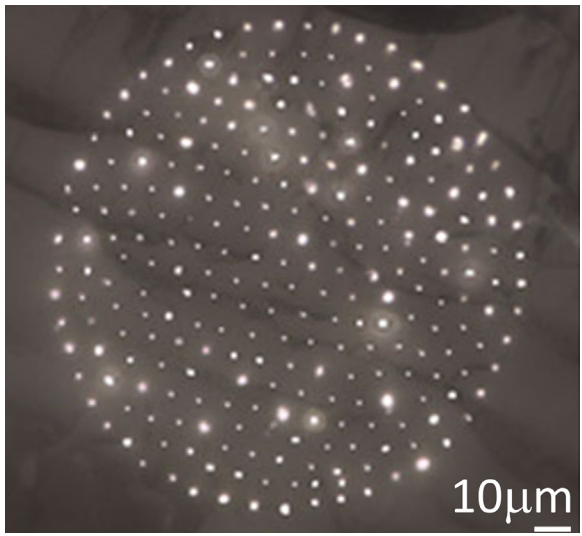


**Figure 2.14** Cross section of a wire array metamaterial fibre drawn to small-wire diameter. Variations in wire diameter are due to Rayleigh−Plateau instability.
Adapted from Naman et al. (2013).

potentially glass). Such columns of liquids inside other liquids are known to be unstable and have the tendency to break up into a series of droplets due to the surface tension acting to minimise surface area. Any perturbation on the surface of the inner cylinder is amplified by the surface tension until the cylinder breaks into spherical droplets. The growth of the amplitude of perturbations $A(t)$ over time $t$ in a simplified model of the process is exponential, with a gain term proportional to the surface tension $\sigma$ and inversely proportional to the radius $r$ and the viscosity of the outer (polymer or glass) material $\mu$ (Naman et al., 2013; Tomotika, 1935)

$$A(t) = A(0)e^{\frac{\sigma}{2r\mu}t}. \tag{2.13}$$

The dependence on radius makes the instability an increasing problem for smaller diameter wires and hence poses the limitation on minimum wire diameter.

The instability becomes irrelevant if the rate of growth is slow compared to the time for which the metal is liquid during the draw process − that is, the time it takes to transition from the neck-down region to the fibre 'freezing'. However, reducing the radius of the metal exponentially increases the rate of growth of the perturbations that cause break up. A cross section of a metamaterial fibre at the onset of this effect is shown in Figure 2.14 where variations in wire diameter are evident.

Experiments and modelling to date indicate that it is impractical to co-draw indium wires in PMMA or Zeonex to diameters below 1 μm. Figure 2.15 shows the dimensions required to achieve wire arrays with effective plasma frequencies in different parts of the spectrum, using Eqn (2.3) (Naman et al., 2013). Whilst wires of approximately 1 μm diameter, giving a plasma frequency at 15 THz, were demonstrated, to move into the near-IR and visible would require wire diameters of 300 nm and below.

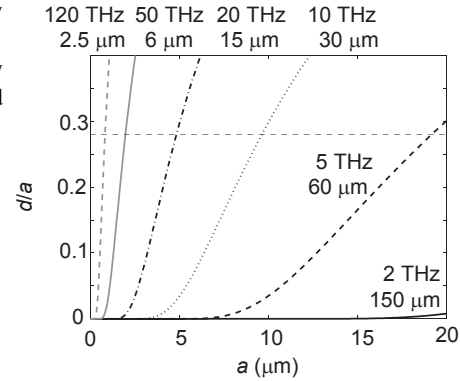


**Figure 2.15** Dependence of plasma frequency calculated using Eqn (2.3), and hence minimum operating wavelength, on wire array metamaterial parameters: wire separation $a$ and diameter $d$. Note that the maximum $d/a$ ratio shown by the horizontal line corresponds to $a < \lambda/2n_d$, required to make the array subwavelength.
Adapted from Naman et al. (2013).

As the growth of the instability also depends on the viscosity of the outer fluid (polymer or glass) and the surface tension between that and the metal, there is a scope for decreasing the rate of growth by increasing the viscosity of the outer material or decreasing the surface tension. For the combination of materials used to date, there is a very limited scope in practice. The surface tension is determined by the material choice, and whilst the viscosity can be increased by reducing the draw temperature, an upper limit is reached beyond which drawing is no longer possible and the fibre breaks due to the high tensions required for drawing. However, a different material choice may allow for a substantially lower surface tension or drawing at higher viscosity than the current indium/polymer combination.

Whilst new material combinations offer a promising direction, they also come with the possibility of new problems. Higher drawing temperatures mean that mismatched thermal expansions and the consequent stresses may become a problem, and glasses will be more brittle than the current polymers. Importantly, it should be noted that there are examples of co-drawing wire array structures to the nanoscale. Badinter et al. report drawing bismuth and lead−tin alloy wires in borosilicate glass producing regular arrays of nanowires as small as 50 nm diameter; they state they 'selected a compatible glass […] to provide a minimum value of the interfacial tension between the glass and the melt' (Badinter, Iosher, Monaico, Postolache, & Tiginyanu, 2010). This approach can clearly be made to work for some metal−glass combinations, and it is reasonable to expect that it can be made to work for combinations including metals with good optical properties at short wavelengths, as required for metamaterials.

The extension of this fabrication technique to smaller structure would translate to an extension of the applications. Continuing with the example from above, a particularly attractive possibility is the development of a mid-IR hyperlens. The mid-IR is a hugely important spectral region as there are strong spectral signals for a large array of important molecules, with obvious applications to biology and medicine. Extrapolating the THz hyperlens performance would suggest submicron, even 100 nm, resolution in the mid-IR, allowing a precise identification of organic molecules at substantially subcellular resolutions. As noted above, the drawing method is perfectly suited to the fabrication of hyperlenses.

In addition to hyperlenses, another application that is well suited to drawn metamaterials is waveguides, having a compatible geometry. There are few choices for waveguides in the Far IR and THz, partly because of the lack of suitable materials and partly because at these wavelengths conventional waveguides may have large diameters such that they may become impractical or inflexible (Setti, Vincetti, & Argyros, 2013; Wu, Argyros, & Leon-Saval, 2011). Waveguides with metamaterial cladding offer a potential solution to both problems: they can have air cores and can achieve subwavelength confinement with waveguide diameters smaller than the wavelengths of the radiation they guide (Atakaramians, Argyros, Fleming, & Kuhlmey, 2012, 2013). A subset of such waveguide designs may be compatible with the geometries produced by the draw process.

If the drawing technique can be pushed to the fabrication of nanometre-sized wires, more intriguing possibilities emerge. For instance, we have numerically shown that an invisible fibre could be realisable with this fabrication technique (Tuniz et al., 2010). This would require a wire array with 100 nm pitch and 13.5-nm-diameter silver nanowires in a silica matrix. Numerical simulations demonstrate this to be an invisible fibre-reducing shadowing and scattering by over 95% at 633 nm over a 13 nm bandwidth and at normal incidence $\pm 10^{\circ}$. Furthermore, with similar sized wires included in the core of a doped optical fibre, the extreme density of states provided by indefinite materials (Jacob et al., 2010) could open up new avenues for emission control for fibre lasers.

Whilst longitudinal invariance is a key property of drawn metamaterials, it should be noted that further possibilities arise if that invariance is broken. This can be achieved through post-processing, such as laser patterning (Tuniz et al., 2012). There is also the possibility of utilising the Rayleigh−Plateau instability to produce controlled longitudinal patterning during the draw (Kaufman et al., 2012). Finally, given the intrinsic fibre form, weaving of metamaterial fibres might be used to achieve more complex metamaterials. For example, a magnetic resonator fibre with negative permeability and a wire array fibre with negative permittivity can produce a sheet of negative refractive index material.

## 2.7 Conclusions

Metamaterials hold out great promise. Their extraordinary properties can provide functionality that would be impossible, or at least impractical, with natural materials. These properties include negative index, indefinite permittivities and designer magnetic responses, with functionalities ranging from invisibility and cloaking to subresolution imaging. Due to their dimensions and composition from dissimilar materials, they are very difficult to fabricate, especially on the scale required to realise practical devices. The fibre fabrication technique, as developed for drawing microstructured fibres, has been adapted to draw metamaterials in the form of fibres where the microstructure is comprised of metals. This well-established fabrication technique should be applicable to economically manufacture metamaterials in commercial quantities.

To date, this adapted technique has been successfully applied to research demonstrations of polymer/indium metamaterials with tailored electric and magnetic properties in the THz, and Far IR, spectral regions. Furthermore, these metamaterials have been used to make a THz hyperlens, demonstrating their practical application to deliver significant and novel functionality of $\lambda/50$ resolution in the THz. There is a very good prospect of extending this approach to a range of combinations of glasses and metals to provide metamaterials and devices made from these, operating in the mid- to near-IR and even the visible. By applying knowledge from microstructured fibre fabrication, metamaterials are poised to move from being a fascinating research topic to an applied technology solving real-world problems.

## References

Anthony, J., Leonhardt, R., Argyros, A., & Large, M. C. J. (2011). THz properties of a microstructured Zeonex polymer fibre. *Journal of the Optical Society of America B, 28*(5), 1013−1018.

Argyros, A. (2009). Microstructured polymer optical fibres. *Journal of Lightwave Technology, 27*(11), 1571−1579.

Argyros, A. (2013). Microstructures in polymer fibres for optical fibres, THz waveguides and fibre-based metamaterials. *ISRN Optics, 2013*, 785162.

Atakaramians, S., Argyros, A., Fleming, S. C., & Kuhlmey, B. T. (2012). Hollow-core waveguides with uniaxial metamaterial cladding: modal equations and guidance conditions. *Journal of the Optical Society of America B, 29*(9), 2462−2477.

Atakaramians, S., Argyros, A., Fleming, S. C., & Kuhlmey, B. T. (2013). Hollow-core uniaxial metamaterial clad fibers with dispersive metamaterials. *Journal of the Optical Society of America B, 30*(4), 851−867.

Badinter, E., Iosher, A., Monaico, E., Postolache, V., & Tiginyanu, I. M. (2010). Exceptional integration of metal or semimetal nanowires in human-hair-like glass fiber. *Materials Letters, 64*(17), 1902−1904.

Barlow, H. M., & Cullen, A. L. (1953). Surface waves. *Proceedings of the IEE-Part III: Radio and Communication Engineering, 100*(68), 329−341.

Belov, P. A., Marques, R., Maslovski, S. I., Nefedov, I. S., Silveirinha, M., Simovski, C. R., et al. (2003). Strong spatial dispersion in wire media in the very large wavelength limit. *Physical Review B, 67*(11), 113103.

Belov, P. A., Palikaras, G. K., Zhao, Y., Rahman, A., Simovski, C. R., Hao, Y., et al. (2010). Experimental demonstration of multiwire endoscopes capable of manipulating near-fields with subwavelength resolution. *Applied Physics Letters, 97*(19), 191905.

Belov, P. A., & Silveirinha, M. G. (2006). Resolution of subwavelength transmission devices formed by a wire medium. *Physical Review E, 73*(5), 056607.

Belov, P. A., Simovski, C. R., & Ikonen, P. (2005). Canalization of subwavelength images by electromagnetic crystals. *Physical Review B, 71*(18), 193105.

Bitzer, A., Ortner, A., & Walther, M. (2010). Terahertz near-field microscopy with subwavelength spatial resolution based on photoconductive antennas. *Applied Optics, 49*(19), E1−E6.

Capolino, F. (2009), Metamaterials handbook (Vol. 2). Applications of Metamaterials 3−17. CRC Press.

Casse, B. D. F., Lu, W. T., Huang, Y. J., Gultepe, E., Menon, L., & Sridhar, S. (2010). Superresolution imaging using a three-dimensional metamaterials nanolens. *Applied Physics Letters, 96*(2), 023114.

Hou, J., Bird, D., George, A., Maier, S., Kuhlmey, B. T., & Knight, J. C. (2008). Metallic mode confinement in microstructured fibres. *Optics Express, 16*, 5983−5990.

Jacob, Z., Kim, J.-Y., Naik, G. V., Boltasseva, A., Narimanov, E. E., & Shalaev, V. M. (2010). Engineering photonic density of states using metamaterials. *Applied Physics B, 100*, 215−218.

Kaufman, J. J., Tao, Guangming, Shabahang, S., Banaei, E.-H., Deng, D. S., Liang, Xiangdong, et al. (2012). Structured spheres generated by an in-fibre fluid instability. *Nature, 487*, 463−467.

Knight, J. C., Birks, T. A., Russell, P. St. J., & Atkin, D. M. (1996). All-silica single-mode optical fiber with photonic crystal cladding. *Optics Letters, 21*, 1547−1549.

Lemoult, F., Fink, M., & Lerosey, G. (2011). Far-field sub-wavelength imaging and focusing using a wire medium based resonant metalens. *Waves in Random and Complex Media, 21*(4), 614−627.

Lemoult, F., Kaina, N., Fink, M., & Lerosey, G. (2013). Wave propagation control at the deep subwavelength scale in metamaterials. *Nature Physics, 9*, 55−60.

Leonhardt, U. (2006). Optical conformal mapping. *Science, 312*, 1777−1780.

Maslovski, S. I., & Silveirinha, M. G. (2009). Nonlocal permittivity from a quasistatic model for a class of wire media. *Physical Review B, 80*(24), 245101.

McPhedran, R. C., Shadrivov, I. V., Kuhlmey, B. T., & Kivshar, Y. S. (2011). Metamaterials and metaoptics. *NPG Asia Materials, 3*, 100−108.

Naman, O. T., New-Tolley, M. R., Lwin, R., Tuniz, A., Al-Janabi, A. H., Karatchevtseva, I., et al. (2013). Indefinite media based on wire array metamaterials for the THz and mid-IR. *Advanced Optical Materials*. http://dx.doi.org/10.1002/adom.201300402.

Pendry, J. B. (2000). Negative refraction makes a perfect lens. *Physical Review Letters, 85*(18), 3966−3969.

Pendry, J. B., Holden, A. J., Robbins, D. J., & Stewart, W. J. (1999). Magnetism from conductors and enhanced nonlinear phenomena. *IEEE Transactions on Microwave Theory and Techniques, 47*(11), 2075−2084.

Pendry, J. B., Holden, A. J., Stewart, W. J., & Youngs, I. (1996). Extremely low frequency plasmons in metallic mesostructures. *Physical Review Letters, 76*(25), 4773−4776.

Pendry, J. B., Schurig, D., & Smith, D. R. (2006). Controlling electromagnetic fields. *Science, 312*, 1780−1782.

Rotman, W. (1962). Plasma simulation by artificial dielectrics and parallel-plate media. *IRE Transactions on Antennas and Propagation, 10*(1), 82−95.

Russell, P. St. J. (2006). Photonic crystal fibers. *Journal of Lightwave Technology, 24*, 4729−4749.

Schurig, D., Mock, J. J., Justice, B. J., Cummer, S. A., Pendry, J. B., Starr, A. F., et al. (2006). Metamaterial electromagnetic cloak at microwave frequencies. *Science, 314*, 977−980.

Setti, V., Vincetti, L., & Argyros, A. (2013). Flexible tube lattice fibers for terahertz applications. *Optics Express, 21*(3), 3388−3399.

Silveirinha, M. G., Belov, P. A., & Simovski, C. R. (2008). Ultimate limit of resolution of subwavelength imaging devices formed by metallic rods. *Optics Letters, 33*(15), 1726−1728.

Simovski, C. R., Belov, P. A., Atrashchenko, A. V., & Kivshar, Y. S. (2012). Wire metamaterials: physics and applications. *Advanced Materials, 24*(31), 4229−4248.

Singh, N., Tuniz, A., Lwin, R., Atakaramians, S., Argyros, A., Fleming, S. C., et al. (2012). Fiber-drawn double split ring resonators in the terahertz range. *Optical Materials Express, 2*(9), 1254−1259.

Smith, D. R., & Kroll, N. (2000). Negative refractive index in left handed materials. *Physical Review Letters, 85*, 2933.

Smith, D. R., Padilla, W. J., Vier, D. C., Nemat-Nasser, S. C., & Schultz, S. (2000). Composite medium with simultaneously negative permeability and permittivity. *Physical Review Letters, 84*(18), 4184.

Smith, D. R., & Schurig, D. (2003). Electromagnetic wave propagation in media with indefinite permittivity and permeability tensors. *Physical Review Letters, 90*(7), 77405.

Taylor, G. F. (1924). A method of drawing metallic filaments and a discussion of their properties and uses. *Physical Review, 23*(5), 655.

Tomotika, S. (1935). On the instability of a cylindrical thread of a viscous liquid surrounded by another viscous fluid. *Proceedings of the Royal Society of London. Series A, Mathematical and Physical Sciences, 150*(870), 322−337.

Tomotika, S. (1936). Breaking up of a drop of viscous liquid immersed in another viscous fluid which is extending at a uniform rate. *Proceedings of the Royal Society of London. Series A, Mathematical and Physical Sciences, 153*(879), 302−318.

Tuniz, A., Ireland, D., Poladian, L., Argyros, A., de Sterke, C. M., & Kuhlmey, B. T. (2014). Imaging performance of finite uniaxial metamaterials with large anisotropy. *Optics Letters, 39*(11), 3286−3289.

Tuniz, A., Kaltenecker, K. J., Fischer, B. M., Walther, M., Fleming, S. C., Argyros, A., et al. (2013). Metamaterial fibres for subdiffraction imaging and focussing at terahertz frequencies over optically long distances. *Nature Communications, 4*, 2706. http://dx.doi.org/10.1038/ncomms3706.

Tuniz, A., Kuhlmey, B. T., Chen, P., & Fleming, S. C. (2010). Weaving the invisible thread: design of an optically invisible metamaterial fibre. *Optics Express, 18*(17), 18095−18105.

Tuniz, A., Kuhlmey, B. T., Lwin, R., Wang, A., Anthony, J., Leonhardt, R., et al. (2010). Drawn metamaterials with plasmonic response at terahertz frequencies. *Applied Physics Letters, 96*, 191101.

Tuniz, A., Lwin, R., Argyros, A., Fleming, S. C., & Kuhlmey, B. T. (2012). Fabricating metamaterials using the fiber drawing method. *Journal of Visualised Experiments, 68*, e4299. http://dx.doi.org/10.3791/4299.

Tuniz, A., Lwin, R., Argyros, A., Fleming, S. C., Pogson, E. M., Constable, E., et al. (2011). Stacked-and-drawn metamaterials with magnetic resonances in the terahertz range. *Optics Express, 19*(17), 16480−16490.

Tuniz, A., Pope, B., Wang, A., Large, M. C. J., Atakaramians, S., Min, S.-S., et al. (2012). Spatial dispersion in three-dimensional drawn magnetic metamaterials. *Optics Express, 20*(11), 11924−11935.

Veselago, V. G. (1968). The electrodynamics of substances with simultaneously negative values of ε and μ. *Soviet Physics Uspekhi, 10*(4), 509−514.

Walser, R. M. (2003). In W. S. Weiglhofer, & A. Lakhtakia (Eds.), *Introduction to complex mediums for optics and electromagnetics*. Washington: SPIE Press (Part IV).

Wu, D. S., Argyros, A., & Leon-Saval, S. G. (2011). Reducing the size of hollow terahertz waveguides. *Journal of Lightwave Technology, 29*(1), 97−103.

Xu, T., Agrawal, A., Abashin, M., Chau, K. J., & Lezec, H. J. (2013). All-angle negative refraction and active flat lensing of ultraviolet light. *Nature, 497*, 470−474.

Yao, J., Liu, Z., Liu, Y., Wang, Y., Sun, C., Bartal, G., et al. (2008). Optical negative refraction in bulk metamaterial nanowires. *Science, 321*, 930.

# Liquid crystal-infiltrated photonic crystal fibres for switching applications

3

*D.C. Zografopoulos*[1], *A. Pitilakis*[2], *E.E. Kriezis*[2]
[1]Istituto per la Microelettronica e Microsistemi (IMM), Consiglio Nazionale delle Ricerche (CNR), Roma, Italy; [2]Department of Electrical and Computer Engineering, Aristotle University of Thessaloniki, Thessaloniki, Greece

## 3.1 Introduction

Photonic crystal fibres (PCFs) are a special class of optical fibres characterized by a periodical arrangement of microcapillaries that form the fibre's cladding around a solid or hollow defect core. Light propagation and potential applications of PCFs have drawn remarkable attention since the late 1990s (Russell, 2006). The engineering of the PCF geometry combined with an ample selection of available materials for their fabrication provides extensive degrees of freedom for the tailoring of their optical properties, such as modal area, chromatic dispersion, nonlinearity and birefringence. Compared to their conventional counterparts, PCFs can exhibit unprecedented performance in a broad range of applications which span from large-mode-area endlessly single-mode fibres, dispersion compensation, single-polarization and high-birefringence guidance, and nonlinear applications. For example, such applications include supercontinuum generation and pulse shaping, high-power pulse delivery in hollow-core PCFs, high-power fibre lasers, and fibre components for metrology and spectroscopy (Cerqueira, 2010; Hansen, 2005; Hänsch, 2006; Knight, 2007).

The presence of the cylindrical capillaries in the PCF cladding, and often in the core, provides a natural possibility for their infiltration with fluid materials that can enhance their properties or introduce a means for dynamic control. Polymers and liquids are possible candidates, as their refractive index can be thermally tuned via the thermo-optic effect. Some examples which fall in this category include tunable birefringence in polymer-infiltrated PCFs (Kerbage & Eggleton, 2002) and tunable bandgaps (Du, Liu, Wang, Liu, et al., 2008) or nonlinear focusing (Rosberg et al., 2007) in isotropic liquid-infiltrated PCFs. Nevertheless, functionalities that are more extensive are offered by infiltrating PCFs with nematic liquid crystals (LCs), a class of organic materials sharing properties of both isotropic liquids and solid crystals. Owing to their large inherent optical anisotropy and the capability of controlling their molecular orientation via the application of external stimuli such as electric or magnetic fields, LCs have long stood out as the active material in low-power consumption tunable photonic devices (Zografopoulos, Asquini, Kriezis, d'Alessandro, & Beccherelli, 2012). Not surprisingly,

**Optofluidics, Sensors and Actuators in Microstructured Optical Fibers.** http://dx.doi.org/10.1016/B978-1-78242-329-4.00003-5

LC-based PCFs have also been under intense investigation since the first experimental study of LC-PCF tunable switches (Larsen, Bjarklev, Hermann, & Broeng, 2003). Thereafter, numerous LC-PCF in-line components for telecom applications in optical fibre systems have been demonstrated, such as tunable bandgap switches (Alkeskjold et al., 2004, 2006), notch filters (Noordegraaf et al., 2008), polarizers (Ertman et al., 2012; Haakestad et al., 2005; Wei et al., 2009), polarization rotators (Wei, Alkeskjold, & Bjarklev, 2010), noise filtering devices (Petersen et al., 2008), tunable long-period gratings (Liou, Chang, Lin, & Yu, 2011; Wei, Weirich, Alkeskjold, & Bjarklev, 2009), Sagnac filters (Du, Liu, Wang, Zou, et al., 2008) and tunable-fibre lasers (Olausson et al., 2010). In a different context, LC-PCFs have also been proposed as sensing elements, for instance in the measurement of electric fields (Mathews, Semenova, & Farrell, 2009) or temperature and hydrostatic pressure (Woliński et al., 2008).

Infiltration of the PCF capillaries with LC materials is typically performed by capillary action at high temperatures so that the LC is in the isotropic state (Alkeskjold et al., 2004). The filling time is on the order of tens of minutes for the infiltration of a few centimetres, which provides adequate optical length for most applications. Vacuum pumps can be used to accelerate the procedure, though care must be taken to avoid the formation of defects. When the partial infiltration of a single capillary with larger dimensions is required, which in most cases forms the PCF's defect core, arc-fusion techniques can be used to collapse the smaller capillaries and expose the target (Xiao et al., 2005). In general, selective infiltration is possible by taking advantage of the different filling speed amongst capillaries of different radii (Huang, Xu, & Yariv, 2004), whereas other sophisticated methods provide even more accurate control (Vieweg et al., 2010; Wang, Yuan, Hansen, & Bang, 2011).

The dynamic control of the LC-infiltrated PCF sections is usually achieved via their thermal, electrical or optical addressing. In the temperature range far from their clearing point, LC materials show similar thermo-optic coefficients (TOCs) with optical isotropic fluids and thus offer no significant advantage. However, in the proximity of the nematic to isotropic transition, the TOC obtains large values and tunability is enhanced (Alkeskjold et al., 2006). Another interesting configuration is controlling the operation temperature within a range corresponding to different states of the LC material, in which their optical properties change abruptly within very small temperature intervals (Larsen et al., 2003). Optical addressing takes advantage of the *cis*−*trans* isomerization of specially synthetized azo-dyes that are dispersed in the LC mixture and permit the switching between a disordered, isotropic-like structure and the standard uniaxial nematic state (Hsiao & Ko, 2008; Liou et al., 2011). Nevertheless, the majority of LC-PCF devices rely on the electro-optic control of the LC molecules, as this allows for a greater dynamic control of the fibre properties. The control voltage is applied across the PCF's cross-section via metallic electrodes. The accurate positioning of the electrodes can be achieved using V-grooves as in Figure 3.1(a) (Alkeskjold & Bjarklev, 2007). Photolithographic techniques allow for patterning more complicated electrode configurations, such as periodic combs in LC-PCF long-period gratings (Wei, Weirich, et al., 2009). The grooved structures can also serve as the fixing element for the fibre and achieve mechanical splicing with non-infiltrated PCFs or conventional single-mode fibres (Wei, Alkeskjold, et al., 2009). Fusion splicing is avoided, as the locally

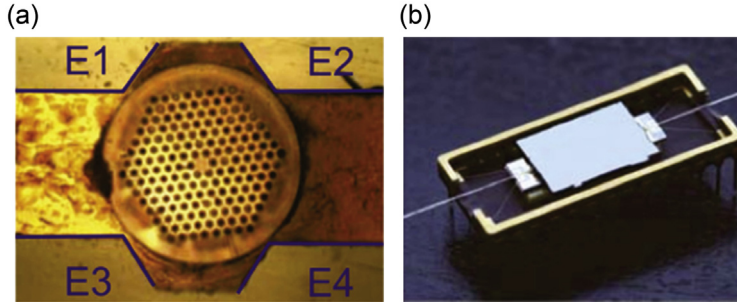


**Figure 3.1** (a) A liquid crystal-photonic crystal fibre (LC-PCF) placed in a V-groove assembly with four 200 nm gold-deposited electrodes (Alkeskjold & Bjarklev, 2007). (b) A packaged LC-PCF device pigtailed to two SMF-28 single-mode fibres, wire bonded for electrical access (Alkeskjold et al., 2007).

generated high temperatures may irreversibly damage the LC material. Such techniques permit the overall packaging and low-loss in-line connection of LC-PCF components in optical fibre networks, as in the example shown in Figure 3.1(b) (Alkeskjold et al., 2007).

The tunability range offered by LC-PCF components depends on various factors, such as the type of the fibreglass and LC material, the alignment and addressing of the LC, the geometry and the physics involved, for example, the light-guiding mechanism of the PCF. To achieve the target properties, the LC-PCF has to be designed by rigorously taking into account these parameters. In this work, we present the key aspects regarding the physics of LC-PCFs and show how the fibre's properties can be tuned by electro-optical addressing in the context of switching applications for fibre telecom networks. Section 3.2 presents the physics governing the LC switching mechanism in cylindrical capillaries in the presence of an applied control voltage. Light guidance in LC-infiltrated PCFs is comprehensively studied in Section 3.3, covering the known light-guiding mechanisms in PCFs and the most common designs with respect to the LC infiltration and PCF geometry. Section 3.4 tackles the design and assesses the performance of three switching elements that reflect the potentialities offered by LC-PCFs, namely a single-polarization switch, a complete polarization controller and a dual-core LC-PCF polarization splitter. Finally, conclusions are drawn and potential future directions are discussed in Section 3.5.

## 3.2 LCs in cylindrical capillaries

### *3.2.1 LC switching in cylindrical capillaries*

Light guidance in LC-PCFs is very strongly related to the effective refractive indices presented by the LC material which is contained in the cylindrical capillaries, which in turn are determined by the LC molecular orientation. Thus, the first step to be taken is

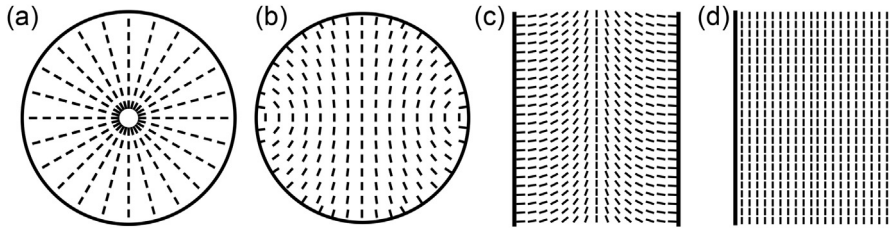


**Figure 3.2** Typical liquid crystal (LC) textures in a cylindrical capillary: (a) planar radial, (b) planar polar, (c) escaped radial and (d) axial.

the study of the LC orientation and electro-optical addressing in the containing cylindrical capillaries, in a framework which allows for accurate quantitative predictions.

The local molecular orientation is designated by the unit vector $\hat{\mathbf{n}}$, which will be referred to as the nematic director; the director varies with position over the fibre's cross-section. Anticipated equilibrium configurations (known as textures) in a cylindrical capillary are strongly dependent on the director orientation along the cylindrical boundary, together with the anchoring strength, the capillary's dimensions and the LC material properties. Figure 3.2(a)−(c) depict three possible textures with homeotropic anchoring (i.e. $\hat{\mathbf{n}}$ is perpendicular to the boundary) in the absence of any external stimuli: Figure 3.2(a) is the planar radial (PR), Figure 3.2(b) the planar polar (PP) and Figure 3.2(c) the escaped radial (ER) texture. The first two are purely planar distortions with the director contained in the plane normal to the fibre axis, whereas in the third case the deformation takes place in all three dimensions. The PR and PP textures involve regions of abrupt LC re-orientation, which are known as defects. The particular texture which is anticipated to develop under equilibrium conditions, for given anchoring conditions (strength), is actually related to the specific ratio of the elastic constants (to be introduced further down) and the capillary's radius, as analysed in (Burylov, 1997). In general, small-sized capillaries ($R < 0.5$ μm) tend to promote the PP or the PR texture, whereas the ER corresponds to larger radii.

We are mainly interested in capillaries with radii in the range of few microns, formed in a host fibreglass material such as silica or other. It has been experimentally proved (Alkeskjold et al., 2004) that, for the above range of conditions, a commonly acquired texture is that of Figure 3.2(d) with the LC material aligning along the cylinder axis at rest position; this is a typical case of homogeneous anchoring referred to as axial (AX) texture. The very same texture can be recovered also from Figure 3.2(c) at the weak anchoring limit.

Switching of the axially aligned LC in the cylindrical geometry when subjected to an electric voltage is remarkably similar to the LC switching in a planar cell, which is the archetype of most flat-panel LC-based displays. A convenient framework to study LC switching is provided by the continuum theory, taking into account the interplay of elastic properties, anchoring conditions, geometry and impressed electric fields by voltage application (Pitilakis, Zografopoulos, & Kriezis, 2011). The salient building blocks of this framework will be provided, albeit in a terse manner.

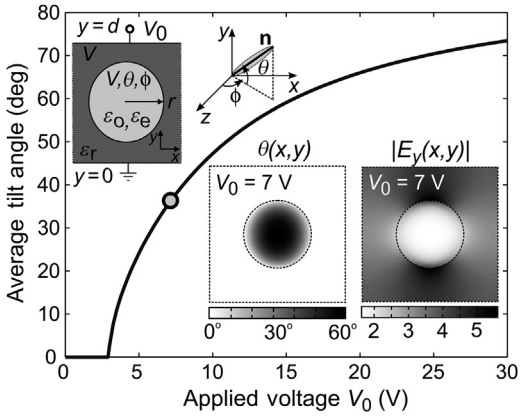


**Figure 3.3** Average tilt angle versus applied voltage for an isolated capillary, according to the layout shown as top left inset. The two bottom insets depict the tilt angle and the electric field intensity distribution at 7 V. The electric field shows high level of uniformity over the capillary's extent.

The nematic director, following the convention of the inset in Figure 3.3, is written as

$$\hat{\mathbf{n}} = n_x\hat{\mathbf{x}}_0 + n_y\hat{\mathbf{y}}_0 + n_z\hat{\mathbf{z}}_0 = \cos\theta\sin\varphi\hat{\mathbf{x}}_0 + \sin\theta\hat{\mathbf{y}}_0 + \cos\theta\cos\varphi\hat{\mathbf{z}}_0, \tag{3.1}$$

with $\theta$ and $\varphi$ being the tilt and twist angles, respectively, which are allowed to vary in the $x-y$ cross-section. LC deformations account for an elastic energy density $F_{\text{elast}}$ with three discrete contributions from splaying, twisting and bending, according to the expression

$$\begin{aligned} F_{\text{elast}} &= F_{\text{splay}} + F_{\text{twist}} + F_{\text{bend}} = \\ &\frac{1}{2}K_{11}\left(\nabla\cdot\hat{\mathbf{n}}\right)^2 + \frac{1}{2}K_{22}\left(\hat{\mathbf{n}}\cdot\nabla\times\hat{\mathbf{n}}\right)^2 + \frac{1}{2}K_{33}\left(\hat{\mathbf{n}}\times\nabla\times\hat{\mathbf{n}}\right)^2, \end{aligned} \tag{3.2}$$

$K_{ii}\,(i = 1 \ldots 3)$ standing for the corresponding elastic constants, typically measured in pN.

Applying an electric field across a nematic LC induces a polarization vector and, provided that the dielectric anisotropy is positive ($\Delta\varepsilon = \varepsilon_{//}^{\text{static}} - \varepsilon_{\perp}^{\text{static}} > 0$), as in most common LC mixtures, forces the LC molecules to an alignment parallel to the electric field vector. The re-orientation of the LC under the application of an external field, or switching in short, is accompanied by a substantial change in optical properties, due to the appreciable LC birefringence. When the applied electric field originates from a constant voltage across the LC region (Yang & Wu, 2006), which is almost exclusively the case of practical importance, the distribution of the nematic director should minimize the energy functional

$$F_{\text{tot}} = \iiint_V F_{\text{d}}\,\text{d}v = \iiint_V \left(F_{\text{elast}} - \frac{1}{2}\mathbf{D}\cdot\mathbf{E}\right)\text{d}v. \tag{3.3}$$

The second term which accounts for the electric field energy density explicitly depends on the nematic director,

$$\frac{1}{2}\mathbf{D}\cdot\mathbf{E} = \frac{1}{2}\varepsilon_0\left(\varepsilon_{\perp}^{\text{static}}|\mathbf{E}|^2 + \Delta\varepsilon\left(\mathbf{E}\cdot\hat{\mathbf{n}}\right)^2\right). \tag{3.4}$$

The minimization of the total energy is accomplished by deriving and subsequently solving the corresponding Euler−Lagrange equations

$$\frac{\partial F_{\text{d}}}{\partial\xi} = \frac{\partial}{\partial x}\left(\frac{\partial F_{\text{d}}}{\partial\xi_x}\right) + \frac{\partial}{\partial y}\left(\frac{\partial F_{\text{d}}}{\partial\xi_y}\right), \tag{3.5}$$

with $\xi$ standing for each of the tilt $\theta(x, y)$ and twist $\varphi(x, y)$ angles which fully determine the nematic director, and $\xi_u \equiv \partial\xi/\partial u$. The mathematic framework is complemented by enforcing the zero divergence of the dielectric displacement

$$\nabla\cdot\mathbf{D} = \nabla\cdot(\varepsilon_0\tilde{\varepsilon}_r\mathbf{E}) = 0, \tag{3.6}$$

with the electric field intensity being the negative potential gradient, $\mathbf{E} = -\nabla V(x,y)$. The relative permittivity elements are simply related to the nematic director via

$$\varepsilon_{ij} = \varepsilon_{\perp}^{\text{static}}\delta_{ij} + \Delta\varepsilon n_i n_j. \tag{3.7}$$

The above equations develop a system of coupled partial differential equations with respect to the triplet ($\theta$, $\varphi$,$V$) in the two-dimensional $x-y$ space. Numerical solution is necessary for almost all cases of practical importance; this can be accomplished, for instance, by employing the finite-element method.

A comprehensive depiction of LC switching in a single (isolated) LC capillary is provided in Figure 3.3. A radius $r = 0.5$ μm is assumed, with the electrodes placed above and below at a distance $d = 2$ μm. The nematic material is E7 ($\varepsilon_{\perp}^{\text{static}} = 5.4$, $\varepsilon_{//}^{\text{static}} = 19.54$, $K_{11} = 11.4$ pN, $K_{22} = 6.6$ pN, $K_{33} = 18.2$ pN) and the surrounding fibreglass is silica ($\varepsilon_{\text{r}} = 3.91$). Strong homogeneous anchoring conditions have been assumed on the cylindrical boundary. The average tilt angle is plotted versus the applied voltage and demonstrates a threshold effect around 3 V. Up to this voltage the LC molecules retain their rest position and, when the threshold is exceeded, they start to progressively tilt away from the capillary axis. The threshold existence is an anticipated feature, in full analogy to the threshold occurring in planar LC cells that is equal to $E_{\text{th}} = \frac{\pi}{d}\sqrt{K/\varepsilon_0\Delta\varepsilon}$ (Stewart, 2004). A typical tilt profile $\theta(x, y)$ is shown in the bottom left inset at 7 V, demonstrating azimuthal symmetry. Tilting is by far the main distortion in this arrangement, originating from the major electric field component which is vertical (i.e. along the $y$ axis) and also demonstrates high levels of uniformity as shown in the bottom right inset. The switched state is complemented by faint levels of twisting (not shown), due to the minor (horizontal) electric field

component. This secondary effect has a vanishingly small contribution to the overall optical response.

The dynamics of switching are primarily governed by the rotational viscosity of the LC material (typically in the range of 50−200 mPa s), the elastic constants and the LC thickness. For typical nematic LC materials, the switching speed is in the millisecond scale. We will provide some further quantitative information on this point in Section 3.4.1, including rise times and relaxation times, for a particular LC-PCF device.

### 3.2.2 LC switching in infiltrated PCF lattices

In Section 3.2.1, we have examined LC switching in an isolated cylindrical capillary in the context of the continuum theory. It is reasonable to further investigate the case of the infiltrated PCF lattice, in which case many tens or a few hundreds of infiltrated capillaries are actually involved. Figure 3.4 depicts a typical PCF with a triangular lattice of circular voids, extending to seven rings around a solid core. All voids are filled by the nematic material E7 and the fibreglass is silica. Voltage is applied via a pair of planar electrodes in contact with the external circumference of the fibre. Figure 3.4(a) presents the tilt angle at 150 V, whereas Figure 3.4(b) presents the corresponding dominant (vertical) electric field component at the same voltage. The tilt distribution per individual capillary is almost uniform, with the tunability factor (average measure of the nematic director deviation from the rest axial position) varying by less than 1% over the different rings. The corresponding twist angles are bounded to very low values, below 2°, as in the isolated capillary case, thus minimally impacting the overall response.

It should be stressed that only a fraction of the applied voltage ($\Delta V/V_0$) is actually dropped across the capillaries, and thus is engaged in the LC switching mechanism. This fraction is directly related to the fibre's diameter, the fibreglass dielectric

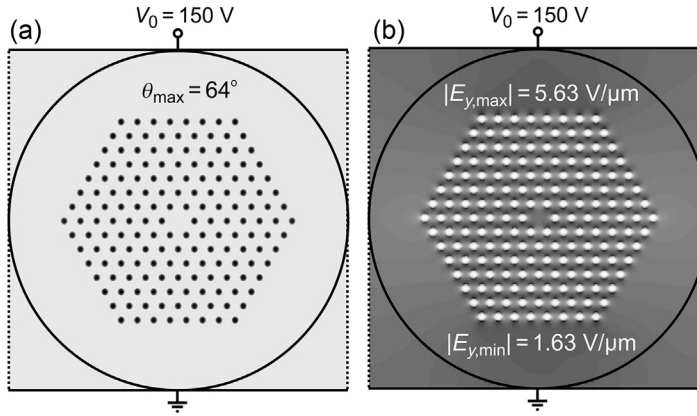


**Figure 3.4** Photonic crystal fibres (PCFs) with LC-infiltrated triangular lattice of seven rings: (a) tilt distribution and (b) dominant electric field component at an applied voltage of 150 V.

permittivity, the LC static permittivities and the level of switching (thus $V_0$ itself). In particular, for a positive anisotropy material such as E7, the fraction $\Delta V/V_0$ dropped across the capillaries is significantly higher at low tilt angles and shrinks as the molecules tilt further away from the capillary axis. Observing Figure 3.4(b) we notice the appreciable variation of the electric field in the fibre's cross-section ($E_{y,\min} = 1.63$ V/μm, $E_{y,\max} = 5.63$ V/μm); however, the electric field intensity inside every capillary is almost constant, leading to uniform switching.

The necessary voltage for switching the complete lattice seems, at least at first instance, quite excessive, and this necessitates some further commenting. The required voltage can be reduced up to an extent with more elaborate electrode design, for instance polishing a standard 125 μm fibre in order to bring the electrodes closer to the LC cladding or directly integrating the electrodes in the fibreglass material. Such approaches have been experimentally demonstrated (Chesini et al., 2009). More importantly, the high voltage does not necessarily imply high-power consumption, as well. The power consumption associated with LC-PCF devices stems from the fact that the voltage applied is actually an AC one at low frequency (typically around 1 kHz) in order to drive the LC material without ionic migrations or impairments. As in other devices relying on capacitive operation, this power can be estimated by $P = (1/2)CV^2f$, with $C$ being the total component capacitance, $V$ the driving peak-to-peak voltage and $f$ the LC driving frequency. A rudimentary calculation predicts capacitance values in the range of tens of pF/μm, which for device lengths in the millimetre scale, driving voltages of tens of volts and a driving frequency of 1 kHz finally translate into a theoretical power consumption in the μW regime. This is an astonishingly small value that provides strong evidence that sub-mW LC-PCF devices are possible.

## 3.3 Light guidance in LC-infiltrated PCFs

Compared to their conventional counterparts, light guidance in PCFs involves more complicated mechanisms and much richer physics. This is owing to the particular features, unique to PCFs, that include the cladding's design and periodicity, the geometry of the defect core, the adjustability of the various geometrical parameters and the possibility to fill – selectively or not – the PCF capillaries with materials characterized by properties different than those of the host fibreglass.

In the most standard configuration, the PCF core is solid and the cladding is composed of a triangular periodic lattice of void microcapillaries. In this case, the core shows a higher refractive index compared to the composite glass/air cladding and light is guided through the fibre's core by index guiding, a mechanism which shows certain similarities to total internal reflection in standard optical fibres, albeit with some notable differences. First, the refractive index of the PCF cladding is highly dispersive, a property that, by proper design, can lead to extraordinary properties, such as endlessly single-mode operation (Birks, Knight, & Russell, 1997) or targeted dispersion profiles (Roberts et al., 2005). Second, all guided modes in index-guiding PCFs suffer from inherent confinement losses, stemming from light tunnelling from the core towards the bulk fibre cladding in the exterior of the microstructured region.

Although the periodicity of the cladding is not a prerequisite in index-guided PCFs (Monro, Bennett, Broderick, & Richardson, 2000), it is almost always present as it facilitates both the fabrication process and the PCF design.

Bandgap guidance arises from the periodicity of the cladding that, under appropriate conditions, acts as a mirror within certain spectral windows − the photonic bandgaps − and permits light confinement in the PCF's core, provided the latter exhibits a lower refractive index than that of the cladding. These conditions are, for instance, fulfilled when the PCF capillaries are infiltrated with a material, liquid or solid, of higher refractive index than that of the fibreglass − even slightly higher (Argyros, Birks, Leon-Saval, Cordeiro, & Russell, 2005) − or when an extra air capillary is introduced in the core, thus reducing its average refractive index, as in hollow-core (Amezcua-Correa et al., 2008) or honeycomb-lattice PCFs (Knight, Broeng, Birks, & Russell, 1998).

Depending on the fibre design and the refractive indices of the materials used, LC infiltrated PCFs can rely on either of the two light-guiding mechanisms. Common nematic compounds are characterized in the infrared by an ordinary index around 1.5 and an extraordinary one which can vary from 1.55 up to 2.1, for high $\Delta n$ materials (Catanescu, Wu, & Chien, 2004). The fibreglass index typically starts from $n_g = 1.444$ for pure silica at 1550 nm and can be increased by adding various metal oxides up to more than 2.0, as in the case of telluride or chalcogenide fibres. Various PCFs relying on the aforementioned high-index glasses have been fabricated using techniques such as stack-and-draw, sol−gel casting or ultrasonic drilling (Feng, Mairaj, Hewak, & Monro, 2005).

As discussed in Section 3.2, in most cases the LC molecules in infiltrated capillaries tend to lie parallel to the fibre axis when no voltage is applied, because this configuration minimizes their total energy. This implies that light of either polarization, $x$ or $y$, senses the LC ordinary index, and the fibre is not birefringent, regardless of the guiding mechanism. In the extreme case of perfect LC alignment along the direction of the applied electric field, the two polarizations inside the capillary sense a maximum index difference, equal to the LC birefringence $\Delta n$. Given the ample selection of available materials and the degrees of freedom provided by the fibre's geometry, one can design LC-PCFs with tailored properties, such as selective single-polarization or high-birefringence guidance, examples of which are described in the rest of this section.

The rigorous analysis of the optical properties of LC-PCFs requires the use of numerical tools capable of taking into account the fully anisotropic nature of the nematic materials. To this end, amongst the various methods used for the study and design of PCFs (Scarmozzino, Gopinath, Pregla, & Helfert, 2000), we have utilized the plane-wave expansion method for the extraction of the bandgaps of infinite periodic claddings (Johnson & Joannopoulos, 2001), finite-element eigensolvers (Zografopoulos, Pitilakis, & Kriezis, 2013) and finite-difference time-domain formulations (Zografopoulos, Kriezis, & Tsiboukis, 2006b) for the extraction of the modal properties, that is, modal effective index, confinement losses and modal area, the beam-propagation method (Pitilakis et al., 2011) and an eigenvalue expansion method (Zografopoulos et al., 2013) to study light guidance and polarization conversion phenomena in LC-PCFs.

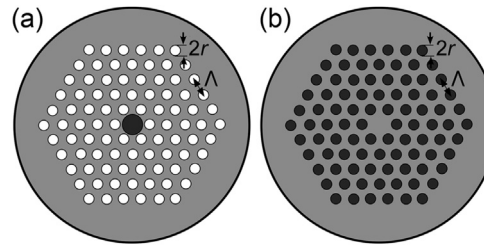


**Figure 3.5** Schematic layout of two triangular lattice index-guiding LC-PCFs: (a) LC-core/air-cladding and (b) solid-core/LC-cladding. Dark grey indicates the LC-infiltrated parts.

### 3.3.1 Index guidance in LC-PCFs

Two generic LC-PCF designs which rely on the index-guiding mechanism are schematically shown in Figure 3.5. In the layout of Figure 3.5(a), an extra capillary is added in the defect core and selectively infiltrated with a nematic material, whereas the cladding capillaries remain void. When no voltage is applied, the LC molecules rest along the fibre axis and the defect core is characterized by the ordinary LC index $n_o$. Light guidance depends on the effective index of the cladding, which is highly dispersive and corresponds to the dispersion curve of the fundamental space-filling mode, that is, the highest-index mode supported by the infinite periodic lattice of air capillaries, also termed as the radiation line (Koshiba & Saitoh, 2004; Zografopoulos, Kriezis, & Tsiboukis, 2006a). If $n_o$ is sufficiently low, then the LC-PCF cannot guide light in the rest case. In the case of uniform LC alignment along either of the orthogonal axes, that is, in the limit of an infinite electric field, the polarization perpendicular to the applied field still senses a low-index core, whereas the parallel one senses a higher index core, close to the extraordinary LC index $n_e$. By proper design and selection of materials, fibreglass and LC, the LC-PCF can guide either a single-polarization, or both with high modal birefringence (Zografopoulos et al., 2006a).

A specific design that targets voltage-controlled single-polarization operation, is investigated in Figure 3.6. The PCF is made of the high-index $PbO/SiO_2$ glass SF6, which has been experimentally demonstrated as a successful fibreglass material for PCFs (Hundertmark et al., 2009). Its refractive index at 1529.6 nm is $n_g = 1.764$ and its dispersion is described by a Sellmeier formula (Schott). Its low-frequency permittivity is equal to $\varepsilon_r = 12.5$ (Cohen, Uhlmann, & Shaw, 1973). The PCF cladding consists of seven rings of air capillaries with radius $r = 0.75$ μm, and the lattice pitch is $\Lambda = 3$ μm. The central defect capillary is larger ($r_c = 1$ μm), and it is infiltrated with the nematic material E44, characterized by $K_{11} = 15.5$ pN, $K_{22} = 13$ pN, $K_{33} = 28$ pN (Cui, Zola, Yang, & Yang, 2012) and $\varepsilon_o = 5.2$, $\varepsilon_e = 22$ (Wang, Wang, & Bos, 2004). Its refractive indices are described by a Cauchy model and they obtain the values $n_o = 1.5044$ and $n_e = 1.7337$ at 1550 nm (Li, Wen, Gauza, Lu, & Wu, 2005). The control voltage is applied across a fibre diameter of 62.5 μm and the fibre is assumed to reside in an index-matching gel.

For this selection of materials, the polarization sensing $n_o$ in the core cannot be guided, as $n_o$ is significantly lower than $n_g$. Although $n_e$ is also lower than $n_g$, light

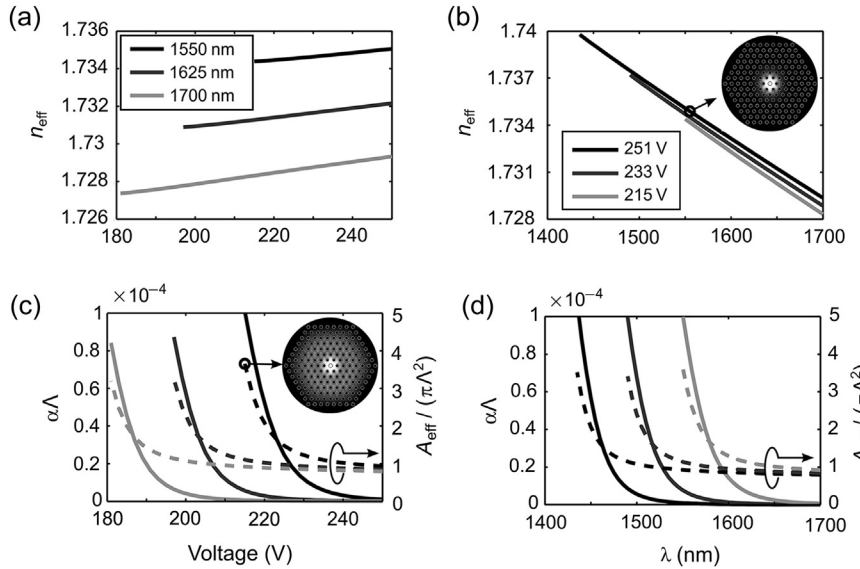


**Figure 3.6** Modal properties of the proposed LC-core single-polarization PCF: (a) modal effective index as a function of the applied voltage for three wavelengths. (b) Modal effective index as a function of wavelength for three values of applied voltage. Inset shows the electric field modal profile at 1550 nm and $V_0 = 251$ V. (c) Normalized confinement losses and effective modal area as a function of the applied voltage, in which $\alpha$ is the imaginary part of the mode propagation constant. Inset shows the modal profile at 1550 nm and close to the cutoff voltage, showing extensive leakage of the optical field in the PCF cladding. (d) Normalized confinement losses and effective modal area as a function of the operation wavelength.

can still be guided in the PCF with such a depressed-index core, provided this difference is small enough at the given wavelength (Mangan, Arriaga, Birks, Knight, & Russell, 2001). This is demonstrated in the results of Figure 3.6, in which the effective modal index, confinement losses and modal area are calculated as a function of the applied voltage in the wavelength range between 1400 and 1700 nm. The LC profiles in the infiltrated capillaries were calculated according to the methodology described in Section 3.2 and the modal properties by a fully anisotropic finite-element eigensolver (Zografopoulos et al., 2013). A voltage threshold is associated with each wavelength that indicates that the average index sensed by the guided polarization becomes enough to permit sufficient light confinement in the PCF core. It is interesting to point out that this threshold is lower for higher wavelengths. The SF6 fibreglass shows a much stronger normal dispersion than E44, and therefore the difference $n_g - n_e$ drops with increasing wavelength, thus relaxing the condition for the switching of the LC molecules. Therefore, this PCF allows for single-polarization guidance, only for sufficiently high applied-voltage values. This property can be exploited for the design of a single-polarization in-fibre switch, as will be discussed in Section 3.4.1.

Figure 3.5(b) shows the layout of a different approach towards functional index-guiding LC-PCFs. The fibre's core is solid and the cladding capillaries are infiltrated

with a nematic material. The fibre matrix is made of the lead-silicate fibreglass SF57 (Schott; Tiwari, & Janyani, 2011), whereas the capillaries of the PCF are infiltrated with the nematic mixture E7 (Li, Wu, Brugioni, Meucci, & Faetti, 2005). The fibreglass index is higher than both the ordinary and the extraordinary indices of the LC, meaning that the PCF is index guiding for both polarizations for any LC orientation. The pitch of the host matrix is $\Lambda = 3$ μm and the radius of the LC-filled capillaries is $r = 0.25\Lambda$. Placing the fibre between electrodes at a distance of $D = 45$ μm (the fibre resides inside an index-matching gel) can provide for electric control over the orientation of the LC, which subsequently affects the birefringence of the fibre. When the applied voltage is low, the LC molecules are aligned with the fibre axis, at which state the modal birefringence is zero. As the voltage is increased, the LC molecules are titled and progressively align with the electric field ($y$-axis), perpendicularly to the propagation direction; this transverse direction is the slow axis of the highly birefringent LC-PCF. In this case, the vertically polarized $HE_y$ fundamental mode senses a higher refractive index in the capillaries, compared to the horizontally polarized $HE_x$-mode, which in all cases senses an index very close to the ordinary index of the anisotropic material. As a result, the fibre's modal birefringence, $\Delta n_{\text{eff}} = n_{\text{eff},y} - n_{\text{eff},x}$, rises for higher values of the applied voltage. This is demonstrated in Figure 3.7(a), in which the modal birefringence is calculated as a function of the applied voltage and wavelength. High values of $\Delta n$, up to more than 0.001, can be readily achieved.

When the light launched in the birefringent LC-PCF is polarized at an angle with its slow axis, polarization rotation occurs along the propagation direction. For maximum conversion efficiency, light should be launched at $\pi/4$ with respect to the slow axis of the fibre (Hameed & Obayya, 2010). When the fibre length is equal to $L_\pi = 0.5\lambda/\Delta n$, a maximum polarization rotation is achieved, amounting to a $\pi$-phase retardation. Figure 3.7(b) shows that this polarization rotation can be extremely efficient, with very low values of crosstalk. The possibility to electro-optically control the LC-PCF's birefringence can be the key element for the operation of tunable-fibre components, such as the complete polarization controller investigated in Section 3.4.2.

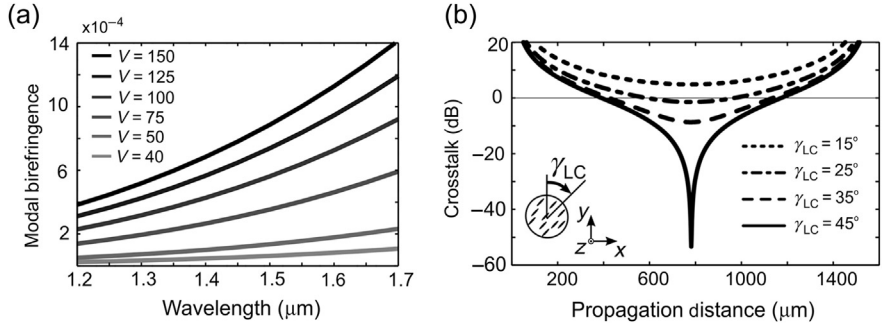


**Figure 3.7** (a) Modal birefringence of a high-index soft-glass SF57 PCF infiltrated with the nematic mixture E7 as a function of the applied voltage and the operation wavelength. Birefringence values higher than 0.001 are achievable for sufficiently high control voltage values. (b) Crosstalk of the $HE_x$ to $HE_y$ polarization conversion along the light propagation direction for different angles of the LC nematic director principal axis with respect to the fibre's slow axis (Pitilakis et al., 2011).

### 3.3.2 Bandgap guidance in LC-PCFs

Light propagation via the bandgap-guiding mechanism can be achieved in LC-PCFs, when the periodic cladding leads to the formation of bandgap windows, within which light can be confined in the central defect core. The most direct approach, which has been extensively studied both theoretically and experimentally in the literature, is to infiltrate triangular-lattice silica PCFs with a nematic material. Except for rare cases regarding the visible spectrum (Woliński et al., 2007), both LC indices are higher than that of silica. The presence of high-index inclusions in the silica PCF matrix leads to the formation of bandgaps. In the case of LC-PCFs, these bandgaps depend not only on the material, but also on the polarization and the LC orientation. In the extreme case, the two orthogonal polarizations sense a high-index cladding with an effective capillary index difference equal to the LC material birefringence $\Delta n = n_e - n_o$. Thus, the bandgaps are polarization-dependent, so that the LC-PCF can support single-polarization guidance, when the bandgap exists for a sole polarization, or high-birefringence guidance, when both polarizations are guided within their corresponding bandgaps (Ren, Shum, Hu, Yu, & Gong, 2008).

The optical properties of such an LC-PCF are investigated in Figure 3.8. A typical silica PCF, as in Figure 3.5(b), is infiltrated with the nematic mixture E7. The

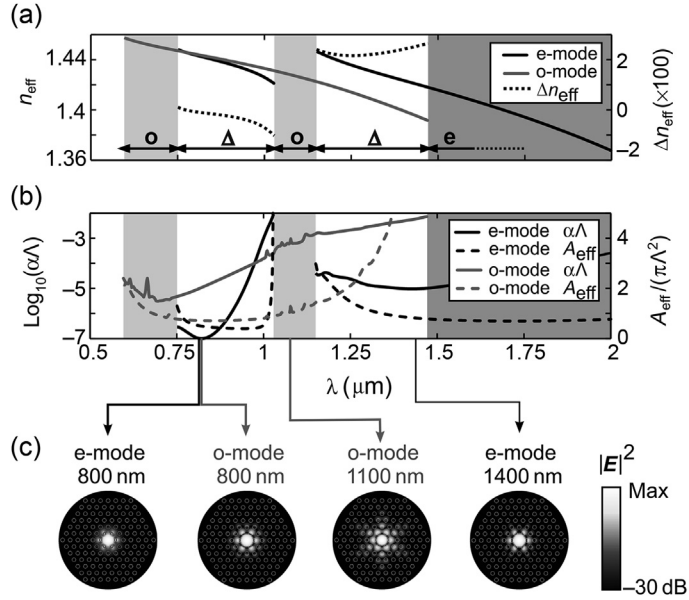


**Figure 3.8** (a) Modal effective indices and birefringence for the bandgap-guiding $SiO_2$/E7 LC-PCF studied. Shaded regions indicate single-polarization spectral windows. (b) Normalized confinement losses and modal effective area, and (c) optical power profiles for guided modes of *o*- and *e*-polarization calculated at different operational wavelengths.

triangular lattice pitch in the six-ring cladding is $\Lambda = 2$ μm, and the capillary radius $r = 0.5$ μm. The LC-PCF's properties are studied by means of a fully anisotropic finite-element eigensolver. The material index dispersion of both $SiO_2$ and E7 is taken into account. Figure 3.8(a) shows the effective modal indices for the two orthogonal polarizations and the corresponding modal birefringence $\Delta n_{\text{eff}}$, assuming a perfect alignment of the LC molecules along the *e*-axis. The bandgaps for each polarization define the spectral windows of high transmittance. When these overlap, both polarizations are guided, exhibiting very high values of $\Delta n_{\text{eff}}$. As one approaches the bandgap edges, the confinement losses and the effective modal area become higher, as shown in Figure 3.8(b). It is stressed that the results presented in Figure 3.8 are calculated for the extreme case of perfect alignment of the LC molecules along one of the orthogonal axes, that is, in the limit of infinite voltage. By adjusting the control voltage, it is possible to shift the bandgaps in an intermediate state for *e*-polarized light, and thus tune both the value of $\Delta n_{\text{eff}}$ and the propagation losses.

A different design of a bandgap-guiding LC-PCF is depicted in Figure 3.9(a), based on the honeycomb cladding structure, one of the first reported bandgap-guided PCFs (Knight et al., 1998; Lægsgaard, Mortensen, & Bjarklev, 2003). The PCF is made from a high-index tellurite glass with $n_g = 2.1$ and the cladding holes are infiltrated with E7 (Zografopoulos et al., 2006b). The radius of the cladding holes is $r = 0.25\Lambda$ and that of the void central defect $r_c = 0.2\Lambda$. The fibre is placed between a pair of electrodes and immersed in an index-matching gel. Under these conditions, the PCF supports bandgaps below the radiation line, which are shown in Figure 3.9(b) for the ideal case of perfect LC alignment. The guided modes of the two orthogonal polarizations of the fundamental mode are guided within their respective bandgaps and, consequently, they exhibit different dispersion curves. Modal birefringence can obtain values higher than 0.01, one to two orders of magnitude higher than that of conventional highly birefringent optical fibres.

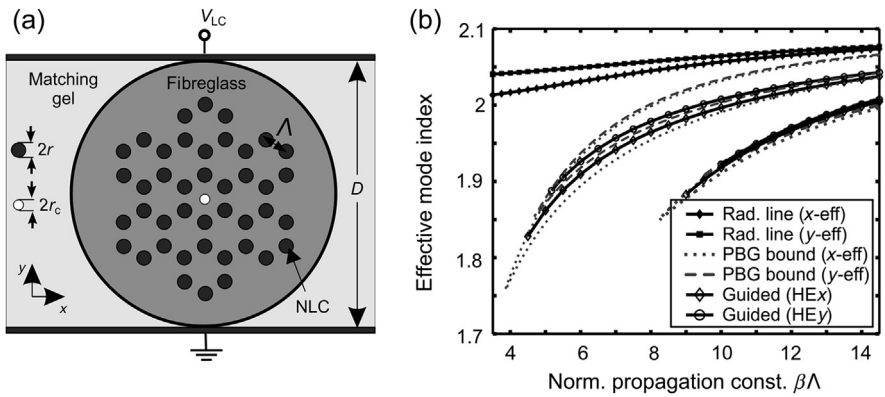


**Figure 3.9** (a) Layout of the proposed honeycomb-lattice LC-infiltrated bandgap-guiding PCF. (b) Radiation lines, bandgaps and guided-mode dispersion curves, showing high-birefringence operation in the interval of $5.5 < \beta\Lambda < 8.5$ (Zografopoulos et al., 2006b).

### 3.3.3 Hybrid guidance in LC-PCFs

It has been thus far shown that LC-PCFs can be designed to guide light via either the index- or bandgap-guiding physical mechanism. By taking advantage of the large LC optical anisotropy, a third class of LC-PCFs can be derived that combine the properties of both types. Such fibres exhibit hybrid guidance, that is, the two orthogonal polarizations are guided via different physical mechanisms (Sun & Chan, 2007). This particular case is not only interesting from the fundamental scientific point of view, but it also extends the range of property values and functionalities achievable by purely index- or bandgap-guiding LC-PCF.

A hybrid-guiding LC-PCF has been designed based on the generic layout of Figure 3.5(b) (Zografopoulos & Kriezis, 2009). The PCF cladding shows four air-hole rings, the radius for which is $r = 0.25\Lambda$, and the fibre is placed between a pair of electrodes, as in other LC-PCF designs here presented. The critical parameter is the selection of the materials, namely fibreglass and LC, which should satisfy the condition $n_o < n_g < n_e$. In this example, the fluorine-doped fibreglass F2 is selected (Buczynski et al., 2009), characterized by $n_g = 1.595$ at 1530 nm (Schott). The nematic material is a high $\Delta n$ mixture with $n_o = 1.51$ and $n_e = 1.86$ at 1550 nm (Gauza et al., 2005).

When no voltage is applied, light senses low-index capillaries and the two polarizations of the fundamental mode are degenerate, that is, modal birefringence is zero. As the control voltage is applied, for example along the $y$-axis, the LC molecules are tilted in the $y-z$ plane, attempting to align parallel to the applied electric field. This modifies the effective cladding index sensed by $y$-polarized light, which progressively obtains higher values. For low values of tilt, both polarizations are still index guided, yet $y$-polarized light senses a higher index, and therefore exhibits a higher effective modal index. This is demonstrated in Figure 3.10(a), in which the modal curves for

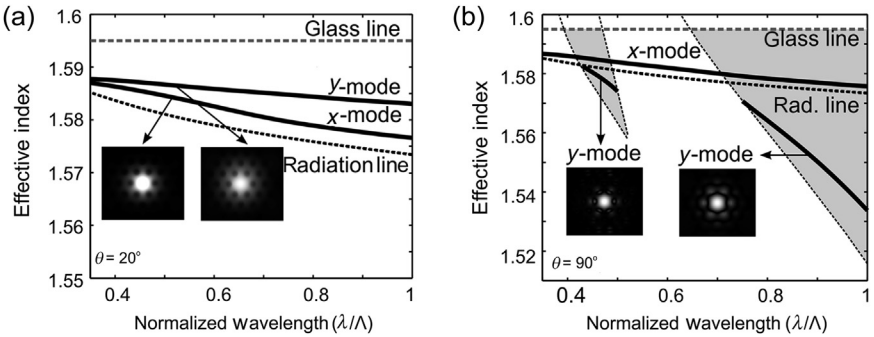


**Figure 3.10** Radiation line and modal dispersion curves for the two orthogonal fibre polarizations calculated at (a) $\theta = 20°$ and (b) $\theta = 90°$. For low tilt angle values the fibre is index guiding for both polarizations, whereas for higher tilt angles $y$-polarized light is bandgap guided and $x$-polarized light is index guided, indicating hybrid guidance for the LC-PCF (Zografopoulos & Kriezis, 2009).

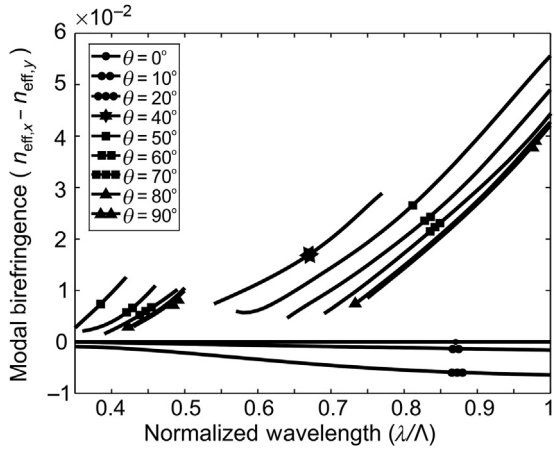


**Figure 3.11** Family of birefringence curves for various values of the LC tilt angle. As the tilt angle increases, the fibre passes through different operation modes: degenerate guidance, highly birefringent index guidance, single polarization and, finally, highly birefringent hybrid guidance (Zografopoulos & Kriezis, 2009).

both polarizations are calculated, assuming a uniform tilt angle. It is clear that both are index guided, with modal indices higher than the cladding's radiation line corresponding to the LC rest position. The higher cladding index sensed by *y*-polarized light also leads to weaker confinement, as shown in the modal profiles of Figure 3.10(a). For a certain voltage/tilt range, the capillary index for *y*-polarized light is close to $n_g$, and the mode suffers from very high confinement losses, indicating single-polarization operation.

When the voltage is further increased, the capillaries show a higher index than the fibreglass, and thus bandgap formation and guidance is allowed. The modal profiles for the extreme case of fully switched molecules are shown in Figure 3.10(b). Although the *x*-polarization is still index guided with the same properties, the orthogonal one is bandgap guided within the corresponding spectral windows. It is remarked that in this state the effective modal index of *y*-polarized light is lower than the radiation line and therefore the modal birefringence sign is inverted compared to the low tilt angle scenario of Figure 3.10(a). The dependence of the hybrid LC-PCF's modal birefringence on the tilt angle is summarized in Figure 3.11. For low tilt angles both modes are guided in the whole spectral window under investigation with $\Delta n_{\text{eff}} = n_{\text{eff},x} - n_{\text{eff},y} < 0$. For high tilt angles, the sign of $\Delta n_{\text{eff}}$ is reversed and can obtain extremely high values, up to 0.05, which are unachievable by conventional highly birefringent fibres. In general, hybrid-guiding LC-PCFs provide richer possibilities for the tuning of the fibre's polarization properties, as they combine the properties of both standard PCF light-guiding mechanisms. Via proper design, they could be promising as in-line polarization control components for light switching and manipulation in fibre optical systems.

## 3.4 Switching components based on LC-infiltrated PCFs

The examples presented in Section 3.3 demonstrate that by exploiting the inherent anisotropy of nematic materials and the tailoring capabilities offered by the design of PCFs one can tune a range of key properties by controlling the orientation of the nematic molecules. Such possibilities can be utilized in the design of LC-PCF all-in-fibre components, which can provide extensive control of light propagation in fibre optics networks. In the present section, we investigate three such LC-PCF-based switching components: a single-polarization switch, a complete polarization controller and a polarization splitter.

### 3.4.1 Single-polarization switch

The LC-PCF single-polarization switch under investigation is based on the LC-core fibre discussed in Section 3.3.1. It was shown that the fibre guides only one polarization, when the applied voltage is high enough to sufficiently tilt the LC molecules and raise the core effective index sensed by the transmitted polarization. This voltage threshold was found equal to 215 V for the wavelength of 1550 nm. To assess the fibre's performance as a switch, a rectangular pulse is applied. The peak voltage is set to 251 V. At $t = 0$ the fibre is in the rest position and LC molecules lie along its axis. When the pulse is applied at $t = 1$ ms, they start to reorient in order to follow the direction of the applied field. Allowing enough time for the LC to reach the steady state, the pulse is removed at $t = 10$ ms. The LC molecules follow an elastic relaxation and progressively return back to the rest position. The LC switching dynamics are modelled in the frame of the continuum theory presented in Section 3.2. To include the temporal dynamics, Eqn (3.5) takes the following form:

$$\frac{\partial F_{\mathrm{d}}}{\partial \xi} - \frac{\partial}{\partial x}\left(\frac{\partial F_{\mathrm{d}}}{\partial \xi_x}\right) - \frac{\partial}{\partial y}\left(\frac{\partial F_{\mathrm{d}}}{\partial \xi_y}\right) = \gamma_1 \frac{\partial \xi}{\partial t}. \tag{3.8}$$

The introduction of the time-dependent term in the right-hand side allows for the study of the molecular orientation in time. The rise and fall times are proportional to the rotational viscosity of the LC, which for E44 is $\gamma_1 = 280$ mPa s (Wang et al., 2004). The rise time, in general, drops for higher voltage values, whereas the fall time depends on the LC elastic constants and the dimensions of the cavity (Stewart, 2004).

Figure 3.12 shows the maximum tilt, at the centre of the LC-capillary, and the average tilt values as a function of time. The LC reaches the steady state after approximately 1.5 ms from the application of the control voltage and relaxes much slower, more than 10 ms after its removal. The fibre's response, described by the normalized confinement losses, is also shown in the same plot for comparison. During the switching of the LC molecules, losses remain high almost until the steady state is reached, because of the large voltage threshold that is 85% of the peak voltage value as extracted from Figure 3.6(c). On the contrary, when the pulse is switched off the fibre optical response is much faster than the LC relaxation dynamics, because a small

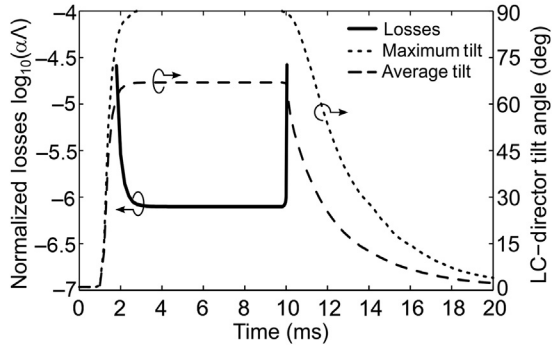


**Figure 3.12** Switching dynamics in the LC-core PCF investigated in Section 3.3.1. A rectangular voltage pulse peaking at 251 V is applied to the LC electrodes for the time interval between 1 and 10 ms, tilting the nematic director and allowing the guiding of a low-loss *y*-polarized mode, at 1550 nm. The LC molecules are assumed pretilted at 1°. When the pulse is switched off, the fibre's optical response follows much faster dynamics than the LC elastic relaxation.

decrease of the tilt angle reduces the effective refractive index in the LC core and inhibits light confinement. For the case here investigated, the switch is in the ON state when the guided-mode confinement losses are very small (less than approximately 0.1 dB/cm); these losses can be further reduced by adding more rings in the cladding. On the contrary, in the OFF state, in which no guided mode is supported, the insertion losses of the fibre become extremely high for fibre lengths larger than 1 mm.

The operation of the polarization switch demonstrates that, depending on the LC-PCF design, the dynamics of the fibre's tunable properties do not necessarily follow those of the nematic LC. In the case studied, the fibre's response time is determined by the LC rise time, which in turn depends on the applied voltage and is more than one order of magnitude faster than the fall time. These results suggest that, by proper fibre design and selection of the nematic material, components with even faster response times can be envisaged. For instance, commercially available nematic mixtures exist with high birefringence and viscosity lower than 100 mPa s, which is approximately three times lower than that of E44 or that of the common nematic mixture E7. Considering such a material in the single-polarization fibre switch here investigated would imply submillisecond response times, which is state of the art for nematic-LC-based photonic/optical components (Jiao, Ge, Wu, & Choi, 2008).

### 3.4.2 Complete polarization controller

A compact-sized in-fibre electrically tunable polarization controller can be designed exploiting the tunable birefringence in LC-infiltrated glass-core PCFs (Pitilakis et al., 2011), as presented in Section 3.3.1. This component performs arbitrary conversions between the input and output state of polarization (SoP), using a set of three voltages, similarly to the set of three wave plates used in classical polarization controllers. The SoP of light propagating in a fibre is calculated by means of the Stokes parameters

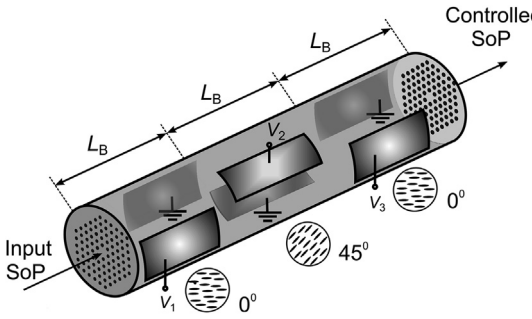


**Figure 3.13** The proposed polarization controller is made of an LC-PCF divided into three sections, each one with its own pair of electrodes; the electrode orientation in the middle section is at an angle of $\pi/4$ with respect to the input and output ones. The three sections are of equal length, each one providing a relative phase retardation of $0-2\pi$, proportional to the applied voltage (0−150 V).

(Zhuang, Suh, & Patel, 1999) and its evolution can be mapped on the surface of a Poincaré sphere. The LC-PCF employed supports *y*-polarized ($HE_y$) and *x*-polarized ($HE_x$) modes, which are assumed quasi-transverse electromagnetic for the purposes of polarization rotation.

The polarization controller relies on the LC-PCF with controllable high-birefringence studied in Section 3.3.1. The layout of the polarization controller component is shown in Figure 3.13 and it is composed of three consecutive sections of the aforementioned LC-PCF. All three sections are of length $L_B = 2L_\pi$, each one providing a relative phase retardation of up to $2\pi$, between the orthogonally polarized modes of the fibre at the design wavelength. The phase retardation is proportional to the applied voltage in each section, effectuated by three pairs of electrodes, placed so that the fibre's slow axis in the second section is rotated by $\pi/4$ with respect to the axis of the other two sections. This configuration can provide dynamic polarization control at the fibre's output (Oh, Kwon, Shin, Choi, & Oh, 2004). The component is designed for operation at 1.55 μm and for a maximum voltage of $V_{max} = 150$ V, leading to a device length $L_{tot} = 6L_\pi = 4.65$ mm, in which $L_\pi = 0.5\lambda/\Delta n_{eff}(V_{max})$. The maximum voltage can be reduced at the expense of increasing the length of the fibre sections.

To demonstrate the functionality of the polarization controller, two rotation examples are assessed (Pitilakis et al., 2011). The input SoP is in both cases a polarization near the characteristic point 'P', whereas $HE_x$ (point 'H') or $HE_y$ (point 'V') are the targeted SoP at the output. The point 'P' corresponds to an equal proportion of 'V' and 'H' polarizations. The necessary phase shifts, and subsequently modal birefringence values, were calculated by the Stokes parameters of the selected input and output SoP (Zhuang et al., 1999). The voltages which lead to the required $\Delta n$ in each of the three sections are equal to 116, 58 and 100 V, respectively, for the 'P-to-H' conversion, and 116, 113 and 68 V, respectively, for the 'P-to-V' conversion. The nematic director profiles at the fibre's cross-section are consistently calculated by solving the coupled electrostatic and elastic problem using the formulation described in Section 3.2. The LC profiles for each of the three sections were then fed into an in-house fully anisotropic finite element-based beam propagation method (BPM), to model light propagation and quantify the polarization rotation along the tunable birefringent LC-PCF.

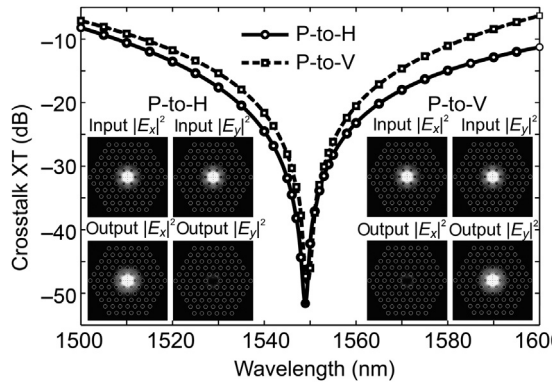


**Figure 3.14** Spectral response of the LC-PCF polarization controller, depicting the crosstalk (XT) between the two orthogonal polarizations at the fibre output, for the 'P-to-H' and 'P-to-V' conversions. XT values lower than −20 dB in a range of 30 nm, or more, are predicted. The insets show the modal intensity profiles of the two transverse components (Pitilakis et al., 2011).

The efficiency of the proposed polarization controller is numerically evaluated by calculating the crosstalk (XT) between the two orthogonal polarizations. The XT is defined as the ratio of the guided power in each of the two polarizations which is, in turn, calculated via vector overlap integrals of the electric field at the component output (for a given voltage value at each of the three sections) with the reference $HE_x$ and $HE_y$ modes of the fibre at-rest state (low voltage). The spectral response of the component for the two conversion examples studied is presented in Figure 3.14. The XT is found to be below −20 dB for a range larger than 40 and 30 nm for the 'P-to-H' and 'P-to-V' cases, respectively, whereas the corresponding minima are −53 and −48 dB both found near the design wavelength of 1.55 μm. The insets of Figure 3.14 depict the cross-section intensity profiles of the input and output electric fields for the 'P-to-H' and 'P-to-V' conversions in the vicinity of 1.55 μm. These results demonstrate the efficiency of the dynamic polarization control provided by the electrically tunable LC-PCF.

### 3.4.3 Polarization splitter

Compact tunable all-in-fibre polarization splitters can be designed utilizing the dual-core PCF depicted in Figure 3.15(a). The solid-glass core of the PCF lies in proximity to an LC-infiltrated capillary of a radius larger compared to the rest of the lattice capillaries, which are void; the LC-infiltrated capillary serves as the second core of the fibre. Electro-optical control of the LC-core's guiding properties allows for tuning of the polarization-dependent coupling length ($L_C$) between the two cores which can be used to design a polarization splitter (LC-PCF-PS) component (Zografopoulos et al., 2013).

The schematic of the proposed dual-core LC-PCF-PS is shown in Figure 3.15(a). The radius of the LC-filled capillary is $R = 0.5\Lambda$, in which $\Lambda = 2.15$ μm is the pitch of the cladding's triangular lattice, formed by four rings of void capillaries of radius $r = 0.25\Lambda$. The LC material is the nematic mixture E7 with ordinary and extraordinary refractive indices $n_o = 1.5024$ and $n_e = 1.697$, respectively, at 1550 nm and at 25 °C;

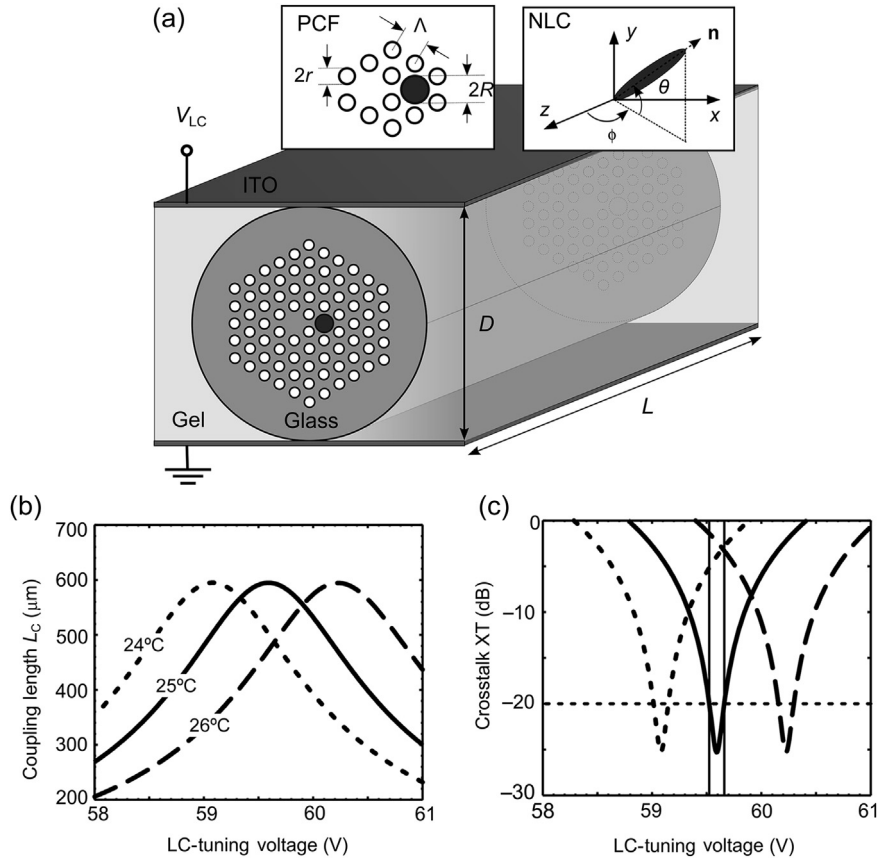


**Figure 3.15** (a) Schematic of the dual-core LC-infiltrated PCF where all structural parameters are annotated. (b) Coupling length for the *y*-polarized modes of the fibre as a function of $V_{LC}$ at 1550 nm. (c) Output-port crosstalk as a function of $V_{LC}$, for a *y*-polarized input excitation of the F2-glass core of the dual-core LC-PCF-PS and for a fibre length equal to the $L_C$ of each voltage (Zografopoulos et al., 2013).

accurately fitted frequency- and temperature-dispersion formulas for the E7 can be found in Li et al. (2005). The fibreglass material is the high-index lead-silicate Schott F2 glass, with an index of $n_g = 1.595$ at 1550 nm, in between the E7 indices; the frequency dispersion for F2 is provided by a three-term Sellmeier formula (Schott). The fibre diameter is $D = 50$ μm, and it is immersed in an index-matching gel, bounded by a pair of planar indium-tin-oxide electrodes which apply an external voltage $V_{LC}$ across the fibre. The cross-section distribution of the nematic director inside the LC-filled capillary is acquired by rigorously solving the coupled electrostatic/elastic problem, for a given voltage value, as presented in Section 3.2.1 (Pitilakis et al., 2011). The modal properties of the fibre are extracted using a finite element-based eigenmode solver and are then used to design and model the component.

The operating principle of the electrically tunable LC-PCF-PS is as follows: At the rest case ($V_{LC} = 0$), the LC molecules align along the fibre axis ($z$) and both $x$- and $y$-polarized light in the LC-core senses the low ordinary index. No guided mode is supported by the LC-core for these conditions, and hence coupling between the two cores is not allowed. When $V_{LC}$, applied along the $y$-axis, exceeds a certain threshold, then the LC molecules progressively align with that axis and their tilt angle, denoted by $\theta$ in the inset of Figure 3.15(a), increases. In this case, a $y$-polarized mode guided inside the LC-core, emerges from cutoff. As the relation $n_o < n_g < n_e$ is satisfied, there exists a certain voltage at which the effective index of the mode situated in the LC-core equals that of the (voltage-independent) mode situated in the solid core, for the $y$-polarized light only. This is the synchronized state of the component, in which the $L_C$ is maximal and complete power transfer is possible between the two cores. Note that $x$-polarized light is unaffected by the applied voltage and can only be guided in the solid core of the fibre. The voltage-dependence of the $L_C$ for $y$-polarized light at 1550 nm is depicted in Figure 3.15(b) in which we observe that a voltage approximately equal to 60 V is required to synchronize the device at a maximum coupling length of 595 μm. Finally, the temperature sensitivity of the device is also investigated, by introducing appropriate changes to the material properties at both the electrostatic/elastic and the optical waveguiding problems (Zografopoulos et al., 2013). Allowing for a 1 K deviation from the nominal temperature, the synchronization voltage is found to be marginally shifted, whereas the maximum coupling length − which is the parameter of interest − is negligibly affected.

To quantify the performance of the LC-PCF-PS component, the output-port crosstalk (XT) is used, defined as the ratio of the guided power between the solid- and LC-core of the fibre, for $y$-polarized light (Zografopoulos et al., 2013). When light is launched into the solid core of the PCF and the fibre length is equal to an even (or odd) multiple of $L_C$, $y$-polarized light exits through the solid (or LC) core. As the $x$-polarized light is unable to couple to the LC-core, it always exits through the solid core. Consequently, polarization splitting is achieved at the output of the fibre when its length is an odd multiple of the voltage-dependent $L_C$. The voltage dependence of the XT is depicted in Figure 3.15(c) in which we observe that satisfactory XT values of less than −20 dB are attained when the LC-PCF-PS is synchronized. The fibre length is, in all cases, equal to the $L_C$ for the given voltage, as given by Figure 3.15(b). The optical field profile at the fibre output is acquired by means of an eigenmode expansion model utilizing the guided LC-PCF modes for a given set of voltage, fibre length and input excitation. The validity of this semi-analytical approach was crosschecked with a fully vectorial BPM.

By properly adjusting the overall length of the fibre, the LC-PCF-PS can achieve selectable dual-band operation. The synchronization voltage at 1300 nm is slightly different compared to 1550 nm, but the corresponding (maximal) coupling length is considerably different, 930 versus 595 μm. Consequently, if an overall fibre length which equals an odd multiple of the $L_C$ for both wavelength bands is chosen, then selectable dual-band operation can be achieved. For the given LC-PCF parameters, this length equals 6530 μm, which approximately satisfies the condition $6530 \approx 11 \times 595 \approx 7 \times 930$. The performance of the component, in terms of the output-port XT, is depicted in

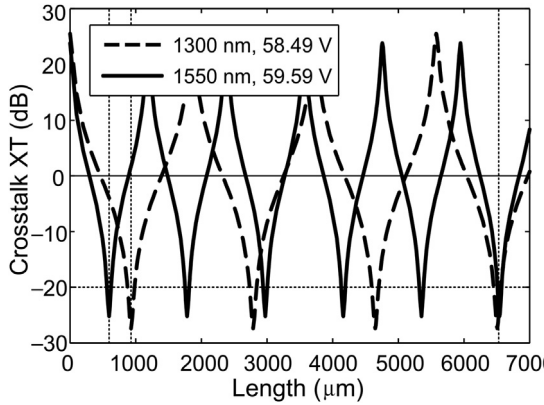


**Figure 3.16** Output-port crosstalk calculated along the LC-PCF-PS for a *y*-polarized input at the two target wavelengths of 1300 and 1550 nm for an applied voltage of $V_{s1} = 58.49$ V and $V_{s2} = 59.59$ V, respectively. The first XT minima occur at the corresponding coupling lengths $L_{c1} = 929.7$ mm and $L_{c2} = 594.7$ mm, which are the optimum fibre lengths for single-band operation. When the fibre length is approximately 6530 mm, selectable dual-band operation is possible, in which XT values below -20 dB are attained for both wavelength bands (Zografopoulos et al., 2013).

Figure 3.16 as a function of the fibre length for which the single- and dual-band regimes are clearly identified. The corresponding spectral response over a range of 100 nm is depicted in Figure 3.17(a) for the 1300 nm band, and in Figure 3.17(b) for the 1550 nm band. These figures reveal the excellent performance of the device, allowing

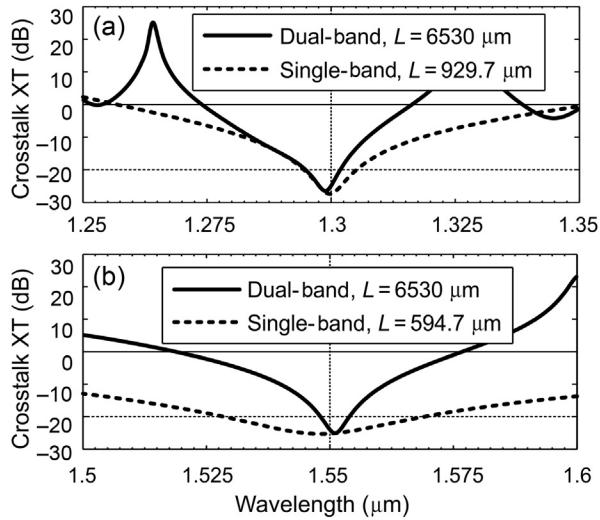


**Figure 3.17** Spectral response of the polarization splitter for both single- and dual-band operation at the target wavelengths of (a) 1300 nm and (b) 1550 nm. The LC voltage values used for each wavelength window are the same as in Figure 3.16 (Zografopoulos et al., 2013).

for crosstalk values lower than −20 dB in a 40-nm window at 1550 nm, for an ultra-compact length less than 0.6 mm.

## 3.5 Concluding remarks

In the decade following the first demonstration of LC-based PCF components (Larsen et al., 2003), this scientific field has expanded rapidly in terms of both the demonstration of new functionalities and novel solutions in practical problems, such as splicing, LC alignment, addressing and reduction of scattering losses. Taking advantage of the diverse physical mechanisms of light guiding and manipulating in PCFs, as well as of the inherent properties of liquid crystalline materials, numerous tunable components have been demonstrated, envisaged as essential parts of fibre optic networks.

Although the basic principles regarding the switching properties of LC-PCF have already been demonstrated, there is still plenty of space for the design and development of LC-PCF components with enhanced or entirely new features. The continuous progress in the chemical synthesis of novel LC materials promises the delivery of nematic mixtures with higher birefringence and lower viscosities, thus extending the range of tunable LC-PCF devices and reducing their response speed. Another promising route, the exploration of which has already been launched, is the use of 'exotic' LC compounds, such as polymerizable LCs (Zito & Pissadakis, 2013), LCs with controllable defects for bistable devices, LCs with nanoparticle dispersions (Scolari et al., 2009), azo-dyes for all-optical switching and blue phases. These materials are characterized by unique physical and chemical properties that provide additional possibilities, thus far unexplored.

In parallel, building on the accrued experience, progress in fabrication technologies is expected to offer new solutions for key issues, such as electrode definition or integration, LC infiltration and alignment quality, and in- and out-splicing of the LC-PCF. Such improvements are expected to lower the component's insertion losses and power budget and will ease their integration in fibre optics networks and systems. Thus, by merging the potential of PCFs (a special class of optical fibres with unprecedented properties) and LC materials (a traditional solution for the low-power electro-optical control of photonic components), LC-PCFs can emerge as a promising solution of in-line integrated fibre components for switchable light routing and polarization control.

## Acknowledgements

This work was supported by the European Union (European Social Fund − ESF) and Greek national funds through the Operational Programme 'Education and Lifelong Learning' of the National Strategic Reference Framework (NSRF) Research Funding Programme THALES 'Reinforcement of the interdisciplinary and/or interinstitutional research and innovation' (Project ANEMOS).

## References


Alkeskjold, T. T., & Bjarklev, A. (2007). Electrically controlled broadband liquid crystal photonic bandgap fiber polarimeter. *Optics Letters, 32*, 1707−1709. http://dx.doi.org/10.1364/OL.32.001707.

Alkeskjold, T. T., Lægsgaard, J., Bjarklev, A., Hermann, D. S., Broeng, J., Li, J., et al. (2006). Highly tunable large-core single-mode liquid-crystal photonic bandgap fiber. *Applied Optics, 45*, 2261−2264. http://dx.doi.org/10.1364/AO.45.002261.

Alkeskjold, T. T., Lægsgaard, J., Bjarklev, A., Hermann, D. S., Broeng, J., Li, J., et al. (2004). All-optical modulation in dye-doped nematic liquid crystal photonic bandgap fibers. *Optics Express, 12*, 5857−5871. http://dx.doi.org/10.1364/OPEX.12.005857.

Alkeskjold, T. T., Scolari, L., Noordegraaf, D., Lægsgaard, J., Weirich, J., Wei, L., et al. (2007). Integrating liquid crystal based optical devices in photonic crystal fibers. *Optical and Quantum Electronics, 39*, 1009−1019. http://dx.doi.org/10.1007/s11082-007-9139-8.

Amezcua-Correa, R., Gèrôme, F., Leon-Saval, Broderick, N. G. R., Birks, T. A., & Knight, J. C. (2008). Control of surface modes in low loss hollow-core photonic bandgap fibers. *Optics Express, 16*, 1142−1149. http://dx.doi.org/10.1364/OE.16.001142.

Argyros, A., Birks, T. A., Leon-Saval, S. G., Cordeiro, C. M. B., & Russell, P. St. J. (2005). Guidance properties of low-contrast photonic bandgap fibers. *Optics Express, 13*, 2503−2511. http://dx.doi.org/10.1364/OPEX.13.002503.

Birks, T. A., Knight, J. C., & Russell, P. St. J. (1997). Endlessly single-mode photonic crystal fiber. *Optics Letters, 22*, 961−963. http://dx.doi.org/10.1364/OL.22.000961.

Buczynski, R., Pysz, D., Martynkien, T., Lorenc, D., Kujawa, I., Nasilowski, T., et al. (2009). Ultra flat supercontinuum generation in silicate dual core microstructured fiber. *Laser Physics Letters, 8*, 575−581. http://dx.doi.org/10.1002/lapl.200810143.

Burylov, S. V. (1997). Equilibrium configuration of a nematic liquid crystal confined to a cylindrical cavity. *JETP, 85*, 873−886. http://dx.doi.org/10.1134/1.558425.

Catanescu, C. O., Wu, S.-T., & Chien, L.-C. (2004). Tailoring the physical properties of some high birefringence isothiocyanato-based liquid crystals. *Liquid Crystals, 31*, 541−555. http://dx.doi.org/10.1080/02678290410001662240.

Cerqueira, S. A., Jr. (2010). Recent progress and novel applications of photonic crystal fibers. *Reports on Progress in Physics, 73*, 024401. http://dx.doi.org/10.1088/0034−4885/73/2/024401.

Chesini, G., Cordeiro, C. M. B., de Matos, C. J. S., Fokine, M., Carvalho, I. C. S., & Knight, J. C. (2009). All-fiber devices based on photonic crystal fibers with integrated electrodes. *Optics Express, 17*, 1660−1665. http://dx.doi.org/10.1364/OE.17.001660.

Cohen, B. M., Uhlmann, D. R., & Shaw, R. R. (1973). Optical and electrical properties of lead silicate glasses. *Journal of Non-Crystalline Solids, 12*, 177−188. http://dx.doi.org/10.1016/0022-3093(73)90067-7.

Cui, Y., Zola, R. S., Yang, Y.-C., & Yang, D.-K. (2012). Alignment layers with variable anchoring strengths from polyvinyl alcohol. *Journal of Applied Physics, 111*, 063520. http://dx.doi.org/10.1063/1.3697680.

Du, J., Liu, Y., Wang, Z., Liu, Z., Zou, B., Jin, L., et al. (2008). Thermally tunable dual-core photonic bandgap fiber based on the infusion of a temperature-responsive liquid. *Optics Express, 16*, 4263−4269. http://dx.doi.org/10.1364/OE.16.004263.

Du, J., Liu, Y., Wang, Z., Zou, B., Liu, B., & Dong, X. (2008). Electrically tunable Sagnac filter based on a photonic bandgap fiber with liquid crystal infused. *Optics Letters, 33*, 2215−2217. http://dx.doi.org/10.1364/OL.33.002215.

Ertman, S., Rodríguez, A. H., Tefelska, M. M., Chychłowski, Pysz, D., Buczyński, et al. (2012). Index guiding photonic liquid crystal fibers for practical applications. *Journal of Lightwave Technology, 30*, 1208−1214. http://dx.doi.org/10.1109/JLT.2011.2172393.

Feng, X., Mairaj, A. K., Hewak, D. W., & Monro, T. M. (2005). Nonsilica glasses for holey fibers. *Journal of Lightwave Technology, 23*, 2046−2054. http://dx.doi.org/10.1109/JLT.2005.849945.

Gauza, S., Li, J., Wu, S.-T., Spadło, A., Dąbrowski, R., Tzeng, Y.-N., et al. (2005). High birefringence and high resistivity isothiocyanate-based nematic liquid crystal mixtures. *Liquid Crystals, 32*, 1077−1085. http://dx.doi.org/10.1080/02678290500303007.

Haakestad, M. W., Alkeskjold, T. T., Nielsen, M. D., Scolari, L., Riishede, J., Engan, H. E., et al. (2005). Electrically tunable photonic bandgap guidance in a liquid-crystal-filled photonic crystal fiber. *IEEE Photonics Technology Letters, 17*, 819−821. http://dx.doi.org/10.1109/LPT.2004.842793.

Hameed, M. F. O., & Obayya, S. S. A. (2010). Analysis of polarization rotator based on nematic liquid crystal photonic crystal fiber. *Journal of Lightwave Technology, 28*, 806−815. http://dx.doi.org/10.1109/JLT.2010.2040581.

Hänsch, T. W. (2006). Passion for precision (nobel lecture). *ChemPhysChem, 7*, 1170−1187. http://dx.doi.org/10.1002/cphc.200690024.

Hansen, K. P. (2005). Introduction to nonlinear photonic crystal fibers. *Journal of Optical and Fiber Communications Reports, 2*, 226−254. http://dx.doi.org/10.1007/s10297-004-0021-1.

Hsiao, V. K. S., & Ko, C.-Y. (2008). Light-controllable photoresponsive liquid-crystal photonic crystal fiber. *Optics Express, 16*, 12670−12676. http://dx.doi.org/10.1364/OE.16.012670.

Huang, Y., Xu, Y., & Yariv, A. (2004). Fabrication of functional microstructured optical fibers through a selective-filling technique. *Applied Physics Letters, 85*, 5182−5184. http://dx.doi.org/10.1063/1.1828593.

Hundertmark, H., Rammler, S., Wilken, T., Holzwarth, R., Hänsch, T. W., & Russell, P. St. J. (2009). Octave-spanning supercontinuum generated in SF6-glass PCF by a 1060 nm mode-locked fibre laser delivering 20 pJ per pulse. *Optics Express, 17*, 1919−1924. http://dx.doi.org/10.1364/OE.17.001919.

Jiao, M., Ge, Z., Wu, S.-T., & Choi, W.-K. (2008). Submillisecond response nematic liquid crystal modulators using dual fringe field switching in a vertically aligned cell. *Applied Physics Letters, 92*, 111101. http://dx.doi.org/10.1063/1.2896650.

Johnson, S. G., & Joannopoulos, J. D. (2001). Block-iterative frequency-domain methods for Maxwell's equations in a planewave basis. *Optics Express, 8*, 173−190. http://dx.doi.org/10.1364/OE.8.000173.

Kerbage, C., & Eggleton, B. J. (2002). Numerical analysis and experimental design of tunable birefringence in microstructured optical fiber. *Optics Express, 10*, 246−255. http://dx.doi.org/10.1364/OE.10.000246.

Knight, J. C. (2007). Photonic crystal fibers and fiber lasers (invited). *Journal of the Optical Society of America B, 24*, 1661−1668. http://dx.doi.org/10.1364/JOSAB.24.001661.

Knight, J. C., Broeng, J., Birks, T. A., & Russell, P. St. J. (1998). Photonic band gap guidance in optical fibers. *Science, 282*, 1476−1478. http://dx.doi.org/10.1126/science.282.5393.1476.

Koshiba, M., & Saitoh, K. (2004). Applicability of classical optical fiber theories to holey fibers. *Optics Letters, 29*, 1739−1741. http://dx.doi.org/10.1364/OL.29.001739.

Larsen, T. T., Bjarklev, A., Hermann, D. S., & Broeng, J. (2003). Optical devices based on liquid crystal photonic bandgap fibers. *Optics Express, 11*, 2589−2596. http://dx.doi.org/10.1364/OE.11.002589.

Liou, J.-H., Chang, T.-H., Lin, T., & Yu, C.-P. (2011). Reversible photo-induced long-period fiber gratings in photonic liquid crystal fibers. *Optics Express, 19*, 6756−6761. http://dx.doi.org/10.1364/OE.19.006756.

Li, J., Wen, C.-H., Gauza, S., Lu, R., & Wu, S.-T. (2005). Refractive indices of liquid crystals for display applications. *IEEE/OSA Journal of Display Technology, 1*, 51−61. http://dx.doi.org/10.1109/JDT.2005.853357.

Li, J., Wu, S.-T., Brugioni, S., Meucci, R., & Faetti, S. (2005). Infrared refractive indices of liquid crystals. *Journal of Applied Physics, 97*, 073501. http://dx.doi.org/10.1063/1.1877815.

Lægsgaard, J., Mortensen, N. A., & Bjarklev, A. (2003). Mode areas and field-energy distribution in honeycomb photonic bandgap fibers. *Journal of the Optical Society of America B, 20*, 2037−2045. http://dx.doi.org/10.1364/JOSAB.20.002037.

Mangan, B. J., Arriaga, J., Birks, T. A., Knight, J. C., & Russell, P. St. J. (2001). Fundamental-mode cutoff in a photonic crystal fiber with a depressed-index core. *Optics Letters, 26*, 1469−1471. http://dx.doi.org/10.1364/OL.26.001469.

Mathews, S., Semenova, Y., & Farrell, G. (2009). Electronic tunability of ferroelectric liquid crystal infiltrated photonic crystal fibre. *Electronics Letters, 45*, 617−618. http://dx.doi.org/10.1049/el.2009.0580.

Monro, T. M., Bennett, P. J., Broderick, N. G. R., & Richardson, D. J. (2000). Holey fibers with random cladding distributions. *Optics Letters, 25*, 206−208. http://dx.doi.org/10.1364/OL.25.000206.

Noordegraaf, D., Scolari, L., Lægsgaard, J., Alkeskjold, T. T., Tartarini, G., Borelli, E., et al. (2008). Avoided-crossing-based liquid-crystal photonic-bandgap notch filter. *Optics Letters, 33*, 986−988. http://dx.doi.org/10.1364/OL.33.000986.

Oh, Y.-H., Kwon, M.-S., Shin, S.-Y., Choi, S., & Oh, K. (2004). In-line polarization controller that uses a hollow optical fiber filled with a liquid crystal. *Optics Letters, 29*, 2605−2607. http://dx.doi.org/10.1364/OL.29.002605.

Olausson, C. B., Scolari, L., Wei, L., Noordegraaf, D., Weirich, J., Alkeskjold, T. T., et al. (2010). Electrically tunable Yb-doped fiber laser based on a liquid crystal photonic bandgap fiber device. *Optics Express, 18*, 8229−8238. http://dx.doi.org/10.1364/OE.18.008229.

Petersen, M. N., Scolari, L., Tokle, T., Alkeskjold, T. T., Gauza, S., Wu, S.-T., et al. (2008). Noise filtering in a multi-channel system using a tunable liquid crystal photonic bandgap fiber. *Optics Express, 16*, 20067−20072. http://dx.doi.org/10.1364/OE.16.020067.

Pitilakis, A. K., Zografopoulos, D. C., & Kriezis, E. E. (2011). In-line polarization controller based on liquid-crystal photonic crystal fibers. *Journal of Lightwave Technology, 29*, 2560−2569. http://dx.doi.org/10.1109/JLT.2011.2160523.

Ren, G., Shum, P., Hu, J., Yu, X., & Gong, Y. (2008). Polarization-dependent bandgap splitting and mode guiding in liquid crystal photonic bandgap fibers. *Journal of Lightwave Technology, 22*, 3650−3659. http://dx.doi.org/10.1109/JLT.2008.920125.

Roberts, P. J., Mangan, B. J., Sabert, H., Couny, F., Birks, T. A., Knight, J. C., et al. (2005). Control of dispersion in photonic crystal fibers. *Optical and Fiber Communications Reports, 2*, 435−461. http://dx.doi.org/10.1007/978-0-387-48948-3_9.

Rosberg, C. R., Bennet, F. H., Neshev, D. N., Rasmussen, P. D., Bang, O., Krolikowski, W., et al. (2007). Tunable diffraction and self-defocusing in liquid-filled photonic crystal fibers. *Optics Express, 15*, 12145−12150. http://dx.doi.org/10.1364/OE.15.012145.

Russell, P. St. J. (2006). Photonic-crystal fibers. *Journal of Lightwave Technology, 24*, 4729−4749. http://dx.doi.org/10.1109/JLT.2006.885258.

Scarmozzino, R., Gopinath, A., Pregla, R., & Helfert, S. (2000). Numerical techniques for modeling guided-wave photonic devices. *IEEE J Sel Top Quantum Electron, 6*, 150−162. http://dx.doi.org/10.1109/2944.826883.

SCHOTT, A. G. *Lead-oxide optical fiberglass series*. http://www.schott.com.

Scolari, L., Gauza, S., Xianyu, H., Zhai, L., Eskildsen, L., Alkeskjold, T. T., et al. (2009). Frequency tunability of solid-core photonic crystal fibers filled with nanoparticle-doped liquid crystals. *Optics Express, 17*, 3754−3764. http://dx.doi.org/10.1364/OE.17.003754.

Stewart, I. W. (2004). *The static and dynamic continuum theory of liquid crystals*. London and New York: Taylor & Francis.

Sun, J., & Chan, C. C. (2007). Hybrid guiding in liquid-crystal photonic crystal fibers. *Journal of the Optical Society of America B, 24*, 2640−2646. http://dx.doi.org/10.1364/JOSAB.24.002640.

Tiwari, M., & Janyani, V. (2011). Two-octave spanning supercontinuum in a soft glass photonic crystal fiber suitable for 1.55 μm pumping. *Journal of Lightwave Technology, 29*, 3560−3565. http://dx.doi.org/10.1109/JLT.2011.2170958.

Vieweg, M., Gissibl, T., Pricking, S., Kuhlmey, B. T., Wu, D. C., Eggleton, B. J., et al. (2010). Ultrafast nonlinear optofluidics in selectively liquid-filled photonic crystal fibers. *Optics Express, 18*, 25232−25240. http://dx.doi.org/10.1364/OE.18.025232.

Wang, B., Wang, X., & Bos, P. J. (2004). Optimizing the nematic liquid crystal relaxation speed by magnetic field. *Journal of Applied Physics, 96*, 1785−1789. http://dx.doi.org/10.1063/1.1767289.

Wang, F., Yuan, H., Hansen, O., & Bang, O. (2011). Selective filling of photonic crystal fibers using focused ion beam milled microchannels. *Optics Express, 19*, 17585−17590. http://dx.doi.org/10.1364/OE.19.017585.

Wei, L., Alkeskjold, T. T., & Bjarklev, A. (2009). Compact design of an electrically tunable and rotatable polarizer based on a liquid crystal photonic bandgap fiber. *IEEE Photonics Technology Letters, 21*, 1633−1635. http://dx.doi.org/10.1109/LPT.2009.2028156.

Wei, L., Alkeskjold, T. T., & Bjarklev, A. (2010). Tunable and rotatable polarization controller using photonic crystal fiber filled with liquid crystal. *Applied Physics Letters, 96*, 241104. http://dx.doi.org/10.1063/1.3455105.

Wei, L., Weirich, J., Alkeskjold, T. T., & Bjarklev, A. (2009). On-chip tunable long-period grating devices based on liquid crystal photonic bandgap fibers. *Optics Letters, 34*, 3818−3820. http://dx.doi.org/10.1364/OL.34.003818.

Woliński, T. R., Czapla, A., Ertman, S., Tefelska, M., Domański, A. W., Wójcik, J., et al. (2008). Photonic liquid crystal fibers for sensing applications. *IEEE Transactions on Instrumentation and Measurement, 57*, 1796−1802. http://dx.doi.org/10.1109/TIM.2008.922077.

Woliński, T. R., Ertman, S., Czapla, A., Lesiak, P., Nowecka, K., Domański, A. W., et al. (2007). Influence of temperature and electrical fields on propagation properties of photonic liquid-crystal fibres. *Measurement Science and Technology, 18*, 3061−3069. http://dx.doi.org/10.1088/0957-0233/17/5/S08.

Xiao, L., Jin, W., Demokan, M. S., Ho, H. L., Hoo, Y. L., & Zhao, C. (2005). Fabrication of selective injection microstructured optical fibers with a conventional fusion splicer. *Optics Express, 13*, 9014−9022. http://dx.doi.org/10.1364/OPEX.13.009014.

Yang, D.-K., & Wu, S.-T. (2006). *Fundamentals of liquid crystal devices*. John Wiley & Sons.

Zhuang, Z., Suh, S.-W., & Patel, J. S. (1999). Polarization controller using nematic liquid crystals. *Optics Letters, 24*, 694−696. http://dx.doi.org/10.1364/OL.24.000694.

Zito, G., & Pissadakis, S. (2013). Holographic polymer-dispersed liquid crystal Bragg grating integrated inside a solid core photonic crystal fiber. *Optics Letters, 38*, 3253−3255. http://dx.doi.org/10.1364/OL.38.003253.

Zografopoulos, D. C., Asquini, R., Kriezis, E. E., d'Alessandro, A., & Beccherelli, R. (2012). Guided-wave liquid-crystal photonics. *Lab on a Chip, 12*, 3598−3610. http://dx.doi.org/10.1039/C2LC40514H.

Zografopoulos, D. C., & Kriezis, E. E. (2009). Tunable polarization properties of hybrid-guiding liquid-crystal photonic crystal fibers. *Journal of Lightwave Technology, 27*, 773−779. http://dx.doi.org/10.1109/JLT.2008.928186.

Zografopoulos, D. C., Kriezis, E. E., & Tsiboukis, T. D. (2006). Photonic crystal-liquid crystal fibers for single-polarization or high-birefringence guidance. *Optics Express, 14*, 914−925. http://dx.doi.org/10.1364/OPEX.14.000914.

Zografopoulos, D. C., Kriezis, E. E., & Tsiboukis, T. D. (2006). Tunable highly birefringent bandgap-guiding liquid-crystal microstructured fibers. *Journal of Lightwave Technology, 24*, 3427−3432. http://dx.doi.org/10.1109/JLT.2006.878495.

Zografopoulos, D. C., Pitilakis, A. K., & Kriezis, E. E. (2013). Dual-band electro-optic polarization switch based on dual-core liquid-crystal photonic crystal fibers. *Applied Optics, 52*, 6439−6444. http://dx.doi.org/10.1364/AO.52.006439.

This page intentionally left blank

# Microstructured optical fiber filled with carbon nanotubes

4

*M. Pisco, M. Consales, A. Cutolo, A. Cusano*
University of Sannio, Benevento, Italy

## 4.1 Introduction

Microstructured optical fibers (MOFs), being composed of a periodic distribution of micrometric air holes running uniformly along the fiber length, are a promising building block to realizing multifunctional optical fiber devices. The microstructuration of the cladding as well as the presence of the air core allows for the development of new functionalized devices by filling the hollow-core optical fibers (HOF) holes with specific functional materials. Furthermore, by exploiting the properties of the in-fiber integrated materials, the guiding features of the MOF itself can be properly changed in order to develop new tunable photonic devices (Canning, Stevenson, Yip, Lim, & Martelli, 2008; Domachuk, Nguyen, Eggleton, Straub, & Gu, 2004; Larsen, Bjarklev, Hermann, & Broeng, 2003) as well as optical fiber sensors (Corradini & Selleri, 2012, Chapter 11).

In this regard, single-walled carbon nanotubes (SWCNTs) constitute an effective material for integration within MOFs for the realization of photonic devices in light of their unique electrical and mechanical properties (Dresselhaus, Dresselhaus, & Avouris, 2001).

In our previous research activities, we integrated SWCNTs with HOFs to realize sensing probes basically composed of a piece of HOF, spliced at one end with an SOF and covered and partially filled with SWCNTs at the other termination.

The sensing capability of the HOF sensors was first investigated in 2006 by exposure to traces of tetrahydrofuran (Cusano, Consales, et al., 2006). After this feasibility analysis, following studies were aimed at investigating the far-field transmission characteristics of SWCNTs−HOF probes with different deposition conditions in order to study the influence of the deposition process on the guiding properties of the final structure (Pisco et al., 2009). Successively, we demonstrated the sensing capability of the proposed sensors toward VOCs (Pisco et al., 2008, 2010).

This chapter reviews the research activities devoted to the integration of MOFs with SWCNTs for the realization of all-in-fiber sensing probes. It starts with a description of the CNTs' main properties and techniques for their integration with optical fibers. The attention is then focused on the integration of MOFs and SWCNTs using the Langmuir−Blodgett (LB) technique and on the individuation of the main trends and correlations between the deposition process parameters and the MOF guiding properties modifications due to the SWCNTs integration. To this aim, both morphological characterizations and far-field transmission measurements were performed. The integration activities have been hence finalized and exploited for

**Optofluidics, Sensors and Actuators in Microstructured Optical Fibers.** http://dx.doi.org/10.1016/B978-1-78242-329-4.00004-7

VOCs detection applications. In this framework, several sensing probes fabricated with different process features have been characterized in terms of reflectance spectrum in order to get more information on the nanotubes filling within MOF holes. Realized sensors, employed in single wavelength reflectometric configuration, have then been exposed in a test chamber to several VOCs pulses at room temperature in order to demonstrate their capability to work for sensing applications.

## 4.2 Carbon nanotubes as advanced materials for environmental monitoring

Carbon-based nanostructures exhibit unique properties and morphological flexibility, which renders them inherently multifunctional and compatible with organic and inorganic systems. In particular, CNTs were first discovered by Sumio Iijima in the early 1990s (Iijima, 1991) and since then they have become a prominent material for an amazing breadth of scientific and technological disciplines ranging from structural and material science to chemistry, biology, and electronics (Rivas et al., 2009).

CNTs are structures from the fullerene family consisting of a honeycomb sheet of sp2-bonded carbon atoms rolled seamlessly into itself to form a cylinder with a diameter of few nanometers and a length ranging from 1 to 100 μm. They have been widely used as sensitive materials for the construction of chemical and biological sensors thanks to their unique electronic, chemical, structural, optical, mechanical, and thermal properties depending on their specific hollow nanostructure (Rivas et al., 2009; Yellampalli, 2011). Indeed, due to their unique morphology, CNTs possess an excellent ability to reversibly absorb molecules of environmental pollutants undergoing a modulation of their electrical, geometric, and optical properties, such as conductivity, thickness, and refractive index, thus they are particularly suitable for use as sensitive materials in chemical and biological sensing (Ye & Sheu, 2007).

CNTs can be distinguished into SWCNTs or multiwalled carbon nanotubes (MWCNTs), depending on whether only one layer or many layers of graphite are concentrically rolled up together; they also can behave as either metallic or semiconductors, depending upon their diameter and chirality (Terrones, 2003). A further distinction is usually made between closed-end or opened-end CNTs, depending upon whether the ends of the tubes are capped or uncapped (Dresselhaus, Dresselhaus, & Eklund, 2006).

The first CNTs-based chemical sensor was designed in 1997 (Tans et al., 1977), after the problem of electric contact between the nanotubes and electrode was solved. Initially, CNTs were mainly applied in field effect transistor (FET) (Chen et al., 2003; Collins, Bradley, Ishigami, & Zettl, 2000; Kong et al., 2000; Qi et al., 2003; Varghese et al., 2001; Zahab, Spina, Poncharal, & Marliere, 2000) and amperometric-based sensors for the detection of various gases (such as $NO_2$, $NH_3$, $O_2$, CO, and $CO_2$) and $H_2O$ vapors (Luque, Ferreyra, & Rivas, 2007; Manso, Mena, Yanez-Sedeno, & Pingarron, 2007; Tkac, Whittaker, & Ruzgas, 2007; Yan, Chen, Tay, & Khor, 2007; Zare & Nasirizadeh, 2007).

In particular, the operation of semiconductor CNTs-based FETs is underlain by extremely high sensitivity of their electric properties to the adsorbed substances and the charge transfer effect.

Wei, Lin, and Lin (2003) demonstrated a gas sensor depositing CNT bundles onto a piezoelectric quartz crystal, which detected CO, $NO_2$, $N_2$, and Hydrogen ($H_2$) by detecting changes in oscillation frequency and was more effective at higher temperatures (200 °C). Recently, Marzari et al. studied sensing mechanisms for CNTs-based $NH_3$ sensors (Peng, Zhang, Chow, Tan, & Marzari, 2009). They found that at higher temperatures (150 °C or above), charge transfer process contributes to the sensing signal and $NH_3$ adsorption is to be facilitated by environmental oxygen.

Bao et al. fabricated Thin-film Transistor (TFT) sensors consisting of aligned, sorted nanotube networks (Roberts, LeMieux, & Bao, 2009). These SWCNT−TFTs were used to detect trace concentrations (down to 2 ppb) of dimethyl methylphosphonate and trinitrotoluene in aqueous solutions.

Penza, Antolini, and Antisari (2004) developed surface acoustic wave and quartz crystal microbalance sensors coated with SWCNTs and MWCNTs and used them to detect VOCs such as ethanol, ethylacetate, and toluene by measuring the downshift in the resonance frequency of the acoustic transducers.

Another possibility, explored by several researchers, is to integrate CNTs in chemical sensors, modifying the carbon nanotubes surface with polymer films enhancing the selectivity of sensors (Du, Ye, Cai, Liu, & Zhang, 2010; Firdoz et al. 2010; Qi et al., 2003; Zhang, Mubeen, Myung, & Deshusses, 2008). For example, sensors with a polyetylenimine coating are capable of selectively measuring very low $NO_2$ concentrations (about 100 ppt) against the background of many other gases, and sensors with a Nafion film coating can detect $NH_3$ against the $NO_2$ background (Qi et al., 2003).

On the same principle, nanoparticles made from transition metals such as gold, platinum, palladium (Pd), copper, silver, and nickel (well known for their high catalytic activity) have been widely utilized to enhance the performance of carbonaceous materials, increasing their sensitivity toward a specific analyte (Day, Unwin, Wilson, & Macpherson, 2005; Du, Wang, Cai, Qin, & Zhang, 2010; Penza, Rossi, Alvisi, & Serra, 2010).

CNTs have also been successfully employed as sensitive materials in chemo-optical sensors, as demonstrated by Barone, Baik, Heller, and Strano (2005), who developed a device for β-D-glucose sensing in solution phase.

Over the last few years, great effort to develop optical biochemical sensors based on CNTs has been made by two groups (one at the Massachusetts Institute of Technology and the other at Rice University) who solved single-molecule adsorption on the SWCNT sidewall through the quenching of excitons (Cognet et al., 2007; Heller et al., 2009; Jin, Heller, Kim, & Strano, 2008; Jin et al., 2010; Siitonen, Tsyboulski, Bachilo, & Weisman, 2010a,b), enabling a new generation of optical sensors capable of the ultimate detection limit (e.g., single molecules). The recorded fluorescence modulation, supplemented with proper calibration, provides a means for evaluating the concentration of the quencher molecule, even at low concentrations (Jin et al., 2008, 2010; Kim et al., 2009).

Moreover, Heller et al. recently used a peptide structure to modulate the SWCNT fluorescence to realize a chaperone sensor for nitroaromatics (Heller et al., 2011). They described an indirect detection mechanism, as well as an additional exciton quenching-based optical nitroaromatic detection method, illustrating that functionalization of CNT surface can result in completely unique sites for recognition, resolvable at the single-molecule level.

Finally, great attention has recently been focused on the capability of SWCNT overlays, deposited on the facet of standard single-mode optical fibers, to undergo changes in their geometrical and/or geometrical properties as a consequence of the adsorption of target analyte molecules, enabling the exploitation of such materials for the development of fiber nanosensors for a wide range of strategic environmental applications, such as chemical detection in gaseous and liquid phase at room temperature (Consales et al., 2006, 2007, 2009; Cusano, Pisco, et al., 2006; Penza et al., 2005), as well as for hydrogen detection at cryogenic temperatures (Cusano, Pisco, et al., 2006).

In particular, the possibility of integrating such materials with the optical fiber technology has enabled the development of advanced nanosensors capable of air and water quality monitoring, characterized by parts per million (ppm) and sub-ppm resolutions, good recovery features, and fast responses, as will be seen in the following paragraphs.

## 4.3 Carbon nanotubes integration techniques with optical fibers

The realization of homogeneous thin films of CNTs with a controllable thickness is an important basis for the development of their scientific understanding and technological applications. Since CNTs are nanosized materials and tend to aggregate in mats, their precise and controlled handling represents one of the most challenging issues to deal with for their integration into devices.

Proper manipulation techniques are required to apply thin films of CNTs onto small and unconventional substrates (such as the optical fiber one) in such a way as to control their morphological and geometrical characteristics as well as to fully benefit from their properties and to mathematically schematize the final device for a rational design of its performance.

At the same time, simple and low cost fabrication procedures and equipment are required for a fast and cost−effective transition of the CNTs-based devices from the laboratories to the market.

So far, several techniques have been implemented to integrate CNTs with optical fibers for the development of in-fiber devices (either for sensing or telecommunications applications). In what follows, we describe the reported approaches, focusing particular attention on the LB deposition method, which is the technique we used for the realization of MOF sensing probes.

### 4.3.1 Spraying method

CNT spraying is a very simple method proposed in 2004 by Set et al. to coat the terminal face of an optical fiber with a thin layer of CNTs (Kashiwagi & Yamashita, 2010; Set, Yaguchi, Tanaka, & Jablonski, 2004). It mainly consists of two steps: first a dispersed solution of CNTs is sprayed on the fiber facet (Kashiwagi & Yamashita, 2010; Set et al., 2004) and then successively the residual solvent is evaporated by heat treatments.

Since CNTs tend to entangle with each other, not many types of solvents can be used to disperse them with high uniformity and fewer entanglements. Set et al. used dimethylformamide, one of the most commonly employed solvents, to disperse CNTs. The main advantage of this method relies on its simplicity (it is possible to realize optical devices using a simple setup). However, it has low control of the morphological and geometrical features of the sprayed layer (the sprayed solution typically spreads around the chosen target position) and suffers from poor efficiency of CNT use.

### 4.3.2 Direct synthesis

A further integration technique was proposed by Yamashita et al. and relies on the direct growth of CNTs onto the facet of standard optical fibers (Yamashita et al., 2004). With this technique, the cleaved end of an optical fiber is first submerged into a bimetal acetate solution of Mo and Co and is then placed in a furnace maintained at 400 °C in air to decompose acetates or any other organic residues to form an oxide of bimetallic Mo/Co catalyst. Successively the realized device is placed on a quartz boat, which in turn is positioned in a quartz tube inside an electric furnace. $Ar/H_2$ gas is supplied during the heat-up, stopped at the desired temperature, and evacuated. Then, ethanol vapor is supplied. After the reaction, the electric furnace is turned off and cooled down to room temperature with $Ar/H_2$ flow. Figure 4.1 shows the field emission scanning electron microscope (FE-SEM) images of the synthesized

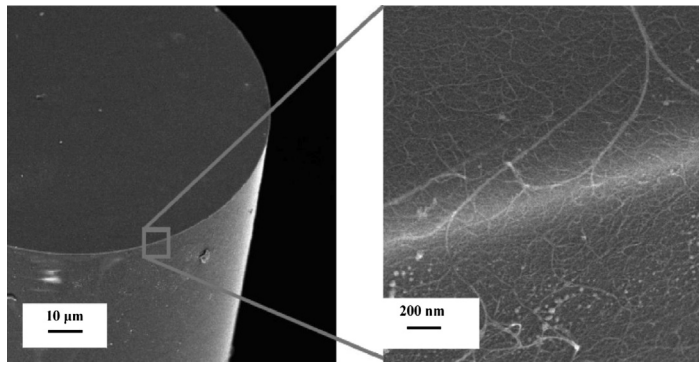


**Figure 4.1** FE-SEM images of SWCNTs directly synthesized onto the cleaved end of a single-mode fiber (Yamashita et al., 2004).

SWCNTs, where a tangled network of SWCNT is clearly appreciable on the cleaved face of the fiber. This direct growth approach has the advantage of direct integration with the fibers; however, there is no method to remove impurities in as-synthesized CNT. Consequently, it requires the ability to manufacture high purity nanotubes (Yamashita et al., 2004).

### 4.3.3 Transferring using hot water

A new method for transferring films of vertically aligned single-walled carbon nanotubes (VA-SWCNT) onto a D-shaped fiber using hot water was also introduced (Song, Yamashita, Einarsson, & Maruyama, 2007).

The CNT film is firstly grown on a quartz substrate by an alcohol catalytic chemical vapor deposition method. To this aim, catalyst particles are loaded onto a quartz substrate by dip-coating into an ethanol solution incorporating Mo−Co bimetallic acetates; the catalyst-coated substrate is then inserted into a tube furnace and heated under 40 kPa of Ar/$H_2$ gas (3% $H_2$). Ethanol is supplied as a carbon source, forming into SWCNTs on the surface of the metal catalyst particles. As the CNTs grow, the high nanotube density causes the initially randomized growth direction to align perpendicular to the substrate, resulting in vertically aligned growth. Successively, the VA-SWCNT film is peeled from the substrate by submersion into hot water (60 °C) and attached onto the flat face of the D-fiber. The realized device is finally dried at 80 °C for 2 h. The optical absorption properties of the film remain the same before and after the film transfer. In Figure 4.2 the scanning electron microscope (SEM) images of the VA-SWCNT film grown on a quartz substrate (Figure 4.2(a)) and the VA-SWCNT film peeled away from the substrate (Figure 4.2(b)) are shown.

This new preparation procedure guarantees almost 100% yield by the safe and easy process of forming CNT devices and enables the maximization of CNT interaction with the field of propagating light.

### 4.3.4 Optically assisted deposition

Recently, a novel technique was also proposed that exploits the optical radiation propagating through an optical fiber as a means of integrating CNTs onto its facet

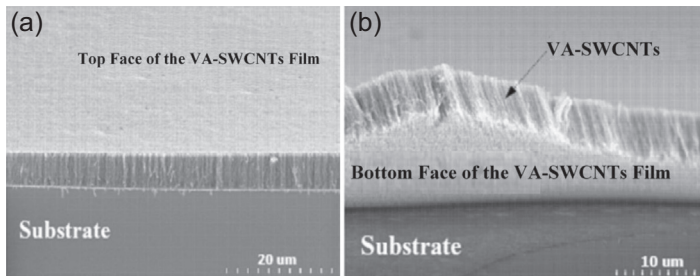


**Figure 4.2** (a) SEM image of the VA-SWCNT film grown on a quartz substrate (×2 k) and (b) carpet-like VA-SWCNT film peeled away from the substrate (×3 k) (Song et al., 2007).

(Kashiwagi, Yamashita, & Set, 2007; Nicholson, 2007; Nicholson, Windeler, & Di Giovanni, 2007). With reference to the schematic representation of Figure 4.3, the method requires only a light source and enables the deposition of CNTs preferentially onto the core region of the fiber by injecting a light beam from the fiber end into a CNT-dispersed dimethylformamide (Kashiwagi et al., 2007) or ethanol (Nicholson, 2007; Nicholson et al., 2007) solution. This allows for optimal interaction with propagating radiation, while at the same time minimizing the waste of the nanotubes during device preparation.

The basic principle of the optically assisted CNT deposition is not yet confirmed. However, the authors presume that one possible mechanism could be the optical tweezer effect, which is caused by the optical intensity diversion of light in a solution. Another possible mechanism could be the flow of solution due to the injected light. Indeed, the light might thermally induce convection and swirl near the core, enabling the attachment of entangled CNTs.

This technique possesses many advantages in terms of efficiency of CNT use and simplicity of the device fabrication process compared to alternative fabrication techniques. However, it requires very precise control of the light injection power to deposit a uniform and less scattered CNT layer. In particular, smaller CNT entanglements require higher injection power, whereas high power injection makes the CNT layer form around the core, not on the core. The upper limit of optical intensity depends on the flow speed caused by the injected light. Additional techniques are therefore needed to optimize the injection power for each solution.

In 2009 Kashiwagi et al. proposed the use of optical reflectometry as a means of providing an in situ monitoring of the CNT layer deposition process and to precisely control the optical power injection (Kashiwagi, Yamashita, & Set, 2009). With this method the thickness can be controlled by changing the light injection period after the increase of reflectivity due to the first entanglement deposition. In Figure 4.4, the FE-SEM images of thin and thick CNTs layers deposited by this technique on an area of about 15 μm around the fiber core are reported.

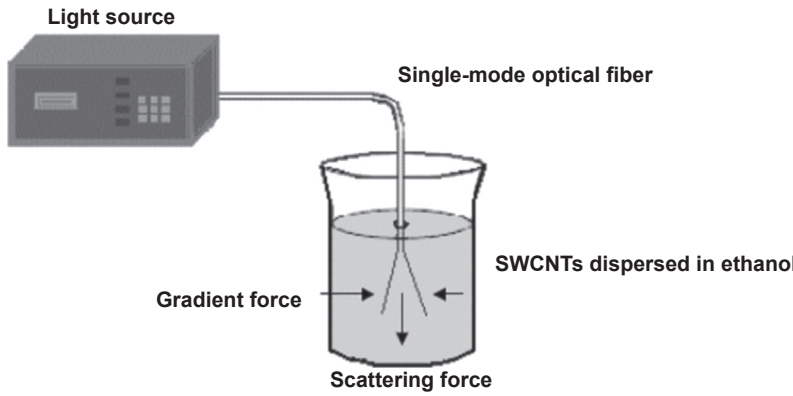


**Figure 4.3** Setup for depositing carbon nanotubes on the facet of cleaved optical fibers using optical radiation.

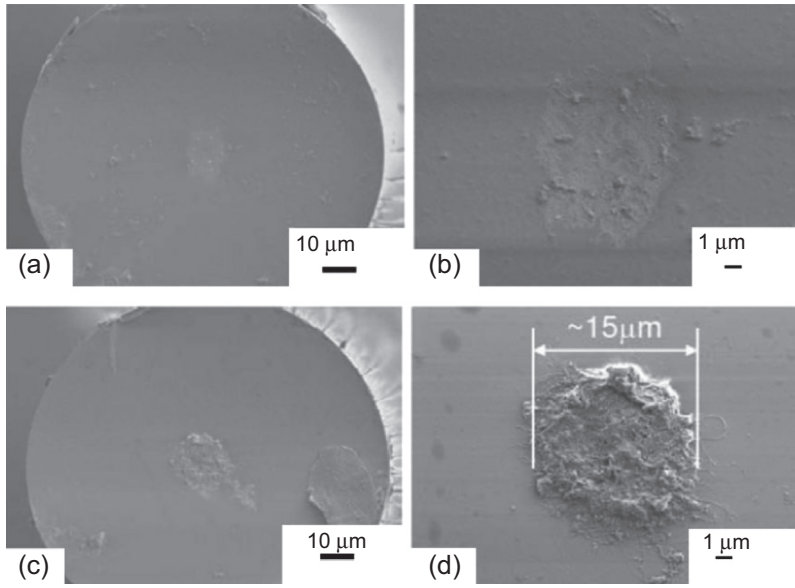


**Figure 4.4** FE-SEM images of the fiber end with the thin layer [(a) whole fiber end (b) magnified around the core region] and with the thick layer [(c) whole fiber end (d) magnified around the core region] (Kashiwagi et al., 2009).

### 4.3.5 Langmuir–Blodgett layer by layer deposition

The LB technique is a well-known method that allows the manipulation of material at the molecular level for depositing defect-free, ultra-thin organic films with accurate control over the architecture of the films at the nanoscale level (Petty, 1996). The technique, schematically represented in Figure 4.5, is based on the production of organic monolayer films, first oriented on a subphase and subsequently transferred, layer by layer, onto a solid surface at room temperature and molecule specific surface pressure.

Usually, the LB film is constituted by amphiphilic molecules that have hydrophobic and hydrophilic tail or head groups (Peterson, 1990; Petty, 1996). A monolayer of the material is at first formed by dispersing the molecules onto the surface of a subphase in the form of a solution. The solvent evaporates, leaving the molecules dispersed across the water surface and oriented with the hydrophobic part upwards and the hydrophilic part in water, creating a suspended monolayer. Reducing the surface area by means of moving barriers, the molecules start to repel one another, modifying the surface pressure (Peterson, 1991). At the first compression, the molecules are randomly oriented and experience weak interaction with each other. Upon further compression, they are pressed closer together with the hydrophobic tails of the molecules that engage to lift from the surface. The molecules undergo a transition from the gas phase to a liquid-condensed phase, accompanied by a steep rise in surface pressure. Additional compression decreases the surface area occupied by each

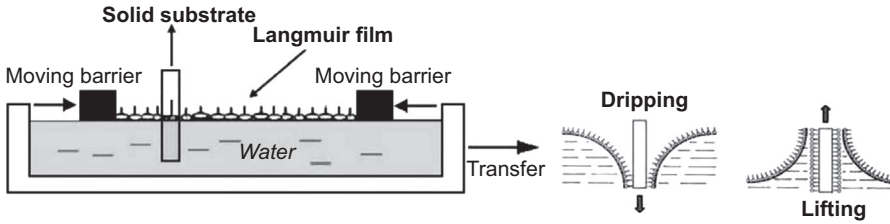


**Figure 4.5** Schematics of the Langmuir−Blodgett deposition procedure.

molecule close to its cross-sectional area, producing a solid phase in which the molecules are packed in an ordered array. From this phase, the molecules may be transferred to a properly cleaned and prepared solid substrate, dipping it through the condensed Langmuir layer to realize the LB film (Peterson, 1990; Petty, 1996). Repeated dipping of the same substrate is also possible, resulting in the deposition of a thin film one monolayer at a time.

This procedure provides a high-resolution control and uniformity of film thickness (about 1−3 nm per layer) and is thus ideal for the optical interference principle used in the reflectometric configuration to convert dielectric constant changes into optical intensity variations. An additional advantage of the LB technique is that monolayers can be transferred onto almost any kind of solid substrate. However, these advantages have to be traded with the low speed of the deposition procedure as well as the limited number of materials suitable for this technique.

## 4.4 Sensing probes fabrication

Several samples have been arranged by infiltrating SWCNTs within the air holes of the MOF, and the MOF Photonic Bandgap (PBG) features' dependence on the deposition parameters has been investigated by far-field transmission measurements. The samples were composed by a piece of MOF, spliced at one end with an SOF and covered and partially filled with SWCNTs at the other termination, as schematically shown in Figure 4.6. Before the MOF−SOF splicing, the deposition of SWCNTs was performed at atmospheric pressure by means of the LB technique.

In particular, for the integration within MOFs, a solution (0.2 mg/ml) of SWCNTs pristine material (purchased from Carbon Nanotechnologies Inc., Houston, USA) in chloroform has been spread onto a subphase constituted by deionized water (18 MΩ) with 10-4 M of $CdCl_2$. The subphase pH and the temperature are 6.0 and 23 °C, respectively. The monolayer has been compressed with a barrier rate of 15 mm/min until the surface pressure of 45 mN/m is reached. The single layer has been deposited with a dipping rate of 3 mm/min and the transfer ratio of the monolayer from the subphase to the substrate surface is in the range 0.5−0.7.

Although the LB deposition method is a well-assessed technique, the employment of the LB technique to integrate carbon nanotubes monolayers within the MOF holes yields substantial changes in the deposition process.

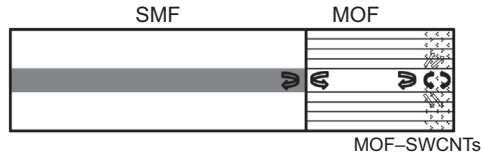


**Figure 4.6** Schematic view of the sensing head of the MOF−SWCNTs samples.

The fiber substrate microstructuration, that is, the MOF, affects the deposition process because of the micrometric dimensions of its air holes, which in turn enables capillarity phenomena to occur (Nielsen, Noordegraaf, Sørensen, Bjarklev, & Hansen, 2005; Zhmud, Tiberg, & Hallstensson, 2000). During the vertical MOF dipping, performed with the rate of 3 mm/min and for a depth of 1 mm, the LB suspension penetrates within the MOF holes because of the dipping itself; at the same time it penetrates within the MOF holes for capillarity.

It is worth highlighting that the penetration depth of the LB suspension within the MOF holes does not correspond to the penetration depth of the SWCNTs within the MOF holes. The SWCNTs deposition, indeed, occurs with a high efficiency at a given suspension surface pressure while in this case the dipping of the MOF substrate, breaking the superficial regularity of the suspension, locally changes the parameters ruling the effectiveness of the carbon nanotubes deposition on the microstructured substrate. Furthermore, the extension of the region onto the holes' sides where the nanotubes adhered is also limited from the quantity of carbon nanotubes "available" at the dipping time. Differently from the classic LB deposition on a planar substrate accomplished with a constant surface pressure, even if the overall surface pressure is held constant by the barrier movement, locally at each MOF hole, only the nanotubes subphase corresponding to the MOF hole affects the deposition during the dipping. In summary it is expected that the transfer of SWCNTs thin monolayers within the MOF holes by means of the LB deposition method would be the result of the dipping movement and capillarity's phenomena rising at the dipping time, which is strongly dependent on the surface pressure. It is noteworthy that while the capillarity phenomena impose differences in the carbon nanotubes penetration depth between the core and cladding holes due to the different diameters, the dipping movement into the suspension reduces the differences, forcing the suspension penetration at the dipping time. Nevertheless, although a complete understanding of the adhesion and penetration mechanisms has not yet been achieved, the experimental results revealed the capability to deposit SWCNTs within the MOF holes and to consequently modify the MOF guiding properties.

After the SWCNTs are infiltrated within the MOF holes, the open end of the MOF piece is spliced at the input end to a single mode optical fiber (SOF) by using an electrical arc splicing system (Fujikura FSM-50S). The fibers' ends, both cleaved, have been aligned and pressed against each other using the splicer precision motors. In order to avoid the complete collapse of air holes during the splicing, a splicing procedure has been developed ad hoc. In particular, a series of 10 arcs with short duration (100 ms) and high power (80 bit power) have been forced, in place of a single arc with lower

power (40 bit) and longer extension (800 ms) usually used for SOF−SOF splicing. The splicing process was previously tested and the losses were estimated to be about 1 dB by means of the comparison between the measurements of the transmitted power in Butt-coupling configuration and after the optical fibers' fusion, respectively. In addition, the bonding achieved between the two fibers, weak with respect to the bending, has been enforced by using a heating protection sleeve.

## 4.5 Experimental results

The SWCNTs monolayers deposition has been accomplished on several pieces of MOF with different lengths on the order of a few centimeters, and it was performed at atmospheric pressure with the other MOF termination not connected. As previously described, after the SWCNTs deposition, for each sample, the free termination has been spliced at a single-mode SOF. Several samples have been realized with the LB technique by changing the monolayer number and thus the amount of carbon nanotubes able to fill the MOF holes. In the following, the analysis is focused on five samples fabricated according to Table 4.1. The influence of the external pressure at the dipping time has been investigated by depositing 20 monolayers of SWCNTs onto an MOF piece previously spliced to an SOF (sample 5).

### 4.5.1 Morphological and far-field characterizations

In order to investigate the morphological characteristic of the fabricated MOF samples, a SEM has been used. The analysis with the SEM has been performed on several samples. The retrieved images of the observed samples show a quite uniform overlay covering the fibers' holes. In Figure 4.7(a) and (b) an atomic force microscope (AFM) image of an MOF before the deposition and the SEM image of the same MOF after the deposition of 10 monolayers of SWCNTs are shown, demonstrating the success of the SWCNTs deposition onto the MOFs. In Figure 4.7(c) and (d), the SEM image of a bare MOF and the SEM image of the

**Table 4.1 Samples main features**

| Sample | Length (cm) | Monolayer |
|---|---|---|
| 1 | 13.3 | 10 |
| 2 | 11.0 | 16 |
| 3 | 4.0 | 20 |
| 4 | 10.0 | 20 |
| 5[a] | 6.5 | 20 |

[a]SWCNTs deposited after the SOF−MOF splicing.

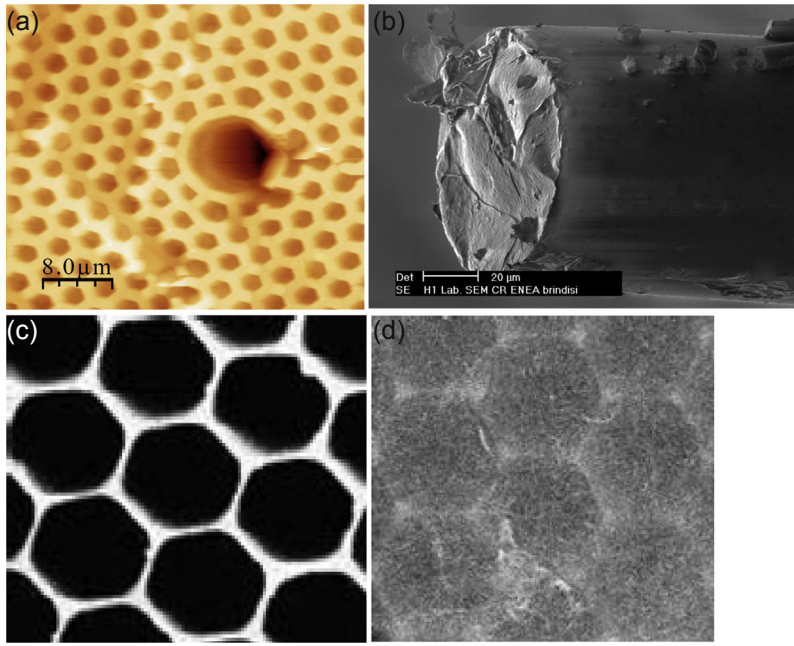


**Figure 4.7** (a) AFM image of a bare MOF, (b) SEM image of the MOF after the deposition of 10 monolayers of SWCNTs, (c) SEM image of a bare MOF, and (d) SEM image of the MOF after the deposition of 16 monolayers of SWCNTs (Pisco et al., 2009).

MOF after the deposition of 16 monolayers of SWCNTs (sample 2) are shown. The SEM images, showing a particular of the MOF cladding, reveal a web-like overlay covering the MOF holes, demonstrating the success of the SWCNTs deposition onto the MOFs.

In order to characterize the MOF−SWCNTs guiding properties modifications and the SWCNTs filling capability, the optical far field emerging from the samples has been collected by means of an infrared vidicon camera (Hamamatsu C2741-03) while a narrowband laser source at 1550 nm lights the samples. The camera has been screen-shielded from the visible light to reduce the environmental noise and a proper holder for the fiber has been provided in order to guarantee the repeatability in the positioning of different samples. The end face of the samples has been positioned in front of the receiving lens.

In Figure 4.8(a) the transmitted field, revealed in the far-field mode, of an MOF without nanotubes is shown for reference. The far field emerging from an MOF is basically featured by a Gaussian shape and by little peaks of circular shapes located in correspondence to the MOF cladding holes close to the core.

In Figure 4.8(b) and (c) the emerging far fields from the samples 1 and 2 realized with 10 and 16 monolayers are shown, respectively. As can be seen, the presence of the SWCNTs is not able to strongly modify the field distribution of the propagating mode, which basically keeps the Gaussian shape. Nevertheless, while for sample 1 a

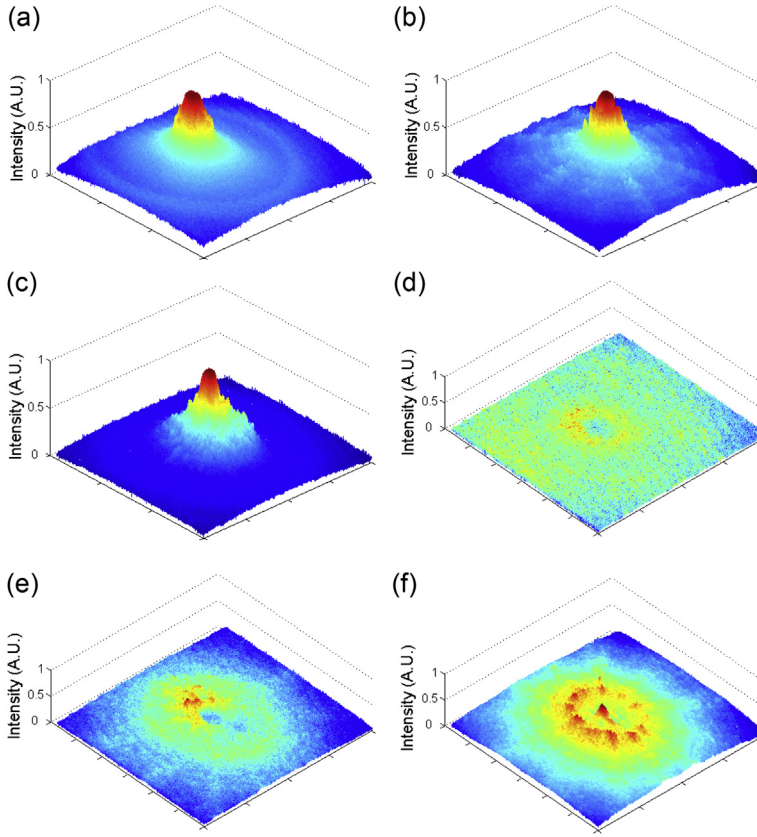


**Figure 4.8** Distribution of the far field of the bare MOF (a) and of the MOF samples 1−5 (b−f), respectively (Pisco et al., 2009).

slightly higher light content can be observed in correspondence to the MOF cladding in the coated case, the same spreading of the far field is more evident for sample 2, which exhibits a stronger increase of the field amplitude external to the corresponding fiber core.

The far-field spreading increases with the monolayer number and thus accordingly to the higher SWCNTs content. As evident, the main effect of SWCNTs filling is a worse confinement of the fundamental mode, consistent with a refractive index contrast reduction induced by a partial filling of the core and cladding holes. It is noteworthy that the core refractive index increase (with no cladding holes filled) is expected to lead to an increase of the core confinement power, while the cladding holes refractive index increase (with core unperturbed) as well as the core and cladding holes refractive indexes simultaneous increase would lead to a diminution of the fundamental mode confinement power. Hence the field spreading observed between the samples with 10 and 16 monolayers and the bare MOF is in agreement either with an increase of the cladding holes refractive index or with an increase of

the core and cladding holes refractive indices. Nevertheless, the exclusive cladding holes filling is not expected on the basis of the deposition technique used, except for differences in the carbon nanotubes penetration between the core and cladding holes due to the different capillary diameters. With regard to sample 3, a strong modification of the field distribution occurs and the amount of power transmitted is strongly reduced, as shown in Figure 4.8(d). The emerging field presents a circular crown shape and the core mode is no longer visible. In other words, the larger amount of SWCNTs used for sample 3 is able to induce a strong diminution of the fundamental mode power, attributable to the modification of the PBG occurring in consequence of the MOF holes filling.

Overall, the far field emerging from sample 3, in agreement with the field exhibited from samples 1 and 2, demonstrates the capability of the LB technique to infiltrate SWCNTs within the MOF holes. In particular, the deposition of 20 monolayers (or more) yields the functionalized MOF, which is not capable of meaningfully guiding the light. As matter of fact, the PBG modification particularly affects the field distribution of sample 3, which was fabricated with a higher number of monolayers with respect to samples 1 and 2.

In order to study the influence of the MOF length, the far field emerging from sample 4 has been characterized and shown in Figure 4.8(e). Samples 3 and 4 have both been obtained by depositing 20 SWCNTs monolayers, but the MOF pieces are long: 4 and 10 cm, respectively. It is observable that the far field keeps the circular crown shape and the fundamental core mode has been suppressed again. The field emerging from sample 4, however, is slightly circularly asymmetric and the light content is slightly higher. The comparison thus reveals that the MOF length doesn't meaningfully rule the field distribution in transmission. In addition, it confirms the important role of monolayers number in the PBG modification and thus on the resulting field distribution. It is noteworthy that this result is consistent with the deposition process previously described. In fact, assuming the deposition as the resultant of dipping and capillarity mechanisms, any dependence on the fiber length was not expected. Congruently the SWCNTs deposition is strongly affected by the number of dipping and not by the capillaries' lengths.

Finally, Figure 4.8(f) shows the far field emerging from an additional sample on which 20 monolayers of SWCNTs have been deposited after the splicing procedure. The connection at the fiber termination is responsible for a change in the air pressure within the MOF holes and thus a less efficient filling is expected. As observable, the far field emerging from the sample still presents a circular crown shape and a little peak in correspondence to the MOF core is visible. The deposition of 20 monolayers is able to strongly modify the PBG, but the core mode is not completely suppressed. In this case, during the deposition stage, the LB suspension, in order to penetrate within the MOF capillaries, had to overcome the pressure offered by the air present within the MOF. The elasticity of the air thus determines a pressure variable during the MOF dipping and it represents a good exemplification of the effect of the pressure on the deposition, which can be otherwise properly controlled.

In summary, the far-field characterizations reveal the success of the SWCNTs deposition, demonstrating the partial filling of the nanotubes within MOFs. Also, the

obtained results demonstrate that the main effect of SWCNTs filling is the significant modification of the guiding properties and thus of the local PBG at the termination of the MOF. Also, by using the LB deposition method, we demonstrate how by acting on the process parameters and especially on the monolayers number and pressure conditioning at the free termination, it would be possible to optimize and tailor the SWCNTs filling, enabling the local control of the MOF PBG. The proper modification of the MOF PBG features, by filling (also selectively) the MOF holes with SWCNTs, can supply to the final device advanced functionalities and can be properly exploited to develop high-performance sensors based on PBG modifications as well as multimaterial and multifunctional fibers.

### 4.5.2 Sensing features

In this section, we report on the exploitation of the experimental results previously described regarding the integration between MOFs and SWCNTs in order to develop an all fiber optochemical sensor useful for VOCs detection.

In particular, an analysis of the sensing properties of samples 1 and 3 is reported. Sensor 1 is made up of a 13.3 cm long MOF with 10 monolayers of SWCNTs, whereas sensor 3 is made up of a 4 cm long MOF and 20 SWCNTs monolayers. Both sensors have been characterized by reflectance spectra in order to get more information on the nanotubes filling within the MOF holes.

#### 4.5.2.1 Reflectance characterization

Reflectance characterization of the realized probes has been carried out within the MOF bandwidth. The spectral reflectance measurements were carried out by illuminating the fiber tip with a tunable laser source (covering the wavelength range 1520−1620 nm) and redirecting the reflected light (via a $2 \times 1$ directional coupler) to an optical spectrum analyzer (Ando AQ6317C) used in synchronous mode, allowing 1pm wavelength resolution in the selected spectral range.

In Figures 4.9 and 4.10, we display the reflected spectra of the two samples. Reflectance spectra exhibit several interference fringes and their envelope offers a quite periodic behavior. In particular, in the reflectance of sensor 1, two different harmonic contents, fast and slow, can be clearly distinguished. The observation of two different harmonic contents suggests the presence of a double cavity interferometer, as schematically shown in Figure 4.6. From the wavelength separation of the fringes the optical path length weighted by the medium effective refractive index of each interferometer can be approximately retrieved, according to

$$2 \cdot \mathrm{neq} \cdot d = \frac{\lambda_1 \cdot \lambda_2}{(\lambda_2 - \lambda_1)} \tag{4.1}$$

where $d$ is the length of the interferometer, neq is the medium effective refractive index of the propagating mode, and $\lambda_1$ and $\lambda_2$ are the wavelengths corresponding to two adjacent maxima. Thus, by twice applying Eqn (4.1) at the reflectance spectrum, the

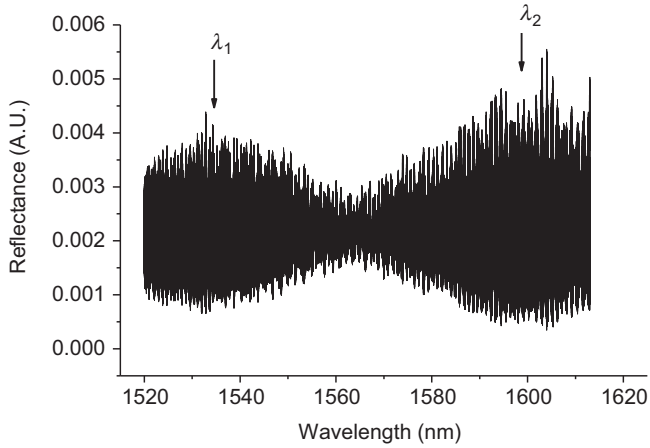


**Figure 4.9** Reflectance of MOF sensor 1. The arrows indicate the wavelengths corresponding to two adjacent envelope relative maxima (Pisco et al., 2008).

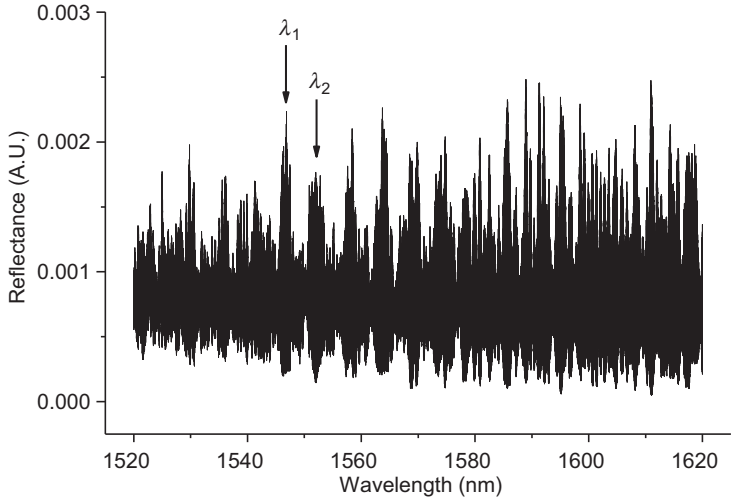


**Figure 4.10** Reflectance of MOF sensor 3. The arrows indicate the wavelengths corresponding to two adjacent envelope relative maxima (Pisco et al., 2008).

features of the double interferometer, in both fast and slow regime, can be deduced. The optical path lengths weighted by the medium effective refractive index obtained for sensor 1 are approximately 26.6 cm and 40 μm, respectively.

The former coincides approximately with the double length of the MOF piece, by considering the MOF effective refractive index equal to one (not filled by SWCNTs). The latter represents the extension of the region, on a micrometric scale, constituted by the deposited SWCNTs within the MOF holes at the fiber tip.

The two cavities, hence, can be attributed to the piece of MOF and to the SWCNTs region. In turn, from the analysis of the reflectance of sensor 3, although the fast oscillating component is again clearly observable, the envelope of the reflectance seems to be periodic, mostly in the wavelength range 1545−1575 nm, while a periodic behavior for the envelope in the remaining spectral range is less recognizable.

Nevertheless, by also twice applying Eqn (4.1) in this case, optical path lengths weighted by the medium effective refractive index of 8 cm and 460 μm are obtained for sensor 3. The fast oscillating behavior is still attributed to the piece of MOF, which is 4 cm long, whereas the SWCNTs seem to cover a region of hundreds of microns consistently with the larger amount of SWCNTs deposited in the case of sensor 3 (20 monolayers). Also, on the basis of previous works (Penza et al., 2005) dealing with the SWCNTs deposition onto the end face of SOFs, 10 and 20 monolayers of SWCNTs are not capable of producing an external cavity able to produce interference fringes in the investigated wavelength range. Hence, the results obtained from the spectral characterization of both sensors reveal that the carbon nanotubes are penetrated at least in the MOF central hole and their distribution along the MOF axis, which cannot be assumed spatially uniform, extends for tens and hundreds microns, respectively.

It is noteworthy that Eqn (4.1) is rigorously valid under the hypothesis of transparent media, which in turn is not truly verified for carbon nanotubes-based materials. In addition, the estimation of the equivalent cavity length by means of the interference fringes together with the trivial measurement of the length of the MOF piece before the deposition are not able to discriminate the fraction of nanotubes penetrated inside the holes from the fraction of nanotubes which composes an external overlay at MOF termination (Cusano, Consales, et al., 2006). Nevertheless, insight into the double interferometer behavior of the sensing probe is obtained, and an approximated estimation of the extension of the SWCNTs region can be retrieved.

#### 4.5.2.2 Sensor modeling

On the basis of reflectance and far-field characterizations, the sensing probe reflectance of sensor 1 can be modeled as a Fabry−Perot double interferometer, while the behavior of sensor 3 cannot be trivially assumed like a simple double interferometer in agreement with the spectral and far-field analysis. In the MOF region with SWCNTs the optical fiber guiding properties are changed and significant losses can be expected. In Eqn (4.2) the model of the reflectance of sensor 1 is reported. The symbols $r$, $n$, $d$, and $A$ represent the reflection coefficient, the complex effective refractive index, the cavity length, and the absorbance (due to the coupling and splicing losses), respectively, while the subscript indices and labels indicate respectively the interface and the cavity they are referred to. In particular, subscript 12 refers to the SOF−MOF interface, 23 to the MOF−SWCNTs interface, and 34 to the SWCNTs−external medium interface, while the subscript labels SOF, MOF, and SWCNTs have obvious meaning. The reflectance $R$ is ruled by several factors involved in the propagation of the lightwave through the MOF and the MOF filled with SWCNTs. In particular, any change in the SWCNTs dielectric function affects the reflectance $R$ through the reflection

coefficients $r_{23}$ and $r_{34}$, the absorbance $A_{23}$, and the propagation constant $\beta_{\mathrm{SWCNTs}}$, according to Eqns (4.2) and (4.3)

$$R = \left| \frac{r_{12} + r_{23}\cdot(1-A_{12})\cdot e^{j\cdot\beta_{\mathrm{MOF}}} + r_{34}\cdot(1-A_{12})\cdot(1-A_{23})\cdot e^{j\cdot(\beta_{\mathrm{MOF}}+\beta_{\mathrm{SWCNTs}})} + r_{12}\cdot r_{23}\cdot r_{34}\cdot e^{j\cdot\beta_{\mathrm{SWCNTs}}}}{1 + r_{12}\cdot r_{23}\cdot e^{j\cdot\beta_{\mathrm{MOF}}} + r_{12}\cdot r_{34}\cdot(1-A_{23})\cdot e^{j\cdot(\beta_{\mathrm{MOF}}+\beta_{\mathrm{SWCNTs}})} + r_{23}\cdot r_{34}\cdot e^{j\cdot\beta_{\mathrm{SWCNTs}}}} \right|^2 \tag{4.2}$$

with

$$\begin{gathered} r_{12} = \frac{n_{\mathrm{SOF}} - n_{\mathrm{MOF}}}{n_{\mathrm{SOF}} + n_{\mathrm{MOF}}};\ r_{23} = \frac{n_{\mathrm{MOF}} - n_{\mathrm{SWCNTs}}}{n_{\mathrm{MOF}} + n_{\mathrm{SWCNTs}}};\ r_{34} = \frac{n_{\mathrm{SWCNTs}} - n_{\mathrm{ext}}}{n_{\mathrm{SWCNTs}} + n_{\mathrm{ext}}}; \\ \beta_{\mathrm{MOF}} = \left(\frac{4\cdot\pi}{\lambda}\right)\cdot n_{\mathrm{MOF}}\cdot d_{\mathrm{MOF}};\ \beta_{\mathrm{SWCNTs}} = \left(\frac{4\cdot\pi}{\lambda}\right)\cdot n_{\mathrm{SWCNTs}}\cdot d_{\mathrm{SWCNTs}} \end{gathered} \tag{4.3}$$

It is noteworthy that the sensor sensitivity to chemically induced changes in the dielectric properties of the sensitive material used to functionalize MOFs cannot be thought of as derived by a simple Fabry–Perot effect in light of the PBG modifications. For instance, at the interface between the MOF and the MOF filled with SWCNTs, coupling losses due to the modal overlap between modes propagating in the sections with different guiding properties affect the reflectance $R$. This means that as the dielectric function of the SWCNTs is modified by chemical sorption, consequent changes are expected in the coupling coefficients as well as in the reflectance $R$. On the other hand, the propagation losses within the MOF region filled with SWCNTs depend on the SWCNTs dielectric function and hence contribute to the reflectance variations. In summary, the SWCNTs effective dielectric function variations within the MOF filled with SWCNTs determine, in combination with the penetration depth of the carbon nanotubes, the sensing probe reflectance changes by affecting the propagation features of the sensing probe itself.

#### 4.5.2.3 Sensor response to traces of volatile organic compounds

In order to investigate the sensing capability of the fabricated MOF sensors, they have been placed in a test chamber (Consales et al., 2006, 2007) and exposed to traces of VOCs. At the same time, a reflectometric system, which allows reflectance measurements at a single wavelength, has been employed. In order to light the sensing probes a superluminescent light emitting diode with 40 nm bandwidth centered at 1550 nm has been used. The light source is split by means of an optical coupler, as schematically shown in Figure 4.11. One of the arms of the coupler is connected directly to a photodiode in order to provide a monitoring of the source power level. The other arm is connected to the sensing probes by means of an optical switch, which is responsible for the time division multiplexing, allowing the simultaneous interrogation of several sensors. The time-multiplexed reflected signal is collected by another photodiode. The electrical signals coming from the photodetectors are acquired by a data acquisition (DAQ) system and stored in a computer,

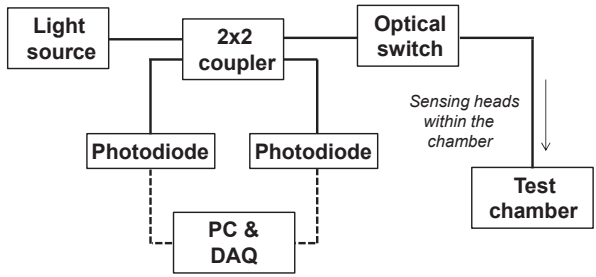


**Figure 4.11** Experimental setup for volatile organic compounds exposure.

which provides the time demultiplexing of the retrieved signals. The optoelectronic sensor output consists of the ratio between the reflected signal at the sensing interface and the source reference signal.

Since the light source is featured by a bandwidth much wider than the separation of the faster interference fringes, the sensing performance exploited by each sensor basically depends on the slow features of the reflectance spectrum and thus mainly on the SWCNTs cavity. During the measurements, the temperature within the chamber has been monitored by using a commercial thermocouple. The sensors' sensitivity to temperature variations was previously characterized and used in order to properly compensate the sensors' output.

The optical sensors have been located in a test chamber for toluene traces exposure measurements. Dry air has been used as reference gas and carrier gas to transport the VOCs of toluene with different concentration pulses. The test cell containing the sensor has a volume of 1200 ml, whereas the total flow rate for each exposure has been kept constant at 1000 ml/min. The gas flow rate has been controlled by a mass flow meter driven by a controller unit. The VOCs vapors have been generated by the bubbling method with a thermo-stated flask containing the liquid analyte.

Here a comparison among the performances exploited by sensors 1 and 3 is carried out by considering their relative reflectance change due to toluene exposure. To this aim, both sensors have been exposed to three toluene pulses of 45 min with increasing concentrations in the ppm range. Figure 4.12 reports the time responses of both sensors. Upon exposures, the reflectance of sensor 1 decreases linearly with the toluene concentration, as confirmed by further exposure measurements resumed in Figure 4.13. Conversely, sensor 3 reflectance increases upon exposure, presenting a significantly lower sensitivity. Moreover, sensor 3 is not able to reach a steady state within 45 min, especially for high concentration exposures; this also limits the maximum reflectance change observed during the exposure tests. The higher response times and the lower sensitivity of sensor 3 can be explained on the basis of the higher extension of the SWCNTs region (higher diffusion times and higher losses in the filled region). In fact, the VOCs, able to interact with the SWCNTs, lead to a change of the SWCNTs agglomerate dielectric function, and the shortest the SWCNTs region the fastest the detection of induced variations. In addition, as

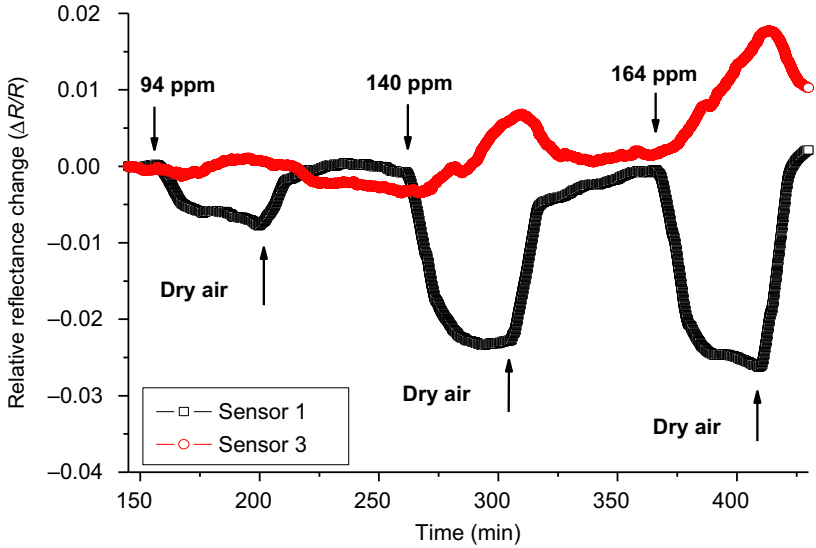


**Figure 4.12** Time responses of MOF sensors 1 and 3 to three toluene impulses (Pisco et al., 2008).

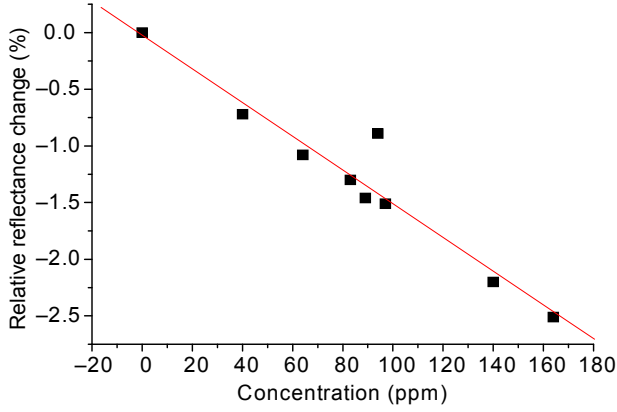


**Figure 4.13** Relative reflectance change (Δ*R*/*R*) of sensor 1 corresponding to the steady states reached upon exposures to different concentration pulses of toluene (Pisco et al., 2008).

demonstrated by the far-field characterization, the SWCNTs penetration depth in sensor 3 yields the functionalized MOF unable to guide the light, and thus it reduces the capability of the light to interact with the sensitive material. Further investigation is required to assess the sensitivity dependence on the SWCNTs distribution within the MOF structure and also to identify characterization features able to predict the correct functioning and the performance of the final device.

## 4.6 Conclusions

The research activities devoted to the integration of MOFs with SWCNTs in order to develop new in-fiber active and passive optoelectronic devices are reviewed. The infiltration of SWCNTs inside the MOF holes has been accomplished through the deposition of multiple SWCNTs monolayers by means of the LB method. The far-field characterizations revealed the success of the SWCNTs deposition demonstrating the partial filling of the nanotubes within MOFs. Also, the obtained results demonstrated that the main effect of SWCNTs filling is the significant modification of the guiding properties and thus of the local PBG at the termination of the MOF. Also, by using the LB deposition method, we demonstrate how by acting on the process parameters and especially on monolayers number and pressure conditioning at the free termination, it would be possible to optimize and tailor the SWCNTs filling, enabling the local control of the MOF PBG. The proper modification of the MOF PBG features, by filling (also selectively) the MOF holes with SWCNTs, can supply to the final device advanced functionalities and can be properly exploited to develop high performance sensors based on PBG modification as well as multimaterial and multifunctional fibers. On the basis of the retrieved results, a novel optochemical sensor for VOCs detection has been developed and its sensing capability has been proved by exposure to VOCs traces in a proper test chamber. The presented experimental results demonstrated that the fabrication parameters strongly affect the sensors' performances and that the proposed optochemical sensor is able to perform VOCs detection with a good sensitivity and fast response times.

## References

Barone, P. W., Baik, S., Heller, D. A., & Strano, M. S. (2005). Near-infrared optical sensors based on single-walled carbon nanotubes. *Nature Materials, 4*(1), 86−92.

Canning, J., Stevenson, M., Yip, T. K., Lim, S. K., & Martelli, C. (2008). White light sources based on multiple precision selective micro-filling of structured optical waveguides. *Optics Express, 16*(20), 15700−15708.

Chen, R. J., Bangsaruntip, S., Drouvalakis, K. A., et al. (2003). Noncovalent functionalization of carbon nanotubes for highly specific electronic biosensors. *Proceedings of the National Academy of Sciences of the United States of America, 100*, 4984−4989.

Cognet, L., Tsyboulski, D. A., Rocha, J. D. R., Doyle, C. D., Tour, J. M., & Weisman, R. B. (2007). Stepwise quenching of exciton fluorescence in carbon nanotubes by single molecule reactions. *Science, 316*, 1465−1483.

Collins, P. G., Bradley, K., Ishigami, M., & Zettl, A. (2000). Extreme oxygen sensitivity of electronic properties of carbon nanotubes. *Science, 287*, 1801−1804.

Consales, M., Campopiano, S., Cutolo, A., Penza, M., Aversa, P., Cassano, G., et al. (2006). Carbon nanotubes thin films fiber optic and acoustic VOCs sensors: performances analysis. *Sensors and Actuators B, 118*(1−2), 232−242.

Consales, M., Crescitelli, A., Campopiano, S., Cutolo, A., Penza, M., Aversa, P., et al. (2007). Chemical detection in water by single-walled carbon nanotubes-based optical fiber sensors. *IEEE Sensors Journal, 7*(7), 1004−1005.

Consales, M., Crescitelli, A., Penza, M., Aversa, P., Veneri, P. D., Giordano, M., et al. (2009). SWCNT nano-composite optical sensors for VOC and gas trace detection. *Sensors and Actuators B, 138*(1), 351−361.

Corradini, R., & Selleri, S. (2012). Photonic crystal fibers for physical, chemical and biological sensing. In M. Pisco, A. Cusano & A. Cutolo (Eds.), *Photonic bandgap structures: A novel technological platform for physical, chemical and biological sensing* (pp. 189−202). Bentham Science Publishers. e-book.

Cusano, A., Consales, M., Cutolo, A., Penza, M., Aversa, P., Giordano, M., et al. (2006). Optical probes based on optical fibers and single-walled carbon nanotubes for hydrogen detection at cryogenic temperatures. *Applied Physics Letters, 89*(20), 3.

Cusano, A., Pisco, M., Consales, M., Cutolo, A., Giordano, M., Penza, M., et al. (2006). Novel optochemical sensors based on hollow fibers and single walled carbon nanotubes. *IEEE Photonics Technology Letters, 18*(22), 2431−2433.

Day, T. M., Unwin, P. R., Wilson, N. R., & Macpherson, J. V. (2005). Electrochemical templating of metal nanoparticles and nanowires on single-walled carbon nanotube networks. *Journal of the American Chemical Society, 127*(30), 10639−10647.

Domachuk, P., Nguyen, H. C., Eggleton, B. J., Straub, M., & Gu, M. (2004). Microfluidic tunable photonic band-gap device. *Applied Physics Letters, 84*(11), 1838−1840.

Dresselhaus, M. S., Dresselhaus, G., & Avouris, P. (2001). Carbon nanotubes: synthesis, structure, properties, and applications. In *Topics in applied physics* (Vol. 80). Berlin: Springer. ISBN 978-3-540-41086-7.

Dresselhaus, M., Dresselhaus, G., & Eklund, P. C. (2006). *Science of fullerenes and carbon nanotubes*. San Diego, USA: Academic Press.

Du, D., Ye, X. X., Cai, J., Liu, J., & Zhang, A. (2010). Acetylcholinesterase biosensor design based on carbon nanotube-encapsulated polypyrrole and polyaniline copolymer for amperometric detection of organophosphates. *Biosensors and Bioelectronics, 25*, 2503−2508.

Du, D., Wang, M., Cai, J., Qin, Y., & Zhang, A. (2010). One-step synthesis of multiwalled carbon nanotubes-gold nanocomposites for fabricating amperometric acetylcholinesterase biosensor. *Sensors and Actuators B, 143*(2), 524−529.

Firdoz, S., Ma, F., Yue, X. L., Dai, Z. F., Kumar, A., & Jiang, B. (2010). A novel amperometric biosensor based on single walled carbon nanotubes with acetylcholine esterase for the detection of carbaryl pesticide in water. *Talanta, 83*, 269−273.

Heller, D. A., Jin, H., Martinez, B. M., Patel, D., Miller, B. M., Yeung, T., et al. (2009). Multimodal optical sensing and analyte specificity using single-walled carbon nanotubes. *Nature Nanotechnology, 4*, 114−120.

Heller, D. A., Pratt, G. W., Zhang, J., Nair, N., Hansborough, A. J., Boghossian, A. A., et al. (2011). Peptide secondary structure modulates single-walled carbon nanotube fluorescence as a chaperone sensor for nitroaromatics. *Proceedings of the National Academy of Sciences of the United States of America, 108*, 8544−8549.

Iijima, S. (1991). Helical microtubules of graphitic carbon. *Nature, 354*(6348), 56−58.

Hong, J., Heller, D. A., Kalbacova, M., Kim, J., Zhang, J., Boghossian, A. A., et al. (2010). Detection of single-molecule $H_2O_2$ signaling from epidermal growth factor receptor using fluorescent single-walled carbon nanotubes. *Nature Nanotechnology, 5*, 302−332.

Jin, H., Heller, D. A., Kim, J. H., & Strano, M. S. (2008). Stochastic analysis of stepwise fluorescence quenching reactions on single-walled carbon nanotubes: single molecule sensors. *Nano Letters, 8*(12), 4299−4304.

Kashiwagi, K., & Yamashita, S. (2010). Optical deposition of carbon nanotubes for fiber-based device fabrication. In B. Pal (Ed.), *Frontiers in guided wave optics and optoelectronics* (pp. 674−691). Croatia: INTECH.

Kashiwagi, K., Yamashita, S., & Set, S. Y. (2007). Novel cost effective carbon nanotubes deposition technique using optical tweezer effect. In A. M. Earman & R. T. Chen (Eds.), *Proceedings of the SPIE vol. 6478; photonics packaging, integration and interconnects VII* (pp. 6478−6515). SPIE.

Kashiwagi, K., Yamashita, S., & Set, S. Y. (2009). In-situ monitoring of optical deposition of carbon nanotubes onto fiber end. *Optics Express, 17*(7), 5711−5715.

Kim, J., Heller, D. A., Hong, J., Barone, P. W., Song, C., Zhang, J., et al. (2009). The rational design of nitric oxide selectivity in single-walled carbon nanotube near infrared fluorescence sensors for biological detection. *Nature Chemistry, 1*, 473−481.

Kong, J., Franklin, N. R., Zhou, C., Chapline, M. G., Peng, S., Cho, K., et al. (2000). Nanotube molecular wires as chemical sensors. *Science, 287*, 622−625.

Larsen, T. T., Bjarklev, A., Hermann, D. S., & Broeng, J. (2003). Optical devices based on liquid crystal photonic bandgap fibres. *Optics Express, 11*(2), 2589−2596.

Luque, G. L., Ferreyra, N. F., & Rivas, G. A. (2007). Electrochemical sensor for amino acids and albumin based on composites containing carbon nanotubes and copper microparticles. *Talanta, 71*(3), 1282−1287.

Manso, J., Mena, M. L., Yanez-Sedeno, P., & Pingarron, J. (2007). Electrochemical biosensors based on colloidal gold−carbon nanotubes composite electrodes. *Journal of Electroanalytical Chemistry, 603*, 1−7.

Nicholson, J. W. (2007). Optically assisted deposition of carbon nanotube saturable absorbers. In *Paper presented at the conference on lasers and electro-optics/quantum electronics and laser science conference and photonic applications systems technologies*. Washington, DC: Optical Society of America.

Nicholson, J. W., Windeler, R. S., & Di Giovanni, D. J. (2007). Optically driven deposition of single-walled carbon-nanotube saturable absorbers on optical fiber end-faces. *Optics Express, 15*(15), 9176−9183.

Nielsen, K., Noordegraaf, D., Sørensen, T., Bjarklev, A., & Hansen, T. P. (2005). Selective filling of photonic crystal fibres. *Journal of Optics A: Pure and Applied Optics, 7*(8), L13−L20.

Peng, N., Zhang, Q., Chow, C. L., Tan, O. K., & Marzari, N. (2009). Sensing mechanisms for carbon nanotube based $NH_3$ gas detection. *Nano Letters, 9*, 1626−1630.

Penza, M., Antolini, F., & Antisari, M. V. (2004). Carbon nanotubes as SAW chemical sensors materials. *Sensors and Actuators B, 100*(1−2), 47−59.

Penza, M., Cassano, G., Aversa, P., Cusano, A., Cutolo, A., Giordano, M., et al. (2005). Carbon nanotube acoustic and optical sensors for volatile organic compound detection. *Nanotechnology, 16*(11), 2536−2547.

Penza, M., Rossi, R., Alvisi, M., & Serra, E. (2010). Metal-modified and vertically aligned carbon nanotube sensors array for landfill gas monitoring applications. *Nanotechnology, 21*(10), 105501.

Peterson, I. R. (1990). Langmuir−Blodgett films. *Journal of Physics D: Applied Physics, 23*, 379−395.

Peterson, I. R. (1991). Langmuir−Blodgett films. In G. J. Ashwell (Ed.), *Molecular electronics*. Taunton, UK: Research Studies Press.

Petty, M. C. (1996). *Langmuir Blodgett films: An introduction*. Cambridge: Cambridge University Press.

Pisco, M., Consales, M., Cutolo, A., Aversa, P., Penza, M., Giordano, M., et al. (2010). Microstructured optical fibers filled with carbon nanotubes: photonic bandgap modification and sensing applications. In *"Carbon Nanotubes" a cura di José Mauricio Marulanda, Intech* (pp. 507−522). ISBN 978-953-307-054-4.

Pisco, M., Consales, M., Cutolo, A., Penza, M., Aversa, P., & Cusano, A. (2008). Hollow fibers integrated with single walled carbon nanotubes: bandgap modification and chemical sensing capability. *Sensors and Actuator B: Chemical, 129*(1), 163−170.

Pisco, M., Consales, M., Penza, M., Aversa, P., Giordano, M., Cutolo, A., et al. (2009). Photonic bandgap modification in hollow optical fibers integrated with single walled carbon nanotubes. *Microwave and Optical Technology Letters, 51*(11), 2729−2732.

Qi, P., Vermesh, O., Grecu, M., Javey, A., Wang, Q., & Dai, H. (2003). Toward large arrays of multiplex functionalized carbon nanotube sensors for highly sensitive and selective molecular detection. *Nano Letters, 3*(3), 347−352.

Rivas, G. A., Rubianes, M. D., Pedano, M. L., Ferreyra, N. F., Luque, G., & Miscoria, S. A. (2009). *Carbon nanotubes: A new alternative for electrochemical sensors*. New York: Nova Science Publishers, Inc.

Roberts, M. E., LeMieux, M. C., & Bao, Z. (2009). Sorted and aligned single-walled carbon nanotube networks for transistor-based aqueous chemical sensors. *ACS Nano, 10*, 3287−3293.

Set, S. Y., Yaguchi, H., Tanaka, Y., & Jablonski, M. (2004). Ultrafast fiber pulsed lasers incorporating carbon nanotubes. *IEEE Journal on Selected Topics in Quantum Electronics, 10*(1), 137−146.

Siitonen, A. J., Tsyboulski, D. A., Bachilo, S. M., & Weisman, R. B. (2010a). Surfactant-dependent exciton mobility in single-walled carbon nanotubes studied by single-molecule reactions. *Nano Letters, 10*(5), 1595−1599.

Siitonen, A. J., Tsyboulski, D. A., Bachilo, S. M., & Weisman, R. B. (2010b). Dependence of exciton mobility on structure in single-walled carbon nanotubes. *Journal of Physical Chemistry Letters, 1*(14), 2189−2192.

Song, Y.-W., Yamashita, S., Einarsson, E., & Maruyama, S. (2007). All-fiber pulsed lasers passively mode-locked by transferable vertically aligned carbon nanotube film. *Optics Letters, 32*(11), 1399−1401.

Tans, S. J., Devoret, M. H., Dai, H., Thess, A., Smalley, R. E., Geerligs, L. J., et al. (1977). Individual single-wall carbon nanotubes as quantum wires. *Nature, 386*, 474−477.

Terrones, M. (2003). Science and technology of the twenty-first century: synthesis, properties, and applications of carbon nanotubes. *Annual Review of Materials Research, 33*, 419−501.

Tkac, J., Whittaker, J. W., & Ruzgas, T. (2007). The use of single walled carbon nanotubes dispersed in a chitosan matrix for preparation of a galactose biosensor. *Biosensors and Bioelectronics, 22*(8), 1820−1824.

Varghese, O. K., Kichambre, P. D., Gong, D., Ong, K. G., Dickey, E. C., & Grimes, C. A. (2001). Gas sensing characteristics of multi-wall carbon nanotubes. *Sensors and Actuators B, 81*, 32−41.

Wei, B.-Y., Lin, C.-S., & Lin, H.-M. (2003). Examining the gas sensing behaviors of carbon nanotubes using a piezoelectric quartz crystal microbalance. *Sensors and Materials, 15*(4), 177−190.

Yamashita, S., Inoue, Y., Maruyama, S., Murakami, Y., Yaguchi, H., Jablonski, M., et al. (2004). Saturable absorbers incorporating carbon nanotubes directly syntehsized onto substrates and fibers and their application to mode-locked fiber lasers. *Optics Letters, 29*, 1581−1583.

Yan, X. B., Chen, X. J., Tay, B. K., & Khor, K. A. (2007). Transparent and flexible glucose biosensor via layer-by-layer assembly of multi-wall carbon nanotubes and glucose oxidase. *Electrochemistry Communications, 9*(6), 1269−1275.

Ye, J., & Sheu, F-S. (2007). Carbon nanotube-based sensor. In C. S. S. R. Kumar (Ed.), *Nanomaterials for biosensors*. Wiley-VCH Verlag GmbH & Co.

Yellampalli, S. (2011). *Carbon nanotubes-synthesis, characterization, applications*. 51000 Rijeka, Croatia: InTech, Janeza Trdine 9.

Zahab, A., Spina, L., Poncharal, P., & Marliere, C. (2000). Water-vapor effect on the electrical conductivity of a single-walled carbon nanotube mat. *Physical Review B, 62*(15), 10000−10003.

Zare, H. R., & Nasirizadeh, N. (2007). Hematoxylin multi-wall carbon nanotubes modified glassy carbon electrode for electrocatalytic oxidation of hydrazine. *Electrochimica Acta, 52*, 4153−4160.

Zhang, T., Mubeen, S., Myung, N. V., & Deshusses, M. A. (2008). Recent progress in carbon nanotube based gas sensors. *Nanotechnology, 19*, 332001.

Zhmud, B. V., Tiberg, F., & Hallstensson, K. (2000). Dynamics of capillary rise. *Journal of Colloid and Interface Science, 228*, 263−269.

This page intentionally left blank

# Molten glass-infiltrated photonic crystal fibers

5

*I. Konidakis*
Foundation for Research and Technology – Hellas (FORTH), Institute of Electronic Structure and Laser (IESL), Heraklion, Greece

## 5.1 Glassy materials: and why glass-infiltrated photonic crystal fibers (PCFs)?

The material called glass may be defined in three different ways (Ingram, 2001; West, 1984). The first deals with the traditional ways of glass preparation. According to this definition, glass is the solid and rigid material that is formed on cooling from the liquid to the solid state, without any crystallization occurring. The material becomes rigid because the cooling process involves an increase in viscosity. The second definition deals with the structure of glass and states that glass is an amorphous material in which no long-range order of periodicity exists in how the constituent atoms are arranged. Finally, a third definition states that glass is any solid that exhibits a glass transition upon heating. Nevertheless, none of the above definitions are entirely flawless, and additional structural criteria are often considered for the classification of glassy materials.

However, research studies of glasses over the years have made the point that a direct correlation exists between their structure and thermal history with their properties, including, optical, thermal, and mechanical characteristics. Thus, upon selecting suitable glass-forming components their properties can be tuned accordingly. For instance, phosphate glasses are soft and exhibit relatively low glass transition temperatures in comparison to typical silicate or borosilicate glasses, which are characterized by elevated glass transition temperatures and networks of high rigidity.

Upon infiltration of photonic crystal fiber (PCF) capillaries with glasses, the coupling of light between the core and the infiltrated capillaries of the periodic cladding is modified, inducing the existence of photonic bandgap (PBG) guidance transmission characteristics. Moreover, the PBG transmission profiles of the infiltrated all-glass composite PCFs can be tuned accordingly by the selection of the glass infiltration medium, for the realization of multicomponent waveguide fiber devices with unique optical and physical properties. Such an approach is highly promising toward the development of in-fiber devices for a wide variety of applications including light emitting and sensing probes, supercontinuum (SC) generation, broadband amplifiers, as well as in-fiber polarizers (see next sections).

Furthermore, there are two more practical reasons for seeking the fabrication of all-glass composite PCFs. First, soft glasses like phosphate glasses cannot be drawn easily into fibers. Nevertheless, their distinct optical properties and plasmonic features can be

**Optofluidics, Sensors and Actuators in Microstructured Optical Fibers.** http://dx.doi.org/10.1016/B978-1-78242-329-4.00005-9

exploited for most of the aforementioned applications, and thus their encapsulation within fiber capillaries opens the way toward the exploitation of their potential and the design of state-of-the-art in-fiber devices. Second, the investigation of glass formation within the constrained environment of the fiber capillaries remains by itself an open scientific challenge, that is, the study of glass formation within micrometric dimensions. It is also worth noting that likewise PCFs, microstructured optical fibers (MOFs), with nonperiodic capillary structure, are also suitable fibers for glass infiltration toward the fabrication of all-glass composite fibers.

In the following section, the advantages of composite all-glass PCFs toward potential applications and in-fiber devices will be presented, along with in-lab fabrication methods and the reasons for selecting specific types of glass-infiltration mediums. In Section 5.3, key results on the guiding properties and characteristics of recently developed composite all-glass PCFs will be discussed in detail. In Section 5.4, future prospects and possible research directions will be expressed, whereas the significant points of the chapter are summarized in Section 5.5.

## 5.2 Glass-infiltrated PCFs: state of the art and fabrication techniques

By suitably choosing a PCF exhibiting modified total internal reflection properties, PBG guidance can be observed when the fiber capillaries are filled with glassy materials of refractive index significantly greater than that of the PCF body. In such a case, PBG guidance relies on the existence of stopbands in the transmission spectrum of a PCF consisting of a defect core of low refractive index $n_L$ embedded in a periodic microstructured cladding of high refractive index $n_H$ (Abeeluck, Litchinitser, Headley, & Eggleton, 2002; Knight, Broeng, Birks, & Russell, 1998). In such a configuration, the light propagation into the core is allowed for specific spectral bands with modal indices of $n < n_L$, whereas for optical wavelengths in the stopbands light escapes from the fiber core into the higher-index rods, which support resonance waveguiding in the sort wavelength limit. Typically, PBG guidance in all-solid PCFs is associated with high refractive index contrast; however, all-solid PBG fibers with an index contrast of only 1% have been demonstrated by Argyros, Birks, Leon-Saval, Cordeiro, and Russell (2005).

Based on the existence of PBG guidance, all-glass composite PCFs can be exploited toward the development of several functional in-fiber devices suitable for a wide variety of applications (Cerqueira, 2010; Russell, 2006). Exploitation of all-glass PCFs toward SC generation has attracted significant scientific interest over the years. SC relies on significant spectral broadening of the original source, for example, a picosecond or femtosecond laser beam. Over the years, several research efforts have focused on extending the broadening to both higher and lower frequencies, thus expanding the range of potential applications of in-fiber devices to fields, such as optical coherence tomography, frequency metrology, and several kinds of spectroscopy.

Due to their unique optical properties, all-glass PBG fibers can also be used as fiber lasers and amplifiers, with many scientific and technological advantages such as diffraction-limited and high beam quality and good efficiency. Doping the silica PCF and/or the filling glass with rare earth elements, such as erbium, ytterbium, and terbium, is a typical procedure for enhancing laser power and efficiency. Furthermore, the development of many nonlinear optical components is based on the exploitation of PBG fibers transmission profiles. For instance, Lousteau et al. (2012) have reported recently on PBG confinement in an all-solid tellurite glass PCF, in which tellurite glass nonlinear optical and dispersive properties are exploited toward the development of optical components of great interest. In a similar manner, Schmidt et al. (2009) propose the use of tellurite glass-filled silica PCFs for the realization of inline fiber devices suitable for wavelength-filtering applications, while significantly extending the emission range.

Furthermore, the infiltration of PCFs with highly functional glasses can lead to the development of exotic applications like integrated optical isolators and electrically driven in-fiber devices. The use of magneto-optic glasses as filling components allows modifying and controlling the PBG transmission characteristics of the all-glass PCF upon exposure to an external magnetic field. Such glasses typically contain high concentrations of large mass and polarizability ions, that is, lead ($Pb^{2+}$) and bismuth ($Bi^{3+}$) and so on, that modulate the refractive index of glass according to magnetic field strength (Golis & Ingram, 2007). Along the same lines, when fast ion-conducting (FIC) glasses are employed, the transmission profile can be modified by external electric field application, prompting the realization of electrically driven in-fiber devices in which light−current and current−light interactions take place (Noginova, Yakim, Soimo, Gu, & Noginov, 2011). However, several challenges lay ahead regarding these latter two applications, and they will be considered, among others, in Section 5.4.

PCF-based optical sensors offer opportunities spanning many topics and novel potential applications including biomedical sensing, environmental monitoring, and structural health monitoring (Cerqueira, 2010; Russell, 2006). Over the last few decades, fiber optics-based sensors have been extensively investigated as they can easily fulfill all the market requirements, that is, small size, low power consumption, and low weight. Molten glass-infiltrated PCFs and the exploitation of PBG guidance characteristics have great potential to add to this topic. Recently, Konidakis, Konstantaki, and Pissadakis (2014) reported on the isopropanol solvent (2-propanol, $C_3H_7OH$)-sensing ability of thermally poled phosphate glass-layer/silica PBG fibers. Sensing mechanism relies on the plasmon resonance polarization-dependent loss induced by the formation of silver nanoparticles (AgNPs) on the surface of the phosphate glass, and the reduction in the index contrast between the isopropanol-filled capillaries and the phosphate glass layer compared to the empty capillaries and the identical glass layer. Biosensing applications become plausible upon exploitation of surface plasmon resonance phenomena in PCFs (Hautakorpi, Mattinen, & Ludvigsen, 2008; Seise et al., 2012), and the use of molten glass-infiltrated PBG fibers may create new ways for presenting novel functionalities while optimizing sensing ability and efficiency.

An important advantage of all-glass composite PCFs is the ability to select the infiltration matrix among numerous choices of functional glasses, and thus control

the transmission profiles of the fabricated-composite PCF according to desired guiding properties and targeted applications. For instance, it was mentioned earlier that tellurite glasses enable the development of all-glass PBG fibers suitable for optical amplification covering extended optical high-yield photon emission. On a different approach, chalcogenide glass-silica PBG fibers are investigated toward shifting the SC spectrum to longer wavelength, that is, toward the mid-far-IR region, thus expanding further the operating range of the composite fibers to serve emerging safety and security as well as sensing applications (Granzow et al., 2011; Markos, Yannopoulos, & Vlachos, 2012).

Recent research work of Konidakis, Zito, and Pissadakis (2012) and Konidakis and Pissadakis (2014) presented in this chapter (Section 5.3) is based on silica PCFs infiltrated with silver metaphosphate ($AgPO_3$) glass and silver iodide (AgI)-doped FIC glasses of the family $x\text{AgI} + (1 - x)\text{AgPO}_3$. These selections were prompted by multiple reasons. First, the photosensitivity characteristics of the silver binary glass ($AgPO_3$) can be exploited to modulate the PBG guidance profiles of the composite fibers. Second, the relative soft nature of the phosphate glass (glass transition temperature $T_g = 192\ ^\circ\text{C}$), accompanied by low melt viscosity at modest annealing temperatures ($\eta = 0.05$ Pa s at 700 °C), allow the formation of highly homogeneous phosphate-glass strands inside the air capillaries of the silica PCF. Moreover, the existence of the characteristic silver plasmonic band can be further exploited for tuning the guidance mechanism of the composite fiber by applying an external electric field.

Amenability to doping is an additional advantage of $AgPO_3$-based glasses and a powerful tool for modifying their physical characteristics. Indicatively, additions of AgI significantly enhance the mobility of silver cations while suppressing the glass transition temperature ($T_g$), making possible the modulations of the fiber transmission patterns upon electric field application and variation of the fabrication protocol, whereas doping with rare earth elements is really promising toward PBG fiber laser applications. Finally, it is worth noting that $AgPO_3$ glass is relatively easy to prepare under lab ambient conditions by melting equimolar amounts of low-cost starting materials, that is, $AgNO_3$ and $NH_4H_2PO_4$ dry powders, within an electrical furnace (Konidakis, Varsamis, & Kamitsos, 2011).

We move on now to consider fabrication techniques of all-glass PCFs. Fabrication of composite all-glass PCFs can be achieved by direct fiber drawing from preforms constructed from two different glass types (Lousteau et al., 2012; Russell, 2006) or by filling of the PCF air capillaries with glass melt by means of either pressure-assisted or vacuum-assisted infiltration techniques. Infiltration-based methods permit the realization of all-glass PCFs without the necessity of fiber-drawing facility. The temperature and duration of the infiltration process depend upon the glass type and melt viscosity, as well as the PCF characteristics. Namely, Hagen−Poiseuille law (Atkins, 1998) as expressed in the form of Eqn (5.1) can be used to estimate the filling distance $d$ of the PCF capillaries, after a period of time $t$, at which $p$ denotes the infiltration pressure, $R$ the capillary radius, and $\eta$ the melt viscosity:

$$d = \sqrt{pR^2t/4\eta}. \tag{5.1}$$

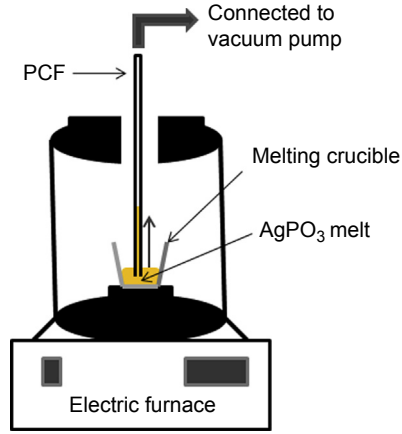


**Figure 5.1** Schematic representation of the vacuum-assisted infiltration of an air/silica PCF with $AgPO_3$ molten glass. The infiltration process is performed at a constant temperature of 700 °C.

Schmidt et al. (2009) and Granzow et al. (2011) follow the pressure-assisted melt-filling protocol by using a highly sophisticated PCF infiltration pressurized chamber with remarkable operating efficiency and robustness. However, composite all-glass PCF samples of equally good quality can be prepared following even simpler in-lab infiltration procedures. For instance, Markos et al. (2012) exploit the capillarity effect to infuse the PCF capillaries with amine solvents in which the bulk $As_2S_3$ glass is dissolved, whereas Konidakis , Zito, and Pissadakis (2012, 2014) prepare their all-glass PCF samples by means of vacuum-assisted infiltration techniques. In the latter approach, the free end face of the PCF is directly immersed inside the glass melt, whereas the second end face is constrained into a vacuum chamber (Figure 5.1). Following the infiltration process, the PCFs are removed from the furnace and are allowed to cool down to room temperature, resulting in the formation of phosphate glass strands along the infiltrated length of the PCF capillaries. A typical filling ratio following this vacuum-assisted infiltration procedure is ∼5 cm of filled PCF in ∼4 h. Scanning electron microscopy (SEM) analysis is performed on the fabricated all-glass PCFs to confirm the success of the infiltration process. Figure 5.2 shows SEM scans of a cleaved end face of a phosphate glass-infiltrated silica PCF (LMA-10, drawn by NKT Photonics Ltd), along with details of the phosphate glass strands emerging from the PCF's cleaved end face and magnified area of the glass-filled capillaries.

## 5.3 PBG guidance characteristics of composite all-glass PCFs

This section includes results and discussion on three versions of all-solid molten glass-infiltrated PCFs fabricated by utilizing different glass compositions and post-fabrication treatment. The three types are: (1) $AgPO_3$ glass PCFs (Section 5.3.1),

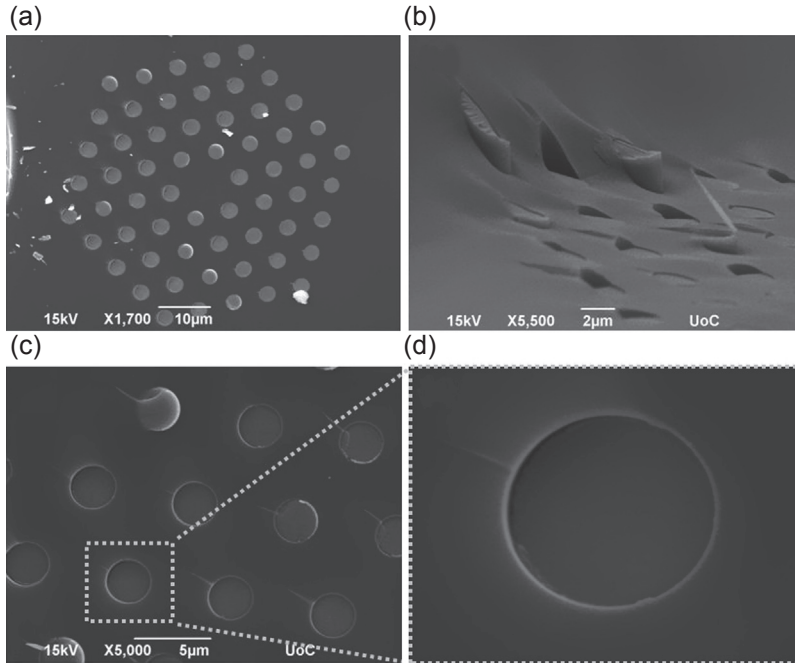


**Figure 5.2** SEM scan of a cleaved cross-section of an infiltrated LMA-10 PCF (a), with details of phosphate glass strands emerging from the PCF's cleaved end face (b) and infiltrated capillaries (c and d).

(2) thermal poling of composite all-glass PCFs (Section 5.3.2), and (3) AgI-doped FIC glass PCFs (Section 5.3.3). For the experiments presented herein, a commercially available all-silica solid-core PCF was used, that is, LMA-10 drawn by NKT Photonics Ltd (Birkerod, Denmark). The microstructured LMA-10 fiber has a periodic four-ring lattice of hollow capillaries running through the entire length of the PCF. The total fiber diameter is 125 μm and the average diameter of the capillaries is 2.85 μm as determined by SEM studies, whereas the lattice constant is found to be 6.4 μm.

### 5.3.1 Silver metaphosphate glass PCFs

In this section, work on the $AgPO_3$ glass LMA-10 fiber will be presented. Onward, all-glass composite PCFs of this type will be denoted as $AgPO_3$/LMA-10. SEM scans of this type of composite fiber were presented earlier (Figure 5.2). Inspection of Figure 5.2 reveals the formation of $AgPO_3$ glass strands of excellent quality and homogeneity within the silica LMA-10 fiber capillaries. As a common practice, SEM analysis was performed in various cross-sections of the entire infiltrated length of all LMA-10 samples to ensure axial homogeneity of the phosphate glass strands. Notably, SEM analysis revealed the presence of hollow inclusions within the

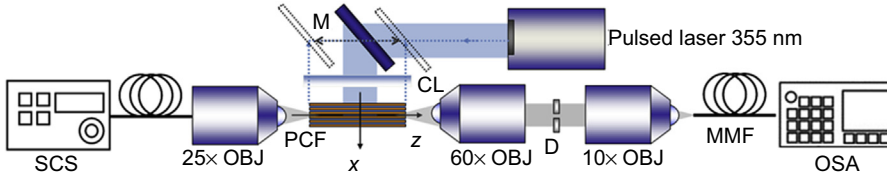


**Figure 5.3** Schematic representation of microscope objective coupling-in/out experimental setup employed for optical transmission measurements of the composite all-glass PCFs.

phosphate glass strands, but only in the few millimeters regions toward the vacuum chamber-connected end face, which actually correspond to the initial moments of vacuum-assisted infiltration. The effect of such inhomogeneities on the guiding properties of the $AgPO_3$/LMA-10 fiber was considered individually by performing transmission measurements on filled samples within this "initial" few millimeters infiltration region, that is, for the sake of comparison with corresponding transmission profiles of samples from the homogeneously filled-centimeters region (Konidakis et al., 2012).

Transmission spectra of $AgPO_3$/LMA-10 PCFs of length ranging from 3 to 30 mm were measured by using a standard microscope objective coupling-in/out setup and a broadband SC source (SCS, 350−2000 nm), as shown schematically in Figure 5.3. In particular, a 25× microscope objective was used to couple light into the silica core of the LMA-10 fiber, whereas a 60× objective collected the near-field light from the fiber end face. An iris diaphragm (D) was used to select the core-only guided output light, and reduce the stopband noise level originating from light propagation through the $AgPO_3$ glass strands. As shown in Figure 5.4, fine featured modes propagating through $AgPO_3$ strands at the $AgPO_3$/LMA-10 fiber end face are clearly visible. Figure 5.4 presents also the white-light far-field diffraction pattern outcoupled from the $AgPO_3$/LMA-10 fiber and projected through a phase mask, which shows a discontinuous dispersion pattern with characteristic evidence of the existence of visible stopbands in the transmission spectrum.

The core-only detected light was coupled through a multimode fiber (MMF) to an optical spectrum analyzer (OSA). Figure 5.5(a) presents a typical experimental transmission spectrum of a 5-mm long $AgPO_3$/LMA-10 fiber, normalized to the transmission of a pristine LMA-10 fiber of the same length. As evident from the aforementioned phase mask projection of light guided through the fiber core, the actual transmission pattern of the composite fiber demonstrated PBG guidance in all of the measurement range, that is, 350−1650 nm. The transmission-to-stopband extinction ratio was found to have a typical value of ∼30 dB/cm. Moreover, it was found to be almost independent from the length of the $AgPO_3$/LMA-10 fiber sample, as revealed from experimental studies of composite fibers of various lengths (Konidakis et al., 2012).

However, a transmission loss of a few dB/cm proportional to the fiber length and independent from the wavelength was determined. Such transmission losses are mainly attributed to three factors: (1) the optical absorption of $AgPO_3$ glass, (2) the mode-confinement losses due to relatively low refractive index contrast between silica

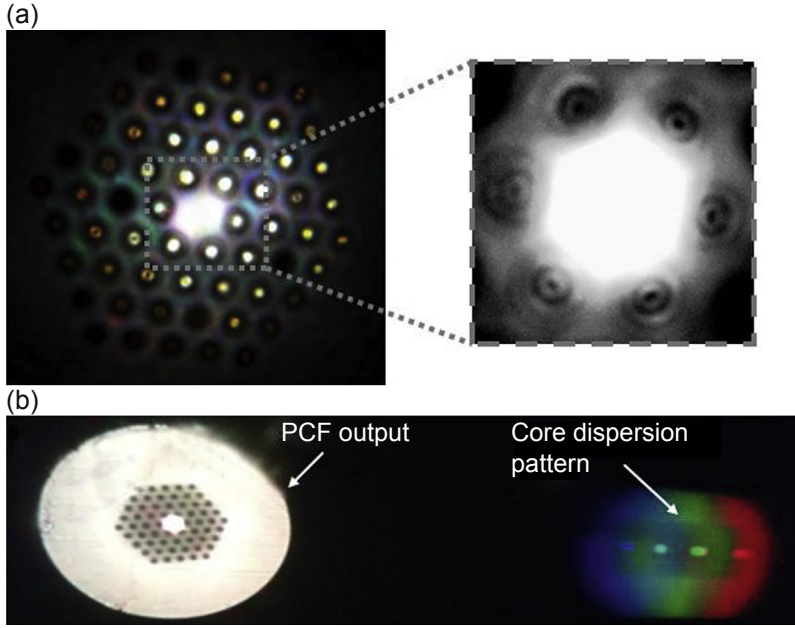


**Figure 5.4** (a) Fine featured modes at the all-glass $AgPO_3$/LMA-10 fiber end face propagating through the $AgPO_3$ glass strands in the cladding, along with detail of the first ring of cladding and core. (b) White-light far-field diffraction pattern outcoupled from the $AgPO_3$/LMA-10 fiber and projected through a phase mask.

and the $AgPO_3$ glass, as well as the few rings of the PBG structure of the LMA-10 fiber (Argyros et al., 2005), and (3) scattering induced by AgNP precipitation. The latter is of great importance regarding the guiding properties and related applications of all-glass $AgPO_3$/LMA-10 fibers, and will be thoroughly considered in the following two sections.

Remarkably, tuning of the spectral allocation of the transmission stopbands of the $AgPO_3$/LMA-10 PBG fibers is achieved by varying silver concentration of the phosphate glass. Namely, reduction of silver concentration from 50% of the metaphosphate composition to 35% causes a refractive index decrease from $\sim$1.75 to $\sim$1.68, as obtained from ellipsometry measurements performed on the corresponding splat-quenched phosphate glass samples. Inspection of Figure 5.5(a) shows that such refractive index variation of the infiltration medium is enough to cause significant changes in the transmission profile of the all-glass composite fibers, that is, both bandwidth and band positions are modified, as well as the transmission-to-stopband extinction ratio particularly in the short wavelengths. Thus, altering silver concentration is a powerful and straightforward tool for controlling the PBG guidance characteristics of all-glass PCFs, and can be of great scientific and technological importance in terms of in-fiber devices in the application fields of SC generation and narrowband amplification (Konidakis et al., 2012).

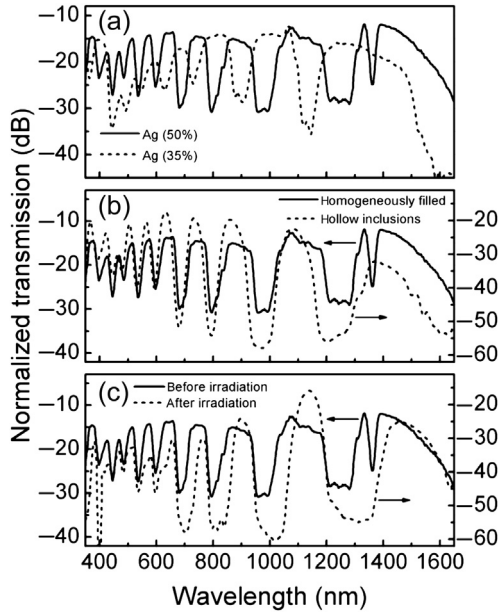


**Figure 5.5** (a) Experimental transmission spectra of 5-mm-long $AgPO_3$/LMA-10 and 0.35Ag−0.65$PO_3$/LMA-10 fibers. (b) Comparison between the homogeneously filled LMA-10 section and the first infiltrated section containing hollow inclusions (see text). (c) Transmission spectra measured on the same $AgPO_3$/LMA-10 sample before and after 355 nm laser irradiation. All spectra are normalized to the corresponding transmission spectrum of a pristine LMA-10 PCF.

Additionally, we consider the effect of hollow inclusion presence in the $AgPO_3$ glass strands on the PBG guiding profile of $AgPO_3$/LMA-10 fiber by comparing the transmissions of a homogeneously filled sample with an inhomogeneously filled one taken from the few millimeter region toward the vacuum chamber connected end face (Figure 5.5(b)), that is, regions in which hollow inclusions and air bubbles were found after SEM analysis. Inspection of Figure 5.5(b) reveals an increase of the bandgap extinction ratio to a maximum value of 60 dB/cm at 1100 nm. Such remarkable enhancement of the transmission contrast is attributed to the high scattering losses occurring within the phosphate glass strands that largely attenuate the stopband light propagation through fiber capillaries; that is, hollow inclusions located in the phosphate glass strands act as centers of scattering, and thus significantly induce losses, especially near the band-edge transmission slope.

Another important feature of the composite all-glass $AgPO_3$/LMA-10 PBG fiber is the effect of the $AgPO_3$ glass photosensitivity on the fiber's guiding properties. Such an effect was explored by irradiating the homogeneous filled sample with the third harmonic at 355 nm of a 150 ps Nd:YAG laser (Figure 5.3). The fiber was irradiated with a total fluence of $\sim 3$ J/cm$^2$, whereas the laser beam was scanned by a mirror (M) along the fiber length through a cylindrical lens (CL), as shown schematically in Figure 5.3. Figure 5.5(c) shows the comparison of the output transmission spectra measured on the

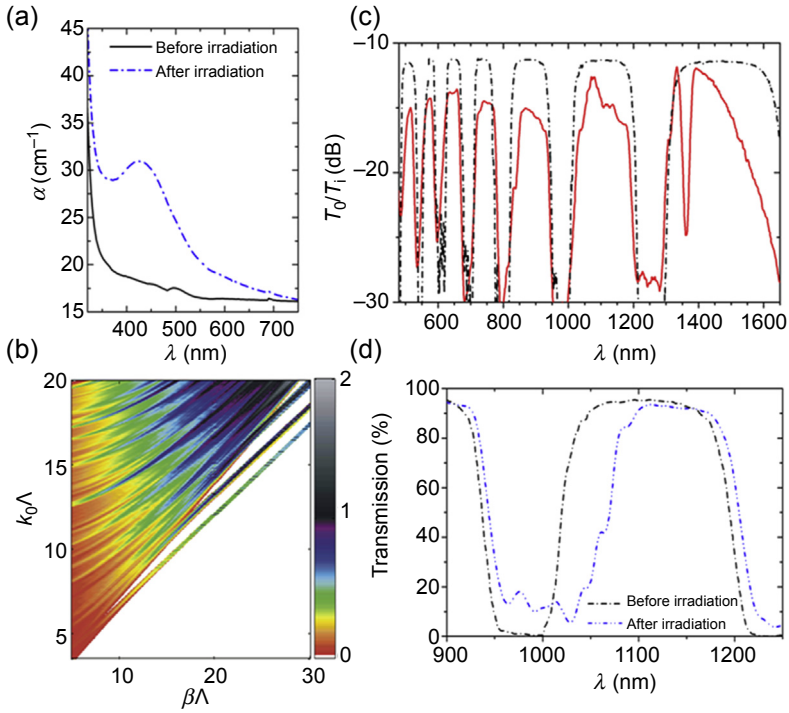


**Figure 5.6** (a) Experimentally measured absorption coefficient spectra of $AgPO_3$ splat-quenched glass before and after 355 nm laser irradiation. (b) Normalized projected density of states (DOS) map; see text for units and further details. (c) Experimental (solid line) and numerically calculated (dashed line) transmission spectra of the $AgPO_3$/LMA-10 PCF. (d) Numerical simulation results of laser irradiation effect (see text).

same $AgPO_3$/LMA-10 sample, before and after laser exposure. The laser exposure induced an average signal attenuation of $\sim$15 dB, and even more importantly, a strong enhancement of the transmission-to-stopband extinction ratio from 30 to 90 dB/cm in the 1100-nm-centered band. Moreover, upon laser irradiation, a narrowing of the transmission bandwidths up to 50 and 80 nm in the bands centered at 1100 and 1450 nm, respectively, was observed with a distinct left band-edge red shift. Such spectral allocation effects are directly correlated with the high photosensitivity of the $AgPO_3$ glass (Pissadakis, Ikiades, Hua, Sheridan, & Wilkinson, 2004).

It is known that silver-containing phosphate glasses photo-darken under ultraviolet laser irradiation, resulting in increased optical absorption accompanied by refractive index variations of the magnitude $\Delta n = \sim 10^{-2}$ (Pissadakis et al., 2004). Figure 5.6(a) demonstrates measured absorption coefficient spectra of the $AgPO_3$ glass splat quenched sample, that is, prepared from identical melt to the one used for filling the air-capillaries of the all-glass LMA-10 fiber, before and after 355 nm laser irradiation. It becomes apparent that, upon laser irradiation, the optical absorption of the phosphate glass drastically increases below 500 nm. Consequently, in the

case of $AgPO_3$/LMA-10 fiber, the modes propagating through the phosphate glass strands are drastically suppressed, resulting in the strong increase of the signal attenuation in the fiber core stopbands. Thus, the transmission-to-stopband ratio enhancement is primarily associated with the augmentation of the absorption losses, rather than on the increase of the laser irradiation-exposed $AgPO_3$ glass refractive index. Additionally, the observed left band-edge red shift (Figure 5.5(c)) arises from the inhomogeneous penetration of the 355 nm laser radiation into the glass strands near the LMA-10 core, due to capillary scattering and enhanced optical absorption effects. The last statement is verified by theoretical model predictions discussed below.

Finally, in a recent study by Konidakis et al. (2012), numerical calculations of the photonic density of states (DOS) were performed for the two-glass (phosphate and silica) configuration of the PBG structure. For the DOS calculations, a plane-wave expansion technique as a function of the (out-of-plane) propagation constant $\beta$ was employed. Figure 5.6(b) presents a normalized projected DOS map with normalized frequency $k_0\Lambda$ and normalized $\beta\Lambda$ being the units. Moreover, numerical simulations of the transmission profile of the $AgPO_3$/LMA-10 fiber utilizing the beam propagation method (BPM) were reported (Figure 5.6(c) and (d)) to explore further the left band-edge red shift upon laser irradiation observed in the experimental transmission spectrum (Figure 5.5(c)).

The two-glass composite fiber was simulated by a radial approximation of its two-dimensional index profile (Abeeluck et al., 2002), while taking into account the $AgPO_3$ glass dispersion independently measured by ellipsometry. Figure 5.6(c) reveals a good agreement between the experimentally measured transmission spectrum and the simulation, thus proving the validity of the theoretical model. The simulation of the photo-induced left band-edge red shift was approximated by adding a linear increase of the $AgPO_3$ glass refractive index with an average value of 0.02 along the diameter direction. In such an approach, the theoretical model accounts plausibly for the absorption attenuation of the $AgPO_3$ glass along the axis of the irradiating laser beam. Figure 5.6(d) shows the comparison between the calculated transmission band centered at 1100 nm before and after laser irradiation. The simulation model confirms a left-edge red shift of $\sim$50 nm in good agreement with the experimental data presented previously in Figure 5.5(c).

### 5.3.2 Thermal poling of composite all-glass PCFs

We move on now to consider thermal poling experiments on the recently realized all-glass $AgPO_3$/LMA-10 PBG fiber, starting from the question, what is the motivation behind it? Beyond the photo-chromic characteristics of $AgPO_3$ glass described in the previous section, the existence of a silver distinct plasmonic spectral signature turns out to be of great importance for tuning and further exploiting the PBG-guiding properties of $AgPO_3$/LMA-10 fiber. This distinct plasmonic signature arises from the existence of AgNPs inside the phosphate glass strands (Kreibig, 1974; Sönnichsen, Franzl, Wilk, Plessen, & Feldmann, 2002). As will become apparent, thermal poling of composite $AgPO_3$/LMA-10 fibers induces the formation

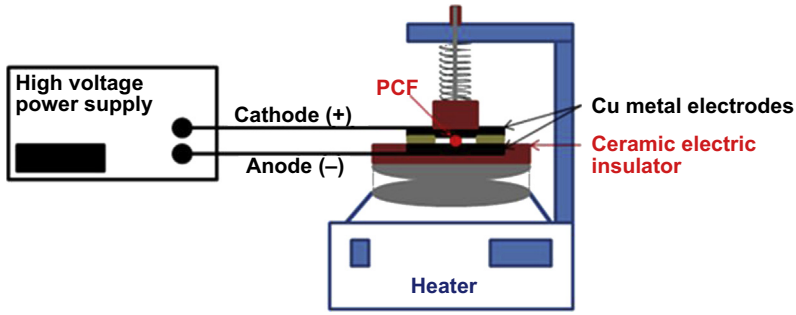


**Figure 5.7** Schematic representation of thermal poling experimental setup.

of AgNPs within the confined volume of the PCF capillaries. Fine examples of MOFs based on inherent plasmonic characteristics have been presented (Hassani & Skorobogatiy, 2007; Hautakorpi et al., 2008), attracting substantial interest in terms of the development of in-fiber electrically driven devices (Noginova et al., 2011) and biosensors (Seise et al., 2012).

In the case of $AgPO_3$/LMA-10 fiber, the application of an external electric field resulted in the polarization-dependent tuning of the PBG guidance via the formation of AgNPs within the phosphate glass strands that add a metallic contribution to the electromagnetic plasmon−polariton response of the fiber, consequently affecting the guiding mechanism (Konidakis, Zito, et al., 2014). In addition to the fully infiltrated $AgPO_3$/LMA-10 samples, fiber samples in which only a layer of $AgPO_3$ glass is deposited within the air capillaries of the LMA-10 PCF were also fabricated and studied. Fiber samples of this type will be denoted as $AgPO_3$-layered/LMA-10. The first step of the fabrication process of those samples is identical to that of $AgPO_3$/LMA-10 samples (described in Section 5.2). Following the initial infiltration process, the fully filled fibers were reheated at 700 °C, while pressurized nitrogen gas was forcing the $AgPO_3$ glass out of the fiber capillaries. By using nitrogen gas pressures of ∼5 bars for 4 h, the $AgPO_3$ glass was removed from the LMA-10 capillaries, however, leaving behind glass layers attached onto the silica surface of the capillary walls. As was the case for $AgPO_3$/LMA-10 samples, $AgPO_3$-layered/LMA-10 fibers were also studied by SEM to examine the quality of the $AgPO_3$ layer formation.

For the electric field thermal poling experiments, a homemade experimental setup was employed (Figure 5.7). A ∼2 cm piece of infiltrated LMA-10 fiber was placed between two optically polished copper metal electrodes, separated by two sheets of insulating mica clay of 0.4 mm thickness. To achieve maximum temperature control, the bottom electrode is positioned onto a ceramic base that is placed directly on a heating plate of great temperature accuracy. After the desired temperature is reached and stabilized, the electric field is applied, that is, generated from a 5 kV DC voltage power supply. The duration of the experiment was varied upon the fabricated-composite fiber type, while several tests were performed to discover optimum thermal poling conditions. Namely, these were found to be 6 and 2 h for the $AgPO_3$/LMA-10 and the $AgPO_3$-layered/LMA-10 samples, respectively. Poling attempts

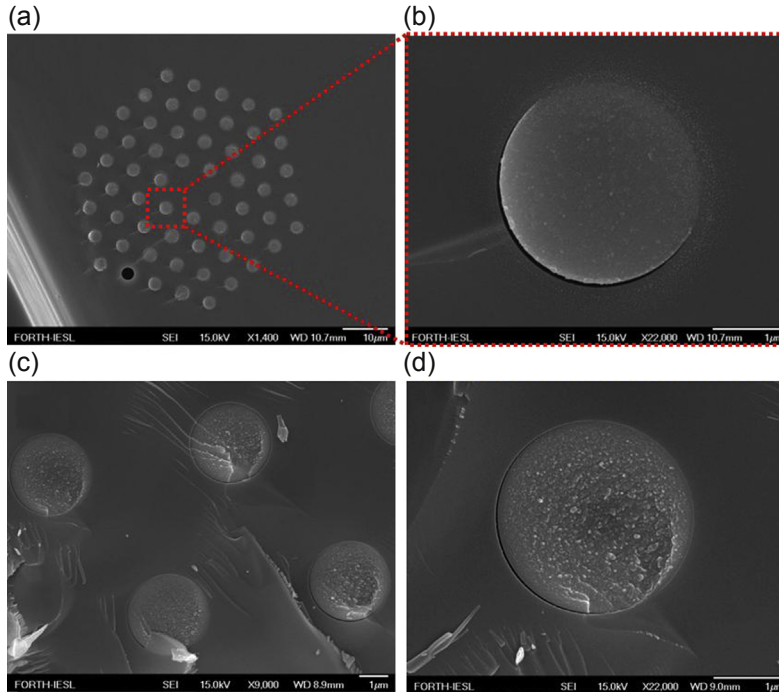


**Figure 5.8** SEM scan of cleaved cross-section of $AgPO_3$/LMA-10 fiber before electric field exposure (a), with details of an infiltrated capillary (b). (c and d) Details of infiltrated capillaries from a different cross-section of the same fiber, after electric field exposure at a poling voltage of 800 V.

were performed with 600 and 800 V at 150 °C, that is, ∼40 °C below the glass transition temperature ($T_g$) of $AgPO_3$ glass (Konidakis et al., 2011). At that temperature range, silver cation migration is assisted by glass network movements, whereas the glass retains its form and stability. Based on these poling conditions, nominal electric field is estimated on the order of $2 \times 10^6$ V/m, that is, well below the breakdown point of silica glass.

Figure 5.8 shows SEM scans of a cleaved cross-section of an $AgPO_3$/LMA-10 fiber sample along with details of a glass-infiltrated capillary prior to electric field exposure (a and b), and corresponding shots from cross-sections exposed to external electric field (c and d). It is worth noting that both pieces originate from the same fiber sample, and the nonexposed one is just taken from a cross-section outside the 2-cm-long exposed region. Inspection of Figure 5.8 by image analysis using "Image J" software, revealed an average size of ∼10 nm for the AgNPs located within pristine phosphate glass, that is, prior to poling, whereas the average size of the AgNPs after the thermal poling process increases remarkably to a figure of ∼90 nm. In the case of pristine samples the observed minimal AgNP precipitation originates unavoidably from the relative slow cooldown of the glass within the LMA-10 capillaries after the infiltration,

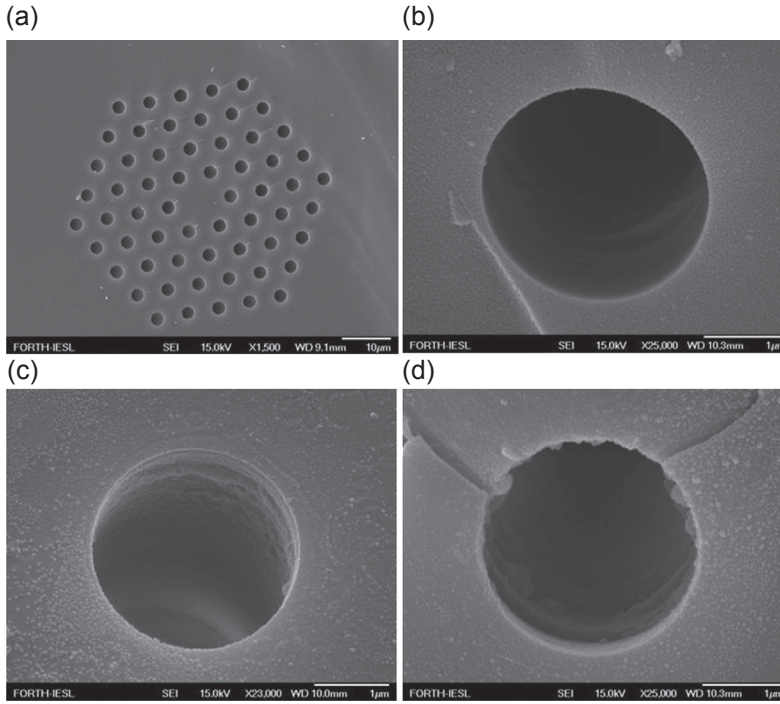


**Figure 5.9** (a) SEM scan of a cleaved cross-section of $AgPO_3$-layered/LMA-10 fiber with magnified images of $AgPO_3$ glass layer deposited on the fiber capillaries before (b) and after (c and d) electric field exposure at a poling voltage of 800 V.

that is, compared to rapid cooling of typical splat quenched glasses. In a different manner, the formation of large AgNPs and clusters within the glass strands of $AgPO_3$/LMA-10 fibers exposed to external electric field (Figure 5.8(c) and (d)) is attributed to the enhanced silver-cation migration within the constrained environment of the encapsulated phosphate glass network, induced by the electric field application, and gradually resulting in silver-rich agglomerated regions of AgNPs and clusters (Konidakis, Zito, et al., 2014).

Similar SEM examination was performed on $AgPO_3$-layered/LMA-10 samples. Figure 5.9(a) displays a cleaved cross-section of $AgPO_3$-layered/LMA-10 fiber, whereas Figure 5.9(b) shows details of the glass layer before thermal poling. SEM scans at different cross-sections reveal the formation of a smooth $AgPO_3$ glass layer of $\sim$50 nm thickness on the silica capillary surface. Before thermal poling treatment, only a minor glass layer thickness variation of $\pm$5 nm was obtained. Notably, after the poling process (Figure 5.9(c) and (d)), the surface of the $AgPO_3$ glass layer becomes rough and full of silver-rich bumps due to AgNPs agglomeration. The so-formed AgNPs are of typical dimension $<$150 nm and, as will become evident later, they constitute a dominant propagation loss mechanism of great significance in the case of $AgPO_3$-layered/LMA-10 fibers.

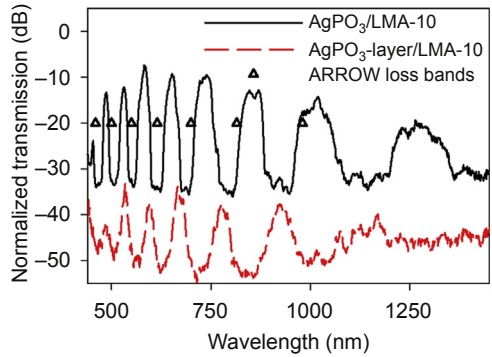


**Figure 5.10** Typical transmission spectra of 1-cm-long $AgPO_3$/LMA-10 and $AgPO_3$-layered/LMA-10 fibers before thermal poling. Both spectra are normalized to the corresponding transmission spectrum of a pristine LMA-10 PCF. △ denote ARROW model predictions for the position of the PBG loss bands (see text).

Experimental transmission spectra of 1-cm-long $AgPO_3$/LMA-10 and $AgPO_3$-layered/LMA-10 fibers prior to thermal poling treatment are presented in Figure 5.10, along with simple antiresonant reflecting optical waveguide (ARROW) guidance theoretical predictions for the PBG loss bands, which agree well with the experimental measurements. As mentioned earlier, theoretical modeling takes into account dispersion data obtained for the corresponding splat-quenched $AgPO_3$ glass samples using ellipsometry. The transmission profile of the $AgPO_3$/LMA-10 fiber is characterized by PBG guidance with extinction ratios up to ∼25 dB/cm, whereas the transmission bands of the $AgPO_3$-layered/LMA-10 fiber are of greater loss and narrower bandwidth, that is, features related with the homogeneity of the glass layer deposited in the capillaries. In both types of composite fibers, the PBG extinction ratio was found independent of the infiltration length. The origins of the transmission losses in both profiles have been identified in the previous section, and are attributed to scattering effects induced by AgNPs precipitation during cool down, $AgPO_3$ glass inherent absorption, and mode confinement losses due to low index contrast and the few rings of the PBG structure of the LMA-10 PCF.

The aforementioned transmission spectra of $AgPO_3$/LMA-10 and $AgPO_3$-layered/LMA-10 fibers shown in Figure 5.10 were measured by using a microscope objective coupling-in/out setup and the SC source as described earlier in Section 5.3.1 (Figure 5.3). However, to proceed to polarization transmission analysis of the PBG patterns, the transmitted light through the PCF core was filtered using a Rochon polarizer, before being coupled through a MMF to the OSA. Notably, prior to any thermal poling treatment of the fibers, filtering the transmitted light through the polarizer revealed no detectable differences with respect to the polarization state. This holds for both types of the fabricated all-glass LMA-10 PCFs presented herein.

Identical polarization analysis was repeated on the same $AgPO_3$/LMA-10 and $AgPO_3$-layered/LMA-10 fiber samples, after thermal poling, that is, exposure to an external electric field of 800 V at 150 °C, and results are shown in Figure 5.11. After thermal poling, both fully filled and layered LMA-10 fibers exhibited significant

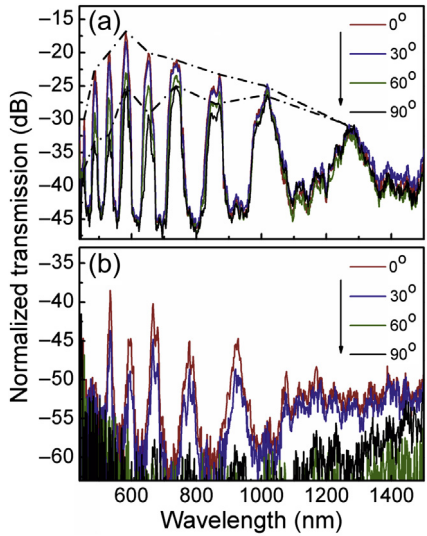


**Figure 5.11** Transmission spectra of 1-cm-long $AgPO_3$/LMA-10 (a) and $AgPO_3$-layered/LMA-10 (b) fibers after electric field exposure, filtered though a Rochon polarizer at various angles. All spectra are normalized to the transmission spectrum of a pristine LMA-10 PCF. Dash-dot connection lines in (a) are only used as a guideline to the eye (see text). Poling voltage employed was 800 V.

changes in their transmission spectra. In particular, overall transmission losses increased more than ∼5 dB/cm for both types of fibers. Moreover, remarkable polarization-dependent spectral changes were detected upon thermal poling. For the fully filled $AgPO_3$/LMA-10 samples, rotation of the polarizer axis from 0° to 90°, results in a decrease in the intensity of the transmission stopbands of the ∼500−1000 nm region. At specific bands of transmission, the polarization-dependent loss exceeded ∼10 dB.

The results of Figure 5.11 reveal even more pronounce variations in the filtered transmission spectra of the $AgPO_3$-layered/LMA-10 fibers upon thermal poling. Remarkably, for specific polarization states for angles between 60° and 90°, light transmission through the fiber core is no longer detectable, thus the loss is dramatically enhanced for the $AgPO_3$-layered fiber compared to the fully filled one. This extremely enhanced polarization loss is mainly attributed to two parameters: first, to the large size of AgNPs and clusters formed within the glass layer and on its surface and contribute drastically to overall scattering loss; and second, to the high refractive index contrast between the empty space of the fiber capillary and the $AgPO_3$ glass layer, which highly confines the guiding mode into it, resulting in high light interactions with the so-formed embedded AgNPs (Konidakis, Zito, et al., 2014). At this point it is important to emphasize that identical thermal poling experiments performed on an empty LMA-10 PCF using the same voltage and temperature conditions showed absolutely no alteration on the guiding properties of the pristine fiber. Even more importantly, the same holds for sole thermal treatment, that is, without electric field application, of the $AgPO_3$ glass composite fibers considered here.

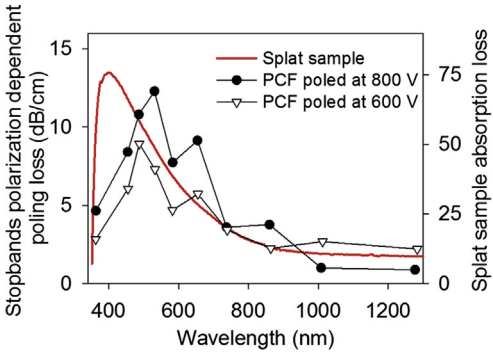


**Figure 5.12** Measured absorption coefficient difference $\Delta\alpha(\lambda)$ of $AgPO_3$ splat-quenched glass before and after thermal poling treatment, and polarization-dependent stopband poling loss of $AgPO_3$/LMA-10 fibers poled using electric fields of 600 and 800 V.

It was clear from the early stages of this project that the polarization-dependent transmission profiles of $AgPO_3$/LMA-10 and $AgPO_3$-layered/LMA-10 fibers correlated with the thermal poling effects on the structural and optical properties of the $AgPO_3$ glass. To more deeply investigate the effects of thermal poling on the structural properties of the $AgPO_3$ glass, micro-Raman vibrational spectroscopy has been carried out on a splat-quenched glass specimen prior to and after thermal poling experiment, that is, poling conditions employed were identical to the ones to which the fabricated composite fibers were exposed. The performed structural analysis confirms the anticipated silver-cation displacements from the anode surface of the glass during thermal poling and their migration toward the cathode side (Konidakis, Zito, et al., 2014).

In addition, thermal poling effects on the absorption coefficient $\alpha(\lambda)$ of the splat $AgPO_3$ glass were measured, and compared to those obtained from the bandgap modulation of the $AgPO_3$/LMA-10 composite fiber. Figure 5.12 shows the difference $\Delta\alpha(\lambda)$ between the $\alpha(\lambda)$ of the same $AgPO_3$ glass specimen before and after thermal poling. The resulting $\Delta\alpha(\lambda)$ extinction spectrum is characterized by a peak having its maximum at 402 nm, in good agreement with typically reported silver plasmon bands in various phosphate glasses (Baia, Baia, Kiefer, Popp, & Simon, 2006; Kreibig, 1976).

The polarization-dependent poling loss corresponding to the PBG transmission stopbands of the $AgPO_3$/LMA-10 fiber, also shown in Figure 5.12, exhibited a rather different shape compared to the one obtained for the $AgPO_3$ splat-quenched glass. The former consistently shows a double-peak profile for thermal poling performed with electric fields of 600 and 800 V. It is characterized by two peaks located at approximately 531 and 654 nm, and an intermediate notch at 583 nm. Such a prominent plasmon resonance absorption feature suggests that the electric field-induced AgNP formation within the $AgPO_3$ glass strands results in the formation of AgNPs of great size, broad distribution, and eccentric shape. Simple theoretical modeling simulations reported by Konidakis, Zito, et al. (2014) employ the Mie scattering method, whereas assuming a single spherical AgNP of $\sim$90 nm size produced a bell-shaped loss-spectra profile peaking at 560 nm with a bandwidth of 244 nm, that is, comparable to the experimentally obtained one shown in Figure 5.12 for the $AgPO_3$/LMA-10 fiber bandgaps.

We consider now the two main reasons causing the observed differences in the data of Figure 5.12, that is, between the $\Delta\alpha(\lambda)$ extinction spectrum and the polarization-dependent poling loss corresponding to the PBG transmission stopbands. The first reason is the different thermal history and cooling rate of the splat-quenched $AgPO_3$ glass and the corresponding glass filling the PCF capillaries. The latter glass is subjected to significantly slower cooling rates for avoiding PCF thermal shock, thus allowing formation of larger silver-seed NPs, which are further augmented upon electric field application. A more thorough study on the effect of thermal history and cooling rate of the infiltrated glass on the guiding properties of the composite PCFs will be presented in the following section. The second reason is related to the pressure exerted in the $AgPO_3$ glass strands confined in the silica walls of the PCF capillaries due to the twice-larger thermal expansion coefficient of the phosphate glass compared to that of silica. It is well known that pressure effects are able to enhance medium-range order topological constraints within the phosphate glass network, leading to glasses with higher packing density and enhanced densification ability (Hutchinson, Ingram, & Robertson, 1992). As a result, in the $AgPO_3$ glass strands within the fiber capillaries even minimum migration of silver cations upon electric field application induces rapid AgNP agglomeration. This also provides a plausible explanation why AgNPs are not only formed toward the cathode side of the capillaries, in which silver-rich regions were expected, but instead they are randomly distributed within the glass strands as depicted by SEM analysis (Figure 5.8).

### 5.3.3 AgI-doped FIC glass PCFs

In this section, we exploit the advantages of another set of functional glasses as PCF infiltration mediums. Recently, Konidakis and Pissadakis (2014) reported on the fabrication of all-glass PBG fiber by infiltration of FIC phosphate glasses of the family $xAgI + (1 - x)AgPO_3$ into the LMA-10 fiber capillaries. Doping the base $AgPO_3$ glass with AgI results in FIC glasses with superior ionic conductivities up to $10^{-2}$ S/cm at room temperature; that is, such enhanced conductivity values are analogous to those of molten salt electrolytes like $KNO_3$ widely used for battery applications (Ingram, 1987). The remarkable conductivity of FIC glasses is also indicative of the high mobility of silver cations within the glass matrix, which act as charge carriers.

So why infiltrate PCFs with FIC glasses? Such decision is mainly prompted by two key reasons. First, the high ionic conductivity of FIC glasses can be of great importance toward the design of novel in-fiber electrically driven devices (see next section). Second, the enhanced cation mobility strongly favors the formation of AgNPs, thus opening the way to further exploitation of the plasmonic characteristics of the composite all-glass PCFs, as demonstrated in the previous section. Adding to this, it is interesting to note that the introduction of AgI halide salt also supports the formation of seed AgI-rich microdomains and/or clusters within the glass matrix. As discussed in previous sections, such formations act as centers of scattering, and thus the concentration of AgI is by its own right a direct and powerful tool for controlling and tuning the PBG guidance characteristics of the composite PCFs. Furthermore, the high tendency

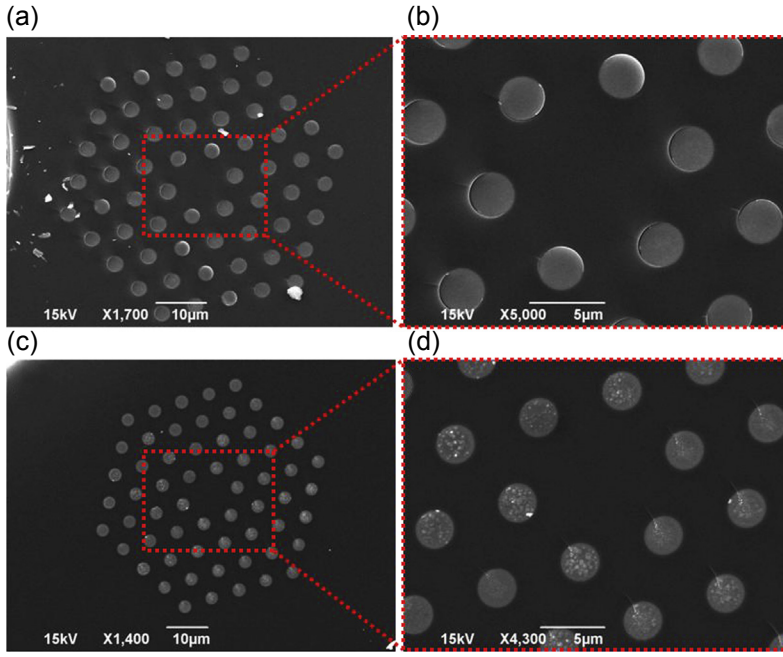


**Figure 5.13** (a) SEM scan of a cleaved cross-section of $0.3AgI + 0.7AgPO_3$/LMA-10 fiber prepared following the fast-cooling method. (b) Magnified area of panel (a). (c) SEM scan of the same type of composite fiber prepared following the slow-cooling method. (d) Magnified area of panel (c).

of FIC glasses to form silver clusters and microdomains is exploited even more in terms of the cooling protocol followed during all-glass PCF fabrication. Upon this basis, we subsequently consider both the effects of AgI concentration as well as the cooling method employed for the glass formation on the PBG transmission profiles of composite $xAgI + (1 - x)AgPO_3$-glass/LMA-10 fibers, whereas all samples are examined by SEM to inspect glass-filling quality and monitor the formation of silver microdomains.

The $xAgI + (1 - x)AgPO_3$-glass/LMA-10 fibers were infiltrated following the vacuum-assisted procedure described in Section 5.2, whereas FIC glass melts were prepared from the appropriate amounts of AgI, $AgNO_3$, and $NH_4H_2PO_4$ dry powders (Konidakis & Pissadakis, 2014). After the infiltration stage, two distinct cooling methods of the glass melt were followed, namely fast cooling (f.c.) and slow cooling (s.c.). Following the fast-cooling method, the infiltrated LMA-10 fiber was abruptly removed from the electric furnace and exposed to ambient lab temperature. On the contrary, by adopting the slow-cooling approach, after the infiltration period the fiber was simply removed from the glass melt with the aid of a micrometric stage, while it remained within the furnace to sustain a controlled cooling rate of $\sim 5\,^{\circ}C/min$.

Figure 5.13(a) and (b) shows SEM scans of a cleaved cross-section of $0.3AgI + 0.7AgPO_3$/LMA-10 fiber prepared following the fast-cooling method. Thorough

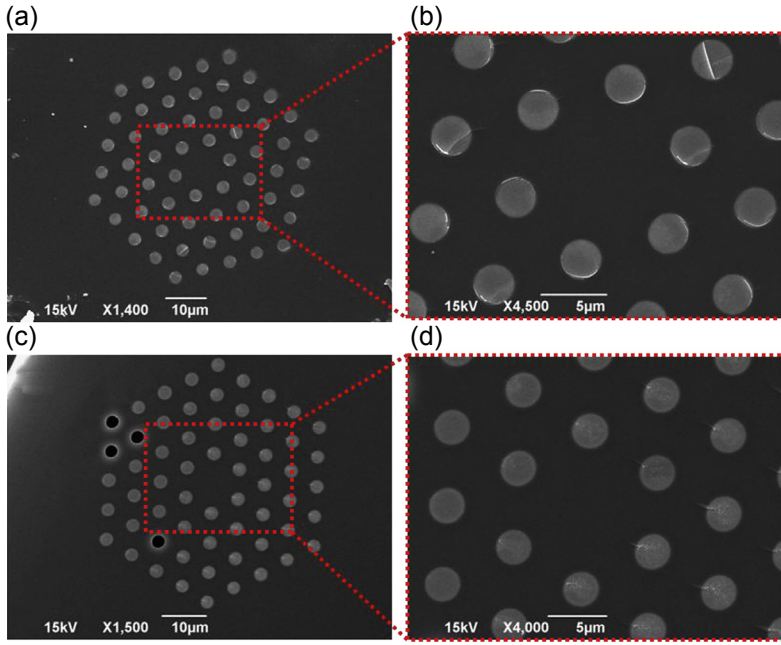


**Figure 5.14** (a) SEM scan of a cleaved cross-section of $0.55AgI + 0.45AgPO_3$/LMA-10 fiber prepared following the fast-cooling method. (b) Magnified area of panel (a). (c) SEM scan of the same type of composite fiber prepared following the slow-cooling method. (d) Magnified area of panel (c).

image analysis revealed that the fast-cooled $0.3AgI + 0.7AgPO_3$ glass strands appear to exhibit minimal cluster formation of average size less than 15 nm. Such a cluster size is comparable to the size of AgNPs reported in previous sections for the binary $AgPO_3$ glass, that is, prepared under equivalent cooling conditions. However, inspection of Figure 5.13(c) and (d) reveals an average size of $\sim$350 nm for the clusters embedded within the corresponding slow-cooled glass strands.

Similar SEM examination was performed on $0.55AgI + 0.45AgPO_3$/LMA-10 fiber samples. Figure 5.14 displays details of a cross-section of samples fabricated following fast-cooling protocol (a and b), and the corresponding scans for fibers of the slow-cooling protocol (c and d). Once again, for the fast-cooled FIC glass, AgNPs of negligible size of less than 15 nm are revealed, whereas their size increases significantly to a figure of $\sim$150 nm when the slow-cooling method is adopted. Overall, SEM analysis of the fabricated FIC glass PCFs revealed good quality of glass strands along the infiltrated length of the capillaries.

Experimental transmission spectra of 1-cm-long $xAgI + (1 - x)AgPO_3$/LMA-10 fibers for $x = 0$, 0.3, and 0.55, prepared by fast-cooling protocol are shown in Figure 5.15. Transmission profiles exhibit PBG guidance with extinction ratios of $\sim$20 dB/cm for the AgI-doped FIC glasses and $\sim$25 dB/cm for the binary $AgPO_3$ glass. More importantly, we note that, due to the higher refractive index of the FIC

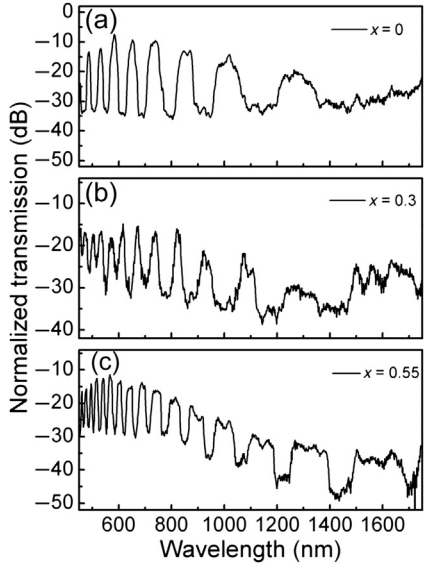


**Figure 5.15** Experimental transmission spectra of 1-cm-long $x$AgI + $(1 - x)$$AgPO_3$/LMA-10 fibers, for $x = 0$, 0.3, and 0.55, prepared following the fast-cooling method. All spectra are normalized to the transmission spectrum of a pristine LMA-10 PCF.

glasses compared to the base $AgPO_3$ glass, that is, indexes for the AgI-doped glasses are 1.90 and 2.1 for $x = 0.3$ and 0.55, respectively (Benassi, Fontana, & Rodrigues, 1991), additional optical bands are introduced in the transmission spectra of FIC-glass/LMA-10 fibers. Namely, the extra bands are mainly inserted in the short wavelength regimes, as predicted by ARROW model theory. Moreover, the transmission losses for the AgI-doped glass infiltrated LMA-10 fibers appear higher than those of the $AgPO_3$/LMA-10 fiber, mainly due to the greater absorption loss of the AgI-containing glasses.

We consider now the effect of the cooling method followed during sample fabrication, that is, fast and slow cooling, on the PBG guidance characteristics of the composite FIC-glass/LMA-10 fibers. Figure 5.16 presents transmission spectra of $x$AgI + $(1 - x)$ $AgPO_3$/LMA-10 fibers, measured with the use of the standard objective coupling-in/out set up (Figure 5.3). For fiber with $x = 0.3$ (Figure 5.16(a)), slow-cooling protocol leads to enhancement of the overall transmission loss by as much as $\sim$10 dB/cm at specific bands of transmission. Moreover, two key spectral features characterize the transmission spectra: First, the extinction ratio of the transmission stopbands drastically increases from $\sim$15 to 30 dB/cm, and second, the full-width half-maximum (FWHM) broadening of the discrete stopbands up to a factor of two for specific bands of transmission. These specific spectral features are related to the extensive AgI agglomeration promoted strongly by the slow-cooling process, which is allowing more time for ion movements while the glass network is extremely soft during cool down (Konidakis & Pissadakis, 2014). In addition, we speculate that the broadening of the FWHM of

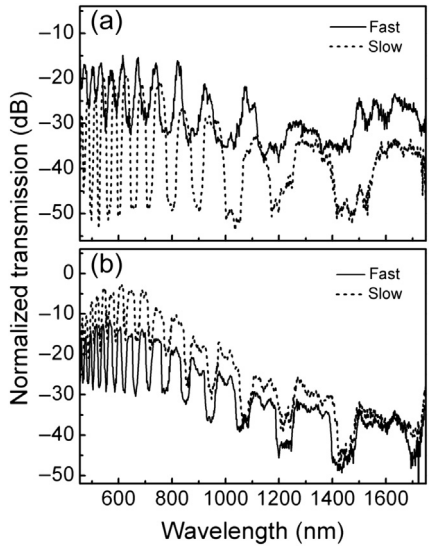


**Figure 5.16** Experimental transmission spectra of 1-cm-long $x$AgI + $(1 - x)$$AgPO_3$/LMA-10 fibers fabricated via the fast-cooling and slow-cooling methods, for $x = 0.3$ (a) and $x = 0.55$ (b). All spectra are normalized to the transmission spectrum of a pristine LMA-10 PCF.

the stopbands is attributed to the high refractive index of the so-formed AgI microdomains, which consequently affect the light confinement in these infiltrated PCFs. The pronounced AgI agglomeration within the glass strands of this particular phosphate glass was verified by SEM studies presented in Figure 5.13.

The effect of cooling method on the PBG guiding properties of the 0.55AgI + 0.45$AgPO_3$/LMA-10 fiber (Figure 5.16b) is of rather different effect and less prominent compared to the FIC glass of lower AgI concentration ($x = 0.3$). Figure 5.16(b) shows that the slow-cooling protocol almost diminishes transmission losses of the composite PCF in the short wavelength regimes, whereas it reduces loss throughout the entire spectral region. We recall now on the corresponding SEM scans of this fiber shown earlier in Figure 5.14, in which even following the slow-cooling route, the so-formed AgI microdomains did not exceed the size of ~150 nm, despite the higher amount of AgI concentration compared to FIC glass with $x = 0.3$. It is known for such glass systems that the devitrification and maximum tendency for crystallization is normally expected close to the highest content of AgI (Tomasi, Mustarelli, Magistris, & Ricci, 2002). However, in the case of glasses formed within the constraint environment of the fiber capillaries, the crystallization bias is pushed toward lower contents of AgI. In addition, among the samples presented herein, the 0.55AgI + 0.45$AgPO_3$/LMA-10 fiber exhibits the highest refractive index contrast between silica and the phosphate glass, which consequently results in impressive reduction of mode confinement losses. Thus, as long as its capillaries remain free of exceptionally large AgI particles, that is, as depicted by SEM analysis, it is expected to exhibit the most optimum transmission behavior. Finally, among the two cooling protocols,

slow-cooling exhibits even better transmission performance due to the fact that during the elongated cooling period the residual stresses between silica and the soft FIC glass vanish, helping to reduce losses even further.

## 5.4 Prospects and future directions

In this section, likely future trends and research directions toward the design and fabrication of advanced in-fiber devices will be considered. Light transmission tuning through fiber devices by electric or magnetic field could be of great importance in a sense that the desired light propagation is controlled entirely by the external field application. So far, as presented in previous sections, an electric field was employed to induce plasmonic characteristics of all-glass PCFs and generate transmission-dependent losses. However such an approach is more useful toward sensing applications (see below), because once the plasmonic features are generated they cannot be reversed. For advanced light transmission control, it is believed that the next crucial step would be the tuning of PBG guidance properties upon application of external voltage on the fiber end faces, and via the exploitation of the enhanced-charge carrier mobility within FIC glass infiltration mediums. This can be vital for devices targeting light amplification, lasing, and SC generation applications. Nevertheless, such a process involves several scientific challenges, for instance the use of highly conductive but also transparent electrodes at the fiber end faces, and ongoing research work focuses on successfully overcoming these issues.

Let us now consider the infiltration of PCFs with "smart" functional magneto-optic glasses. Typical glasses of this type contain cations of large mass and high polarizability, such as lead ($Pb^{2+}$) and bismuth ($Bi^{3+}$), and exhibit interesting properties in terms of magneto-optics and nonlinear-optics phenomena, which can result in highly sophisticated optoelectronic, as well as, biomedical applications (Golis & Ingram, 2007). For instance, the generation and magnitude variation of a magnetic field within a magnetic tomography device could be monitored by an all-magneto-optic-glass PCF probe, by means of the light transmitted through the fiber, resulting in accurate medical screening. A major drawback of lead- and bismuth-doped glasses is their relatively high melting temperatures that can be close to the fusion temperature of pristine silica glass, and thus silica PCFs. Thus, for these glasses to be exploited, new fabrication techniques may be required, namely involving the pre-melting of the cation oxides prior to mixing with the phosphate precursors and before the PCF infiltration stage.

Regarding sensing and biosensing applications a lot of potential arises from the exploitation of silver plasmonic characteristics of the phosphate glass-layered PCFs presented in Section 5.3.2. First, a basic sensing principle relies on the scattering effects induced by the formation of plasmon nanoparticles and their interactions with the target liquid solvents or gases. Second, the use of functional molecules that provide binding sites for proteins and DNA on the surface of the plasmon particles is highly promising toward the evolution of applications in the biosensing discipline (Abbas, Linman, & Cheng, 2011; Homola, Yee, & Gauglitz, 1999; Santiago-Cordoba,

Cetinkaya, Boriskina, Vollmer, & Demirel, 2012). It is noted also that the overall procedure is based on the lab-in-a-fiber idea, in which all processes take place within the PCF capillaries, and thus making biosensing probing easy, whereas is safe at the same time due to the biocompatibility of the phosphate glass. Ongoing work involves the identification of appropriate absorbing molecules and their uniform deployment within the constraint environment of the PCF capillaries.

Finally, it is worth noting that continuous research effort is planted for shifting the SC generation toward longer wavelengths, in which interesting molecular spectroscopy and medicine applications may arise (Schmidt, 2013). Moreover, emphasis will always be given on the design and fabrication of upgraded PBG/PCF configurations that reduce losses and improve confinement, and thus enhance their potential use toward all application fields and commercialization of novel products.

## 5.5 Conclusions and final remarks

Within this chapter a subjective selection of topics in the field of molten glass-infiltrated PCFs was presented and discussed, aiming to demonstrate their advantages toward the design of novel in-fiber devices and potential applications. Different types of all-glass PCFs were considered along with a review on the employed fabrication methods and techniques. Recent scientific studies by the author on various types of phosphate glass infiltrated silica PCFs were presented and discussed in detail.

In particular, for the case of all-glass $AgPO_3$/silica PBG fiber, it was shown that the phosphate glass photosensitivity allows the modulation of the fiber transmission by photo-induced variation of the refractive index. Furthermore, the transmission characteristics of this type of composite fiber were tuned by using thermal poling processes, resulting in polarization-dependent transmission. The observed polarization effects were induced by the formation of AgNPs within the infiltrated $AgPO_3$ glass and the introduction of silver plasmonic characteristics. Finally, the transmission characteristics of composite $x$AgI + $(1 - x)$$AgPO_3$/LMA-10 fibers were presented. The introduction of AgI salt within the phosphate glass induces additional transmission stopbands in the PBG spectra along with spectral allocations attributed to the variation of the refractive index contrast between the silica core and the AgI-doped FIC phosphate glass strands. The effect of the phosphate glass cooling protocol during sample fabrication on the transmission behavior of the fiber was also considered.

In conclusion, it is believed that recent findings on the field of molten glass-infiltrated PCFs appear promising toward the realization of several in-fiber devices suitable for a wide variety of applications, including SC and second harmonic generation, narrowband amplification, solid state lasers, nonlinear and magneto-optics, as well as, sensing and biosensing. Ongoing research interest is focused on the development and optimization of advanced in-fiber devices suitable for the aforementioned applications, and the near future should see many of these applications transformed into widely used commercial products.

## Acknowledgments

All experimental work presented in Section 5.3 has been performed by the author in the Photonic Materials and Devices Laboratory (PMDL), of the Institute of Electronic Structure and Laser (IESL), Foundation for Research and Technology-Hellas (FORTH), under the supervision of Stavros Pissadakis whom I would like to sincerely thank for his guidance and advice throughout the years.

The research disciplines investigated by the author are currently funded by the State Scholarship Foundation (IKY) within the framework of IKY Fellowships of Excellence for Postgraduate Research in Greece − Siemens Program, CN: SR-22091/13. Before that, financial support from the EU Projects SP4-Capacities "IASIS" CN 232479 and CA "ASPICE" CN 287637, and Greek "THALES" project NA(Z) NOWIRE-380252 is gratefully acknowledged.

Finally, I would like to dedicate this chapter to my sister Katerina and to my parents.

## References

Abbas, A., Linman, M. J., & Cheng, Q. (2011). New trends in instrumental design for surface plasmon resonance-based biosensors. *Biosensors & Bioelectronics, 26*, 1815−1824.

Abeeluck, A. K., Litchinitser, N. M., Headley, C., & Eggleton, B. J. (2002). Analysis of spectral characteristics of photonic bandgap waveguides. *Optics Express, 10*, 1320−1333.

Argyros, A., Birks, T. A., Leon-Saval, S. G., Cordeiro, C. M. B., & Russell, P. S. J. (2005). Guidance properties of low-contrast photonic bandgap fibres. *Optics Express, 13*, 2503−2511.

Atkins, P. (1998). *Physical chemistry-6th edition*. Oxford: Oxford University Press.

Baia, L., Baia, M., Kiefer, W., Popp, J., & Simon, S. (2006). Structural and morphological properties of silver nanoparticles-phosphate glass composites. *Chemical Physics, 327*, 63−69.

Benassi, P., Fontana, A., & Rodrigues, P. A. M. (1991). Light-scattering in superionic glasses $(AgI)_x(AgPO_3)_{1-x}$ Brillouin and Raman scattering. *Physical Review B, 43*, 1756−1762.

Cerqueira, A. S., Jr. (2010). Recent progress and novel applications of photonic crystal fibers. *Reports on Progress in Physics, 73*, 024401−024422.

Golis, E. P., & Ingram, A. (2007). Investigations of magneto-optic properties in PbO-$Bi_2O_3$-$GeO_2$ glass system. *Journal of Physics: Conference Series, 79*, 012003−012005.

Granzow, N., Uebel, P., Schmidt, M. A., Tverjanovich, A. S., Wondraczek, L., & Russell, P. S. J. (2011). Bandgap guidance in hybrid chalcogenide−silica photonic crystal fibers. *Optics Letters, 36*, 2432−2434.

Hassani, A., & Skorobogatiy, M. (2007). Design criteria for microstructured-optical-fiber-based surface-plasmon-resonance sensors. *Journal of the Optical Society of America B, 24*, 1423−1429.

Hautakorpi, M., Mattinen, M., & Ludvigsen, H. (2008). Surface-plasmon-resonance sensor based on three-hole microstructured optical fiber. *Optics Express, 16*, 8427−8432.

Homola, J., Yee, S. S., & Gauglitz, G. (1999). Surface plasmon resonance sensors: review. *Sensors and Actuators B, 54*, 3−15.

Hutchinson, J. M., Ingram, M. D., & Robertson, A. H. J. (1992). The effects of pressure and densification on ionic conductivities in silver iodomolybdate glasses. *Philosophical Magazine Part B, 66*, 449−461.

Ingram, M. D. (1987). Ionic-conductivity in glass. *Physics and Chemistry of Glasses, 28*, 215−234.

Ingram, M. D. (2001). *Glass science-4th year undergraduate course*. Aberdeen: University of Aberdeen.

Knight, J. C., Broeng, J., Birks, T. A., & Russell, P. S. J. (1998). Photonic band gap guidance in optical fibers. *Science, 282*, 1476−1478.

Konidakis, I., Konstantaki, M., & Pissadakis, S. (2014). Materials growth and processing in the capillaries of photonic crystal fibres: towards the lab-in-a-fibre protocol. *Proceedings of SPIE, 8982*, 89820C-1.

Konidakis, I., & Pissadakis, S. (2014). Optical spectra tuning of all-glass photonic bandgap fiber infiltrated with silver fast-ion-conducting glasses. *Materials, 7*, 5735−5745.

Konidakis, I., Varsamis, C. P. E., & Kamitsos, E. I. (2011). Effect of synthesis method on the structure and properties of $AgPO_3$-based glasses. *Journal of Non-Crystalline Solids, 357*, 2684−2689.

Konidakis, I., Zito, G., & Pissadakis, S. (2014). Silver plasmon resonance effects in $AgPO_3$/silica photonic bandgap fiber. *Optics Letters, 39*, 3374−3377.

Konidakis, I., Zito, G., & Pissadakis, S. (2012). Photosensitive, all-glass $AgPO_3$/silica photonic bandgap fiber. *Optics Letters, 37*, 2499−2501.

Kreibig, U. (1974). Electronic properties of small silver particles: the optical constants and their temperature dependence. *Journal of Physics F: Metal Physics, 4*, 999−1014.

Kreibig, U. (1976). Small silver particles in photosensitive glass: their nucleation and growth. *Applied Physics, 10*, 255−264.

Lousteau, J., Scarpignato, G., Athanasiou, G., Mura, E., Boetti, N., Olivero, M., et al. (2012). Photonic bandgap confinement in an all-solid tellurite-glass photonic crystal fiber. *Optics Letters, 37*, 4922−4924.

Markos, C., Yannopoulos, S. N., & Vlachos, K. (2012). Chalcogenide glass layers in silica photonic crystal fibers. *Optics Express, 20*, 14814−14824.

Noginova, N., Yakim, A. V., Soimo, J., Gu, L., & Noginov, M. A. (2011). Light-to-current and current-to-light coupling in plasmonic systems. *Physical Review B, 84*, 035447−035451.

Pissadakis, S., Ikiades, A., Hua, P., Sheridan, A., & Wilkinson, J. (2004). Photosensitivity of ion-exchanged Er-doped phosphate glass using 248nm excimer laser radiation. *Optics Express, 12*, 3131−3136.

Russell, P. S. J. (2006). Photonic-crystal fibers. *Journal of Lightwave Technology, 24*, 4729−4749.

Santiago-Cordoba, M. A., Cetinkaya, M., Boriskina, S. V., Vollmer, F., & Demirel, M. C. (2012). Ultrasensitive detection of a protein by optical trapping in a photonic-plasmonic microcavity. *Journal of Biophotonics, 5*, 629−638.

Schmidt, M. A. (2013). *Chalcogenide-silica fibers: A new base for linear and nonlinear nanophotonic devices*. ICTON-2013, Tu.C6.1.

Schmidt, M. A., Granzow, N., Da, N., Peng, M., Wondraczek, L., & Russell, P. S. J. (2009). All-solid bandgap guiding in tellurite-filled silica photonic crystal fibers. *Optics Letters, 34*, 1946−1948.

Seise, B., Csaki, A., Schwuchow, A., Fritzsche, W., Weber, K., Cialla, D., et al. (2012). Microstructured optical fibre as biosensor for pathogen detection on DNA-level. *Biomedical Engineering/Biomedizinische Technik, 57*(SI-1), 339.

Sönnichsen, C., Franzl, T., Wilk, T., Plessen, G., & Feldmann, J. (2002). Plasmon resonances in large noble-metal clusters. *New Journal of Physics, 4*, 93.1−93.8.

Tomasi, C., Mustarelli, P., Magistris, A., & Ricci, O. (2002). Devitrification and phase equilibria in the $xAgI(1-x)AgPO_3$ system. *The Journal of Physical Chemistry B, 106*, 2962−2966.

West, A. R. (1984). *Solid state chemistry and its applications*. New York: John Wiley & Sons.

# Part Two

# Sensing and optofluidic applications

This page intentionally left blank

# Microstructured optical fibre-based sensors for structural health monitoring applications

6

*F. Berghmans, T. Geernaert, C. Sonnenfeld, S. Sulejmani, H. Thienpont*
Vrije Universiteit Brussel (VUB), Brussels, Belgium

## 6.1 Introduction to structural health monitoring applications and fibre Bragg grating sensors

When browsing through handbooks dealing with Structural Health Monitoring (SHM) one encounters several definitions for this particular field of engineering science. In a very broad sense, SHM refers to diagnosing the state of a structure or of its constituent parts or materials and following up on that state as a function of time, considering that it will be affected by aging as a result of normal usage, the influence of the environment, accidental events and the initiation and propagation of damage. More specifically, SHM involves observing a structure over time using measurements from an array of sensors, the extraction of damage-sensitive features from these measurements and the statistical analysis of these features to determine the current state of the structure's health (Sohn et al., 2004). Examples of structures exposed to severe stress conditions over long periods and therefore requiring SHM are multiple: bridges, dams, buildings, pipelines, train rails and carriages, aircraft fuselages and wings, wind turbine structures and blades, and so on. Knowledge about the integrity of the structure and of the evolution of that integrity has become crucial as it allows optimizing the design and usage of the structure, replacing scheduled and periodic maintenance by condition-based maintenance, minimizing downtime, extending the operational life cycle and preventing the occurrence of catastrophic failure. Depending on the type of structure and on its usage, the implementation of SHM approaches are essentially driven by the potential for obtaining enhanced designs, for more efficiently managing the maintenance costs, for improving reliability and for ensuring safer operation of the structure (Balageas, Fritzen, & Güemes, 2006).

SHM is often mentioned along with Non-Destructive Testing or Non-Destructive Evaluation (NDT or NDE, respectively) techniques (Herlier, 2013; Mix, 2005; Shull, 2002). NDT relies on examinations of the structure to assess the existence of damage or geometry changes mainly using visual inspections, often combined with ultrasonic, acoustic emission, radiographic testing or another measurement techniques. We note upfront that our intention is not to provide an exhaustive review of NDT techniques and SHM approaches. A wealth of literature exists on these subjects, and we invite the interested reader to consult the set of handbooks already referenced. We limit

**Optofluidics, Sensors and Actuators in Microstructured Optical Fibers.** http://dx.doi.org/10.1016/B978-1-78242-329-4.00006-0

ourselves to stating that current damage tolerance design methodology requires the structures to be able to withstand the occurrence and development of damage up to certain levels without failure and calls for damage to be detectable by periodic NDT-based inspection before growing to critical size. However, damage can still occur and increase beyond acceptance levels between two inspection routines and may go unnoticed for long times, with possibly catastrophic consequences. Therefore, many efforts now target the development of NDT sensors which can become an integral part of the material or structure to be monitored with the aim to return in situ and continuous information about the structure and hence to support effective SHM. A supplementary approach is to develop new so-called 'smart' materials which not only possess the classical properties of stiffness and strength, but which can also act as actuators under a variety of external stimuli, provide passive and active response to enable SHM, facilitate advanced NDT strategies, and even enable shape-changing and morphing structures (Elhajjar, Saponara, & Muliana, 2013; Schwartz, 2008). In this chapter we report on our efforts in these respects, and more specifically on dedicated microstructured optical fibre (MOF)-based sensors which allow carrying out multi-dimensional strain measurements when embedded inside structural materials, such as for example fibre-reinforced polymer composite materials (Campbell, 2010).

The ability to accurately measure mechanical strain is crucial in many SHM applications. Strain measurements can be used to identify the presence, location and severity of damage in structures (Li, 2010). It can also return information on the mechanical load or vibrations experienced by the structure. Such strain measurements can be achieved with optical fibre-based sensors, which have already been considered multiple times for SHM-related applications (Glisic & Inaudi, 2007; Lopez-Higuera, Rodriguez Cobo, Quintela Incera, & Cobo, 2011; Udd, 1995). These sensors have a number of advantages which can be essential for SHM, including immunity to electromagnetic interference, low weight, small size and limited intrusiveness. In addition and depending on the type of sensor, they can be multiplexed in large sensor arrays to return quasi-distributed measurements, and they enable fully distributed measurements (Berghmans & Geernaert, 2011; Thevenaz, 2011).

In the remainder of this chapter, we will mainly deal with one particular type of optical fibre-based sensor, that is, a fibre Bragg grating (FBG) sensor, which has evolved over the last 30 years into one of the most mature fibre sensor technologies (Cusano, Cutolo, & Albert, 2011). It combines all the advantages of optical fibre sensors with excellent resistance to fatigue at high loads when adequately manufactured and handled (Davis, Tejedor, Grabovac, Kopczyk, & Nuyens, 2012; Schukar, Kusche, Kalinka, & Habel, 2013), which is also a very important asset in SHM applications. An FBG is created as a periodic modulation of the refractive index in the core of a single-mode optical fibre. It acts as a wavelength-selective mirror for light travelling along the fibre and reflects a narrow band of wavelengths centred on the so-called Bragg wavelength $\lambda_B$. This wavelength is defined as:

$$\lambda_B = 2n_{\text{eff}}\Lambda \tag{6.1}$$

in which $n_{\text{eff}}$ is the effective refractive index of the mode propagating in the fibre and $\Lambda$ is the period of the grating (Hill & Meltz, 1997). When an FBG experiences mechanical strain or a change in temperature, the Bragg wavelength shifts due to mechanical deformation, thermal expansion, the thermo-optic effect and the strain-optic effect (Othonos & Kalli, 1999). FBGs are mostly used to measure strain in the direction along the axis of the optical fibre. The general equation governing the change of $\lambda_B$ with longitudinal strain $\varepsilon$ is given by:

$$\frac{d\lambda_B}{\varepsilon} = \lambda_B \left\{ 1 - \frac{n_{\text{eff}}^2}{2} \left[ p_{12} - \nu (p_{11} + p_{12}) \right] \right\} \tag{6.2}$$

in which $\nu$ is the Poisson coefficient of the fibre glass, and $p_{11}$ and $p_{12}$ are two components of the elasto-optic tensor of glass. Using the values of $p_{11} = 0.113$, $p_{12} = 0.252$, $\nu = 0.16$ and $n_{\text{eff}} = 1.482$ from Barlow & Payne (1983) returns an axial strain sensitivity of the Bragg wavelength of about 1 pm/μstrain around a wavelength of 1550 nm. The Bragg wavelength is also sensitive to changes in temperature $T$ according to:

$$\frac{d\lambda_B}{dT} = \lambda_B (\alpha + \xi) \tag{6.3}$$

in which $\alpha$ is the thermal expansion coefficient of the fibre glass and $\xi$ is the thermo-optic coefficient of the fibre. With values $\xi = 8.6 \times 10^{-6}\ \text{K}^{-1}$ for a germanium-doped silica core optical fibre and $\alpha = 0.55 \times 10^{-6}\ \text{K}^{-1}$ (considering a pure silica cladding) the change of $\lambda_B$ with temperature is around 10 pm/K around 1550 nm. Finally, the Bragg wavelength of a conventional FBG is only weakly sensitive to pressure P, that is, a few tenths of a pm/bar as given by:

$$\frac{d\lambda_B}{dP} = \lambda_B \left\{ -\frac{1 - 2\nu}{E} + \frac{n_{\text{eff}}^2}{2E} \left[ 1 - 2\nu (p_{11} + 2p_{12}) \right] \right\} \tag{6.4}$$

with $E$ Young′s modulus of the fibre glass.

FBG sensors in conventional optical fibres are now widely used for axial strain measurements in many SHM-related applications (Antunes et al., 2011). However, their cross-sensitivity to both thermal and mechanical perturbations requires taking special precautions, and strain measurements should always be corrected for the influence of temperature changes. This can be done by using two FBGs which are sufficiently closely spaced for both gratings to experience the same temperature changes, whilst only one of them is exposed to the mechanical strain. Subtraction of the two Bragg wavelength shifts then returns a signal which is only dependent on axial strain. Several other techniques for discriminating between temperature and strain effects are available as well (Kinet et al., 2014). Furthermore and due to the limited sensitivity of the Bragg wavelength to transverse load, regular FBGs are not ideally suited for carrying out transverse strain

**Table 6.1 Summary of conventional fibre-based sensor techniques which were proposed to discriminate between temperature and strain effect and/or to enable multi-axial strain measurements**

| References | Optical fibre and sensor type |
|---|---|
| Lawrence, Nelson, and Udd (1996) | Two FBGs operating at widely spaced wavelengths written at the same location in a single PM fibre (elliptical core) |
| Nelson et al. (1998) | Two FBGs operating at widely spaced wavelengths written at the same location in a single PM fibre (elliptical core and bow-tie stress-applying parts) |
| Lawrence, Nelson, Udd, and Bennett (1999) | One FBG in a single PM fibre (elliptical stress-applying region) |
| Abe et al. (2004) | Two FBGs at relatively closely spaced wavelengths written at the same location in a single PM fibre (elliptical stress-applying region) |
| Luyckx et al. (2007) | Two FBGs at relatively closely spaced wavelengths written at different but closely spaced locations in a single PM fibre (bow-tie stress-applying parts), with one of the FBGs inserted in a capillary |
| Mawatari and Nelson (2008) | Two FBGs operating at widely spaced wavelengths written at the same location in a single PM fibre (bow-tie stress-applying parts) |
| Voet, Luyckx, De Waele, and Degrieck (2010) | Two FBGs written in regular optical fibre, one of which is encapsulated in a capillary |

measurements (Bosia et al., 2003). Transverse strain information could nevertheless prove crucial for SHM purposes, for example to detect or prevent delamination in composite materials. In such materials, the reinforcement fibres enhance the mechanical strength of the composite in the plane of the structure, but a relative fragility and substantial residual strain can still exist in the transverse direction.

Several techniques were proposed to deal with the shortcomings mentioned above (Udd, 2007). A summary of references explaining such techniques is provided in Table 6.1. They mostly relied on exploiting the polarization properties of light propagating in birefringent or polarization-maintaining (PM) optical fibres equipped with an FBG. Transverse strain and temperature influence the birefringence of these fibres, which is translated into a change in spectral distance between the two Bragg wavelengths reflected by the FBG in the PM fibre. In spite of the relative simplicity of this transduction mechanism, the performance of the sensor systems remained limited, on the one hand due to the relatively low sensitivity of the birefringence of classical optical fibres to transverse strain and on the other hand due to the non-negligible cross-sensitivity of that same birefringence to temperature.

## 6.2 Microstructured optical fibres for temperature-insensitive pressure and transverse strain sensing

The issues of cross-sensitivity to temperature and relatively low sensitivity to pressure and transverse strain mentioned in the previous section can both be dealt with by using Bragg grating sensors fabricated in MOF. This brings us to the story on how MOFs fit in the SHM picture. As also explained in other chapters of this volume, an MOF is an optical fibre which has a transverse wavelength-scale microstructure which typically consists of air holes running along the entire length of the waveguide. MOFs have emerged in the 1990s as optical waveguides which featured unprecedented properties (Arismar Cerqueira, 2010; Knight, Birks, Russell, & Atkin, 1996; Russell, 2003, 2006). This essentially results from the great flexibility which MOFs offer in terms of tailoring their optical waveguiding and sensing properties and adapting these properties to suit a wide range of applications. Examples of such applications include supercontinuum generation (Dudley, Genty, & Coen, 2006; Ranka, Windeler, & Stentz, 2000), optical fibre lasers and amplifiers (Knight, 2007) and fibre-optic sensing (Frazão, Santos, Araújo, & Ferreira, 2008; Pinto & Lopez-Amo, 2012). Another aspect which has largely contributed to their success is that MOFs can be made from a single material, in contrast to conventional fibres. Furthermore, FBGs can be fabricated in MOFs using conventional photo-inscription methods, leading to so-called microstructured optical fibre Bragg gratings or MOFBGs.

The combination of the unique properties of MOFs with the sensor functionalities of an FBG allows leveraging the potential of grating-based fibre sensors (Berghmans, Geernaert, Baghdasaryan, & Thienpont, 2014). This is also true in SHM-related applications, for which MOF-based sensors have mostly been combined with gratings inscribed in these fibres to enable measurements of mechanical quantities, precisely with an emphasis on discriminating between strain and temperature effects. A non-exhaustive list of examples includes pressure, transverse force, strain and bend sensing (Berghmans, Geernaert, Sonnenfeld, et al., 2014; Berghmans, Sonnenfeld, et al., 2014; Chen et al., 2008; Fernandes et al., 2012; Frazão, Carvalho, Ferreira, Araújo, & Santos, 2005; Geernaert et al., 2009, 2014; Jin, Jin, & Ju, 2009; Jin et al., 2007; Luyckx et al., 2009; Osorio et al., 2014; Sørensen, Canning, Lægsgaard, & Hansen, 2006; Tenderenda et al., 2014; Wang et al., 2009; Zhang, Liu, Wang, Ji, & Lu, 2012).

MOFs can indeed be designed to feature sensitivities to particular measurands which cannot be achieved with their conventional counterparts. In the remainder of this section, we focus on a highly birefringent MOF which has been designed specifically for temperature-insensitive pressure or transverse mechanical load sensing and to which we will refer as 'butterfly' MOF. It essentially exploits the sensing principle which was previously used with PM fibres as mentioned in Section 6.1 and which is illustrated for the sake of clarity in Figure 6.1. An FBG fabricated in this MOF reflects two distinctly separated Bragg wavelengths – referred to as $\lambda_{B,1}$ and $\lambda_{B,2}$ – that is, one for each of the two orthogonally polarized modes which are guided by the MOF.

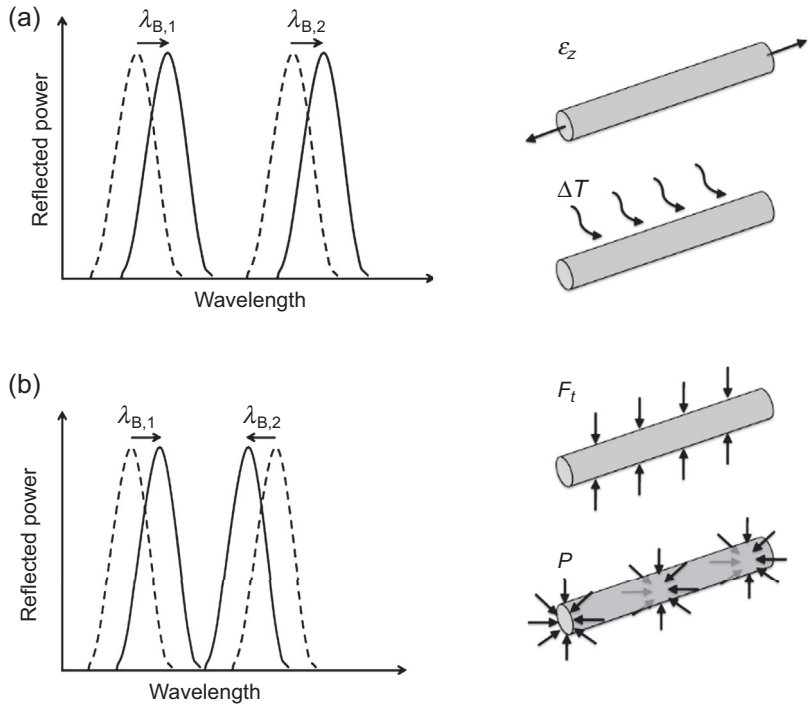


**Figure 6.1** Simplified illustration of the sensing principle of the butterfly MOFBG. Load applied transversally to the MOF is encoded in the spacing $\Delta\lambda$ between the two Bragg peaks. (a) Response of the sensor to temperature changes or axial strain – both peaks move in the same way and $\Delta\lambda$ remains unchanged. (b) Response of the sensor to transverse load – the peaks move in the opposite direction and $\Delta\lambda$ changes.
Adapted from Berghmans, Sonnenfeld, et al. (2014), Berghmans, Geernaert, Sonnenfeld, et al. (2014).

A mechanical load applied transversally to the fibre is encoded in the spacing $\Delta\lambda$ between the two Bragg peaks, with:

$$\Delta\lambda = \lambda_{B,2} - \lambda_{B,1} \tag{6.5}$$

The individual Bragg wavelength shifts resulting from mechanical load (in isothermal conditions) can be derived from the total strain field present in the centre of the MOF core as:

$$\frac{d\lambda_{B,1}}{\lambda_{B,1}} = \varepsilon_3 - \frac{n_1^2}{2}\Big[p_{11}\varepsilon_1 + p_{12}(\varepsilon_2 + \varepsilon_3)\Big] \tag{6.6}$$

$$\frac{d\lambda_{B,2}}{\lambda_{B,2}} = \varepsilon_3 - \frac{n_2^2}{2}\Big[p_{11}\varepsilon_2 + p_{12}(\varepsilon_1 + \varepsilon_3)\Big] \tag{6.7}$$

in which $\varepsilon_1$, $\varepsilon_2$, $\varepsilon_3$ are the principal strain components along the axes of the coordinate system of the optical fibre ($\varepsilon_3$ being the axial strain), and $n_1$ and $n_2$ are the effective refractive indices for the two orthogonally polarized modes, along the fast and slow axis, respectively (see also Figure 6.2(a)). Note that the strains $\varepsilon_1$, $\varepsilon_2$, $\varepsilon_3$ ideally stand for the average over the mode field of the propagating mode, but according to the so-called 'centre-strain approximation', they are taken equal to those found in the centre of the fibre core. Equations (6.6) and (6.7) clearly show that in the presence of transverse strains $\varepsilon_1$ and $\varepsilon_2$, the two Bragg wavelengths respond differently.

The cross-section of the butterfly MOF is shown in Figure 6.2, together with typical values of the parameters of the microstructure (Berghmans, Geernaert, Sonnenfeld, et al., 2014). This optimized microstructure has been obtained following extensive modelling efforts and feedback cycles between manufacturing and modelling (Martynkien et al., 2010; Sulejmani et al., 2012). The strategy of the modelling approach is outlined below.

An essential figure of merit for the optimization is the ratio of the polarimetric sensitivity to pressure $K_P$ and the polarimetric sensitivity to temperature $K_T$. These sensitivities are defined using a most important parameter of the highly birefringent butterfly MOF, that is, its phase modal birefringence $B$, with:

$$B = \frac{\lambda}{2\pi}(\beta_2 - \beta_1) = n_2 - n_1 \tag{6.8}$$

and in which $\beta_1$ and $\beta_2$ are the propagation constants and $n_1$ and $n_2$ the effective refractive indices of the fundamental modes orthogonally polarized along the fast and slow axes, respectively.

The polarimetric pressure and temperature sensitivities are then given by:

$$K_P = \frac{2\pi}{\lambda}\frac{\mathrm{d}B}{\mathrm{d}P} \tag{6.9}$$

and

$$K_T = \frac{2\pi}{\lambda}\left(\frac{\mathrm{d}B}{\mathrm{d}T} + B\alpha\right) \tag{6.10}$$

The first term in the equation for $K_T$ represents the contribution to the overall sensitivity related only to temperature-induced changes in modal birefringence, whereas the second term represents the contribution related to thermal fibre expansion. The relation between the spectral spacing $\Delta\lambda$ between the two Bragg peaks, reflected by an FBG inscribed in the MOF and the phase modal birefringence $B$, is given by:

$$\Delta\lambda = 2B\Lambda \tag{6.11}$$

and hence optimizing the polarimetric sensitivities to pressure and temperature also optimizes the sensitivity of $\Delta\lambda$ to these measurands.

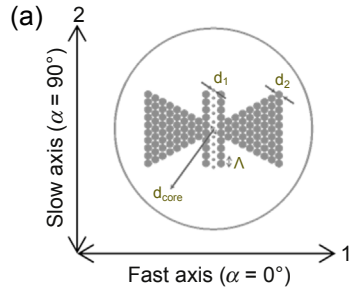


(b)

| Parameter | Typical value |
|---|---|
| Outer cladding diameter | 125 µm |
| Number of airhole rings | 6–9 |
| Airhole pitch $\Lambda$ | 3.5–4 µm |
| $d_1/\Lambda$ | 0.225 |
| $d_2/\Lambda$ | 0.95–0.99 |
| $d_{core}/\Lambda$ | 0.9 |
| Core region doping concentration | 3 mol% |

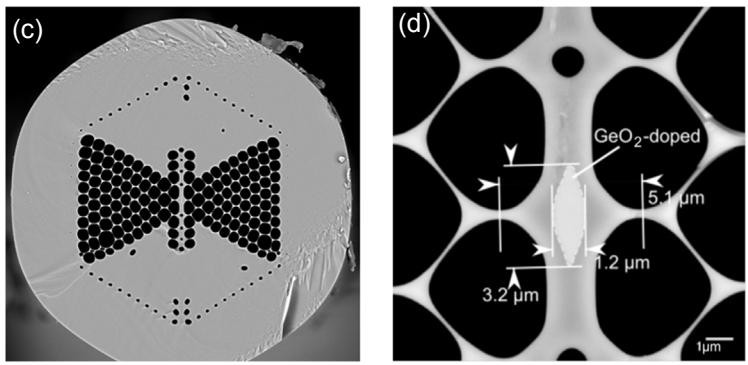


**Figure 6.2** (a) Ideal cross-section of the butterfly MOF with indication of the slow and fast axes, or 1- and 2-axis, respectively. The 3-axis corresponds to the axial direction of the fibre. (b) Typical parameter set of the butterfly microstructure. (c) Scanning electron microscope photograph of the cross-section of the fabricated butterfly MOF. (d) Close-up of the core region of the MOF with indication of the Ge-doped zone.
Adapted from Berghmans, Geernaert, Sonnenfeld, et al. (2014).

Because we want to obtain an MOF which is very sensitive to pressure whilst being – in as much as possible – insensitive to temperature changes, the ratio $K_P/K_T$ should be as high as reasonably achievable. $K_P/K_T$ is maximized by means of a dedicated microstructure layout with hole diameters and pitch values which are optimized for

that purpose, but which still allow for repeatable manufacturing of the fibre based on current stack-and-draw technology (Poli, Cucinotta, & Selleri, 2007). $K_P$ and $K_T$ can be calculated as follows. When hydrostatic pressure acts on the birefringent MOF, it induces a specific stress distribution in the fibre cross-section and deforms the fibre structure. Stress induced by hydrostatic pressure causes the initially isotropic glass to become birefringent. The principal refractive indices are given by the following set of equations:

$$\begin{cases} n_1 = n + C_1\sigma_1 + C_2(\sigma_2 + \sigma_3) \\ n_2 = n + C_1\sigma_2 + C_2(\sigma_1 + \sigma_3) \\ n_3 = n + C_1\sigma_3 + C_2(\sigma_1 + \sigma_2) \end{cases} \tag{6.12}$$

with $C_1$ and $C_2$ the stress-optic coefficients and $\sigma_1$, $\sigma_2$, and $\sigma_3$ the principal components of the pressure-induced stress. The principal stresses $\sigma_1$ and $\sigma_2$ for load applied parallel to an arbitrary Cartesian $(x, y)$ plane, which is parallel to the fibre's cross-sectional (1, 2) plane, are calculated using the following relation:

$$\sigma_{1,2} = \frac{(\sigma_x + \sigma_y) \pm \sqrt{(\sigma_x - \sigma_y)^2 + 4\tau_{xy}^2}}{2} \tag{6.13}$$

For normal load the contribution of the shear stress $\tau_{xy}$ to the principal stress components $\sigma_1$ and $\sigma_2$ is relatively small in the core region and in its neighbourhood, and one can assume that the principal axes of the anisotropic fibre and the Cartesian axes of the coordinate system coincide. The distribution of the refractive index $n_i(x, y)$ in the stressed fibre is then given as:

$$n_i(x, y) = n_{\text{mat}}(x, y) + \Delta n_i(x, y) \tag{6.14}$$

with $i = 1$ or 2 for the fast or slow polarized modes, respectively. $n_{\text{mat}}$ is the refractive index of the MOF silica, and the correction terms $\Delta n_i(x, y)$ represent the pressure-induced modifications of the refractive index distributions. These are given by:

$$\begin{cases} \Delta n_1(x, y) = C_1\sigma_1(x, y) + C_2[\sigma_2(x, y) + \sigma_3(x, y)] \\ \Delta n_2(x, y) = C_1\sigma_2(x, y) + C_2[\sigma_1(x, y) + \sigma_3(x, y)] \end{cases} \tag{6.15}$$

To find the distribution of $\Delta n_1(x, y)$ and $\Delta n_2(x, y)$ in the fibre cross-section, one first determines the normal stress components $\sigma_x$, $\sigma_y$ and the shear stress component $\tau_{xy}$ using finite element software, in this case the Structural Mechanics module of the commercially available COMSOL Multiphysics® software (COMSOL). In a second step, one calculates the principal stresses using Eqn (6.13).

Knowledge of the stress-optic coefficients $C_1$ and $C_2$ then allows calculating the correction terms $\Delta n_1(x, y)$ and $\Delta n_2(x, y)$ and hence the stress birefringence $\sigma_1(x, y) - \sigma_2(x, y)$ in the cross-section of the MOF (illustrated in Figure 6.3) and material birefringence $n_2(x, y) - n_1(x, y)$. Once the deformations of the MOF and the stress-induced corrections to the refractive indexes are known, these data are used as input to the RF Module of COMSOL Multiphysics®, which allows calculating the propagation constants $\beta_1$ and $\beta_2$ and hence the effective refractive indices $n_1$ and $n_2$. Because both mechanical and electromagnetic calculations are carried out using a finite element method, it is straightforward to transfer the initial and deformed meshes between the mechanical and electromagnetic software modules, which not only

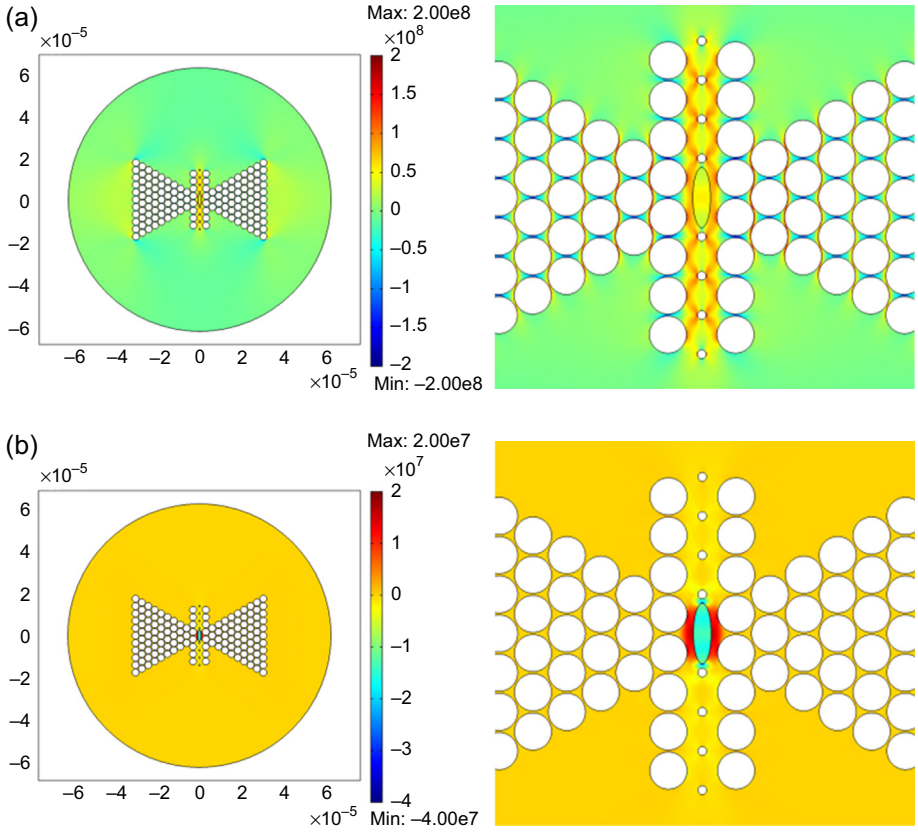


**Figure 6.3** (a) Distribution of the stress birefringence in the cross-section of our highly birefringent microstructured optical fibre (MOF) induced by hydrostatic pressure $P = 20$ MPa. (b) Distribution of the stress birefringence in the cross-section of our highly birefringent MOF, induced by residual thermal stress. The external fibre diameter is 125 μm.
Adapted from Berghmans, Geernaert, Napierala, Baghdasaryan, Sonnenfeld, Sulejmani, et al. (2012).

simplifies the data exchange procedures but also increases the accuracy of the calculations. For the sake of completeness, we mention that the triangular mesh used to model the MOF consisted of $10^5$ up to $3 \times 10^5$ elements.

To determine the overall sensitivity to pressure, one calculates $B$ for the unloaded fibre, that is, $B_P = 0$ assuming that the refractive index of silica $n_{\text{mat}}$ satisfies the Sellmeier equation. In the second step, one determines the structural deformations and the stress-related corrections of the refractive indices $\Delta n_1$ and $\Delta n_2$ for an applied pressure $P = 1$ GPa. In the third step, one transfers the coordinates of the deformed mesh to the software module for electromagnetic calculations and adds the correction terms $\Delta n_x$ and $\Delta n_y$ to the initial value of refractive index $n_{\text{mat}}$. Finally, using these input data and the resulting propagation constants $\beta_1$ and $\beta_2$, one can calculate $B_P = 1$ GPa which is the phase modal birefringence at a pressure of 1 GPa.

The overall pressure sensitivity of the phase modal birefringence versus wavelength can be finally calculated according to the following equation:

$$\frac{\mathrm{d}B}{\mathrm{d}P} = \frac{B_{P=1\ \text{GPa}} - B_{P=0}}{P} \tag{6.16}$$

As stated earlier the sensor elements in the highly birefringent MOF are Bragg gratings. To facilitate the fabrication of these gratings using conventional UV laser-based photo-inscription, a germanium-doped inclusion was added in the core of the MOF. This yields thermal stress arising from the differences in thermal expansion coefficients between pure and doped silica, which also contributes to the overall temperature response. To account for this effect one follows an approach similar to the case of hydrostatic pressure. The sensitivity of the modal birefringence to temperature becomes:

$$\frac{\mathrm{d}B}{\mathrm{d}T} = \frac{B_{T_0} - B_{T_1}}{\Delta T} \tag{6.17}$$

with $\Delta T = T_0 - T_1$. To determine the change of the birefringence with temperature, one first calculates the temperature-dependent distribution of residual thermal stress components $\sigma_1(x, y, \Delta T)$, $\sigma_2(x, y, \Delta T)$, $\sigma_3(x, y, \Delta T)$ using the COMSOL Structural Mechanics module, as shown in Figure 6.3(b). In the next step, one determines the temperature-induced corrections of the refractive index distribution in the glass part of the MOF cross-section, which takes into account both the stress and the thermo-optic effects:

$$\begin{cases} \Delta n_1(x,y,\Delta T) = C_1\sigma_1(x,y,\Delta T) + C_2[\sigma_2(x,y,\Delta T) + \sigma_3(x,y,\Delta T)] + \dfrac{\mathrm{d}n_{\text{mat}}}{\mathrm{d}T}\Delta T \\ \Delta n_2(x,y,\Delta T) = C_1\sigma_2(x,y,\Delta T) + C_2[\sigma_1(x,y,\Delta T) + \sigma_3(x,y,\Delta T)] + \dfrac{\mathrm{d}n_{\text{mat}}}{\mathrm{d}T}\Delta T \end{cases} \tag{6.18}$$

**Table 6.2 Absolute values of the polarimetric sensitivity to pressure and of the ratio of the polarimetric sensitivities to pressure and to temperature for different types of polarization maintaining optical fibres**

| | Bow-tie PM fibre (Urbanczyk et al., 2007) | Side-hole PM fibre (Moon et al., 2007) | NKT photonics PM-1550 MOF (NKT photonics) | Butterfly MOF (Martynkien et al., 2010) |
|---|---|---|---|---|
| $\lvert K_P \rvert$ (rad/m MPa) | 4.4 | 60 | 7.5 | 43 |
| $\lvert K_P/K_T \rvert$ (K/MPa) | 10 | 150 | 610 | 5400 |

Using the modelling approach and the quantities mentioned above, one can calculate the figure of merit $K_P/K_T$ for different types of optical fibres based on their idealized – that is, not as-built – cross-section. This is done in Table 6.2 for a regular bow-tie PM fibre, a side-hole PM fibre with an elliptical core, a commercially available PM MOF and the butterfly MOF.

Whilst the butterfly MOF has a pressure sensitivity with a magnitude comparable to that of the side-hole PM fibre, it is substantially less sensitive to temperature and hence the figure of merit reaches considerably larger values. This low sensitivity to temperature changes stems from the low content of materials with different thermal expansion coefficients and from the origin of the modal birefringence which is mainly due to waveguide birefringence. Furthermore, the pressure sensitivity of the butterfly MOF can be controlled to be either negative or positive by adapting the fabrication process, as discussed in Sulejmani et al. (2012). Polarimetric pressure sensitivities for fabricated butterfly MOFs of −56 and 126 rad/m MPa have been obtained at a wavelength of 1.55 μm, which are the largest values reported for highly birefringent MOFs.

Owing to the germanium doping of the butterfly MOF core region, FBGs can be routinely inscribed in this fibre using conventional UV photo-inscription techniques (Geernaert et al., 2010). A reflection spectrum of an FBG inscribed in the butterfly MOF shown in Figure 6.2(c) is shown in Figure 6.4.

The typical sensitivity of the wavelength separation of a butterfly MOFBG to a transverse line load is shown in Figure 6.5. This result was obtained by compressing the MOFBG between a metal and a glass plate with a line load of 0.2 N/mm and monitoring the Bragg wavelength shifts using an amplified spontaneous emission source, a circulator and a commercially available FBG interrogator with a peak wavelength detection resolution of 1 pm. Because the holey microstructure is asymmetric, the transverse line load sensitivity varies with the angular orientation of the applied force with respect to the MOF cross-section. The grating sensitivity is determined as the slope of a linear fit of the Bragg peak wavelength shift versus the applied transversal

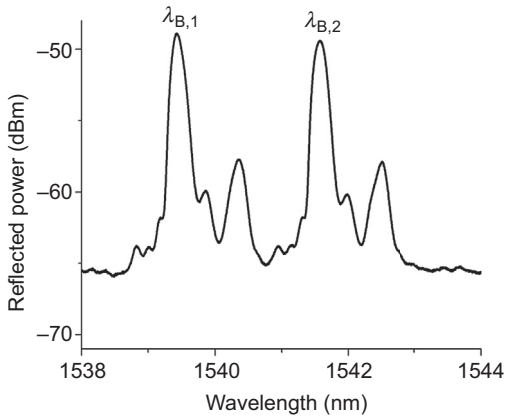


**Figure 6.4** Reflection spectrum of a butterfly MOFBG with identification of the two Bragg wavelengths $\lambda_{B,1}$ and $\lambda_{B,2}$.

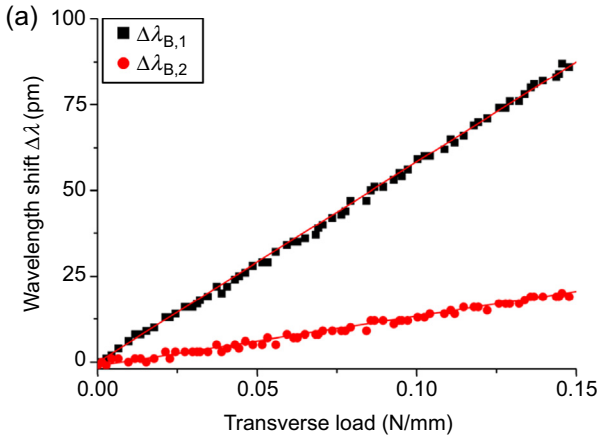


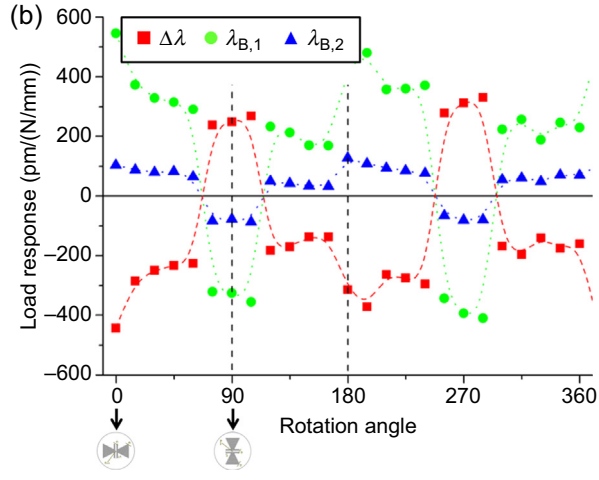


**Figure 6.5** (a) Wavelength shift of the two Bragg wavelengths versus transversal line load for one particular rotation angle. The red solid lines represent the linear fit of the data. (b) Sensitivity against the rotation angle of the MOF for a vertically applied line load (see also Figure 6.2(a)). Adapted from Sonnenfeld, Sulejmani, Geernaert, Eve, Lammens, Luyckx, et al. (2011).

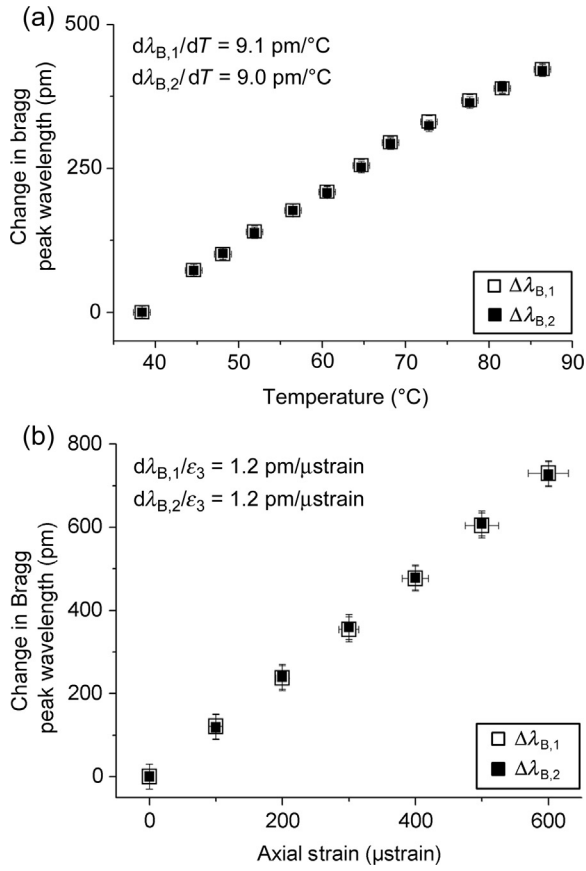


**Figure 6.6** (a) Measured change of $\lambda_{B,1}$ and $\lambda_{B,2}$ of a butterfly MOFBG with temperature with indication of linear fit regression coefficient. (b) Measured change of $\lambda_{B,1}$ and $\lambda_{B,2}$ of a butterfly MOFBG with axial strain with indication of linear fit regression coefficient.

line load (Figure 6.5(a)). The highest sensitivity of $\Delta\lambda$ to the transverse force is obtained when the load is applied along the slow axis of the MOF. The sensor response exhibits, as anticipated, a periodic behaviour when plotted against the angular orientation of the microstructure (Figure 6.5(b)) (Sonnenfeld et al., 2011; Sulejmani et al., 2011).

The temperature sensitivity of a bare MOFBG sensor was measured in a range from room temperature to 100 °C. Although the individual Bragg wavelengths $\lambda_{B,1}$ and $\lambda_{B,2}$ showed a temperature sensitivity of around 9 pm/°C, the Bragg wavelength separation $\Delta\lambda$ had a very low temperature sensitivity of $-0.1$ pm/°C only, as shown in Figure 6.6(a), for reasons already explained earlier in the text. The axial strain sensitivity of the sensor was measured by fixing both fibre ends between translation stages and monitoring the change in Bragg wavelengths as a function of the axial displacement. Figure 6.6(b) shows that the axial strain sensitivity of the individual Bragg wavelengths was 1.2 pm/μstrain, whilst the wavelength separation showed no detectable sensitivity to axial strain.

The pressure sensitivity of the bare MOFBG sensor was determined with both numerical simulations and experiments, as detailed in Sulejmani et al. (2011). A hydrostatic pressure sensitivity of −15 pm/MPa was obtained for the Bragg peak separation, which is an order of magnitude increase over FBG based pressure sensors made in regular bow-tie PM optical fibre.

## 6.3 Structural health monitoring-related applications of the butterfly microstructured optical fibres

In this section, we illustrate potential uses of butterfly MOFBGs as sensors which may support structural health monitoring (SHM). To do so we selected three distinct applications, which take advantage of the features of these sensors explained in the previous section: the large sensitivity to transverse load of the butterfly MOF, the dependence of that sensitivity on the angular orientation of the MOF with respect to the direction of the applied mechanical load, and the insensitivity of the sensor response to temperature variations.

### *6.3.1 Monitoring the cure cycle of fibre-reinforced polymer composite materials*

One of the challenges in the manufacturing of fibre-reinforced composite materials is to avoid excessive residual stresses which appear within the material during their production. Such stresses can cause visible distortion of the structure and can lead to premature failure of the composite. Residual stresses may initiate matrix cracking and delamination, which result in a decreased strength of the composite structure (Hoa, 2009). In this respect, achieving accurate measurements of stress buildup in a composite material as it cures can be crucial.

Studying composite curing with optical fibre-based sensors has already been reported several times in the literature. FBG sensors in particular have proven their effectiveness for in situ monitoring of the cure cycle of composite materials, as they have shown to provide information about the degree of cure and about the evolution of the process-induced strain. It is beyond the scope of this chapter to provide a detailed overview of these techniques. Examples of cure monitoring in plain resins can be found in Antonucci, Cusano, Giordano, Nasser, and Nicolais (2006); Colpo, Humbert, & Botsis (2007); Giordano et al. (2004); Harsch, Karger-Kocsis, and Herzog (2007); Karalekas, Cugnoni, and Botsis (2008); Parlevliet, Bersee, and Beukers (2010). The techniques mainly relied on measuring the axial strain along the fibre direction. Other reports describe the use of FBG sensors for measuring the residual strain in a composite material cured in actual manufacturing conditions, such as Guo, 2007; Khoun, de Oliveira, Michaud, and Hubert (2011); Marin, Robert, Triollet, and Ouerdane (2012); Montanini and D'Acquisto (2007); Mulle, Collombet, Olivier, and Grunevald (2009); O'Dwyer, Maistros, James, Tatam, and Partridge (1998); Parlevliet et al. (2010). Most of these studies combined an optical sensing system consisting of an

FBG sensor subjected to in-plane strain along the fibre and temperature variations, and a thermometer (either a thermocouple or another FBG) to discriminate between the contributions of temperature and strain to the Bragg wavelength changes. Nevertheless, during the cure of a composite material (and particularly in the case of a thick composite), anisotropic strains arise in the three directions of space, due to the difference in thermal behaviour between the matrix and the reinforcing fibres. This leads to stress-induced birefringence which may allow quantifying the transversally induced strain into the optical fibre, both in plane and along the direction through the thickness of the composite laminate. One can, for example, take advantage of the peak splitting of the reflected Bragg spectrum or from polarization-dependent loss in an FBG, resulting from the induced birefringence in the optical fibre core due to the occurrence of non-axisymmetric thermal residual stress, as described in Guemes and Menéndez (2002); Lammens et al. (2013); Okabe et al. (2002); Sorensen, Gmür, and Botsis (2006). The cure shrinkage strain in the direction through the thickness of composite materials has also been measured by directly embedding the FBG sensor along that direction in the composite sample during the lay-up phase (Minakuchi, 2013).

The use of FBG sensors fabricated in highly birefringent optical fibres has also already been proposed as a solution for multi-axial strain sensing during the cure cycle of composite materials (Black et al., 2002; Chehura et al., 2005). Those FBG sensors allowed distinguishing between the strains arising in the longitudinal direction of the FBG sensor from those arising in the transverse directions. In Chehura et al. (2005) FBG sensors were embedded such that the slow axis of the sensor was aligned with the plane of the material. This allowed measuring an effective transverse strain (the difference between the in-plane and out-of-plane transverse strain components) and returned a good correlation with the progress of the cure reaction indicating that this technique would be able to follow the chemical resin shrinkage during the cure cycle. More extensive information on the use of strain measurements in composite laminates can be found in Luyckx, Voet, Lammens, and Degrieck (2011).

To demonstrate the potential of butterfly MOFBGs for measuring the through-the-thickness strain buildup as a carbon−epoxy composite laminate cures, such sensors were embedded during the lay-up operation between plies of the composite laminate (Sonnenfeld, Luyckx, Collombet, Grunevald, et al., 2013a, 2013b; Sonnenfeld, Luyckx, Collombet, Geernaert, et al., 2013). The curing was carried out in a semi-industrial autoclave, which is representative for industrial composite manufacturing (Collombet et al., 2013). Because the phase modal birefringence of the MOF sensor is inherently insensitive to temperature, the changes in peak separation $\Delta\lambda$ of the MOFBG are only due to thermally induced strain related to the modification of the strain state in the material. As such, no need exists for adding an additional sensor to correct for temperature variations.

Prior to carrying out the actual curing experiment, the calibration of embedded butterfly MOFBG sensors was done by means of experiments on cross-ply laminate carbon fibre-reinforced composite coupons, in which MOFBG sensors were embedded at mid-thickness and submitted to different loadings along the three principal directions of the laminate composite. We have already explained that the response of the peak

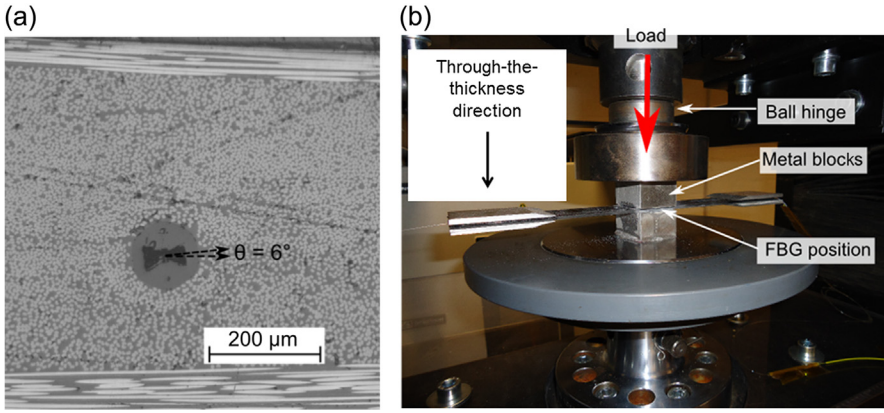


**Figure 6.7** (a) Scanning electron micrograph of a butterfly MOF embedded with the 0° orientation in a cross-ply composite laminate. An orientation error of 6° was detected. (b) Experimental setup used for the transverse out-of- plane loading. The composite sample is compressed between two metal blocks along the direction through the thickness.

separation exhibits the highest sensitivity when the MOF is embedded at a 0° angular orientation with respect to the direction of the applied force (see Figure 6.5(b)). For that reason the MOFBG sensors were embedded with that particular orientation along the through-the-thickness direction of the coupon, as illustrated in Figure 6.7(a). The experimental transverse out-of-plane strain sensitivity of the embedded MOFBG as measured with the setup shown in Figure 6.7(b) was −0.2 pm/µstrain at this 0° orientation (see Figure 6.8). This sensitivity is 3.5 times larger than when the coupon is loaded along its transversal in-plane direction and eight times larger than when the sensor is submitted to longitudinal strain. Therefore, the peak separation changes of the MOFBG embedded with that orientation are mainly due to transversal out-of-plane strain.

Figure 6.9(a) shows the actual instrumented composite laminate piece cured in the autoclave. The positions of the different sensors, including the MOFBG, regular FBGs and thermocouples, are indicated in Figure 6.9(b). The autoclave temperature, vacuum and pressure cycle are illustrated in Figure 6.10. The peak separation of the MOFBG sensor was recorded all along this cycle, during which the MOFBG is compressed in all directions. We recall that the peak separation of the MOFBG depends on the difference between the transversal in-plane and out-of-plane strains. Because here it is embedded in a quasi-isotropic structure − that is, with much lower in-plane strain than out-of-plane strain − and with a 0° orientation with respect to the through-the-thickness direction, we can assume that the strain arising through the thickness is mainly responsible for the changes in the peak separation $\Delta\lambda$. Furthermore, because the phase modal birefringence of the butterfly MOF is inherently insensitive to temperature, the changes in $\Delta\lambda$ are due to thermally induced transverse strain resulting from the changing strain state in the composite material as it cures.

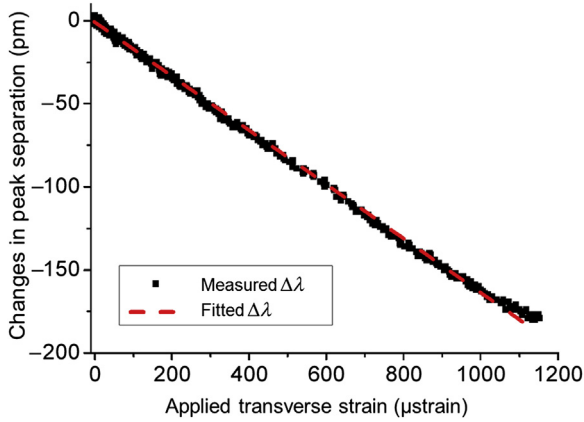


**Figure 6.8** Change of the peak separation $\Delta\lambda$ of the MOFBG embedded in a cross-ply composite laminate coupon as a function of strain applied along the through-the-thickness direction. Adapted from Sonnenfeld, Luyckx, Collombet, Geernaert, et al. (2013).

Figure 6.10 shows a first drop of $\Delta\lambda$ (part A) which corresponds to the polymerization of the sample. Using the calibration data mentioned above, this drop corresponds to a transverse compressive strain of −95 μstrain. In part B, the sensor signal remains constant, meaning that no transverse strain is measured by the MOF sensor. One can therefore reasonably assume that the cure reaction has been completed and that the composite material is formed. The cooling phase (part C) features a large decrease of $\Delta\lambda$ associated with the buildup of a substantial transversal residual strain of about −1150 μstrain (Berghmans, Geernaert, Sonnenfeld, et al., 2014). The MOFBG sensor response thus clearly records the onset of gelation in the composite at around the 106th minute of the cycle (start of part A in Figure 6.10), the onset of vitrification (start of part B in Figure 6.10 at around the 130th minute of the cycle) and the consolidation of the composite (part C).

The above shows that a single MOFBG sensor can potentially characterize, in real time and in situ, the cure process of a composite material on a semi-industrial scale, which may eventually help optimizing that process. The main drawback of the butterfly MOF is the rotational variance of the sensitivity to transverse load, which requires the fibre to be properly oriented as it is being embedded in the composite. This can be done using microscopic observation of the MOF end face in a laboratory environment. However, for industrial-scale applications of this technique, it would be preferable to use a technique which allows for automated and repeatable placement of the fibre sensor.

### 6.3.2 *Measuring shear stress in lap joints*

As discussed in the previous paragraphs many research efforts have focused on the measurement of normal stresses and hydrostatic pressure. The detection of shear stress

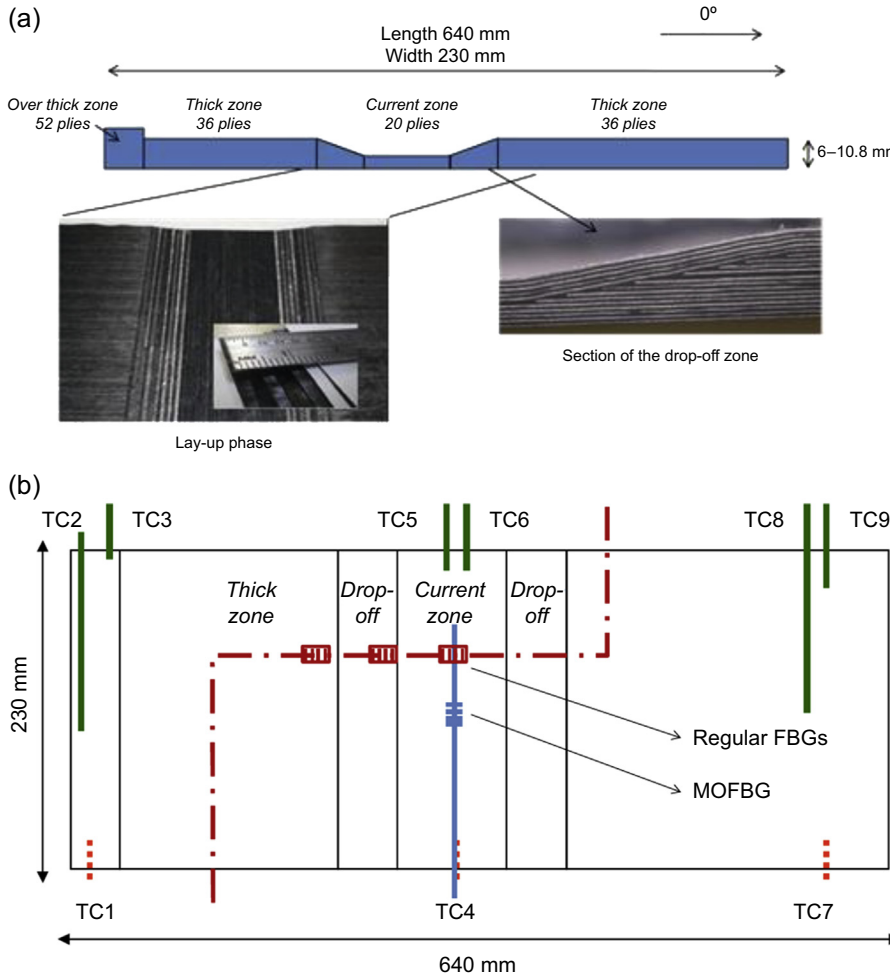


**Figure 6.9** (a) Schematic of the carbon−epoxy laminate manufactured using the autoclave vacuum bag technique with picture of the so-called drop-off zone. (b) Schematic of the optical fibre sensor network embedded in the composite specimen. TC stands for thermocouple. Adapted from Sonnenfeld, Luyckx, Collombet, Geernaert, et al. (2013).

remained mostly unaddressed. Yet the existence of shear stress is driving the appearance of important structural defects such as delamination in laminated composite materials, disbonding of adhesive joints or buckling of beams (Adams, Comyn, & Wake, 1997; Voyiadjis & Woelke, 2008). Several attempts have been made at measuring shear stress with FBG-based sensors. The use of an FBG in a conventional fibre embedded under a small tilt angle in a deformable layer has been proposed as a possible technique (Tjin, Suresh, & Ngo, 2004). Shear load applied to the deformable

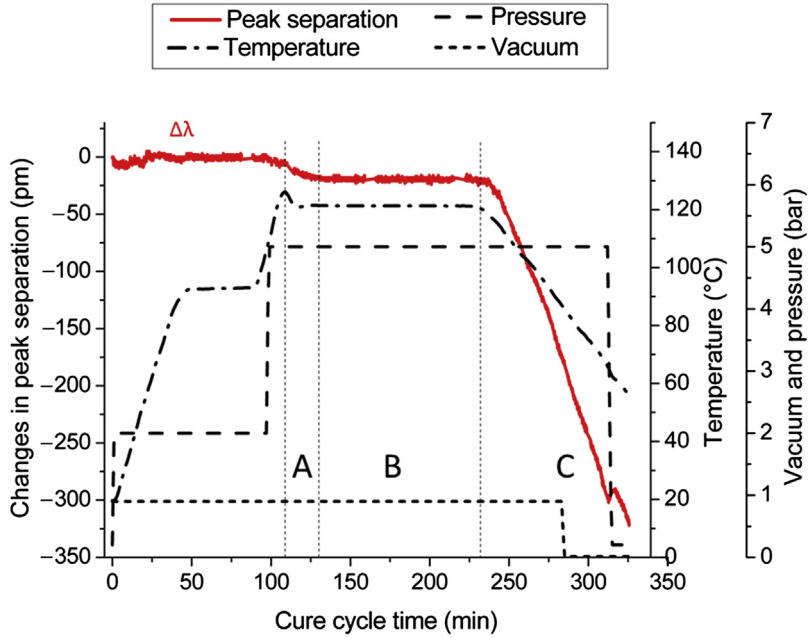


**Figure 6.10** Illustration of the autoclave cure cycle environmental conditions (black lines) and of the MOFBG peak separation $\Delta\lambda$ measured along the entire cure cycle.

layer resulted in axial strain applied to the fibre, which was straightforwardly measured by the Bragg peak wavelength shift. A shear displacement sensor has also been described that used a ferrofluidic-infiltrated MOFBG sensor and a magnet embedded in a polymer foil (Candiani, Margulis, Konstantaki, & Pissadakis, 2012). Shear load applied to the foil modified the location of the ferrofluidic segment in the MOFBG sensor, which influenced the MOFBG reflection spectrum. Other research efforts have been reported in McKenzie, Jones, Marshall, and Galea (2000); Ning, Murayama, Kageyama, Uzawa, and Wada (2012); Palaniappan et al. (2008); Takeda, Yamamoto, Okabe, and Takeda (2007). A first FBG sensor shear stress monitoring, however, was based on a PM fibre embedded in a material along the direction perpendicular to that of applied shear load (Schulz et al., 1999). When the fundamental optical axes of the fibre were aligned with the directions of principal stress, the optical fibre experienced the shear load as if it were a transverse load. The shear load induced a change in material birefringence of the optical fibre, and hence also a change in its modal birefringence, which can be straightforwardly detected by monitoring the FBG reflection spectrum. This measurement principle is very attractive, but the sensor itself suffered low transverse shear strain sensitivity and significant thermal cross-sensitivity. In the remaining paragraphs of this section, we show how this can be improved by using the butterfly MOFBG-based sensor and how this sensor can be used for monitoring disbonding in adhesive joints (Sulejmani et al., 2013; Sulejmani et al., 2014a, 2014b).

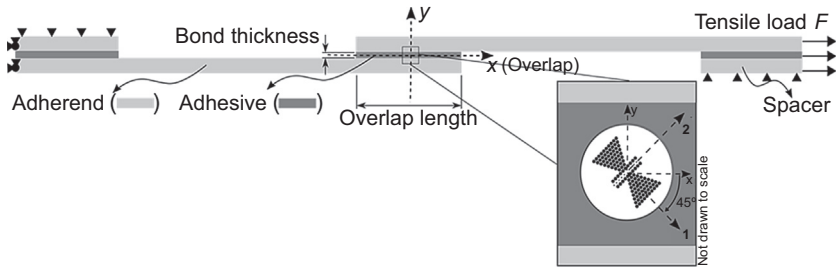


**Figure 6.11** Arrangement of a single-lap joint with an MOFBG embedded in the centre ($x = y = 0$) of the adhesive layer. The MOF is oriented so that its principal axes are oriented at 45° with respect to the ($x$, $y$) axes system.
Adapted from Sulejmani et al. (2013).

We consider the arrangement shown in Figure 6.11. An MOFBG was embedded in a single-lap joint (SLJ). Such an SLJ is a simple structure consisting of a uniform adhesive layer sandwiched between two adherend plates. When a tensile load F is applied along the direction shown in Figure 6.11, a shear stress distribution appears in the adhesive layer. For such a structure this shear stress distribution is very well known and can be described by analytical models. As mentioned earlier, the influence of the shear stress (see the term $\tau_{xy}$ in Eqn (6.13)) is often neglected when the transverse stress sensitivity of an MOFBG sensor is considered. However, when investigating the shear stress sensitivity of these sensors, the contribution of this component is crucial. We have also already described that owing to the asymmetry in the design of the butterfly MOF cross-section, the sensitivity of the sensor to transverse load depends on the angular orientation of the MOF with respect to the direction of the load, and looking at this structure one understands that the magnitude of the transverse load sensitivity will be the smallest when transverse load is applied at ±45° with respect to the slow or fast axis of the MOF. This also means that if the MOFBG is embedded in a shear-loaded adhesive layer at an angle of ±45°, as shown in Figure 6.11, it can now detect the shear strain load-induced transverse strain in the fibre. Because the butterfly MOF exhibits much higher transverse stress sensitivity than conventional PM fibres, one can expect it to be much more sensitive to shear stress as well, if it is properly embedded. To verify this, the sensitivity of the butterfly MOFBG was calculated with a finite element model and compared to that of a side-hole and a bow-tie PM fibre when embedded in an SLJ. The bow-tie FBG sensor and side-hole FBG sensor yield a shear stress sensitivity of 16.0 and 16.2 pm/MPa, respectively, whilst the shear stress sensitivity for the butterfly MOFBG is almost four times larger. The experimental evidence is shown in Figure 6.12. The butterfly MOFBG sensor returns a shear stress sensitivity of 59.8 pm/MPa, which would correspond to a shear strain sensitivity of 0.01 pm/μstrain considering the material properties of the adhesive (Sulejmani et al., 2013).

The butterfly MOFBG thus features an enhanced shear stress sensitivity compared to conventional PM FBG-based sensors. Furthermore, disbonding of the adhesive/adherend interface or the appearance of cracks in the bond will lead to a

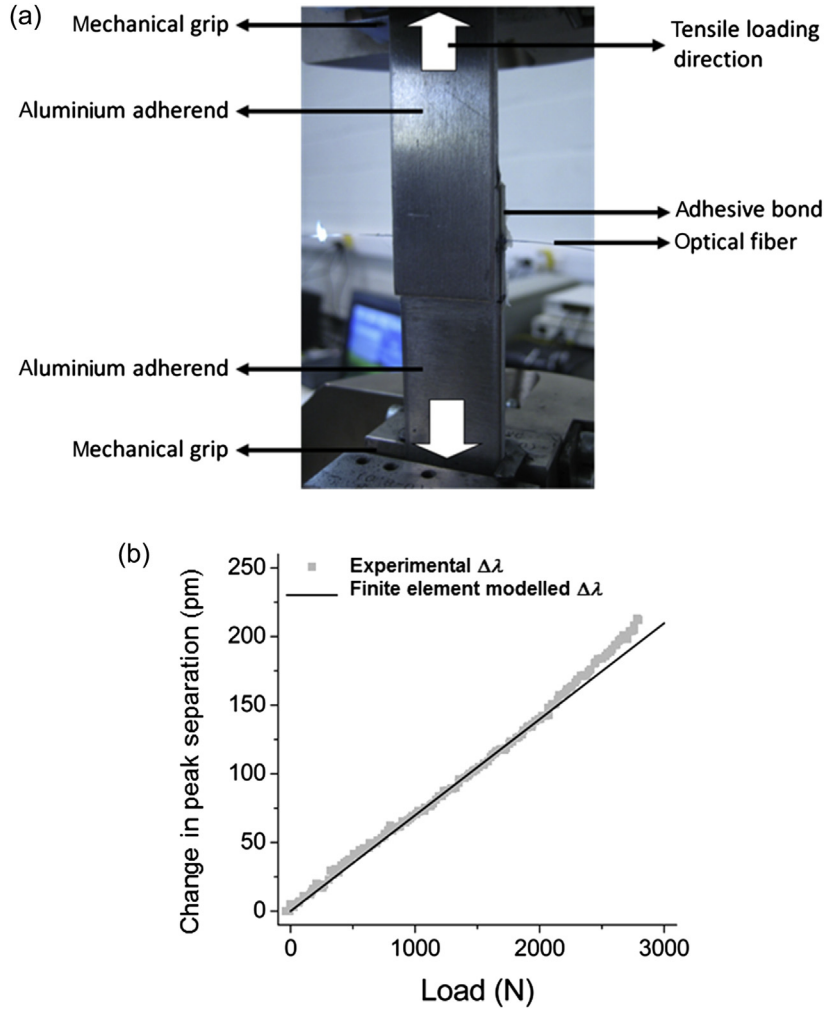


**Figure 6.12** (a) Illustration of the SLJ test sample gripped in the tensile test machine. (b) Bragg peak separation of the MOFBG $\Delta\lambda$ as a function of applied tensile load.
Adapted from Sulejmani et al. (2013).

redistribution of the shear stress profile in the adhesive layer, and following up on the shear stress distribution in the adhesive bond will therefore also return information about the bond quality. One can therefore consider using the butterfly MOFBG as a tool for monitoring the adhesive bond layer quality. A way to do so has been detailed in Sulejmani et al. (2013). Three MOFBG sensors were embedded with a 45° orientation in single-lap adhesive joint as pictured in Figure 6.13(a). When tensile load is applied to the SLJ, the peak separations $\Delta\lambda$ of the three MOFBGs change with different rates. Sensors 1 and 3 are close to the edges of the joint, in which the shear

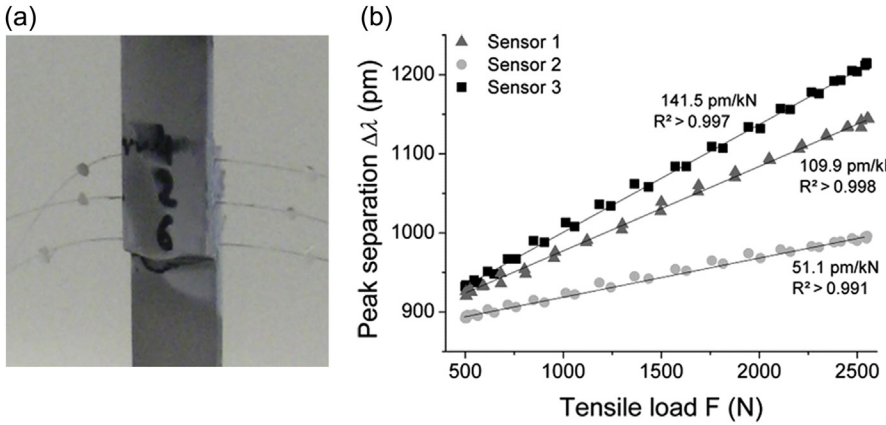


**Figure 6.13** (a) Photograph of the experimental SLJ with three embedded butterfly MOFBGs. (b) Response of the three butterfly MOFBG sensors when embedded as a function of static tensile load applied to the SLJ.
Adapted from Sulejmani et al. (2014a).

stress is larger and hence these sensors will experience more shear loading, resulting in a larger sensor response.

The SLJ was then submitted to a fatigue test with the response of the three MOFBGs being recorded at regular intervals. The evolution of the sensor responses throughout the entire test characterizes the redistribution of the shear stress in the bond layer, which results from the appearance of disbonds at either side of the joint and the propagation of these disbonds. Using this technique it has been shown in Sulejmani et al. (2013) that a disbond with a length of 1% of the initial joint length can change the sensor response by 10%. An elegant way to follow up on the propagation of the disbond without the need for calibrating the sensors is to consider the ratios $R_{12}$ and $R_{32}$ of the MOFBG sensor responses, as given by:

$$R_{12} = \frac{\Delta\lambda_{\text{sensor 1}} - \Delta\lambda_{i,\text{sensor 1}}}{\Delta\lambda_{\text{sensor 2}} - \Delta\lambda_{i,\text{sensor 2}}} = \frac{\mathrm{d}(\Delta\lambda_{\text{sensor 1}})}{\mathrm{d}(\Delta\lambda_{\text{sensor 2}})} \tag{6.19}$$

and

$$R_{32} = \frac{\Delta\lambda_{\text{sensor 3}} - \Delta\lambda_{i,\text{sensor 3}}}{\Delta\lambda_{\text{sensor 2}} - \Delta\lambda_{i,\text{sensor 2}}} = \frac{\mathrm{d}(\Delta\lambda_{\text{sensor 3}})}{\mathrm{d}(\Delta\lambda_{\text{sensor 2}})} \tag{6.20}$$

with the response of sensor 2 as a reference signal. $\Delta\lambda_{i,\text{sensor } j}$ ($j = 1, 2, 3$) are the initial peak separations of the sensors, which should be measured when the unloaded adhesive bond is still intact. As soon as the structure is loaded, these peak separations $\Delta\lambda_{\text{sensor } j}$ ($j = 1, 2, 3$) change. The magnitude of the change depends on the loading level, on the occurrence of a disbond, as well as on the

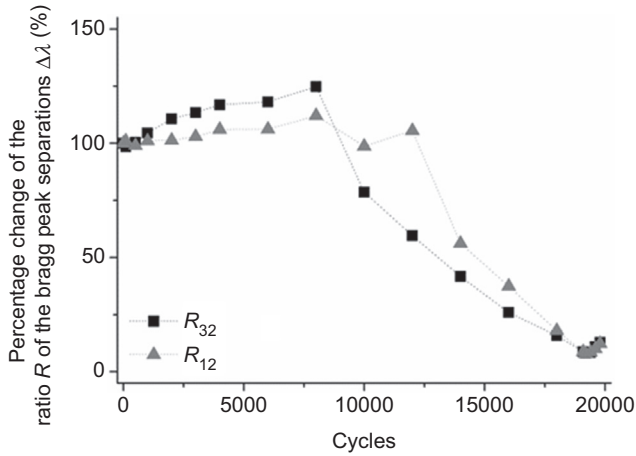


**Figure 6.14** Evolution of the ratios $R_{12}$ and $R_{32}$ of the Bragg peak separations of the three MOFBG sensors embedded in the single-lap joint shown in Figure 6.13(a). Adapted from Sulejmani et al. (2014a).

location and on the angular orientation of the MOFBG sensors. As long as the adhesive joint remains intact, the ratios $R_{12}$ and $R_{32}$ stay constant. As soon as a significant disbond appears at one or at both sides of the joint, these ratios change. This stems from the induced redistributions of shear stress which initially have a large effect on the outer sensors only. Figure 6.14 shows the evolution of the ratios $R_{12}$ and $R_{32}$ during the fatigue test. The increase of the sensor sensitivity of sensors 1 and 3 during the first part of the test stems from the initiation and growth of disbonds at both sides of the overlap. Their responses increase as the shear stress level at their location rises because the overall effective overlap length decreases. The small disbonds do not yet significantly influence the shear stress level in the centre of the bond and hence the response of the central MOFBG (sensor 2) does not change. At around 8000 cycles, a change occurs in evolution of the response of sensor 3. From there on sensor 3 is located in a region strongly affected by the shear stress redistribution due to the disbond at that side of the joint. Sensor 1 is not yet affected, because the disbond on its side is not sufficiently long. Once this disbond has propagated that far, sensor 1 is no longer located in the high shear stress region, and its sensor response will also decrease. This can be seen by the change in $R_{12}$ trend around 10,000 cycles. Beyond 10,000 cycles, the responses of sensors 1 and 3 decrease, whereas the response of sensor 2 increases abruptly from 16,000 onwards. This is attributed to the shorter overall overlap length of the bond, which generates a larger shear stress along the bond line.

The above demonstrates that one can take advantage of the high transverse strain sensitivity of the butterfly MOFBG and the dependence of the sensitivity to orientation with respect to the direction of the load to carry out shear stress measurements with unprecedented resolution compared to conventional fibre-based sensors, and that these features can also potentially be exploited for adhesive bond monitoring.

### 6.3.3 Vibration measurements

The capability of carrying out accurate vibration measurements can be an important asset in many SHM-related applications (Balageas et al., 2006). Vibration data obtained from dynamic strain measurements can, for example, be used to detect and locate damage in civil structures (Adewuyi & Wu, 2009). Several vibration or dynamic strain sensor techniques which are based on conventional optical fibre have been developed over the years, each coming with their own advantages and drawbacks (Rodriguez Garcia, Corres, & Goicoechea, 2010). More recently, MOFs have also been considered for carrying out vibration measurements (Ramakrishnan, Rajan, Semenova, Callaghan, & Farrell, 2014; Ramakrishnan, Rajan, Semenova, Wolinski, & Farrell, 2012; Thakur, Nalawade, Saxena, & Grattan, 2011). Here we discuss the potential of exploiting the temperature insensitivity and enhanced transverse strain sensitivity of the birefringence of the butterfly MOF to realize a temperature-insensitive vibration sensor.

Such a sensor can be fairly straightforwardly constructed by foreseeing a vibration transducer acting on a portion of the MOF and by monitoring how the state of polarization (SOP) of light propagating through the MOF varies around an operating point, as detailed in Chah et al. (2012), Chah, Caucheteur, et al. (2014). In contrast to the previous Subsections 6.3.1 and 6.3.2, no FBGs are used as sensor elements. The principle of the measurement is illustrated in Figure 6.15. Vibration transferred to the MOF using a mechanical transducer varies the birefringence of the MOF. The time-varying birefringence yields a changing phase shift $\phi$ induced between the two polarization eigenmodes propagating in the MOF and hence a time-varying SOP at the fibre output. The analyser converts the SOP fluctuation into a change of output optical power $P_{\mathrm{OUT}}$, the magnitude of the latter depending on the stress applied to the MOF and on the input optical power $P_{\mathrm{IN}}$.

The total phase shift $\phi$ can be written to consist of three contributions:

$$\phi = \phi_i + \phi_T + \phi_F \tag{6.21}$$

in which $\phi_i$ stems from the initial phase modal birefringence of the MOF, $\phi_T$ results from temperature variations and $\phi_F$ is the result of the vibration load applied to the MOF with the mechanical transducer. For a sinusoidal time-varying applied-vibration force with frequency $f$, $\phi_F$ can be written as:

$$\phi_F = \phi_M \sin(2\pi f t) \tag{6.22}$$

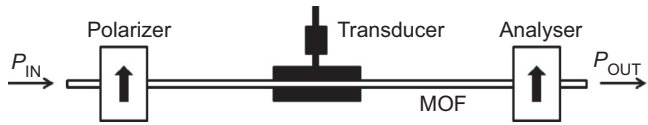


**Figure 6.15** Simplified scheme of the vibration measurement set-up. Adapted from Chah et al. (2012).

As further detailed in Chah et al. (2012), when orienting the linear polarizer at 45° with respect to the slow- and fast-axis system of the MOF and the analyser at −45°, the detected output power can be written as a function of the input power according to

$$P_{\mathrm{OUT}} = \frac{1}{2} P_{\mathrm{IN}} \left\{ 1 + \cos[\phi_i + \phi_T + \phi_M \sin(2\pi f t)] \right\} \tag{6.23}$$

Figure 6.16 shows the calculated normalized AC component of the sensor response for different temperatures and types of optical fibres, the butterfly MOF, a panda-type PM fibre and a standard communication-grade single mode fibre, with $\phi_i = 90°$ and an applied force amplitude of 5 N (Chah et al., 2012). In isothermal conditions ($\Delta T = 0\ °C$), the response of the butterfly MOF is clearly larger than that of the other fibres. This stems from the large sensitivity of the modal birefringence of the MOF to transverse load. Figure 6.16 also shows that, when $\Delta T \neq 0\ °C$, the sensor response of the butterfly MOF and standard single mode fibres do not vary significantly with changing temperature, in contrast to that of the panda fibre. Note that because the standard single mode fibre is not polarization maintaining and although it features low sensitivity to temperature changes, it cannot provide stable measurements because the SOP can change in time because of any uncontrolled displacement of the fibre. The above illustrates that the low polarimetric temperature sensitivity of the butterfly MOF and its relatively high transverse load sensitivity offer the possibility to use this fibre as a stable sensing element for polarization-based vibration measurements.

## 6.4 Conclusion and trends

In this chapter, the potential of using MOF-based sensors to support SHM-related applications has been highlighted. This potential stems from the enhanced properties which such microstructured fibres can possess over conventional optical fibres, when properly designed and manufactured. To illustrate this we have focused on one particular fibre: the so-called butterfly MOF. The core region of this butterfly MOF was Ge-doped to allow for the fabrication of FBGs using conventional ultraviolet photo-inscription methods, and its microstructure has been designed such that the fibre is highly birefringent, with a birefringence which features a large sensitivity to transverse load or pressure, whilst exhibiting a negligible sensitivity to temperature. Possible applications of this fibre include monitoring the cure cycle of composite materials and quantifying the amount of transverse residual strain in composite laminates, carrying out shear strain measurements with unprecedented resolution in adhesive bonds, monitoring the propagation of disbonding in single lap glue joints and finally measuring vibrations in a temperature-insensitive manner.

In terms of future developments of MOF-based sensor technology in the realm of SHM, it is not straightforward to look into a crystal ball and forecast what will happen in the next decades or which MOF-based sensors will eventually find their

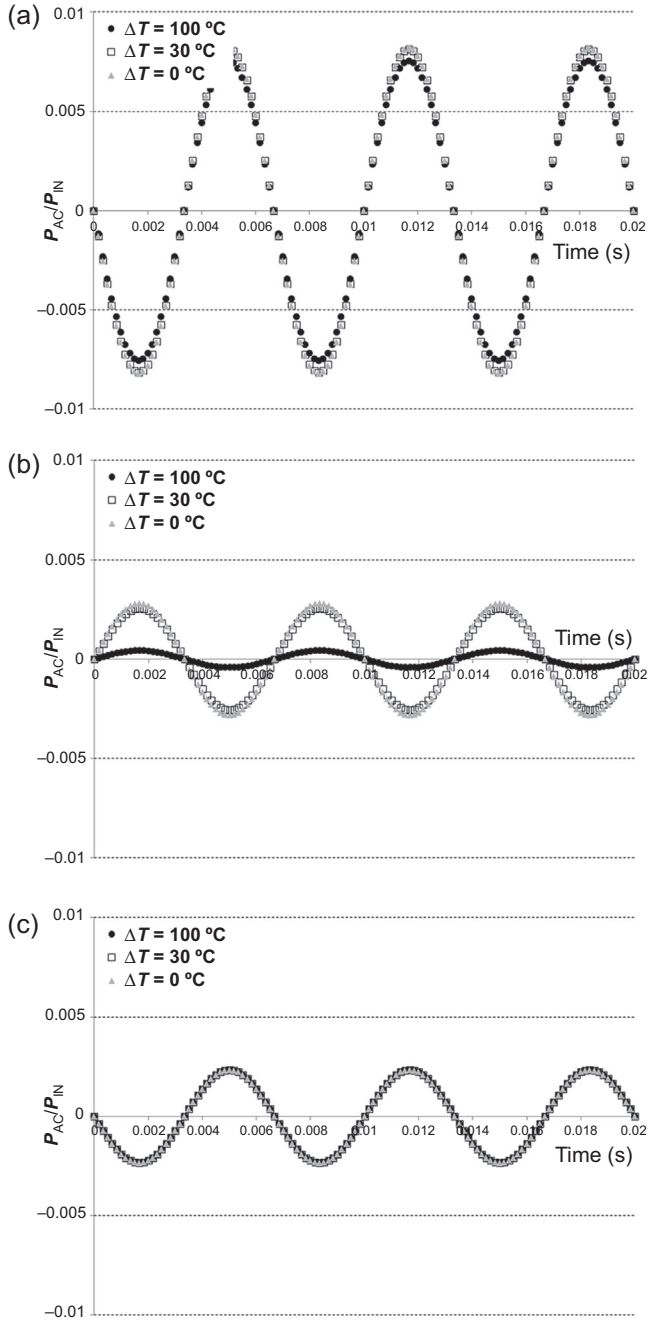


**Figure 6.16** Calculated response of (a) a butterfly MOF, (b) a panda-type fibre and (c) a regular single mode fibre submitted to an applied sinusoidal vibration with a force amplitude of 5 N and an initial phase shift $\phi_i = 90°$.
Adapted from Chah et al. (2012).

way to actual industrial applications. Yet a number of opportunities exist which deserve further exploration and are worth mentioning in the context of this chapter.

With regard to fibre-based sensors embedded within composite materials, using fibres with a small outer diameter is trending (e.g., 40 or 60 μm cladding diameter), to minimize the effect of the integration of the fibre on the mechanical properties of the composite and improve on the strain transfer between composite and fibre sensor (Takeda, Okabe, Kuwahara, Kojima, & Ogisu, 2005; Voet et al., 2014). Micro- or nanofibre-based sensors may create opportunities here, and it may be worth investigating whether ultra-small diameter MOFs with enhanced properties can be developed and embedded within composites (Chen, Ding, Newson, & Brambilla, 2013; Yu et al., 2014). A second trend may lie in the combination of MOFs with distributed optical fibre sensor techniques based, for example, on optical frequency domain interrogation or on Brillouin scattering techniques (Dong, Bao, & Chen, 2009; Muryama, Wada, & Igawa, 2013; Thevenaz & Thévenaz, 2011). Here also the specific properties of MOFs may help achieving an enhanced response to specific measurands which are relevant to SHM. A last example of a possible trend to watch relates to MOF technology itself. The fibres which we have been dealing with so far in this chapter were all made from silica. However, MOFs can also be fabricated in polymer materials to obtain so-called microstructured polymer optical fibres or mPOFs (Large, Poladian, Barton, & van Eijkelenborg, 2007). Such devices can combine the unique features of MOFs with the peculiar material properties of polymers to obtain sensors with unprecedented characteristics (Berghmans & Thienpont, 2014; Kalli & Webb, 2011; Liehr & Mukhopadhyay, 2011; Peters, 2011). For SHM purposes and when the measurement of mechanical quantities is considered, an important advantage is that mPOF can cope with much larger strains than glass MOF, and hence the mPOF sensors can potentially measure much larger strain ranges than their glass counterparts. Furthermore, the lower Young′s modulus of mPOFs can help obtaining devices with a higher sensitivity to strain or to pressure than glass fibre sensors. Finally, great advances have occurred in the field of Bragg grating fabrication in mPOF as well, which may further leverage the sensor capabilities of such gratings (Berghmans, Geernaert, Baghdasaryan, et al., 2014).

To close, we are convinced that the field can benefit from MOF-based sensors. Realizing their true potential and moving to real-life applications will not only depend on bringing the cost of MOF technology to acceptable levels, but will also greatly rest on the ability to demonstrate the maturity of MOF-based sensors, and on the efforts of the MOF community to reach out to increase the popularity of these devices. We hope that our chapter has somehow contributed to that.

## Acknowledgements

The authors would like to acknowledge the funding received from various sources to accomplish parts of the work described in this chapter. More particularly, the authors thank the European Commission for Grant Agreements 224058 (PHOSFOS project)

and 251649 (SMARTSOCKET project). The authors also appreciate the support received from the Flemish Agency for Innovation by Science and Technology (IWT) for the SBO project grants 110070 (eSHM with AM) and 120024 (SSC). The authors express their gratitude as well to the Research Foundation − Flanders for projects G099014N, and for Thomas Geernaert's post-doctoral fellowship 12D6615N. Belgian Science Policy is acknowledged for the Interuniversity Attraction Pole P7/35 Photonics@be: towards smart photonics in 2020. The COST TD1001 action OFSESA is acknowledged for providing networking opportunities and a forum which allowed discussing parts of the results described in this chapter with international experts. Finally, the Flemish Hercules Foundation is recognized for the investments in the research and laboratory infrastructure at Vrije Universiteit Brussel as well as the Vrije Universiteit Brussel's for Hugo Thienpont's Methusalem fellowship.

## References

Abe, I., Kalinowski, H. J., Frazão, O., Santos, J. L., Nogueira, R. N., & Pinto, J. L. (2004). Superimposed Bragg gratings in high-birefringence fibre optics: three-parameter simultaneous measurements. *Measurement Science and Technology, 15*(8), 1453.

Adams, R. D., Comyn, J., & Wake, W. C. (1997). *Structural adhesive joints in engineering* (2nd ed.). London: Chapman & Hall.

Adewuyi, A. P., & Wu, Z. S. (2009). Vibration-based structural health monitoring technique using statistical features from strain measurements. *ARPN Journal of Engineering and Applied Sciences, 4*(3), 38−47.

Antonucci, V., Cusano, A., Giordano, M., Nasser, J., & Nicolais, L. (2006). Cure-induced residual strain build-up in a thermoset resin. *Composites Part A: Applied Science and Manufacturing, 37*(4), 592−601.

Antunes, P., Lima, H., Alberto, N., Bilro, L., Pinto, P., Costa, A., et al. (2011). Optical sensors based on fiber Bragg gratings for structural health monitoring. In S. C. Mukhopadhyay (Ed.), *New developments in sensing technology for structural health monitoring*. Berlin: Springer-Verlag.

Arismar Cerqueira, S., Jr. (2010). 2010. Recent progress and novel applications of photonic crystal fibers. *Reports on Progress in Physics, 73*, 024401.

Balageas, D., Fritzen, C.-P., & Güemes, A. (Eds.). (2006). *Structural health monitoring*. London: ISTE Ltd.

Barlow, A., & Payne, D. (1983). The stress-optic effect in optical fibers. *IEEE Journal of Quantum Electronics, 19*(5), 834−839.

Berghmans, F., & Geernaert, T. (2011). Optical fiber Point sensors. In L. Thévenaz (Ed.), *Advanced fiber Optics: Concepts and technology* (pp. 309−344). Lausanne: EPFL Press.

Berghmans, F., Geernaert, T., Baghdasaryan, T., & Thienpont, H. (2014). Challenges in the fabrication of fibre Bragg gratings in silica and polymer microstructured fibres. *Laser & Photonics Reviews, 8*(1), 27−52.

Berghmans, F., Geernaert, T., Napierala, M., Baghdasaryan, T., Sonnenfeld, C., Sulejmani, S., et al. (2012). Applying optical design methods to the development of application specific photonic crystal fibres. In P. Benitez (Ed.), *Proceedings of SPIE: Vol. 8550. Optical systems design 2012*. pp. 85500B-1-17.

Berghmans, F., Geernaert, T., Sonnenfeld, C., Sulejmani, S., Luyckx, G., Lammens, N., et al. (2014). Microstructured optical fibre Bragg grating sensors for structural health monitoring applications. In *Proceedings of the 7th European workshop on structural health monitoring. Nantes, France, 8–11 July 2014* (pp. 962–969). Rennes: Inria.

Berghmans, F., Sonnenfeld, C., Sulejmani, S., Geernaert, T., Luyckx, G., Lammens, N., et al. (2014). Opportunities for structural health monitoring of composite material structures with novel microstructured optical fiber sensors. In F.-K. Chang (Ed.), *Structural health monitoring 2013: A roadmap to intelligent structures. Proceedings of the ninth international workshop on structural health monitoring.* Stanford, CA, USA, 10–12 September 2013. Lancaster: DEStech Publications, Inc.

Berghmans, F., & Thienpont, H. (2014). Plastic optical fibers for sensing applications. In *Optical fiber communication conference, OSA technical digest (online), San Francisco, United States, 9–13 March 2014*. Optical Society of America. pp. Tu3K.2.

Black, C. A., Udd, E., Schulz, W. L., Kreger, S. T., Kunzler, M., Taylor, T., et al. (2002). Using multi-axis fiber grating strain sensors to measure transverse strain and transverse strain gradients in composite materials with complex weave structures. In , *Proceedings of SPIE: Vol. 4694. Smart structures and materials 2002: Smart sensor technology and measurement systems* (pp. 128–134).

Bosia, F., Giaccari, P., Botsis, J., Facchini, M., Limberger, H., & Salathe, R. (2003). Characterization of the response of fibre Bragg grating sensors subjected to a two-dimensional strain field. *Smart Materials and Structures, 12*(6), 925–934.

Campbell, F. C. (2010). *Introduction to composite materials*. Structural composite materials. ASM International.

Candiani, A., Margulis, W., Konstantaki, M., & Pissadakis, S. (2012). A shear-displacement sensor based on a ferrofluidic defected microstructured optical fibre Bragg grating. In *Advanced photonics congress, OSA technical digest (online). Colorado Springs, United States, 17–20 June 2012*. Optical Society of America. pp. BTu2E.2.

Chah, K., Caucheteur, C., Mégret, P., Sulejmani, S., Geernaert, T., Thienpont, H., et al. (2014). Reflective polarimetric vibration sensor based on temperature-independent FBG in HiBi microstructured optical fiber. In *Proceedings of SPIE: Vol. 9141. Optical sensing and detection III* (p. 91410U).

Chah, K., Linze, N., Caucheteur, C., Mégret, P., Tihon, P., Verlinden, O., et al. (2012). Temperature-insensitive polarimetric vibration sensor based on HiBi microstructured optical fiber. *Applied Optics, 52*(25), 6130–6138.

Chehura, E., Skordos, A. A., Ye, C.-C., James, S. W., Partridge, I. K., & Tatam, R. P. (2005). Strain development in curing epoxy resin and glass fibre/epoxy composites monitored by fibre Bragg grating sensors in birefringent optical fibre. *Smart Materials and Structures, 14*(2), 354–362.

Chen, G. Y., Ding, M., Newson, T. P., & Brambilla, G. (2013). A review of microfiber and nanofiber based optical sensors. *The Open Optics Journal, 7*(Suppl. 1, M3), 32–57.

Chen, C., Laronche, A., Bouwmans, G., Bigot, L., Quiquempois, Y., & Albert, J. (2008). Sensitivity of photonic crystal fiber modes to temperature, strain and external refractive index. *Optics Express, 16*(13), 9645–9653.

Collombet, F., Luyckx, G., Sonnenfeld, C., Grunevald, Y.-H., Davila, Y., Torres, M., et al. (2013). Cure monitoring of an autoclave manufactured industrial part: added value of complementary instrumentation. In *Proceedings of the international conference on composite materials 2013 (ICCM-19). Montreal, Canada, 28 July–2 August 2013* (pp. 1178–1187). Canadian Association for Composite Structures and Materials.

Colpo, F., Humbert, L., & Botsis, J. (2007). Characterisation of residual stresses in a single fibre composite with FBG sensor. *Composites Science and Technology, 67*(9), 1830−1841.

Available at http://www.comsol.com/ Accessed 01.08.14.

Cusano, A., Cutolo, A., & Albert, J. (Eds.). (2011). *Fiber Bragg grating sensors: Recent advancements, industrial applications and market Exploitation*. Bentham Science Publishers.

Davis, C., Tejedor, S., Grabovac, I., Kopczyk, J., & Nuyens, T. (2012). High-strain fiber Bragg gratings for structural fatigue testing of military aircraft. *Photonic Sensors, 2*(3), 215−224.

Dong, Y., Bao, X., & Chen, L. (2009). Distributed temperature sensing based on birefringence effect on transient Brillouin grating in a polarization-maintaining photonic crystal fiber. *Optics Letters, 34*(17), 2590−2592.

Dudley, J., Genty, G., & Coen, S. (2006). Supercontinuum generation in photonic crystal fiber. *Reviews of Modern Physics, 78*, 1135−1184.

Elhajjar, R., Saponara, V. L., & Muliana, A. (Eds.). (2013). *Smart composites: Mechanics and design*. Boca Raton: CRC Press−Taylor & Francis Group, LLC.

Fernandes, L. A., Becker, M., Frazão, O., Schuster, K., Kobelke, J., Rothhardt, M., et al. (2012). Temperature and strain sensing with femtosecond laser written Bragg gratings in defect and nondefect suspended-silica-core fibers. *IEEE Photonics Technology Letters, 24*(7), 554−556.

Frazão, O., Carvalho, J. P., Ferreira, L. A., Araújo, F. M., & Santos, J. L. (2005). Discrimination of strain and temperature using Bragg gratings in microstructured and standard optical fibres. *Measurement Science and Technology, 16*, 2109−2113.

Frazão, O., Santos, J. L., Araújo, F. M., & Ferreira, L. A. (2008). Optical sensing with photonic crystal fibers. *Laser & Photonics Reviews, 2*(6), 449−459.

Geernaert, T., Becker, M., Mergo, P., Nasilowski, T., Wojcik, J., Urbanczyk, W., et al. (2010). Bragg grating inscription in $GeO_2$-doped microstructured optical fibers. *Journal of Lightwave Technology, 28*(5), 1459−1467.

Geernaert, T., Luyckx, G., Voet, E., Nasilowski, T., Chah, K., Becker, M., et al. (2009). Transversal load sensing with fiber Bragg gratings in microstructured optical fibers. *IEEE Photonics Technology Letters, 21*(1), 6−8.

Geernaert, T., Sulejmani, S., Sonnenfled, C., Chah, K., Luyckx, G., Lammens, N., et al. (2014). Internal strain monitoring in composite materials with embedded photonic crystal fiber Bragg gratings. In E. W. Taylor, & D. A. Cardimona (Eds.), *Proceedings of SPIE: Vol. 9226. Nanophotonics and macrophotonics for space environments VIII* (p. 92260D).

Giordano, M., Laudati, A., Nasser, J., Nicolais, L., Cusano, A., & Cutolo, A. (2004). Monitoring by a single fiber Bragg grating of the process induced chemo-physical transformations of a model thermoset. *Sensors and Actuators A: Physical, 113*(2), 166−173.

Glisic, B., & Inaudi, D. (2007). *Fiber optic methods for structural health monitoring*. Chichester: John Wiley &Sons, Ltd.

Guemes, J. A., & Menéndez, J. M. (2002). Response of Bragg grating fiber-optic sensors when embedded in composite laminates. *Composites Science and Technology, 62*(7−8), 959−966.

Guo, Z.-S. (2007). Strain and temperature monitoring of asymmetric composite laminate using FBG hybrid sensors. *Structural Health Monitoring, 6*(3), 191−197.

Harsch, M., Karger-Kocsis, J., & Herzog, F. (2007). Influence of cure regime on the strain development in an epoxy resin as monitored by a fiber Bragg grating sensor. *Macromolecular Materials and Engineering, 292*(4), 474−483.

Herlier, C. (2013). *Handbook of nondestructive evaluation* (2nd ed.). The McGraw-Hill Companies, Inc.

Hill, K. O., & Meltz, G. (1997). Fiber Bragg grating technology fundamentals and overview. *Journal of Lightwave Technology, 15*(8), 1263−1276.

Hoa, S. V. (2009). *Principles of the manufacturing of composite materials*. Lancaster: DEStech Publications, Inc.

Jin, L., Jin, W., & Ju, J. (2009). Directional Bend sensing with a $CO_2$-laser-inscribed long period grating in a photonic Crystal fiber. *Journal of Lightwave Technology, 27*(21), 4884−4891.

Jin, L., Wang, Z., Fang, Q., Liu, Y., Liu, B., Kai, G., et al. (2007). Spectral characteristics and bend response of Bragg gratings inscribed in all-solid bandgap fibers. *Optics Express, 15*(23), 15555−15565.

Kalli, K., & Webb, D. J. (2011). Polymer optical fiber-based sensors. In L. Thévenaz (Ed.), *Advanced fiber optics: Concepts and technology*. Lausanne: EPFL Press.

Karalekas, D., Cugnoni, J., & Botsis, J. (2008). Monitoring of process induced strains in a single fibre composite using FBG sensor: a methodological study. *Composites Part A: Applied Science and Manufacturing, 39*(7), 1118−1127.

Khoun, L., de Oliveira, R., Michaud, V., & Hubert, P. (2011). Investigation of process-induced strains development by fibre Bragg grating sensors in resin transfer moulded composites. *Composites Part A: Applied Science and Manufacturing, 42*(3), 274−282.

Kinet, D., Mégret, P., Goossen, K. W., Qiu, L., Heider, D., & Caucheteur, C. (2014). Fiber Bragg grating sensors toward structural health monitoring in composite materials: challenges and solutions. *Sensors, 14*, 7394−7419.

Knight, J. C. (2007). Photonic crystal fibers and fiber lasers. *Journal of the Optical Society of America B, 24*(8), 1661−1668.

Knight, J. C., Birks, T. A., Russell, P. St. J., & Atkin, D. M. (1996). All-silica single-mode optical fiber with photonic crystal cladding. *Optics Letters, 21*(19), 1547−1549.

Lammens, N., Kinet, D., Chah, K., Luyckx, G., Caucheteur, C., Degrieck, J., et al. (2013). Residual strain monitoring of out-of-autoclaved cured parts by use of polarization dependent loss measurements in embedded optical fiber Bragg gratings. *Composites Part A: Applied Science and Manufacturing, 52*, 38−44.

Large, M. C. J., Poladian, L., Barton, G. W., & van Eijkelenborg, M. A. (2007). *Microstructured polymer optical fibres*. New York: Springer.

Lawrence, C. M., Nelson, D. V., & Udd, E. (1996). Multi-parameter sensing with fiber Bragg gratings. In *Proceedings of SPIE: Vol. 2872. Second Pacific Northwest fiber optic sensor workshop* (pp. 24−31).

Lawrence, C. M., Nelson, D. V., Udd, E., & Bennett, T. (1999). A fiber optic sensor for transverse strain measurement. *Experimental Mechanics, 39*(3), 202−209.

Li, Y. Y. (2010). Hypersensitivity of strain-based indicators for structural damage identification: a review. *Mechanical Systems and Signal Processing, 24*(3), 653−664.

Liehr, S. (2011). Polymer optical fiber sensors in structural health monitoring. In S. C. Mukhopadhyay (Ed.), *New developments in sensing technology for structural health monitoring*. Berlin: Springer-Verlag.

Lopez-Higuera, J. M., Rodriguez Cobo, L., Quintela Incera, A., & Cobo, A. (2011). Fiber optic sensors in structural health monitoring. *Journal of Lightwave Technology, 29*(4), 587−608.

Luyckx, G., De Waele, W., Degrieck, J., Van Paepegem, W., Vlekken, J., Vandamme, S., et al. (2007). Three-dimensional strain and temperature monitoring of composite laminates. *Insight, 49*(1), 10−16.

Luyckx, G., Voet, E., Geernaert, T., Chah, K., Nasilowski, T., De Waele, W., et al. (2009). Response of FBGs in microstructured and Bow tie fibers embedded in laminated composite. *IEEE Photonics Technology Letters, 21*(18), 1290−1292.

Luyckx, G., Voet, E., Lammens, N., & Degrieck, J. (2011). Strain measurements of composite laminates with embedded fibre Bragg gratings: criticism and opportunities for research. *Sensors, 11*(1), 384−408.

Marin, E., Robert, L., Triollet, S., & Ouerdane, Y. (2012). Liquid resin infusion process monitoring with superimposed fibre Bragg grating sensor. *Polymer Testing, 31*(8), 1045−1052.

Martynkien, T., Statkiewicz-Barabach, G., Olszewski, J., Wojcik, J., Mergo, P., Geernaert, T., et al. (2010). Highly birefringent microstructured fibers with enhanced sensitivity to hydrostatic pressure. *Optics Express, 17*(14), 15113−15121.

Mawatari, T., & Nelson, D. (2008). A multi-parameter Bragg grating fiber optic sensor and triaxial strain measurement. *Smart Materials and Structures, 17*(3), 035033.

McKenzie, I., Jones, R., Marshall, I. H., & Galea, S. (2000). Optical fibre sensors for health monitoring of bonded repair systems. *Composite Structures, 50*(4), 405−416.

Minakuchi, S. (2013). Direct measurement of out-of-plane and in-plane cure shrinkage strain in compsoites by embedded fiber-optic sensors. In *Proceedings of the international conference on composite materials 2013 (ICCM-19). Montreal, Canada, 28 July−2 August 2013* (pp. 3979−3986). Canadian Association for Composite Structures and Materials.

Mix, P. E. (2005). *Introduction to nondestructive testing: A training guide* (2nd ed.). Hoboken: John Wiley & Sons, Inc.

Montanini, R., & D'Acquisto, L. (2007). Simultaneous measurement of temperature and strain in glass fiber/epoxy composites by embedded fiber optic sensors: II. Post-cure testing. *Smart Materials and Structures, 16*(5), 1727−1735.

Moon, D. S., Kim, B. H., Lin, A., Sun, G., Han, Y.-G., Han, W.-T., et al. (2007). The temperature sensitivity of sagnac loop interferometer based on polarization maintaining side-hole fiber. *Optics Express, 15*(13), 7962−7967.

Mulle, M., Collombet, F., Olivier, P., & Grunevald, Y.-H. (2009). Assessment of cure residual strains through the thickness of carbon−epoxy laminates using FBGs, Part I: elementary specimen. *Composites Part A: Applied Science and Manufacturing, 40*(1), 94−104.

Muryama, H., Wada, D., & Igawa, H. (2013). Structural health monitoring by using fiber-optic distributed strain sensors with high spatial resolution. *Photonic Sensors, 3*(4), 355−376.

Nelson, D. V., Makino, A., Lawrence, C. M., Seim, J. M., Schulz, W. L., & Udd, E. (1998). Determination of the K-matrix for the multi-parameter fiber grating sensor in AD072 fibercore fiber. In , *Proceedings of SPIE: Vol. 3489. Fourth Pacific Northwest fiber optic sensor workshop* (pp. 79−85).

Ning, X., Murayama, H., Kageyama, K., Uzawa, K., & Wada, D. (2012). Measurement of longitudinal strain and estimation of peel stress in adhesive-bonded single-lap joint of CFRP adherend using embedded FBG sensor. In M. Tomizuka, C.-B. Yun, & J. P. Lynch (Eds.), *Proceedings of SPIE: Vol. 8354. Sensors and smart structures technologies for civil, mechanical, and aerospace systems*. pp. 83451I-83451I-10.

Available at http://www.nktphotonics.com/files/files/PM-1550-120402.pdf Accessed 12.08.14.

Okabe, Y., Yashiro, S., Tsuji, R., Mizutani, T., & Takeda, N. (2002). Effect of thermal residual stress on the reflection spectrum from fiber Bragg grating sensors embedded in CFRP laminates. *Composites Part A: Applied Science and Manufacturing, 33*(7), 991−999.

Osorio, J. H., Hayashi, J. G., Espinel, Y. A. V., Franco, M. A. R., Andres, M. V., & Cordeiro, M. B. (2014). Photonic-crystal fiber-based pressure sensor for dual environment monitoring. *Applied Optics, 53*(7), 3668−3672.

Othonos, A., & Kalli, K. (1999). *Fiber Bragg gratings: Fundamentals and applications in telecommunications and sensing*. New York: Artech House.

O'Dwyer, M. J., Maistros, G. M., James, S. W., Tatam, R. P., & Partridge, I. K. (1998). Relating the state of cure to the real-time internal strain development in a curing composite using in-fibre Bragg gratings and dielectric sensors. *Measurement Science and Technology, 9*(8), 1153−1158.

Palaniappan, J., Ogin, S. L., Thorne, A. M., Reed, G. T., Crocombe, A. D., Capell, T. F., et al. (2008). Disbond growth detection in composite-composite single-lap joints using chirped FBG sensors. *Composites Science and Technology, 68*(12), 2410−2417.

Parlevliet, P. P., Bersee, H. E. N., & Beukers, A. (2010). Measurement of (post-)curing strain development with fibre Bragg gratings. *Polymer Testing, 29*(3), 291−301.

Peters, K. (2011). Polymer optical fiber sensors − a review. *Smart Materials and Structures, 20*, 013002.

Pinto, A. M. R., & Lopez-Amo, M. (2012). Photonic Crystal fibers for sensing applications. *Journal of Sensors, 2012*, 598178.

Poli, F., Cucinotta, A., & Selleri, S. (2007). Photonic crystal fibers: Properties and applications. In *Springer series in materials science* (Vol. 102). Dordrecht: Springer.

Ramakrishnan, M., Rajan, G., Semenova, Y., Callaghan, D., & Farrell, G. (2014). Investigation of the effect of vibration amplitude on vibration measurements of polarimetric fiber sensors embedded in composite beams. *Smart Materials and Structures, 23*(4), 045037.

Ramakrishnan, M., Rajan, G., Semenova, Y., Wolinski, T., & Farrell, G. (2012). Comparison of vibration measurements in composite materials using different types of polarimetric sensors. In , *Proceedings of SPIE: Vol. 8421. OFS2012 22nd international conference on optical fiber sensors* (p. 842178).

Ranka, J. K., Windeler, R. S., & Stentz, A. J. (2000). Visible continuum generation in air−silica microstructure optical fibers with anomalous dispersion at 800 nm. *Optics Letters, 25*(1), 25−27.

Rodriguez Garcia, Y., Corres, J. M., & Goicoechea, J. (2010). Vibration detection using optical fiber sensors. *Journal of Sensors, 2010*, 936487.

Russell, P. (2003). Photonic Crystal fibers. *Science, 299*, 358−362.

Russell, P. St. J. (2006). Photonic-Crystal fibers. *Journal of Lightwave Technology, 24*(12), 4729−4749.

Schukar, V., Kusche, N., Kalinka, G., & Habel, W. (2013). Field deployable fiber Bragg grating strain patch for long-term stable health monitoring applications. *Applied Sciences, 3*, 39−45.

Schulz, W. L., Udd, E., Morrell, M., Seim, J. M., Perez, I. M., & Trego, A. (1999). Health monitoring of an adhesive joint using a multiaxis fiber grating strain sensor system. In , *Proceedings of SPIE: Vol. 3586. Nondestructive evaluation of aging aircraft, airports, and aerospace hardware III* (pp. 41−52).

Schwartz, M. (Ed.). (2008). *Smart materials*. Boca Raton: CRC Press−Taylor & Francis Group, LLC.

Shull, P. J. (Ed.). (2002). *Nondestructive Evaluation: Theory, techniques, and applications*. New York: Marcel Dekker, inc.

Sohn, H., Farrar, C. R., Hemez, F. M., Shunk, D. D., Stinemates, D. W., Nadler, B. R., et al. (2004). *A review of structural health monitoring literature: 1996−2001*. Los Alamos National Laboratory Report, LA-13976-MS.

Sonnenfeld, C., Luyckx, G., Collombet, F., Geernaert, T., Sulejmani, S., Thienpont, H., et al. (2013). Cure cycle monitoring of laminated carbon fiber-reinforced plastic by fiber Bragg gratings in microstructured optical fiber. In *Proceedings of the 19th international*

*conference on composite materials (ICCM 2013), Montréal, Canada, 28 July−2 August 2013* (pp. 3327−3335).

Sonnenfeld, C., Luyckx, G., Collombet, F., Grunevald, Y.-H., Douchin, B., Crouzeix, L., et al. (2013a). Integration of microstructured optical fibres into carbon fibre reinforced plastic materials − determination of the initial strain state. In O. T. Thomsen, B. F. Sorensen, & C. Berggreen (Eds.), *CompTest 2013 − Book of abstracts, Aalborg, Denmark, 22−24 April 2013* (pp. 157−158). Aalborg: Aalborg University.

Sonnenfeld, C., Luyckx, G., Collombet, F., Grunevald, Y.-H., Douchin, B., Crouzeix, L., et al. (2013b). Embedded fibre Bragg gratings in photonic crystal fibres for cure cycle monitoring of carbon fibre reinforced polymer materials. In *Proceedings of SPIE: Vol. 8775. Microstructured and Specialty optical fibres II* (p. 87750).

Sonnenfeld, C., Sulejmani, S., Geernaert, T., Eve, S., Lammens, N., et al. (2011). Microstructured optical fiber sensors embedded in a laminate composite for smart material applications. *Sensors, 11*, 2566−2579.

Sørensen, H. R., Canning, J., Lægsgaard, J., & Hansen, K. (2006). Control of the wavelength dependent thermooptic coefficients in structured fibres. *Optics Express, 14*(14), 6428−6433.

Sorensen, L., Gmür, T., & Botsis, J. (2006). Residual strain development in an AS4/PPS thermoplastic composite measured using fibre Bragg grating sensors. *Composites Part A: Applied Science and Manufacturing, 37*(2), 270−281.

Sulejmani, S., Sonnenfeld, C., Geernaert, T., Berghmans, F., Thienpont, H., Eve, S., et al. (2011). Towards micro-structured optical fiber sensors for transverse strain sensing in smart composite materials. In *IEEE sensors 2011 proceedings. Limerick, Ireland, 28−31 October 2011* (pp. 109−112). IEEE.

Sulejmani, S., Sonnenfeld, C., Geernaert, T., Luyckx, G., Mergo, P., Urbanczyk, W., et al. (2014). Disbond monitoring in adhesive joints using shear stress optical fiber sensors. *Smart Materials and Structures, 23*, 075006.

Sulejmani, F., Sonnenfeld, C., Geernaert, T., Luyckx, G., Mergo, P., Urbanczyk, W., et al. (2014). Adhesive bond monitoring with microstructured optical fiber Bragg grating sensors. In *Proceedings of the 7th european Workshop on structural health monitoring. Nantes, France, 8−11 July 2014* (pp. 1194−1199). Rennes: Inria.

Sulejmani, S., Sonnenfeld, C., Geernaert, T., Luyckx, G., Van Hemelrijk, D., Mergo, P., et al. (2013). Shear stress sensing with Bragg grating-based sensors in microstructured optical fibers. *Optics Express, 21*(17), 20404−20416.

Sulejmani, S., Sonnenfeld, C., Geernaert, T., Mergo, P., Makara, M., Poturaj, K., et al. (2012). Control over the pressure sensitivity of Bragg grating based sensors in highly birefringent microstructured optical fibers. *IEEE Photonics Technology Letters, 24*(6), 527−529.

Takeda, N., Okabe, Y., Kuwahara, J., Kojima, S., & Ogisu, T. (2005). Development of smart composite structures with small-diameter fiber Bragg grating sensors for damage detection: quantitative evaluation of delamination length in CFRP laminates using Lamb wave sensing. *Composites Science and Technology, 65*(15−16), 2575−2587.

Takeda, S., Yamamoto, T., Okabe, Y., & Takeda, N. (2007). Debonding monitoring of composite repair patches using embedded small-diameter FBG sensors. *Smart Materials and Structures, 16*(3), 763−770.

Tenderenda, T., Murawski, M., Szymanski, M., Szostkiewicz, L., Becker, M., Rothhardt, M., et al. (2014). Longitudinal strain sensing with photonic crystal fibers and fiber Bragg

gratings. In M. G. F. Digonnet, & S. Jiang (Eds.), *Proceedings of SPIE: Vol. 8982. Optical components and materials XI* (p. 898219).

Thakur, H. V., Nalawade, S. M., Saxena, Y., & Grattan, K. T. V. (2011). All-fiber embedded PM-PCF vibration sensor for structural health monitoring of composite. *Sensors and Actuators A: Physical, 167*(2), 204−212.

Thevenaz, L. (2011). Inelastic scatterings and applications to distributed sensing. In L. Thévenaz (Ed.), *Advanced fiber optics: Concepts and technology* (pp. 263−307). Lausanne: EPFL Press.

Tjin, S. C., Suresh, R., & Ngo, N. Q. (2004). Fiber Bragg grating based shear-force sensor: modeling and testing. *Journal of Lightwave Technology, 22*(7), 1728−1733.

Udd, E. (Ed.). (1995). *Fiber optic smart structures*. New York: John Wiley & Sons, Inc.

Udd, E. (2007). Review of multi-parameter fiber grating sensors. In E. Udd (Ed.), *Proceedings of SPIE: Vol. 6770. Fiber optic sensors and applications V*. pp. 677002-1-10.

Urbanczyk, W., Martynkien, T., Szpulak, M., Statkiewicz, B., Olszewski, J., Golojuch, G., et al. (2007). Photonic crystal fibers: new opportunities for sensing. In , *Proceedings of SPIE: Vol. 6619. Third european workshop on optical fibre sensors* (p. 66190G).

Voet, E., Ahmed, T., Lindner, E., Luyckx, G., Brødsjø, A., & Degrieck, J. (2014). Smaller diameter optical fibre sensor for automated embedding in composite laminates. In *Proceedings of the 7th European workshop on structural health monitoring. Nantes, France, 8−11 July 2014* (pp. 1473−1480). Rennes: Inria.

Voet, E., Luyckx, G., De Waele, W., & Degrieck, J. (2010). Multi-axial strain transfer from laminated CFRP composites to embedded Bragg sensor: II. Experimental validation. *Smart Materials and Structures, 19*(10), 105018.

Voyiadjis, G. Z., & Woelke, P. (2008). *Elasto-plastic and damage analysis of plates and shells*. Berlin: Springer-Verlag.

Wang, Y., Bartelt, H., Ecke, W., Willsch, R., Kobelke, J., Kautz, M., et al. (2009). Sensing properties of fiber Bragg gratings in small-core Ge-doped photonic crystal fibers. *Optics Communications, 282*, 1129−1134.

Yu, C., Chen, X., Gong, Y., Wu, Y., Rao, Y., & Peng, G. (2014). Simultaneous force and temperature measurement using optical microfiber asymmetrical interferometer. *Photonic Sensors, 4*(3), 242−247.

Zhang, J.-H., Liu, N.-L., Wang, Y., Ji, L.-L., & Lu, P.-X. (2012). Dual-peak Bragg gratings inscribed in an all-solid photonic bandgap fiber for sensing applications. *Chinese Physics Letters, 29*(7), 074205-1-4.

# Liquid crystals infiltrated photonic crystal fibers (PCFs) for electromagnetic field sensing

7

*T.R. Woliński, S. Ertman, K.A. Rutkowska*
Warsaw University of Technology, Warsaw, Poland

## 7.1 Introduction—state of the art: photonic liquid crystal fibers for electromagnetic field sensing

Between 2000 and 2010, photonic crystal fibers (PCFs) (Russell, 2003) have attracted increasing scientific interest, due to a great number of potential applications, including the fabrication of a new class of in-fiber devices. Their core is usually made by a defect in the periodical structure of the PCF cross-section (missed or additional rod/tube). In this way either a hollow-core PCF or a solid-core PCF can be manufactured. Optical waveguiding in a PCF is governed by one of two principal mechanisms responsible for light trapping within the core. While the first one is a classical propagation effect based on the modified total internal reflection (mTIR or index guiding) phenomenon, which is well known and similar to the waveguiding effect within a conventional fiber, the second, referred to as the photonic bandgap (PBG) effect, occurs if the refractive index of the core is lower than the mean reflective index of the cladding region.

PCFs are formed by the periodic matrix (typically square or triangular) of microscopic air channels and/or microrods distributed in a solid material [e.g., in pure silica (Russell, 2003), nonsilica high-index/multicomponent glasses (Désévédavy et al., 2010; Feng, Monro, Petropoulos, Finazzi, & Hewak, 2003), silver-halide crystalline materials (Millo, Lobachinsky, & Katzir, 2008), or polymers (Argyros, van Eijkelenborg, Large, & Bassett, 2006; van Eijkelenborg et al., 2001)]. The core region of PCFs can either be made of solid materials (as in conventional fibers) (Désévédavy et al., 2010; Feng et al., 2003; Millo et al., 2008; Russell, 2003; van Eijkelenborg et al., 2001) or remain hollow (Argyros et al., 2006; Désévédavy et al., 2010; Russell, 2003). Hollow-core PCFs allow for air guiding (thus exhibiting low nonlinearity and high damage threshold), as well as for liquid and gas sensing.

One of the most important features of PCFs is the high flexibility of their design. The possibility to control the geometrical and material parameters of PCFs allows for the fiber with specific optical parameters to be fabricated in accordance to particular applications (Poli, Cucinotta, & Selleri, 2007). Specifically, depending on fiber composition and its geometry, light guiding in a PCF can be governed by one of two principal mechanisms—namely by the mTIR or by the PBG mechanism. On the other hand, when microchannels are infiltrated with a high-index material, the

**Optofluidics, Sensors and Actuators in Microstructured Optical Fibers.** http://dx.doi.org/10.1016/B978-1-78242-329-4.00007-2

PCF can also be considered as a two-dimensional photonic lattice (with spatial periodic modulation of the refractive index in two dimensions), allowing (in specific cases) for discrete light propagation as typical for waveguide arrays and photonic lattices (Garanovich, Longhi, Sukhorukov, & Kivshar, 2012; Lederer et al., 2008).

Therefore, there is great interest among the scientific community in employing PCF in the field of optical sensing. The biggest advantage of PCFs is that by varying the size and location of the holes and core it is possible to change the fiber transmission spectrum, mode shape, nonlinearity, dispersion, and birefringence in an easy way not achievable in conventional optical fibers. The existence of air channels gives another possibility of light propagation in air or ability of their infiltration with gaseous or liquid materials. PCFs with their specific features have introduced a great number of new and improved applications in the fiber-optic sensing technology (Frazão, Santos, Araújo, & Ferreira, 2008).

To date, many magnetic fluid-based photonic devices, including magnetic field fiber sensors, have been demonstrated (Hu, Zhao, Li, Chen, & Lv, 2010; Zu, Chan, Lew, Jin, et al., 2012b). Recently, PCF has also been applied, making fiber sensors more adjustable and customizable. By infiltrating PCF with a magnetic fluid it is possible to implement magnetic field sensing (Thakur, Nalawade, Gupta, Kitture, & Kale, 2011; Zu, Chan, Gong, et al., 2012a; Zu, Chan, Lew, Hu, et al., 2012c).

Usually, a strong magnetic field is needed to study magnetic-field-induced changes in the optical properties of LCs, which are mainly due to relatively small anisotropy of diamagnetic susceptibility ($\Delta\chi$) of these materials. To lower the applied magnetic field requirement, ferronematic materials (i.e., nematic liquid crystals (NLCs) doped with ferro- or ferrimagnetic particles) have been proposed (Burylov & Raikher, 1995; Wang, Pu, Ji, & Yu, 2012).

The propagation properties of PCFs can be dynamically changed (including switching between different guiding mechanisms) by introducing gaseous, liquid, or solid media into the air channels (Du, Lu, & Wu, 2004; Larsen, Bjarklev, Hermann, & Broeng, 2003; Laudyn et al., 2008; Mathews, Farrell, & Semenova, 2011; Pinto & Lopez-Amo, 2012; Poli et al., 2007; Rosberg et al., 2007; Woliński, Szaniawska et al., 2006). This simple idea has been found to be very useful while broadening the applicability of PCFs [also in terms of sensing applications (Frazão et al., 2008; Pinto & Lopez-Amo, 2012)]. Specifically, the concept of using liquid crystals (LCs), resulting in a new type of active optical fiber, has gained a significant amount of scientific attention. These particular photonic structures are often referred to as photonic liquid crystal fibers (PLCFs) (Woliński et al., 2004), liquid crystal-photonic crystal fibers (LC-PCFs) (Du et al., 2004), or liquid crystal-photonic bandgap fibers (Larsen et al., 2003). LCs are anisotropic and, in most cases, their refractive indices are higher than those of silica glass. Furthermore, the refractive indices of LCs can be engineered and dynamically adjusted (Khoo, 2007). High tunability of optical properties of PLCFs (e.g., manifested by tuning the guiding mechanisms or changes in discrete propagation), achieved by applying external factors such as temperature, strain, pressure, and electric and magnetic fields, as well as by the light beam itself (e.g., when nonlinear effects in LCs are considered), enable various potential applications in the field of fiber optics and optical sensing.

Infiltrating the air holes with different materials allows for the creation of a special class of infused PCFs with enhanced optical properties. In this context, the application of LCs has gained particular attention, resulting in new highly tunable photonic structures (Larsen et al., 2003), or PLCFs (Woliński et al., 2004), in which light propagation conditions are determined by both an LC "guest" material and a PCF "host" structure. While the properties of effective PLCF structures depend heavily on LC molecular orientation, the techniques for efficient orientation of an LC within PCF holes have to be developed (Chychłowski et al., 2010). In this way PLCFs benefiting from the merger of passive PCF host structures with active LC guest materials are responsible for the diversity of new propagation, spectral, and polarization properties.

Light-guiding dynamics, including switching between both mechanisms of propagation, can be simply achieved in PLCFs thanks to the unique properties of an infiltrating LC. Due to high electro-, magneto-, and thermo-optic responses of LCs, their refractive indices may be relatively easily changed either by temperature or by external physical fields. In this context, thermal and electrical tuning along with unusual spectral and polarization properties of PLCFs have been studied over the last few years (Woliński, 2008; Woliński et al., 2008; Woliński, Ertman, et al., 2006; Woliński, Szaniawska, et al., 2006; Woliński, 2012). After the demonstration of tunable PBGs using thermo-optic tuning of LC (Woliński, Szaniawska, et al., 2006), one of the most spectacular phenomena was the successful realization of temperature-induced switching between the two mechanisms of light propagation (Figure 7.1).

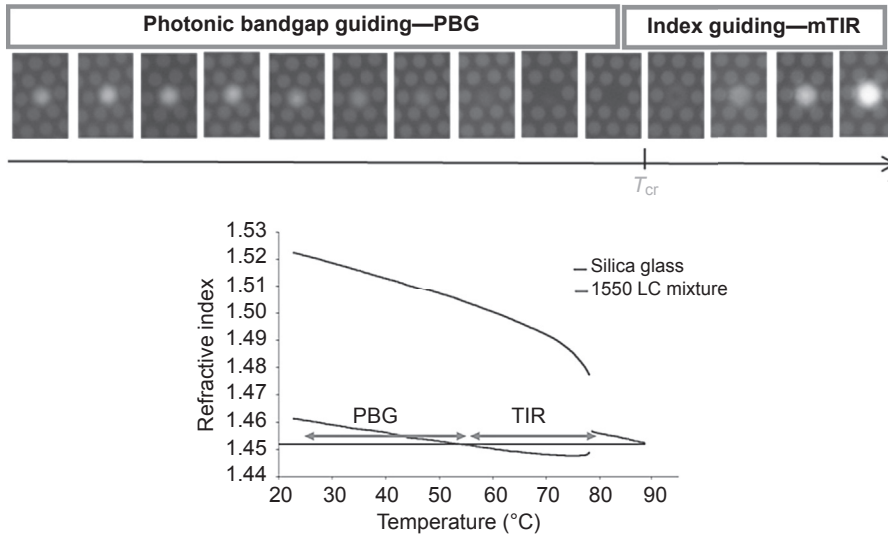


**Figure 7.1** Temperature-induced reversible PBG/mTIR propagation mechanisms switching in 1023 MCSU PCF infiltrated with 1550 LC; $T_{cr}$ corresponds to the temperature in which the refractive index of silica glass and the ordinary refractive index of the 1550 LC are equal, resulting in the lack of propagation (Woliński, Ertman, et al., 2006).

Tunability in highly birefringent solid-core PLCF has also been demonstrated (Haakestad et al., 2005). The latter achievement is related to polarization properties of the analyzed photonic structures that can be dynamically tuned via external fields-induced reorientation of LC molecules. Due to high sensitivity to external conditions, PLCFs were also used for switching and sensing applications (e.g., Woliński, 2008) when subjected to the influence of temperature, electric field, or hydrostatic pressure. Resultant devices can find potential applications as threshold sensors, in birefringence measurements, temperature and pressure sensors, all-optical multiparameter sensors, tunable filters, and all-fiber attenuators. In addition, research on high-index-glass-based PLCFs is also performed (Ertman et al., 2009). It allows for index-guiding propagation in a wide range of LC guest materials and enables continuous and repeatable broadband birefringence tuning, as well as continuous adjustment of polarization dependent losses.

While the refractive index of LCs can be tuned by external fields, it is possible to dynamically modify the guiding properties of PCFs. LC used as infiltration makes PCF sensitive to variations of external fields—and thus PLCFs can be successfully applied to fabricate all-fiber sensors for different variables such as temperature and magnetic and electric field strength.

The aim of this chapter is to demonstrate the most spectacular features of PLCFs that are used for dynamically controlled and tunable photonic devices that might be used for electromagnetic field sensing. The chapter is organized as follows: Section 7.2 presents an overview of LCs infiltrated microstructured optical fibers. Section 7.3 discusses selected issues related to electric field sensing with PLCFs. Apart from thermally, electrically, and magnetically induced modifications, it is possible to obtain optically induced changes in the refractive indices of LC due to optical nonlinearity. In the optical fiber sensing context, nonlinear optics may be applied either as a measurand sensitive to the interaction mechanism or as an optical signal processing technique to assist in configuring the optical signal used to probe a sensor. In Section 7.4, the results of theoretical analyses and experimental tests related to nonlinear discrete light propagation in PLCFs are presented. Considering the fiber as a matrix of mutually parallel waveguide channels, when optical nonlinearity is taken into account, spatial light localization and/or delocalization can be obtained, with the final scenario implemented by the optical power level and the molecular orientation of LC. In special cases, a discrete spatial soliton can be obtained, paving the way for all-optical sensing and switching to be developed in PLCFs. Final conclusions on future research directions (Section 7.5) summarizes the chapter.

## 7.2 LCs infiltrated microstructured optical fibers

### *7.2.1 Circular- and elliptical-core LCs fibers*

Hollow-core fibers were initially used as a guest medium for LC infiltration. Early experimental demonstration of light propagation in liquid crystal-core optical fibers (LCFs) obtained from hollow-core fibers (capillary tubes of radii between 5 and

30 μm) filled with low-birefringence NLCs were presented in the late 1990s (Woliński et al., 1998). In theory, the propagation properties of the $TE_{01}$ and $TM_{01}$ modes have been analyzed in the waveguide composed of a low-birefringence NLC acting as an optical fiber anisotropic core characterized by an index ellipsoid. It was shown that for smaller diameters of the LC-core, the $TE_{01}$ mode was guided while $TM_{01}$ was the leaky mode; however, for bigger diameters the differences between both modes decreased. The experimental results were compared with theoretical calculations in view of some typical optical fiber parameters, such as numerical aperture, suggesting a great potential of LC-core fibers for environmental sensing. Since the liquid crystalline-core fiber is characterized by an index ellipsoid, it can serve as a fiber with easily controlled birefringence. Consequently, external stresses modify the propagation properties of the liquid crystalline fiber due to reorientation of liquid crystalline molecules, resulting in sensing possibilities.

In order to control the polarization properties of the lowest-order LP modes within a LC-core optical fiber, an elliptical-core cylindrical waveguide was proposed and manufactured. The elliptical-core (4 × 18 μm, Figure 7.2) fiber was filled with a specially designed low-birefringence LC (Woliński & Szymańska, 2001) with homogeneous transverse orientation of the LC molecules. Since both refractive indices (ordinary and extraordinary) of the LC are thermally dependent, at a certain temperature range the elliptical-core LCF could propagate only the light polarized along the major *x*-axis of the ellipse. Consequently, the elliptical-core LCF exhibited single-polarization propagation due to the fact that the modes associated with polarization along the major *y*-axis of the ellipse are radiated out of the fiber (the LC ordinary refractive index was lower than the refractive index of silica cladding). The elliptical-core LCF is a unique example of a multimode single-polarization optical fiber.

To investigate polarization phenomena in elliptical-core LCFs, a set of extremely low-birefringence LC mixtures was synthesized at the Military University of Technology, Warsaw, Poland. The LC mixtures had their ordinary ($n_o$) refractive indices below the refractive index ($n = 1.4580$ at $\lambda = 583$ nm) of the fused silica in a certain

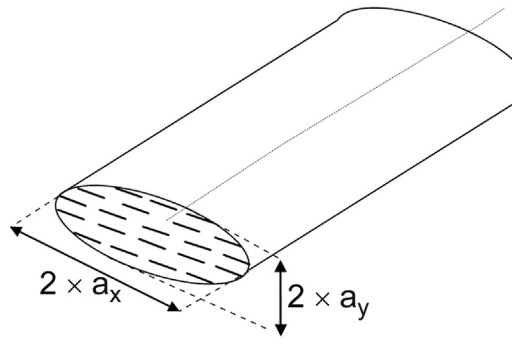


**Figure 7.2** LC molecules transversely oriented inside the elliptical-core liquid crystal fiber.

temperature range. The elliptical-core LC fibers were subjected to the influence of an external electric field, temperature, and hydrostatic pressure and the experimental polarization characteristics were obtained. The results indicated a possibility of single-polarization propagation within the LC fiber, suggesting a great potential of LC-core fibers for multiparameter sensing.

### 7.2.2 PLCFs based on silica glass, multicomponent glasses, and on polymer photonic crystal fibers

Due to the appearance of PCFs at the beginning of the twenty-first century, the concept of using LCs for PCFs infiltration resulted in a new type of active optical fibers, that is, PLCFs, gaining a significant amount of scientific attention. The main advantage of infiltrating solid-core PCFs with LCs is the limiting attenuation of LCFs due to the fact that the light is being propagated not in a lossy LC—as in the case of LC-core fibers—but in (silica) glass, whereas the LC could strongly influence and tune propagation parameters.

In order to study the optical properties of PLCFs, different types of both silica glass and high-index glass PCF structures have been used. Initially, isotropic PCFs based on silica glass fibers manufactured at the Maria Curie-Skłodowska University (MCSU) in Lublin, Poland were used along with commercially available host PCFs, for example, PM-1550-01 (polarization-maintaining) and LMA-25 PCF (produced by NKT Photonics, Denmark) (Figure 7.3). The third type of host fibers was a specially designed high-index PCF that was manufactured at the Institute of Electronic Materials Technology ITME, Warsaw, Poland. According to the ITME, the fiber denoted as PCF14(6) was made by the stack-and-draw technique from lead bismuthgallate (Pb-Bi-Ga)-based glass designated as PBG08, which is characterized by a high refractive index $\sim$1.95.

Recently more attention has been directed toward microstructured polymer optical fibers (mPOFs). Plastic materials like poly(methyl methacrylate) (PMMA, acrylic glass which has a refractive index of 1.49 at 588 nm) and also Zeonex (Cyclo Olefin 480R with a refractive index of 1.52 at 588 nm) are very interesting optical materials with high mechanical strength. Some of the key advantages of mPOFs are their high flexibility and greater resistance to mechanical stress than that of silica glass fibers.

Research activities on microstructured optical fibers made from polymers started between 2000 and 2010 as a consequence of PCF technology development. This originates mainly from the possibilities opened up by different material properties of polymers and silica glass. The microstructured Zeonex polymer optical fiber fabricated by Kiriama Pty. Ltd. in Sydney, Australia (Figure 7.4) has a large core to obtain good core-guiding propagation. An analogous type of PCF made of silica glass yielded to exceptionally low attenuation when infiltrated with an LC (Tefelska, Ertman, & Wolinski, 2012). A specific type of this optical material, namely 480R, is characterized by high mechanical strength, good light transmittance, low water and moisture absorption, good chemical, UV light, and heat resistance. As PCFs have periodic air holes, it is possible to fill some holes selectively, leaving the others empty. In this way, the creativity has no limits and a very

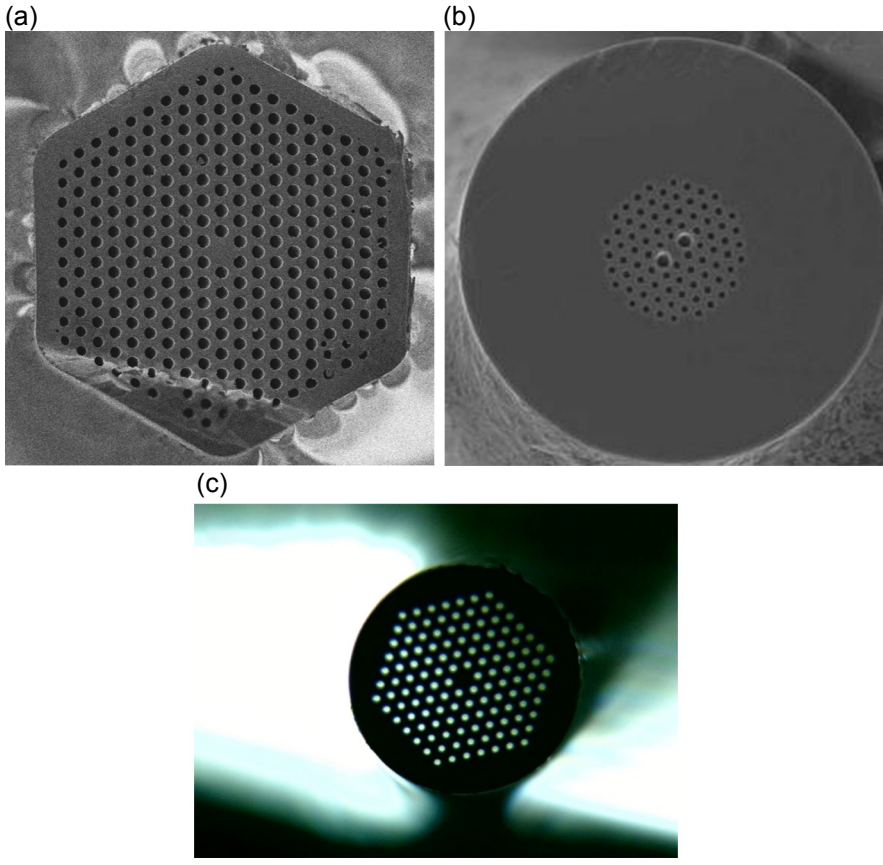


**Figure 7.3** PCFs produced by (a) MCSU Lublin: 1023, (b) NKT Photonics: PM-1550-01, and (c) LMA-25.

different configuration could be developed with the same fiber and the same infiltrated material, changing only the order and periodicity of the filled holes.

LC and polymer-based PCFs constitute a new solution based on unique properties of LCs and mPOFs, opening up new areas in innovative sensing and photonic devices applications (Woliński, Tefelska et al., 2014; Woliński, Mileńko et al., 2014). Compared with their silica-based microstructured fibers, it is easier to fabricate exotic mPOFs by extrusion or drilling at low temperature; their nonlinearity is potentially stronger, the range of available polymers that may be drawn is more diverse, and the biocompatibility of polymers is often better. LCs, due to their attractive properties, that is, high birefringence and high electro-optic and thermo-optic effects, are a very good candidate for mPOF infiltration to obtain tunable all-in-fiber innovative photonic devices for sensing and security applications.

One of the material candidates to be infiltrated inside PCFs is polydimethylsiloxane (Poudereux, Mileńko, Dybko, Otón, & Woliński, 2014). Although the primary field of

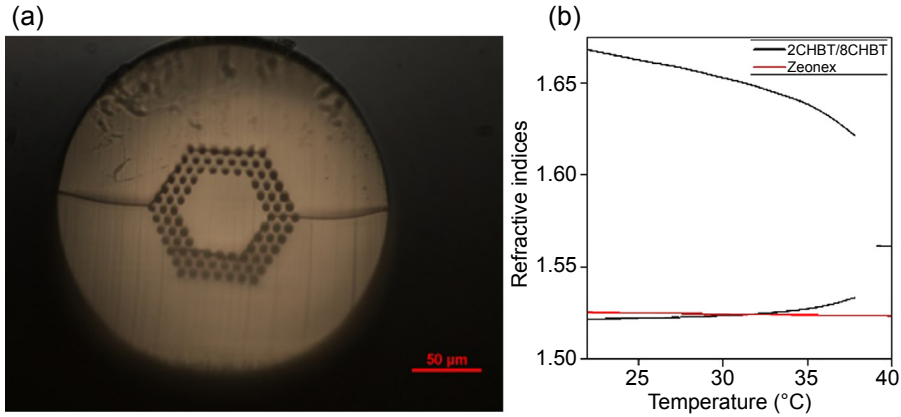


**Figure 7.4** (a) Large-core polymer (Zeonex) microstructured optical fiber manufactured by Kiriama Pty. Ltd. (Sydney, Australia): outer diameter 225 µm, core diameter $R = 55$ µm, holes diameter $d = 5.3-5.8$ µm, pitch $\Lambda = 8.0-8.4$ µm; (b) thermal dependences of Zeonex and 2CHBT/8CHBT LC mixture (Woliński, Mileńko et al., 2014).

application of this silicone elastomer is the embedding of electronic components, it is also used in micro- and nanotechnologies and especially as a basic material for optofluidic technologies.

### 7.2.3 LCs for PLCFs—low- and high-birefringence nematics, chiral nematics and blue phases, ferroelectric LCs

NLCs have only a long-range orientation order of the molecules' long axes, but their centers of gravity are randomly distributed. To fabricate PLCFs, NLCs with low-(LB), medium-(MB), and high-(HB) birefringence were used. NLCs of LB have been prepared in the form of prototype mixtures designated as 1800, 1110, 1550, and 1550A (obtained by doping the 1550 material with propyl propenylbicyclohexane). These LB NLC mixtures are especially interesting for silica glass fibers, as their ordinary refractive index in the specific temperature ranges is lower than that of silica glass. As NLCs with MB, the two commonly known nematics—5CB and 6CHBT—are a good solution. In addition, three experimental NLC mixtures with HB, abbreviated as 1294-1b, 1658A, and 1679, were used for PCFs infiltration. A special class of MB NLC, for example, 2CHBT/8CHBT LC mixture, was synthesized for polymer-based PCFs infiltration. All of these materials were synthesized at the Military University of Technology, Warsaw, Poland.

Host PCFs could also be filled with chiral NLCs (ChNLCs), that is, nematics doped with chiral compounds—optically active dopants (OADs), for example, cholesteric dopants, azo-compounds, dyes that can modify the switching and sensing possibilities of PLCFs. ChNLCs, due to their spatial periodicity, are characterized by unique optical properties such as selective Bragg reflection, circular dichroism, and optical activity. The selective Bragg reflection is a total reflection of circularly polarized light (having

the same handedness as the helical pitch of the chiral structure), occurring at the wavelength $\lambda = <n> P$ where $<n>$ is the mean refractive index and $P$ is the pitch (defined as the distance it takes for the director to rotate one full turn in the helix). A cholesteric (or chiral nematic) LC resembles a NLC in all physical properties except that the molecules tend to arrange themselves in a helical structure with the helical axis perpendicular to the director. The length over which the LC director rotates $2\pi$ is defined as helical pitch, which indicates the twist extent of LC molecules. An optical filtering by temperature-induced tuning of the PBGs in a PCF infiltrated with a cholesteric LC was proposed by Tefelska, Woliński, Dąbrowski, and Wójcik (2010).

Cholesteric LCs present a blue phase (BP) in a narrow range of temperatures. This chiral mesophase is formed by a three-dimensional fluid unity cell with cubic defects and has the property of being macroscopically isotropic but exhibiting Bragg reflections. Recently, it has been reported that the BP as a fiber waveguiding core is optically isotropic, polarization insensitive, and relatively low loss (Khoo, Hong, Zhao, Ma, & Lin, 2013), and due to the tightly wound director axis arrangement in the BP, the scattering loss associated with director axis fluctuations is largely reduced, allowing good transmission through several mm interaction lengths. BP LC is a promising material to infiltrate PCFs since LC molecules in this phase are self-aligned, without any alignment layer needed.

Also, chiral smectic C* ferroelectric LCs that are characterized by μs switching time in the electric field could be used for PCF infiltration (Budaszewski, Woliński, Geday, & Otón, 2010).

## 7.3 Electric field-induced effects

### 7.3.1 *Impact of an external electric field on LC molecular orientation inside microholes*

LC molecular alignment has a crucial impact on guiding properties of PLCFs. An external electric field can be used to reorient LC molecules, making PLCFs a good candidate for sensing. Usually, typical LC molecules tend to align parallel to the direction of an electric field, but for LCs with negative dielectric anisotropy ($\Delta\varepsilon < 0$) they tend to orient perpendicular to the direction of the field.

PLCF's response to the electric field relies on a few main factors, in particular: material and geometrical properties of a host fiber, physical properties of a guest LC, and initial orientation of the LC molecules inside the host fiber. The initial orientation of LC molecules is defined when a PLCF sample is being created and it depends on orientation techniques used at this stage. Although the filling process with LCs is always realized in a similar way (capillary action, sometimes assisted with pressure or vacuum) there are still differences in the pretreatment of microholes. In the simplest approach, fibers are filled without any additional preparation. Usually, in such cases planar alignment of LC molecules is observed, that is, molecules align parallel to the axis of the microcapillary (Larsen et al., 2003; Du et al., 2004; Woliński et al., 2005).

Planar alignment (Figure 7.5(a)) could be obtained without any aligning layers due to two main reasons—"orientation by flow" during infiltration and van der Waals interactions between molecules responsible for orientational order. However, in some cases a splay alignment of LC molecules (Figure 7.5(b)) can be observed, if the interaction between holes surface and LC molecules is strong enough to create homeotropic anchoring (Tartarini, Alkeskjold, Scolari, Bjarklev, & Bassi, 2007). Other alignments, as transverse or transverse-tilted (Figure 7.5(c−d)), are not possible to obtain without special aligning techniques. The most flexible method for LC molecules alignment control inside of fibers' microholes is based on so-called "photoalignment" (Chigrinov, Kozenkov, & Kwok, 2008). It has been recently demonstrated that with this technique it is possible to obtain a stable planar, transverse, or tilted alignment or even patterned textures with strictly defined sections consisting of two or more types of alignment (Chychłowski, Yaroshchuk, Kravchuk, & Woliński, 2012; Ertman, Srivastava, Chigrinov, Chychłowski, & Woliński, 2013).

The transverse alignment of LC molecules can also be obtained if PLCF is placed in a transverse electric field strong enough to reorient the majority of molecules (assuming that LC has positive dielectric anisotropy). Similarly, if the field is directed at some angle to the axis of PLCF, the expected alignment should be close to transverse-tilted (Figure 7.5(d)). However, if the intensity of the field is not strong enough to ensure total reorientation, the resulting alignment would be somewhere between the initial alignment and that expected at strong fields. It is possible to use numerical models to predict the alignment of LC molecules for any value of the electric field, but such calculations are quite complicated. There is quite a long list of factors that should be included in such rigorous modeling of LC reorientation, including the definition of initial alignment with well estimated anchoring energy, all complex physical properties of modeled LCs, and finally the nonuniformity of the electric field and its changes with the accruing reorientation. Although such calculations are possible (James, Willman, Fernandez, & Day, 2006), in the case of PLCF the results obtained by using such "expansive" rigorous calculations are

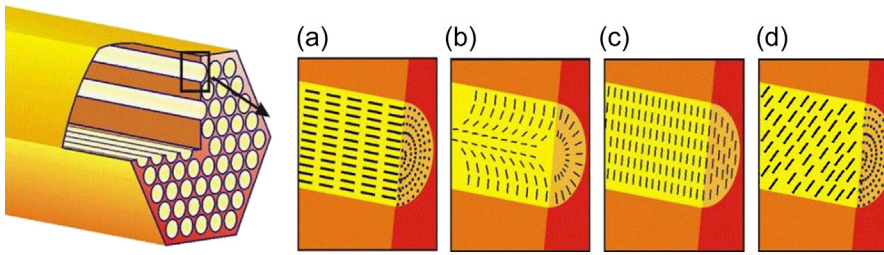


**Figure 7.5** Typical LC molecules alignment in a microcapillary: (a) planar (the most common alignment obtained even without any pretreatment due to so-called "flow-induced orientation"); (b) splay (also known as axial or escaped radial); (c) transverse (such an alignment can be induced at the manufacturing level but is also possible to obtain with a strong electric field applied perpendicularly to the fiber axis, assuming positive dielectric anisotropy of the LC); (d) transverse-tilted (could be induced by special aligning layers or by a strong electric field directed at some angle to the fiber axis).

in good agreement with the modeling in which simplified reorientation models are applied (Ertman et al., 2010). In other words, to obtain fast results, the simplest approach is to assume some well-defined initial alignment of molecules (with a known or possible to define permittivity tensor), some well-defined expected alignment at high intensities of the electric field, and, if needed, also consider some intermediate, easy-to-mode-numerically alignments. With such an approach it is easy to predict tuning ranges or in the case of sensing applications it is possible to predict the sensing range of a modeled fiber.

### 7.3.2 Selected electrode configurations used to steer PLCFs

In order to characterize the response of PLCFs to the electric field, there should be a way to apply various intensities (and directions) of the electric field to the sample. The simplest approach is to place a PLCF between two flat electrodes (Figure 7.6(a)), so the electric field would be directed perpendicularly to the fiber axis and its value can easily be controlled by changing the voltage applied to the electrodes. However, in some cases such steering is not sufficient; for example, if the initial alignment of the LC molecules inside the holes is transverse, the response to the transverse electric field would be changing if the angle between the initial orientation direction of molecules and the direction of the field were varied. The same situation could be considered in the case of a birefringent PLCF based on PCFs selectively filled with LCs.

In this context, more complicated sets of electrodes should be used to allow dynamic changes not only in the intensity but also in the direction of the electric field. The steering with two sets of orthogonal electrodes (Figure 7.6(b−c)) allows for an easy change of direction in four different field orientations: 0°, 90°, +45°, and −45°, taking into account the fact that not only opposite electrodes could be used but also electrodes could be paired (Ertman & Woliński, 2008).

More complex steering could be realized with the six electrode setup (Figure 7.6(d)): depending on wiring, six different directions (0°, 30°, 60°, 90°, 120°, and 150°) of an electric field can be easily obtained by using a single source of voltage. However, additional calculations proved that if two pairs of opposite electrodes are independently tuned, the electric field can be adjusted in any direction (Ertman & Woliński, 2014). In addition to being useful for characterizing PLCFs samples in the context of sensing applications, such complicated electrode configurations are also predominantly designed to build effectively tunable devices based on the PLCFs in which the axes of birefringence or polarization dependent losses could be easily redefined.

### 7.3.3 Impact of an external electric field on the guiding properties of PLCFs

It is evident that application of an external electric field results in reorientation of LC molecules in the direction of the electric field, assuming positive LC dielectric anisotropy ($\Delta\varepsilon > 0$). The impact of such reorientation on the guiding properties of a PLCF is

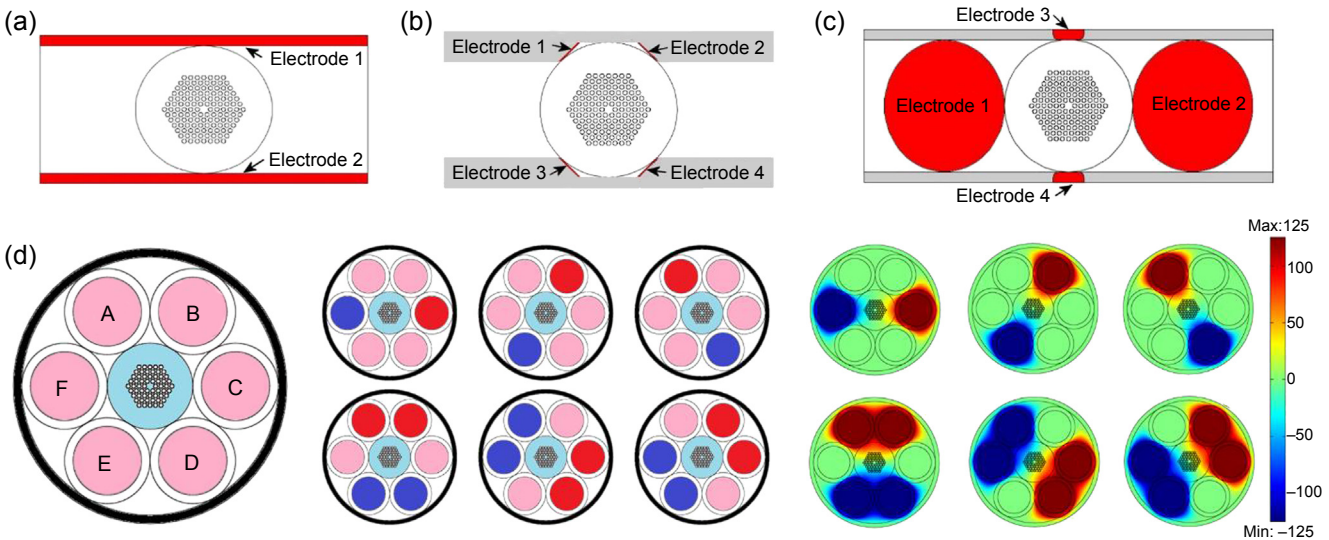


**Figure 7.6** Selected types of electrodes that could be used to apply an electric field to PLCFs: (a) two flat parallel electrodes; (b) four electrode setup based on the v-groove assembly; (c) setup with two short electrodes embedded in the two parallel dielectric plates and with two metal rods placed on the both sides of the fiber; (d) the six electrode setup—the PLCF is surrounded by six microwires with the same diameters as the fiber (it should allow for easy stacking); the six possible steering scenarios and resulting distribution of the electric potential are also included.
(a–c): Ertman, S., & Woliński, T. R. (2008). Electric field control of liquid crystal infiltrated photonic crystal fibers by using various electrode configurations. *Proceedings of SPIE 7120*, 712004. (d): Ertman, S., & Woliński, T.R. (2014). Six microelectrodes assembly for tunable optical fibers. *Proceedings of SPIE 9157*, 915735.

strongly dependent on the relation between the refractive index of the core of a host fiber ($n_{PCF}$) and the refractive indices of a crystal (ordinary, $n_{LCo}$ and extraordinary, $n_{LCe}$). Generally, by taking into account the relation between these indices, PLCFs could be divided into three classes: low index-core PLCFs (if $n_{PCF} < n_{LCo} < n_{LCe}$), medium index-core PLCFs ($n_{LCo} < n_{PCF} < n_{LCe}$), and high index-core PLCFs ($n_{LCo} < n_{LCe} < n_{PCF}$). The impact of an electric field on the properties of all three types of PLCFs is substantially different.

In the case of low index-core PCLFs only PBG guiding is possible, no matter what type of alignment of molecules is obtained inside microholes. Such a situation is typical for the majority of PLCFs based on PCFs made of silica glass, since the refractive indices of most LCs are higher than the index of silica glass. The reorientation of LC molecules would result in a change of the effective refractive index of inclusions, and thus changes in the transmission spectra would be observed. When reorientation starts, in practice increased LC scattering is usually observed along with no continuous change of the transmission bands. However, in most cases of intermediate intensities of the electric field, attenuation tends to increase (Figure 7.7(a)), and for high intensities, a new band of propagation appears (Figure 7.7(b)). Such behavior could be directly utilized to build intensity-based sensors of electric field intensity. Moreover, relying on a single sample, the response of the sensor could be adjusted by changing the operating wavelength (Figure 7.7(c)).

Medium index-core PLCFs are based on solid-core PCFs made of glass, whose refractive index is below an extraordinary and above an ordinary refractive index of LC ($n_{LCo} < n_{PCF} < n_{LCe}$). In such fibers the guiding properties strongly depend on the alignment of LC molecules and polarization of the light. In particular, if all molecules are parallel to the fiber axis (planar alignment) both polarizations are index guided and the fiber is nonbirefingent (assuming that hexagonal symmetry of the PCF is maintained). On the contrary, if all molecules are perpendicular to the fiber axis, one polarization is index guided, since for orthogonal polarization only selected wavelengths can be guided by the PBG effect. Such fibers have been proven to be an excellent candidate for building effectively tunable all in-fiber polarizers whose polarization dependent attenuation is close to zero in the absence of an electric field and could be increased up to 40 dB/10 cm (Ertman et al., 2012). In the context of sensing applications, medium index-core PLCFs could be very interesting since they are strongly sensitive to any changes of molecular alignment. However, it should be remembered that in most cases the reorientation of molecules is connected with a simultaneous increase in birefringence and polarization dependent losses.

The last class of the proposed division consists of high index-core PLCFs, in which the refractive index of a solid-core host-PCF is higher than both refractive indices of an LC ($n_{LCo} < n_{LCe} < n_{PCF}$). In such a case the refractive index of the core is always higher than that of the cladding. It means that conditions for index guiding are always fulfilled in such fibers (no matter how the LC molecules are aligned). It is a very interesting feature since index-guiding modes are strongly localized in the core and their confinement losses are smaller than those observed in the PBG modes. Moreover, it has been experimentally confirmed that the attenuation of index-guiding PLCFs is much lower than in the case of PBG guiding,

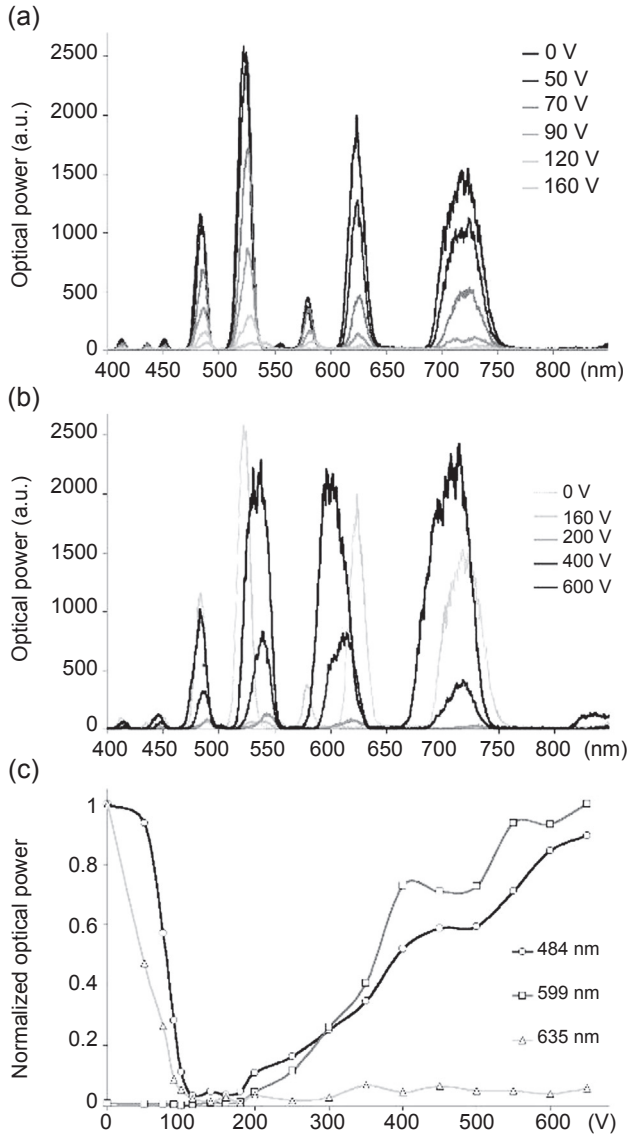


**Figure 7.7** Impact of an electric field on the guiding properties of PCF made of silica filled with a 1294-1b nematic liquid crystal (Ertman et al., 2005); (a) initially, an increase of electric field intensity causes increased scattering and a drop of optical power guided in the fiber; (b) for higher intensities of an electric field, a new band of propagation appears; (c) in the context of intensity-based sensors of an electric field, the response could be tailored by choosing the operating wavelength.

Ertman, S., Wolinski, T.R., Szaniawska, K., Lesiak, P., Domanski, A.W., Dabrowski, R., Nowinowski-Kruszelnicki, E., & Wojcik, J. (2005). Influence of electrical field on light propagation in microstructured liquid crystal fibers. *Proceedings of SPIE 5950*, 326−332.

because the impact of light scattering by LC molecules is strongly reduced (according to numerical simulations, more than 99% of optical power is usually guided in glass). Although reorientation of molecules with an electric field will not cause any significant changes of attenuation, it is possible to obtain effective broadband tuning of birefringence. A continuous change of birefringence from 0 to $2 \times 10^{-4}$ has recently been demonstrated (Ertman et al., 2009). Such fibers can find application as tunable phase shifters, tunable retarders, or even for building all in-fiber polarization controllers. Moreover, such fibers can also be used to build polarimetric sensors of an electric field (Mathews et al., 2011). The advantage of high index-core PLCFs in the context of electric field sensing is that their losses are very low, so in practice it could be possible to use a number of sensing parts in a single optical fiber link, and the analysis of a phase change in the output could provide information about the average electric field in the vicinity of sensing parts. Moreover, by using two perpendicular sets of such links (in the form of a matrix), it could be possible to determine the map of electric field intensity distribution over a specified area.

### 7.3.4 Detection of an electric field direction with PLCF-based sensors

The electric field sensing with typical PLCFs described above has one significant limitation—the sensor could not detect the direction of an electric field but only its intensity. Moreover, this detection is correct only if the direction of the field is perpendicular to the fiber axis. It could be imagined that if the direction of the field was parallel to the initial orientation of the LC molecules, then there would be no response of the fiber since molecules would not change their orientation, no matter how high the intensity of the field would be. The most straightforward solution for this issue is to use a set of three orthogonally oriented sensors, each of which would be measuring one component of an electric field intensity vector.

However, it must be mentioned that it is possible to build PLCFs which could be more practical in detecting electric field direction. For example, if a sensor was based on the PLCF in which the initial alignment of LC molecules is perpendicular to the fiber axis, its response would be highest only if the electric field would be oriented not only perpendicularly to the fiber axis but also perpendicularly to the initial direction of LC molecules alignment. Two such fibers mounted in that way, where the initial orientation of molecules in both fibers would be orthogonal, would allow for two-dimensional detection of field direction. A third dimension could be added, for example, by using PLCFs based on an LC with negative dielectric anisotropy and initial planar orientation. For such a fiber, if the electric field was directed along the fiber axis, the molecules would tend to change their alignment from planar to transverse. As a result, the dimensional detection of electric field direction (and intensity) could be realized by three parallel fibers, which is more practical than using three mutually perpendicular fibers (in the context of size and scalability).

The detection of electric field direction is also possible by using selectively filled highly birefringent PLCFs whose response is also strongly dependent on the direction of the field in respect to the birefringence axis of the fiber (Mileńko et al., 2013, 2014).

## 7.4 Optical field-induced effects

### 7.4.1 Discrete light propagation in two-dimensional waveguide arrays

Discrete light propagation, typical for photonic structures with a periodically modulated (in space) refractive index, takes place when the light is confined in weakly guiding waveguide channels and switching between them occurs via an evanescing coupling. It can be considered as light propagation in a multicore directional coupler and can be studied in both planar systems (i.e., periodic in one transverse direction) and in two-dimensional structures. Discrete photonic systems (of different dimensionality) have been practically achieved in various materials, giving rise to various phenomena which are not accessible in homogeneous bulk media. An overview of theoretical and experimental developments in the field of discrete light propagation can be found in Garanovich et al. (2012) and Lederer et al. (2008), with particular attention devoted to a rich family of discrete solitons (Lederer et al., 2008). To date, two-dimensional waveguide lattices have been demonstrated in photorefractive materials, cubic and hexagonal waveguide arrays written with fs-laser pulses in fused silica, and in multicore optical fibers. Most of these solutions require specialized fabrication techniques, high energy densities needed for lattice fabrication, or do not offer dynamic tunability.

Recently, the concept of discrete light propagation in two-dimensional periodic optical systems has also been transferred to the fluid-filled microstructured fibers which are ideally suited to be combined with liquid media. Hollow sections of PCFs can be easily infiltrated with the use of capillary forces or high pressure. More complicated patterns can be obtained by selective infiltration with the use of a needle method or a direct laser writing technique (Vieweg et al., 2010). Thanks to a large variety of host (PCF) structures and guest materials (commercially available or customized) it is possible to obtain PCF-based waveguide matrices with almost arbitrary coupling parameters (and also with tunable features). In this way, completely (Laudyn et al., 2008; Rosberg et al., 2007) and selectively (Vieweg et al., 2010, 2011, 2012) fluid-infiltrated PCFs have been adopted to the needs of discrete optics, with the main advantage stemming from the well-established fabrication process. The latter allows for a structural regularity of periodic photonic structures to be easily accomplished. Moreover, relatively long propagation distances (when compared to few millimeters-long arrays and lattices etched in semiconductors or optically induced in photorefractive and few centimeters-long waveguide arrays in silica) which can be achieved in PCF-based

photonic systems allow for a wide range of different discrete propagation effects to be obtained, including spatiotemporal nonlinear ones. In particular, beam self-defocusing at high optical powers has been demonstrated in a standard PCF infiltrated with a high-index nonlinear liquid by employing thermal nonlinearity (Rosberg et al., 2007). Moreover, spatial solitons in optofluidic systems in the form of selectively fluid-filled PCFs and relying on the ultrafast Kerr nonlinearity in highly nonlinear liquids have been also shown (Vieweg et al., 2012).

PLCF-based waveguide matrices represent a special group in the class of fluid-infiltrated PCFs. The advantage in their application stems from: (1) the possibility of dynamical changes in light propagation (e.g., by applied fields and factors), allowing for adjusting diffraction and dispersion properties and resulting in optical devices (including sensors) with tunable characteristics and (2) enhanced nonlinear properties. Specifically, nonlinear effects (related to reorientational and thermal nonlinearities in LCs) may result in dramatic changes in propagation characteristics (e.g., when discrete solitons are observed, as described below).

### 7.4.2 Optical nonlinearities in LCs

Apart from thermally or electrically/magnetically induced modifications, it is possible to obtain optically induced changes of LCs refractive indices thanks to optical nonlinearity (Khoo, 2007). In the case of LCs both positive ($n_2 > 0$) and negative ($n_2 < 0$), Kerr-type nonlinearity (with refractive index changing linearly with light intensity I according to the relation: $n = n_L + n_2 I$, where $n_L$ is the linear refractive index and $n_2$ is the optical Kerr constant) occurs due to molecular reorientation and thermal effects, respectively. The electronic contribution to the third-order nonlinear effects in LCs can be neglected as it is of the same order of magnitude as in ordinary liquids. While the thermal effects (even if still significant, $|n_2| \approx 10^{-5}$ cm$^2$/W in nematic phase) are similar to those observed in other materials, the reorientational ones (arising from the collective motion of molecules) are unique, characteristic of the liquid crystalline phase. Not only does the reorientational nonlinearity induce extremely large intensity dependent changes in refractive indices at relatively low power levels, but such changes can be modified by external fields. The reorientational nonlinearity of LCs turns out to be many orders of magnitude greater than the conventional Kerr effect in dielectric media. The optical Kerr constant ($n_2$) obtained due to appreciable light-induced molecular reorientation typically takes the values up to $10^{-3}$ cm$^2$/W (Khoo, 2007) and can be significantly increased (by six orders of magnitudes) by suitable dopants (Khoo, 2011).

### 7.4.3 Influence of reorientational and thermal nonlinearities on discrete light propagation in PLCFs

#### 7.4.3.1 PLCF sample tested

The PCF to be tested (shown in Figure 7.8(a)) has been manufactured at the Marie Curie-Skłodowska University in Lublin, Poland. Its cladding region consists of air

channels with the diameter $d = 4.4$ μm, arranged in a hexagonal pattern with an interhole distance (pitch) $\Lambda = 5.9$ μm. This particular geometry (with no defect in a periodic structure, contrary to typical solid-core PCFs) has been chosen to study discrete light propagation in conditions analogous to those in uniform waveguide arrays and matrices (Garanovich et al., 2012; Lederer et al., 2008). Being typically nematic, 6CHBT (also known as 6CPS) has been selected as a liquid crystalline material for infiltration.

As already mentioned, when introducing an LC into the air channels of a PCF, different molecular arrangements can be obtained [e.g., due to suitable orientation treatment (Chychłowski et al., 2010; Ertman et al., 2007) or/and under the influence of external fields (Du et al., 2004)] with three distinctive cases schematically shown in Figure 7.1(b). Such arrangements determine the values of LC refractive indices to be considered (for a particular state of polarization). When the molecular orientation of an LC after infiltration is random and not predictable, an average refractive index of an LC ($\tilde{n}$) can be assumed (e.g., for calculations).

### 7.4.3.2 Theoretical predictions

For numerical simulations, a finite difference (FD) scheme has been applied for a beam propagation method (BPM) with a square mesh grid. The disadvantage of a typical FD-BPM in this case is the impossibility of structure geometry to be precisely

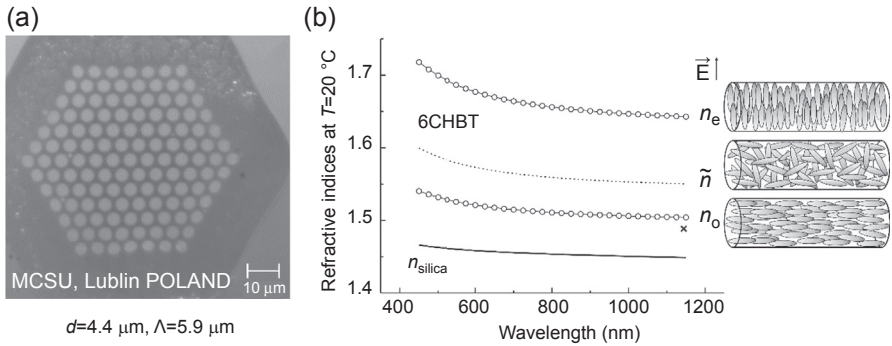


**Figure 7.8** (a) Photo of a hollow-core PCF manufactured at the Marie Curie-Skłodowska University (MCSU), Lublin. The diameters of the air channels and interhole distance are equal to 4.4 and 5.9 μm, respectively, which gives the diameter-to-pitch ratio of 0.746. (b) The refractive indices of the 6CHBT LC at a temperature of 20 °C (Baran, Raszewski, Dabrowski, Kedzierski, & Rutkowska, 1985; Schirmer et al., 1997), where $n_o$ is the ordinary and $n_e$ is the extraordinary refractive index in a nematic phase and $n_{iso}$ is the refractive index in an isotropic phase. The average value of the refractive index in a nematic phase, given by the following formula: $\tilde{n} = 2n_o/3 + n_e/3$ (dashed line), can be considered when random orientation of LCs within a PCF structure is assumed. The refractive index of silica ($n_{silica}$) at 20 °C (Medhat, El-Zaiat, Radi, & Omar, 2002) is also shown for comparison (solid line).

represented by points placed in the nods of a mesh grid. The application of a square mesh for the structure with hexagonal symmetry results in numerical size, shape, and distances which are changing between individual air channels after the digitalization process. It causes the digital representation of a periodic structure not to consist of identical circular elements. The numerical representation of refractive index distribution in a PCF cross-section can be improved when: (1) triangular grid mesh (Rutkowska, Rutkowski, Chychłowski, & Woliński, 2008), (2) radial coordinates (Rutkowska et al., 2007), (3) index-averaging technique (Zhu & Brown, 2002), or (4) the FD-BPM with the exact boundary conditions (EBCs) (Jung & Karpierz, 2012a,b) are implemented. In the latter case, the FD semivectorial scheme is applied together with the boundary conditions derived from the Maxwell equations, but suitable corrections implemented make calculations more demanding and time consuming.

In our simulations, with the results shown in Figures 7.9–7.11, the numerical problem (with a scalar and quasivectorial FD-BPM with EBCs) has been simplified by the assumption of homogenous distribution of the refractive index (taken as $n_o$ or $n_e$ for totally oriented and $\tilde{n}$ for completely disoriented molecules of LC) inside liquid crystalline rods. The grid period of the square mesh was equal to 0.1 μm and the calculation window set to (106 × 106) $\mu m^2$ in order to enclose the whole PLCF structure. Please note that only the central part of the calculation window (limited to the area of (60 × 60) $\mu m^2$) is shown in the graphs below.

Figure 7.9 (a) shows light propagation in a linear regime when the Gaussian beam with an initial width of 5 μm is launched into the center of a periodic structure. While the values of the refractive indices ($n_o$, $n$, and $n_e$) of the 6CHBT LC are higher than those of silica ($n_{silica}$), discrete propagation (resulting from light guidance in the LC cores) is obtained (based, in principle, on the index-guiding mechanism). The light is coupling and spreading into an increasing number of LC waveguide channels, broadening its spatial profile. The efficiency of the coupling between liquid crystalline waveguide cores strongly depends on the wavelength and index contrast. In principle, for a defined PLCF structure, the shorter the wavelength, the longer the coupling distance. In addition, by increasing the index contrast it is also possible to reduce light transfer between waveguide channels and to narrow the angular divergence of a light beam. In particular, when an extraordinary refractive index of 6CHBT LC is considered, a 5 μm Gaussian beam launched to the center of a PLCF remains confined within the first ring of waveguide channels. Moreover, in this case the index contrast is so high that higher-order modes are induced in the liquid crystalline waveguide channels. On the other hand, at longer wavelengths (and for a relatively low index contrast) the coupling distance is decreasing, and thus a strongly diffracting beam reaches the boundaries of the hollow cladding. Due to the limited area of a periodic structure the light passes into and out from the central waveguide channel (i.e., the light beam alternately broadens and narrows in space). In this case, the symmetry is broken due to boundary effects. The magnitude of discrete diffraction depends on the initial width of a Gaussian beam (see e.g., Figure 7.9(b)). As one can see, the more waveguide channels are illuminated at the input facet, the less visible are the features and effects characteristics for discrete diffraction (see e.g., the last two rows in Figure 7.9(b)).

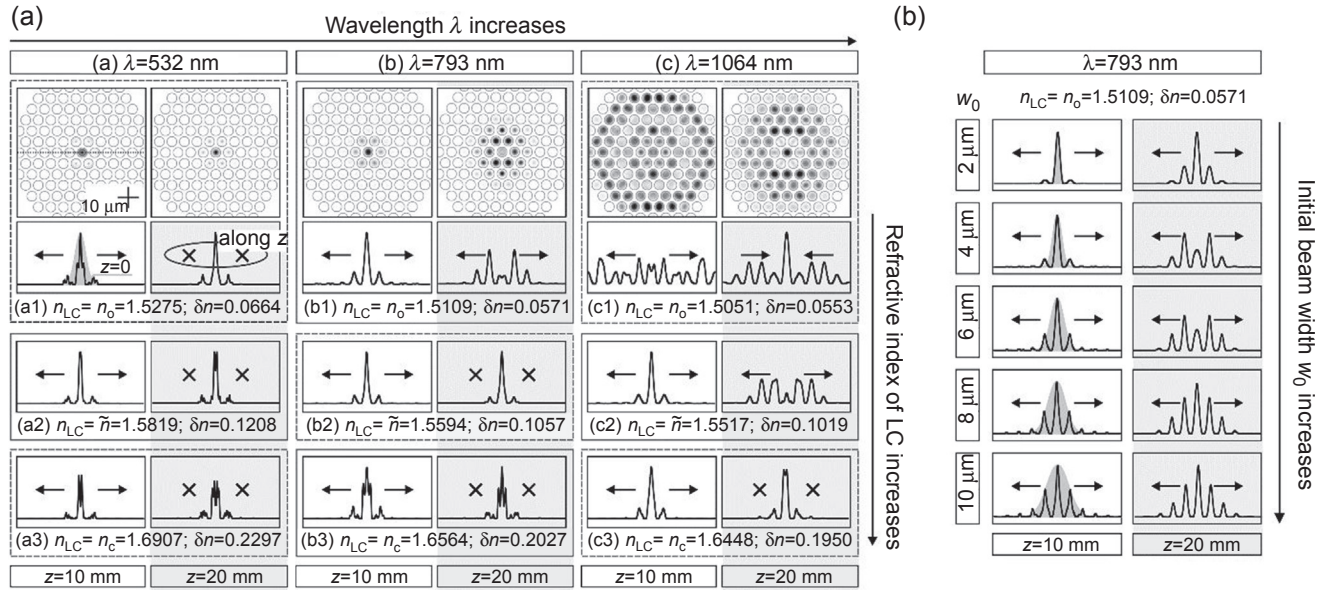


**Figure 7.9** (a) Numerical results showing the discrete diffraction of a low-power Gaussian beam with an initial width of 5 μm launched into the central waveguide channel for a wavelength of 532 nm (a), 793 nm (b), and 1064 nm (c). Please note that the color-inverted scale has been applied for the intensity profiles (i.e., darker colors correspond to higher light intensity). In addition, normalized intensity beam transverse profiles (along the central horizontal line marked in dashed) are also shown at specific propagation distance (i.e., for 10 and 20 mm). The black arrows and crosses used in the latter graphs indicate if the beam width extends or not in space on the way of propagation. The refractive indices of 6CHBT LC and index contrast (between LC and silica) $\delta n$ taken for calculations are specified in each panel. (b) Numerical results showing discrete diffraction of the Gaussian beams with different initial widths $w_0$ for a wavelength of 793 nm and for the PLCF with fixed optical parameters.

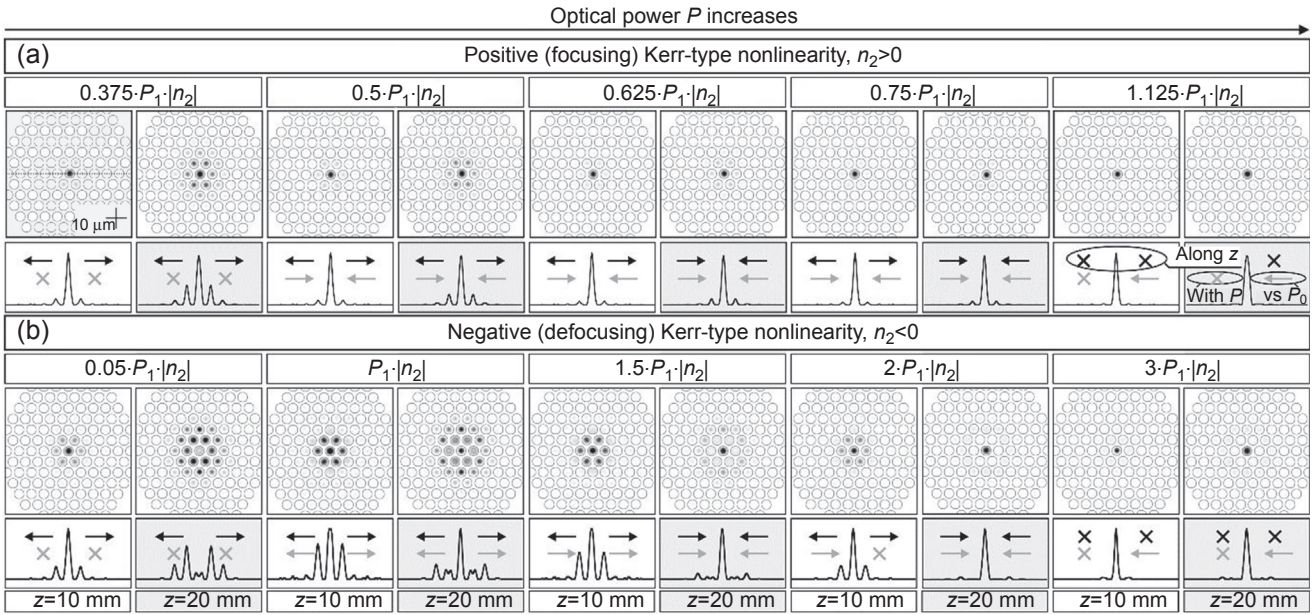


**Figure 7.10** (a–b) Numerical results showing spatial light intensity distribution (after 10- and 20-mm propagation) as a function of the optical power $P$. (a) When positive/focusing Kerr-type nonlinearity is considered ($n_2 > 0$), higher optical power results in stronger spatial localization of the beam (with the possibility of discrete spatial soliton generation). (b) For negative/defocusing Kerr-type nonlinearity ($n_2 < 0$) light delocalization and then localization are observed for increasing power, leading eventually to discrete soliton formation. In the present notation $|n_2|P_1 = 7.85 \cdot 10^{-4}$ μm$^2$. The black signs (arrows and crosses) used in the graphs with beam intensity profiles show how the beam width changes on the way of propagation (for a fixed value of power), while the gray ones indicate (for the specific power and for fixed propagation distance of 10 or 20 mm) how the beam width varies with power (sign on the left-hand side) and how it changes with respect to the linear case (sign on the right-hand side).

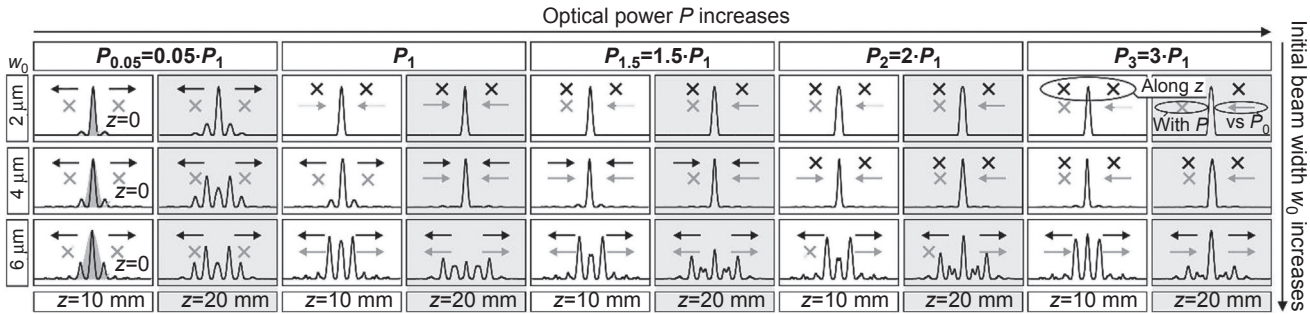


**Figure 7.11** Numerical results obtained for the Gaussian beams with different initial widths showing how discrete light propagation changes with optical power (with the assumption of negative/defocusing Kerr-type nonlinearity). Marks indicating how the beam width changes with propagation distance (black) and with optical power are used in an analogous way, as in Figure 7.3.

The results shown in Figure 7.9 indicate that for the fixed geometry of a PCF (i.e., for a specific size and spatial location of air channels) the coupling strength between adjacent LC waveguide channels (and thus the intensity profile at the output facet of a fiber with a fixed length) can be easily modified by changing beam parameters (including wavelength, initial width, and state of polarization) and refractive indices of LCs (Brzdąkiewicz, Laudyn, Karpierz, Woliński, & Wójcik, 2006). The latter can be tuned not only thermally and by external fields applied (forcing the molecules to be aligned along a specific direction) but also (particularly important in the context of this section) by nonlinear effects taking place when the optical power of a propagating beam is high enough, leading to the potential formation of sensors, with the aforementioned fields and factors used as measurands.

Going from a linear to a nonlinear regime (when the power of a propagating beam increases), the refractive index of illuminated liquid crystalline waveguide cores can be modified by nonlinear effects. It means that the optical parameters of a PLCF structure and its guiding features can be affected by the propagating beam itself. As a result, discrete diffraction can be effectively counteracted by power-induced detuning of waveguide channel(s) from the rest of the matrix due to the differences in propagation constants of the adjacent liquid crystalline cores. In other words, in a nonlinear regime light induces a defect in the periodic structure, thus changing its guiding characteristics.

In the case of focusing Kerr-type nonlinearity (i.e., for $n_2 > 0$ what is for reorientational nonlinearity in LCs), when optical power increases, higher index contrast between LC cores and silica cladding results in stronger guiding in the region of liquid crystalline cores and thus the light beam profile narrows in space (as shown in Figure 7.10(a)). Finally, when the power of an input beam is high enough, nonlinearity completely balances diffraction and the light beam propagates being transversely localized in a limited region of the waveguide matrix or, for high enough excitations, in a single (central) waveguide channel. Such a beam, which propagates maintaining an invariant transverse profile (here for $1.125 \cdot n_2 P_1 = 8.83 \cdot 10^{-4}$ μm$^2$ in the case of focusing Kerr-type nonlinearity), is called a discrete spatial soliton (Lederer et al., 2008). The way to obtain discrete spatial soliton is slightly different in the case of defocusing (negative) Kerr-type nonlinearity (which is thermal nonlinearity in LCs). Initially, when optical power gets higher, a decrease in the index contrast between liquid crystalline waveguide cores and silica glass results in a shorter coupling distance and thus in wider broadening of the beam in space. This spatial light delocalization is then followed by spatial light localization (specifically manifested by the central peak formed by the light beam focused in a single LC channel) which occurs when the power constantly increases. It is caused by the propagation constant of the central liquid crystalline waveguide channel being completely different from the others. The light localization observed may eventually lead (if the power is high enough) to a discrete soliton (also referred to as a nonlinear defect mode) with its propagation parameters completely decoupled from the rest of the waveguide matrix—predicted here for $|n_2 P| > 2.35 \cdot 10^{-3}$ μm$^2$ for $w_0 = 5$ μm (see the last two columns in Figure 7.10(b)).

In Figure 7.11, a deviation is considered in spatial broadening for the beams characterized by different initial widths (with numerical analyses limited to the case of thermal optical nonlinearity in LCs, dominant as suggested by experimental observations). As one can see, the narrower the beam at the input, the lower the optical power required for each phase in the delocalization and localization processes (characteristic for negative Kerr-type nonlinearity) described above.

### 7.4.3.3 Experimental results

The above numerical results, suggesting that the strength of an electromagnetic field can be monitored with use of a PLCF, have been confirmed experimentally. Suitable measurements have been performed (with the use of a Ti:Sapphire ($\lambda = 793$ nm) laser) in 10- and 20-mm-long pieces of PCF infiltrated with 6CHBT. The description of the experimental setup, in which the light is coupled to and decoupled from a PLCF with the use of long working-distance microscope objectives, can be found in (Rutkowska, Laudyn, & Jung, 2012). For several samples tested in the experiment, a special procedure based on the photoalignment (with use of SE-130 polymer) (Chychłowski et al., 2010) allowed the introduction of planar anchoring on capillaries walls, forcing specific orientation of LC molecules inside a PCF (with ordinary refractive index of LC considered for any state of light polarization). What is important from an experimental point of view is that the defined orientation of the LC molecules inside the air channels allows for the reduction of transmission losses, typically taking place in PLCFs as an effect of light scattering, which is particularly strong in a disordered nematic phase. In addition, it has to be underlined that owning to their quasicrystalline and nonuniform nature, LCs introduce a further challenge in the experimental observation of discrete diffraction in PLCFs. Specifically, even small changes in the homogeneity of infiltration (e.g., when air channels are not fully infiltrated or different orientation occurs of liquid crystalline molecules within succeeding air channels) result in a heterogeneous array formed by waveguides with different optical parameters, which in turn may lead to deterioration of the coupling mechanism.

The measurements, whose results are shown in Figure 7.12, have been performed at room temperature and for varying optical power of the pump beam. As one can see, in principle for low-power excitation, the light beam coupled into a single waveguide channel is switching into the surrounding liquid crystalline rods. Beam broadening in the form of discrete diffraction is observed, with the coupling length depending on the index contrast, wavelength, and the initial beam width. For a small input spot size and short wavelength (corresponding to a long coupling distance) the beam is confined in the central part of the matrix despite the optical power level. The experimental data acquired with the use of light beam from a Ti:Sapphire laser show the power-dependence of a beam profile at the output facet of a PLCF and confirm the influence of defocusing nonlinearity on the PLCF under test (see Figure 7.12(a–d)). In the first phase of power increment, slight light delocalization is observed, and it transforms later into light localization (when most of light intensity is concentrated in the central LC channel) when the optical power constantly increases.

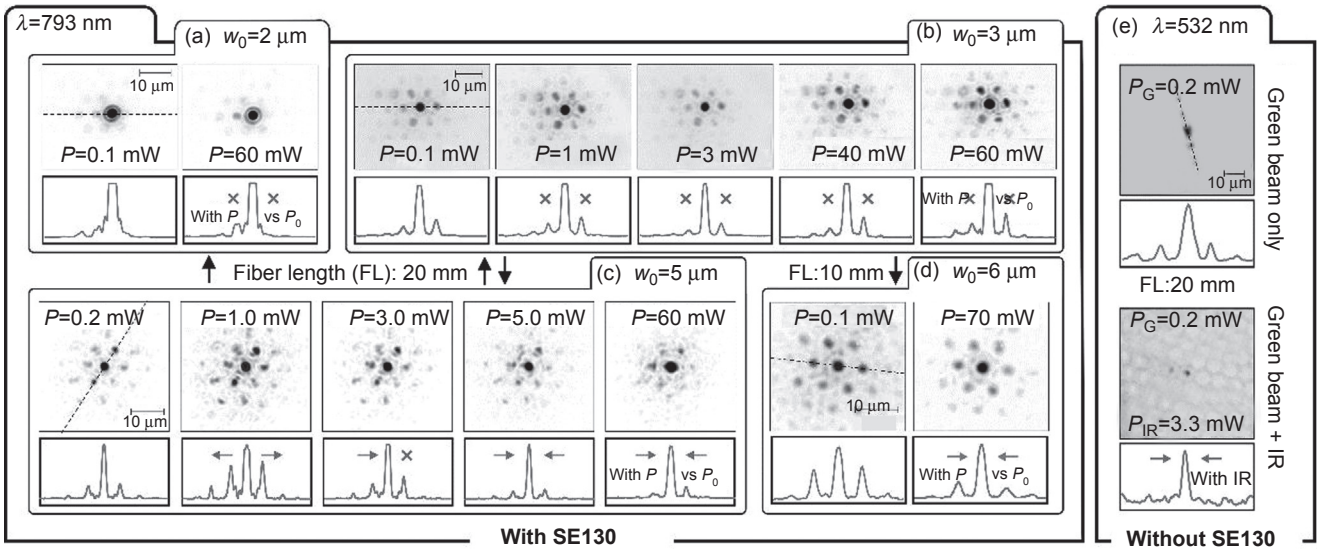


**Figure 7.12** Experimental results showing output intensity profiles at the output facet of 20- (a−c, e) and 10-mm-long PCF infiltrated with 6CHBT LC obtained for a wavelength of 793 nm (a−d) and 532 nm (e) and representing optical power dependence of discrete light propagation in a PLCF for different input beam widths (as marked in each panel), respectively. Please note that the intensity of images registered in the experimental conditions has been controlled with the use of neutral density filters and thus the color levels in the gray scales used in each photosentence do not correspond to the same value of light intensity. Moreover, for two beam interactions (e) a bandpass color filter has been applied to ensure that only green light intensity at the output facet is registered by a CCD camera.

No dependence of linear polarization direction on registered effects observed in experimental conditions indicates the domination of thermal nonlinearity.

In the second part of the experiment, the influence of an electromagnetic wave on the optical properties of a PLCF has been tested with the use of two laser beams launched simultaneously into the fiber (with the experimental setup described in (Murek & Rutkowska, 2014)). For this purpose a low-power signal beam at a wavelength of 532 nm (from a DPSS laser based on Nd:YAG) has been applied to monitor how the liquid crystalline waveguide channel(s) is (are) decoupled from the rest of the matrix under the influence of a pump laser beam. The latter (from CW Nd:YAG laser, $\lambda = 1064$ nm) has been colaunched with a signal beam to confirm the power-dependence of optical properties of the fiber (modified by the pump) while observing the signal beam profile at the output facet of a PLCF (see Figure 7.12(e)). Both laser beams with the initial widths of a few micrometers have been launched axially to the same liquid crystalline core of PLCF with the length of 20 mm. The signal beam has been characterized by low power (in the range of a fraction of milliwatts) to ensure that all effects of thermal nonlinearity in LCs are induced by the pump beam. Please note that spatial light intensity distribution for only green light (even if an IR beam, served as a pump, is present in the system) is presented in Figure 7.5(e) thanks to the bandpass colored glass filter applied (with nonzero transmission for the wavelengths in the range from 355 to 610 nm). As one can see, a severe change in light intensity (and spatial profile) of the signal beam at the output facet of the fiber has been obtained, thus proving that the propagation properties of PLCFs for a low-power signal beam can be obtained using variable power of the pump.

When summarizing the results of the experimental measurements presented above it is worth underlining that direct quantitative comparison between experimental and theoretical data is not accessible, mainly due to the fact that structural regularity (assumed in simulations and hardly achieved in experimental conditions) is required for predictable and repeatable results. Our tests suggest that a homogeneous array with constant coupling coefficients was not formed in experimental conditions; nevertheless, the coupling strength has not varied much while switching between different input waveguide channels in the array. Moreover, we have noticed that for some PLCF samples under testing, defocusing and focusing behavior was obtained only for a specific input position in the photonic lattice and it could indicate its nonuniformity. However, we believe that, in general, our PLCF structure is suitable for light self-localization in the form of discrete soliton.

### 7.4.4 Potential applications (optical sensors based on all-optical switching and routing in PLCFs)

In this section, theoretical and experimental work has been presented on discrete light propagation in a two-dimensional waveguide array based on a PLCF structure. Experimental observations regarding how the intensity pattern at the output facet of a PLCF changes with optical power (performed for the input Gaussian beams of different widths and wavelengths) are in qualitative agreement with the results of numerical simulations. Specifically, taking advantage of thermal nonlinearity in LCs, spatial light

delocalization and localization (particularly in the form of a discrete (gap) soliton) have been demonstrated. Such a feature allows, that is, for all-optical switching, routing, and electromagnetic sensing to be potentially developed in PLCFs.

It is worthwhile to note that the functionality of our photonic structure relies on the discreteness of the system, as well as on high tunability and nonlinearity of LCs used as infiltration. The universal access and commercial availability of PCFs (with almost unlimited configuration) and LCs (with given optical parameters), as well as the well-established fabrication process make PLCFs ideal candidates for the study of discrete light propagation (including a variety of nonlinear effects and other phenomena known from discrete optics) with a possibility of further applications. The results presented in this section could be found to be very useful for applications which rely on a defined (but also tunable) coupling between (relatively easily reconfigurable and versatile) adjacent waveguides, as well as for the investigation of nonlinear effects (such as discrete solitons). The proposed solution allows for tailoring the spatial coupling of a waveguide matrix, as well as optical nonlinearity in a two-dimensional discrete system, which is an important feature for potential electromagnetic sensing.

## 7.5 Conclusions and research directions

LC infiltrated PCFs, benefiting from a merger between "passive" PCF host microstructures and a variety of "active" LC guest materials, create a new challenge both for fiber optics and for LC photonics. They introduce new levels of tunability to PCFs and boost the performance of these fibers due to a diversity of new propagation, spectral, thermo-optic, electro-optic, and polarization properties, simultaneously demonstrating that optical fibers can be more special and unique than previously thought. Apart from their high sensitivity to temperature as well as electrical/magnetic/optical fields, the use of different LC molecular orientation "scenarios" within the microholes can determine either index guiding or PBG propagation mechanisms and reversible switching between them.

PLCFs—due to infiltration of LCs into PCFs—form a novel and common platform that addresses the need for an all in-fiber configuration suitable for optical sensing. The possibility of sensing applications arises in particular from the presence of LCs characterized by high optical tunability with external and internal factors, such as temperature, electric, magnetic, and optical fields, deformations, and the introduction of dopants, dyes, nanoparticles, or other chemicals.

Consequently, the resulting PLCFs are highly sensitive to external physical fields such as temperature and electric/magnetic field, so they can be used in various types of prospective optical fiber sensors. It is evident that by using different combinations of PCFs and LCs, new methods of optical fiber sensing with wide sensitivity ranges and operating regions can be implemented. Moreover, this particular new sensing method allows for measuring external factors distribution in a specified area by using an array of PLCF sensing elements. The main advantage of the proposed solution is its compactness, simplicity, and relatively low cost.

Prospective sensing devices based on PLCFs may also find their applications in so-called lab-on-a-chip structures. Moreover, a particular use of LCs infiltration for a new class of optofluidic devices allows for many additional distinguished applications. LCs will thus play a fundamental role in upgrading and innovating already existing optofluidic systems, typically where isotropic fluids are used, by allowing them to exploit fully the unique and remarkable properties of anisotropic fluidic infiltration. PLCF-based optofluidic devices can be used in various physical, chemical, and biological sensing schemes because of their low cost, capability of multiplexed measurements, and fast response as well as compatibility with a wide range of surface chemistries that can enable high specificity and sensitivity. These structures will allow us to measure the influence of external factors, such as temperature and electric/magnetic field, as well as to perform the "lab-in-a-fiber" biochemical analysis. Unquestionably, the impact of PLCF-based devices for optical sensing will be significant.

## Acknowledgments

The authors gratefully acknowledge the support of the Polish National Science Center (NCN) under the grant no. 2011/01/B/ST7/05015.

S.E. would like to acknowledge the support of the National Center for Research and Development in the frame of the project LIDER/05/208/L3-11/NCiBR/2012., whereas, K.A.R. would like to acknowledge *Homing Plus Programme* (HOMING PLUS/2010-2/11) granted by the Foundation for the Polish Science and cofinanced by the European Regional Development Fund.

## References

Argyros, A., van Eijkelenborg, M. A., Large, M. C., & Bassett, I. M. (2006). Hollow-core microstructured polymer optical fiber. *Optics Letters, 31*(2), 172−174.

Baran, W., Raszewski, Z., Dabrowski, R., Kedzierski, J., & Rutkowska, J. (1985). Some physical properties of mesogenic 4-(trans-4′-n-alkylcyclohexyl) isothiocyanatobenzenes. *Molecular Crystals and Liquid Crystals, 123*(1), 237−245.

Brzdąkiewicz, K., Laudyn, U., Karpierz, M., Woliński, T., & Wójcik, J. (2006). Linear and nonlinear properties of photonic crystal fibers filled with nematic liquid crystals. *Opto-Electronics Review, 14*(4), 287−292.

Budaszewski, D., Woliński, T. R., Geday, M., & Otón, J. M. (2010). Photonic crystal fibers infiltrated with ferroelectric liquid crystals. *Photonics Letters of Poland, 2*(3), 110−112.

Burylov, S. V., & Raikher, Y. L. (1995). Ferronematics: enhanced magneto-optical response of a liquid crystalline system. *Materials Science and Engineering: C, 2*(4), 235−241.

Chigrinov, V. G., Kozenkov, V. M., & Kwok, H. S. (2008). *Photoalignment of liquid crystal materials: Physics and application*. UK: Wiley−SID series.

Chychłowski, M., Ertman, S., Tefelska, M., Woliński, T. R., Nowinowski-Kruszelnicki, E., & Yaroshchuk, O. (2010). Photo-induced orientation of nematic liquid crystals in microcapillaries. *Acta Physica Polonica A, 118*, 1100.

Chychłowski, M., Yaroshchuk, O., Kravchuk, R., & Woliński, T. (2012). Liquid crystal alignment in cylindrical microcapillaries. *Opto-Electronics Review, 20*, 47−52.

Désévédavy, F., Renversez, G., Troles, J., Houizot, P., Brilland, L., Vasilief, I., et al. (2010). Chalcogenide glass hollow core photonic crystal fibers. *Optical Materials, 32*(11), 1532−1539.

Du, F., Lu, Y., & Wu, S. (2004). Electrically tunable liquid-crystal photonic crystal fiber. *Applied Physics Letters, 85*(12), 2181−2183.

Ertman, S., Srivastava, A. K., Chigrinov, V. G., Chychłowski, M., & Woliński, T. R. (2013). Patterned alignment of liquid crystal molecules in silica micro-capillaries. *Liquid Crystals, 40*, 1−6.

Ertman, S., Tefelska, M., Chylowski, M., Rodriquez, A., Pysz, D., Buczynski, R., et al. (2012). Index guiding photonic liquid crystal fibers for practical applications. *Journal of Lightwave Technology, 30*, 1208−1214.

Ertman, S., Wolinski, T. R., Beeckman, J., Neyts, K., Vanbrabant, P. J. M., James, R., et al. (2010). Numerical simulations of electrically induced birefringence in photonic liquid crystal fibers. *Acta Physica Polonica A, 118*, 1113−1117.

Ertman, S., Wolinski, T. R., Szaniawska, K., Lesiak, P., Domanski, A. W., Dabrowski, R., et al. (2005). Influence of electrical field on light propagation in microstructured liquid crystal fibers. *Proceedings of SPIE, 5950*, 326−332.

Ertman, S., & Woliński, T. R. (2008). Electric field control of liquid crystal infiltrated photonic crystal fibers by using various electrode configurations. *Proceedings of SPIE, 7120*, 712004.

Ertman, S., & Woliński, T. R. (2014). Six microelectrodes assembly for tunable optical fibers. *Proceedings of SPIE, 9157*, 915735.

Ertman, S., Woliński, T. R., Czapla, A., Nowecka, K., Nowinowski-Kruszelnicki, E., & Wójcik, J. (2007). Liquid crystal molecular orientation in photonic liquid crystal fibers with photopolymer layers. *Proceedings of SPIE, 6587*, 658706.

Ertman, S., Woliński, T. R., Pysz, D., Buczynski, R., Nowinowski-Kruszelnicki, E., & Dabrowski, R. (2009). Low-loss propagation and continuously tunable birefringence in high-index photonic crystal fibers filled with nematics liquid crystals. *Optics Express, 17*, 19298−19310.

Feng, X., Monro, T., Petropoulos, P., Finazzi, V., & Hewak, D. (2003). Solid microstructured optical fiber. *Optics Express, 11*(18), 2225−2230.

Frazão, O., Santos, J. L., Araújo, F. M., & Ferreira, L. A. (2008). Optical sensing with photonic crystal fibers. *Laser & Photonics Reviews, 2*(6), 449−459.

Garanovich, I. L., Longhi, S., Sukhorukov, A. A., & Kivshar, Y. S. (2012). Light propagation and localization in modulated photonic lattices and waveguides. *Physics Reports, 518*(1), 1−79.

Haakestad, M. W., Alkeskjold, T. T., Nielsen, M. D., Scolari, L., Riishede, J., Engan, H. E., et al. (2005). Electrically tunable photonic bandgap guidance in a liquid-crystal-filled photonic crystal fiber. *IEEE Photonics Technology Letters, 17*(4), 819−821.

Hu, T., Zhao, Y., Li, X., Chen, J., & Lv, Z. (2010). Novel optical fiber current sensor based on magnetic fluid. *Chinese Optics Letters, 8*(4), 392−394.

James, J., Willman, E., Fernandez, F. A., & Day, S. E. (2006). Finite-element modeling of liquid-crystal hydrodynamics with a variable degree of order. *IEEE Transactions on Electron Devices, 53*, 1575−1582.

Jung, P., & Karpierz, M. (2012). Analysis of light propagation in optical fibers with a high step index. *Acta Physica Polonica-Series A General Physics, 122*(5), 829.

Jung, P., & Karpierz, M. A. (2012). Beam propagation method in rectangular structures with a high step index. *Optics Communications, 285*(21−22), 4184−4189.

Khoo, I. (2007). *Liquid crystals*. Hoboken.

Khoo, I. (2011). Extreme nonlinear optics of nematic liquid crystals (invited). *JOSA B, 28*(12), A45−A55.

Khoo, I. C., Hong, K. L., Zhao, S., Ma, D., & Lin, T.-H. (2013). Blue-phase liquid crystal cored optical fiber array with photonic bandgaps and nonlinear transmission properties. *Optics Express, 21*(4), 4319−4327.

Larsen, T., Bjarklev, A., Hermann, D., & Broeng, J. (2003). Optical devices based on liquid crystal photonic bandgap fibres. *Optics Express, 11*(20), 2589−2596.

Laudyn, U. A., Rutkowska, K. A., Rutkowski, R. T., Karpierz, M. A., Woliński, T. R., & Wójcik, J. (2008). Nonlinear effects in photonic crystal fibers filled with nematic liquid crystals. *Central European Journal of Physics, 6*(3), 612−618.

Lederer, F., Stegeman, G. I., Christodoulides, D. N., Assanto, G., Segev, M., & Silberberg, Y. (2008). Discrete solitons in optics. *Physics Reports, 463*(1), 1−126.

Mathews, S., Farrell, G., & Semenova, Y. (2011). All-fiber polarimetric electric field sensing using liquid crystal infiltrated photonic crystal fibers. *Sensors and Actuators A: Physical, 167*(1), 54−59.

Medhat, M., El-Zaiat, S., Radi, A., & Omar, M. (2002). Application of fringes of equal chromatic order for investigating the effect of temperature on optical parameters of a GRIN optical fibre. *Journal of Optics A: Pure and Applied Optics, 4*(2), 174.

Milenko, K., Ertman, S., & Woliński, T. R. (2013). Numerical analysis of birefringence tuning in high index microstructured fiber selectively filled with liquid crystal. *Proceedings of SPIE, 8794*, 87942C.

Milenko, K., Ertman, S., & Woliński, T. R. (2014). *Numerical analysis of the phase birefringence of the photonic crystal fibers selectively filled with liquid crystal*. Molecular Crystals and Liquid Crystals − accepted for publication.

Millo, A., Lobachinsky, L., & Katzir, A. (2008). Single-mode index-guiding photonic crystal fibers for the middle infrared. *Photonics Technology Letters, IEEE, 20*(10), 869−871.

Murek, M., & Rutkowska, K. A. (2014). Two laser beams interaction in photonic crystal fibers infiltrated with highly nonlinear materials. *Photonics Letters of Poland, 6*(2), 74−76.

Pinto, A. M., & Lopez-Amo, M. (2012). Photonic crystal fibers for sensing applications. *Journal of Sensors, 2012*. http://dx.doi.org/10.1155/2012/598178.

Poli, F., Cucinotta, A., & Selleri, S. (2007). *Photonic crystal fibers: Properties and applications*. Springer.

Poudereux, D., Mileńko, K., Dybko, A., Otón, J. M., & Woliński, T. R. (2014). Polarization properties of polymer-based photonic crystal fibers. *Photonics Letters of Poland, 6*(2), 59−61.

Rosberg, C. R., Bennet, F. H., Neshev, D. N., Rasmussen, P. D., Bang, O., Krolikowski, W., et al. (2007). Tunable diffraction and self-defocusing in liquid-filled photonic crystal fibers. *Optics Express, 15*, 12145−12150.

Russell, P. St. J. (2003). Photonic crystal fibers. *Science, 299*(5605), 358−362.

Rutkowska, K. A., Laudyn, U. A., & Jung, P. S. (2012). Discrete light propagation in photonic liquid crystal fibers. In *IEEE xplore photonics global conference (PGC), Singapore*.

Rutkowska, K. A., Laudyn, U. A., Rutkowski, R. T., Karpierz, M. A., Woliński, T.. R., & Wójcik, J. (2007). Nonlinear light propagation in photonic crystal fibers filled with nematic liquid crystals. *Proceedings of SPIE, 6582*, 658215.

Rutkowska, K. A., Rutkowski, R. T., Chychłowski, M. S., & Woliński, T. R. (2008). Analyses of light propagation in photonic liquid crystal fibers. *Proceedings of SPIE, 7120*, 712003.

Schirmer, J., Kohns, P., Schmidt-Kaler, T., Muravski, A. A., Yakovenko, S. Y., Bezborodov, V. S., et al. (1997). Birefringence and refractive indices dispersion of different liquid crystalline structures. *Molecular Crystals and Liquid Crystals, 307*(1), 17−42.

Tartarini, G., Alkeskjold, T. T., Scolari, L., Bjarklev, A., & Bassi, P. (2007). Spectral properties of liquid crystal photonic bandgap fibres with splay-aligned mesogens. *Optical and Quantum Electronics, 39*, 913–925.

Tefelska, M. M., Ertman, S., & Wolinski, T. R. (2012). Large area multimode photonic band gap propagation in photonic liquid crystal fiber. *IEEE Photonics Technology Letters, 24*, 631–633.

Tefelska, M. M., Woliński, T. R., Dąbrowski, R., & Wójcik, J. (2010). Chiral nematic liquid crystals as an alternative filling in photonic crystal fibers. *Photonics Letters of Poland, 2*(1), 28–30.

Thakur, H. V., Nalawade, S. M., Gupta, S., Kitture, R., & Kale, S. (2011). Photonic crystal fiber injected with $Fe_3O_4$ nanofluid for magnetic field detection. *Applied Physics Letters, 99*(16), 161101.

van Eijkelenborg, M., Large, M., Argyros, A., Zagari, J., Manos, S., Issa, N., et al. (2001). Microstructured polymer optical fibre. *Optics Express, 9*(7), 319–327.

Vieweg, M., Gissibl, T., & Giessen, H. (2011). Nonlinear optics-photonic-crystal fibers are selectively filled with nonlinear liquids. *Laser Focus World, 47*(6), 53.

Vieweg, M., Gissibl, T., Kartashov, Y. V., Torner, L., & Giessen, H. (2012). Spatial solitons in optofluidic waveguide arrays with focusing ultrafast Kerr nonlinearity. *Optics Letters, 37*(13), 2454–2456.

Vieweg, M., Gissibl, T., Pricking, S., Kuhlmey, B., Wu, D., Eggleton, B., et al. (2010). Ultrafast nonlinear optofluidics in selectively liquid-filled photonic crystal fibers. *Optics Express, 18*(24), 25232–25240.

Wang, X., Pu, S., Ji, H., & Yu, G. (2012). Enhanced magnetic-field-induced optical properties of nanostructured magnetic fluids by doping nematic liquid crystals. *Nanoscale Research Letters, 7*(1), 1–7.

Woliński, T. R. (2008). Photonic liquid-crystal fibers: new sensing opportunities. In *Optical waveguide sensing and imaging. NATO science for peace and security series B: Physics and biophysics* (pp. 51–72). Springer.

Woliński, T. R. (2012). Photonic liquid crystal fiber sensors for safety and security monitoring. In G. Xiao, & W. J. Bock (Eds.), *Photonics sensing: Principle and applications for safety and security monitoring* (pp. 147–181). New Jersey: Wiley.

Woliński, T. R., Bondarczuk, K., Szaniawska, K., Lesiak, P., Domański, A. W., Dąbrowski, R., et al. (2004). Propagation effects in a photonic crystal fiber filled with low-birefringent liquid crystal. *Proceedings of SPIE, 5518*, 232–237.

Woliński, T. R., Czapla, A., Ertman, S., Tefelska, M., Domański, A., Wójcik, J., et al. (2008). Photonic liquid crystal fibers for sensing applications. *IEEE Transactions on Instrumentation and Measurement, 57*(8), 1796–1802.

Woliński, T. R., Ertman, S., Lesiak, P., Domański, A., Czapla, A., Dąbrowski, R., et al. (2006). Photonic liquid crystal fibers—A new challenge for fiber optics and liquid crystals photonics. *Opto-Electronics Review, 14*(4), 329–334.

Woliński, T. R., Szaniawska, K., Bondarczuk, K., Lesiak, P., Domanski, A. W., Dabrowski, R., et al. (2005). Propagation properties of photonic crystals fibers filled with nematic liquid crystals. *Opto-Electronics Review, 13*(2), 59–64.

Woliński, T. R., Szaniawska, K., Ertman, S., Lesiak, P., Domański, A. W., Dąbrowski, R., et al. (2006). Influence of temperature and electrical fields on propagation properties of photonic liquid crystal fibers. *Measurement Science and Technology, 17*, 985–991.

Woliński, T. R., & Szymańska, A. (2001). Polarimetric optical fibers with elliptical liquid-crystal core. *Measurement Science and Technology, 12*, 948–951.

Woliński, T. R., Szymańska, A., Nasiłowski, T., Karpierz, M. A., Kujawski, A., & Dąbrowski, R. (1998). Propagation effects in liquid crystal-core optical fiber waveguides. *Molecular Crystals and Liquid Crystals, 321*, 113−124.

Woliński, T. R., Tefelska, M. M., Chychłowski, M. S., Godyń, K., Dąbrowski, R., Wójcik, J., et al. (2009). Multi-parameter sensing based on photonic liquid crystal fibers. *Molecular Crystals and Liquid Crystals, 502*, 220−234.

Woliński, T. R., Tefelska, M., Mileńko, K., Rutkowska, K., Domański, A. W., Ertman, S., et al. (2014). Propagation effects in a polymer-based photonic liquid crystal fiber. *Applied Physics A, 115*(2), 569−574.

Woliński, T. R., Mileńko, K., Tefelska, M., Rutkowska, K. A., Domański, A. W., Ertman, S., et al. (2014). Liquid crystals and polymer-based photonic crystal fibers. *Molecular Crystals and Liquid Crystals, 594*(1), 55−62.

Zhu, Z., & Brown, T. (2002). Full-vectorial finite-difference analysis of microstructured optical fibers. *Optics Express, 10*(17), 853−864.

Zu, P., Chan, C. C., Gong, T., Jin, Y., Wong, W. C., & Dong, X. (2012). Magneto-optical fiber sensor based on bandgap effect of photonic crystal fiber infiltrated with magnetic fluid. *Applied Physics Letters, 101*(24), 241118.

Zu, P., Chan, C. C., Lew, W. S., Hu, L., Jin, Y., Liew, H. F., et al. (2012). Temperature-insensitive magnetic field sensor based on nanoparticle magnetic fluid and photonic crystal fiber. *Photonics Journal, IEEE, 4*(2), 491−498.

Zu, P., Chan, C. C., Lew, W. S., Jin, Y., Zhang, Y., Liew, H. F., et al. (2012). Magneto-optical fiber sensor based on magnetic fluid. *Optics Letters, 37*(3), 398−400.

# Polymer micro and microstructured fiber Bragg gratings: recent advancements and applications

8

*G. Rajan, G.D. Peng*
School of Electrical Engineering and Telecommunications, UNSW Australia, Sydney, NSW, Australia

## 8.1 Introduction

Since the first demonstration of polymer optical fiber Bragg gratings (POFBGs) in 1999, significant research efforts have been devoted to their sensing applications. In recent times, advancement in the fabrication of single-mode polymer fiber enhanced the research and development of Bragg grating sensors for different applications. Their unique advantages compared to their silica counterparts, such as high flexibility, large strain and temperature measurement range, low Young's modulus, biocompatibility, and so on (Peng, Xiong, & Chu, 1999a) have led to further research in device development and application of POFBGs. Some application-oriented research works are reported (Kuang, Quek, Koh, Cantwell, & Scully, 2009; Webb et al., 2009) and further efforts are ongoing in exploring the further potential of POFBGs.

Since the demonstration of the first POFBG, further development occurred with single-mode polymer fibers, such as the emergence of microstructured polymer fiber, improved photosensitive single-mode polymer fibers, and polymer microfibers. In this chapter, we present an overview on the recent progress in the development of POFBG sensors including polymer microstructured FBGs, polymer microfiber Bragg gratings, and POFBG arrays. The sensing applications of POFBGs are an emerging area with some promising research ongoing in a number of fields. In this chapter, we discuss some of the recent developments in this area, such as POFBG-based accelerometers, fast-response humidity sensors, force and pressure measurements, and so forth.

## 8.2 Polymer optical fibers

The majority of optical fiber sensors are based on silica optical fibers due to their wide use in telecommunication applications and the wide availability of components, instrumentation, and optical fiber specifications. However, polymer optical fibers (POFs) have experienced a surge in applications for short-haul telecommunication systems due to their ease of implementation. More interestingly, many researchers have

**Optofluidics, Sensors and Actuators in Microstructured Optical Fibers.** http://dx.doi.org/10.1016/B978-1-78242-329-4.00008-4

realized their unique properties for the sensing of strain, temperature, humidity, and so on and have looked into the sensing potential of polymer fibers (Peters, 2011). Simultaneously, researchers also focused on the development of POFs with new properties including single-mode fibers, microstructured fibers, and polymer microfibers. In addition, the unique material properties of polymer fiber have been used to expand the envelope of sensing applications beyond those previously realized with silica optical fiber sensors.

When coming to single-mode fibers, silica fiber technology is abundant whereas POF technology has focused exclusively on large core step and graded index multimode fibers. The first reported single-mode polymer was in the early 1990s and was demonstrated by Kuzyk, Paek, & Dirk (1991). These fibers had dye-doped cores, the core size was approximately 8 μm, and the cladding diameter was 125 μm. Single-mode fibers with copolymer for both core and cladding were later reported by Bosc & Toinen (1992) in which compositions of the copolymer in the core and cladding were adjusted to get a refractive index profile that yielded single-mode guidance. However, the studies on the photosensitivity of the polymethyl methacrylate (PMMA) polymer fiber led to the surge in research on Bragg gratings based on POF. Photosensitivity of PMMA has been discovered decades ago and the earliest report on photosensitivity of PMMA was by Tomlinson, Kaminow, Chanderross, Fork, & Silfvast (1970) in the 1970s. In this work, a properly prepared PMMA (through oxidation of monomer) exhibited a substantial increase in refractive index after irradiation with UV light at 325 nm (He−Cd laser) or 365 nm (Hg arc). A subsequent report related to photosensitivity of PMMA was found in an article on dye-doped polymer laser (Kaminov, Weber, & Chanderross, 1971). Research carried out by Chu and Peng et al. (Peng & Chu, 2000; Peng, Chu, Lou, & Chaplin, 1995; Peng, Xiong, & Chu, 1999b) during the latter 1990s and early 2000s on the photosensitivities of various PMMA-based POFs led to the development of several PMMA POFs made from undoped, dye-doped, or oxidated preforms, and those were examined under varying irradiation wavelengths, intensities, and time. Various reasons for the photosensitivity of polymer fibers are explained in the literature, such as photo polymerization, photo-cross linking, photolysis, or chain scission (Bolle, Lazare, Blanc, & Wilmes, 1992; Decker, 1998; Tao, Yu, & Tam, 2007).

One of the most photosensitive polymer fiber so far reported was fabricated at the University of New South Wales (UNSW) by Peng et al (Liu, Peng, & Chu, 2002; Xiong, Peng, Wu, & Chu, 1999), in which the core monomer mixture is PMMA doped with benzyl methacrylate (BzMA) to meet the requirement of the refractive index, whereas the cladding is PMMA without dopants. Single-mode photosensitive POF with different diameters are reported ranging from 100 to 240 μm for the cladding and the core diameter ranging from 6 to 12 μm (Liu et al., 2002; Liu, Liu, Peng, & Chu, 2004; Xiong et al., 1999). The reported difference in the refractive index between the core and the cladding is 0.0086. These fibers are typically single mode only in the infrared (IR) region, suffer high transmission loss in the C-L band, and are approximately 0.5 dB/cm, which is considerably higher compared to the silica fiber standards. Doped photosensitive single-mode POFs are still experimental, with only one commercial manufacturer, Paradigm Optics, that supplies single-mode POFs.

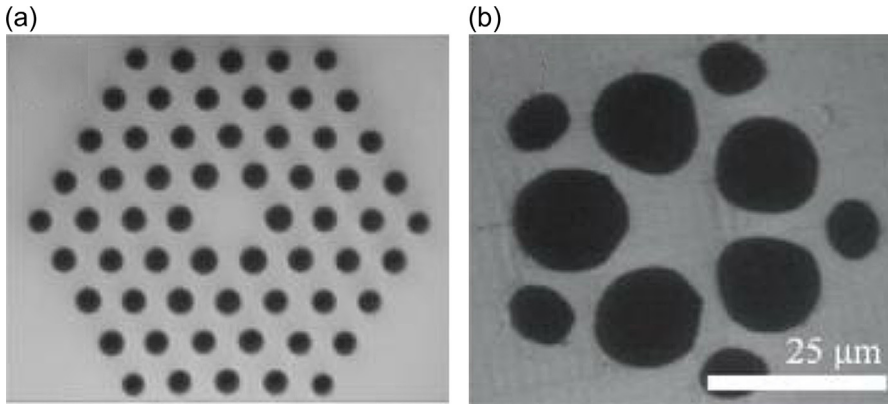


**Figure 8.1** (a) Cross-section of a typical single-mode mPOF and (b) an alternative single-mode design.
Courtesy of Kiriama Pvt Ltd.

It can be seen that conventional single-mode polymer fiber faces challenges in its fabrication and suffers high transmission loss in the near-mid IR wavelengths, only short sensing lengths of single-mode POFs can be used (Abdi, Peters, Kowalsky, & Hassan, 2011). A promising solution to these issues is the use of microstructured polymer optical fibers (mPOFs), first developed by researchers at the University of Sydney (Large, Barton, Poladian, & van Eijkelenborg, 2007; Van Eijkelenborg et al., 2001), which can be endlessly single mode with very low transmission loss (Figure 8.1). Microstructured POFs have a large air fraction in the cross-section of the fiber that significantly reduces the attenuation of a light wave propagating through the fiber. Additionally, the confinement effect on the light wave, created by the holes in the microstructure, enables single-mode propagation over a wide wavelength range. This means that by using microstructure single-mode mPOFs could be easily fabricated for any wavelength of operation. The loss of single-mode mPOF is typically 1 dB/m across the visible, and the core size varies from 1 to 15 µm depending on the wavelength guided (Argyros, 2013). These advantages, therefore, make mPOFs ideal for the inscription of Bragg gratings to serve as highly tunable FBG sensors without the power losses inherent in solid-core single-mode POFs.

## 8.3 Polymer fiber Bragg gratings

Initial work with the POFBGs was undertaken by Peng and Chu et al. at UNSW Australia. Gratings in single-mode fiber were demonstrated with very high reflectivity (Figure 8.2(a)), a 28 dB transmission rejection (Liu et al., 2002), and a large (70 nm) tuning range (Xiong et al., 1999). The polymer fibers used in the reported work were made in-house as solid core fibers as described in the previous section. The FBG inscription process included a side illumination inscription setup which consisted of

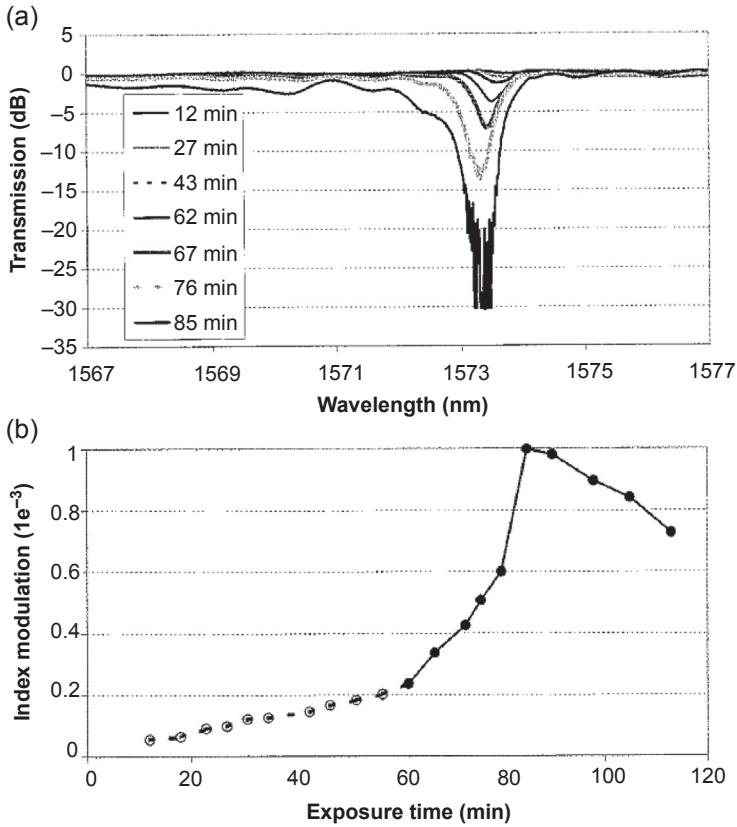


**Figure 8.2** (a) Transmission spectra of POF gratings at different UV exposure times; (b) refractive index modulation of POF gratings at different UV radiation times (Liu et al., 2002).

a modified Sagnac interferometer. Index changes up to $10^{-3}$ were achieved without apparent material damage (Figure 8.2(b)).

Another reported work is by Yu, Tao, & Tam (2004), in which POFBG is demonstrated in a fiber with an MMA-EMA-BzMA core doped with *trans*-4-stilbenemethanol. The fiber was irradiated with 325 nm laser light using a phase mask setup. A maximum index change of $-9 \times 10^{-3}$ was achieved. Xu, Ming, & Zhang (2002) realized birefringent gratings in azobenzene-doped PMMA fibers written with 532 nm laser light. Progress in the single-mode fiber fabrication and improved photosensitivity lead to reduced inscription times, with grating inscription time reported in minutes. Researchers from Aston University also demonstrated Bragg gratings inscribed in polymer fibers using photosensitive single-mode polymer fibers, and also its use for humidity sensing applications (Zhang, Webb, & Peng, 2012a). They have also investigated the time response of polymer FBGs with change in humidity. An electrically tunable Bragg grating filter in polymer optical fiber is also reported by this group (Kalli et al., 2007).

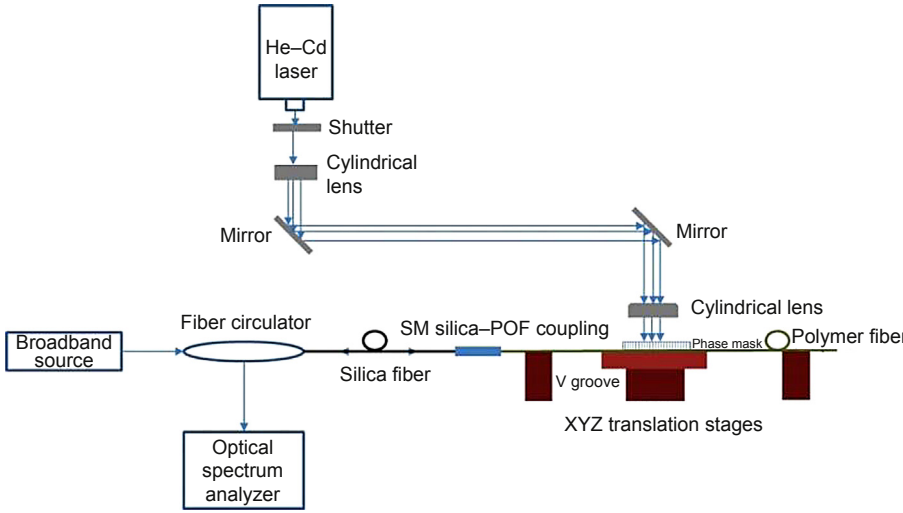


**Figure 8.3** Schematic of a standard polymer FBG fabrication setup.

Other reported works on POFBG include the ones with peak reflected wavelength of 962 nm, a study on the intrinsic temperature sensitivity of polymer FBG, and thermo-optic effects in polymer fiber gratings (Zhang, Zhang, Tao, Wang, & Peng, 2010). In recent history, most researchers use a 325 nm He−Cd laser and the phase mask technology to inscribe grating in polymer fibers as shown in Figure 8.3 (Rajan, Noor, Ambikiarajah, & Peng, 2014; Rajan, Ramakrishnan, et al., 2014). The reflectivity of the gratings depends on the inscription setup as UV laser power, inscription time, stability and alignment, POF type, and so on and research is ongoing in improving the inscription techniques. As the transmission loss is considerably high, only a small length of POF is used and is either glued or butt coupled to a silica fiber to obtain the measurements. Another reported research with polymer FBG includes a study on inscription of Bragg grating in polymer fibers using a 248 nm laser (Rajkumar et al., 2013).

The recent research work on polymer FBGs includes inscription of gratings in polymer mPOF using different techniques to reduce the inscription writing time, grating in polymer microfiber, and polymer Bragg grating arrays. The following sections give an update of those developments in polymer fiber grating research.

### 8.3.1 Microstructured polymer fiber Bragg gratings

The microstructured geometry makes the Bragg grating inscription more difficult in mPOFs due to the multiple interfaces encountered when exposing the mPOF to side illumination. The several rings of holes surrounding the core in the mPOF can scatter the incident beam, leading to significant reduction in the optical intensity in the core region of the fiber. However, researchers have successfully written FBG sensors to microstructured polymer fibers. Dobb et al. (2005) inscribed Bragg grating in

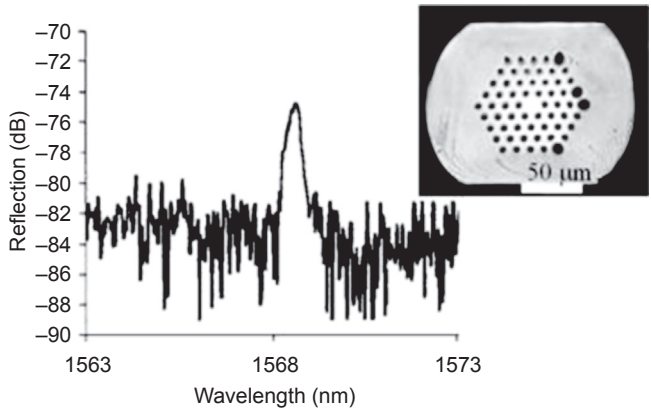


**Figure 8.4** Reflection spectrum of a Bragg grating inscribed in a single-mode mPOF (Dobb et al., 2005).
Reused with permission.

mPOF using a low-power continuous-wave laser source and using the phase mask technology. In this case, the orientation of the fiber and the separation between the fiber and the phase mask are optimized to improve the grating strength and inscription time. Reflection profile of the fabricated FBG is shown in Figure 8.4. The fiber was exposed to the UV radiation for approximately 60 min before obtaining saturation, and the obtained reflectivity is approximately 10%.

Another addition to mPOF Bragg gratings is the one reported by Yuan et al., in which gratings are inscribed in humidity-insensitive TOPAS and PMMA mPOFs (Stefani, Yuan, Markos, & Bang, 2011; Yuan et al., 2011), with peak reflected wavelength at 850 nm. The 850 nm window is a region where polymers typically have low-attenuation properties, and telecommunication sources and detectors are commercially available. The growth dynamics of the grating were also studied, and it was found that after 300 min the grating strength begins to saturate. The reported strain and temperature sensitivity of the TOPAS mPOF Bragg gratings were 0.64 pm/με and −78 pm/°C respectively (Figure 8.5). The biggest advantage of TOPAS grating is that it is 50 times less humidity sensitive compared to other POFBGs, which makes it suitable for a range of applications with negligible cross-sensitivity to humidity.

In contrast to PMMA, TOPAS has a very low moisture absorption rate and a significantly high glass transition temperature ($T_g$), around 135 °C. Markos et al. (2013) inscribed FBGs into a TOPAS mPOF with a Bragg wavelength of 853 nm. The authors were able to perform strain sensing over a large strain range at elevated temperatures up to 110 °C. It was also demonstrated that the low moisture absorption of TOPAS did not create apparent thermal strain in the sensor. The thermally induced blue shift in the Bragg wavelength was not recovered at room temperature, indicating that permanent changes had occurred to the mPOF during the extended thermal loading. This result again emphasizes that the loading and thermal history of a POF sensor must be taken into account when analyzing data from the sensor. Figure 8.6(a) shows a microscope

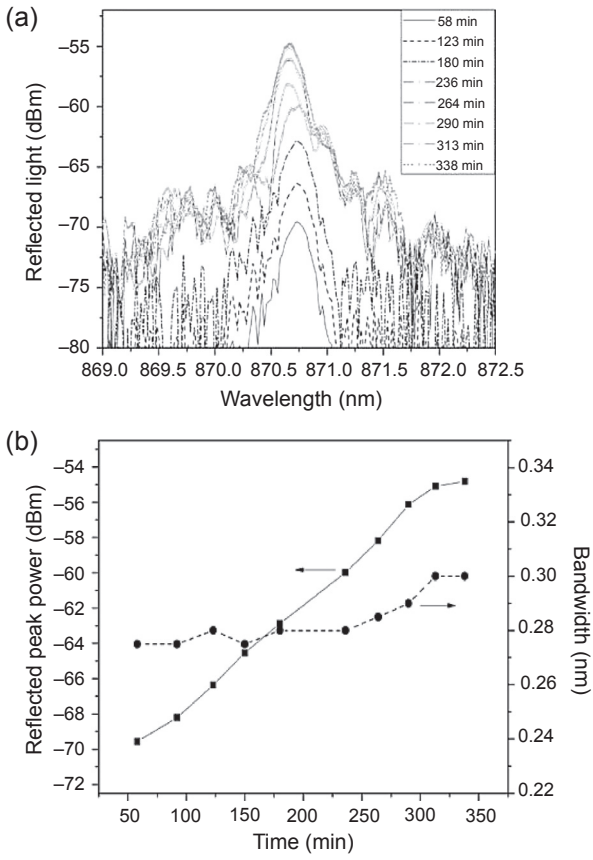


**Figure 8.5** (a) Reflection spectra of the FBG in a TOPAS mPOF at different writing times; (b) growth dynamics of the peak intensity and bandwidth of a 10 mm FBG during inscription (Yuan et al., 2011).
Reused with permission.

image of the mPOF cross-section, as well as the reflected spectrum of the FBG sensor. The FBG was exposed to 110 °C for 7 h, after which the mPOF was returned to room temperature, as seen in Figure 8.6(b).

We have noted that the inscription time of gratings is considerably long; it makes mPOF grating procedure time consuming, thus less productive, and is a serious problem for applications requiring mass production. Recent works carried out by Stefani, Stecher, Town, & Bang (2012), and Bundalo, Nielsen, Markos, & Bang (2014), considerably reduced the grating inscription time in mPOFs. Direct writing on FBGs in mPOFs are reported by Stefani et al., in which gratings are inscribed in 2.5 s. A fourth-order grating with a resonance wavelength of 1518.67 nm was reported in this case. In the work reported by Bundalo et al., gratings are inscribed in PMMA mPOF in less than 7 min. This is achieved by optimizing the alignment between the cylindrical lens, phase mask, and the polymer fiber used in the experiment. Due to the added scattering in mPOF, to improve the inscription time it is necessary to focus the writing beam well aligned with the core of the fiber. The grating fabricated was

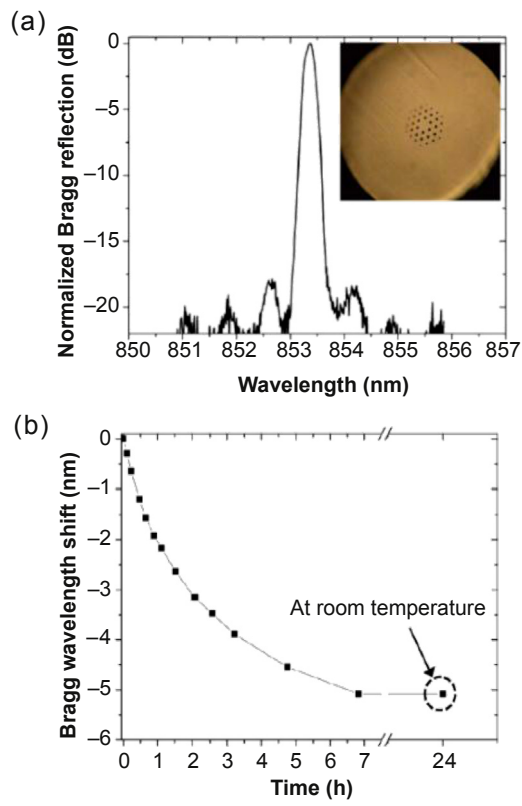


**Figure 8.6** (a) Reflection spectrum of high-$T_g$ TOPAS FBG at room temperature; (b) variation of Bragg wavelength with time (Markos et al., 2013). Reused with permission.

centered at 632.6 nm, had an FWHM of 0.3−0.4 nm, the grating strength was 26 dB, and the growth rate was 7.9 dB/min.

In the work reported by Yuan, Stefani, & Bang (2012), they took advantage of the high-strain capabilities of POFs and wrote a dual-wavelength FBG with a single setup, by writing a single grating and then tensioning the POF prior to writing a second FBG. Figure 8.7 shows FBG resonance wavelength versus applied force, and the reflection spectra of the fabricated dual FBG is also shown in the inset. They have demonstrated a temperature- and humidity-compensated POFBG strain sensor, which is based on a dual FBG architecture in a single-mode PMMA mPOF that operates at the low loss wavelength of 850 nm. The resonance wavelength has been tuned by 7 m by applying strain up to 1%, and the upper limit of this technique allows tuning the FBG resonance by 12 nm with 2.25% strain.

Long-period gratings (LPGs) have also been demonstrated in mPOFs, written through mechanical stamping of a heated mPOF (Durana et al., 2012) and UV inscription (Sáez-Rodríguez et al., 2010). Sáez-Rodríguez et al. (2010) applied the LPG for humidity sensing, using the high diffusion coefficient of PMMA ($6.7 \times 10^{-9}$ cm$^2$/s at

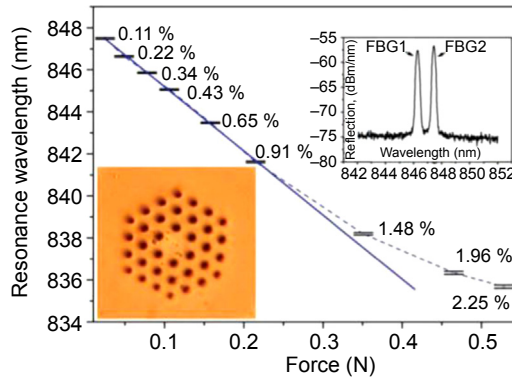


**Figure 8.7** FBG resonance wavelength versus applied force; inset: reflection spectra of the fabricated dual FBG (Yuan et al., 2012).
Reused with permission.

room temperature) producing a 250 nm shift in one of the cladding mode resonances at maximum moisture absorption, orders of magnitude larger than can be obtained with silica optical fiber-based sensors.

### 8.3.2 Polymer microfiber gratings

Polymer microfiber Bragg grating is another recent addition to the polymer FBG family, which can improve the measurement capabilities of the polymer gratings. A two-stage process was reported by Rajan, Noor, Ambikiarajah, Farrell, & Peng (2013) to fabricate the polymer microfiber in which the fiber was etched to a certain diameter and then tapered down to a final diameter. This method ensured that a sufficient amount of photosensitive core was retained within the fiber. After etching, the fiber is placed in between the heating plates (temperature is around 160 °C) for 5 min to ensure that the fiber was heated uniformly, and then it is pulled from both sides using a pair of translation stages, resulting in a polymer microfiber with a diameter of 16 μm. Figure 8.8 shows the micrographs of the unetched fiber, etched fiber, and the final tapered fiber.

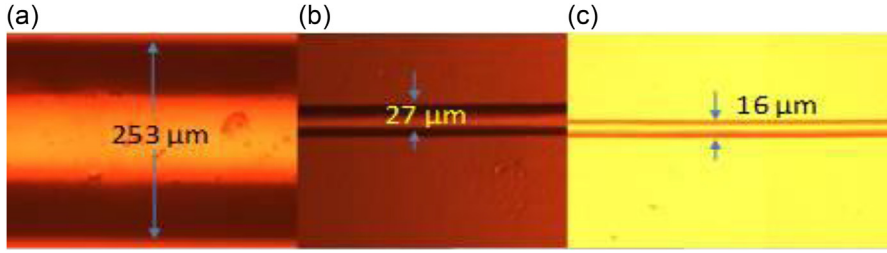


**Figure 8.8** Micrographs of (a) original polymer fiber, (b) etched polymer fiber, and (c) polymer microfiber.

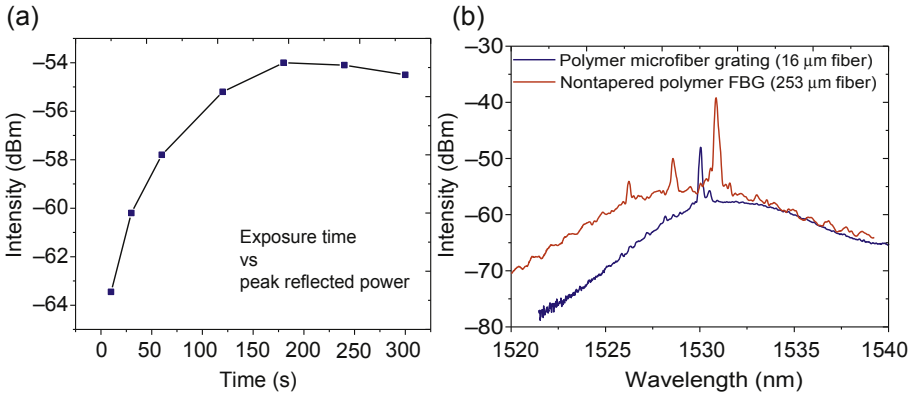


**Figure 8.9** (a) Variation in peak intensity with UV exposure time, and (b) comparison of reflection spectra of the original PFBG and the polymer microfiber grating.

The Bragg grating structures were fabricated in the polymer microfiber by a phase mask technique using a He−Cd laser emitting light at 325 nm. The Bragg peak started appearing just after the fiber was illuminated with the UV laser and grew thereafter, reaching saturation, and then decreasing as shown in Figure 8.8 with maximum reflected power obtained in 3 min. This grating growth behavior was similar to that of the original photosensitive polymer fibers, but the exposure time to obtain the maximum peak was lower than that of nontapered PFBG, which is normally 7−10 min with the same experimental setup. This phenomenon is attributed to the relation between the thickness of the polymer fiber and the UV laser power, in which the effective power in the core of the fiber is dependent on the penetration depth. Figure 8.9 shows a comparison of reflection spectra in the microfiber Bragg grating and polymer fiber Bragg grating. A small shift is observed for the reflection peak of the polymer microfiber grating due to the decrease in the effective refractive index of the polymer fiber at smaller radii.

Figure 8.10 shows the temperature and strain sensitivity of polymer microfiber gratings and its comparison with the nontapered polymer FBG. In the case of POFs, due to the relatively large thermal expansion coefficient and the negative thermo-optic effect and positive grating period effect, the temperature-induced wavelength shift of a polymer fiber Bragg grating is far more complex than a silica fiber Bragg grating (Zhang & Tao, 2013). The measured temperature sensitivity of microfiber grating (150.5 pm/°C) was approximately two times larger than that of the nontapered polymer grating (88 pm/°C), which is mainly due to the reduced size of the fiber. The strain sensitivity of the microfiber grating (1.2 pm/με) and the original polymer FBG (1.34 pm/με) is approximately in the same range. The small variation observed is due to the change in the $n_{\text{eff}}$ of the microfiber.

The fabricated POFBGs can be used in a number of applications in which high-sensitivity measurements are required. Compared to silica microfibers, polymer microfiber gratings can be advantageous due to their high-temperature sensitivity, very low

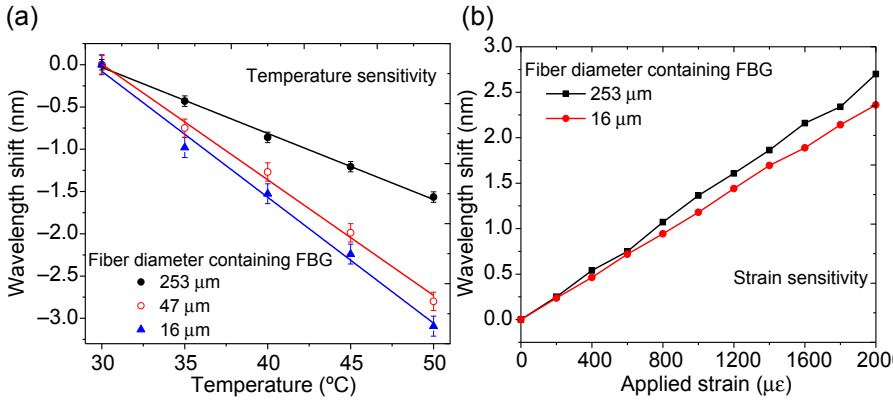


**Figure 8.10** (a) Temperature sensitivity and (b) strain sensitivity of original polymer FBG and polymer microfiber grating.

Young's modulus, and their flexibility. These features of the polymer microfiber grating would make it ideal for medical applications such as in medical textiles.

### 8.3.3 Polymer fiber Bragg grating arrays

As the FBGs are ideal wavelength-selective components for detecting multiple sensing parameters, a method is described to inscribe multiple FBGs on a single-mode polymer fiber using a single phase mask and by applying strain to the fiber (Rajan, Noor, et al., 2014). Five FBGs were fabricated in the same fiber at different locations by changing the position of the fiber using a motorized translation stage and by applying the strain to the fiber. The schematic of the location of the FBGs in the FBG array is shown in Figure 8.11.

In this technique, initially a grating is inscribed at zero-strain condition and then, at each step, an elongation of 0.2% was applied to the fiber using a translation stage and the position of the UV-exposed region was changed by moving the fiber using the motorized translation stage. The measured reflection spectra of the polymer FBG array are shown in Figure 8.12. The dotted spectrum is the one measured at the maximum-strain state (0.8% elongation) and the bold spectrum shows the FBG spectrum at the zero-strain condition.

To see any effects of applied elongation during the grating inscription on the reflected spectra, the 3 dB bandwidth of the polymer FBGs was also measured. The

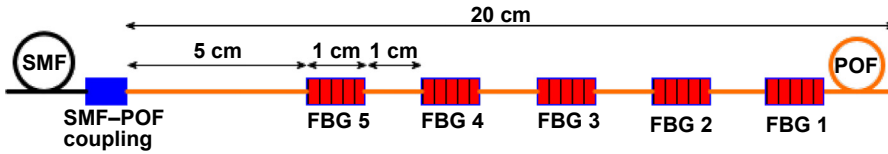


**Figure 8.11** Schematic of the location of different FBGs on the grating array.

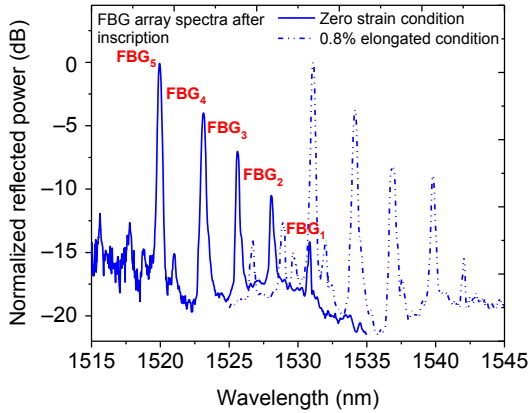


**Figure 8.12** Reflected spectrum of the Bragg grating array at zero-strain condition and at 0.8% elongated condition.

measured 3 dB bandwith of the grating with elongation 1.25% was 0.86 nm, and for the grating inscribed at 0.9% elongation condition it was 0.33 nm, a slight increase from other gratings (Figure 8.13). The measured reflectivity of the grating inscribed with 1.25% elongation was also lower than that of the other FBGs, which is only 6% compared to ∼20% reflectivity of other FBGs. From these results, it is clear that the prolonged elongation for 5 min during UV exposure and the resulted creep and hysteresis during the inscription can affect the quality of the inscribed grating at higher strain states. The UV laser-induced temperature change in the polymer fiber can also enhance this effect. Therefore, to have a good-quality FBG array inscribed into the fiber using this technique, the elongation should be restricted to below 0.9%; otherwise, the reflectivity of the grating is affected due to creep and hystersis of the fiber during the inscription of the grating.

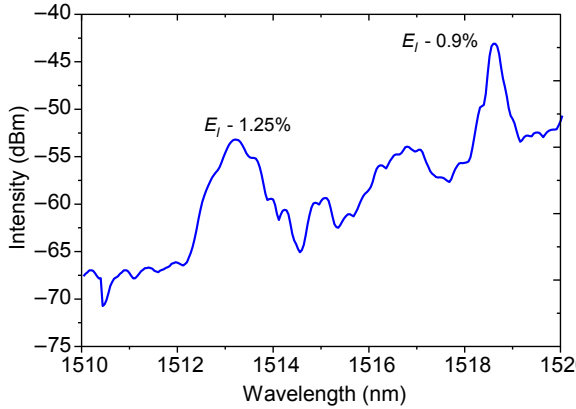


**Figure 8.13** Reflection spectra of FBGs inscribed at 0.9% and 1.25% fiber elongation.

## 8.4 Applications of polymer fiber Bragg grating sensors

The potential of fabricated POFBGs is demonstrated in a number of applications in which the use of the polymer FBG can be of a distinct advantage. Given the low Young's modulus, high failure strain, and intrinsic humidity sensitivity, FBGs based on polymer fibers are generally used in applications in these sensing areas. In this section, we give an update of some of recently reported research work on applications of polymer FBGs, both microstructured and standard FBGs.

*Polymer FBG-based accelerometer*: Stefani, Andresen, Yuan, Rasmussen, & Bang (2012) reported the first polymer FBG-based accelerometer, in which an mPOF grating with wavelengths of 1550 and 850 nm is used. The schematic of the accelerometer characterization setup is shown in Figure 8.14. The demonstrated accelerometers have a linear response for accelerations up to 15 g and a flat frequency response of 1 kHz for a fixed acceleration of 1 g. They have also compared the performance of the polymer FBGs with silica counterparts and the use of polymer FBGs increased the sensitivity by a factor of about four. In addition, the ultimate strain of the polymer material is much higher than that of silica; therefore, the maximum acceleration potential is also much higher.

*Humidity sensors based on polymer FBGs*: One of the unique advantages of polymer FBG is its intrinsic sensitivity to humidity, which arises from the properties of PMMA. For humidity measurements, polymer FBG with reduced cladding thickness can give a better response time compared to unetched polymer FBGs. Rajan, Noor, Liu et al. (2013) and Zhang et al. (2012a) reported humidity sensors based on polymer

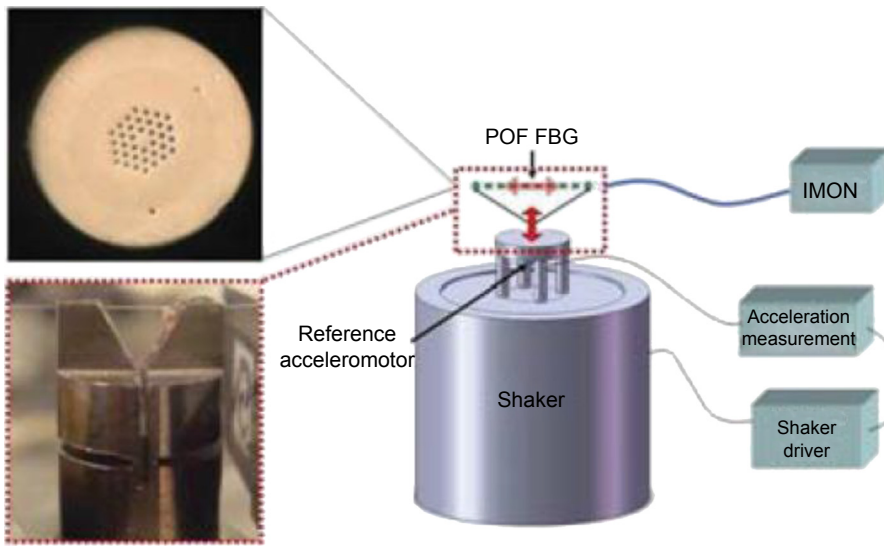


**Figure 8.14** Schematic of a microstructured polymer FBG accelerometer characterization setup (Stefani, Andresen et al., 2012).
Reused with permission.

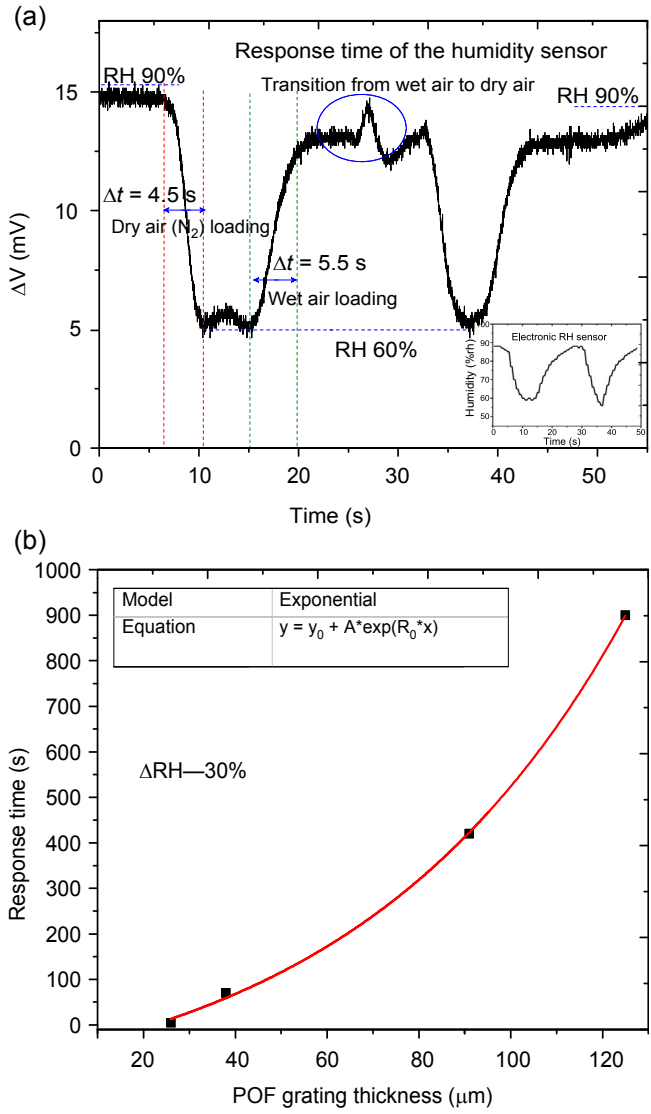


**Figure 8.15** (a) Plot showing response time of the humidity sensor, and (b) response time of humidity sensor with different thicknesses.

FBG with reduced cladding thickness. The time response of the polymer FBG humidity sensor with a thickness of 25 μm is shown in Figure 8.15(a), in which when the relative humidity (RH) is changed from 90% to 60% and a voltage variation of 9.8 mV is observed in 4.5 s, whereas for an RH change of 60−90% a voltage variation of 8.2 mV is observed in 5.5 s. A nonlinear decrease in response time is also reported with a decrease in the polymer FBG diameter as shown in

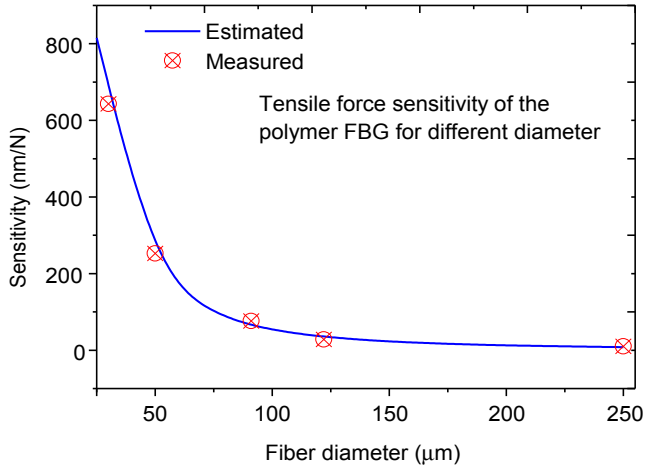


**Figure 8.16** Force sensitivity of the polymer fiber Bragg grating with different fiber diameters.

Figure 8.15(b). The exponential nature of the change in response time is mainly attributed to the absorption mechanism of PMMA. The results demonstrate that polymer FBGs can respond to a change in humidity within seconds if etched to micron level diameter and could be ideal for many industrial applications in which real-time humidity measurements are required.

*Force- and pressure-sensitivity polymer FBGs:* Typically, the force and pressure sensitivity of an FBG depends on the cross-sectional area of the fiber, which can be increased by reducing the diameter of the fiber. Rajan, Liu, Luo, Ambikiarajah, and Peng (2013) reported a sensitivity of 680 nm/N for a polymer FBG with a diameter of 30 μm (Kuang et al., 2009). The focus of the measurement range was at the lower end of the spectrum ranging from 0.005 to 0.05 N. Force sensitivity of polymer FBG with different diameters is calculated and compared with the measured one as shown in Figure 8.16. Sensitivity increases considerably with decrease in fiber diameter.

Bhowmik et al. (Bhowmik, Rajan, Ambikiarajah, & Peng, 2014) has recently reported the inherent pressure sensitivity of polymer FBG with different cladding thicknesses. It was found that the polymer FBG pressure sensitivity increases with reduced cladding thickness by etching. The reason attributed for this phenomenon is due to the etching effects on the fiber, which makes the polymer fiber soft after etching and increases the pressure sensitivity. The reported pressure sensitivity of the polymer FBG with different thicknesses for applied pressure is shown in Figure 8.17.

Rajan, Liu, et al. (2013) also demonstrated high sensitivity pressure using a POF grating-based sensor, in which a thin vinyl diaphragm, which has low Young's modulus, is used to transfer the applied pressure to the POF grating. A prestrained POF grating is attached to the diaphragm vertically as shown in Figure 8.18(a). Due to the very low Young's modulus (2−2.5 GPa) of the vinyl material, higher strain can be produced for very low pressure. The maximum deformation that can occur at the middle of the diaphragm for an applied pressure also depends on the diaphragm

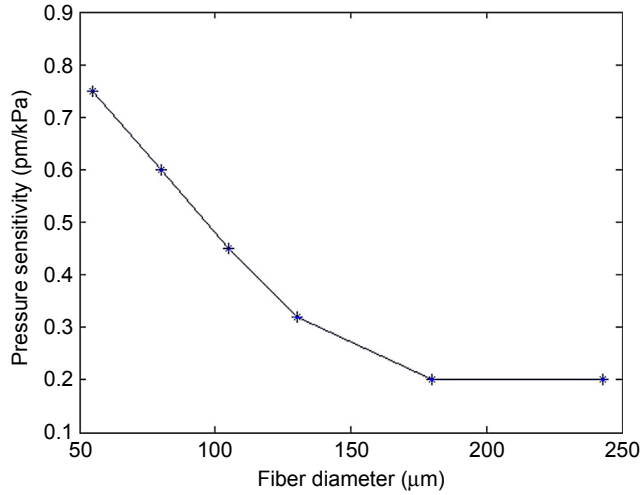


**Figure 8.17** Diameter effects on pressure sensitivity of a polymer FBG.

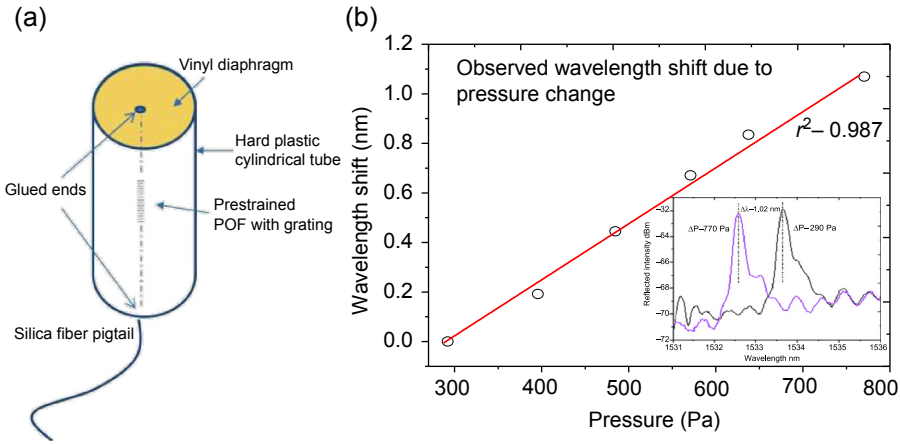


**Figure 8.18** (a) Schematic of the pressure transducer and (b) pressure-induced wavelength shift (inset: shift in the spectral response).

radius and thickness. The observed wavelength shift for the pressure transducer for a range of applied pressure is shown in Figure 8.18(b). For a configuration with a 91 μm diameter POF grating attached perpendicular at the middle of an 8 mm diameter vinyl diaphragm, a sensitivity of approximately 1.32 pm/Pa was estimated. The total length of the fiber containing the grating was 7.5 cm and the thickness of the diaphragm was approximately 60 μm. This sensitivity can be further improved by changing the

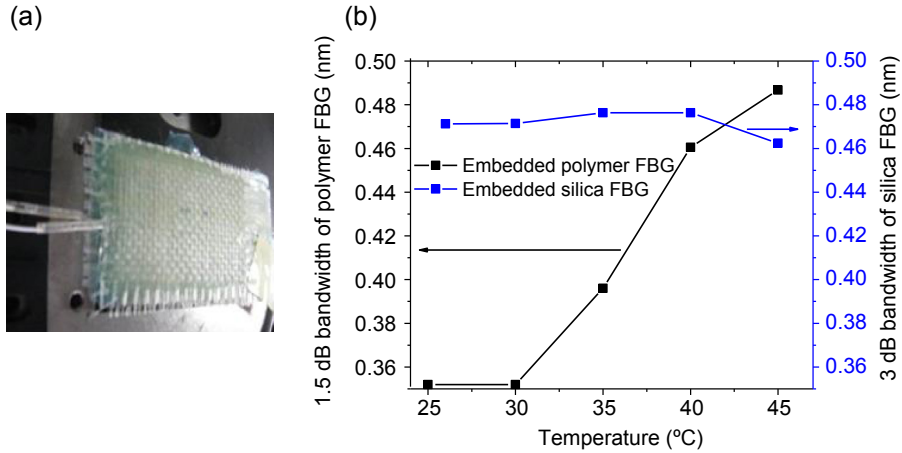


**Figure 8.19** (a) Cured composite material with embedded polymer FBGs. (b) Measured 1.5 dB bandwidth of polymer FBG and 3 dB bandwidth of silica FBG at different temperatures.

diameter of the fiber. That means for high-sensitivity tensile force and pressure measurements, an etched polymer FBG will be a good alternative.

*Composite materials with embedded polymer FBGs*: Composite material structures are widely used in the aerospace, aviation, marine, and civil industries because of their advantages of high strength and stiffness with less weight. For composite materials, the attractive characteristics of polymer FBGs include their high temperature sensitivity, large strain range, and the absence of buffer coating. In a recent work reported by Rajan, Ramakrishnan, et al. (2014), for a polymer FBG embedded in a glass-reinforced composite material, a spectral broadening was observed due to the thermal expansion of the composite, but the sensitivity of the embedded polymer FBG to temperature remains the same as that of the free-space polymer FBG.

A cured composite sample with embedded polymer FBG is shown in Figure 8.19(a) and the measured 1.5 dB bandwidth of the polymer FBG is shown in Figure 8.19(b); it can be seen that the bandwidth increases as the temperature increases. The measured bandwidth change for the embedded polymer FBG within a temperature range of 30−45 °C was 8.5 pm/°C. This indicates that with appropriate calibration, the temperature and thermal expansion of the composite can be measured using the embedded polymer FBG.

*Biochemical concentration sensor*: Another reported application of polymer FBG is a biochemical concentration sensor (Zhang, Webb, & Peng, 2012b). A sensor based on polymer FBG is demonstration for the measurement of saline concentration, in which the concept is based on the process of osmosis. The sensor response against step change in saline concentration is shown in Figure 8.20. If solute exits in the water, then the water content absorbed in the polymer fiber will change because of the process of osmosis. That the sensor is reversible and thus can be used for in situ repeatable measurement and monitoring of concentration is also reported.

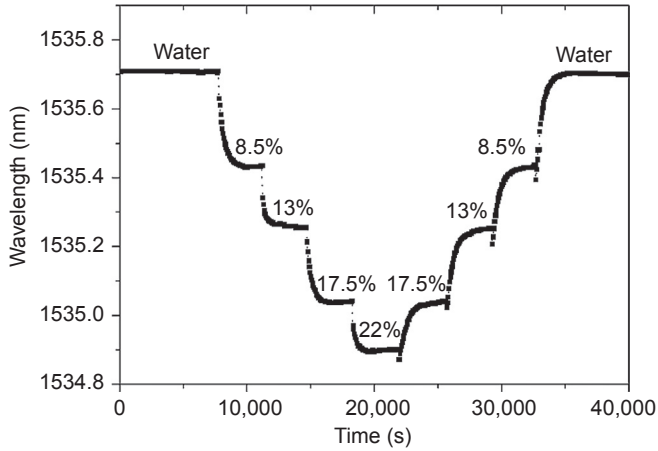


**Figure 8.20** Polymer FBG sensors response against step change of saline concentration (Zhang et al., 2012b).

**Emerging Areas:** Compared to silica FBGs, the research on polymer FBGs do not excel due to the lack of commercially available single-mode polymer fibers, standardization issues, high loss, fabrication difficulty, and so on. But polymer FBGs have advantages such as low Young's modulus, high temperature sensitivity, large strain range, and so forth, which can find applications in niche areas such as biomedical. An example of one of the emerging potential areas in which microstructured polymer FBGs can play a vital role is in the biosensing and biomedical engineering applications. A recent work carried out by Emiliyanov, E Hoiby, Pedersen, & Bang (2013) on a selective serial multi-analyte fluorescene-based fiber optic biosensor using polymer TOPAS fiber point in that direction. The authors suggest that the selective and label-free multi-antibody biosensing with polymer FBG with multiple central wavelengths will soon be demonstrated. Another potential area in which polymer FBG can make an impact is in the biomedical engineering area, in which high-sensitivity pressure measurements are required. With the current development on polymer FBG-based pressure and force sensors, it can be assumed that in the near future, such devices will be available for demonstration in biomedical applications.

## 8.5 Conclusions

In this chapter, we have reviewed the recent updates of research on polymer FBG sensors and their applications. Recent research on microstructured polymer FBGs is reviewed, and that it is an emerging area with potential in biosensing and biomedical engineering applications is noted. A review of polymer microfiber grating and polymer FBG were also presented. The development of these sensors could be vital in a number of application areas, and some examples of the devices based on polymer FBGs were presented. With the ongoing research activities on single-mode polymer FBGs, the research has a bright future with potential applications in niche areas such as biomedical.

## References


Abdi, O., Peters, K., Kowalsky, M., & Hassan, T. (2011). Validation of a single-mode polymer optical fibre sensor and interrogator for large strain measurements. *Measurement Science and Technology, 22*(075207).

Argyros, A. (2013). Microstructures in polymer fibres for optical fibres, THz waveguides and fibre-based metamaterials. id 785162 *ISRN Optics, 2013*.

Bhowmik, K., Rajan, G., Ambikiarajah, E., & Peng, G.-D. (2014). Hydrostatic pressure sensitivity of standard singlemode polymer fibre bragg gratings and etched polymer fibre bragg gratings. *Proc. SPIE 9157, 23rd International Conference on Optical Fibre Sensors, 91573G* (June 2, 2014).

Bolle, M., Lazare, S., Blanc, M. L., & Wilmes, A. (1992). Submicron periodic structures produced on polymer surfaces with polarized excimer laser ultraviolet radiation. *Applied Physics Letters, 60*, 674−676.

Bosc, D., & Toinen, C. (1992). Full polymer single-mode optical fibre. *IEEE Photonics Technology Letters, 4*(7), 749−750.

Bundalo, I. L., Nielsen, K., Markos, C., & Bang, O. (2014). Bragg grating writing in PMMA microstructured polymer optical fibres in less than 7 minutes. *Optics Express, 22*, 5270−5276.

Decker, C. (1998). The use of UV irradiation in polymerization. *Polymer International, 45*, 133.

Dobb, H., Webb, D. J., Kalli, K., Argyros, A., Large, M. C. J., & van Eijkelenborg, M. A. (2005). Continuous wave ultraviolet light-induced fibre Bragg gratings in few-and single-mode microstructured polymer optical fibres. *Optics Letters, 30*(24), 3196−3298.

Durana, G., Gómez, J., Aldabaldetreku, G., Zubia, J., Montero, A., & Ocáriz, Sáez de (2012). Assessment of an LPG mPOF for strain sensing. *IEEE Sensors Journal, 12*, 2668−2673.

Emiliyanov, G., E Hoiby, P., Pedersen, L. H., & Bang, O. (2013). Selective serial multi-antibody biosensing with TOPAS microstructured polymer optical fibres. *Sensors, 13*(3), 3242−3251.

Kalli, K., Dobb, H. L., Webb, D. J., Carroll, K., Themistos, C., Komodromos, M., et al. (2007). Development of an electrically tuneable Bragg grating filter in polymer optical fibre operating at 1.55 μm. *Measurement Science and Technology, 17*, 3155−3164.

Kaminov, I. P., Weber, H. P., & Chanderross, E. A. (1971). *Applied Physics Letters, 18*(497).

Kuang, K. S. C., Quek, S. T., Koh, C. G., Cantwell, W. J., & Scully, P. J. (2009). Plastic optical fibre sensors for structural health monitoring: a review of recent progress, 312053 *Journal of Sensors, 2009*.

Kuzyk, M. G., Paek, U. C., & Dirk, C. W. (1991). Guest-host polymer fibres for nonlinear optics. *Applied Physics Letters, 59*(8), 902−904.

Large, M. C. J., Barton, G. W., Poladian, L., & van Eijkelenborg, M. A. (2007). *Microstructured polymer optical fibres*. Berlin, Germany: Springer.

Liu, H. B., Liu, H. Y., Peng, G. D., & Chu, P. L. (2004). Novel growth behaviors of fibre Bragg gratings in polymer optical fibre under UV irradiation with low power. *IEEE Photonics Technology Letters, 16*(1), 159−161.

Liu, H. Y., Peng, G. D., & Chu, P. L. (2002). Polymer fibre bragg gratings with 28-dB transmission rejection. *IEEE Photonics Technology Letters, 14*, 935−937.

Markos, C., Stefani, A., Nielsen, K., Rasmussen, H. K., Yuan, W., & Bang, O. (2013). High-Tg TOPAS microstructured polymer optical fibre for fibre Bragg grating strain sensing at 110 degrees. *Optics Express, 21*, 4758−4765.

Peng, G. D., & Chu, P. L. (2000). Polymer optical fibre photosensitivities and highly tunable fibre gratings. *Fibre and Integrated Optics, 19*, 277−293.

Peng, G. D., Chu, P. L., Lou, X., & Chaplin, R. A. (1995). Fabrication and characterization of polymer optical fibres. *Journal of Electrical and Electronics Engineering, Australia, 15*(3), 289−296.

Peng, G. D., Xiong, Z., & Chu, P. L. (1999a). Photosensitivity and gratings in dye-doped polymer optical fibres. *Optical Fibre Technology, 5*, 242−251.

Peng, G. D., Xiong, Z., & Chu, P. L. (1999b). Photosensitivity in dye-doped polymer optical fibres. *Optical Fibre Technology, 5*, 242−251.

Peters, K. (2011). Polymer optical fibre sensors- a review. *Smart Materials and Structures, 20*(013002), 12.

Rajan, G., Liu, B., Luo, Y., Ambikiarajah, E., & Peng, G.-D. (2013). High sensitivity force and pressure measurements using etched singlemode polymer fibre Bragg gratings. *IEEE Sensors Journal, 13*(5), 1794−1800.

Rajan, G., Noor, M. Y. M., Ambikiarajah, E., Farrell, G., & Peng, G.-D. (2013). Polymer microfibre Bragg grating. *Optics Letters, 38*(17), 3359−3362.

Rajan, G., Noor, M. Y. M., Ambikiarajah, E., & Peng, G. D. (2014). Inscription of multiple bragg gratings in a singlemode polymer optical fibre using phase mask and its analysis. *IEEE Sensors Journal, 14*(17), 2384−2388.

Rajan, G., Noor, M. Y. M., Liu, B., Ambikiarajah, E., Webb, D., & Peng, G.-D. (2013). A fast response intrinsic humidity sensor based on an etched singlemode polymer fibre bragg grating. *Sensors and Actuators A: Physical, 203*, 107−111.

Rajan, G., Ramakrishnan, M., Semenova, Y., Ambikiarajah, E., Farrell, G., & Peng, G.-D. (2014). Experimental study and analysis of a polymer fibre bragg grating embedded in a composite material. *Journal of Lightwave Technology, 32*, 1726−1733.

Rajkumar, R., Mathews, S., Rajan, G., Semenova, Y., Farrell, G., & Srinivasan, B. (November 2013). Fabrication and characterization of bragg gratings in polymer optical fibres using 248 nm irradiation. In *Proc. ACP 2013, Beijing, China*.

Sáez-Rodríguez, D., Cruz, J. L., Johnson, I., Webb, D. J., Large, M. C. J., & Argyros, A. (2010). Water diffusion into UV inscripted long period grating in microstructured polymer fibre. *IEEE Sensors Journal, 10*, 1169−1173.

Stefani, A., Andresen, A., Yuan, W., Rasmussen, N. H., & Bang, O. (2012). High sensitivity polymer optical fibre Bragg grating based accelerometer. *IEEE Photonics Technology Letters, 24*(9), 763−765.

Stefani, A., Stecher, M., Town, G. E., & Bang, O. (2012). Direct writing of fibre Bragg grating in microstructured polymer optical fibre. *IEEE Photonics Technology Letters, 24*(13), 1148−1150.

Stefani, A., Yuan, W., Markos, C., & Bang, O. (2011). Narrow bandwidth 850-nm fibre Bragg gratings in few-mode polymer optical fibres. *IEEE Photonics Technology Letters, 23*, 660−662.

Tao, X. M., Yu, J. M., & Tam, H. Y. (2007). Photosensitive polymer optical fibres and gratings. *Transactions of the Institute of Measurement and Control, 29*(3−4), 255−270.

Tomlinson, W. J., Kaminow, I. P., Chanderross, E. A., Fork, R. L., & Silfvast, W. T. (1970). Photoinduced refractive index increase in poly(methyl methacrylate) and its applications. *Applied Physics Letters, 16*(12), 486−488.

Van Eijkelenborg, M. A., Large, M. C. J., Argyros, A., et al. (2001). Microstructured polymer optical fibre. *Optics Express, 9*(7), 319−327.

Webb, D. J., Kalli, K., Zhang, C., Johnson, I., Chen, X. F. G., Rodriguez, D. S., et al. (September 9−11, 2009). Applications of polymer fibre grating sensors. In *The 18th international conference on plastic optical fibres*.

Xiong, Z., Peng, G. D., Wu, B., & Chu, P. L. (1999). Highly tunable bragg gratings in single-mode polymer optical fibres. *IEEE Photonics Technology Letters, 11*, 352−354.

Xu, X., Ming, H., & Zhang, Q. (2002). Properties of polarized laser-induced birefringent gratings in azobenzene-doped poly(methyl methecrylate) optical fibres. *Optics Communications, 204*(1−6), 137−143.

Yuan, W., Khan, L., Webb, D. J., Kalli, K., Rasmussen, H. K., Stefani, A., et al. (2011). Humidity insensitive TOPAS polymer fibre Bragg grating sensor. *Optics Express, 19*, 19731−19739.

Yuan, W., Stefani, A., & Bang, O. (2012). Tunable polymer fibre Bragg grating (FBG) inscription: fabrication of dual-FBG temperature compensated polymer optical fibre strain sensors. *IEEE Photonics Technology Letters, 24*, 401−403.

Yu, J. M., Tao, X. M., & Tam, H. Y. (2004). Trans-4-stilbenemethanol-doped photosensitive polymer fibres and gratings. *Optics Letters, 29*(2), 156−158.

Zhang, Z. F., & Tao, X. M. (2013). Intrinsic temperature sensitivity of fibre Bragg gratings in PMMA-based optical fibres. *IEEE Photonics Technology Letters, 25*(3), 310−312.

Zhang, W., Webb, D. J., & Peng, G.-D. (2012). Investigation into time response of polymer fibre Bragg grating based humidity sensors. *Journal of Lightwave Technology, 30*, 1090−1096.

Zhang, W., Webb, D., & Peng, G.-D. (2012). Polymer optical fibre Bragg grating acting as an intrinsic biochemical concentration sensor. *Optics Letters, 37*(8), 1370−1372.

Zhang, Z. F., Zhang, C., Tao, X. M., Wang, G. F., & Peng, G.-D. (2010). Inscription of polymer optical fibre Bragg grating at 962 nm and its potential in strain sensing. *IEEE Photonics Technology Letters, 22*(21), 1562−1564.

This page intentionally left blank

# Functionalized microstructured optical fibers for specific nucleic acid detection

9

*A. Candiani, A. Cucinotta*
University of Parma, Parma, Italy

## 9.1 Introduction

The need for new, fast, and cheap technologies for medical and healthcare diagnostic equipment is the driving force behind and investment and research in biosensor technology (Loung, Male, & Glennon, 2008). Among the different principles of detection, optical-based biosensing is one of the most widely investigated transduction methods. In particular, optical fiber sensors offer the main advantage of small and flexible shape, connecting a remote light source to a small in situ sensing element; they are able to give rapid and sensitive detection of the target in real time, especially if the detection is performed using a label-free scheme.

In such a context, microstructured optical fibers (MOFs), also known as photonic crystal fibers (PCFs), offer a number of unique advantages in biological and chemical sensing applications. Due to the presence of air holes running along their entire lengths, these fibers have the ability to accommodate biological and chemical samples in gaseous or liquid form in the immediate vicinity of the fiber core or even inside the core. MOFs can be used simultaneously for light guiding and as fluidic channels, leading to a strong light/sample overlap. Such channels can be further functionalized with biorecognition layers that can bind and progressively accumulate target sample, thus enhancing sensor sensitivity and specificity. Due to the small size of MOF core and cladding air holes and the high degree of overlap between sample and light, a very small fluid volume is required for sensing. The amount of volume needed using these fibers is on the order of hundreds of nanoliters to tens of microliters, whereas in conventional optics measurement techniques the volumes needed are on the order of 1−10 mL. The use of an extremely small volume is of huge interest for biochemical applications, such as analyte detection or protein/DNA recognition (Corradini & Selleri, 2012, Chapter 11; Skorobogatiy, 2009).

Various research groups have implemented very attractive and interesting classes of MOF-based sensors for bioapplications. Jensen et al. (2004) have described a sensor for detection of biomolecules in an aqueous solution using an MOF without a solid core. By infiltrating fluorophore-labeled DNA in the air holes of the microstructured part of the fiber, the transmission peak located in the absorption region of the fluorophore revealed the presence of the target biomolecule. Ruan, Schartner, Ebendorff-Heidepriem, Hoffmann, and Monro (2007) have used soft-glass MOFs to

**Optofluidics, Sensors and Actuators in Microstructured Optical Fibers.** http://dx.doi.org/10.1016/B978-1-78242-329-4.00009-6

detect quantum dot-labeled proteins, achieving a detection limit of 1 nM. Afshar, Warren-Smith, and Monro (2007) have developed a generic model of excitation and fluorescence recapturing, supported by the experimental results, within filled solid-core MOFs. Moreover, the small core of MOF can actually be an advantage for approaches exploiting the inherent nonlinearity of the PCF, like the four-wave mixing-based biosensor first proposed in Ott, Heuck, Agger, Rasmussen, & Bang (2008) and experimentally demonstrated in Frosz, Stefani, and Bang (2011). Polymeric MOFs, which have attractive material and biochemical properties, have been also used successfully in such a photonic approach for biosensing. The first demonstration of biosensing with a polymer MOF was in 2005, when the polymethylmethacrylate microstructured fiber was used for fluorescence-based selective detection of the antibody streptavidin (Jensen et al., 2005). Emiliyanov et al. (2007a,b) have presented a microstructured-polymer optical fiber (mPOF) fabricated from Topas cyclic olefin copolymer, in which localized sensor layers could be activated on the inner side of the air holes in a predetermined section of the fiber, and the detection of fluorophore-labeled antibodies was proven. Moving on to label-free techniques, different approaches can be implemented to detect specific biological targets; Markos, Yuan, Vlachos, Town, and Bang (2011) realized a dual-core mPOF biosensor that detects change of the layer thickness of antibody biomolecules by monitoring the change in the coupling length between the two cores.

Furthermore, the possibility to inscribe a Bragg or long period grating (LPG) in the core of the microstructured-fiber detection increases the interrogation efficiency of the system. Rindorf et al. (2006) observed the shift of the resonant peak of an LPG, measuring the thickness of a monolayer of poly-L-lysine and double-stranded DNA. One of the major challenges in DNA detection is the discrimination of different sequences differing only for a single nucleobase, that is, point mutations or single nucleotide polymorphisms. This characteristic is particularly important because point mutations can be related to genetic diseases, such as cystic fibrosis (CF) or thalassemia, and are frequently found in the DNA of tumor cells (Greenman et al., 2007).

In this chapter, we will report a novel DNA photonic-sensing approach based on peptide nucleic acids (PNA)-functionalized MOF Bragg grating. By employing Bragg gratings, the signal is monitored in reflection mode allowing the use of the fiber itself as a probe. Theoretical models have been developed to characterize Bragg gratings as transduction elements in MOF biosensors (Burani & Lægsgaard, 2005; Rindorf & Bang, 2008). Here we demonstrate experimentally the feasibility of such a scheme adopting the following approach. The inner surface of different MOFs has been functionalized using a PNA probe, an oligonucleotide (ON) mimic that is well suited for specific DNA target sequence detection. In our case, PNA probes have been used to detect DNA chains of great relevance for medical and food industry applications. After the solution of DNA molecules had been infiltrated inside the fiber capillaries and hybridization had occurred, oligonucleotide-functionalized gold nanoparticles (ONAuNPs) were added and used to form a sandwich-like system to achieve signal amplification, as observed in other optical techniques (D'Agata, Corradini, Grasso, Marchelli, & Spoto, 2008). The results obtained will be presented in the following paragraphs, describing the advantages and the effectiveness of such a method.

## 9.2 Functionalization and hybridization process

A biosensor is an analytical device comprising two elements: a biological recognition element able to interact specifically with a target, and a transducer able to convert the recognition event into a measurable signal. The biorecognition element consists of PNA, a nucleic acid analog that can very effectively bind to complementary DNA strands, and the transducer consists of an MOF Bragg grating. PNA molecules are not able to be strongly adsorbed to the fiber surface, so a derivatization of the surfaces is needed to obtain a suitable substrate. In several works, the modification of optical fiber and waveguide silica surfaces has been described. The most stable modification can be obtained by tethering of sensors or biomolecules to the silica surface through a silanization procedure (Chen et al., 2007; Cordek, Wang, & Tan, 1999; Tazawa, Kanie, & Katayama, 2007).

To test the applicability of sequence-selective detection of DNA by the fibers, a series of tests aimed at the introduction of very selective DNA-binding molecules at the fiber surface has been carried out on a suspended core MOF (Coscelli et al., 2010). The derivatization procedure was tested using tetramethylrhodamine. To obtain a PNA-modified surface, the functionalization on the internal channels of the fiber was carried out according to the scheme reported in Figure 9.1.

The protocol used is described by the following steps:

1. Cleaning and activation of the silica surface with acidic treatment (HCl:methanol = 1:1), which, according to the literature, is the best performing technique for subsequent derivatization (Han, Mayer, Offenhauser, & Ingebrandt, 2006).
2. Silanization with (3-aminopropyl)triethoxysilane (5% in ethanol) overnight (Han et al., 2006).
3. Reaction of the amino group with succinic anhydride (0.25 M in *N*,*N*-dimethylformamide [DMF], overnight) to obtain a carboxylic acid functional group attached to the fiber.
4. Activation of the carboxylic function with *N*,*N*-diisopropylcarbodiimide and *N*-hydroxysuccinimide in DMF as a solvent (0.25 M both) overnight.
5. Reaction of the activated ester with the end terminal amino group of the PNA probe overnight (30 μM of probe in 100 mM carbonate buffer in water:acetonitrile = 90:10 containing 0.001% sodium dodecyl sulfate, pH = 9), according to previous procedures used for microarray spotting (Germini et al., 2005; Rossi, Scaravelli, Corradini, Fogher, & Marchelli, 2006).
6. Quenching of the excessive activated esters with an excess of ethanolamine (50 mM in aqueous Tris buffer pH = 9.0, room temperature for 3 h).

Internal derivatization was obtained by applying a nitrogen pressure of 2 atm to a polytetrafluoroethylene (PTFE) tubing reservoir (100 μL), connected to the terminal part of the fiber through a polyetheretherketone ferrule junction and a PTFE adapter. The flow through the fiber was checked by the appearance of a liquid flow at the opposite end. After each treatment, the liquid was removed from the fiber by means of at least 30 min nitrogen flux, as checked by optical microscope inspection.

To test the protocol used and to check that the PNA probes were effectively attached on the surface, hybridization experiments have been performed with fluorescently labeled full complementary and single mismatched DNA ONs, reported in

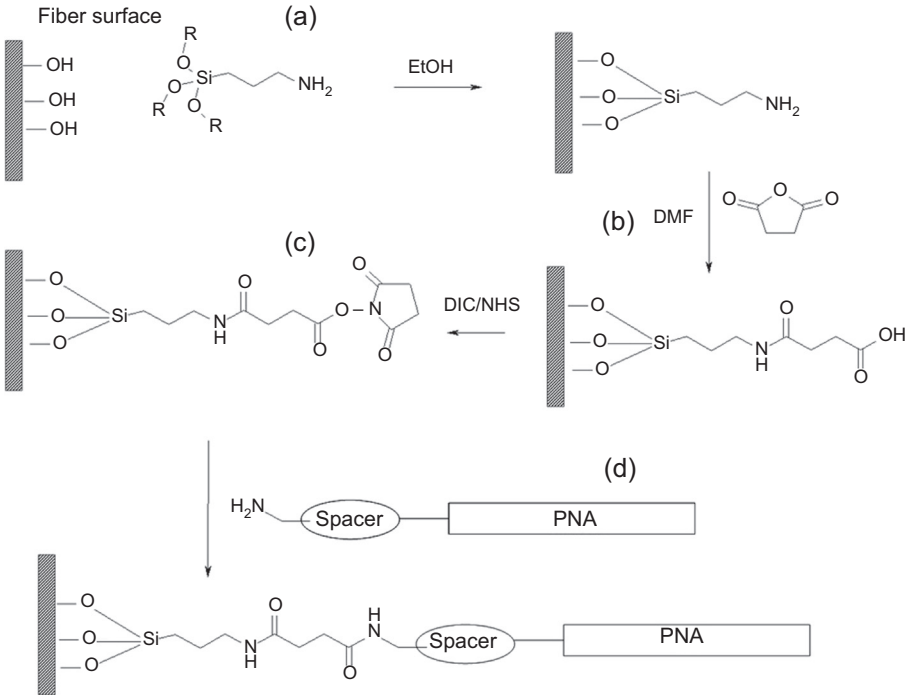


**Figure 9.1** Derivatization scheme used for the PNA-modified solid core (SC)-PCF. (a) Silanization. (b) Reaction with succinic anhydride. (c) Activation of the carboxylic moiety. (d) Covalent link to the PNA through the terminal amino group. Experimental details are described in the text (Coscelli et al., 2010).

Table 9.1. The hybridization has been evaluated by means of a microarray fluorescence reader, the ScanArray Express by Perkin Elmer, which performs fluorescence scanning of the samples deposited on a glass slide using two different laser sources for excitation of the fluorophores (543 nm for the Cy3 channel and 633 nm for the Cy5 channel) and different emission filters for selecting the fluorescence emitted.

Several 5-cm-long samples of the same fiber, internally modified with PNA, have been treated separately, one series with the Cy3-modified full match (DNA 1) and

**Table 9.1 Sequences of the PNA probes and of DNA targets**

| Oligo | Sequence | Role |
|---|---|---|
| PNA | H-O-O-TTACTC**A**TTCACC-NH2 | Probe |
| DNA 1 | Cy3-GGTGAA**T**GAGTAA | Cy3-full match |
| DNA 2 | Cy3-GGTGAA**A**GAGTAA | Cy3-mismatch |

Note: O: 2-(2-aminoethoxy)ethoxyacetyl spacer. The bold underscored letter denotes the position of the matched/mismatched base.

one with the mismatched (DNA 2) ONs, as described in Table 9.1. The solutions have been diluted to 100 nM concentration and their fluorescence-emission intensities have been checked to be the same as before hybridization. The hybridization has been performed by flowing each solution through the fiber by means of a high-performance liquid chromatography 100 μL syringe with moderate pressure for 2 h. Thirty-four microliters of each solution has passed through either of the two fibers, in large excess if compared to the ultra-small internal volume (around 23 nL). The fibers have been then dried with a flux of air and washed with excess phosphate buffer solution (PBS) (15−20 μL), and then dried again. The two fibers have then been analyzed using the ScanArray Express reader, and the fluorescence was quantified using the instrument software. An example of the results is reported in Figure 9.2(b). The same measurement was repeated in triplicate with reproducible results. Unmodified fibers treated with the 100 nM solution of the DNA 1, using the same procedure, showed very low

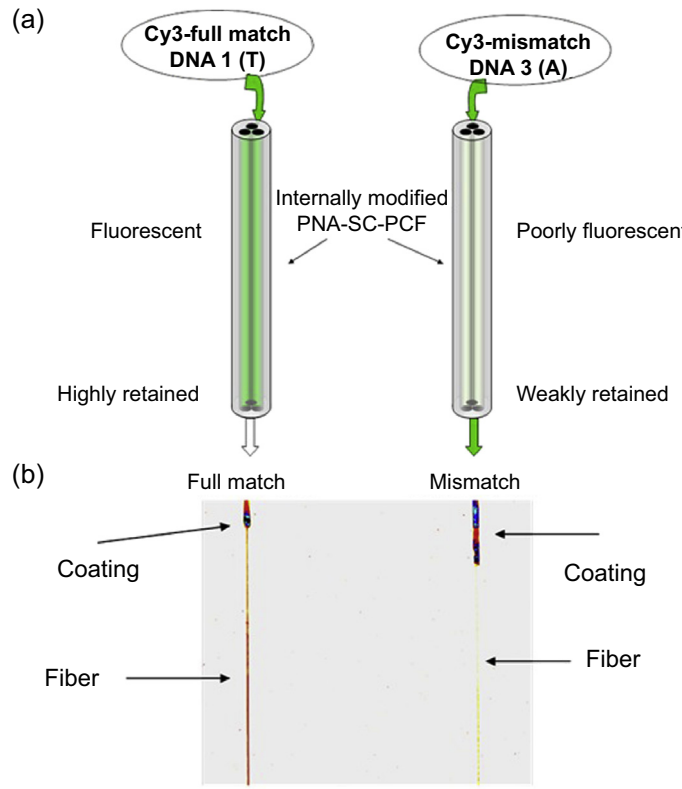


**Figure 9.2** (a) Schematic representation of the hybridization experiment using PNA internally modified SC-PCF. (b) ScanArray images (Cy3 channel; λex = 543 nm and λem = 570 nm) of the fibers after hybridization; PNA SC-PCF hybridized with (left) full-match DNA 1 and (right) mismatched DNA 3. Negative image intensity is color-encoded from (low) yellow to (high) blue; full scale: black (Coscelli et al., 2010).

fluorescence, whereas the intensity of the PNA-modified fibers treated with the same solution was significantly higher (fluorescence ratio PNA-modified/unmodified fibers = 53, std. dev. = 14), thus showing that the PNA induces efficient capturing of the target DNA within the fiber. Furthermore, the full-match DNA 1 was captured by the PNA-modified fibers more efficiently than the singly mismatched DNA 2 (fluorescence ratio DNA 1/DNA 2 = 3.0, std. dev. = 0.9). This indicates a role of the PNA probe in binding to the target DNA and in discriminating the DNA with only a single-base difference.

The experiment reported has demonstrated the possibility to use ON probes to functionalize the internal channel surface of an MOF. The implemented protocol was then used to realize highly selective DNA biosensors, which will be presented and discussed in the following paragraphs.

## 9.3 Label-free DNA biosensors based on PNA-functionalized microstructured optical fiber gratings

Initially, the bioderivatization described above has been applied on the external surface of standard silica fibers previously inscribed with gratings, which represent a powerful investigative tool, able to greatly amplify the spectral response of the fiber. On the basis of the measurement of refractive index changes induced by a chemical and biochemical interaction that occurs at the interface-cladding analyte on the outer surface of the fiber, the transmission spectrum is modulated. First, a standard optical fiber with LPG has been externally functionalized using PNA probes. The hybridization PNA−DNA that happened on the silica surface modifies the effective refractive index $n_{\text{eff}}$, thus modulating the transmission mode propagation (Sozzi et al., 2011). A similar approach has been applied using a double tilted fiber Bragg grating (DTFBG). In this configuration, the coupling between the forward-propagating core mode and the counter-propagating cladding mode occurs, and the molecular recognition event is measured through the spectral transmission response of the DTFBG modified by the external refractive-index changes (Candiani et al., 2012).

In both of these initial experiments, the target molecules were detected through interaction with the cladding modes, and the system was read in transmission mode. Moreover, a liquid-handling Teflon tubing system has been used for the packaging of the fiber and for keeping the solution close to the fibers for which milliliter quantities of analyte are needed.

Using microstructured fibers, many of these limits may be exceeded; the amount of volume needed is on the order of nL/μL, much lower than in the previous approach. Once infiltrated inside the microchannels, the target solution is in contact with the fiber core, thus allowing the interaction between the analyte and the core modes. In addition, the possibility of including a Bragg grating in the core of the fiber makes the approach even more attractive, as it offers the possibility to monitor the reflection modes, allowing the use of the fiber itself as a probe.

In the next paragraphs, we will show two examples of biosensing applications based on PNA-functionalized Bragg grating MOFs for DNA detection for the medical and food industry fields.

### 9.3.1 DNA detection of CF disease using a multimode-doped microstructured optical fiber

The first MOF-based biosensor has been implemented using a grapefruit geometry fiber, having five holes of 20.8-μm diameter, forming an outer core of 16.1 μm that includes a 3.5%wt Ge-doped socket of diameter 8.5 μm, as shown in Figure 9.3. In that fiber, a 22-mm-long Bragg grating was inscribed using a 1067.73 nm phase mask and a 193 nm excimer laser, 10 ns laser radiation (Pissadakis, Livitziis, & Tsibidis, 2009). The grating reflected two major modes, located at 1546 nm (zeroth order) and 1541.6 nm (first order), with strengths 25 and 12 dB, respectively. Profile beam measurements showed that the zeroth-order mode is confined to the Ge-doped core, whereas the first-order mode is defined by the surrounding capillary structure, extending to a greater area (as shown in the right part of Figure 9.3(b)). The inscription of the grating caused a slight birefringence effect in the fiber, and this was observed in the high-order mode spectrum of Figure 9.3(b).

As mentioned, the most stable modification for an optical fiber silica surface can be obtained by tethering of biomolecules or other probes through a silanization procedure. The functionalization of the internal microchannels was realized by following the steps described in the previous paragraph; the PNA sequences used were chosen to mimic the DNA sequence bearing a single-point mutation (W1282X), which is implicated in CF disease (Shoshani et al., 1992), which is the most common mutation present on 50−60% of CF chromosomes in the Ashkenazi Jewish population. The PNA probe used is targeted to the mutated sequence, and ideally should give low or no response to the wild-type DNA, thus revealing only the presence of the mutated sequence.

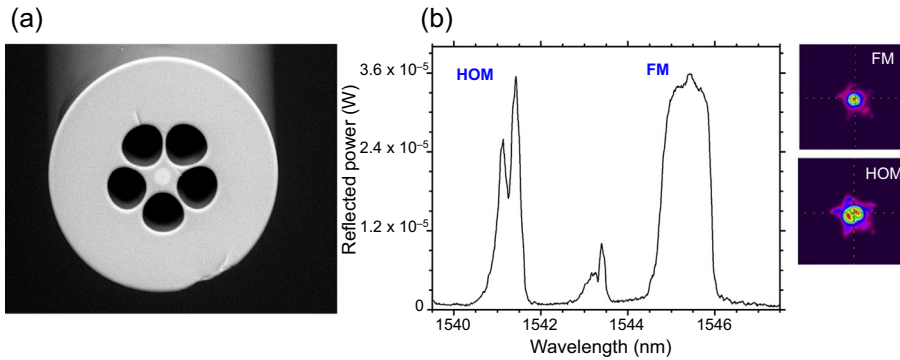


**Figure 9.3** (a) A scanning electron microscope photo of the microstructured fiber used. (b) The reflected spectrum of the MOF, revealing a slight birefringence effect. On the right, the fundamental and high-order mode profiles are reported.

A relatively simple setup has been implemented to monitor the fiber during the functionalization and hybridization processes. An amplified stimulated emission (ASE) source (ASE 1600, NTT Electronics), used as a broadband light source, was connected to a fiber optic circulator 1 × 2 (1530−1570 nm bandwidth), as shown in Figure 9.4. The light was coupled to the functionalized MOF through port2 of the circulator, and the reflected signal was analyzed though port3 using an optical spectrum analyzer (Ando AQ-6315A). The functionalization of the microcapillaries and DNA infiltration process were performed by infiltrating the reagents in the holes of the MOF using a syringe pump (KD Scientific 100 series). The system was connected to a high-pressure microfiltered nitrogen line to empty and dry the fiber after infiltration. To make the setup even more reliable, a high-precision dynamometer was also used to keep the fiber always with the same tension. The measurements were made in a clean room environment with a temperature control system. Spectral measurements of the reflected signal have been recorded at the beginning and at the end of every hybridization phase.

First, to assess the ability of the modified surface to capture complementary DNA even in the presence of dopant agents in the silica substrate, the PNA-modified microstructured fiber and a non-functionalized one were filled with a solution of fluorescently labeled DNA-Full Match (FM)-Cy3 (see Table 9.2) for the hybridization test as described previously. By evaluating the fluorescence intensity from the ScanArray image through the instrument software, the signal-to-noise ratio of the modified fiber, with respect of the background of the plane glass slide, was found to be almost 140; the signal arising from the PNA-modified fiber was found almost nine-fold more intense than that obtained for the non-derivatized one, as reported in Figure 9.5, thus also demonstrating the actual success of the functionalization procedure for this Ge-doped core microstructured fiber. Subsequently, the spectral modulation of the fiber induced by the PNA-DNA hybridization has been studied.

In the label-free detection experiment, unmodified DNA bearing the point mutation and a sequence for AuNP capture was used. Before the infiltration of the DNA solutions, PBS was infiltrated into the microcapillaries to evaluate the stability of the

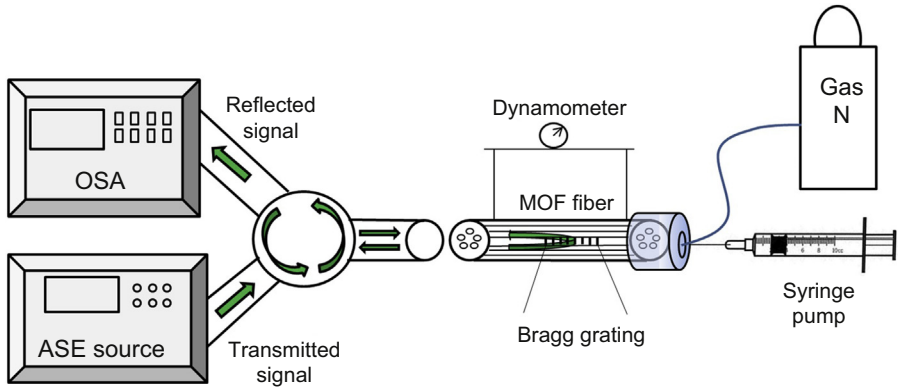


**Figure 9.4** The schematic of the optical setup implemented for the experiment is presented.

**Table 9.2 Sequences of the PNA probes and of DNA targets.**

| Oligo | Sequence | Role |
|---|---|---|
| PNA | H-O-O-CTTTCC*T*TCACTGTT-$NH_2$ | Probe |
| DNA-FM-Cy3 | Cy3-GCAACAGTG*A*AGGAAAGCC | Cy3 full match |
| DNA-FM | **ATCGATGGTGTGTCTT**GGGATTCAATAACTTTGCAACAGTG*A*AGGAAAG | Unlabelled full match (CF mutation) |
| DNA-MM | **ATCGATGGTGTGTCTT**GGGATTCAATAACTTTGCAACAGTG*G*AGGAAAG | Unlabelled single-base mismatch (wild type) |
| AuNP-DNA | AAGACACACCATCGAT − BIOTIN | Biotinylated DNA for AuNP functionalization |

In italics the base corresponding to the W1282X point mutation and in bold the target sequence for ONAuNPs are indicated.
Note: O: 2-(2-aminoethoxy)ethoxyacetyl spacer.

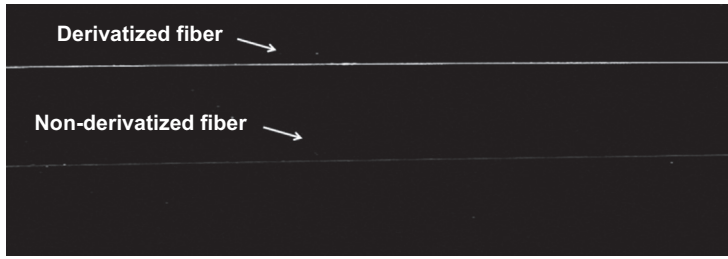


**Figure 9.5** ScanArray Express image of an unmodified fiber (below) and a PNA-derivatized fiber (above) after infiltration of the fluorescently labeled full complementary oligonucleotide (ON) (DNA-FM-Cy3).

signal, which remained unchanged for the duration of approximately 1 h. The syringe pump was used for infiltrating the DNA inside the fiber at a fixed flow rate of 0.25 μL/min, ensuring a continuous renewal of the DNA solution in contact with the surface. The 100 nM DNA solution was infiltrated through the fiber capillaries for 1 h, and then the fiber was emptied using nitrogen at 5 atm, because it has been shown that the sensitivity of fiber-grating sensors is around three times higher when measurements are made in air rather than in liquids (Candiani et al., 2013), and their optical properties were recorded. The reflected signal after the infiltration of DNA-FM showed a small shift of 0.05 nm in the higher order, as illustrated in the red dashed line in Figure 9.6(a).

When the DNA binds to the PNA, it replaces buffer solution molecules within a few nanometers from the surface of the fiber, resulting in a refractive-index change near the sensor surface. At this low DNA concentration, the captured DNA layer is not thick enough to be optically detected, as a shift occurs in the reflected signal, in accordance with the results obtained for the first optical biosensors based on standard fiber gratings and a similar functionalization (Candiani et al., 2012; Sozzi et al., 2011). Subsequently, to enhance the measured shift, the ONAuNPs solution was infiltrated for 1 h, and then the fiber was washed with PBS and emptied again. Nanoparticles and subwavelength-structured materials can lead to strong improvement in the detection limits, and to great simplification of sensing devices and protocols based on DNA and DNA-like probes (D'Agata et al., 2008), especially those in which the response depends on events that take place on nanometer or subnanometer scales on the sensor surface. Therefore, the last process allows the AuNPs to bind to the DNA target, increasing the refractive index contrast between the silica surface of the capillaries and the analyte (see Figure 9.7).

The maximum shift observed for the reflected high-order band in this experiment was around 0.27 nm toward the red, whereas no significant changes were observed in the fundamental mode (Rosi & Mirkin, 2005). The binding of the AuNPs to their target on the DNA captured on the fiber greatly amplify the response of the fiber, because the layer deposited onto the fiber channel surface is greatly incremented, thereby increasing the $n_{\text{eff}}$ of the fiber. This effect is translated into a shift of the reflected high-order Bragg peak, as described by the Bragg condition. In this case,

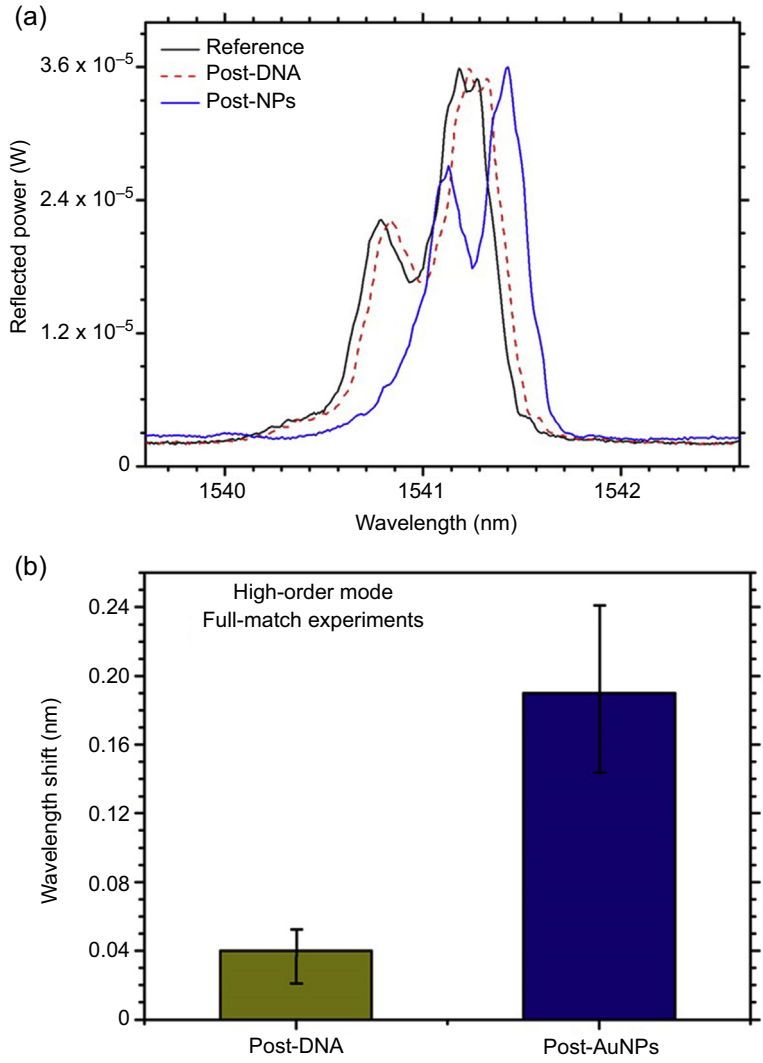


**Figure 9.6** (a) Spectral measurements after the hybridization process with 100 nM full-match DNA solution and gold nanoparticles (NPs). (b) Average of the high-order wavelength shift after DNA infiltration (left) and after oligonucleotide-functionalized gold nanoparticle (ONAuNP) infiltration (right); a small memory effect decreases the modulation observed for each experiment performed on the same fiber.

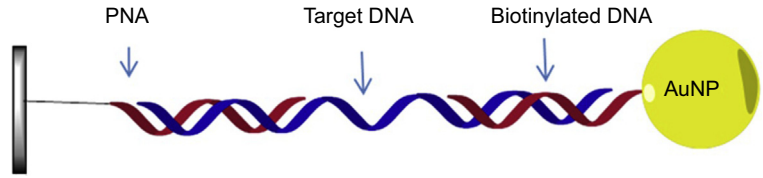


**Figure 9.7** Scheme of sandwich-like system used for DNA detection.

the shift was statistically significant, as reported in Figure 9.6(a). This discrepancy between the two modes was supported by initial experiments on the spectral sensitivity of the two Bragg grating modes in which liquids of different refractive indices were infiltrated in the capillaries. Measurements revealed that the high-order mode is one order of magnitude more sensitive to refractive index changes with respect to the fundamental mode supporting the theoretical calculations of beam profiles shown in Figure 9.3(b). Several measurements were carried out using the same functionalized fiber to evaluate the repeatability of the device. We used the 100 nM DNA solution to verify the reproducibility of a single measurement. The recovery of the fiber was achieved by washing the fiber capillaries with PBS for approximately 24 h with a pressure of 10 atm. The removal of DNA was confirmed spectrally because the reflected signal had shifted back to its initial reference position. Three more rehybridization processes were implemented using the same conditions described earlier, showing very similar results, except for a small memory effect, similar to that previously observed, which tends to decrease the amplitude modulation with the number of tests carried out. The average wavelength shift of the high-order mode was $0.04 \pm 0.02$ nm after DNA hybridization, and $0.19 \pm 0.06$ nm ($n = 3$, relative standard deviation [RSD]% = 35%) after NPs hybridization, as reported in Figure 9.6(b). Finally, the sequence selectivity of the fiber was tested using the mismatched ON (DNA-mismatched [MM]), corresponding to wild-type DNA differing of only one base from DNA-FM, but bearing exactly the same target sequence for ONAuNP. Using the same procedure described above, a 100 nM mismatch DNA solution was infiltrated into the functionalized capillaries, and the capillary was washed and then infiltrated with ONAuNP, after which a spectral measurement was performed. The experiments showed that the total shift was 0.025 nm (Shoshani et al., 1992) much lower than that obtained using FM-DNA. After the measurement, the same fiber was washed with PBS, dried, and the hybridization experiment was repeated using DNA-FM; the response was a final shift of 0.11 nm, consistent with the former ones, thus confirming the sequence selectivity of the optical response.

## 9.4 Detection of unamplified genomic DNA using a large mode area fiber

Another application that has been implemented thanks to our sensing platform based on PNA-functionalized MOF concerns the food industry. The optical systems have been tested on DNA extracted from complex matrix (soy flour), directly diluted, and analyzed, using very small sample volume and no amplification step.

In this experiment, commercially available silica glass large mode area (LMA) fiber manufactured by NKT Photonics has been used. Such fiber has a $\sim$10 μm core whereas the cladding region is formed by 60 holes of 2.85-μm diameter (see Figure 9.8(a)) and an interhole distance of 6.4 μm. As in the previous experiment, for the inscription of the grating, a standard 1073.2 nm period phase mask setup was used (Pissadakis et al., 2009) with a 193 nm high coherence, 10 ns pulse-duration

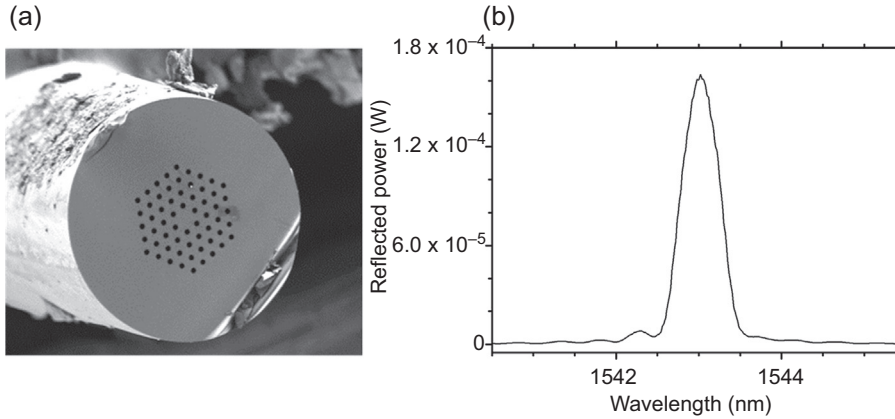


**Figure 9.8** (a) SEM image of the LMA-10 fiber used in the present study, showing the hexagonal geometry of the channels; (b) spectrum of the reflected light of an LMA-10 PCF with Bragg grating inscribed.

excimer laser. The Bragg grating reflected the fundamental mode in the standard C band for telecommunication.

The PNA was covalently bound to the inner surface of the optical fiber channels as described in the previous paragraph. Using this bioconjugated-MOF, we tested the possibility to obtain reproducible wavelength shifts using nonamplified genomic DNA. Thus, a PNA sequence complementary to a specific tract of Roundup Ready (RR) soy was used. The RR-soy was chosen as a DNA model for its relevance in food analysis and because samples of certified DNA content of the target sequence are available and unambiguous for this substrate (genomic DNA from GMO soy flour), and have previously been used to test SPR biosensing devices (Rosi & Mirkin, 2005). The DNA was extracted from reference flour material (GMO material content certified by Institute for Reference Materials and Measurements, IRMM) containing 0%, 0.1%, 1%, and 10% of transgenic soybean flour, using a commercial kit and standard procedures. The concentration of each DNA sample was measured with a Pico200 Picodrop Spectrophotometer and samples containing the same concentration of 30 μg/mL were produced. The DNA was thermally denatured at 90 °C and rapidly frozen (1−2 min), to prevent dsDNA re-annealing, which competes with hybridization with the PNA probe. The frozen samples were melted just before their use and the corresponding solutions were passed through the fiber holes for 50 min. The fibers were subsequently emptied; the position of the reflection band generated by the Bragg grating was at first monitored after infiltration of DNA but no significant shift was observed, as reported in Figure 9.9(a).

A solution of these ONAuNPs was infiltrated in the LMA-10 fibers after the DNA solutions, under the same conditions, and the position of the Bragg-grating band was monitored.

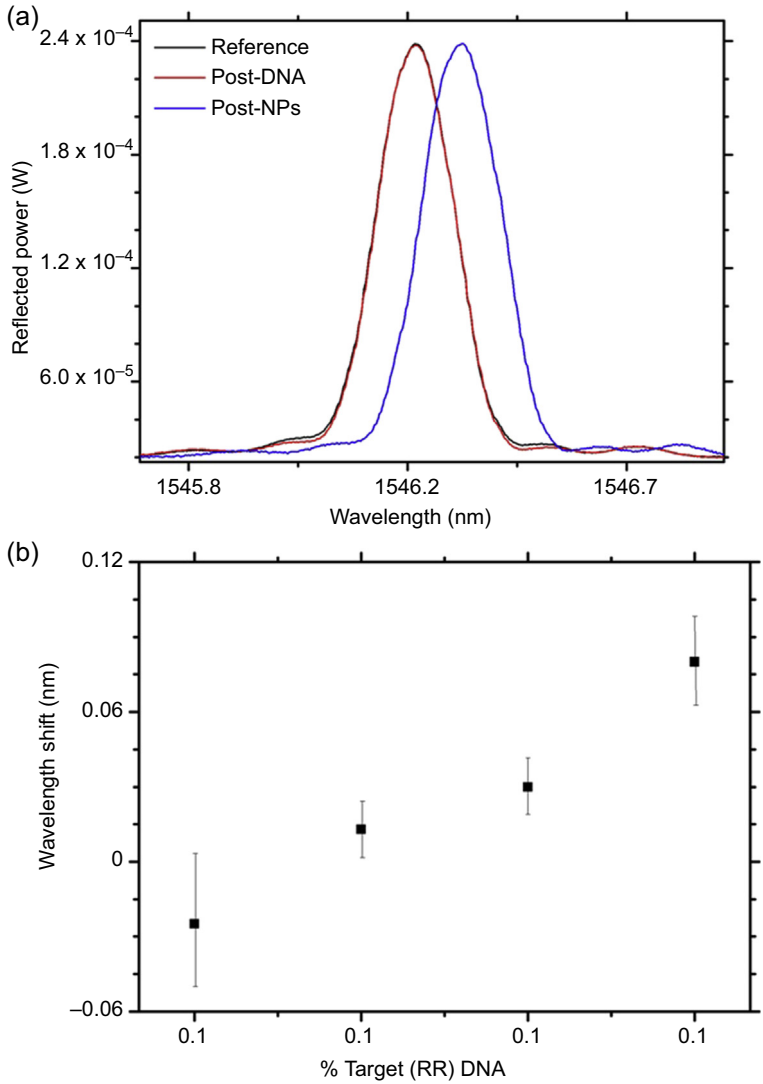


**Figure 9.9** (a) Wavelength shift in the reflection mode obtained for the LMA10-PNA fibers after DNA and ONAuNPs infiltration, using 10% genetically modified organism (GMO) DNA sample, leading to an average shift of 0.08 nm (RSD 27%). (b) Optical shifts obtained using DNA at the same concentration but with different GMO% (vertical bars represent standard deviation).

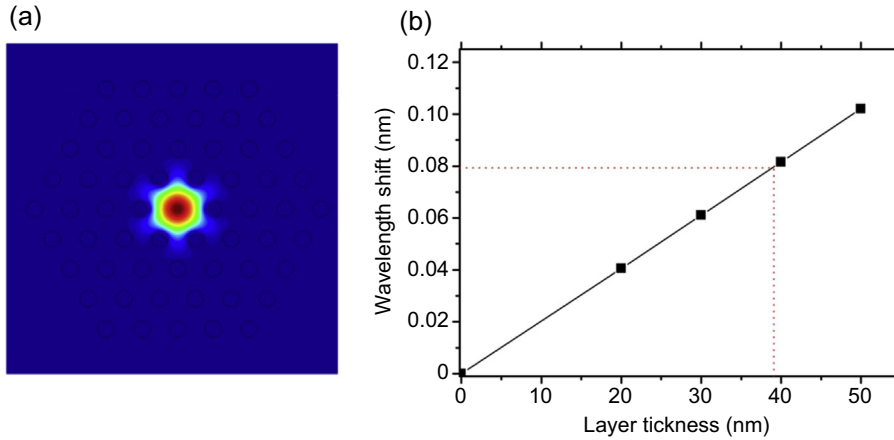


**Figure 9.10** (a) Finite element method (FEM) simulations show the field distribution inside the microstructured optical fiber; (b) wavelength shift versus thickness of the biolayer created by the functionalization and hybridization process.

After data collection, fibers were washed with PBS at pH = 7 to restore initial conditions. Each fiber, after emptying, was reused for subsequent measurements. Quadruplicate measurements were performed by alternating the solutions with different target content, to avoid systematic errors, and significance analysis was carried out. In this case, a significant shift of the Bragg reflection band was observed in the case of 10% RR content, as shown in Figure 9.9(a), whereas a weaker shift was recorded in the case of 0.1 and 1% RR flour, and notably, no statistically significant shift was observed for the sample containing no RR flour.

Unlike customer fiber used in the experiment described above that had some unknown parameters for LMA fiber, finite element method (FEM) solver has been used to simulate the field distribution inside the fiber core, reported in Figure 9.10(a). The effective refractive index $n_{\text{eff}}$ has been evaluated for the reference fiber and for the hybridized fiber (Konstantaki, Childs, Sozzi, & Pissadakis, 2013). Based on the refractive index measured in analogous experiments carried out in the infrared (IR) region (Wang et al., 2009) several simulations were conducted at different biolayer thickness having refractive index of 1.502, corresponding to the organic material deposited on the nanoparticle (Mudraboyina & Sabarinathan, 2011) and covering the surface of the fiber capillaries. Numerical results under these conditions showed an increase of the $n_{\text{eff}}$ of $7.5 \times 10^{-5}$ around 1550 nm, which is consistent with the observed average shift of 0.08 nm for the 10% RR sample, for a layer thickness of 39 nm (Figure 9.10(b)).

Because the size of the nanoparticle used was measured by the Mie model (Haiss, Thanh, Aveyard, & Fernig, 2007) to be $13 \pm 3$ nm, and the streptavidin coating can be evaluated to have 4−5 nm thickness (Kaur & Forrest, 2011) on each side of the NP, the value obtained is consistent with the average deposition of more than one layer of nanoparticle/streptavidin material on the fiber surface (Haiss et al., 2007).

## 9.5 Conclusion

In conclusion, we have reported on a new sensing platform for DNA detection implemented on an MOF formerly functionalized with PNA probes. For the first time, a biodetection technique based on fiber Bragg gratings as transducers and DNA-functionalized AuNPs has been used for signal amplification. In this way, it was possible to observe the reflected signal by the Bragg grating, utilizing the fiber itself as a probe. Two different examples of applications have been reported: in the medical field, the specific DNA sequence that characterizes CF, and in the food industry, the genomic DNA from GMO soy flour. In this last experiment, we demonstrated that direct measurement of genomic DNA without polymerase chain reaction or other amplification reactions can be obtained using IR.

This approach provides some improvements over existing techniques; the use of fiber optics, in addition to the well-known benefits already described at the beginning of the chapter, allows the analysis of very small volumes of solution and a negligible consumption of the sample itself. In addition, the use of PNA probes provides a highly sensitive and selective sensor able to discriminate to single-nucleotide polymorphism, which is a variation of gene material in a single nucleotide. Moreover, the approach can be extended to other recognition elements able to bind target analytes, such as proteins or contaminants.

This technology can thus be very useful for the realization of portable instrumentation suitable for an on-site detection and ultra-low sample concentration and reagent consumption, also taking advantage of the very large number of available tools and processes (e.g., optical fiber can also easily composed in flexible bundles for multichannel sensors), currently developed within the information and communication technology field.

## References

Afshar, V. S., Warren-Smith, S. C., & Monro, T. M. (2007). Enhancement of fluorescence-based sensing using microstructured optical fibers. *Optics Express, 15*(26), 17891−17901.

Burani, N., & Lægsgaard, J. (2005). Perturbative modeling of Bragg-grating based biosensors in photonic-crystal fibers. *Journal of the Optical Society of America B, 22*(11), 2487−2493.

Candiani, A., Bertucci, A., Giannetti, S., Konstantaki, M., Manicardi, A., Pissadakis, S., et al. (2013). Label-free DNA biosensor based on a peptide nucleic acid-functionalized microstructured optical fiber-Bragg grating. *Journal of Biomedical Optics, 18*(5), 57004.

Candiani, A., Sozzi, M., Cucinotta, A., Selleri, S., Veneziano, R., Corradini, R., et al. (2012). Optical fiber ring cavity sensor for label-free DNA detection. *IEEE Journal of Selected Topics in Quantum Electronics, 18*(3), 1176−1183.

Chen, X., Zhang, L., Zhou, K., Davies, E., Sugden, K., Bennion, I., et al. (2007). Real-time detection of DNA interactions with long period fiber-grating-based biosensor. *Optics Letters, 32*, 2541−2543.

Cordek, J., Wang, X., & Tan, W. (1999). Direct immobilization of glutamate dehydrogenase on optical fiber probes for ultrasensitive glutamate detection. *Analytical Chemistry, 71*, 1529−1533.

Corradini, R., & Selleri, S. (2012). Photonic crystal fibers for physical, chemical and biological sensing, e-book. In M. Pisco, A. Cusano, & A. Cutolo (Eds.), *Photonic bandgap structures: A novel technological platform for physical, chemical and biological sensing* (pp. 189−202). Bentham Science Publishers.

Coscelli, E., Sozzi, M., Poli, F., Passaro, D., Cucinotta, A., Selleri, S., et al. (2010). Towards highly specific DNA biosensor: PNA-modified suspended core photonic crystal fiber. *IEEE Journal of Selected Topics in Quantum Electronics, 16*(4), 967−972.

Csaki, A., Jahn, F., Latka, I., Henkel, T., Malsch, D., Schneider, T., et al. (2010). Nanoparticle layer deposition for plasmonic tuning of microstructured optical fibers. *Small, 6*(22), 2584−2589.

D'Agata, R., Corradini, R., Grasso, G., Marchelli, R., & Spoto, G. (2008). Ultrasensitive detection of DNA by PNA and nanoparticle-enhanced surface plasmon resonance imaging. *ChemBioChem, 9*(13), 2067−2070.

Emiliyanov, G., Jensen, J. B., Bang, O., Hoiby, P. E., Pedersen, L. H., Kjær, E. M., et al. (2007a). Localized biosensing with Topas microstructured polymer optical fiber. *Optics Letters, 32*(5), 460−462.

Emiliyanov, G., Jensen, J. B., Bang, O., Hoiby, P. E., Pedersen, L. H., Kjær, E. M., et al. (2007b). Localized biosensing with Topas microstructured polymer optical fiber: erratum. *Optics Letters, 32*(9), 1059.

Frosz, M. H., Stefani, A., & Bang, O. (2011). Highly sensitive and simple refractive index sensing of liquids in photonic crystal fibers using four-wave mixing. *Optics Express, 19*(11), 10471−10484.

Germini, A., Rossi, S., Zanetti, A., Corradini, R., Fogher, C., & Marchelli, R. (2005). Development of a PNA array platform for the detection of genetically modified organisms in food. *Journal of Agricultural and Food Chemistry, 53*, 3958−3962.

Greenman, C., Stephens, P., Smith, R., Dalgliesh, G. L., Hunter, C., Bignell, G., et al. (2007). Patterns of somatic mutation in human cancer genomes. *Nature, 446*(7132), 153−158.

Haiss, W., Thanh, N. T. K., Aveyard, J., & Fernig, D. G. (2007). Determination of size and concentration of gold nanoparticles from UV−Vis spectra. *Analytical Chemistry, 79*(11), 4215−4221.

Han, Y., Mayer, D., Offenhauser, A., & Ingebrandt, S. (2006). Surface activation of thin silicon oxides by wet cleaning and silanization. *Thin Solid Films, 510*, 175−180.

Jensen, J. B., Pedersen, L. H., Hoiby, P. E., Nielsen, L. B., Hansen, T. P., Folkenberg, J. R., et al. (2004). Photonic crystal fiber based evanescent-wave sensor for detection of biomolecules in aqueous solutions. *Optics Letters, 29*(17), 1974−1976.

Jensen, J. B., Hoiby, P. E., Emiliyanov, G., Bang, O., Pedersen, L. H., & Bjarklev, A. (2005). Selective detection of antibodies in microstructured polymer optical fibers. *Optics Express, 13*(15), 5883−5889.

Kaur, K., & Forrest, J. A. (2011). Influence of particle size on the binding activity of proteins adsorbed onto gold nanoparticles. *Langmuir, 28*(5), 2736−2744.

Konstantaki, M., Childs, P., Sozzi, M., & Pissadakis, S. (2013). Relief Bragg reflectors inscribed on the capillary walls of solid-core photonic crystal fibers. *Laser & Photonics Reviews, 7*, 439−443.

Liu, J., Tian, S., Tiefenauer, L., Nielsen, P. E., & Knoll, W. (2005). Simultaneously amplified electrochemical and surface plasmon optical detection of DNA hybridization based on Ferrocene−Streptavidin conjugates. *Analytical Chemistry, 77*(9), 2756−2761.

Loung, J. H. T., Male, K. B., & Glennon, J. (2008). Biosensor technology: technology push versus market pull. *Biotechnology Advances, 26*(5), 492−500.

Markos, C., Yuan, W., Vlachos, K., Town, G. E., & Bang, O. (2011). Label-free biosensing with high sensitivity in dualcore microstructured polymer optical fibers. *Optics Express, 19*(8), 7790−7798.

Mudraboyina, A. K., & Sabarinathan, J. (2011). Protein binding detection using on-chip silicon gratings. *Journal of Sensors, 11*, 11295−11304.

Ott, J. R., Heuck, M., Agger, C., Rasmussen, P. D., & Bang, O. (2008). Label-free and selective nonlinear fiber-optical biosensing. *Optics Express, 16*(25), 20834−20847.

Pissadakis, S., Livitziis, M., & Tsibidis, G. D. (2009). Investigation on the Bragg grating recording in all-silica, standard and microstructured optical fibers using 248 nm 5 ps, laser radiation. *Journal of the European Optical Society, 4*(09049).

Rindorf, L., & Bang, O. (2008). Sensitivity of photonic crystal fiber grating sensors: biosensing, refractive index, strain, and temperature sensing. *Journal of the Optical Society of America B, 25*(3), 310−324.

Rindorf, L., Jensen, J. B., Dufva, M., Pedersen, L. H., Høiby, P. E., & Bang, O. (2006). Photonic crystal fiber long-period gratings for biochemical sensing. *Optics Express, 14*(18), 8224−8231.

Rosi, N. L., & Mirkin, C. A. (2005). Nanostructures in biodiagnostics. *Chemical Reviews, 105*, 1547−1562.

Rossi, S., Scaravelli, E., Corradini, R., Fogher, C., & Marchelli, R. (2006). A PNA-array platform for the detection of hidden allergens in foodstuffs. *European Food Research and Technology, 223*, 1−6.

Ruan, Y., Schartner, E. P., Ebendorff-Heidepriem, H., Hoffmann, P., & Monro, T. M. (2007). Detection of quantum-dot labelled proteins using soft glass microstructured optical fibers. *Optics Express, 15*(26), 17819−17826.

Shopova, S. I., Rajmangal, R., Holler, S., & Arnold, S. (2011). Plasmonic enhancement of a whispering-gallery-mode biosensor for single nanoparticle detection. *Applied Physics Letters, 98*(24), 243104.

Shoshani, T., Augarten, A., Gazit, E., Bashan, N., Yahav, Y., & Rivlin, Y. (1992). Association of a nonsense mutation (W1282X), the most common mutation in the Ashkenazi Jewish cystic fibrosis patients in Israel, with presentation of severe disease. *American Journal of Human Genetics, 50*(1), 222−228.

Skorobogatiy, M. (2009). Microstructured and photonic bandgap fibers for applications in the resonant bio- and chemical sensors. *Journal of Sensors, 2009*.

Sozzi, M., Cucinotta, A., Corradini, R., Marchelli, R., Konstantaki, M., Pissadakis, S., et al. (January 22−27, 2011). *Modification of a long-period grating based fiber optic for DNA biosensing*. San Francisco CA, USA: SPIE Photonics West, 7894-20.

Spoto, G., D'Agata, R., Corradini, R., Ferretti, C., Zanoli, L., Gatti, M., et al. (2010). Ultrasensitive detection of non-amplified genomic DNA by nanoparticle-enhanced surface plasmon resonance imaging. *Biosensors & Bioelectronics, 25*, 2095−2100.

Tazawa, H., Kanie, T., & Katayama, M. (2007). Fiber-optic coupler based refractive index sensor and its application to biosensing. *Applied Physics Letters, 91*, 113901-1−113901-3.

Wang, Z., Heflin, J. R., Van Cott, K., Stolen, R. H., Ramachandran, S., & Ghalmi, S. (2009). Biosensors employing ionic self-assembled multilayers adsorbed on long-period fiber gratings. *Sensors and Actuators B: Chemical, 139*(2), 618−623.

# Photonic bandgap fibers—a roadway to all-fiber refractometer systems for monitoring of liquid analytes

10

*H. Qu, J. Li, M. Skorobogatiy*
Genie Physique, Ecole Polytechnique de Montreal, Montreal, QC, Canada

## 10.1 Introduction

Research and development (R&D) of fiber-optic refractometers has constituted a very interesting topic during the last 20 years. This is due to the appealing properties of fiber-optic sensors, such as low signal attenuation, light weight, immunity to electromagnetic interference, resistance to harsh environments, electrical passivity, and the possibility of multiplexing (Krohn, 1992; Lakhtakia & Mohammod, 2010; Udd & Spillman, 2011). To date, various types of fiber-based refractometers have been demonstrated. The sensing techniques and devices involved in these fiber refractometers may include fiber evanescent-field sensing (Banerjee et al., 2007; Mukherjee et al., 2010; Sheeba, Rajesh, Vallabhan, Nampoori & Radhakrishnan, 2005; Villiatoro, Monzoon-Hernadex & Talavera, 2004), surface plasmon resonance (SPR) (Bhatia & Gupta, 2011; Cennamo, Massarotti, Conte & Zeni, 2011; Lin, 2013), fiber gratings (fiber Bragg gratings and long-period gratings) (Fang, Liao & Wang, 2010; Kapoor & Sharma, 2009; Liang, Huang, Xu, Lee & Yariv, 2005; Schroeder, Ecke, Mueller, Willsch & Andreev, 2001; Yang et al., 2006), whispering gallery mode sensing (Fan, White, Zhu, Suter & Oveys, 2007; White et al., 2007; Zamora, Diez, Andres & Gimeno, 2007), and fiber interferometry (Gao et al., 2012; Juan, Dong, Zhao & Zhao, 2011; Wu et al., 2011). Note that most of these techniques use the interaction between the fiber evanescent field and the test analytes. Namely, the perturbations in the refractive index of test analytes close to the sensor surface are probed by the exponentially decaying optical wave. To increase the modal overlap of the evanescent field with test analytes and thus increase the sensitivity, modifications of the fiber components are usually required, such as fiber tapering or fiber cladding stripping. These treatments would not only bring additional cost to the sensor fabrication but also lead to difficulties in the mass production of the fiber sensors. Besides, the mechanical robustness of the fiber components could be potentially degraded by these treatments.

Developing refractometers based on the photonic bandgap fibers (PBGFs) may circumvent the above-mentioned problems. PBGFs, a subclass of photonic crystal fibers, refer to optical fibers that have specially patterned microsized holes running along all their length or have periodical alternating high- and low-index layers as

**Optofluidics, Sensors and Actuators in Microstructured Optical Fibers.** http://dx.doi.org/10.1016/B978-1-78242-329-4.00010-2

the Bragg reflector in the fiber cladding (the latter is therefore also named Bragg fiber) (Skorobogatiy, 2010). These fibers generally guide by bandgap effect. Only the light within the bandgap of the fiber could be confined and guided in the fiber core due to the destructive interference occurring in the microstructured cladding. When used for sensing of liquid analytes, PBGFs show several unique advantages as compared to the fiber-optic sensors based on evanescent wave detection (Skorobogatiy, 2010). First, PBGFs by their nature could accommodate the analytes within their hollow microstructure. Second, PBGFs generally can be used directly for refractive index measurements without any fiber modifications such as fiber cladding, polishing, or etching. This would benefit the mass production of fiber refractometers. Third, PBGFs could achieve an almost-complete modal overlap with test analytes, thus leading to an extremely high sensitivity for refractive index measurements. These attractive properties potentially make PBGFs a promising candidate for the development of a new generation of fiber refractometers.

Spectroscopic devices play a key role in spectral detection-based refractometers. Traditional spectrometers normally employ moving dispersive elements, such as high-quality Bragg gratings, which lead to high system costs and slow acquisition speeds. Moreover, the resolution of such spectrometers is limited by the length of the spectrometer optical path, which, in turn, makes traditional spectrometers difficult to miniaturize without the loss of resolution (Hollas, 1982; Thorne, 1974). The majority of fiber-optical sensors that use spectroscopic devices for detection are limited to laboratory applications due to high costs and the relatively large size of such systems. Therefore, one of the essential driving forces behind the R&D of spectroscopic instruments is the development of the compact, rapid, and cost-effective spectrometers that can be conveniently integrated into fiber-optic sensing devices. In this respect, we believe that the fiber-based spectrometers may constitute a feasible solution. Existing spectrometers mainly use optical fibers to transfer optical signals from the optical probe to the dispersive element (e.g., gratings) (Lienert, Porter & Sharma, 2009; http://www.oceanoptics.com/Products/usb4000.asp). However, some specialty fibers such as PBGFs can provide the dispersive function, which potentially makes such fibers capable of realizing the function of a spectrometer. Such a fiber spectrometer potentially could be conveniently integrated with other fiber-based devices to constitute an all-fiber sensing system, thus leading to reduced system cost and ease in optical setup assembly.

In this chapter, we demonstrate that an all-fiber refractometer system could be developed from a combination of the hollow-core and solid-core photonic bandgap (PBG) Bragg fibers. Particularly, the proposed all-fiber refractometer system consists of two parts: a liquid-core Bragg fiber sensor for holding and probing liquid analytes and a solid-core Bragg fiber-bundle spectrometer for interrogating the transmission spectrum. The liquid-core Bragg fiber sensor operates on a resonant-sensing mechanism in which the transmission spectrum of the fiber shifts in response to variations in the refractive index of the Bragg fiber core. We show that this Bragg fiber sensor can be used to detect both changes in the bulk refractive index of liquid analytes filling the fiber core (bulk-sensing modality) and changes in the thickness of a layer coated directly on the inner surface of the fiber (surface-sensing modality). The solid-core

Bragg fiber-bundle spectrometer operates based on the optical filtering effect of the individual Bragg fibers. The test light transmitted by all the Bragg fibers inside a bundle is registered by a monochrome charge-coupled device (CCD) camera. By analyzing the intensity image, the test spectrum could be reconstructed using a so-called "transmission matrix" method. By integrating the above-mentioned two devices, an all-fiber refractometer system could be constructed. The main impact of this chapter is in the area of instrumentation of highly integrated optical fiber-based sensors. In this chapter, we demonstrate a modular, all-fiber sensor architecture in which all the elements of a complete sensor system are based on optical fibers. We envision that in the near future, one would be able to assemble a complete all-fiber sensor system by simply splicing various off-the-shelf on-demand fiber modules, such as the light delivery fiber, the fiber refractometer, and the fiber-based spectrometer, which is a very intriguing proposition.

The rest of the chapter is organized as follows. Section 10.2 introduces the general sensing principle of a fiber refractometer operating on a resonant-sensing mechanism. In Sections 10.3 and 10.4, we briefly review the refractometers based on capillary fibers and hollow-core photonic crystal fibers (HC-PCFs), and compare these fiber sensors with our liquid-core Bragg fiber refractometers by analyzing the advantages and drawbacks of each type. In Section 10.5, we propose and experimentally demonstrate the liquid-core Bragg fiber sensor. We show that this fiber sensor could be operated in two modalities: the bulk-sensing modality for detecting changes in the bulk refractive index of the fiber core, and the surface-sensing modality for measuring changes in the thickness of a biolayer coated on the inner surface of the fiber core. Section 10.6 demonstrates a solid-core Bragg fiber-bundle spectrometer. The operating algorithm, calibration process, and practical spectral characterization of this fiber spectrometer are explained in detail. In Section 10.7, we integrate the liquid-core Bragg fiber sensor with the solid-core Bragg fiber spectrometer into an all-fiber refractometer system. Finally, in Section 10.8, we detail the practical applications of the proposed all-fiber refractometer system. We believe that due to its many appealing advantages, all-fiber refractometers could find their applications in a variety of scientific and industrial fields in which monitoring of liquids is required. As an example, we discuss using Bragg fiber refractometers in monitoring concentrations of the commercial coolant and sawing solutions, as well as using Bragg fibers as magnetometers.

## 10.2 Resonant sensing of liquid-core fiber sensors—a theoretical foundation

In this section, we introduce the general sensing principle of a liquid-filled fiber refractometer using a resonant-sensing modality. In resonant sensors, one typically employs fibers with strongly nonuniform spectral transmission characteristics that are sensitive to changes in the analyte refractive index. Here, we take the liquid-filled photonic bandgap (PBG) Bragg fiber sensor as an example. Operation of a resonant Bragg fiber-based sensor relies on changes in the radiation loss of a leaky-core mode due

to changes in the refractive index of an analyte (see Figure 10.1) (Skorobogatiy, 2010). Such a leaky mode is typically confined inside an analyte-filled fiber core by a resonant reflector cladding. The term "leaky mode" generally refers to the guidance mechanism in which the effective refractive index of a propagating mode is smaller than that of the fiber cladding. Such unusual modes are called leaky modes as, outside of a waveguide core, they do not exhibit a traditional evanescent decay into the cladding, but rather they radiate slowly (leak) into the cladding. Unlike the case of common total internal reflection fibers, leaky modes in PBG Bragg fibers are confined by the bandgap of a microstructured reflector, a Bragg mirror consisting of alternating high- and low-index layers. For a particular value of an analyte, the refractive index geometry of such a fiber is chosen to provide strong optical confinement of the leaky-core mode. When changing the refractive index of an analyte, the resonant-guiding condition for mode confinement will change, resulting in shifts in the modal-loss spectrum. Detection of shifts in the transmission spectrum can be then re-interpreted in terms of the changes in the analyte refractive index. Interestingly, the same sensor can also be used in a standard nonresonant interrogation mode for the detection of changes in analyte absorption. Even when operated in a nonresonant regime, sensitivity of the hollow-core Bragg fiber-based sensors is, generally, superior to that of traditional evanescent-field fiber sensors due to greatly improved modal overlap with analyte. Therefore, resonant sensors based on liquid-core Bragg fibers allow detection of minute changes both in the analyte refractive index and in analyte absorption. Note that besides the liquid-core Bragg fiber-based sensors, the above-mentioned

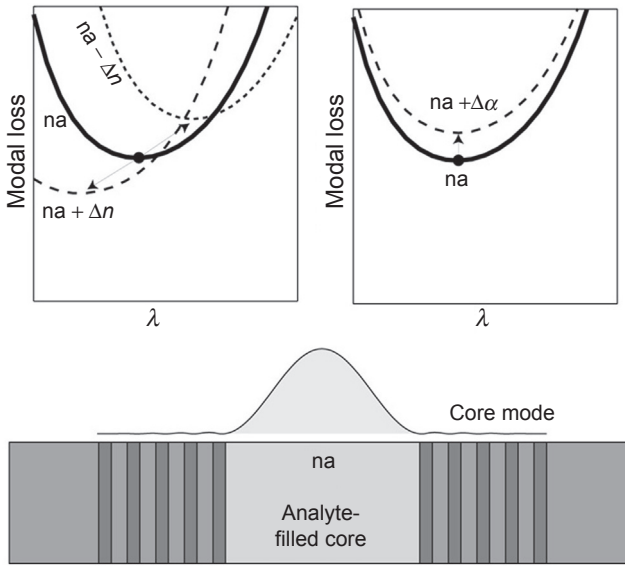


**Figure 10.1** Operational principle and schematics of the analyte-filled Bragg fiber-based sensor. Transmission loss through such a sensor is very sensitive to the analyte refractive index and analyte absorption (Skorobogatiy, 2010).

resonant-sensing mechanism is also applicable to other photonic crystal fiber-based sensors with a PBG guiding principle.

Moreover, besides PBG Bragg fibers, other liquid-core waveguides could be also designed into resonant optical sensors, such as whispering gallery mode sensors, SPR sensors, or inline fiber interferometers introduced in Sections 10.3 and 10.4. In general, these resonant sensors also operate with a spectral-based detection strategy (Skorobogatiy, 2010). The resonant structures in these sensors would lead to formation of spectral signatures (such as spectral peaks or dips) in the transmission spectrum of the sensor. Thus, changes in the analyte refractive index would result in displacement of the spectral signatures, which constitute the resonant-sensing mechanism of these sensors. In the following sections, we will provide a brief review for the resonant sensors based on capillary fiber and hollow-core PCF, respectively. Resonant fiber sensors using a spectral-detection strategy are more accurate than the nonresonant sensors operating on an amplitude-sensing strategy. First, resonant sensors that investigate spectral features are typically immune to the intensity fluctuations of light sources used in the sensor system. Besides, the spectral features under test could be designed to have a narrow spectral width, which would allow a precise reading of the spectral shifts. On the negative side, spectroscopic devices are normally utilized for spectral interrogation of a resonant fiber sensor system, thus increasing the cost of the sensor system.

## 10.3 Capillary fiber sensors

In this section, we provide a brief review of refractometers based on capillary fibers. A capillary fiber could be directly used as a liquid-core fiber sensor operating on an amplitude-sensing mechanism (Miluski & Dorosz, 2006). However, refractive indices of most dielectric materials are greater than those of aqueous analytes ($n \sim 1.33$), such that a capillary fiber filled with aqueous analytes generally does not guide by total internal reflection, but by a leaky-mode guiding principle, thus limiting considerably the sensing length of a capillary fiber sensor (Ma, Scott, Pickrell & Wang, 2010; Miluski & Dorosz, 2006). Currently, only a few polymers, such as Teflon AF ($n \sim 1.29$), have refractive indices lower than those of aqueous analytes.

A capillary fiber can be used in combination with a tapered fiber to constitute a liquid-core optical ring-resonator sensor (LCORRS) operating on a resonant-sensing mechanism. In an LCORRS, the light propagating in the tapered fiber is coupled into the liquid-filled capillary, and excites whispering gallery modes (WGMs) localized on the capillary surface. The resonant wavelength of a WGM shifts when the refractive index of a liquid analyte filling the capillary changes. The sensitivity of an LCORRS can be affected by several factors, such as thickness and radius of the capillary and the mode order of the WGM. Generally, reducing thickness of the wall of the capillary fiber could effectively increase the sensitivity of an LCORRS, because a higher power fraction of the WGM would overlap with test analytes filling the capillary. Several research groups (Luo, Chen, Xu, Chen & Fan, 2014; White, Oveys, & Fan, 2006; White, Oveys, Fan, Smith, & Zhang, 2006; White et al.,

2007) have demonstrated that the sensitivity of an LCORRS is between 10 and 80 nm/refactive index unit (RIU), when the thickness of a capillary wall is in the range of 2−6 μm. Besides, Zamora et al. (2007) showed that the sensitivity could be improved up to ∼800 nm/RIU, if the thickness of a capillary is further reduced to ∼1 μm or submicron. However, reduction of the thickness of a capillary always comes at the cost of its mechanical robustness. Therefore, Sumetsky, Windeler, Dulashko and Fan (2007) proposed to host both a capillary fiber and a tapered fiber within a low-index polymer matrix. In this LCORRS, the wall of the capillary fiber is chemically etched down to the submicron scale. The sensitivity of this LCORRS was measured to be ∼800 nm/RIU. Moreover, Ling and Guo (2007) used a glass prism, instead of a tapered fiber, to couple light into a liquid-filled capillary fiber to increase the modal overlap between the WGMs and test analytes, which resulted in a sensitivity of 600 nm/RIU. Note that, although LCORRSs show relatively high sensitivities to variations of the refractive index, the alignment and maintenance of the LCORRS setups are normally challenging due to fragility of the tapered fibers and the hollow-core capillaries. Also, note that coupling of light from the lead-in waveguide to the capillary fiber always requires accurate positioning of each sensor component. To simplify the optical coupling, several WGM sensors (Lane, Chan, Thiessen & Meldrum, 2014; Manchee, Zamora, Silverstone, Veinot & Meldrum, 2011; Roland, Francois, Hoffmann & Monro, 2013; Silverstone, McFarlane, Manchee & Meldrum, 2012) employed a capillary fiber with a fluorescent or quantum-dot layer coated on its inner surface. Thus, WGMs could be easily excited by the fluorescence generated by the active-coating layers using a simple optical pumping. The sensitivity of these sensors is limited to the range of 10−30 nm/RIU.

As an alternative to the above-mentioned WGM sensors, capillary fibers could also be developed into interferometric refractometers. For example, a short piece of capillary fiber could be spliced between two single-mode fibers (SMFs) as shown in Figure 10.2 (Liu, Peng, Zhang & Qian, 2014; Peng et al., 2014). The light from the lead-in SMF would excite multiple surface modes propagating on the liquid-core capillary, and thus the recombination of these surface modes in the lead-out SMF would generate interference fringes in the transmission spectrum. The interference fringes shift when the refractive index changes in the liquid core of the capillary fiber. The experimental sensitivity was found to be ∼700 nm/RIU in the index range of 1.33−1.35, and ∼1000 nm/RIU in the range of 1.35−1.37 (Liu et al., 2014; Peng et al., 2014). Although a relatively high sensitivity was obtained, the fabrication of this interferometric sensor requires complicated splicing techniques. Besides, Liu, Jang, Zhu, Tang and Shi (2013) proposed and demonstrated a SPR sensor based on a capillary fiber with its inner surface coated with a thin silver layer. When the capillary fiber is filled with high-index liquid analytes, surface plasmon waves would be excited on the interface between the metal layer and the supporting capillary. The SPR excitation would manifest itself as a spectral dip (resonant wavelength) in the transmission spectrum of the sensor. Thus, changes in the refractive index of analytes filling the capillary would shift the resonant wavelength, which constitutes the sensing mechanism of this sensor. A dramatically high sensitivity of ∼6600 nm/RIU was demonstrated. However, the measuring range of this capillary sensor is

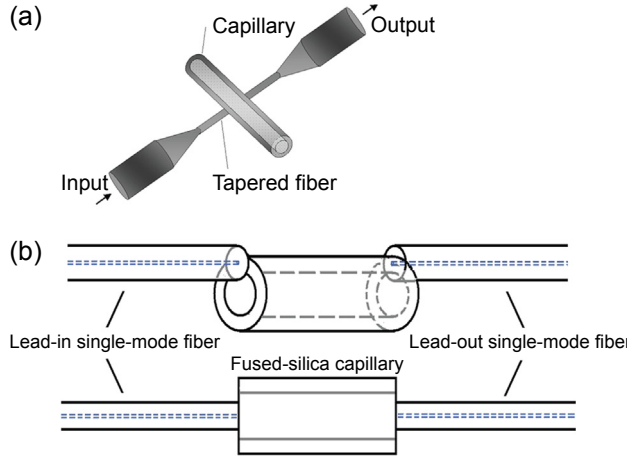


**Figure 10.2** (a) Schematic of an LCORRS (Figure 1 from Zamora et al. (2007)); (b) schematic of a capillary fiber-based interferometer (Figure 1 from Peng, Liu, Zhang, Cheng and Han (2014)).

limited to $n > 1.5$ to satisfy the excitation condition of the SPR mode. Moreover, precise control of the thickness of the coated metal layer was proved to be quite challenging.

## 10.4 Hollow-core photonic crystal fiber sensors

HC-PCF can be generally divided into two classes according to different fiber structures. As shown in Figure 10.3(a) and (b), one type of HC-PCF has a cross-section that features a hollow core surrounded by a periodic array of air holes and the other

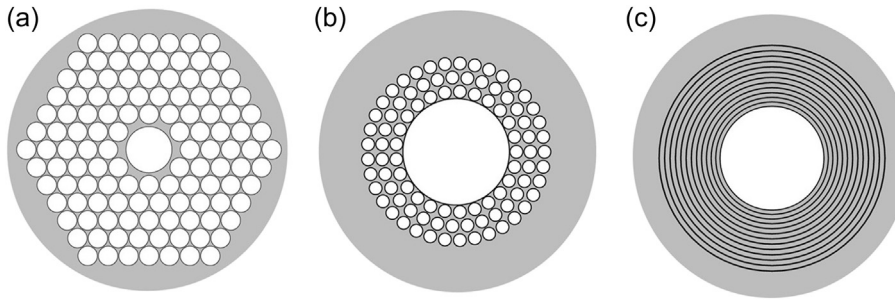


**Figure 10.3** Various types of hollow-core (HC) photonic bandgap fibers (PBGFs). (a) Hollow-core photonic crystal fiber (HC-PCF) featuring small hollow core surrounded by a periodic array of large air holes. (b) HC-PCF featuring medium-size hollow core surrounded by several rings of small air holes separated by nanosize bridges. (c) Bragg fiber featuring large hollow core surrounded by a periodic sequence of high and low-refractive-index layers.
Figure 2 from Skorobogatiy (2010).

type has a cross-section that features a large hollow core surrounded by a periodical sequence of high- and low-refractive-index layers (see Figure 10.3(c)). The latter is typically referred to Bragg fibers, which will be introduced in the following section. In this section, we mainly focus on the sensors based on the first type. HC-PCFs, no matter whether they are filled with liquid analytes, guide by the PBG effect. Practically, bandgaps are defined as frequency regions of enhanced fiber transmission, and they are the result of destructive interference of the core-guided light inside of the fiber-microstructured cladding. When launching spectrally broad light into an HC-PCF, only the spectral component guided by the fiber bandgaps will reach the fiber end, whereas all the spectral components outside of the bandgaps will be irradiated out near the fiber-coupling end. Changes in the refractive index of the liquid analytes filling the HC-PCF would modify the bandgap guidance of the fiber, thus shifting the bandgap position of the fiber. Consequently, the changes in analyte index can be then inferred from spectral shifts of the bandgap, which constitutes the sensing mechanism of such sensors. As mentioned in the Introduction, HC-PCF-based refractometers can achieve almost 100% modal overlap with analytes, thus resulting in a very high sensitivity for refractive index measurements. In Sun and Chan (2007) and Xuan et al. (2007), two HC-PCFs refractometers were experimentally used for sensing of aqueous solutions. The sensitivities of both refractometers were measured to be ~5000 nm/RIU. However, infiltration of the liquid analytes into the microstructure of the fiber was time-consuming (~10 min for 20-cm-long fiber (Rindorf et al., 2006; Sun & Chan, 2007)) due to the microsized holes in the fiber.

HC-PCFs could be also fabricated into inline fiber interferometers for detection of refractive index of liquid analytes. For example, Wang et al. (2013) have demonstrated a Fabry-Pérot (F−P) fiber refractometer that is fabricated by sandwiching a short piece of hollow-core Kagome-lattice fiber between two SMFs. By filling different liquid analytes from the lateral microholes milling on the Kagome-lattice fiber, the optical path length of the F−P cavity is modified, thus leading to the displacement of sensor resonant wavelengths. A sensitivity of ~851.3 nm/RIU was experimentally measured. Jiang, Sui, Jin, Zhang and Jia (2014) reported another F−P fiber refractometer based on a hollow-core PCF. To fabricate the sensor, one end of a short hollow-core PCF is spliced to a lead-in SMF, whereas the other end is spliced to another short section of SMF used as the sensing tip. Thus, the whole sensor structure can be considered as an F−P interferometer comprising three reflectors. Changes in analyte refractive index at the extremity of this sensing tip would modify the Fresnel reflectivity at the SMF/analyte interface, and then change the interference fringe contrast in the reflection spectrum of the sensor. Thus, by studying the interference fringe contrast, a sensor resolution of $1.5 \times 10^{-5}$ was measured. Moreover, Gong, Chan, Zhang, Wong, and Dong (2011) showed a Mach-Zehnder type fiber refractometer that is also fabricated by sandwiching an HC-PCF between two SMFs. With a delicate splicing operation, the air holes are fully collapsed on a short section of each PCF end. Therefore, light from the SMF is first coupled into different modes (including core modes and cladding modes) in the PCF, and then the recombination of these modes would generate interference in the sensor transmission spectrum. Refractive index variations surrounding the PCF could modify the effective refractive index of the cladding mode, leading

to displacement of the interference spectrum of the sensor. The sensitivity was reported to be 24.5 nm/RIU in the index range of 1.35−1.39 and 46.5 nm/RIU in the index range of 1.39−1.43. Note that the fabrication of the in-fiber resonant structures is typically a demanding and time-consuming task that can require significant investments in fiber-processing equipment. The cost of fabrication and complexity of the fabrication process are the two major barriers for the applications of PCF-based interferometric sensors.

## 10.5 Liquid-core Bragg fiber sensors

As shown in Figure 10.3, a special type exists of the hollow-core MOF, that is, the hollow-core PBG Bragg fiber. In 2009, our group (Skorobogatiy, 2009) has proposed the possibility of using a hollow-core Bragg fiber as a fiber refractometer, and theoretically demonstrated that the sensitivity of such a Bragg fiber refractometer could be on the order of 5000 nm/RIU. In this section, we will demonstrate theoretically and experimentally to use Bragg fibers for sensing changes in the bulk refractive index of a liquid analyte filling the fiber core (bulk-sensing modality). The sensitivity of this refractometer is found to be $\sim$1400 nm/RIU. The detection limit of this Bragg fiber refractometer can be as small as $\sim 7 \times 10^{-5}$ RIU, assuming that a spectral shift of $\sim$0.1 nm can be reliably detected. Moreover, we also demonstrate using the Bragg fibers to detect changes in the thickness of a biolayer coated on the inner surface of the fiber (surface-sensing modality). The sensitivity for surface sensing is measured to be $\sim$1 nm/μm.

### *10.5.1 Bragg fiber sensor operating in bulk-sensing mode*

#### *10.5.1.1 Operational principle of liquid-core Bragg fiber sensors*

The all-polymer hollow-core low-refractive-index-contrast Bragg fibers used in our sensors were fabricated inhouse using the fiber-drawing technique. The Bragg fibers feature a large air core (diameter: 0.4−1 mm) surrounded by an alternating polymethyl methacrylate (PMMA)/polystyrene (PS) Bragg reflector (refractive index: 1.487/1.581 @ 589 nm) followed by a PMMA cladding (Figure 10.4). The large core of a Bragg fiber facilitates filling it with aqueous solutions, which might contain biological or chemical reagents. Such a large core also leads to a short response time of a sensor, because the flow resistance of the core decreases polynomially with increasing core radius (Rindorf et al., 2006). Experimentally, the response time of a 40-cm-long sensor is found to be $\sim$1 s.

The guiding and sensing properties of the low-refractive-index-contrast Bragg fiber can be elucidated from the Bragg reflector band diagram (frequency vs propagation constant). In Figure 10.5, we show the band diagram of the TE (transverse electric) and the TM (transverse magnetic) polarized modes propagating inside of an infinite planar Bragg reflector made from PMMA/PS multilayer. Due to the large diameter of the Bragg fiber, the band diagram of the Bragg reflector in a fiber could be

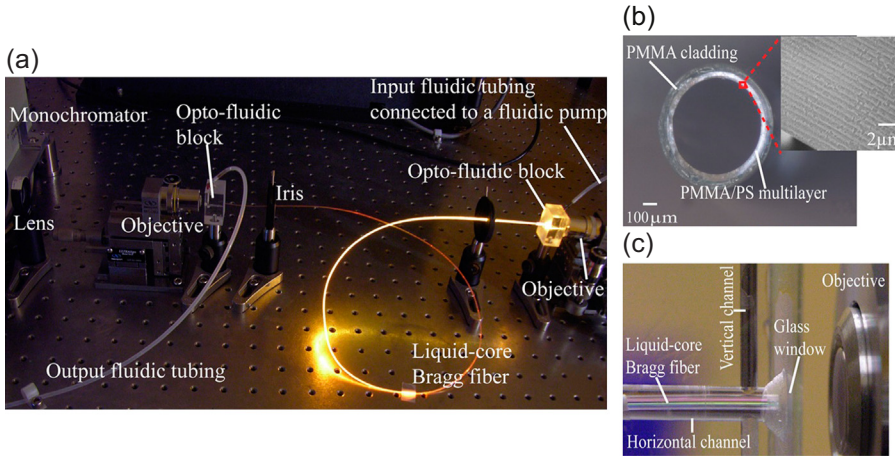


**Figure 10.4** (a) Setup of the Bragg fiber sensor system. An ∼80-cm-long liquid-core Bragg fiber, coiled into an ∼15 cm diameter circle, is integrated into a setup using two opto-fluidic coupling blocks. The beam from a supercontinuum source is coupled into the liquid-core Bragg fiber, and the transmission spectrum of a liquid-core Bragg fiber is then analyzed using a grating monochromator. (b) Cross-section of a hollow-core Bragg fiber; the inset is the graph of the Bragg reflector taken by a scanning electron microscope (SEM). (c) Inner structure of the opto-fluidic block. The tip of a liquid-core Bragg fiber is sealed into the horizontal channel of the coupling block filled with the liquid analyte. The extremity of the horizontal channel is sealed by a glass window through which light is coupled into (or out of) the sensing system. In each coupling block, a vertical channel also connects to the horizontal channel to constitute the fluidic path for fluidic coupling of the Bragg fiber. The colorful appearance of the Bragg fiber is due to the reflection of ambient light from the Bragg reflector.

considered analogous to that of the planar Bragg reflector. This band diagram is calculated by performing a Bloch wave analysis in the Bragg reflector with the plane-wave expansion method (Meade, Rappe, Brommer & Joannopoulos, 1993). Note that the planar Bragg reflector has different bandgaps for TE and TM polarizations, referring to fields purely parallel to the planar interface and fields with a normal component, respectively. To compute this band diagram, we use the values of the refractive indices of the PMMA and PS films measured by a variable-angle spectroscopic ellipsometer (VASE) Ellipsometer (J. A. Woollam Co., Inc.). The average thicknesses of the individual PMMA and PS layers are 0.37 and 0.13 μm, respectively, estimated from the SEM graph (Figure 10.4(b)). Gray regions in Figure 10.5 indicate states delocalized over the whole Bragg reflector. Such states are efficiently irradiated out of the fiber due to scattering on the imperfections in the reflector multilayer. Clear regions (bandgaps) define the parts of the phase space in which light is unable to propagate inside of the Bragg reflector. The black thick curves represent the light line of the liquid analyte, that is, distilled water. Modes guided in the hollow core will have effective refractive indices close to, while somewhat smaller than, that of water (black thick curves in Figure 10.5). Therefore, a mode confined in the liquid core will exist in the regions

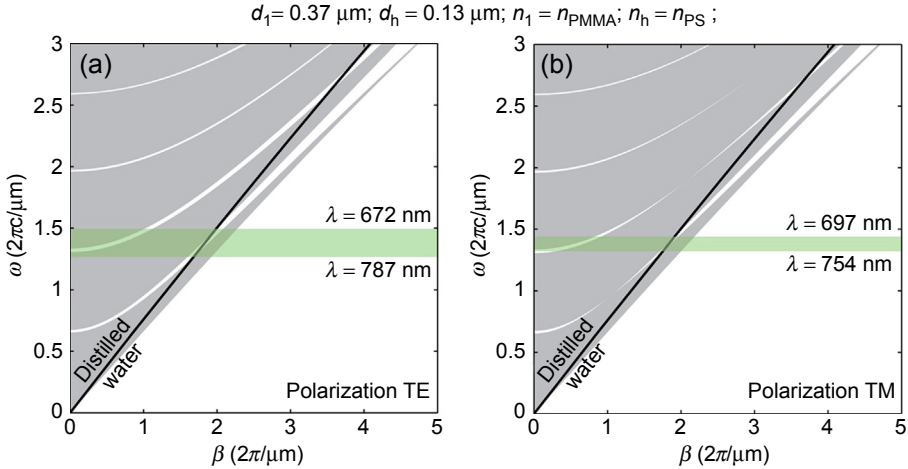


**Figure 10.5** Band diagram of (a) the TE- and (b) the TM-polarized modes of a PMMA/PS Bragg reflector. The gray regions correspond to ($\beta$, $\omega$) for which light can propagate within the Bragg reflector. The clear regions correspond to the parts of the phase space in which light is unable to propagate in the Bragg reflector. Thick black curves represent the light line of distilled water. Transmission bands (green) of the Bragg fiber can be estimated from the intersection of light line of water with the Bragg reflector bandgaps.

of a band diagram in which the light line of water intersects the reflector bandgap (horizontal green regions in Figure 10.5).

From the basic theory (Skorobogatiy, 2010; Qu & Skorobogatiy, 2011) of low-refractive-index-contrast Bragg fibers, the center wavelength, $\lambda_c$, of the fundamental reflector bandgap can be approximately calculated as

$$\lambda_c/2 = d_h\left(n_h^2 - n_c^2\right)^{1/2} + d_l\left(n_l^2 - n_c^2\right)^{1/2}, \tag{10.1}$$

in which $d_l$, $d_h$ are the thicknesses of the low- and high-index layer in the Bragg reflector, respectively; $n_l$, $n_h$ are the refractive indices of the corresponding layers; $n_c$ is the refractive index of the core material. Variations in the refractive index of an analyte filling the fiber core could modify the resonant condition (Eqn (10.1)) of the Bragg fiber, thus resulting in spectral shifts of the resonant wavelength in the fiber transmission, which constitutes the main sensing principle of the Bragg fiber sensor.

We note that low-refractive-index-contrast Bragg fibers have certain advantages for liquid analyte sensing compared to their high-refractive-index-contrast counterparts (Charlton, Temelkuran, Dellemann & Mizaikoff, 2005; Rowland, Afshar, Stolyarov, Fink & Monro, 2012). Previously, high-refractive-index-contrast Bragg fibers have been used for sensing of gas analytes ($n_{analyte} \sim 1$) (Charlton et al., 2005), as well as liquid analytes with high-refractive indices ($n_{analyte} > 1.40$) (Rowland et al., 2012). However, for the high-refractive-index-contrast Bragg fibers used in these works, the TM bandgaps of the Bragg reflector tend to collapse near the light line

of the aqueous material ($n_{analyte} \sim 1.33$) due to the Brewster angle phenomenon, thus leading to high loss for the hybrid expansion (HE/EH) modes propagating in the fiber liquid core. In contrast, low-refractive-index-contrast Bragg fibers show large TM bandgaps in the vicinity of the light line of water, thus resulting in good guidance of HE/EH modes (Figure 10.5). Moreover, we note that low-refractive-index-contrast Bragg fibers are more sensitive to changes in the refractive index of a liquid analyte filling the fiber core, as compared to their high-refractive-index-contrast counterparts. Particularly, from Eqn (10.1), we derive the sensitivity of the sensor, $S$, as

$$S = \frac{d\lambda_c}{dn_c} = 2\left[d_h\left(\frac{n_h^2}{n_c^2} - 1\right)^{-1/2} + d_l\left(\frac{n_l^2}{n_c^2} - 1\right)^{-1/2}\right]. \tag{10.2}$$

According to Eqn (10.2), the closer the value of the core index to those of the individual layers of the Bragg reflector, the more sensitive the Bragg fiber sensor will be to variations in the refractive index of the analyte-filled core, which is exactly the case for our low-refractive-index-contrast Bragg fiber sensor.

#### 10.5.1.2 *Theoretical and experimental characterization of the Bragg fiber sensor*

To theoretically verify the resonant-sensing mechanism, we simulate loss spectra of the fundamental $HE_{11}$ mode of the liquid-core Bragg fiber based on the Transfer Matrix Method (TMM) (Johnson et al., 2001). The structural parameters of the hollow-core Bragg fiber are the same as those used in Section 10.5.1.1 For liquid analytes, we choose a set of NaCl solutions with the weight concentration ranging from 0 to 25% in 5% incremental steps. The corresponding refractive indices of NaCl solutions are shown in the inset of Figure 10.6 (Haynes, 2010, pp. 8−71). The bulk absorption of NaCl solutions in the spectral range of interest was shown to be virtually identical with that of pure water (Sullivan et al., 2006). In our simulations, we compute the propagation loss of the $HE_{11}$ mode taking into account absorption loss of water and dispersion of water and plastics in the Bragg reflector. The simulated loss spectra suggest that the transmission band of the liquid-core Bragg fiber shows a blue-shift as the refractive index of the liquid analyte increases (Figure 10.6(a)).

In our experiments, we employ two opto-fluidic blocks designed to simultaneously enable optical and fluidic coupling of the hollow-core Bragg fiber (Figure 10.4(c)). An ~40-cm-long Bragg fiber, coiled into a 10-cm-diameter circle, is integrated into the sensing system. On each side, the hollow-core Bragg fiber tip is inserted hermetically into the analyte-filled horizontal channel that has a thin glass window attached at the one of its extremities for optical coupling of the Bragg fiber (Figure 10.4(c)). In each block, a vertical channel also connects to the horizontal channel to constitute the fluidic path for fluidic coupling of the Bragg fiber. This design avoids formation of air bubbles in the sensing system, which would strongly suppress fiber transmission. After pumping a liquid analyte into the fiber, we couple the beam from a supercontinuum source into the fiber using a 10× objective, and the transmission spectrum of the

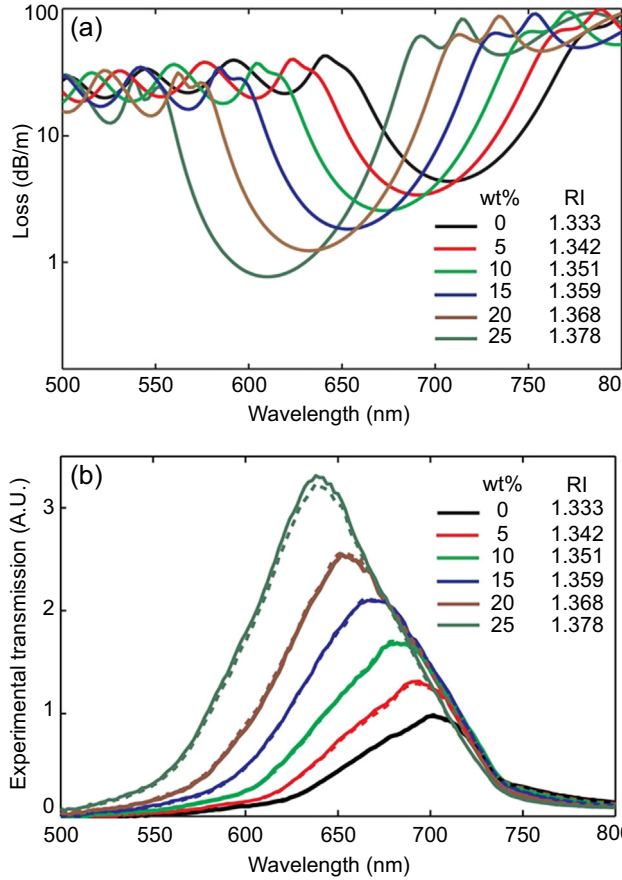


**Figure 10.6** (a) Simulated loss of the fundamental mode ($HE_{11}$ mode) of the Bragg fiber filled with different NaCl solutions. (b) Experimental transmission spectra of an ~40-cm-long Bragg fiber filled with NaCl solutions (solid curves). The dotted curves indicate a repeat of the first experiment after several hours, which demonstrate good repeatability of the measurement. The weight concentrations (wt%) and corresponding refractive indices of the NaCl solutions are listed in both figures as insets.

liquid-core Bragg fiber is then analyzed by the Oriel grating monochromator (Newport, Inc.). To verify the repeatability of the sensor, we repeat the same experiment after 3 h by first purging the setup with distilled water. Figure 10.6(b) shows the results of two consecutive experiments. The solid curve represents the transmission spectra of the first measurement, and it compares well with the results of the second measurement shown as the dotted curve. In the two measurements, we observe no more than 2.51% fluctuation in the detected intensity, whereas the center position of the transmission peak stays at the same position up to the resolution limit (~1 nm) of our spectrometer. As seen in Figure 10.6(b), the experimental transmission spectrum also shows a blue-shift, as the refractive index of the fiber core increases.

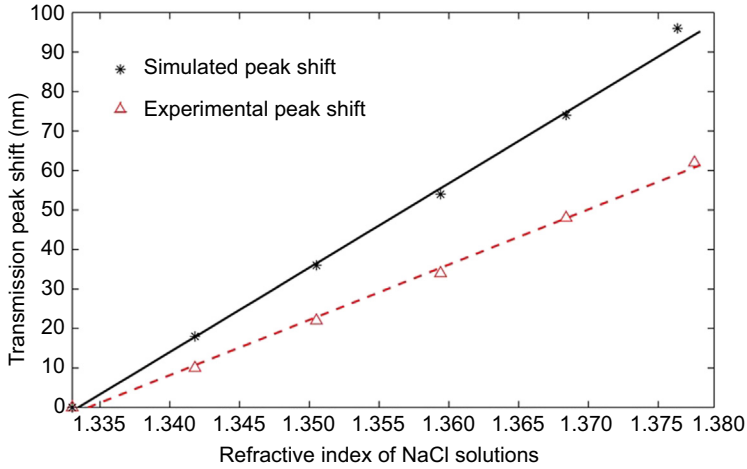


**Figure 10.7** Spectral shifts of the fiber transmission peak obtained from the TMM simulation (black solid line) and the experimental measurements (red dashed line).

Moreover, the spectral shifts of the transmission peak have a linear dependence on the increasing refractive index of the fiber core (see Figure 10.7).

We note that the experimental spectral shifts of the fiber transmission peak are somewhat smaller than the simulated ones. This is likely due to the fact that, in our simulation, we only calculate the spectral shifts of the fundamental $HE_{11}$ mode with its effective refractive index virtually identical to that of the liquid analyte filling the core. Nevertheless, most higher-order core modes have effective refractive indices ($n_{eff}$) lower than those of the $HE_{11}$ mode. Therefore, by substitution of $n_c$ by $n_{eff}$ in Eqn (10.2), we arrive at the conclusion that the spectral shifts of the transmission peaks of higher-order modes are smaller than those of the $HE_{11}$ mode. Due to the large diameter of the Bragg fiber core used in the experiments, many higher-order modes are excited. As these high-order modes are less sensitive than the $HE_{11}$ mode, the experimental spectral shifts are, therefore, smaller than those of the $HE_{11}$ mode. Finally, from Figure 10.7, we conclude that the experimental sensitivity of the liquid-core Bragg fiber sensor is $\sim$1400 nm/RIU. Assuming that a spectral shift of 0.1 nm can be reliably detected, this sensitivity is equivalent to a sensor resolution of $\sim 7 \times 10^{-5}$ RIU. Such sensitivity is comparable to those of the MOF-based sensors (Sun & Chan, 2007; Xuan et al., 2007). Note that compared to other MOF-based sensors, our Bragg fiber sensor is advantageous in terms of its short response time ($\sim$1 s) due to the large core of the Bragg fiber.

### *10.5.1.3 Discussion of factors influencing sensor performance*

#### Dynamic range of the sensor

The operating frequency range of this sensor is mainly determined by the position of the Bragg reflector bandgap. Currently, we routinely produce Bragg fibers with primary bandgaps located in the 500−800 nm spectral range; therefore, all of our

experiments are conducted in this range. Sensitivity of the sensor is so high that by varying the liquid-core refractive index from 1.333 to 1.378, the fiber bandgap already spans this whole operational window (see Figure 10.6). From the band diagram in Figure 10.5, it follows that the largest wavelength of operation is $\lambda \sim 1300$ nm. That is the region in which sensing of low-refractive-index analytes with $n_{\text{eff}} \sim 0$ can be achieved. In application to aqueous analytes, the bulk absorption is generally larger than 50 dB/m at the wavelength above 1 μm, thus limiting the operation range of the sensor in the near-infrared range. Finally, for the high-refractive-index analytes, the fiber bandgap will shift into the blue spectral region; however, no fundamental limit exists for the use of these sensors for high-refractive-index analytes.

### Insertion and coupling loss

Due to the large diameter of the Bragg fiber core (over 0.5 mm), coupling efficiency of the fiber is superb (above 90%), which is one of the well-known advantages of such fibers. Main coupling loss of the sensor comes from the reflection between the air and the glass window covering the fluidic channel (Figure 10.4(c)). The total coupling and out-coupling loss is estimated to be $\sim$10%.

### Dependence of sensitivity on fiber length

To study the dependence of the sensitivity on the length of a Bragg fiber, we first measure the spectral shifts of a 50-cm-long Bragg fiber filled with NaCl solutions with different concentrations. Then, we cut the fiber into 30 cm and 20 cm lengths, and for each length, we repeat the experiment to measure the spectral shifts in response to variations in the refractive index of the liquid core of the Bragg fiber. In Figure 10.8, we plot fiber transmission spectra of the liquid-core Bragg fiber with different lengths.

The transmission spectra of the 50 cm long Bragg fiber show clear spectral shifts caused by variations in the refractive index of the fiber core (Figure 10.8(a)). The sensitivity of the 50-cm-long fiber sensor is $\sim$1300 nm/RIU, which is estimated from the spectral shifts of the specific transmission peak marked by white arrows. In the transmission spectra of the 30-cm-long Bragg fiber, we still observe the spectral shifts of the transmission peak (Figure 10.8(b)); however, the transmission spectra become broader due to reduced fiber attenuation at the bandgap edges because of a shorter fiber length. The experimental sensitivity of the 30-cm-long Bragg fiber sensor is $\sim$1270 nm/RIU (Figure 10.8(d)). Further reduction of the Bragg fiber length to 20 cm leads to even smaller propagation losses at all frequencies. However, the reduced fiber loss causes the difficulty in differentiating specific resonant features in the fiber transmission spectra, and as a result, it becomes difficult to detect spectral shifts.

Therefore, we conclude that the liquid-core Bragg fiber should have a minimal (threshold) length to ensure sufficient attenuation at the wavelengths in the vicinity of bandgap edges to allow the formation of spectral features (such as transmission peaks) in the fiber transmission. We experimentally find the threshold length to be $\sim$10 cm for most Bragg fibers used in our experiments. Once the fiber length is longer than the threshold value, the sensitivity of a Bragg fiber sensor does not strongly depend on the fiber length, which is consistent with the prediction in

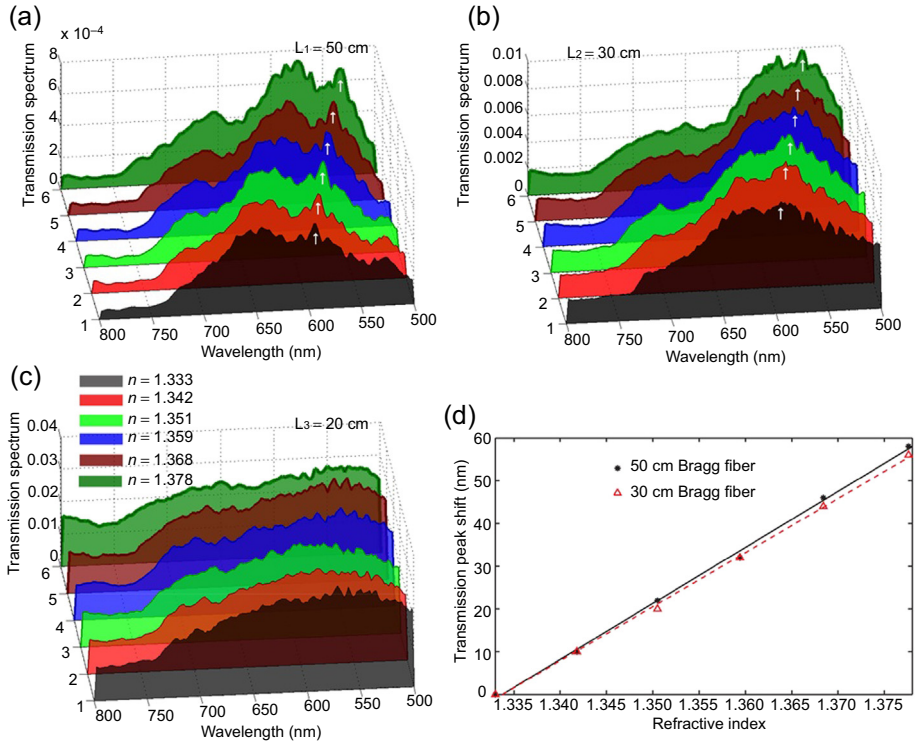


**Figure 10.8** Transmission spectra of the liquid-core Bragg fiber with different lengths: (a) 50 cm; (b) 30 cm; (c) 20 cm. The refractive indices of the analytes filling the fiber core are listed in an inset of (c). The white arrows in (a) and (b) mark the resonant peak positions, which we use to measure the spectral shifts. A linear dependence of the spectral shifts on changes in the refractive index of the fiber core is shown in (d). The black solid line represents the spectral shifts of a 50-cm-long Bragg fiber, and the red dashed line represents the spectral shifts of a 30-cm-long Bragg fiber.

Skorobogatiy (2010). A longer fiber also leads to a stronger attenuation of the higher-order modes, thus acting as a high-order mode stripper, which is also beneficial for sensing. At the same time, signal strength in longer fibers decreases due to increased material absorption and radiation losses, eventually leading to signal-to-noise degradation, which is disadvantageous for sensing. The trade-off between the two above-mentioned factors determines the optimal fiber length. Note that the optimization of the sensing length is not strictly required for sensing applications. Experimentally, we find the maximal sensing length of a Bragg fiber to be $\sim$1 m. With the sensing length smaller than $\sim$1 m, one can always measure the transmission spectrum of a Bragg fiber without much signal-to-noise degradation. Therefore, when sensing a specific liquid analyte, one, in practice, could choose a Bragg fiber with any length between the threshold value ($\sim$10 cm) and the maximal length ($\sim$1 m).

### 10.5.2 Bragg fiber sensor operating in surface-sensing mode

Another application of this Bragg fiber sensor operating on the resonant-sensing modality is to detect changes in the thickness of a thin layer deposited directly on the inner surface of the fiber core. By coating a thin layer, the localized refractive index in the vicinity of the fiber inner surface would change substantially that then modifies the resonant guidance of the Bragg fiber and leads to a spectral shift of the resonant wavelength in the fiber transmission. We take the thickness of the coated layer, $d_a$, as the measurand. Therefore, we could define the sensitivity of the Bragg fiber sensor to changes in the thickness of the coated layer as $S = \partial\lambda_c/\partial d_a$. We note that due to the large core of the Bragg fiber, only a small fraction of core-guided modes can be found in the vicinity of the fiber inner surface, thus leading to a poor modal overlap with the analyte layer. Consequently, we expect the sensitivity in the surface-sensing modality to be moderate.

To study the surface-sensing modality of a Bragg fiber sensor, we first coat an ~3.8 μm thick sucrose layer on the inner surface of a 15 cm long Bragg fiber (from the same preform with the fiber used above). Particularly, a 60 wt% sucrose solution is filled into the Bragg fiber core. Then the fiber is placed in an oven for 6 h to make the sucrose solution more viscous. Subsequently, an air pump is used to blow off most of the sucrose syrup in the fiber core while leaving a thin sucrose layer behind (Figure 10.9(a)). The fiber is then dried again.

For the optical measurements, we first insert the dry sucrose-coated Bragg fiber into the sensing setup and then quickly (~1 s) fill the fiber with distilled water. As the sucrose layer gradually dissolves in water, the bulk refractive index of the fiber core gradually increases. The transmission spectra (Figure 10.9(b)) of the fiber are

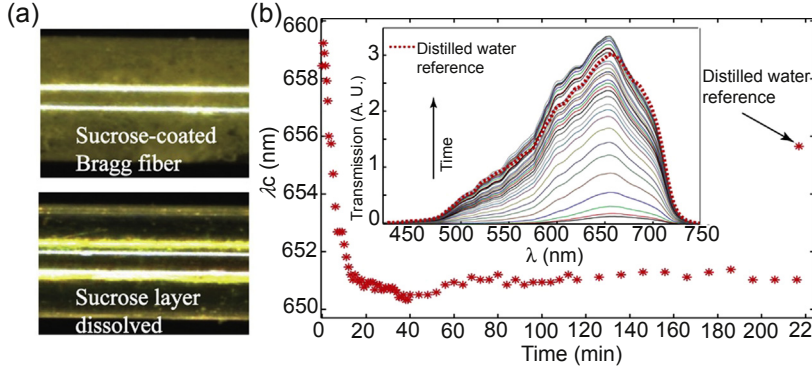


**Figure 10.9** (a) Top: appearance of the Bragg fiber coated with a sucrose layer; bottom: appearance of the Bragg fiber with the coated layer dissolved in the liquid core. (b) Time-dependent spectral changes in the fiber transmission during the dissolution of the thin sucrose layer coated on the inner surface of the fiber core. At $t = 0$, the fiber core is dry; the sucrose layer is 3.8 $\mu$m thick. Then, distilled water is quickly introduced. In the first 20 min, rapid changes in the transmission intensity and peak position are detected. After several hours, the reference is measured by purging the fiber with distilled water.

acquired throughout the dissolution process. Figure 10.9 shows that the transmission spectrum shifts ~8.2 nm toward shorter wavelengths in the first 20 min after filling the fiber with distilled water. During this period, the spectral shift is mostly due to the increase of the bulk refractive index of the fiber core caused by the dissolution of the sucrose layer. No significant spectral shift appears after 20 min, which indicates that most of the sucrose layer is dissolved. In contrast, the transmitted intensity still keeps slowly increasing during the several hours that follow. Visual inspection of the fiber under a microscope indicates that increase of the signal amplitude is probably due to reduction of the scattering losses incurred by the fiber mode on small chunks of the undissolved sucrose. Finally, when the fiber transmission spectrum stops changing (complete dissolution of the sucrose layer), we refill the fiber with distilled water. Consequently, the peak of the transmission spectrum shifts to 655.7 nm. Comparison with the initial peak position, which is measured almost instantaneously after filling the sucrose-coated fiber with water, allows us to conclude that the presence of a 3.8-μm-thick sucrose layer leads to a 3.5 nm red shift of the transmission spectrum of a water-filled fiber, compared to that of a water-filled fiber without a sucrose layer. The corresponding surface sensitivity of our sensor to changes in the sucrose layer thickness is then estimated to be ~0.9 nm/μm. Note that the sensitivity for the surface sensing, in principle, is also strongly independent of the length of the fiber; however, the maximal sensing length is experimentally found to be ~20 cm due to the large scattering loss caused by the sucrose layer.

## 10.6 Solid-core photonic bandgap Bragg fiber spectrometers

As mentioned in the Introduction, the development of the compact, low-cost spectrometer modules that can be easily integrated with fiber-based transduction modules constitutes an active area of optical sensor research. In this section, we propose and experimentally demonstrate an all-fiber spectrometer that consists of a solid-core Bragg fiber bundle and a monochrome CCD camera. Approximately 100 solid-core Bragg fibers that have complementary and overlapping bandgaps are chosen to compose the fiber bundle. The test light filtered by the Bragg fiber bundle is converted into a single intensity image which is then registered by the CCD camera. To reconstruct the test spectrum from the CCD image, we develop an algorithm based on pseudo-inversion of the spectrometer transmission matrix obtained from a calibration measurement. We demonstrate that the center wavelength of a spectral peak can always be reconstructed within several percent of its true value regardless of the peak width or position, and that although the widths of the individual Bragg fiber bandgaps are quite large (60−180 nm), the spectroscopic system has a resolution limit of ~30 nm. Finally, we report fabrication of Bragg fiber bundles containing hundreds of fibers using a two-step drawing technique. This method constitutes a very promising approach toward an industrial-strength fabrication of all-Bragg-fiber spectrometers.

### 10.6.1 Characteristics of the subcomponents: solid-core Bragg fiber, fiber bundle, and CCD camera

#### 10.6.1.1 Solid-core photonic bandgap Bragg fibers

The PBG Bragg fiber is a key element of our spectroscopic system. The solid-core Bragg fibers used in research are fabricated inhouse, and they have been reported previously in Dupuis et al. (2007). An individual solid-core Bragg fiber features a large 300−700-μm-diameter core made of a PMMA plastic. The core region is surrounded with a periodic multilayer reflector featuring ∼100-submicrometer-thick layers of low- and high-refractive-index PMMA/Polystyrene (PS) plastics. Note that bandgap-guidance principle of the liquid-core Bragg fiber described in Section 10.5 is also identical to those of the solid-core Bragg fiber, except that the core's refractive index (RI) of the latter is fixed. A propagation loss of a solid-core Bragg fiber within the reflector bandgap region is ∼10 dB/m, and is mostly determined by the bulk absorption loss of a low-purity PMMA plastic. Outside of the bandgap region scattering loss (on the imperfections in the multilayer structure) dominates, resulting in >60 dB/m propagation loss. In our experiments we used 30-cm-long fibers, so that the loss of guided light was below 3 dB, whereas the loss of nonguided light was >20 dB. The numerical aperture of all the Bragg fibers was in the range of 0.17−0.22.

To construct a fiber-bundle spectrometer, we chose 100 solid-core Bragg fibers with complementary and partially overlapping bandgaps, as shown in Figure 10.10(a). All the fibers in a bundle were drawn from the same preform with the only difference among them being the final diameter. The smaller diameter fibers feature bandgaps shifted toward the blue part of the spectrum. This is easy to rationalize from Eqn (10.1), which predicts that the bandgap center wavelength is proportional to the thickness of the multilayer in the Bragg reflector.

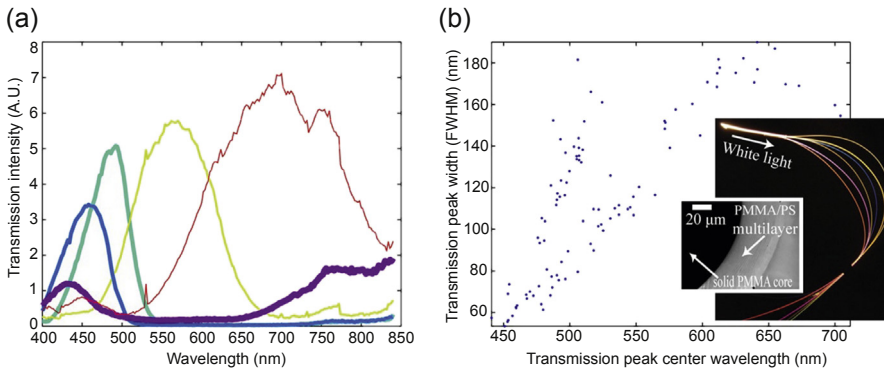


**Figure 10.10** (a) Transmission spectra of five typical Bragg fibers used in the fiber bundle. (b) Distribution of the fiber transmission bandwidth as a function of the fiber bandgap center wavelength for all of the Bragg fibers in a bundle. In the inset: photo of a Bragg fiber cross-section showing a solid-core surrounded by a periodic multilayer reflector.

Figure 10.10(b) also shows the distribution of the fiber transmission bandwidth as a function of the fiber transmission central wavelength. We note that the fiber transmission bandwidth increases with its center frequency (Skorobogatiy, 2005). Thus, in the blue part of a spectrum, the fiber bandgap width is ~60 nm, whereas it increases to ~180 nm in the red part of a spectrum. Two factors contribute to this phenomenon. First, from the basic theory of Bragg fibers (Skorobogatiy, 2005) it follows that the relative width of a PBG (ratio of the bandgap size to the bandgap center frequency) is mostly a function of the refractive index contrasts in the Bragg fiber reflector. As all the fibers used in this project are fabricated from the same preform, it means that the relative bandwidth is approximately constant for all the fibers; hence, the absolute bandgap width should increase with the bandgap center frequency. Second, as we have mentioned in the previous paragraph, fibers featuring bandgaps at longer wavelengths have larger core sizes. In Bragg fibers, modal losses due to radiation and scattering on the reflector imperfections scale as $1/R^3$ with the core size (Johnson et al., 2001; Skorobogatiy, 2005). Therefore, larger core fibers exhibit smaller loss than smaller core fibers. Note that in Figure 10.10, we show the transmission intensities and not the actual losses. Clearly, for the fibers of the same length, smaller core fibers will exhibit spectrally narrower transmission, as wavelengths near the bandgap edge will be attenuated much more strongly than those in the larger core fibers.

### *10.6.1.2 Photonic bandgap Bragg fiber bundle*

The fiber bundle used in our experiments features a 5.6-mm-inner diameter plastic tube that hosted ~100 pieces of 30-cm-long Bragg fibers. The fibers at the input end of a bundle are rigidly attached with epoxy to each other and to the confining tube, and the whole assembly is then polished using optical films of various granularity. On the other end of a bundle, 100 fibers are inserted into a custom-made block featuring holes of diameter 0.8 mm placed in a periodic $10 \times 10$ square array (see Figure 10.11). The block, the tube, and all the fibers are bonded together with epoxy, and the output end is then polished.

The principle of operation of a Bragg fiber-bundle spectrometer can be clearly understood from Figures 10.10 and 10.11. In principle, if all of the fiber bandgaps were spectrally narrow and nonoverlapping, then, at the end of a fiber bundle, the relative intensities of light coming out of the individual fibers would be unambiguously related to the corresponding spectral components of the incoming light. In practice, individual fiber bandgaps are always overlapping, and in our particular implementation, the bandgaps are quite broad. Therefore, to reconstruct the intensity of an incoming light from the intensities of light coming out of the individual fibers, we have to use a deconvolution algorithm.

Another important comment is about the intensity throughput of our spectrometer and its relation to the spectrometer resolution. First of all, if all of the fibers used in the spectrometer were to have strictly complementary and spectrally nonoverlapping bandgaps of width $\delta\lambda$, then, to enable a certain spectrometer

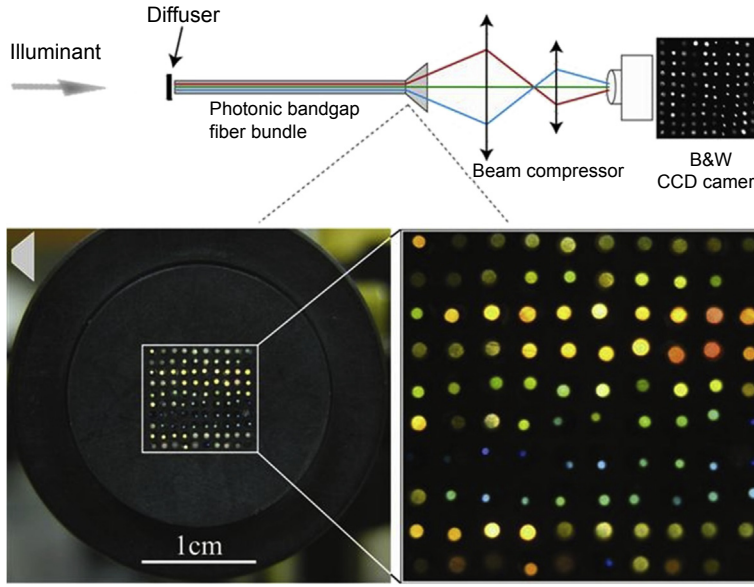


**Figure 10.11** Fiber-bundle spectrometer. Top part: schematic of the spectrometer. Light from the illuminant is launched into the fiber bundle; the image is taken by the monochrome CCD. Lower part: when the broadband light is launched into the fiber bundle, the output is a mosaic of colors selected by the individual Bragg fibers.

range $\Delta\lambda = (\lambda_{max} - \lambda_{min})$, one would need to use $N = \Delta\lambda/\delta\lambda$ fibers. Assuming a broadband light with a unit integral power in the spectral range $\Delta\lambda$, we conclude that the intensity throughput through such a spectrometer would be $\sim 1/N^2$. Indeed, the light beam first has to be physically divided into $N$ parts to be launched into the individual fibers of a bundle; then, an individual fiber would cut out a spectrally narrow ($\sim 1/N$) part of the broadband light.

It is important to realize that our implementation uses $N$ Bragg fibers with relatively large and strongly overlapping bandgaps of spectral width $\delta\lambda >> \Delta\lambda/N$. Spectral resolution of such a spectrometer can be still as small as $\Delta\lambda/N$, while the intensity throughput would be much higher and proportional to $1/N$, rather than $1/N^2$. Such intensity throughput is comparable to the throughput of a grating-based spectrometer with resolution of $\Delta\lambda/N$. Indeed, as we will see in what follows, because of the use of a pseudo-inversion algorithm, the resolution of a fiber-based spectrometer is fundamentally limited only by the number of the spectroscopic elements, such as individual Bragg fibers, regardless of whether they feature overlapping or strictly complementary bandgaps. On the other hand, the throughput of an individual Bragg fiber with a relatively wide bandgap is $\delta\lambda/\Delta\lambda >> 1/N$. The overall $1/N$ scaling of the throughput intensity, therefore, mostly comes from the necessity of subdivision of a test beam into $N$ individual fibers, each of which individually transmits as much as 30−50% of the in-coupled

intensity. In practice, achieving $\Delta\lambda/N$ resolution with $N$ fibers featuring overlapping bandgaps is somewhat challenging, as a pseudo-inverse algorithm used in the spectrum reconstruction is sensitive to the experimental errors.

#### 10.6.1.3 Sensitivity and linear response of the CCD camera

The output of the fiber bundle is a $10 \times 10$ matrix of colored fibers, which is then projected with a beam compressor onto a monochrome CCD array (see Figure 10.11). The sensitivity of a CCD sensor would directly affect the measuring range, the signal-to-noise ratio, and the algorithm that we use to reconstruct the spectrum of an illuminant. The CCD sensor in our experiment is an Opteon Depict 1, E and S Series B1A $652 \times 494$ black and white CCD. The normalized sensitivity for different wavelengths is displayed in Figure 10.12(a), from which it is clear that the sensor covers well all the visible and a part of the near-infrared spectral range. The sensitivity curve, however, is a highly variable function of wavelength, which must be taken into account in the reconstruction algorithm. Figure 10.12(a) was obtained by launching the light form a supercontinuum source into a monochromator the output of which would produce a 2-nm-wide full width at half maximum (FWHM) peak at a desired center wavelength. Light from such a tunable source would then be launched into a commercial multimode fiber of $\sim$1 mm diameter. The output power from such a fiber would then be measured by both the CCD array and a calibrated powermeter; the sensitivity curve is then achieved by dividing one by the other.

As seen in Section 10.6.2.1, one of the key requirements of a CCD array is linearity of its monochromatic response as a function of the intensity of incident light. The near-linear response of a CCD sensor was confirmed at several wavelengths of interest; a typical CCD response (at $\lambda = 560$ nm) is presented in Figure 10.12(b). To obtain Figure 10.12(b), two polarizers were placed between a CCD array and the output of a commercial fiber in a setup described in the previous paragraph. By varying the angle between the two polarizers, we also varied the intensity of light coming onto a CCD array. A reference measurement is performed with a calibrated powermeter for the

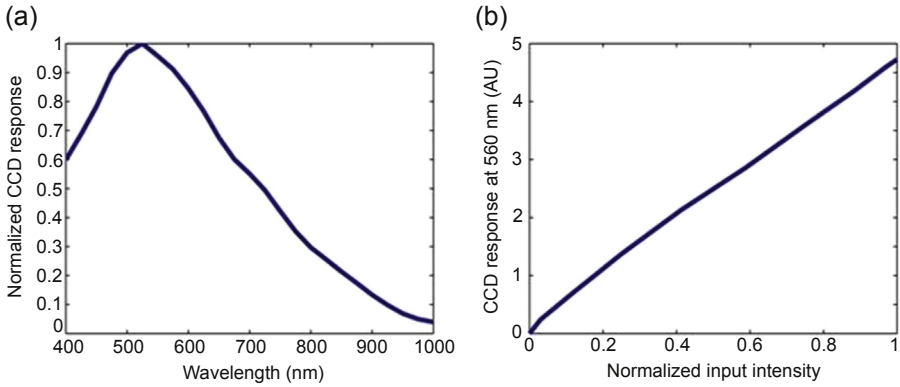


**Figure 10.12** (a) Normalized spectral response of a CCD array. (b) A typical monochromatic near-linear response of a CCD array (at $\lambda = 560$ nm).

same angles between polarizers; the results are compared to establish a near-linear sensor response.

### 10.6.2 Calibration of the fiber-bundle spectrometer and spectrum reconstruction algorithm

In its operation mode, the fiber-bundle spectrometer is illuminated with a test light, which is then spectrally and spatially decomposed by the fiber bundle (see Figure 10.13). The test spectra used in our experiments were either broadband (halogen lamp source), or narrowband (tunable monochromator source). The image of the fiber-bundle output end was then projected onto a monochrome CCD array using a 2:1 beam compressor. Note that a CCD array does not have to be a two-dimensional camera; instead, one can use an economical linear array with the number of pixels matching the number of Bragg fibers in a bundle. The output of each fiber carries information about the intensity of a certain fraction of an illuminant spectrum as filtered by the individual Bragg fibers. It is reasonable to assume, then, that if the Bragg fibers of a bundle feature complementary, while possibly overlapping, bandgaps that together cover the spectral range of interest, then the spectrum of an illuminant could be reconstructed.

#### 10.6.2.1 Transmission matrix method

To interpret a monochrome CCD image, we use a so-called luminance-adaptation model of the fiber spectrometer. In particular, for a fixed exposure time of a CCD array, total intensity $C_n$ registered by an assigned region of a CCD sensor from the output of the $n$th fiber can be presented as

$$C_n = \int_{\lambda_{\min}}^{\lambda_{\max}} I(\lambda) A_n F_n(\lambda) S(\lambda) O_n(\lambda) \mathrm{d}\lambda, \tag{10.3}$$

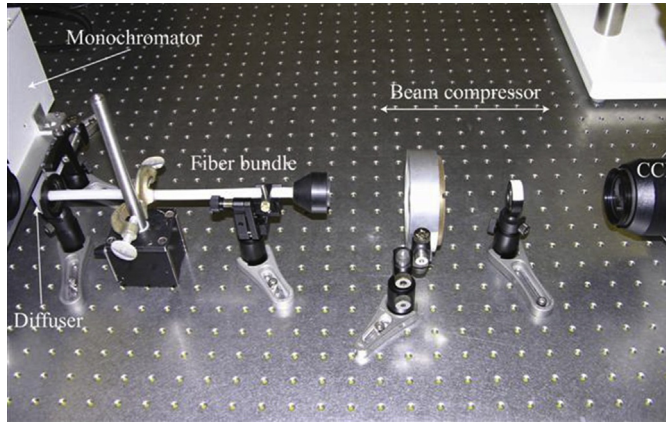


**Figure 10.13** Setup for the spectrometer calibration measurement.

in which $I(\lambda)$ is the illuminant spectral flux density at the fiber-bundle input end, $A_n$ is the area of the $n$th fiber input cross-section, $F_n(\lambda)$ is the transmission function of the $n$th fiber, $S(\lambda)$ is the spectral sensitivity of the CCD array, $O_n(\lambda)$ is a fiber position-dependent transmission function of various optics (diffuser, beam compressor, and a CCD objective), and $\lambda_{\min}$ and $\lambda_{\max}$ define the spectral range of operation. Measuring such transmission functions individually is a daunting task. Instead, we use a calibration procedure that measures a compounded transmission function of our spectrometer, defined as $T_n(\lambda) = A_n F_n(\lambda) S(\lambda) O_n(\lambda)$. Experimentally, the test spectrum can be divided into $N$ equidistant spectral "bins" with the size of each bin to be $\Delta\lambda = (\lambda_{\max} - \lambda_{\min})/N$. Correspondingly, the transmission function $T_n$ for the $n$th Bragg fiber can be discretized into a vector with $N$ elements. The model in Eqn (10.3) could then be rewritten as

$$C_n = \int_{\lambda_{\min}}^{\lambda_{\max}} I(\lambda) T_n(\lambda) \mathrm{d}\lambda = \sum_{i=0}^{N=(\lambda_{\max}-\lambda_{\min})/\Delta\lambda} T_n^i(\lambda_i) \int_{\lambda_i=\lambda_{\min}+i\lambda}^{\lambda_i+\Delta\lambda} I_i(\lambda) \mathrm{d}\lambda = \sum_{i=0}^{N} I_i \cdot T_n^i \tag{10.4}$$

When we take all the Bragg fibers in the bundle into account, Eqn (10.4) presented in the matrix form becomes

$$\begin{bmatrix} C_1 \\ C_2 \\ \cdot\cdot \\ \cdot\cdot \\ C_{100} \end{bmatrix} = \begin{bmatrix} T_{1,1} & T_{1,2} & \cdots & T_{1,N} \\ T_{2,1} & T_{2,2} & \cdots & T_{2,N} \\ \cdot\cdot & & & \\ \cdot\cdot & & & \\ T_{100,1} & T_{100,2} & \cdots & T_{100,N} \end{bmatrix} \begin{bmatrix} I_1 \\ I_2 \\ \cdot\cdot \\ \cdot\cdot \\ I_N \end{bmatrix} \tag{10.5}$$

in which vector $(C)_{100\times1}$ represents the intensities of light coming out of the individual fibers as measured by the CCD sensor, $(T)_{100\times N}$ is a spectrometer transmission matrix, and $(I)_{N\times1}$ is a discretized spectrum of the illuminant. From Eqn (10.5), it follows that a discretized spectrum of the illuminant can be reconstructed from the corresponding CCD image ($C$ vector) by inverting the transmission matrix of a spectrometer.

### 10.6.2.2 Calibration measurement, building a transmission matrix

To construct transmission matrix experimentally, we note that, if the illuminant spectrum is monochromatic ($I_i = 0, \ \forall i \neq i_\lambda$ in Eqn (10.5)), then the measured $C^{i_\lambda}$ vector is proportional to the $i_\lambda$ column of the transmission matrix:

$$C^{i_\lambda}_{(100\times1)} = T^{i_\lambda}_{(100\times1)} \cdot I_{i_\lambda} \tag{10.6}$$

Experimentally, we use a tunable monochromator-based narrowband (2 nm FWHM) source to generate "monochromatic" spectra (see Figure 10.13). In particular, we vary the source center wavelength in 2 nm increments, thus effectively subdividing the 400−840 nm spectral interval under consideration into $N = 221$ equivalent 2-nm-wide bins. For every new position of the source center wavelength, we acquire a $C$ vector using a CCD array and consider it as the next column of the spectrometer transmission matrix. Finally, to finish the calibration we measure the wavelength-dependent intensities $I_i$ of a tunable source by placing a calibrated powermeter directly at the output of a monochromator. By dividing every $C$ vector by the corresponding $I_i$ value, the transmission matrix is constructed.

In our experiments, an halogen lamp source was used with a Newport Oriel 1/8 m monochromator to build a narrowband tunable source of 2 nm FWHM (see Figure 10.13). The light beam from the source was then directed onto a diffuser placed right before the fiber bundle to guarantee a uniform illumination of its input end. At the output end of a fiber bundle, a 2:1 beam compressor was used to image the fiber-bundle output facet onto the 8-bit monochrome CCD sensor array. Individual images were then interpreted using a singular value decomposition (SVD) pseudo-inversion algorithm to construct the corresponding $C$ vectors. The wavelength-dependent intensity of a tunable source was measured using a calibrated Newport 841-PE powermeter.

### 10.6.2.3 Spectral reconstruction algorithm

As noted in Section 10.6.2.1, a discretized spectrum of the illuminant can be reconstructed from the corresponding CCD image ($C$ vector) by inverting the transmission matrix of a spectrometer in Eqn (10.5). However, the immediate problem that one encounters when trying to invert the transmission matrix is that the matrix is nonsquare. Even if the number of spectral bins is chosen to match the number of fibers in the bundle, thus resulting in a square transmission matrix, one finds that such a matrix is ill conditioned. One, therefore, has to resort to an approximate inverse of a transmission matrix. To find a pseudo inverse of a transmission matrix in Eqn (10.5), we employ an SVD algorithm. Particularly, from the linear algebra, we know that any $(100 \times N)$ matrix (suppose that $N > 100$) can be presented in the form

$$\begin{aligned} &(T)_{100\times N} = (U)_{100\times 100}\ (S)_{100\times N}\ \left(V^T\right)_{N\times N} \\ &U^T U = 1;\ \ V^T V = 1;\ \ S = diag(\sigma_1, \sigma_2, \sigma_3, \cdots \sigma_{100}) \\ &\sigma_1 > \sigma_2 > \sigma_3 > \cdots > \sigma_{100} > 0 \end{aligned} \tag{10.7}$$

in which matrixes $U$ and $V$ are unitary, and matrix $S$ is a diagonal matrix of the real positive singular values. For the ill-conditioned matrices, most of the singular values are small and can be taken as zero. By limiting the number of nonzero singular values to $N_\sigma$, Eqn (10.7) can be rewritten as

$$(T)_{100\times N} = (U)_{100\times N_\sigma}\ (S)_{N_\sigma\times N_\sigma}\ \left(V^T\right)_{N_\sigma\times N} \qquad \sigma_1, \sigma_2, \cdots, \sigma_{N_\sigma} \neq 0 \tag{10.8}$$

and a corresponding pseudo inverse of the transmission matrix is then found as

$$(T)^{-1}_{N\times 100} = (V)_{N\times N_\sigma}\ (S)^{-1}_{N_\sigma\times N_\sigma}\ \left(U^T\right)_{N_\sigma\times 100} \tag{10.9}$$

### 10.6.3 Spectral reconstruction experiments

To test our fiber-bundle spectrometer, we perform reconstruction of several test spectra. In one set of experiments, the test spectra is a set of the 25-nm-wide peaks centered at 450, 500, 550, 600, and 700 nm. Such peaks were created using the same monochromator-based tunable source as used for the spectrometer calibration; however, it was adjusted to have a 25 nm bandwidth in the outgoing light. In the second set of experiments, we measure the spectra of four 40-nm-wide bell-shaped curves centered at 450, 500, 550, and 600 nm created using four commercial bandpass filters. In Figure 10.14, we demonstrate, with dashed curves, the test spectra of light beams at the input of a fiber bundle (as resolved by another Oriel monochromator), whereas, with solid curves, we show the corresponding reconstructed spectra using the transmission matrix inversion algorithm. In the figures, we also indicate the optimal number of nonzero singular values used in the matrix inversion procedure (Eqn (10.9)). The choice of the number of nonzero singular values used in the spectrum reconstruction algorithm strongly affects the quality of the reconstructed spectrum. Note, in particular, that although the spectral intensity function should be strictly nonnegative, the reconstructed spectral intensity can take negative values. Therefore, spectrum reconstruction error can be defined as the ratio of the most negative value in the reconstructed spectral intensity to its most positive value:

$$\text{Error}(N_\sigma) = -\min_\lambda\left(I^{\text{reconstr.}}_{N_\sigma}\right) \Big/ \max_\lambda\left(I^{\text{reconstr.}}_{N_\sigma}\right), \tag{10.10}$$

and the optimal $N_\sigma$ to be used in Eqn (10.9) is the one that minimizes the error in Eqn (10.10).

From Figure 10.14 we conclude that the test peak position (the value of the peak center wavelength) can be reconstructed within several percent of its true value in the whole spectral range covered by the spectrometer. Moreover, we note that, although the widths of the individual Bragg fiber bandgaps are quite large (>60 nm), the fiber bundle-based spectroscopic system can resolve peaks of much smaller spectral width. Indeed, in Figure 10.14(a), the widths of the reconstructed spectra are in the 30−50 nm range, with the exception of a peak centered at 600 nm. We mention in passing that we have also conducted measurements using 5, 10, 15, and 20 nm wide peaks. In all of the experiments, we saw that the center wavelength of even the narrowest peak can be reconstructed with high precision; however,

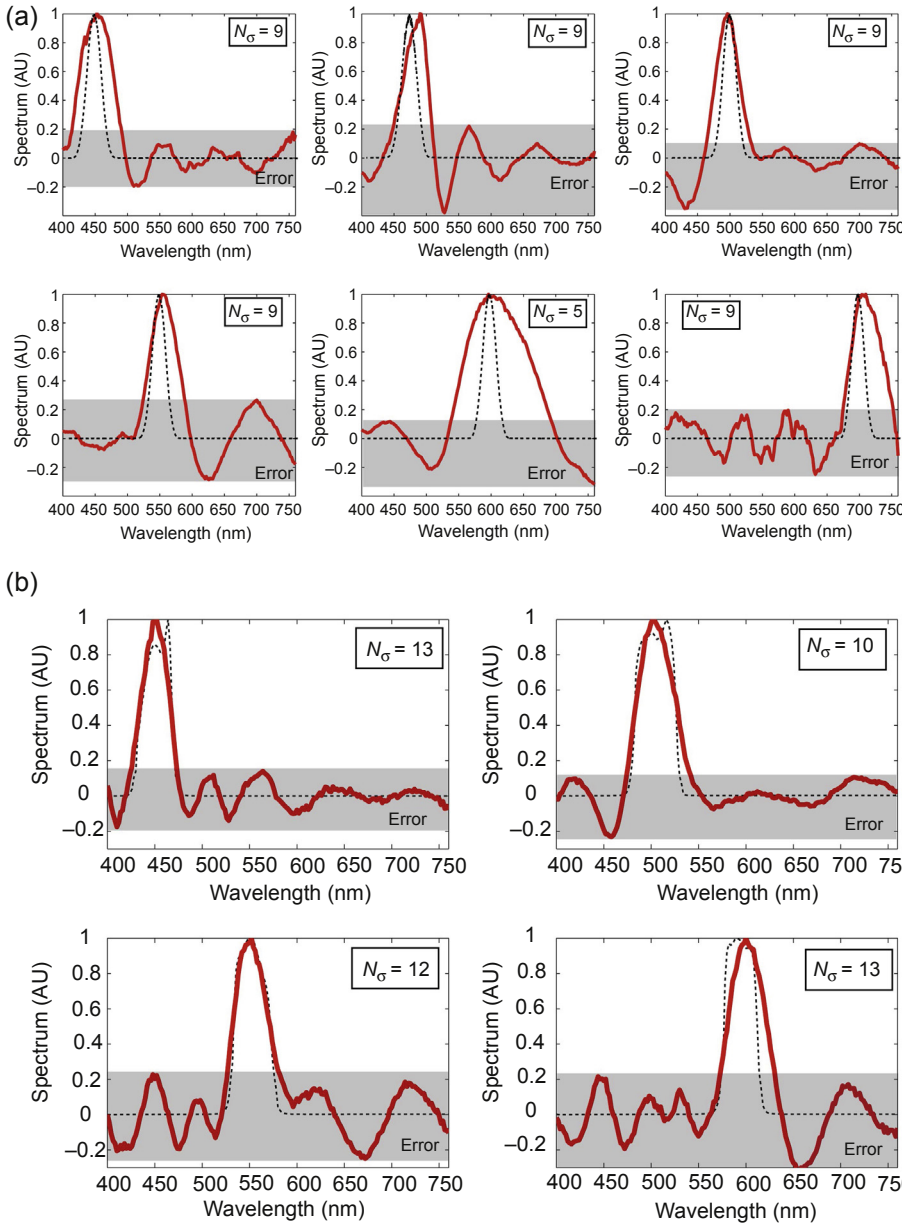


**Figure 10.14** Spectra reconstruction using PBGF bundle-based spectrometer. The top part (a) shows the reconstructed spectra of six 25 nm wide peaks; the bottom part (b) shows the reconstructed spectra of four 40 nm wide bell-shaped spectra. The black dashed lines are the test spectra resolved by another monochromator; the red thick lines are the spectra reconstructed by the fiber-bundle spectrometer. The gray area indicates error level.

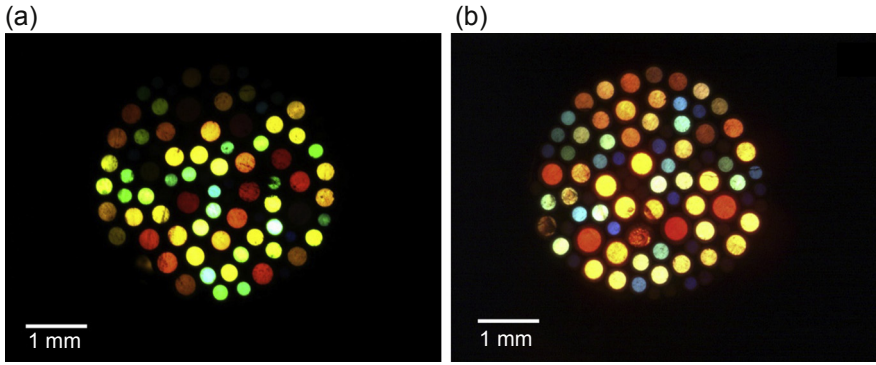


**Figure 10.15** Cross-sections of the PBG fiber bundles fabricated using the two-stage drawing technique. The bundle is illuminated with a broadband halogen lamp. At the output of fiber bundle, a mosaic of colors is visible as the white light is filtered by each fiber inside the bundle.

the reconstructed peak width always stayed around 30 nm. Finally, 40 nm wide test peaks could be well reconstructed in terms of their spectral position and width (see Figure 10.14(b)).

### *10.6.4 Novel technique for drawing PBG fiber bundles*

Finally, we report a two-stage drawing technique for the direct fabrication of the Bragg fiber bundles. This technique constitutes an industrial-strength alternative to the manual bundling of the individual fibers, as presented in Section 10.6.1. The proposed technique comprises two stages. First, we produce a Bragg fiber preform by a co-rolling technique (Gao et al., 2006) and draw it into intermediate preforms with relatively large and variable diameters (1−1.5 mm). Second, we bundle these intermediate preforms, place them into a thin supercladding tube, and, finally, draw this structure into a PBG fiber bundle. Cross-sections of the Bragg fiber bundles are presented in Figure 10.15. Each Bragg fiber bundle is illuminated by light from a broadband source (halogen lamp), and the light is then split by the individual fibers into the respective spectral components, as seen in Figure 10.15. We are currently working on the perfection of the two-stage drawing technique to draw Bragg fiber bundles with reduced outer diameters that eventually enables a fiber bundle to be directly spliced with a single hollow-core Bragg fiber.

## 10.7 Hollow-core Bragg fiber sensor interrogated with all-fiber spectrometer—an all-fiber spectroscopic system

In the two preceding sections, we have detailed a liquid-core Bragg fiber refractometer and a solid-core Bragg fiber spectrometer. In this section, we describe integration of

the two fiber devices into a complete all-fiber spectroscopic system for liquid refractometry.

### 10.7.1 Calibration measurement of the all-Bragg-fiber refractometer system

We start the integration from a calibration measurement to calculate the transmission matrix (Eqn (10.5)) of the Bragg fiber-bundle spectrometer. We first couple the beam from a supercontinuum source into a tunable monochromator (2 nm FWHM) to constitute a tunable light source. The output of the monochromator is then coupled into a 40-cm-long Bragg fiber filled with distilled water. Because the light from the monochromator-based source is relatively weak, the water-filled Bragg fiber is kept straight during the calibration measurement to reduce the propagation loss. The transmitted light from the liquid-core Bragg fiber is coupled into the Bragg fiber-bundle spectrometer using another 10× objective, and a monochrome CCD camera is used to record the intensity image of the Bragg fiber bundle. We then vary the source center wavelength in 2 nm increments, thus effectively subdividing a 560−740 nm spectral interval of interest into 91 bins with equivalent 2 nm widths. At each wavelength, the intensity of the monochromator-based source, $I_i$, is measured by a calibrated powermeter. Besides, at each wavelength, we also acquire a $C_{100\times1}$ vector using the CCD camera (see Eqn (10.5)); a $C_{100\times1}$ vector represents the intensities of light coming out of the individual fibers as measured by the CCD sensor. According to Eqn (10.5), a column of the transmission matrix $T$ can be calculated by dividing a $C_{100\times1}$ vector by the corresponding $I_i$ value. Thus, the complete $T$ matrix can be obtained by repeating the same measurement at every interested wavelength in the 560−740 nm spectral range. Once we have the complete $T$ matrix, a test spectrum (i.e., transmission spectrum of the liquid-core Bragg fiber) can be reconstructed using a pseudo inverse of the $T$ matrix according to Eqn (10.9). Finally, we remove the monochromator from the calibration setup and couple the supercontinuum beam directly into the liquid-core Bragg fiber with a 10× objective. The transmission spectra of the liquid-core Bragg fiber can then be analyzed using the Bragg fiber-bundle spectrometer.

### 10.7.2 Experimental characterization of the all-Bragg-fiber refractometer system

We use NaCl solutions with different concentrations as liquid analytes to experimentally characterize the all-Bragg-fiber refractometric system. The transmission spectra of the liquid-core Bragg fiber measured by the Bragg fiber-bundle spectrometer is shown in Figure 10.16(a). As a reference, we also measure the transmission spectrum of the liquid-core Bragg fiber by directly coupling it to a conventional grating monochromator (Figure 10.16(b)). For ease of comparison, the spectra measured both by the Bragg fiber-bundle spectrometer and by the grating monochromator are normalized to 1. Because the spectra reconstructed by the fiber-bundle spectrometer and measured by the grating monochromator are relatively wide, we therefore calculate the center

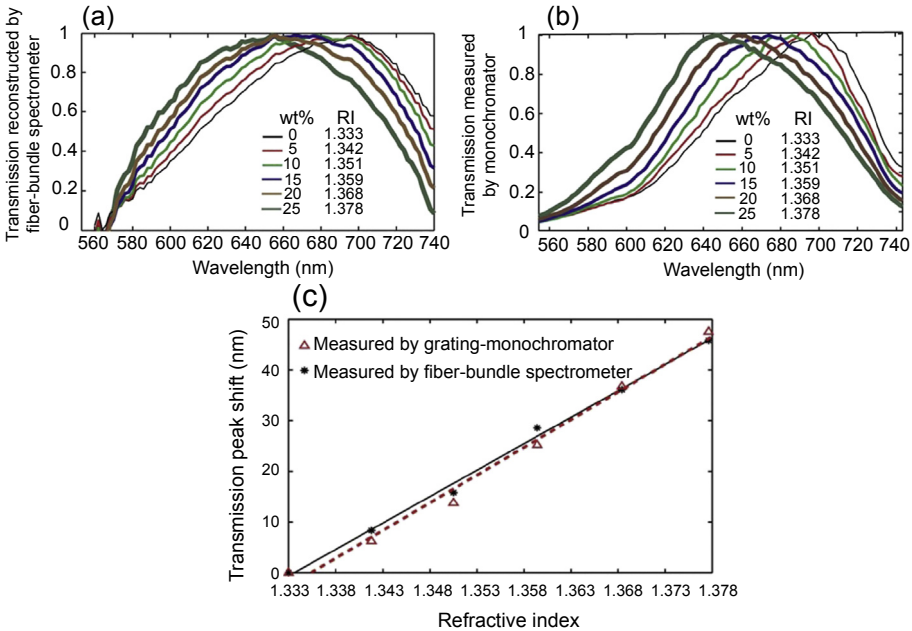


**Figure 10.16** Transmission spectra of an ~40-cm-long liquid-core Bragg fiber measured by (a) the Bragg fiber-bundle spectrometer and (b) a conventional grating monochromator. The concentrations and corresponding refractive indices of the NaCl solutions are listed as the inset. (c) Spectral shifts of the transmission peak measured by the grating monochromator (dashed red line) and by the Bragg fiber-bundle spectrometer (solid black line).

position of a transmission peak by averaging the corresponding wavelengths in which the normalized intensities are above 0.95.

In Figure 10.16(c), we compare the spectral shifts of the transmission peak measured by both the Bragg fiber-bundle spectrometer and the grating monochromator. We note that the spectral shifts of the transmission peak feature a linear dependence with respect to variations in the refractive index of the liquid core of the Bragg fiber. The experimental sensitivity of the liquid-core Bragg fiber sensor is ~1100 nm/RIU measured by the grating monochromator, and is ~1050 nm/RIU measured by the Bragg fiber spectrometer. Note that in both measurements presented in Figure 10.16, the spectral shifts (see Figure 10.16(c)) are marginally smaller than those shown in Figure 10.7. This is likely due to the fact that in the measurements (including the calibration measurements) for Figure 10.16, the liquid-core Bragg fiber is kept straight to reduce the propagation loss of the fiber. Therefore, many high-order modes, which are less sensitive to variations in the refractive index of the fiber core, can propagate through the fiber, thus resulting in smaller spectral shifts. However, in the measurements for Figures 10.6 and 10.7, signal-to-noise degradation is not a critical issue, because we use a more sensitive single-pixel detector for spectral interrogation as compared to the CCD detector used in the Bragg fiber spectrometer. Consequently,

we coil the Bragg fiber piece in a 10 cm diameter circle to strip out high-order modes, thus leading to stronger spectral shifts.

## 10.8 Examples of practical applications of the liquid-core Bragg fiber sensors

Very high sensitivity of the Bragg fiber sensors to changes in the liquid-core refractive index make such sensors desirable for a variety of practical applications that involve monitoring of the industrial liquids. Here, we demonstrate an example of using Bragg fiber refractometers to measure the refractive index and concentration of a commercial coolant solution and an industrial sawing solution. The experimental setup of the Bragg fiber sensor is the same as used in Section 10.5.1. To measure samples with unknown refractive index, we need to calibrate our Bragg fiber. We use a series of NaCl solutions with known refractive indices to characterize the spectral shifts of the Bragg fiber in response to different values of refractive index of the fiber core. In Figure 10.17(a), we present the transmission spectra of the Bragg fiber sensor filled with NaCl solutions of different concentrations. The concentrations and corresponding refractive indices are also listed in the inset of Figure 10.17(a).

In Figure 10.17(d), we present spectral shifts of the transmission peak of the Bragg fiber sensor filled with the reference NaCl solutions. From these measurements, we can then construct a calibration curve (solid blue line in Figure 10.17(d)) that, furthermore, is used to deduce the refractive index of a test sample from the spectral shift of the transmission curve. After constructing the calibration curve, we proceed to measuring the refractive index and concentration of a test coolant solution (Dynalene PG, US) and a test sawing fluid (Lenox, US). The transmission spectra of the coolants and sawing fluids with different concentrations are shown in Figure 10.17(b) and (c). One can make several interesting observations from these measurements. First, from Figure 10.17(b) we note that transmission through the coolant solution improves as the coolant concentration increases. This is in marked contrast to the case of a sawing fluid solution (see Figure 10.17(c)) that shows higher attenuations for higher concentrations of a sawing fluid. This difference in the optical responses of the two fluids is relatively easy to rationalize by noting that the coolant used in our experiments is an optically transparent liquid, whereas the sawing fluid is a semi-opaque yellowish emulsion featuring relatively strong optical absorption. First, as the concentration of a coolant increases, the refractive index of a coolant solution also increases. Consequently, the core refractive index of the liquid-filled Bragg fiber becomes closer to that of the fiber cladding. In the limit when the core refractive index becomes higher than that of the fiber cladding, no radiation losses will occur as the guidance regime will be total internal reflection rather than bandgap guiding. Therefore, it is not surprising to expect that fiber radiation loss should decrease with increasing core refractive index. As the coolant used in our experiments is optically transparent, little or no additional absorption loss occurs with increasing concentration of a coolant. Therefore, the total effect of the increase in the coolant concentration is an improvement in the Bragg

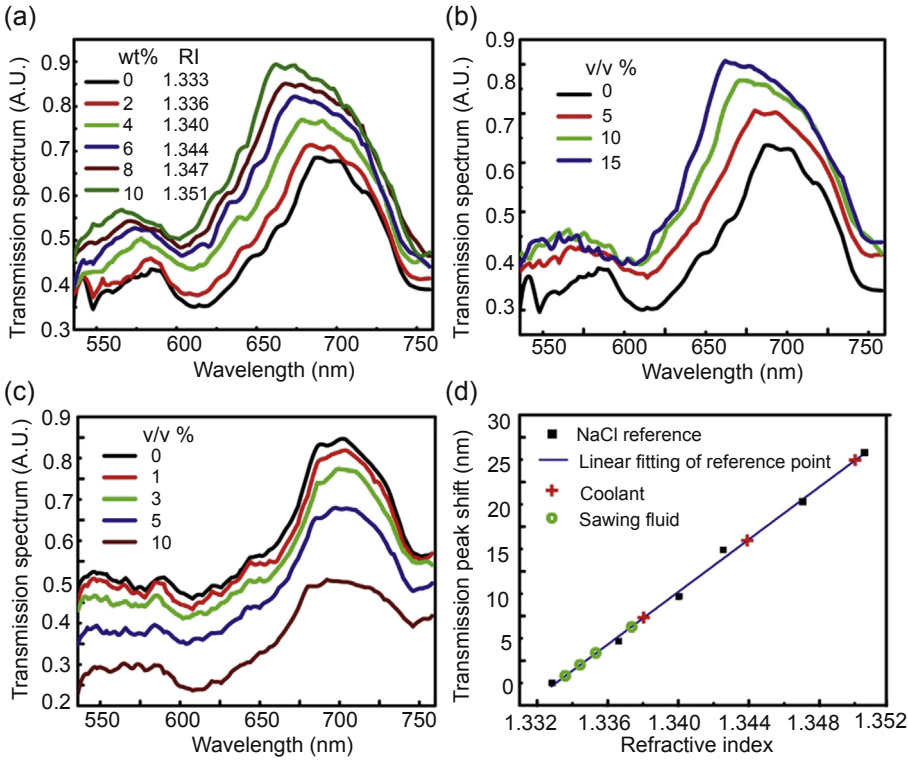


**Figure 10.17** (a) Transmission spectra of the Bragg fiber filled with the reference NaCl solutions of different concentrations. The concentration and corresponding refractive indices of the NaCl solutions are listed in the inset. (b) Transmission spectra of the Bragg fiber filled with a commercial coolant of different concentrations. (c) Transmission spectra of the Bragg fiber filled with a sewing fluid of different concentrations. In (d), we first present the spectral shift of the Bragg fiber filled with the reference NaCl solutions (black square dots), and then use the linear fitting of this spectral shift as a calibration curve to find the refractive index of a test coolant (red cross dots) and a sawing fluid (green circle dots).

fiber transmission. In contrast, as the concentration of a sawing fluid increases, the absorption loss and scattering loss of the liquid core also increase, thus strongly suppressing the transmission through the liquid-core Bragg fiber. Despite the strong absorption loss, from Figure 10.17(c) we see that the spectral features (transmission peaks) in the transmission spectra remain well pronounced even at high concentrations of the sawing fluid. Therefore, we can still use the "resonant-sensing modality" by relating the spectral shifts in the fiber transmission spectrum as a function of the analyte concentration.

Thus, using spectral shifts of the Bragg fiber transmission spectra, the refractive indices of the test fluids can be found as a function of the analyte concentration. In particular, we find the refractive index of the coolant solutions to be 1.3380, 1.3442, and 1.3492, when the volume concentrations of a coolant are 5%, 10%, and

15%, respectively. Similarly, we find the refractive index of the sawing fluid solutions to be 1.3332, 1.3342, 1.3351, 1.3375, when the volume concentrations of a sawing fluid are 1%, 3%, 5%, and 10%, respectively. Comparing these experimentally measured values of the refractive index to the calibration data provided by the coolant suppliers, we conclude that the experimental error in the determination of the coolant concentration is very small and is ~0.04%. Moreover, even in the absence of the calibration data from the supplier (RI vs analyte concentration), one can still infer the analyte concentration from the solution refractive index. This is achieved by treating a two-component solution as an effective medium, and by using one of the analytical models, such as the Bruggeman model (Niklasson, Granqvist & Hunderi, 1981), which relates refractive indices and relative concentrations of the two components to the effective refractive index of their mixture. As shown in Figure 10.18, the calculated concentrations of the coolant and the sawing fluid when using the Bruggeman model agree well with the concentrations used in the experiments. The experimental error in the determination of the coolant concentration in this case is ~0.4%.

We note that the liquid-core Bragg fiber sensors presented in this chapter could also be used for interrogation of other useful properties of the test analytes. For example, the magneto-optic properties of magnetic fluids can be monitored using our Bragg fiber sensor. A well-known effect in magnetic fluids (e.g., $Fe_3O_4$-nanoparticle fluid) is the dependence of their refractive index on the external magnetic field. A Bragg fiber filled with the $Fe_3O_4$-nanoparticle fluid can be used to precisely monitor the fluid refractive index, and, as a consequence, to monitor the strength of the local magnetic field. According to Liu et al. (2008), applying a magnetic intensity of ~1.7 kOe to a $Fe_3O_4$-based solution (weight concentration: 1.2 mg/L) results in a refractive index variation of 0.023 RIU. Thus, ferrofluid-core Bragg fiber can be used as magnetic field sensors with a sensitivity of ~20 nm/kOe, which is comparable

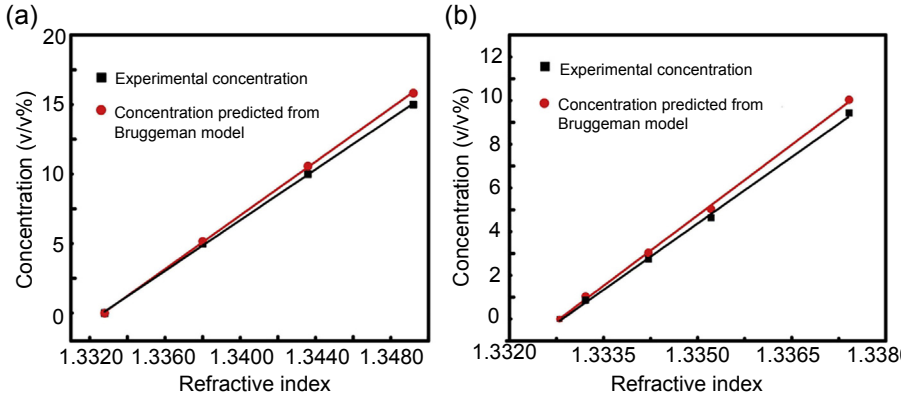


**Figure 10.18** Concentrations of (a) coolant and (b) sawing fluid in their respective solutions as a function of the solution refractive index. The refractive index of each solution is obtained from the spectral shift measurements using the calibration curve presented in Figure 10.17(d). The analyte concentration is then inferred using the Bruggeman model (●), and compared to the known experimental concentrations (■).

to the sensitivities of other magneto-optical sensors based on MOFs and fiber interferometers (Zhao, Lv, Ying & Wang, 2012). The main advantage of using our liquid-filled Bragg fibers in magnetic field sensors is the fact that the resolution of such sensors is virtually independent of the fiber length. This is important as $Fe_3O_4$-based fluid (translucent fluid) features relative high scattering loss, thus limiting sensor length to several centimeters. Besides, liquid-core Bragg fiber sensors can also be used to monitor capillary electrophoresis dynamics. Capillary electrophoresis is a technique, which is frequently used in biological research and pharmaceutical industry, in which separation of ionic species in electrolytic solutions is required. During capillary electrophoresis, analyte local refractive index and absorption become time dependent, which can be monitored optically when using Bragg fibers as capillaries. Finally, Bragg fiber sensors can simply be used as absorption-based sensors for biological and chemical detection. Compared to other absorption-based sensors that use "leaky modes" of capillaries, the Bragg fibers offer much lower propagation losses, thus enabling longer sensing lengths and, hence, higher sensitivities.

## References

Banerjee, A., Mukherjee, S., Verma, R. K., Jana, B., Khan, T. K., Chakroborty, M., et al. (2007). Fiber optic sensing of liquid refractive index. *Sensors and Actuators: B, 123*, 594−605.

Bhatia, P., & Gupta, B. D. (2011). Surface-plasmon-resonance-based fiber-optic refractive index sensor: sensitivity enhancement. *Applied Optics, 50*, 2032.

Cennamo, N., Massarotti, D., Conte, L., & Zeni, L. (2011). Low cost sensors based on SPR in a plastic optical fiber for biosensor implementation. *Sensors, 11*, 11752−11760.

Charlton, C., Temelkuran, B., Dellemann, G., & Mizaikoff, B. (2005). Mid-infrared sensors meet nanotechnology: trace gas sensing with quantum cascade lasers inside photonic band-gap hollow waveguides. *Applied Physics Letters, 86*, 194102.

Dupuis, A., Guo, N., Gauvreau, B., Hassani, A., Pone, E., Boismenu, F., et al. (2007). Guiding in the visible with 'colorful' solid-core Bragg fibers. *Optics Letters, 32*, 2882.

Fan, X. D., White, I. M., Zhu, H. Y., Suter, J. D., & Oveys, H. (2007). Overview of novel integrated optical ring resonantor bio-chemical sensors. *Proceedings of SPIE, 6452*, 1−20.

Fang, X., Liao, C. R., & Wang, D. N. (2010). Femtosecond laser fabricated fiber Bragg grating in microfiber for refractive index sensing. *Optics Letters, 35*, 1007−1009.

Gao, Y., Guo, N., Gauvreau, B., Rajabian, M., Skorobogata, O., Pone, E., et al. (2006). Consecutive solvent evaporation and co-rolling technique for polymer multilayer hollow fiber preform fabrication. *Journal of Material Research, 21*, 2246−2254.

Gao, R. X., Wu, W. J., Wang, Y. Y., Wang, Q., Zhao, F., & Qu, S. L. (2012). Design and fabrication of SMS fiber refractometer for liquid. *Sensors and Actuators: A, 179*, 5−9.

Gong, H., Chan, C. C., Zhang, Y. F., Wong, W. C., & Dong, X. (2011). Miniature refractometer based on modal interference in a hollow-core photonic crystal fiber with collapsed splicing. *Journal of Biomedical Optics, 16*, 017004.

Haynes, W. M. (2010). *CRC handbook of chemistry and physics* (91st ed.). Boca Raton, FL: CRC Press.

Hollas, J. M. (1982). *High resolution spectroscopy* (1st ed.). London: Butterworths.

Jiang, M. S., Sui, Q., Jin, Z., Zhang, F., & Jia, L. (2014). Temperature-independent optical fiber Fabry-Perot refractive index sensor based on hollow-core photonic crystal fiber. *Optik, 125*, 3295.

Johnson, S. G., Ibanescu, M., Skorobogatiy, M., Weiseberg, O., Engeness, T. D., Soljacic, M., et al. (2001). Low-loss asymptotically singlemode propagation in large core omniguide fibers. *Optics Express, 9*, 748.

Juan, K., Dong, X., Zhao, C., & Zhao, Y. (2011). A Sagnac loop sensor for refractive index measurement. In *Photonics and optoelectronics (SOPO), 2011, Symposium on* (pp. 1−4). IEEE.

Kapoor, A., & Sharma, E. K. (2009). Long period grating refractive-index sensor: optical design for single wavelength interrogation. *Applied Optics, 48*, G88.

Krohn, D. A. (1992). *Fiber optic sensors: Fundamentals and applications* (3rd ed.). North Carolina, USA: Instrument Society of America.

Lakhtakia, A., & Mohammod, Z. (2010). Optical guided-wave chemical and biosensors II. In *Springer series on chemical sensors and biosensors* (Vol. 8). Berlin Heidelberg: Springer-Verlag.

Lane, S., Chan, J., Thiessen, T., & Meldrum, A. (2014). Whispering gallery mode structure and refractometric sensitivity of fluorescent capillary-type sensors. *Sensors and Actuators B, 190*, 752.

Liang, W., Huang, Y., Xu, Y., Lee, R. K., & Yariv, A. (2005). Highly sensitive fiber Bragg grating refractive index sensors. *Applied Physics Letters, 86*, 151122.

Lienert, B., Porter, J., & Sharma, S. K. (2009). Simultaneous measurement of spectra at multiple ranges using a single spectrometer. *Applied Optics, 48*, 4762−4766.

Lin, Y. (2013). Characteritics of optical fiber refractive index sensor based on surface plasmon resonance. *Microwave and Optical Technology Letters, 55*, 574.

Ling, T., & Guo, L. (2007). A unique resonance mode observed in a prism-coupled micro-tube resonator sensor with superior index sensitivity. *Optics Express, 15*, 17424.

Liu, T., Chen, X., Di, Z., Zhang, J., Li, X., & Chen, J. (2008). Measurement of the magnetic field-dependent refractive index of magnetic fluids in bulk. *Chinese Optics Letters, 6*, 195.

Liu, B., Jang, Y., Zhu, X., Tang, X., & Shi, Y. (2013). Hollow fiber surface plasmon resonance sensor for the detection of liquid with high refractive index. *Optics Express, 21*, 32349.

Liu, Y., Peng, W., Zhang, X., & Qian, S. (2014). Optical fiber sensor based on capillary wall for highly-sensitive refractive index measurement. *Optics Communications, 319*, 106.

Luo, Y., Chen, X., Xu, M., Chen, Z., & Fan, X. (2014). Optofluidic glucose detection by capillary-based ring resonators. *Optics and Laser Technology, 56*, 12−14.

Ma, C., Scott, B., Pickrell, G., & Wang, A. (2010). Porous capillary tubing waveguide for multigas sensing. *Optics Letters, 35*(3), 315−317.

Manchee, C. P. K., Zamora, V., Silverstone, J. W., Veinot, J. G. C., & Meldrum, A. (2011). Refractometric sensing with fluorescent-core microcapillaries. *Optics Express, 19*, 21540.

Meade, R. D., Rappe, A. M., Brommer, K. D., & Joannopoulos, J. D. (1993). Accurate theoretical analysis of photonic band-gap materials. *Physics Review B, 48*, 8434.

Miluski, P., & Dorosz, D. (2006). Measurement of refractive index using capillary waveguide. In *Photonics applications in astronomy, communications, industry, and high-energy physics experiments 2006*. International Society for Optics and Photonics.

Mukherjee, A., Munsi, D., Saxena, V., Rajput, R., Tewari, P., Singh, V., et al. (2010). Characterization of a fiber optic liquid refractive index sensor. *Sensors and Actuators: B, 145*, 265−271.

Niklasson, G. A., Granqvist, C. G., & Hunderi, O. (1981). Effective medium models for the optical properties of inhomogeneous materials. *Applied Optics, 20*(1), 26−30.

Peng, W., Liu, Y., Zhang, X., Cheng, F., & Han, M. (2014). High sensitivity evanescent field refractometer based on modal interference in micro-capillary wall. *IEEE Sensors Journal, 14*, 430.

Qu, H., & Skorobogatiy, M. (2011). Liquid-core low-refractive-index-contrast Bragg fiber sensor. *Applied Physics Letters, 98*, 201114.

Rindorf, L., Hoiby, P. E., Jensen, J. B., Pedersen, L. H., Bang, O., & Geschke, O. (2006). Towards biochips using microstructured optical fiber sensors. *Analytical and Bioanalytical Chemistry, 385*, 1370−1375.

Roland, K. J., Francois, A., Hoffmann, P., & Monro, T. M. (2013). Fluorescent polymer coated capillaries as optofluidic refractometric sensors. *Optics Express, 21*, 11492.

Rowland, K. J., Afshar, S., Stolyarov, A., Fink, Y., & Monro, T. M. (2012). Bragg waveguides with low-index liquid cores. *Optics Express, 20*, 48.

Schroeder, K., Ecke, W., Mueller, R., Willsch, R., & Andreev, A. (2001). A fibre Bragg grating refractometer. *Measurement Science and Technology, 12*, 757−764.

Sheeba, M., Rajesh, M., Vallabhan, C. P. G., Nampoori, V. P. N., & Radhakrishnan, P. (2005). Fibre optic sensor for the detection of adulterant traces in coconut oil. *Measurement Science and Technology, 16*, 2247−2250.

Silverstone, J. W., McFarlane, S., Manchee, C. P. K., & Meldrum, A. (2012). Ultimate resolution for refractometric sensing with whispering gallery mode microcavities. *Optics Express, 20*, 8284.

Skorobogatiy, M. (2005). Efficient anti-guiding of TE and TM polarizations in low index core waveguides without the need of omnidirectional reflector. *Optics Letters, 30*, 2991.

Skorobogatiy, M. (2009). Microstructured and photonic bandgap fibers for applications in the resonant bio- and chemical sensors. *Journal of Sensors, 2009*, 524237.

Skorobogatiy, M. (2010). Resonant bio- chemical sensors based on photonic bandgap waveguides and fibers. In A. Lakhtakia, & Z. Mohammod (Eds.), *Springer series on chemical sensors and biosensors: Vol. 8. Optical guided-wave chemical and biosensors II* (pp. 43−72). Berlin Heidelberg: Springer-Verlag.

Sullivan, J. M., Twardowski, M. S., Zaneveld, J. R. V., Moore, C. M., Barnard, A. H., Donaghay, P. L., et al. (2006). Hyperspectral temperature and salt dependence of absorption by water and heavy water in the 400−750 nm spectral range. *Applied Optics, 45*.

Sumetsky, M., Windeler, R. S., Dulashko, Y., & Fan, X. (2007). Optical liquid ring resonator sensor. *Optics Express, 15*, 14376.

Sun, J., & Chan, C. C. (2007). Photonic bandgap fiber for refractive index measurement. *Sensors and Acutuators: B, 128*, 46−50.

Thorne, A. P. (1974). *Spetrophysics*. New York: Halsted Press (a Division of John Wiley & Sons, Inc.).

Udd, E., & Spillman, W. B., Jr. (2011). *Fiber optic sensors: An introduction for engineers and scientist* (2nd ed.). Hoboken, New Jersey: John Wiley & Sons Inc.

Villiatoro, J., Monzoon-Hernadex, D., & Talavera, D. (2004). High resolution refractive index sensing with cladded multimode tapered optical fiber. *Electronic Letters, 40*, 106−107.

Wang, Y., Wang, D. N., Liao, C. R., Hu, T., Guo, J., & Wei, H. (2013). Temperature-insensitive refractive index sensing by use of micro Fabry-Perot cavity based on simplified hollow-core photonic crystal fiber. *Optics Letters, 38*, 269.

White, I. M., Oveys, H., & Fan, X. (2006). Liquid-core optical ring-resonator sensors. *Optics Letters, 31*, 1319.

White, I. M., Oveys, H., Fan, X., Smith, T. L., & Zhang, J. (2006). Integrated multiplexed biosensors based on liquid core optical ring resonators and antiresonant reflecting optical waveguides. *Applied Physics Letters, 89*, 191106.

White, I. M., Zhu, H., Suter, J. D., Hanumegowda, N. M., Oveys, H., Zourob, M., et al. (2007). Refractometric sensors for lab-on-a-chip based on optical ring resonators. *IEEE Sensors Journal, 7*, 28.

Wu, Q., Semenova, Y., Yan, B., Ma, Y., Wang, P., Yu, C., et al. (2011). Fiber refractometer based on a fiber Bragg grating and single-mode-multimode- single-mode fiber structure. *Optics Letters, 36*, 2197−2199.

Xuan, H. F., Jin, W., Ju, J., Ho, H. L., Zhang, M., & Liao, Y. B. (2007). Low-contrast photonic bandgap fibers and their potential applications in liquid-base sensors. In *3rd European workshop on optical fiber sensors, Proc. SPIE* (Vol. 6619, p. 661936).

Yang, J., Yang, L., Xu, C.-Q., Xu, C., Huang, W., & Li, Y. (2006). Long-period grating refractive index sensor with a modified cladding structure for large operational range and high sensitivity. *Applied Optics, 45*, 6142.

Zamora, V., Diez, A., Andres, M. V., & Gimeno, B. (2007). Refractometric sensor based on whispering gallery modes of thin capillaries. *Optics Express, 15*, 12011.

Zhao, Y., Lv, R., Ying, Y., & Wang, Q. (2012). Hollow-core photonic crystal fiber Fabry-Perot sensor for magnetic field measurement based on magnetic fluid. *Optics & Laser Technology, 44*, 899−902.

This page intentionally left blank

# Index

*Note:* Page numbers followed by "f" and "t" indicate, figures and tables respectively.